LEABHARLANN CHOLÁISTE NA TRÍONÓIDE, BAILE ÁTHA CLIATH | TRINITY COLLEGE LIBRARY DUBLIN
Ollscoil Átha Cliath | The University of Dublin

**Terms and Conditions of Use of Digitised Theses from Trinity College Library Dublin**

**Copyright statement**

All material supplied by Trinity College Library is protected by copyright (under the Copyright and Related Rights Act, 2000 as amended) and other relevant Intellectual Property Rights. By accessing and using a Digitised Thesis from Trinity College Library you acknowledge that all Intellectual Property Rights in any Works supplied are the sole and exclusive property of the copyright and/or other IPR holder. Specific copyright holders may not be explicitly identified. Use of materials from other sources within a thesis should not be construed as a claim over them.

A non-exclusive, non-transferable licence is hereby granted to those using or reproducing, in whole or in part, the material for valid purposes, providing the copyright owners are acknowledged using the normal conventions. Where specific permission to use material is required, this is identified and such permission must be sought from the copyright holder or agency cited.

**Liability statement**

By using a Digitised Thesis, I accept that Trinity College Dublin bears no legal responsibility for the accuracy, legality or comprehensiveness of materials contained within the thesis, and that Trinity College Dublin accepts no liability for indirect, consequential, or incidental, damages or losses arising from use of the thesis for whatever reason. Information located in a thesis may be subject to specific use constraints, details of which may not be explicitly described. It is the responsibility of potential and actual users to be aware of such constraints and to abide by them. By making use of material from a digitised thesis, you accept these copyright and disclaimer provisions. Where it is brought to the attention of Trinity College Library that there may be a breach of copyright or other restraint, it is the policy to withdraw or take down access to a thesis while the issue is being resolved.

**Access Agreement**

By using a Digitised Thesis from Trinity College Library you are bound by the following Terms & Conditions. Please read them carefully.

I have read and I understand the following statement: All material supplied via a Digitised Thesis from Trinity College Library is protected by copyright and other intellectual property rights, and duplication or sale of all or part of any of a thesis is not permitted, except that material may be duplicated by you for your research use or for educational purposes in electronic or print form providing the copyright owners are acknowledged using the normal conventions. You must obtain permission for any other use. Electronic or print copies may not be offered, whether for sale or otherwise to anyone. This copy has been supplied on the understanding that it is copyright material and that no quotation from the thesis may be published without proper acknowledgement.

# PROCESSES OF MAGMATIC DIFFERENTIATION WITHIN THE SOUTHERN BRITISH AND IRISH PALAEOGENE IGNEOUS PROVINCE

Ph.D. Thesis

2009

Fiona C. Meade

TRINITY COLLEGE
10 AUG 2009
LIBRARY DUBLIN
THESIS
8813

# DECLARATION

I hereby declare that this thesis:

a) has not been submitted as an exercise for a degree at this or any other university,

and

b) it is entirely the work of the author, except where otherwise stated.

I agree that the Library may lend or copy the thesis upon request. This permission covers only single copies made for study purposes, subject to normal conditions of acknowledgement.

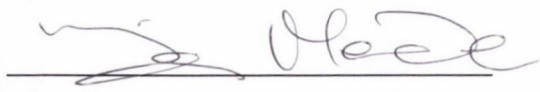

Fiona C. Meade
Sept. 2008

# SUMMARY

This thesis presents a geochemical study of magma - crust interaction within the volcanic centres of the southern British and Irish Palaeogene Igneous Province. Three centres occur in northeast Ireland; the Carlingford Igneous Centre, Co. Louth, the Slieve Gullion Igneous Centre, Co. Armagh and the Mourne Intrusive Centre, Co. Down; while the fourth, the Drumadoon Intrusive Complex, is on the Isle of Arran, south-west Scotland.

Major and trace elements, and Sr, Nd and Pb isotope ratios of both igneous and crustal samples were analysed with the aim of revealing both the extent of magma - crust interaction and processes by which it has occurred. These data allowed the path of the magmas to be traced through the crust and to gauge the processes occurring at various stages during magma storage and ascent, including magma mixing, assimilation during fractional crystallisation and contamination by crustal melts.

The Arran isotope data point towards major assimilation of Grampian terrane lithologies, despite the Drumadoon Igneous Complex being located within the Midland Valley crustal block. Therefore, while the magmas originated on the northern side of the Highland Boundary Fault, they have crossed this boundary at some point during their evolution and ascent, most likely during shallow-level emplacement.

In the case of Carlingford and Mourne, all samples trend markedly towards the local Silurian country rock, reflecting the involvement of a single crustal end member and shallow crustal contamination. Nevertheless, the data imply contamination was not straightforward. Rather, a succession of variably overprinted

processes that form a time sequence of contamination are seen; from initial contamination by crustal partial melts to bulk contamination as the system heats up, and final contamination by the remaining crustal restite. Processes such as xenocryst entrainment, post-contamination fractionation and magma chamber convection were also found to be significant during magma evolution.

On a broader scale, the felsic magmas of the southern British and Irish Palaeogene Igneous Province (BIPIP) appear to result from high levels of contamination during differentiation, producing a characteristic bimodal "Bunsen-Daly" compositional gap, with little intermediate magmatism. There is a broad trend of increasing volumes of felsic rocks as the BIPIP is traversed from north to south, crossing from ancient gneissic terranes in the north into the less metamorphosed Palaeozoic terranes to the south. These southern terranes (Grampian, Midland Valley and Southern Upland terranes) are rich in fusible hydrous minerals (such as muscovite and biotite) and are hence a very fertile contaminant. This appears to have lead to increased production of felsic melts in the southern sectors of the British and Irish Palaeogene Igneous Province.

Significantly, the intermediate compositions that bridge the Bunsen-Daly Gap are not the products of fractional crystallisation, but rather appear to be the result of both mixing of end-member compositions (Arran, Glasdrumman) and restricted amounts of crustal contamination during storage, transport and emplacement (Carlingford).

*"The important thing in science is not so much*

*to obtain new facts as to discover new*

*ways of thinking about them."*

SIR WILLIAM BRAGG

(1862 – 1942)

Nobel laureate in physics (1915) for services in the
analysis of crystal structure by means of X-rays

# 1. TABLE OF CONTENTS

**1. TABLE OF CONTENTS ..... 1**

**2. TABLE OF FIGURES ..... 6**

**3. TABLE OF TABLES ..... 16**

**4. INTRODUCTION ..... 18**

4.1. AIMS OF THIS STUDY ..... 19
4.2. NORTH ATLANTIC IGNEOUS PROVINCE ..... 20
4.3. FORMATION OF THE NORTH ATLANTIC IGNEOUS PROVINCE ..... 21
*4.3.1. Parental magma(s)* ..... *22*
4.4. THE BRITISH AND IRISH PALAEOGENE IGNEOUS PROVINCE ..... 23
*4.4.1. Volcanism within the British and Irish Palaeogene Igneous Province* ..... *26*
4.4.1.1. Lava fields ..... 26
4.4.1.2. Central complexes ..... 29
*4.4.2. Bimodal magmatism* ..... *31*
4.5. REGIONAL GEOLOGY ..... 32
*4.5.1. The Hebridean Terrane* ..... *35*
*4.5.2. The Northern Highlands Terrane* ..... *36*
*4.5.3. The Grampian Terrane* ..... *36*
*4.5.4. The Midland Valley Terrane* ..... *37*
*4.5.5. The Southern Uplands Terrane* ..... *38*
*4.5.6. Post-accretionary geological history* ..... *39*
4.6. THE CENTRES OF THE SOUTHERN BRITISH AND IRISH PALAEOGENE IGNEOUS PROVINCE ..... 40
*4.6.1. Carlingford* ..... *40*
*4.6.2. Arran* ..... *41*
*4.6.3. Mourne* ..... *43*
*4.6.4. Slieve Gullion* ..... *44*
*4.6.5. Tardree* ..... *46*

**5. METHODS ..... 48**

5.1. SAMPLE SELECTION AND PREPARATION ..... 49
5.2. X-RAY FLUORESCENCE ..... 49
*5.2.1. GEOMAR* ..... *49*
*5.2.2. University of St. Andrew's* ..... *50*
*5.2.3. Centre d'Analyses Minérale, University of Lausanne* ..... *50*
5.3. X-RAY DIFFRACTION ..... 50
5.4. INDUCTIVELY COUPLED PLASMA MASS SPECTROMETRY ..... 50
*5.4.1. Scottish Universities Environmental Research Centre* ..... *50*
*5.4.2. Institute F. - A. Forel* ..... *52*
5.5. WHOLE-ROCK ISOTOPE GEOCHEMISTRY ..... 53
*5.5.1. Strontium isotope ratios* ..... *53*
5.5.1.1. Scottish Universities Environmental Research Centre ..... 53
5.5.1.2. Department of Mineralogy, University of Geneva ..... 54
*5.5.2. Neodymium isotopes* ..... *55*
5.5.2.1. Scottish Universities Environmental Research Centre ..... 55
5.5.2.2. Department of Mineralogy, University of Geneva ..... 55
*5.5.3. Lead isotopes* ..... *56*
5.5.3.1. Scottish Universities Environmental Research Centre ..... 56

5.6. Electron microprobe ..... 56
5.7. Microdrilling and micro-Sr isotope analysis ..... 57
5.8. Age dating ..... 59
5.9. Experimental Petrology ..... 60
5.10. Data reproducibility ..... 62
*5.10.1. Major and trace element data* ..... *62*
5.10.1.1. Comparison of XRF major trace element data from different labs 62
5.10.1.2. Institute F. - A. Forel ICP-MS trace element data ..... 64
*5.10.2. Rare earth element data* ..... *65*
5.10.2.1. SUERC ICP-MS rare earth element data ..... 65
*5.10.3. Isotope data* ..... *65*
5.10.3.1. Strontium data repeats ..... 65
5.10.3.2. Leached versus un-leached strontium isotope analysis ..... 66
5.10.3.3. Difficulties with neodymium isotope ratio analysis ..... 67

**6. CARLINGFORD ..... 69**

6.1. Abstract ..... 70
6.2. Introduction ..... 71
6.3. Petrography of major lithologies ..... 75
*6.3.1. Longford-Down meta-siltstone* ..... *75*
*6.3.2. Hornfels* ..... *76*
*6.3.3. Limestone* ..... *78*
*6.3.4. Marble* ..... *79*
*6.3.5. Microgranite* ..... *80*
*6.3.6. Gabbro* ..... *81*
*6.3.7. Plagioclase-phyric Basalt (cone-sheets)* ..... *82*
*6.3.8. Basalt (cone-sheets)* ..... *83*
*6.3.9. Trachy-andesite (cone-sheets)* ..... *84*
*6.3.10. Rhyolite* ..... *85*
6.4. Intrusion sequence of the Carlingford cone-sheets ..... 85
6.5. Sample selection and preparation ..... 86
6.6. Geochemical analysis ..... 87
*6.6.1. X-Ray fluorescence* ..... *87*
*6.6.2. X-Ray diffraction* ..... *87*
*6.6.3. ICP-MS* ..... *88*
*6.6.4. Isotope geochemistry* ..... *88*
*6.6.5. Electron microprobe* ..... *88*
*6.6.6. Microdrilling and micro-Sr isotope analysis* ..... *88*
6.7. Experimental petrology ..... 89
6.8. Major and trace element geochemistry ..... 89
*6.8.1. Major elements* ..... *89*
*6.8.2. Trace elements* ..... *94*
*6.8.3. Rare earth elements* ..... *98*
*6.8.4. Least-squares mixing calculations* ..... *99*
6.9. Isotope geochemistry ..... 100
*6.9.1. Strontium and neodymium isotopes* ..... *101*
*6.9.2. Lead isotopes* ..... *105*
6.10. Microprobe analysis of zoned plagioclase feldspars ..... 108
*6.10.1. Thick section CPD9* ..... *108*
*6.10.2. Thick section CPB* ..... *111*

*6.10.3. Thick section CSRB* ..... *112*
6.11. MICRODRILLING OF ZONED PLAGIOCLASE FELDSPARS ..... 115
*6.11.1. CPD9 18* ..... *117*
*6.11.2. CSRB 1* ..... *117*
*6.11.3. CSRB 11* ..... *117*
6.12. DISCUSSION ..... 118
6.13. CONCLUSIONS ..... 122

**7. ARRAN ..... 124**

7.1. ABSTRACT ..... 125
7.2. INTRODUCTION ..... 125
7.3. THE DRUMADOON INTRUSIVE COMPLEX ..... 128
7.4. PETROLOGY AND PETROGRAPHY ..... 131
*7.4.1. Xenocrystic dolerite/basalt* ..... *131*
*7.4.2. Porphyritic dacite* ..... *132*
*7.4.3. Porphyritic rhyolite* ..... *133*
7.5. CONTACT RELATIONSHIPS ..... 134
7.6. SAMPLE SELECTION AND PREPARATION ..... 136
*7.6.1. Sample preparation* ..... *137*
7.7. GEOCHEMICAL ANALYSIS ..... 137
*7.7.1. X-ray fluorescence* ..... *137*
*7.7.2. ICP-MS* ..... *137*
*7.7.3. Isotope geochemistry* ..... *138*
7.7.3.1. Whole rock isotope ratios for Drumadoon samples ..... 138
7.7.3.2. Whole rock isotope ratios for other Arran samples ..... 139
7.7.3.3. Age dating ..... 139
7.8. MAJOR AND TRACE ELEMENT GEOCHEMISTRY ..... 139
*7.8.1. Major element geochemistry* ..... *139*
*7.8.2. Trace element geochemistry* ..... *141*
*7.8.3. Samples DD-Dol-6 and DD-mDol-16* ..... *144*
7.9. CALCULATION OF THE INITIAL COMPOSITION OF THE MAFIC END MEMBER 147
*7.9.1. Least-squares mixing analysis* ..... *149*
7.10. ISOTOPE GEOCHEMISTRY ..... 150
*7.10.1. Age dating* ..... *150*
*7.10.2. Strontium and neodymium isotope geochemistry* ..... *152*
*7.10.3. The effect of late-stage magma mixing on the isotope ratios of the basaltic and rhyolitic components of the composite intrusion* ..... *153*
7.11. MODELLING OF CRUSTAL CONTAMINATION ..... 156
*7.11.1. Geochemical modelling of contamination by Midland Valley Terrane crust* *157*
*7.11.2. Geochemical modelling of contamination by Grampian Terrane crust* *160*
7.12. DISCUSSION ..... 163
*7.12.1. Major and trace element data* ..... *163*
*7.12.2. Significance of age date* ..... *165*
*7.12.3. Structure of the crust and the magma pathway* ..... *167*
7.13. CONCLUSIONS ..... 170

**8. MOURNE ..... 172**

8.1. ABSTRACT ..... 173

8.2. INTRODUCTION ..... 174
*8.2.1. The Mourne granite complex* ..... *174*
*8.2.2. The Mourne dyke swarm* ..... *176*
8.2.2.1. Dunmore Head dykes ..... 176
8.2.2.2. The Mourne cone-sheet ..... 177
8.3. GEOCHEMICAL ANALYSIS ..... 179
*8.3.1. Sample selection and preparation* ..... *179*
*8.3.2. X-Ray fluorescence* ..... *180*
*8.3.3. ICP-MS* ..... *180*
*8.3.4. Isotope geochemistry* ..... *180*
*8.3.5. Age correction of strontium isotope ratios for the Mourne granites* ... *181*
8.4. THE GLASDRUMMAN CONE-SHEET ..... 183
*8.4.1. Fieldwork* ..... *183*
*8.4.2. Petrology and petrography* ..... *186*
8.4.2.1. Xenocrystic basalt ..... 186
8.4.2.2. Quartz and feldspar-phyric rhyolite ..... 188
8.4.2.3. Hybridised rhyolite ..... 189
8.4.2.4. Mingled rhyolite and basalt ..... 192
*8.4.3. Contact relationships* ..... *193*
*8.4.4. Sample selection* ..... *196*
*8.4.5. Major and trace element geochemistry* ..... *197*
8.4.5.1. Major element data ..... 197
8.4.5.2. Trace element data ..... 200
8.4.5.3. Least-squares mixing analysis ..... 203
8.4.5.4. Rare earth element data ..... 204
*8.4.6. Isotope geochemistry* ..... *206*
8.4.6.1. Whole rock strontium isotope ratios ..... 206
8.4.6.2. Whole rock lead isotope ratios ..... 209
*8.4.7. Discussion* ..... *211*
8.4.7.1. Major and trace element data ..... 211
8.4.7.2. Strontium and lead isotope ratio data ..... 213
*8.4.8. Conclusions* ..... *214*

**9. SLIEVE GULLION ..... 216**

9.1. ABSTRACT ..... 217
9.2. INTRODUCTION ..... 217
9.3. DESCRIPTION OF EXPOSURE ..... 221
9.4. DISCUSSION ..... 239

**10. DISCUSSION AND CONCLUSIONS ..... 243**

**11. FURTHER WORK ..... 250**

**12. ACKNOWLEDGEMENTS ..... 254**

**13. PUBLISHED CONTRIBUTIONS ..... 258**

13.1. PAPERS ..... 259
13.2. CONFERENCE ABSTRACTS ..... 259

**14. BIBLIOGRAPHY ..... 263**

**APPENDICES 1-9 ..... 289**

# 2. TABLE OF FIGURES

Figure 4.1 Distribution of magmatism within the North Atlantic Igneous Province. Plates are reconstructed for the Palaeocene-Eocene boundary. Map modified from Saunders *et al.* (2007) - Figure 7. Black box shows area of Figure 4.11. ..... 21

Figure 4.2 Reconstruction of the North Atlantic at 55 Ma, showing approximate area affected by the mantle plume. Hatched areas are lavas and sills, thin lines are dykes. Area in red represents the axes along which magmatism occurred, suggested to be the surface expression of rising sheets of asthenospheric mantle (Smallwood and White, 2002, Figure 1). ..... 24

Figure 4.3 Map of the British and Irish Palaeogene Igneous Province, showing the major onshore and onshore central complexes and lava fields (after Mussett *et al.*, 1988, Figure 1). ..... 25

Figure 4.4 The theoretical effects of crustal thinspots on rising plume magmas. Figure 1 from Thompson and Gibson (1991). ..... 26

Figure 4.5 Palaeogene lavas unconformably overlying Mesozoic sediments (Cretaceous Chalk) in north Antrim, N. Ireland. ..... 27

Figure 4.6 Columnar basalts from the Giants Causeway (Causeway Tholeiite Member), Antrim, showing colonnade and entablature (after Lyle, 2000). ..... 28

Figure 4.7 The Interbasaltic Formation, including the Post na Spaniagh interbasaltic member (red) lying between the Lower Basalts (below) and the Causeway Tholeiite Member (above). ..... 29

Figure 4.8 Intrusive igneous rocks of the BIPIP, representing crystallised magma chambers. Northern Granite, Glen Sannox, Arran (left) and the Central Igneous Complex of Rum (peridotite) (right). ..... 30

Figure 4.9 The Slieve Gullion Complex, with a central layered intrusion and a surrounding ring-dyke intrusion, representing the upper-levels of the sub-volcanic system. ..... 30

Figure 4.10 Approximate distribution of magma compositions within the BIPIP (right) compared to the proportions expected if magmas evolved exclusively by Bowen-styled fractional crystallisation (left). The paucity of intermediate compositions is known as the "Bunsen-Daly Gap". ..... 32

Figure 4.11 Terrane map of the Northern British Isles. Palaeogene igneous centres are marked as red stars. See also Figure 4.3. Line A-B represents the line along which the cross section seen in Figure 4.12 has been constructed. ..... 33

Figure 4.12 Cross section along line A-B in Figure 4.11. The section was compiled using Figures 1.10 and 1.11 in Trewin and Rollin (2002) and was based on gravity and magnetic data. The magma pathways for the Palaeogene igneous centres of Ireland and Scotland are included (based on this study and that of Nicoll (2008)). Horizontal and vertical scales in kilometres. ..... 34

Figure 4.13 Geology of the Carlingford Igneous Centre (modified from Le Bas, 1967) ..... 41

Figure 4.14 Distribution of Palaeogene igneous rocks on the Isle of Arran ..... 42

Figure 4.15 Map of the eastern and western Mourne granite centres, showing the main granites and their facies. Grey background represents the Longford-Down metasediments (country-rock). Map after Cooper and Johnston (2004), figures 15.3 and 15.4. These figures use the data of Hood (1981) and Gibson (1984) ..... 44

Figure 4.16 Generalised geology of the Slieve Gullion area ..... 45

Figure 4.17 Map of the Tardree Rhyolite Complex, including the Sandy Braes vent. After Cooper (2004), figure 14.6a. Key: pale pink - Lower Basalt Formation, dark pink – Upper Basalt Formation, white – drift cover, blue – Interbasaltic Formation, orange – rhyolite flows, stippled pale pink – pyroclastic rocks, stippled orange – columnar rhyolite, brown – vent agglomerate..... 47

Figure 5.1 Mean values for 36 analyses of the standard, BCR-1 (grey line), with error bars marking the standard deviation of the data. Note the saw-tooth pattern of the values (Oddo-Harkins effect) ..... 51

Figure 5.2 Thermal ionisation mass spectrometer at SUERC, Scotland. ..... 54

Figure 5.3 Cation exchange columns for the separation of Nd from a REE solution, at SUERC, Scotland ..... 55

Figure 5.4 Microdrilling setup at University of Durham, including drill within an over-pressured Perspex clean box and attached computer monitor. ..... 58

Figure 5.5 Screen grab of Merchantek Micromill software showing chosen drill paths. The live video image of the crystal does not copy with the screen grab ..... 58

Figure 5.6 A back scattered electron image of a feldspar that has been micro-drilled. Note the drill paths, showing the collection of two samples, the first from an outer zone and the second from the centre of the crystal ..... 59

Figure 5.7 The Voggenreiter Press and piston cylinder apparatus (yellow) at the Istituto Nazionale i Geofisica e Vulcanologia (INGV) Rome (photo from Deegan, F.M.) ..... 61

Figure 5.8 Plot of the ratio of GEOMAR data divided by Lausanne data for all samples. A ratio of 1 means the analysed values are identical. Values above one indicate the Lausanne data are lower than that of GEOMAR, and below one indicate the Lausanne measurements are higher. ..... 62

Figure 5.9 Plots of selected XRF major element data for both the GEOMAR (black) and Lausanne (grey) labs, showing consistency of the data from both labs. Y-axis is weight % oxide ..... 63

Figure 5.10 Plot showing Zr ppm as analysed by XRF (diamonds) and ICP-MS (circles). Values for both techniques are similar in the low-silica range, but diverge as silica and Zr concentration increases. In these low-silica samples zirconium would be hosted in pyroxene, which would dissolve more readily during ICP-MS preparation ..... 64

Figure 5.11 Plot of repeat analyses for strontium isotope ratio (8 samples). Machine errors on the data are not greater than 0.000044 (2 S.E.). ..... 66

Figure 5.12 Leached and un-leached strontium isotope ratios for samples C-VA1 and CB3. Large points are un-leached, smaller ones are leached. Errors on the data are smaller than the size of the data points. ..... 67

Figure 5.13 Graph showing neodymium concentration (ppm) and whether the samples were measured for isotope ratio or failed. ..... 68

Figure 6.1 Schematic geological map of the Carlingford Igneous Centre, modified from Le Bas (1967). ..... 72

Figure 6.2 Schematic cross-section of the Carlingford Igneous Centre. Compiled after Le Bas (1960; 1967) and O'Driscoll (2006). ..... 74

Figure 6.3 Interbedded siltstones and mudstones showing the upper members of a Bouma sequence... 75

Figure 6.4 Thin section of Longford-Down metasediment (PPL). Note the presence of large amounts of biotite in the darker layers (right), while the paler layers are richer in muscovite and quartz (left). ..... 76

Figure 6.5 Zoom in to a hand sample of a metasedimentary xenolith from the Slate Rock cone-sheet (IJ 17799 11754). Note the occurrence of in-situ partial melting and the formation of a vein network along which melt can be transported. ..... 77

Figure 6.6 Thin section of hornfels xenolith in XPL. The majority of the rock is biotite, with coarse pockets of frozen melt that are rich in plagioclase. See Figure 6.5 for hand sample image ..... 78

Figure 6.7 Thin section of the Carlingford Limestone in plane polarised light, showing skeletal grains in a calcitic matrix. ..... 79

Figure 6.8 A large block of marble within the main gabbro body at IJ 17842 09073, southeast of Barnavave. The block is ~100m long and is entirely crystalline, with recognisable, but sometimes deformed, bedding. ..... 80

Figure 6.9 Microgranite thin section in cross polarised light, exhibiting granophyric texture. ..... 81

Figure 6.10 Gabbro thin section in cross polarised light. Note large plagioclase crystals and considerably smaller olivines and orthopyroxenes ..... 82

Figure 6.11 Porphyritic basalt from the cone-sheet swarm. Thin section is in cross-polarised light and shows a large plagioclase glomerocryst in a fine-grained feldspar, pyroxene and Fe-Ti oxide matrix.....83

Figure 6.12 Basaltic cone-sheet on the Carlingford foreshore, below King John's Castle.....84

Figure 6.13 Thin section image (XPL) of the margin of a hornfels xenolith. The margins of the xenolith show enrichment in opaques and lower proportions of biotite. Melt appears to be sourced from the xenolith, collecting through a small vein (centre) and forming the trachy-andesite.....85

Figure 6.14 Total Alkali v Silica diagram. Data span much of the spectrum from mafic to felsic with an excursion to higher alkalinities in the mid 50% $SiO_2$ range.....90

Figure 6.15 TAS diagram with sedimentary country rocks plotted. Note the hornfelsed metasediments (dark grey field) plot within the trachy-andesite range and low-grade metamorphosed siltstones (pale grey field) within the andesite, dacite and rhyolite ranges. The hornfelsed xenoliths are richer in $K_2O$ than their low grade equivalents, suggesting they have interacted with K-rich metamorphic fluids, and perhaps represent aureole rocks from deeper within the complex.....91

Figure 6.16 Plot of $K_2O$ v $SiO_2$ showing the chemical relationships of intermediate igneous rocks to local country rocks. Country rock fields in grey. The trachy-andesites show high-$K_2O$, similar to the values of the hornfels xenoliths. Arrows show evolution of the magma from basalt to rhyolite, with diversion to low $K_2O$ in the intermediate range, similar to values of the local meta-siltstones.....91

Figure 6.17 Plot of $Na_2O$ v $SiO_2$ showing trend of increasing $Na_2O$ for the gabbros and cone-sheet gabbros. There are low levels of $Na_2O$ within the intermediate range, echoing $Na_2O$ levels within the local crust. The felsic rocks also lie within the meta-siltstone field, while once again, the trachy-andesites plot with the hornfels xenoliths. Arrows represent general evolutionary trends. .....92

Figure 6.18 Plot of CaO v $SiO_2$, showing overall trend of decreasing CaO. Once again the intermediate rocks are displaced towards local crustal values. The rhyolites and microgranites lie within the meta-siltstone field, while the trachy-andesites are again consistently within the hornfels xenolith field.....93

Figure 6.19 Plot of MgO v $SiO_2$ showing overall decrease in MgO, with excursions to anomalously high MgO values within the mid-$SiO_2$ range. These high intermediate MgO values are similar those of the local crust. Again the trachy-andesites lie within the xenolith field. Arrows suggest possible evolutionary trends for intermediate and evolved samples.....93

Figure 6.20 Plot of Rb v $SiO_2$ showing general increase in Rb concentration. There is, however, a dip to lower Rb concentrations at mid-silica ranges, echoing the Rb concentrations of the local crust. While andesite and dacite samples plot near the meta-siltstone, the trachy-andesite plots within the hornfelsed xenolith field.....94

Figure 6.21 Plot of Sr v $SiO_2$ showing a general decrease in Sr concentration. Note the relatively Sr-rich intermediate rocks, which lie within the meta-siltstone field. The trachy-andesites lie close to the hornfels xenoliths.....95

Figure 6.22 Plot of Zr v $SiO_2$ showing a general trend of enrichment similar to that of Rb (Figure 6.20). There is a slight dip to lower Zr concentrations at mid-silica ranges, suggesting the influence of the local crust. While andesite and dacite samples plot near the meta-siltstone, the trachy-andesite plots within the hornfelsed xenolith field. Arrows indicate the general evolutionary trends of the suite, leading to high and low Zr rhyolites. .....96

Figure 6.23 Plot of Zr ppm v Nb ppm. Note decoupling of Zr from Nb at ~Nb=20 ppm, implying addition of Zr by an outside source. This trend is mirrored in the Zr composition of the siltstones, suggesting they may be such a source. The high $SiO_2$ igneous rocks appear to have evolved beyond the composition of the crust, again this may be the result of post-contamination fractional crystallisation, or indeed contamination by a incompatible-rich partial melt of the meta-sedimentary rocks. .....97

Figure 6.24 Chondrite normalised rare earth element plot showing the main cone-sheet lithologies and the local crust. .....98

Figure 6.25 Back scattered electron image of glass resulting from complete melting of Longford-Down metasediment at 1000°C and 5 Kbar. Plagioclase microlites represent areas of recrystallisation. 100

Figure 6.26 $^{87}Sr/^{86}Sr$ v $^{143}Nd/^{144}Nd$ isotope ratios for major lithologies in the Carlingford Igneous Centre, including local metasedimentary crust. The upper curve represents AFC processes using a hornfels end member and r = 0.8, while the lower curve represents AFC processes involving a meta-siltstone end member with r = 0.7. Lower r-values did not fit the dataset, however, the high values used can be justified as the contaminants are highly fusible (See sections 6.7 and 6.8.4). 101

Figure 6.27 $^{87}Sr/^{86}Sr$ v $^{143}Nd/^{144}Nd$ isotope ratios for major lithologies in the Carlingford Igneous Centre, including local metasedimentary crust. The plot shows the trachy-andesites have a very similar isotopic signature to the hornfelsed xenoliths. The curve represents binary mixing of MORB and hornfelsed metasediment end members. 103

Figure 6.28 $^{87}Sr/^{86}Sr$ v Sr ppm, showing potential petrogenetic paths. AFC models are in full lines, with bulk mixing models in dashed lines. Meta-siltstones are labelled by location. Note Carlingford hornfels xenoliths are richer in Sr, and less radiogenic, than their meta-siltstone equivalents. The Slieve Gullion value is from Troll *et al.* (2005). 104

Figure 6.29 Pb isotope plots showing a single point (CS4C) plotting towards the limestone field. The majority of samples plot towards the local Longford-Down crust. BSE values from Allegre et al (1988). MORB and upper and lower crustal fields from Rollinson (1993) (Figure 6.11). 107

Figure 6.30 Feldspar CSRB 1, showing zones in cross-polarised light (left) and back-scattered electron (BSE) image. Bright interference colours in the cross-polarised image are the result of viewing a thick-section (~140$\mu$m) rather than thin section (~30$\mu$m). 108

Figure 6.31 Feldspars from thin section CPD9, showing microprobe spots and An values for the traverses from rim to core of each crystal. X-axis is not to scale, see spots on BSE image for true sampling density. Dashed lines represent the main zone boundaries. Note crystal 16 shows two high-An cores (delineated in white), this may represent a section of the irregular surface of a single resorbed core. Points that lie outside the crystal are groundmass feldspar analyses (see Appendix 2.10). 111

Figure 6.32 Feldspars from thin section CPB, showing microprobe spots and An values for the traverses from rim to core of each crystal. X-axis is not to scale, see spots on BSE image for true sampling density. Dashed lines represent zone boundaries. Note the drilled area in lower left of the BSE image of crystal 1. 112

Figure 6.33 Feldspars from thin section CSRB, showing microprobe spots and An values for the traverses from rim to core of each crystal. X-axis is not to scale, see spots on BSE image for true sampling density. Dashed lines represent the main zone boundaries. Points that lie outside the crystal are groundmass feldspar analyses (see Appendix 2.10). 115

Figure 6.34 Zoned crystals from porphyritic basalt were analysed for An value and micro-drilled for Sr isotopes. The upper graphs show $^{87}Sr/^{86}Sr$ (blocks) and An composition (lines) for the various zones. The central images show back-scattered election (BSE) images of the zoned crystals prior to drilling. The cartoons show zones marked in grey-scale and annotated with chemical composition. Straight lines represent the microprobe traverse for An. 116

Figure 6.35 Summary of processes occurring within the Carlingford cone-sheet magma system. These processes include assimilation of both whole-rock melts and partial melts of local crust, as well as restite assimilation. Xenocryst incorporation also occurs; these xenocrysts may form cores to some large magmatic phenocrysts. Convection is apparent from the presence of resorbed phenocrysts and zonation with phenocrysts. Large xenoliths (>1 m) are also present and have contaminated the magma during transport and intrusion. 121

Figure 7.1 Detailed geology of the Arran region. 127

Figure 7.2 Map of the Drumadoon Intrusive Complex (after Kanaris-Sotiriou and Gibb, 1985) with inset showing an overview of the porphyritic rhyolite sill complexes of Arran. 128

Figure 7.3 Annotated photograph (looking northeast) of the Drumadoon Intrusive Complex. Cliff is approximately 30 m high. 130

Figure 7.4 Xenocrystic dolerite with rounded quartz and potassium feldspar xenocrysts. ..... 131

Figure 7.5 Thin section of xenocrystic basalt, showing chemically eroded xenocrysts of K-feldspar, indicating they were not in equilibrium with the melt ..... 132

Figure 7.6 Polished outcrop of porphyritic dacite, showing its dark matrix and quartz and feldspar phenocrysts. Note the presence of basaltic enclaves up to 5 cm in size. ..... 133

Figure 7.7 Thin section of porphyritic dacite, showing embayed quartz phenocrysts. ..... 133

Figure 7.8 Field photograph of polished rhyolite, showing zoned alkali feldspars and smaller quartz phenocrysts. The feldspar in the centre of the image shows a clear plagioclase rim, while many others do not. ..... 134

Figure 7.9 Unchilled lobate contact and crystal transfer between the porphyritic rhyolite and porphyritic dacite. ..... 135

Figure 7.10 Unchilled but distinct contact between the porphyritic dacite (top) and the xenocrystic basaltic-andesite (bottom). Coin for scale has a diameter of 22 mm. ..... 135

Figure 7.11 Total alkali v silica plot, classifying the Drumadoon rock suite. The suite is sub-alkaline, with the majority of the samples being basaltic andesite and rhyolite/dacite. Small volumes of andesite and low silica dacite represent the Bunsen-Daly gap. Basalt B1 represents a 'normal' Arran basalt, containing no xenocrysts or evidence of mixing (Dickin *et al.*, 1981). ..... 140

Figure 7.12 $TiO_2$ v $SiO_2$ showing mixing line. Key as in Figure 7.11. Basalt B1 was used as the basaltic end member as the most mafic composition seen at Drumadoon, the basaltic andesites, show clear evidence of being the product of mixing themselves (presence of xenocrysts) ..... 141

Figure 7.13 $K_2O$ v $SiO_2$ showing mixing line. Note the distinct drop in $K_2O$ concentrations at high $SiO_2$ concentrations, indicative of potassium feldspar fractionation. Key as in Figure 7.11 ..... 141

Figure 7.14 Plot of Sr v $SiO_2$, once again showing a binary mixing line. More scatter is seen than within the major element data (Figure 7.12 and Figure 7.13), this is most likely due to variations in phenocryst/xenocryst density. Key as in Figure 7.11 ..... 142

Figure 7.15 Plot of Ba v $SiO_2$. Note the distinct downturn in barium concentration at high levels of $SiO_2$; this is in agreement with Figure 7.13, which shows a decrease in $K_2O$, together suggesting fractionation of potassium feldspar. Key as in Figure 7.11 ..... 143

Figure 7.16 Plot of Zr v SiO2. The drop in Zr concentrations is due to late-stage zircon fractionation. Key as in Figure 7.11. ..... 143

Figure 7.17 Chondrite-normalised rare-earth element plot. Rhyolite (*solid black*), basaltic-andesite (*dashed black*), fine-grained Northern Granite (*solid grey*) and coarse-grained Northern Granite (*dashed grey*). Note the granites show enrichment in HREE, while the sill samples are enriched in LREE. ..... 144

Figure 7.18 Graph showing depletion in Cr for samples DD-Dol-6 and DD-mDol-16. ..... 145

Figure 7.19 Plot of V v $SiO_2$. Samples DD-dol-6 and DD-mDol-16 show strong depletion in this transition metals. ..... 146

**Figure 7.20 Plateaux diagrams for dated K-feldspar samples. The upper sample (DD-T) has been treated in Hf, whereas the lower sample (DD-U) is untreated.** ..... 152

Figure 7.21 Bar chart of strontium isotope ratios, showing the ranges of crustal values in the Arran region and the strontium isotope range of igneous samples from the Drumadoon Intrusive Complex (green shading). Note how the igneous samples are displaced from mantle values (grey) towards the crustal realm. (Crustal data fields are from this study and Dickin *et al.*, 1981; Dickin and Bowes, 1991; Halliday *et al.*, 1993; Dickin, 1994). ..... 153

Figure 7.22 Crustal data fields for the Midland Valley Terrane. Crustal data fields from Halliday *et al.* (1993) ..... 159

Figure 7.23 Assimilation and fractional crystallisation (AFC) and binary isotope mixing modelling of crustal contamination in the Drumadoon magma suite. Samples have had the effects of magma mixing "un-mixed" to estimate initial *pre-mixing* isotope ratios. A partial melt of Dalradian metasediment (containing just a fusible mica component, would have a more radiogenic Sr

isotope ratio and plot to the right of its whole rock value. Crustal data fields from Dickin *et al.* (1981), Marcantonio *et al.* (1988), Dickin and Bowes (1991) and Dickin (1994). ..... 162

Figure 7.24 Schematic diagram showing the intrusion sequence of magmas at Drumadoon..... 164

Figure 7.25 Palaeomagnetic stratigraphy of the Paleocene (Gradstein *et al.*, 2004), with recent radiometric dates for the Arran porphyritic rhyolite intrusions and the Northern Granite. Black intervals are periods of normal polarity, while white intervals are reverse polarity. Palaeomagnetic data previously suggested these intrusions all lay within chron 26n (Mussett *et al.*, 1987; Mussett *et al.*, 1989; Hodgson *et al.*, 1990). ..... 167

Figure 7.26 Schematic diagram showing the intrusion pathways of both the rhyolitic (pink) and basaltic (green) magmas. The rhyolite was contaminated in both the upper and lower crust, while the basalt just shows lower crustal influences. The magmas met in the upper crust and mixed and mingled (black square) (see Figure 7.24). They then intruded across the terrane boundary, most likely exploiting the Highland Boundary Fault (purple arrow). ..... 169

Figure 8.1 Map of the Mourne granite complex, showing the various granites (G1-5). Facies within the granites are indicated. Grey background represents the Longford-Down metasediments (country rock). Map after figures 15.3 and 15.4 of Cooper and Johnston (2004),. These figures use the data of Hood (1981) and Gibson (1984). ..... 175

Figure 8.2 Large enclaves of cumulate anorthosite within dyke 60 at Dunmore Head. ..... 177

Figure 8.3 Two large plagioclase phenocrysts within dyke 61 at Dunmore Head..... 177

Figure 8.4 The composite cone-sheet at Glasdrumman Port, showing the basaltic margin (left) and large basaltic enclaves (centre) lying within the central porphyritic rhyolite member. Photograph taken looking south. The dyke dips west beneath the main granite bodies..... 178

Figure 8.5 Plot of strontium isotope ratios for the Mourne granites, with error bars representing the propagated error in the age-corrected Sr data using a ± 5 % analytical uncertainty in Rb/Sr ratio. The data shows that the higher the Rb/Sr ratio, the greater the uncertainty in the data. The yellow box shows the typical range of strontium isotope ratio for the mantle (Saunders *et al.*, 1988). The blue box represents typical crustal ranges within the region. ..... 181

Figure 8.6 Distribution of dip values for the Glasdrumman section of the Mourne cone-sheet. All measurements dip west. The data represent measurements from internal and external boundaries of the dyke..... 183

Figure 8.7 Map of the Glasdrumman composite sheet, with photographs of features as seen along the intrusion. Note, the dark rhyolite (photograph F) occurs all along the intrusion between the basalt and rhyolite, but is too narrow to be seen in map view. See logged section for more lithological detail and key (Figure 8.8). ..... 184

Figure 8.8 Seven logged traverses of the Glasdrumman composite intrusion. Traverses are marked on the map (inset). ..... 185

Figure 8.9 The marginal basalt of the Glasdrumman cone-sheet, showing K-feldspar xenocrysts, most likely originating from a disaggregated enclave of the adjacent porhyritic rhyolite. In some regions these xenocrysts are abundant, though less so in others (see Figure 4.11). ..... 186

Figure 8.10 A purer section of marginal basalt than that seen in Figure 8.9. Note the presence of a small, quartz-rich disaggregated rhyolite enclave..... 187

Figure 8.11 Thin section of Glasdrumman basalt, showing plagioclase laths, with amphibole and chlorite representing weathered mafic minerals..... 187

Figure 8.12 Close-up of quartz and K-feldspar phenocrysts within the Glasdrumman porphyritic rhyolite. The feldspars show very obvious zoning..... 188

Figure 8.13 Thin section of rhyolite, showing quartz and alkali feldspar phenocrysts in a quartz and feldspar groundmass exhibiting graphic texture..... 189

Figure 8.14 Porphyritic rhyolite (left) and dark porphyritic rhyolite (right). The dark rhyolite has a darker groundmass and larger K-feldspar phenocrysts than the adjacent rhyolite. ..... 190

Figure 8.15 Close-up view of phenocrysts within the dark rhyolite. K-feldspar megacrysts show clear zoning with distinct dark pink rims..... 191

Figure 8.16 Thin section image of the hybridised rhyolite, showing a large plagioclase phenocryst in a quartz, feldspar and chlorite groundmass.....192

Figure 8.17 An outcrop of mingled basalt and rhyolite exposed at the northernmost end of the Glasdrumman cone-sheet. Note the density of basalt enclaves and the large feldspar phenocrysts within the rhyolitic groundmass.....193

Figure 8.18 Enclaves of basalt within the dark rhyolite. These enclaves indicate both magmas were liquid at the same time. Note the lack of chilled margins and the presence of xenocrysts of K-feldspar (derived from the rhyolite) within the basaltic enclave. For a close-up view of the area marked by the black box, see Figure 8.19.....194

Figure 8.19 Close-up view of the black box in Figure 8.18. Crystal transfer is clear between the dark rhyolite and the basalt (centre). There is also an obvious absense of chilled margins.....194

Figure 8.20 The lower boundary between the basalt and hybridised rhyolite, showing 'flames" of basalt injecting into the hybridised rhyolite. Interaction is greater within this structure, with a higher concentration of xenocrysts. The segment of the white measuring tape in the top left corner is 25cm in length. See also Figure 8.8 for an overview of the structure of the boundary between the basalt and dark, hybridised rhyolite, especially at the lower margins, where interaction appears greater.....195

Figure 8.21 Total alkali versus silica plot for the Glasdrumman sample suite, with chemical classification of the various lithologies.....197

Figure 8.22 Plot of major elements against distance across the dyke. Coloured stripes represent lithologies detailed in Table 8.1.....198

Figure 8.23 Plot of $SiO_2$ vs. MgO, showing a linear relationship, indicating mixing of basalt and rhyolite to form a hybridised rhyolite.....199

Figure 8.24 plot of $SiO_2$ vs. CaO, again showing a linear relationship between samples, indicating magma mixing between basalt and rhyolite to form hybridised rhyolite. The mixing line indicates a mix of ~25:75.....199

Figure 8.25 Plot of $SiO_2$ v $Na_2O$. Note that the hybridised rhyolites are more enriched in $Na_2O$ than either the basalt or rhyolite.....200

Figure 8.26 Plot of trace element vs. distance across the dyke. Coloured stripes represent lithologies detailed in Table 8.1. For many of the trace elements the hybridised samples show enrichment/depletion beyond the limits of either of the end members (basalt/rhyolite).....201

Figure 8.27 Plot of $SiO_2$ vs. Sr, once again showing a linear relationship, explained by magma mixing. One hybrid sample is slightly enriched, representing the sample from the centre of the hybridised zone. Unlike many of the trace elements, Sr does not show higher concentrations within the hybridised zone than in either of the adjacent zones.....201

Figure 8.28 Plot of $SiO_2$ vs. Ce, showing clearly that the hybridised rhyolite has higher Ce concentrations than either the basalt or the central rhyolite.....202

Figure 8.29 Plot of $SiO_2$ vs. Zr. The hybridised rhyolites have Zr concentrations over twice that of either the basalt or rhyolite. Such high levels of zirconium suggest zircon was concentrated within the hybridised magma, perhaps due to flow differentiation, whereby denser phases were partitioned into the marginal zones of the dyke.....203

Figure 8.30 Abundant mafic enclaves at the lower basalt/dark rhyolite contact (bottom right). The enclaves are irregular in shape and often contain xenocrysts of quartz and alkali feldspar (note the pen in the centre for scale).....204

Figure 8.31 Chondrite-normalised rare earth element concentrations for the rhyolite (pink), basalt (blue) and the hybridised rhyolite (purple). Once again the hybrid magma appears to be enriched in REEs compared to the parent end members. It is particularly enriched in the light rare earth elements (LREEs) compared to both the basalt and rhyolite. Typically a hybrid would be expected to have values intermediate to the two end members. Note the presence of a europium anomaly in both the hybrid and the rhyolite. The rhyolite trough appears more pronounced, however this is a function of the logarithmic scale on the y-axis of the graph.....205

Figure 8.32 Plot of age-corrected strontium isotope ratios for the Glasdrumman cone-sheet, showing the errors introduced by a 5% error on Rb/Sr ratio. Compare to Figure 8.5, where the propagated errors are much higher. Yellow box represents mantle values (Saunders *et al.*, 1988), blue box represents the range for the local Longford-Down crust ..... 207

Figure 8.33 Plot of strontium isotope ratio versus silica. Note the mixing ratios calculated in section 8.4.5.3 are similar, indicating that the hybrid rhyolite is a mix of ~ 75:25 rhyolite to basalt. Also note that the higher silica rhyolites have higher (more radiogenic) strontium ratios than the lower silica basalts. ..... 208

Figure 8.34 Pb isotope plots showing Glasdrumman samples and local crust. All samples plot towards the local Longford-Down crust. BSE values from Allegre et al (1988). MORB and upper and lower crustal fields from Figure 6.11 of Rollinson (1993) ..... 209

Figure 8.35 Close-up of the margin between the marginal basalt and the dark rhyolite, showing a large concentration of phenocrysts at the interface. ..... 212

Figure 8.36 Concentration of phenocrysts at the interface between the basalt and dark rhyolite at the margin of the intrusion. Once again, note the clear boundary, but the lack of a chilled margin, indicating the composite nature of the intrusion. ..... 213

Figure 8.37 Bouguer gravity anomaly map for Northern Ireland. Note the gravity high off the eastern coast, representing a large (~10km thick) mafic body. This body may have been the magma reservoir for magmatism across the region, including the Mourne, Carlingford and Slieve Gullion igneous centres. From Figure 19.2 in Reay (2004). ..... 214

Figure 9.1 Maps of the Slieve Gullion Igneous Centre. Fig 1a: Generalised Geology of the Slieve Gullion Centre after Cooper and Johnston, (2004), showing region of new exposure at Feede Mountain (black box). Fig 1b: Detailed map of the Feede Mountain exposure ..... 218

Figure 9.2 Log of the newly exposed road section at Feede Mountain ..... 220

Figure 9.3 Mafic enclaves in porphyritic microgranite (pG). Coin is 2.5 cm across Inset: Mafic enclave with microgranite xenocryst trace (right) and zoned feldspar in microgranite (left). Coin is 1.7 cm across. ..... 222

Figure 9.4 K-feldspar with plagioclase rim (rapakivi texture) in porphyritic microgranite (pG). Coin is 1.7 cm across ..... 222

Figure 9.5 Porphyritic microgranite (pG) with granophyric texture at start of section (thin section in XPL). ..... 223

Figure 9.6 Porphyritic rhyolite (pR) showing zoned feldspars (at pencil tip) and Newry Granodiorite fragments (e.g. centre right) with plagioclase overgrowths. ..... 224

Figure 9.7 Mafic enclave in porphyritic microgranite (thin section in PPL) ..... 225

Figure 9.8 Porphyritic microgranite (pG) finger (protrusion) in Longford-Down metasediments at 63 m. ..... 226

Figure 9.9 Hornfelsed Longford-Down metasediments striking at approximately 90° to the road. ..... 227

Figure 9.10 Micro-faulting in metasediments. Note the strong colouration in the bands, indicating high-temperature overprint (hornfelsing). ..... 227

Figure 9.11 Southern contact between Longford-Down (LD) metasediments and porphyritic rhyolite (pR) apophysis at 145 m ..... 229

Figure 9.12 Zoned feldspars and xenocryst-bearing enclaves in porphyritic rhyolite (pR) at ~150 m. Coin is 1.7 cm across. ..... 230

Figure 9.13 Porphyritic rhyolite (pR) at offshoot (145 m) (thin section in XPL). Compare groundmass to that of the porphyritic microgranite (Figure 9.5). ..... 230

Figure 9.14 Northern contact of porphyritic rhyolite (pR) apophysis and Longford-Down metasediment at 163 m. GPS instrument for scale ..... 231

Figure 9.15 Main contact (at 225 m) between Longford-Down metasediments (LD) and porphyritic microgranite (pG), which is steeply inclined and at its base dips at ~80° to the SE. ..... 232

Figure 9.16 Crushed zone in Longford-Down metasediments at the main contact at 225 m. Metre stick for scale. ....232

Figure 9.17 Crushed zone in Longford-Down metasediments at 225 m, ca 1 m south of contact (in "damage zone"). Note the presence of angular and strung-out igneous clasts. Coin is 2.5 cm across. ....233

Figure 9.18 Crushing at contact in Longford-Down metasediments and porphyritic microgranite (at ~218 m). (Thin section in XPL). Compare grain size of the porphyritic microgranite (lower right) to that in Figure 9.5 and Figure 9.7. ....234

Figure 9.19 Thin section in PPL of crush zone rocks at ~218 m, showing fine-grained cataclastic groundmass and igneous fragments. ....234

Figure 9.20 Crushed porphyritic microgranite at contact. Note the very small grain-size and the absence of unbroken zoned phenocrysts and enclaves, implying severe physical crushing and inter-mingling. Samples taken from 2 m north of the contact show regular grain-size again. Coin is 2.5 cm across. ....235

Figure 9.21 Wide and extensive mylonitic tuffisite veins in porphyritic microgranite near contact (226/7 m). Inset: Pervasive tuffisite veins near contact (226 m). ....236

Figure 9.22 Mylonitic tuffisite veins at contact (218 m) in porphyritic microgranite (thin section in PPL). ....237

Figure 9.23 Pervasive tuffisite veining with cataclastic crushing in damage zone near main contact (~218 m) (thin section in PPL). ....237

Figure 9.24 Contact of basaltic dyke with microgranite at 276 m. Notebook for scale. ....239

Figure 9.25 Basaltic dyke at 270 m, containing large angular microgranite xenoliths, suggesting that dyke intrusion postdates the solidification of the porphyritic microgranite (pG). ....239

Figure 10.1 Map of crustal terranes throughout the northern British Isles (left). The terranes get younger as boundaries are traversed to the south, and their metamorphic grade generally decreases. The map, right, shows the proportions of mafic (white) and felsic (black) magmas at each of the main igneous centres (from Bell, 1982, Figure 31.1). Note how the granite-rich centres mostly occur in the younger, less metamorphosed terranes. Similarly Lundy, which lies within the Bristol Channel, is 100% felsic rocks. ....246

# 3. TABLE OF TABLES

Table 5.1 Table of mean values for 36 analyses of BCR-1 for rare earth elements with standard deviations, indicating the precision of the data. For a measure of accuracy, the data are compared to the published data for BCR-1 (Raczek *et al.*, 2001). These data all lie with the standard deviation of the data from the current study. ..... 52

Table 7.1 Table of density of xenocryst/phenocryst occurrence in porphyritic rhyolite and xenocrystic dolerite (basaltic-andesite). ..... 147

Table 7.2 $^{40}Ar$-$^{39}Ar$ data from the Drumadoon Igneous Complex. Steps used in calculation of plateau age are in bold. Data is corrected for machine blank, correction factors and $^{37}Ar/^{36}Ar$ post irradiation decay ..... 151

Table 7.3 Re-calculated isotopic values for samples from the Drumadoon Igneous Complex. The effects of binary magma mixing have been removed. Values in bold represent those samples used as the basaltic ($B_i$) and rhyolitic ($R_i$) endmembers ..... 155

Table 7.4 Available radiometric and palaeomagnetic dates for the Arran (and surrounding areas) porphyritic rhyolite sills and the Northern Granite. WMA – weighted mean average. ..... 166

Table 8.1 Table of relative sample locations for traverse 1 (see Figure 8.8) of the Glasdrumman cone-sheet, with lithological boundaries marked. Coloured blocks are not representative of actual thicknesses ..... 196

# 4. INTRODUCTION

*An introduction to the geological history of the British Isles, including discussion of the North Atlantic Igneous Province and the British and Irish Palaeogene Igneous Province.*

## 4.1. Aims of this study

Magma is one of the most important probes into the Earth's interior, preserving isotopic information on its source and/or the crust through which it has passed. In old and lithologically variable crustal terranes, the boundaries between crustal blocks are often marked by extremely diverse lithologies of different ages. These compositional variations are frequently reflected in the radiogenic isotope signature of the rocks (Stone *et al.*, 1999). Such boundaries may, in turn, act as preferential pathways for subsequently ascending magmas. Therefore, due to the juxtaposition of discrete isotopic end members, the course of a magma may be traced isotopically, elucidating not only from which crustal domain the magmas have originated, but also at what point a boundary may have been crossed. This provides a picture of magma ascent and storage at both a local and crustal scale.

Samples from the Drumadoon Igneous Complex, Isle of Arran, the Carlingford Igneous Centre and Mourne Intrusive Complex, NE Ireland, were analysed to elucidate the structure of the crust beneath Southern Scotland and Northeast Ireland and the influence it has had on the magmas that have passed through it. These igneous centres formed within the British and Irish Palaeogene Igneous Province (61-55 Ma), which is itself part of the North Atlantic Igneous Province (Emeleus and Bell, 2005).

Work has also focussed on the formation of intermediate magmas and the processes of magma mixing and crustal contamination. Field observations, whole-rock and micro-scale (crystal-zone) major and trace element data, together with radiogenic isotope data were employed to trace igneous processes, magma-crust interaction and magma pathways, as well as to unravel the long-standing uncertainties regarding petrogenesis of intermediate magmas within the British and

Irish Palaeogene Igneous Province. Detailed field observations have also allowed analysis of intrusion processes at the Slieve Gullion Igneous Centre.

## 4.2. North Atlantic Igneous Province

The North Atlantic Igneous Province (NAIP) stretches from Greenland to Northwest Britain and Ireland. The province has a total estimated area of 1.3 x $10^6$ $km^2$ and a volume of 5-10 x $10^6$ $km^3$ (White and McKenzie, 1989; Eldholm and Grue, 1994; Holbrook *et al.*, 2001). It developed in response to continental break-up of Laurasia when the North American plate began to rift from the Eurasian plate approximately 60 Ma ago (Upton, 1988). The area has had a long history of crustal stretching since Mesozoic times, with thinning of the continental crust and formation of sedimentary basins during the Cretaceous (Anderton, 2000).

The NAIP formed in two main pulses; the first began 62-61 Ma and preceded sea-floor spreading (continental stretching). This first phase comprised a number of central volcanic complexes, as well as several large lava fields (Upton, 1988; Saunders *et al.*, 1997). The rate of magma production slowed ~57 Ma, but increased once again at 56.1 ± 0.5 Ma marking the beginning of Phase 2 (Storey *et al.*, 2007). This, more voluminous, second phase (56-53 Ma) formed during sea-floor spreading (Saunders *et al.*, 1997) and is represented by a 3-8 km thick lava pile, recognised as seaward dipping reflector sequences (Figure 4.1); as well as an addition of ~15 km of igneous material to the lower crust, mostly in the form of sills (White, 1988; White *et al.*, 2008).

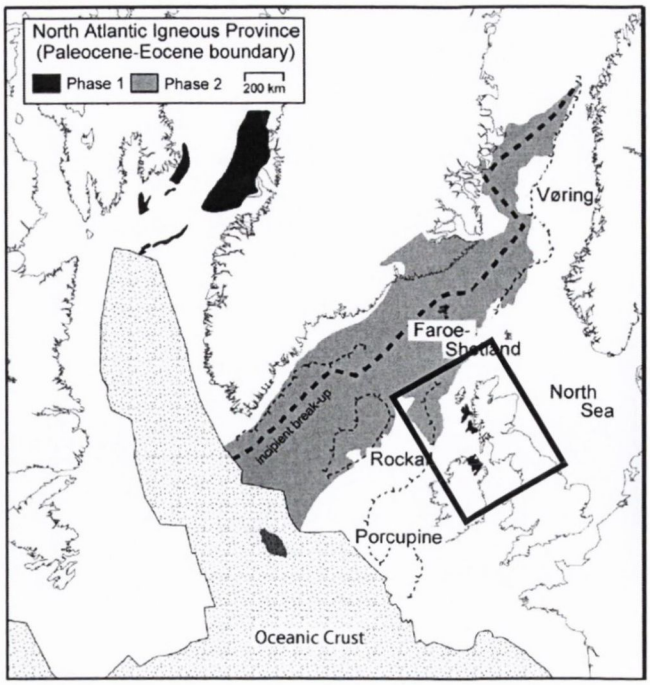


**Figure 4.1 Distribution of magmatism within the North Atlantic Igneous Province. Plates are reconstructed for the Palaeocene-Eocene boundary. Map modified from Saunders *et al.* (2007) - Figure 7. Black box shows area of Figure 4.11.**

## 4.3. Formation of the North Atlantic Igneous Province

Much research has focussed on the formation of the NAIP, and a number of theories have been put forward, ranging from meteorite impact to delamination of the continental lithosphere (Meyer *et al.*, 2007). However, a mantle plume remains the most plausible cause for rifting and magmatism at present (Meyer *et al.*, 2007).

The majority of workers consider continental break-up in the North Atlantic to have occurred due to the interaction of the currently active Iceland mantle plume with continental rift zones (Smallwood and White, 2002). The large head of a *start-up mantle plume* (c.f. Richards *et al.*, 1989; c.f. Campbell and Griffiths, 1990) impacted on the base of the lithosphere and rapidly dispersed, causing initial magmatism over an area 2000 km in diameter, representing Phase 1 of the NAIP. Partial melting is considered to have occurred by decompression melting caused by

active upwelling, elevating mantle temperatures by ~100-150°C (Holbrook *et al.*, 2001; Storey *et al.*, 2007).

Magmatism waned until ~56 Ma, when magma production again increased as the lithosphere thinned and large-scale sea-floor spreading began, with abundant formation of new oceanic crust (Phase 2). This broad area of initial influence quickly reduced to a narrow core, approximately 100 km in diameter (the plume tail), and magmatism focussed on the spreading ridges, as seen today in Iceland and along the North Atlantic mid-ocean ridge (Storey *et al.*, 2007). Assuming the formation of ~50% cumulates, a melt production rate of ~160 $km^3$ per kilometre of rift per million years has been estimated for Phase 1, while a rate of 3000 $km^3$/km/my has been envisaged for Phase 2 (Storey *et al.*, 2007).

### *4.3.1. Parental magma(s)*

Ellam and Stuart (2000) suggested that the NAIP plume had a significant asthenospheric mantle component and they refer to the resulting primary/parental magma as the "North Atlantic End-member (NAEM)". It has strontium and neodymium isotopic ratios akin to depleted mantle (such as an upper mantle N-MORB source), but lead isotope ratios that lie close to the 4.55 Ga geochron (similar to the lower mantle). However, considering the upper mantle-type Sr and Nd isotope signatures, it is likely the similarity of the Pb ratios to primordial lower mantle is coincidental, and therefore they concluded the NAEM had a deep-seated upper mantle source.

Kent and Fitton (2000) also consider the presence of a second mantle source, the 'Icelandic Plume" component, a similarly deep upper mantle source, but relatively enriched in Nb and depleted in other incompatible elements, when

compared to N-MORB. They suggest four main parental magma types (M1-M4), relating to variations in partial melting of these sources. M1 and M2 are tholeiitic to alkalic in composition and represent a partial melt of a depleted N-MORB type source at approximately >100-75 km in depth (garnet-spinel transition field). M1 had a purely N-MORB type source, while M2 gradually incorporated an "Icelandic" source with time. Parental magmas M1 and M2 are recognised throughout the BIPIP.

Magma type M3 is locally known as the Preshal More Tholeiite. It is tholeiitic in composition and represents shallow partial melting (~55 km, spinel field) of an N-MORB source under thinned lithosphere. It is the most common magma type in the Hebrides and Antrim, the BIPIP sites nearest the rifted margins of the NAIP (Kent and Fitton, 2000).

Finally, parental magma type M4 is tholeiitic to mildly alkalic in composition. It represents low degrees of partial melting of a garnet lherzolite (Kerr *et al.*, 1999). M3 and M4 are not seen in the southernmost BIPIP (northern England/Wales/Lundy) (Kent and Fitton, 2000).

## 4.4. The British and Irish Palaeogene Igneous Province

The British and Irish Palaeogene Igneous Province occurs at the south eastern-most extreme of the area influenced by the North Atlantic Igneous Province plume (Figure 4.1, Figure 4.2). This is approximately 1000 km from the centre of the plume head, and there are several theories why such voluminous magmatism occurred so far from the source.

Smallwood and White (2002) (*and references therein*) have suggested the extent and linear expression of the BIPIP relates to intersecting sheets of hot

asthenospheric mantle which have ascended due to instability, evolving into a conventional plume head at the intersection (Figure 4.2).

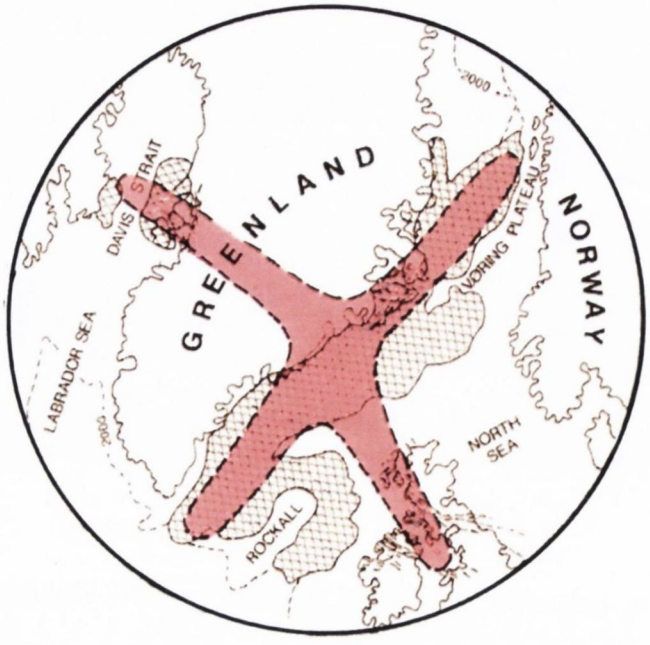


**Figure 4.2 Reconstruction of the North Atlantic at 55 Ma, showing approximate area affected by the mantle plume. Hatched areas are lavas and sills, thin lines are dykes. Area in red represents the axes along which magmatism occurred, suggested to be the surface expression of rising sheets of asthenospheric mantle (Smallwood and White, 2002, Figure 1).**

However, with the availability of detailed seismic data for the regions around the British Isles, it has become apparent that there are many more Palaeogene igneous centres offshore (e.g. Rockall), meaning the BIPIP is probably considerably less linear in its surface expression (compare Figure 4.2 and Figure 4.3).

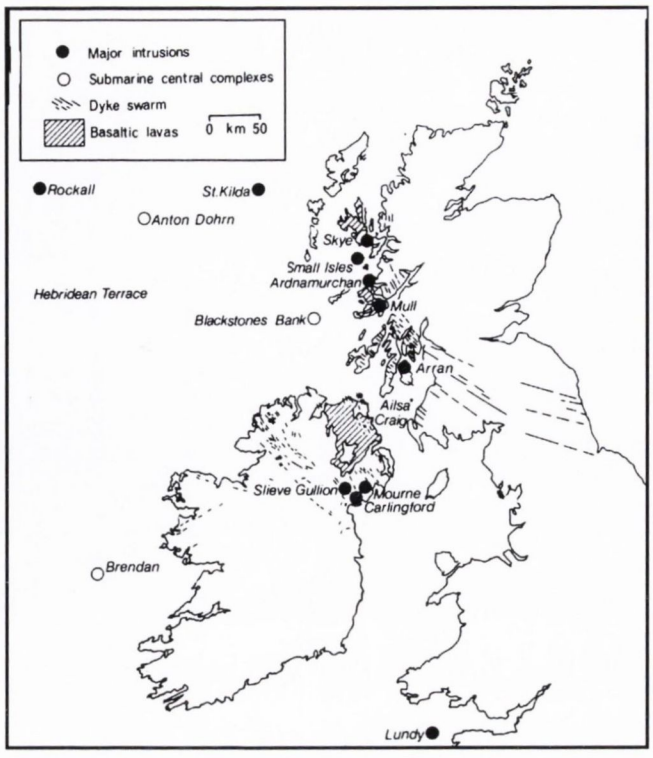


**Figure 4.3 Map of the British and Irish Palaeogene Igneous Province, showing the major onshore and onshore central complexes and lava fields (after Mussett *et al.*, 1988, Figure 1).**

Therefore, as an alternative, *crustal thin spots* have been suggested as the cause for the siting of the British and Irish Palaeogene Igneous Province (Figure 4.4) (Thompson and Gibson, 1991). These crustal thin spots were formed throughout the Mesozoic and caused basin formation, acting as depocentres which resulted in thick successions of Triassic, Jurassic and Cretaceous sediments (Glennie, 2002; Harker, 2002; Hudson and Trewin, 2002). This thinned lithosphere would have focussed magma migration, as well as encouraging decompressional melting, forming central complexes and lava fields, perhaps locally aided by pre-existing faults within these basins and the basement on which they developed (Thompson and Gibson, 1991; Bell and Williamson, 2002).

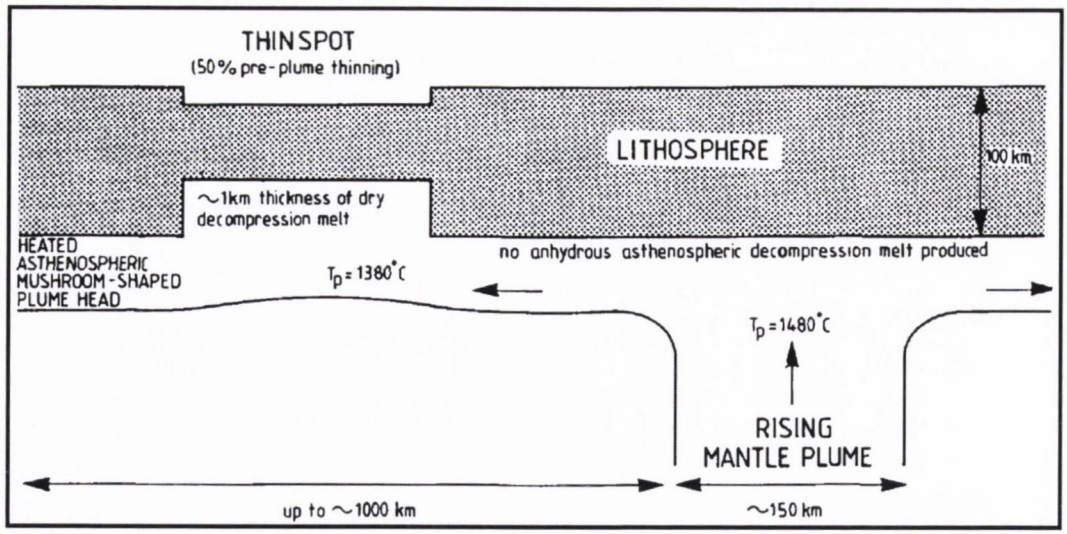


**Figure 4.4 The theoretical effects of crustal thinspots on rising plume magmas. Figure 1 from Thompson and Gibson (1991).**

### *4.4.1. Volcanism within the British and Irish Palaeogene Igneous Province*

The British and Irish Palaeogene Igneous Province mostly formed throughout Phase 1 of the North Atlantic Igneous Province and comprises both lava fields and central complexes. The centres extend from St. Kilda in the north to Lundy in the south and there are extensive lava fields at Skye, Eigg, Mull and in Antrim (Figure 4.3).

#### *4.4.1.1. Lava fields*

The BPIP has four main lava fields. Skye, Eigg and Mull in Scotland and Antrim in Northern Ireland. The Scottish lava fields are associated with, though pre-dating, large central complexes (Skye, Rum and Mull respectively). The Antrim lava field, however, has no associated central complex. The lava fields all formed within the Mesozoic basins of western Scotland and Northern Ireland between 61 and 58

Ma, during Phase 1 of NAIP activity (Cooper and Johnston, 2004; Emeleus and Bell, 2005).

Initial magmatism was often hydroclastic and hyaloclastic, indicating eruption into shallow water, leading on to sub-aerial eruption that was strongly affected by Palaeocene palaeotopography (Figure 4.5). Early flows were often basaltic and hawaiitic in composition, becoming progressively more evolved with time (to mugearite, benmorite and trachyte). Often the less-evolved flows were thin (up to 5 m), getting thicker with more evolved compositions (up to 20 m). Flows gradually filled in the palaeotopography, including narrow valley fills, which cooled with columnar jointing, as seen on Staffa, and at the Giant's Causeway (Figure 4.6) (Bell and Williamson, 2002 *and references therein*).

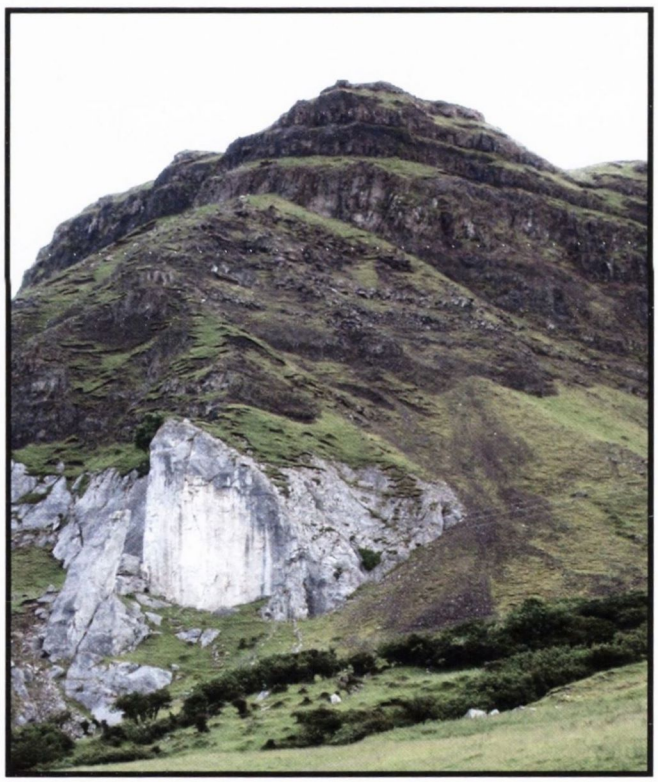

**Figure 4.5 Palaeogene lavas unconformably overlying Mesozoic sediments (Cretaceous Chalk) in north Antrim, N. Ireland.**

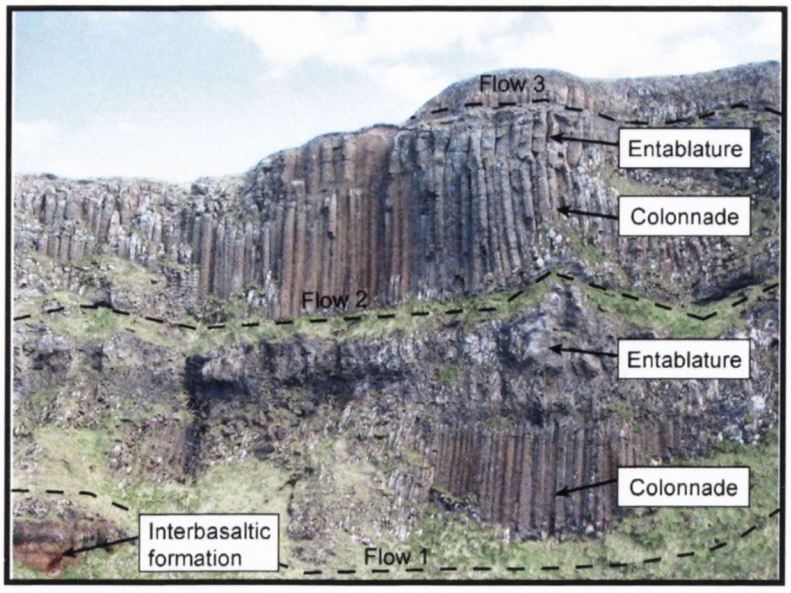


**Figure 4.6 Columnar basalts from the Giants Causeway (Causeway Tholeiite Member), Antrim, showing colonnade and entablature (after Lyle, 2000).**

Many of the lava fields have interbedded sediments, representing hiatuses in volcanism. These boles and palaeosols correspond to time gaps, whereby weathering and deposition occurred between lava flows, the most famous being the *Interbasaltic Formation* of the Antrim Basalts, which represents a time gap of ~1 Ma (Figure 4.6 and Figure 4.7) (Cooper, 2004). During this pause in activity, local extrusive rhyolitic volcanism occurred within the Antrim area, including the Tardree rhyolite dome and the Sandy Braes obsidian (Old, 1975; Cooper, 2004).



**Figure 4.7 The Interbasaltic Formation, including the Post na Spaniagh interbasaltic member (red) lying between the Lower Basalts (below) and the Causeway Tholeiite Member (above).**

#### *4.4.1.2. Central complexes*

The central complexes of the BIPIP represent the eroded roots of large central volcanoes. Variable erosion and faulting throughout the province has resulted in the exposure of various levels of the sub-volcanic system at each centre, from magma chambers (Rum Ultrabasic Intrusion, Arran Northern Granite, Mourne Granites) (Figure 4.8), to the upper reaches of caldera systems/ring-fault intrusions (Slieve Gullion, Rum, Mull, Arran Central Complex) and locally exposed surface eruptive products (Rum, Eigg, Skye) (Figure 4.9) (Bell and Williamson, 2002).

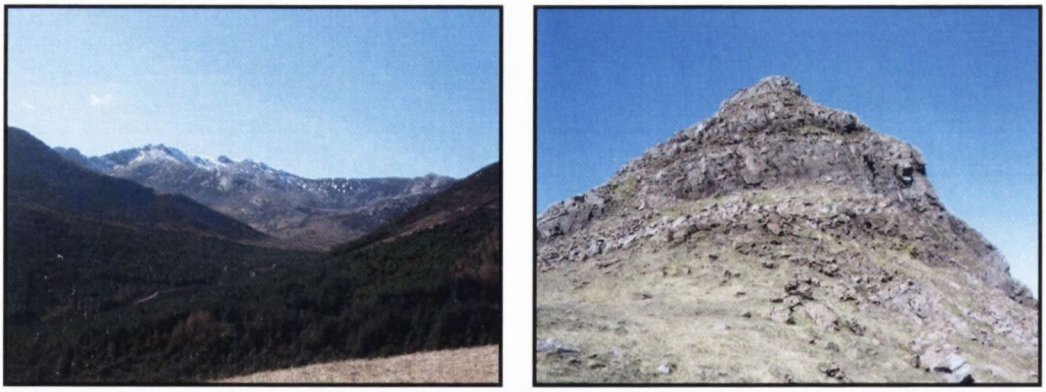

**Figure 4.8 Intrusive igneous rocks of the BIPIP, representing crystallised magma chambers. Northern Granite, Glen Sannox, Arran (left) and the Central Igneous Complex of Rum (peridotite) (right).**



**Figure 4.9 The Slieve Gullion Complex, with a central layered intrusion and a surrounding ring-dyke intrusion, representing the upper-levels of the sub-volcanic system.**

These central complexes appear to be located at intersections of older Caledonian lineaments and the basement highs between the major Mesozoic basins. They were relatively short-lived volcanoes, with magmatism and unroofing at some centres occurring within less than 500 Ka (e.g. Rum) (Hamilton *et al.*, 1998; Chambers *et al.*, 2005; Troll *et al.*, 2008). Despite their short lifespan, these centres had well-developed sub-volcanic systems. These systems were open, and much interaction occurred between the rising/ponding magmas and the surrounding crust.

The development of magma chambers and sophisticated magma storage systems allowed fractional crystallisation to occur, and with that, assimilation, due to the energy release from fractional crystallisation causing large-scale crustal melting. This led to the evolution of silica-rich magmas in the province (Dickin *et al.*, 1981; Gamble *et al.*, 1992; Meighan *et al.*, 1992; Troll *et al.*, 2004; Troll *et al.*, 2005). Almost all centres (Skye, Rum, Mull, Arran, Slieve Gullion, Mourne and Carlingford) have significant granitic and rhyolitic components. Only the Ardnamurchan centre does not have a significant volume of felsic rocks (Bell and Williamson, 2002), however, some rhyolite dykes are present (Geldmacher *et al.*, 1998). Significantly, intermediate rocks are rare at all centres.

### *4.4.2. Bimodal magmatism*

Magmatism within the BIPIP is compositionally bimodal, with large volumes of basalt/gabbro and rhyolite/granite. In contrast, intermediate compositions are both spatially and volumetrically rare, a phenomenon known as the "Bunsen-Daly Gap" (Figure 4.10) (Bunsen, 1851; Daly, 1925). Felsic rocks are almost exclusively associated with the central complexes, where they often form large granitic plutons or laccoliths, e.g. Skye, Arran and Mourne (Thompson, 1969; England, 1992; Stevenson *et al.*, 2007); micro-granite ring-dykes, e.g. Mull and Slieve Gullion (Emeleus, 1962; Sparks, 1988; McDonnell *et al.*, 2004); and thick sill complexes, e.g. Arran and Bute (Smellie, 1914; Harrison, 1925; Kanaris-Sotiriou and Gibb, 1985).

This paucity of intermediate rocks has been a matter of debate for more than 150 years and a number of causes have been suggested. Besides the possibilities of sample bias and trapping of intermediate compositions at lower levels in the magma

system, crustal contamination is currently the main process held responsible (Dickin *et al.*, 1984; Marshall and Sparks, 1984; Geldmacher *et al.*, 1998).

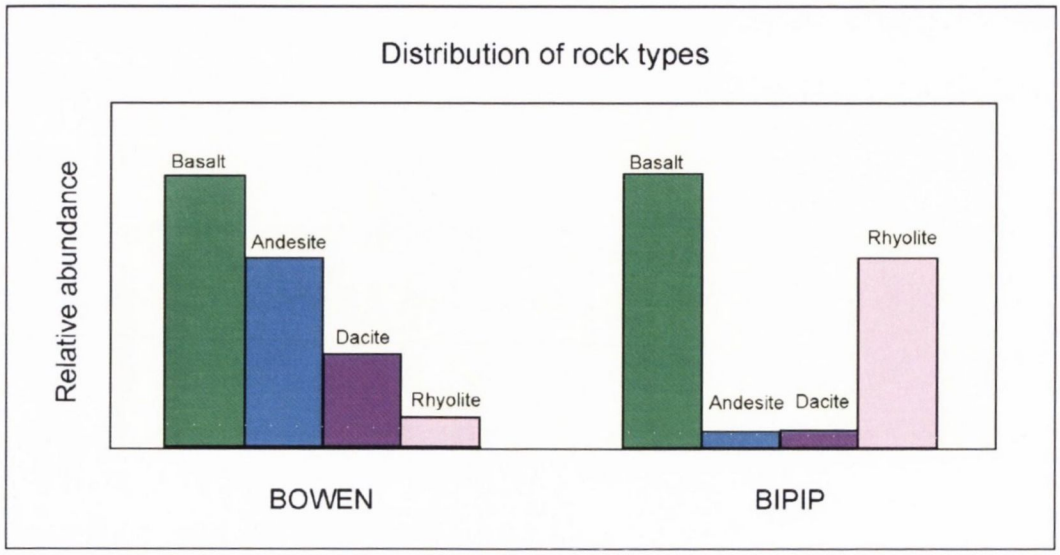


**Figure 4.10 Approximate distribution of magma compositions within the BIPIP (right) compared to the proportions expected if magmas evolved exclusively by Bowen-styled fractional crystallisation (left). The paucity of intermediate compositions is known as the "Bunsen-Daly Gap".**

## 4.5. Regional geology

The northern British Isles comprise five main terranes; the northernmost Hebridean Terrane, the Northern Highlands Terrane, the Grampian Terrane, the Midland Valley Terrane and the Southern Uplands Terrane in the south. All five terranes are exposed sequentially from northern Scotland to northern England, while only the southernmost three are exposed in Ireland. These terranes record a varied and complicated geological history, spanning the last 3000 Ma. This history is summarised below, largely based on Macdonald and Fettes (2007) and the references therein.

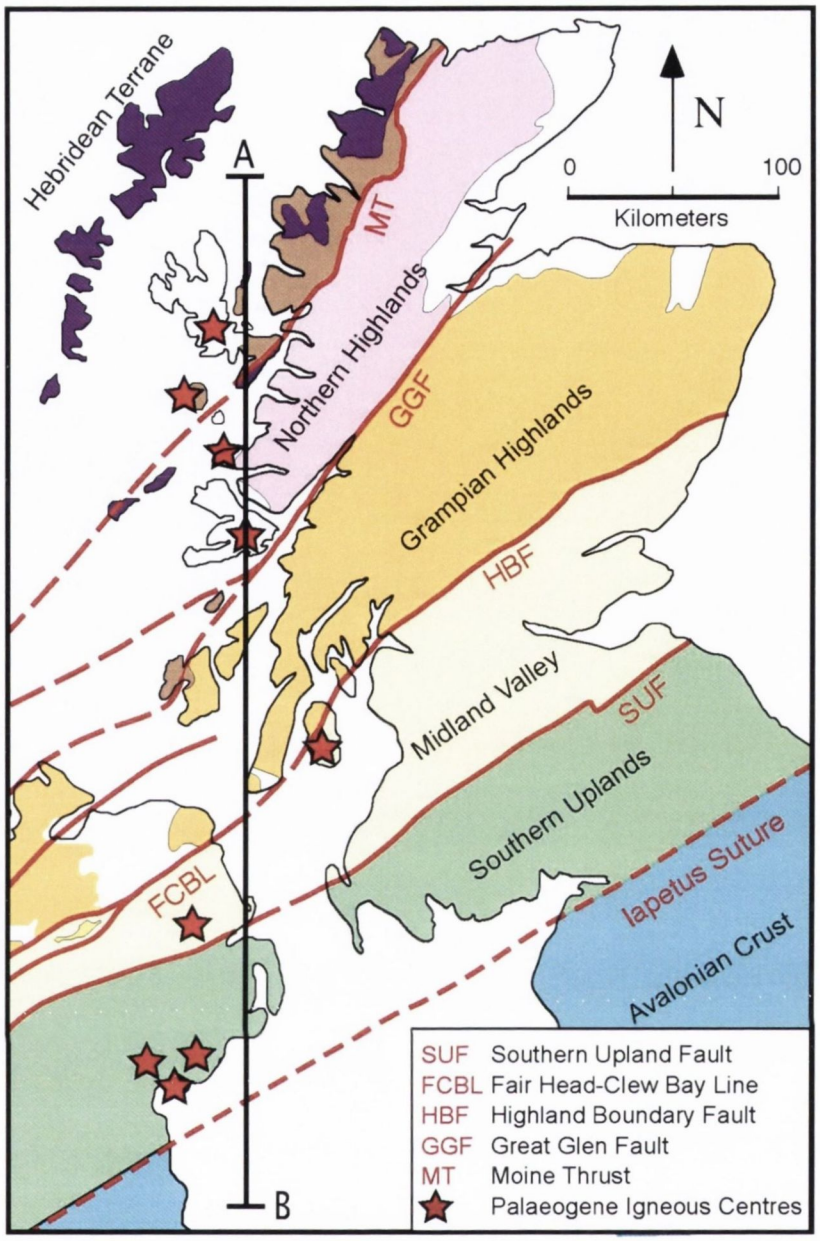


**Figure 4.11 Terrane map of the Northern British Isles. Palaeogene igneous centres are marked as red stars. See also Figure 4.3. Line A-B represents the line along which the cross section seen in Figure 4.12 has been constructed.**

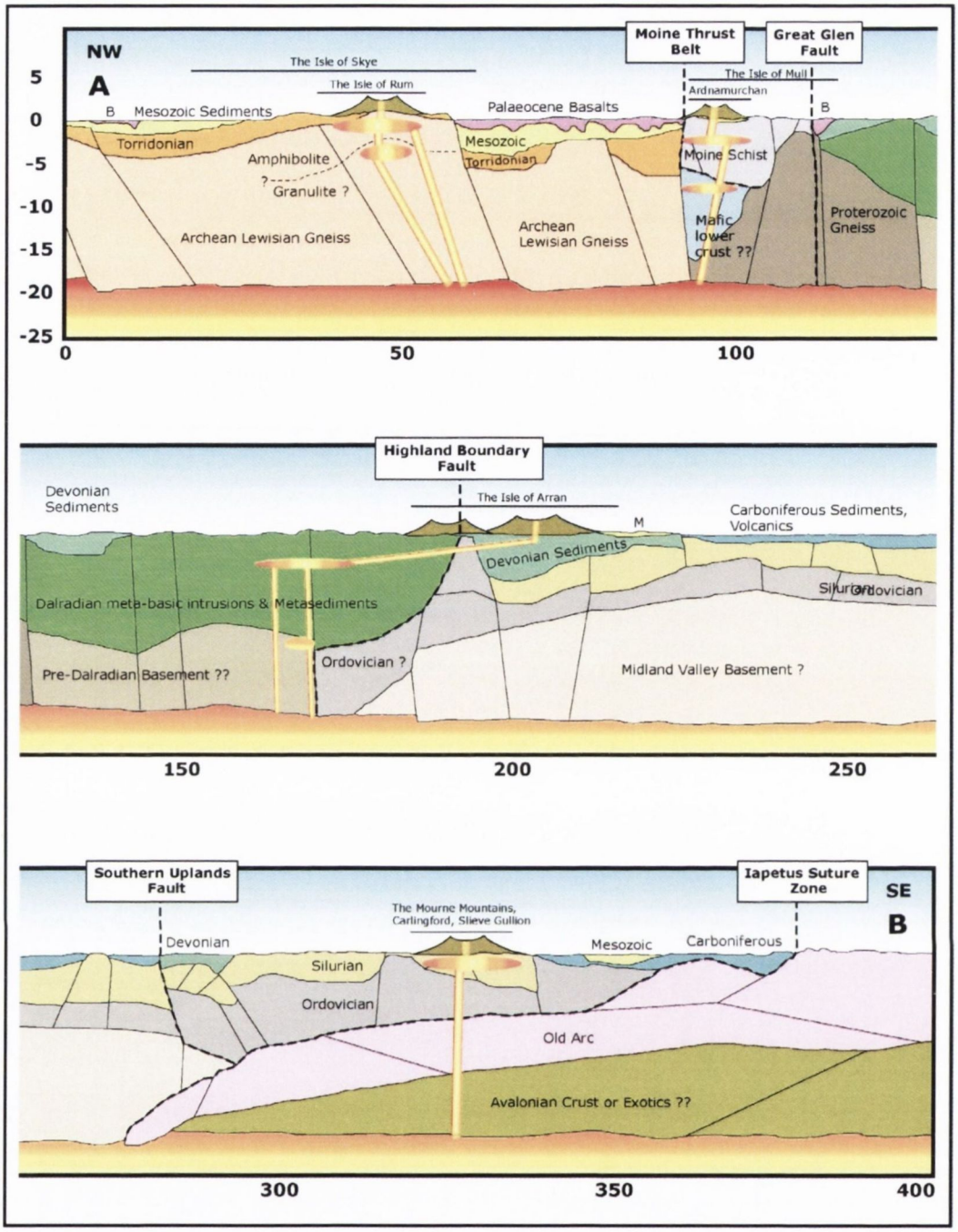


**Figure 4.12 Cross section along line A-B in Figure 4.11. The section was compiled using Figures 1.10 and 1.11 in Trewin and Rollin (2002) and was based on gravity and magnetic data. The magma pathways for the Palaeogene igneous centres of Ireland and Scotland are included (based on this study and that of Nicoll (2008)). Horizontal and vertical scales in kilometres.**

### *4.5.1. The Hebridean Terrane*

The Hebridean Terrane is both the northernmost and oldest terrane in the northern British Isles (Figure 4.11, Figure 4.12). The Archaean Lewisian Gneiss Complex (~3000-1900 Ma) represents the oldest rock suite of NW-Scotland and comprises ancient crust that formed part of the supercontinent Kenorland. It has since been involved in several episodes of metamorphism and deformation and most likely underlies the entire Hebridean Terrane. It also forms the foreland to the younger (overthrust) rocks of the Northern Highlands Terrane. Petrologically, it displays both para- and ortho-gneiss, with extensive metasedimentary rocks intruded by basalts, granodiorites and tonalities. Scourian (2700-2500 Ma) and Laxfordian (~1700 Ma) events have metamorphosed these gneisses to granulite and amphibolite facies, with locally intensely migmatised zones (Trewin and Rollin, 2002; Macdonald and Fettes, 2007).

The Mesoproterozoic to Neoproterozoic Torridonian, a succession of red arkosic sandstones, unconformably overlies the Lewisian Gneisses. They were deposited within a graben on the continent of Rhodinia ~1000-1200 Ma. Zircon ages suggest that the sediment source was not the exposed Lewisian rocks, but rather Precambrian gneisses from Laurentia that give an age range from 2500 to 1100 Ma. On the Isle of Skye, and to the north, the Lewisian and Torridonian rocks are frequently overlain by Cambro-Ordovician shelf deposits, including clastic and carbonate deposits, which formed on the passive margin of Laurentia following the break-up of Rhodinia and the formation of the Iapetus Ocean. The Hebridean Terrane is bounded to the south by the Moine Thrust, and forms the foreland to the over-thrust Northern Highlands Terrane (see Section 4.5.2) (Trewin and Rollin, 2002; Macdonald and Fettes, 2007).

### *4.5.2. The Northern Highlands Terrane*

The Northern Highlands Terrane is bound by the Moine Thrust Belt to the north and the Great Glen Fault to the south (Figure 4.11, Figure 4.12). It consists of extensive outcrops of the Mesoproterozoic Moine Supergroup as well as many inliers of tectonically emplaced exotic gneisses. These Archaean gneisses have not been correlated to the Lewisian gneisses and represent the basement to the Moine rocks, which comprise muds and silts that formed in shallow marine half gräben ~1000-870 Ma (Strachan *et al.*, 2002). These basins formed as East Gondwana rifted from Laurentia (Dalziel and Soper, 2001). The Knoydartian compressional event (~820-750 Ma) caused much of the early deformation in the area, followed by the Grampian Event (480-465 Ma), which significantly deformed the eastern part of the terrane. These events metamorphosed the marine sediments to form schists and psammites. The Scandian Event (435-420 Ma) thrust the terrane several kilometres along the Moine Thrust Fault over the Hebridean foreland to the northwest (Bluck *et al.*, 1997; Macdonald and Fettes, 2007).

### *4.5.3. The Grampian Terrane*

The Grampian Terrane is bounded by the Great Glen Fault to the north and the Highland Boundary Fault to the south (Figure 4.11, Figure 4.12). The Grampian Terrane upper crust comprises the meta-sediments of the Dalradian basin (Anderton, 1982). The basement to the Dalradian has not been directly observed, but has been recognised both geophysically (Hall *et al.*, 1984) and geochemically (Frost and O'Nions, 1985; Dickin and Bowes, 1991; Hitchen *et al.*, 1997; Dickin and Durant, 2002). These authors show crustally contaminated igneous rocks have been

influenced by a composition similar to a Rhinns Complex-type composition (gneiss), and suggest this may compose the underlying basement in the Scottish Grampian Highlands. Work by Daly *et al.* (1991) and Marcantonio *et al.* (1988) links Rhinns Complex gneisses on Islay with those on Inishtrahull in Northern Ireland, extending the region of known Proterozoic gneissic basement to the west. Together, these data suggest the lower crust takes the form of a southward narrowing, wedge-shaped, parallel-sided block, on the order of 600 km (E-W), and extending approximately 100 km N-S, obscured by the overlying Dalradian sequence (Hall *et al.*, 1984; Dickin, 1992).

The terrane is dominated by the Neoproterozoic-Cambrian (~800-520 Ma) rocks of the Dalradian Supergroup, a series of metasedimentary rocks, initially deposited in the Iapetean Dalradian Basin on the passive margin of Laurentia. These sediments were deposited in a deepening basin and comprise sandstones, siltstones and mudstones, which were later metamorphosed to greenshist-amphibolite facies in the Grampian Orogeny (480-465 Ma). This event represented the collision of an island arc with the Laurentian margin as the Iapetus Ocean began to close and was accompanied by extensive granite emplacement (Macdonald and Fettes, 2007).

### *4.5.4. The Midland Valley Terrane*

The Midland Valley Terrane lies between the Highland Boundary Fault and the Southern Uplands Fault (Figure 4.11, Figure 4.12). Structurally, it forms a graben, with mostly Palaeozoic rocks exposed. The Midland Valley Terrane basement is known from xenolith suites in Carboniferous volcanic rocks and comprises both mafic and felsic granulites up to a depth of 7-8 km (Bamford *et al.*, 1977; Graham and Upton, 1978; Halliday *et al.*, 1993). These fragments of

information suggest the Midland Valley basement is likely to be the island arc that caused the Grampian Orogeny (Section 4.5.3). This basement is overlain by both Upper and Lower Palaeozoic sediments, which filled basins throughout the Ordovician, Silurian and Devonian. Carboniferous sandstones throughout Scotland represent deltaic sequences, with shallow marine limestone forming in Ireland (Sevastopulo and Wyse Jackson, 2001). The Permo-Trias, seen in the Arran area, is mostly aeolian and fluvial sandstones (Trewin, 2002).

### *4.5.5. The Southern Uplands Terrane*

To the south of the Southern Uplands fault, and bounded on its southern extreme by the Iapetus Suture, lies the Southern Uplands Terrane (Figure 4.11, Figure 4.12). Once again, only Palaeozoic rocks are exposed with little known of the terrane basement. However, xenolith suites from within Carboniferous lamprophyres show mylonitised meta-sediments, meta-diorites and meta-tonalites that most likely represent an under-thrust meta-igneous succession of Lake District type (island arc) (Anderson and Oliver, 1996).

The exposed rocks of the terrane are Ordovician and Silurian greywackes and mudstones, formed in the Iapetus Ocean (Holland, 2001). On closure of Iapetus these sediments were metamorphosed to greenshist facies and formed an imbricate thrust belt. This event is called the Caledonian Orogeny and influenced both the Midland Valley and Grampian terranes to the north (Phillips, 2001). The southern boundary of the terrane, the Iapetus suture, represents an ancient subduction zone and oceanic arc, and separates the sediments of the "Laurentian" Iapetus from the "Avalonian" Iapetus to the south.

Post-collisional emplacement of highly alkaline magmas occurred widely, both within and around the Caledonian belt. Calc-alkaline granitic plutons intruded throughout the Northern Highlands, Grampian and Southern Uplands terranes, including the Ross of Mull and the Newry granites (Halliday, 1984).

### *4.5.6. Post-accretionary geological history*

Terrane accretion completed with the Caledonian Orogeny and the formation of the supercontinent Laurussia in late Silurian - early Devonian times. The Lower and Upper Old Red Sandstones and conglomerates of late Silurian to early Carboniferous age, such as those on Arran, were deposited by large rivers draining from the N-NE. These Old Red Sandstone deposits, together with the Lower Carboniferous sandstones, siltstones, limestones, and basaltic lavas filled the Midland Valley graben system (Macdonald and Fettes, 2007). In Ireland, the Carboniferous succession is represented by shallow shelf carbonates, rather than interbedded limestones and deltaic sands, as seen in Scotland (Sevastopulo and Wyse Jackson, 2001).

Major sedimentary basins formed from the end of the Palaeozoic, and continued into the Cenozoic, trending approximately N-S. Some marginal basin deposits are found onshore (e.g. northwest Rum, western Arran) while many others are preserved offshore (Glennie, 2002; Harker, 2002; Hudson and Trewin, 2002). These basins represent the onset of crustal thinning in the region, ultimately leading to the opening of the North Atlantic Ocean and culminating in the formation of the North Atlantic Igneous Province during the Palaeogene (Thompson and Gibson, 1991; Anderton, 2000).

## 4.6. The centres of the southern British and Irish Palaeogene Igneous Province

### *4.6.1. Carlingford*

The Carlingford Igneous Centre lies within the Southern Uplands Terrane in Co. Louth, northeastern Ireland. It is the only BIPIP centre entirely in the Republic of Ireland. It formed ~60 Ma years ago (Thompson, 1986) and the earliest activity preserved is a series of basaltic lavas exposed in the south of the centre. These are the sole evidence for the centre's extrusive past. The oldest Palaeogene intrusion recorded is the 'Early Gabbro' of Trumpet Hill, followed by the loppolithic 'Later Gabbros' (Le Bas, 1960). Subsequently, they were intruded by a granophyric micro-granite ring-dyke (Le Bas, 1967) (Figure 4.13).

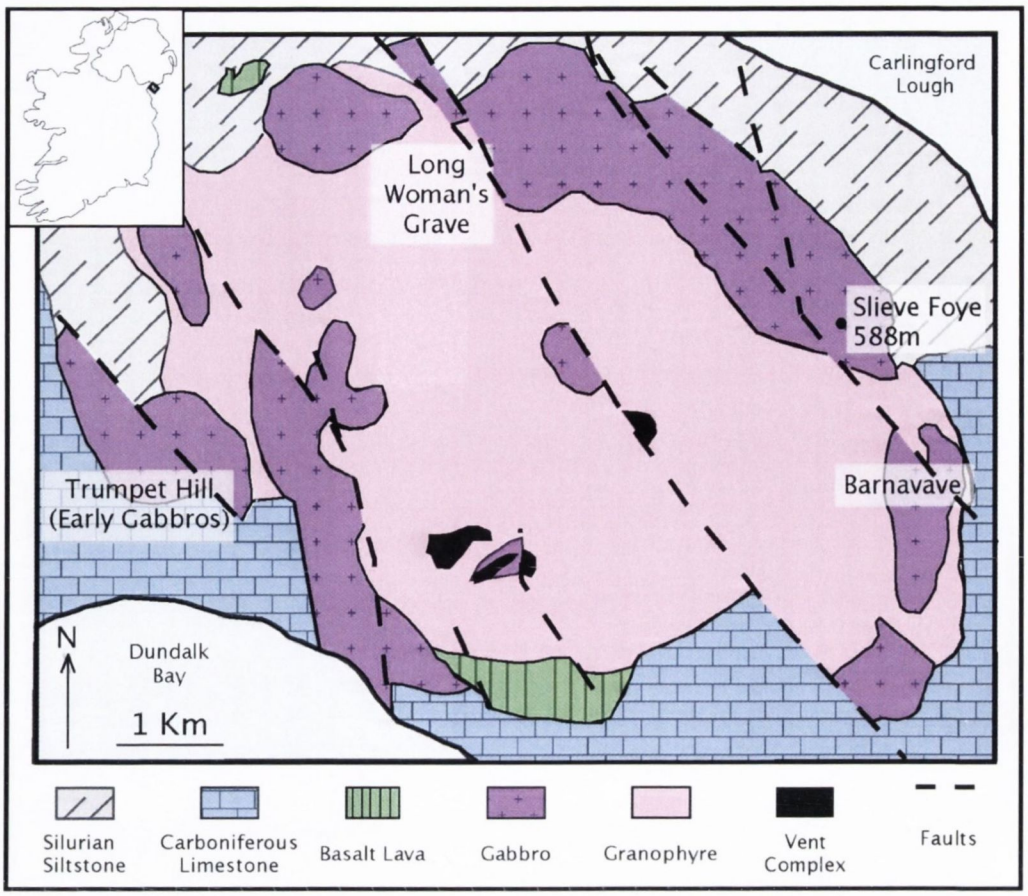


**Figure 4.13 Geology of the Carlingford Igneous Centre (modified from Le Bas, 1967)**

Allen *et al.* (2002) suggested these intrusions were emplaced at ~3-4 km below an extrusive volcanic edifice. Finally the major intrusions were crosscut by a series of aphyric to highly porphyritic basaltic cone-sheets with subordinate rhyolite, basaltic-andesite and trachy-andesite, representing the final phase of intrusive activity preserved at the Carlingford Igneous Centre.

### *4.6.2. Arran*

The Isle of Arran lies within the Firth of Clyde, south-western Scotland. Palaeogene igneous activity on Arran spanned 3 million years, from 61-58 Ma

(Hodgson *et al.*, 1990) and was focussed on two main centres, the Northern Granite (Flett, 1942; England, 1992; Goulty *et al.*, 2001) and the Central Complex (King, 1954; King, 1955; King, 1959; Emeleus and Sutherland, 1982) (Figure 4.14). Arran is also characterised by several pulses of minor intrusion, including a well-developed regional N-S basaltic dyke swarm (Speight *et al.*, 1982).

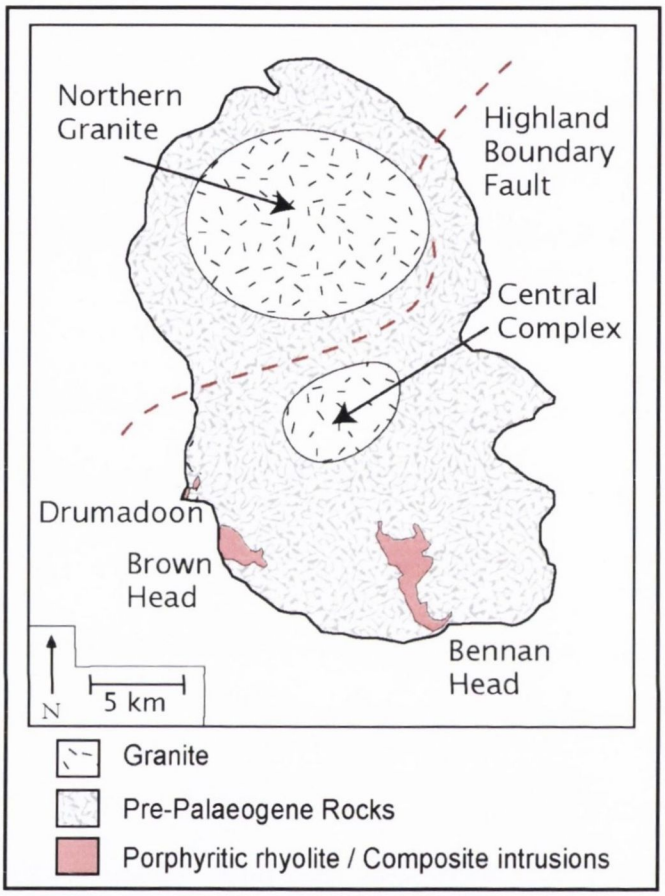


**Figure 4.14 Distribution of Palaeogene igneous rocks on the Isle of Arran**

One of the more distinctive minor intrusive events comprises a series of quartz and feldspar-phyric rhyolites (Figure 4.14). These rhyolites are seen both as large single intrusions (e.g. Brown Head) and as composite dykes and sills with basaltic-andesite margins such as the Drumadoon Intrusive Complex and Beannan Head (Judd, 1893; Harrison, 1925; Kanaris-Sotiriou and Gibb, 1985). The

Drumadoon Intrusive Complex lies to the south of the Highland Boundary Fault, and consists of a dominantly quartz-feldspar-phyric rhyolite sill and the composite intrusions of Drumadoon Point and An Cumhann (comprising a central porphyritic rhyolite flanked by xenocryst-bearing dolerite and zones of porphyritic dacite).

### *4.6.3. Mourne*

The Mourne Igneous Centre is also situated in the Southern Uplands Terrane, and intrudes into crust that is similar to that around Carlingford. The complex consists of a series of five granites, divided into two centres – the Eastern (G1-G2) and Western Mournes (G3-G5) (Figure 4.15) which intruded approximately 56 Ma (Meighan *et al.*, 1984; Gibson *et al.*, 1987; Gamble *et al.*, 1999). These centres were considered by Richey (1927) and Hood (1981) to be a series of stacked ring-dykes relating to cauldron subsidence. However, recent work by Stevenson et al (2007) envisages them to be laccolithic intrusions.

The Glasdrumman composite cone-sheet is exposed at Glasdrumman Port, south of Newcastle, Co. Down and ranges from 12-30 m thick. It is considered to be a cone-sheet to the Mourne granite complex and is exposed sporadically around the north and east of the granites (Akiman, 1973). It is comprised of thin outer basaltic margins, narrow inner zones of dark quartz and feldspar-phyric rhyolite with large feldspar phenocrysts and blobs of basalt and a thick inner pink quartz and feldspar-phyric rhyolite member, forming the majority of the intrusion.

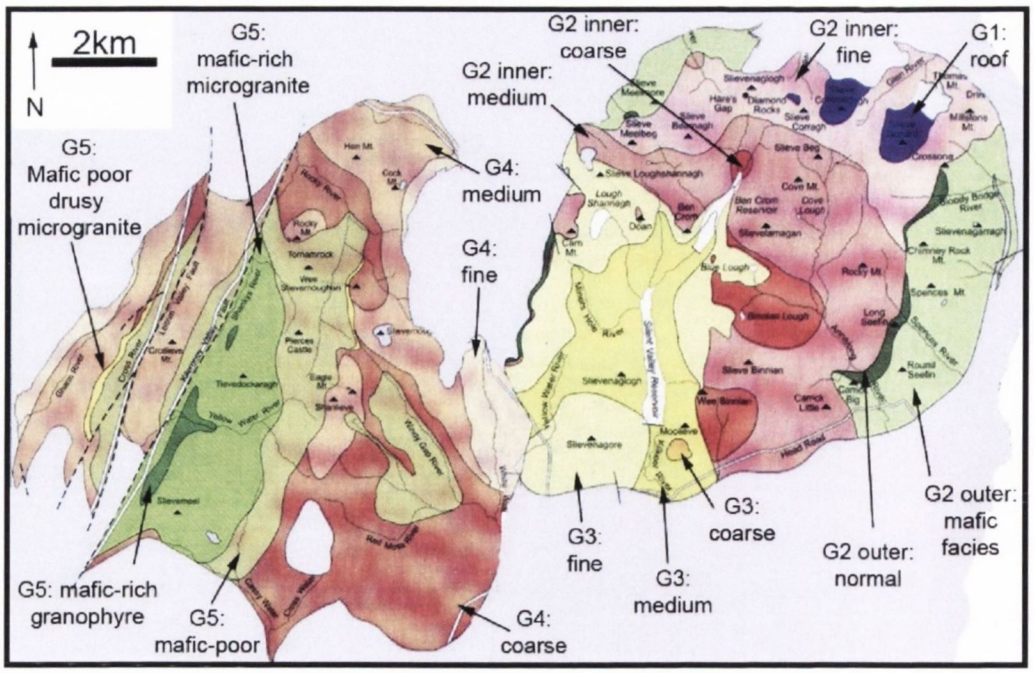


**Figure 4.15 Map of the eastern and western Mourne granite centres, showing the main granites and their facies. Grey background represents the Longford-Down metasediments (country-rock). Map after Cooper and Johnston (2004), figures 15.3 and 15.4. These figures use the data of Hood (1981) and Gibson (1984).**

### *4.6.4. Slieve Gullion*

The Slieve Gullion Igneous Centre formed 56-57 Ma (Meighan *et al.*, 1988; Gamble *et al.*, 1999). It comprises an early ring-complex formed of porphyritic felsite and granophyre, with explosive vent aggregates representative of near-surface volcanism (Richey, 1932; Richey and Thomas, 1932; Emeleus, 1962) (Figure 4.16). Subsequently the centre was intruded by the central Layered Complex, a sequence of flat-lying mafic and felsic sheets (Reynolds, 1951; Gamble, 1979b; Gamble, 1979a; Gamble *et al.*, 1992) (Figure 4.9, Figure 4.16).

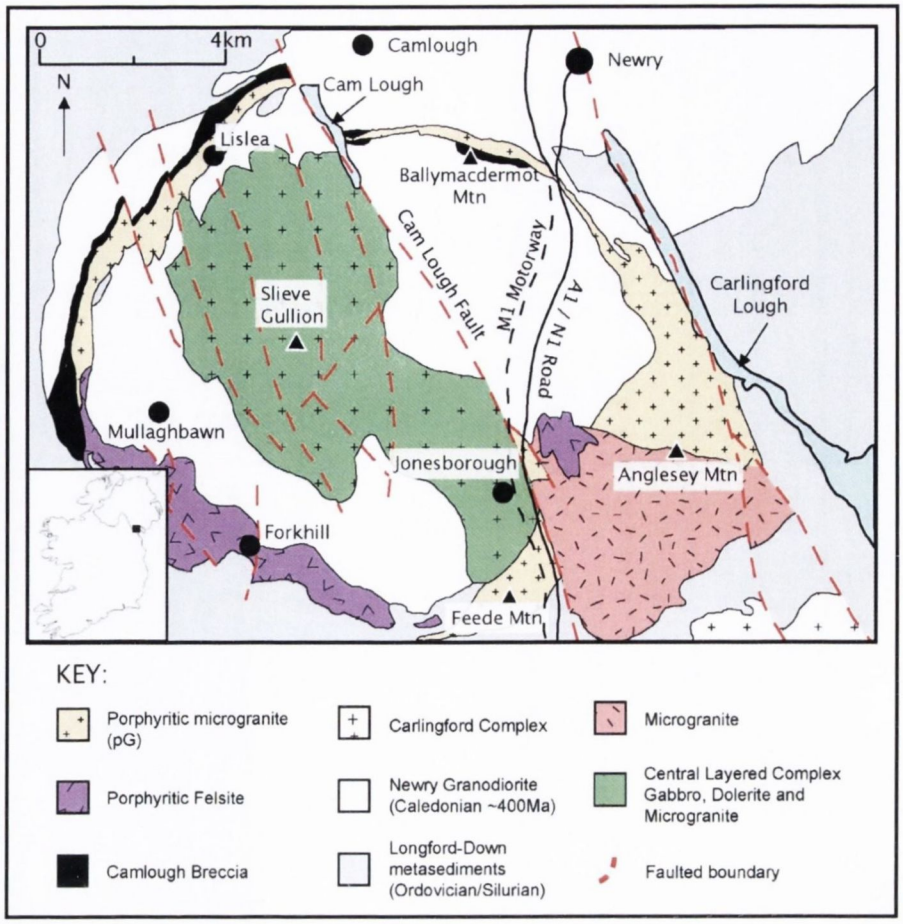


**Figure 4.16 Generalised geology of the Slieve Gullion area**

A number of mechanisms for emplacement of the Slieve Gullion ring centre have been proposed, with Richey's ring-dyke model being widely accepted for the last 80 years (Richey, 1932; Richey and Thomas, 1932; Emeleus, 1962; McDonnell *et al.*, 2004). A recent re-investigation by Stevenson *et al.*(2008), however, proposes a different mode of emplacement. These authors suggest that an early caldera-like volcanic vent complex was intruded by a sub-horizontal sheet of porphyritic microgranite, prior to emplacement of the central layered intrusion.

There is also controversy regarding the age-relationship between the adjacent Carlingford and Slieve Gullion centres. Fieldwork has suggested cone-sheets from the Carlingford centre crosscutting a late microgranite intrusion (Anglesey

Mountain) at Slieve Gullion; however, radiometric dates for both centres suggest Slieve Gullion is in fact younger (Meighan *et al.*, 1988). This relationship is based on dates for the central Layered Complex. Recent $^{40}Ar$-$^{39}Ar$ dating by the Geological Survey of Norway (for which the author supplied the samples) suggests that the Slieve Gullion ring-dyke is older than the Layered complex, however (60.42 ± 0.54 Ma) (M. Ganerød *pers. comm.*), and may be contemporaneous with activity at Carlingford (60.9 ± 0.5 Ma) (cf. Thompson, 1986).

### *4.6.5. Tardree*

The Tardree Rhyolite Complex lies to the southeast of the town of Ballymena, Co. Antrim. It is ~26 km$^2$ and comprises a rhyolite dome and lavas, along with ashes, tuffs and agglomerates representing the products of vent eruptions, as seen at Sandy Braes (Figure 4.17). The rhyolite is pale grey in colour and often columnar. It contains phenocrysts of plagioclase feldspar and quartz. The Sandy Braes Obsidian is a porphyritic black, glassy, welded tuff (Old, 1975; Cooper, 2004).

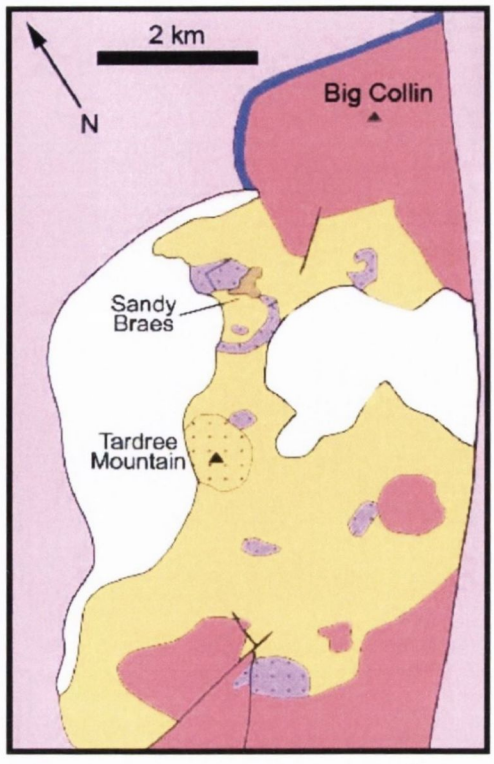


**Figure 4.17 Map of the Tardree Rhyolite Complex, including the Sandy Braes vent. After Cooper (2004), figure 14.6a. Key: pale pink - Lower Basalt Formation, dark pink – Upper Basalt Formation, white – drift cover, blue – Interbasaltic Formation, orange – rhyolite flows, stippled pale pink – pyroclastic rocks, stippled orange – columnar rhyolite, brown – vent agglomerate.**

# 5. METHODS

*Details of the techniques used throughout this study, including the labs visited, machine settings, analytical errors, laboratory blanks and repeatabilty studies of the data.*

## 5.1. Sample selection and preparation

Representative samples of the main igneous and country rock lithologies exposed at each centre were collected. These samples were sliced and weathered edges removed and then crushed in a jaw-crusher to centimetre-sized chips. Chips were washed and representative fresh chips were picked to form a pristine sample. Care was taken not to fractionate porphyritic samples. Chips were powdered in a tungsten carbide TEMA mill. All powders were analysed for major and trace elements and a selected sample set was analysed for rare earth elements and strontium, neodymium and lead isotope ratios.

## 5.2. X-Ray fluorescence

Whole-rock samples were analyzed for major element oxides and trace element concentrations by X-ray fluorescence (XRF) spectroscopy. Three laboratories were used for different sub-projects: GEOMAR Research Centre, Kiel, Germany, the University of St. Andrews, Scotland and Centre d'Analyses Minérale, University of Lausanne, Switzerland.

### *5.2.1. GEOMAR*

Samples were analysed on fused beads using a Philips PW1480 spectrometer. Analyses were performed with a Rh tube and calibration was performed using international geological reference samples. $H_2O$ and $CO_2$ were analysed upon ignition of powders at 1200 °C using a Rosemount CWA 5003 infrared photometer. See Abratis et al. (2002) for further details.

#### *5.2.2. University of St. Andrew's*

Samples were analysed using fused beads on a Spectro X-Lab EDP XRF. All analyses were performed with a Rh tube and calibration was performed using international geological reference samples (http://www.st-andrews.ac.uk/~acc/MAS.htm).

#### *5.2.3. Centre d'Analyses Minérale, University of Lausanne*

Whole-rock samples were analyzed for major oxides by X-ray fluorescence (XRF) spectroscopy using a Phillips PW 1400 spectrometer. Trace elements were not analysed (http://www.unil.ch/cam/page28569_en.html).

## 5.3. X-Ray diffraction

Rock powders were analysed by X-ray diffraction at the Department of Geology, Trinity College Dublin using a Phillips PW1720 X-ray generator with a Phillips PW1050/25 diffractometer and a Phillips PW3313/20 Cu k-alpha anode tube. Results were compared to the "Traces" database (Hiltonbrooks Ltd, http://www.xrays.u-net.com/Software.htm) for mineral identification.

## 5.4. Inductively coupled plasma mass spectrometry

#### *5.4.1. Scottish Universities Environmental Research Centre*

Rare earth elements and U, Th and Pb concentrations of whole-rock powders were determined by inductively coupled plasma mass spectrometry (ICP-MS) at SUERC, East Kilbride, Scotland (http://www.gla.ac.uk/surrc/), using VG Elemental

PQ2 plus ICP-MS fitted with a Meinhard nebulizer and a water-cooled glass, Scott, double pass, spray chamber. For further details on the instrument settings and procedures see Olive *et al.* (2001). Analyses of geological reference standard BCR-1 (n=36) yielded mean values and standard deviations as seen in Figure 5.1 and Table 5.1.

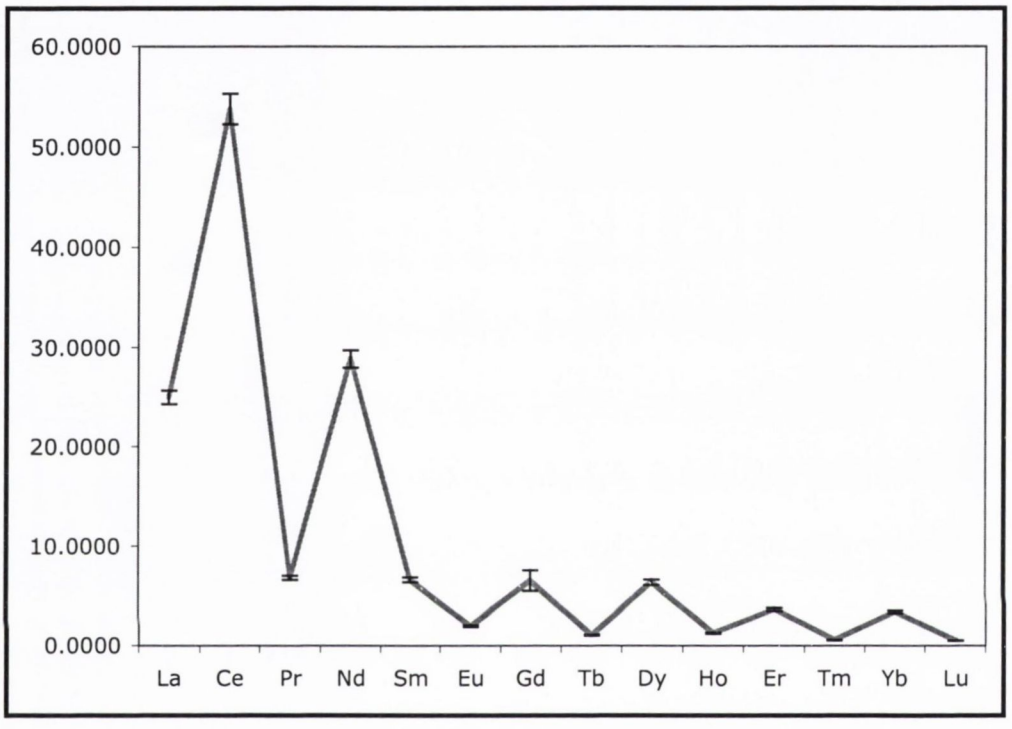


**Figure 5.1 Mean values for 36 analyses of the standard, BCR-1 (grey line), with error bars marking the standard deviation of the data. Note the saw-tooth pattern of the values (Oddo-Harkins effect).**

| | La | Ce | Pr | Nd | Sm | Eu | Gd |
|---|---|---|---|---|---|---|---|
| ***BCR-1 values*** *(Raczek et al., 2001)* | **25.10** | **53.30** | **6.79** | **29.00** | **6.61** | **1.97** | **6.70** |
| **Mean** *(n=36) (ppm)* | 24.97 | 53.77 | 6.81 | 28.87 | 6.61 | 1.95 | 6.56 |
| **Standard Deviation** *(ppm)* | 0.68 | 1.50 | 0.19 | 0.86 | 0.23 | 0.07 | 1.05 |

| | Tb | Dy | Ho | Er | Tm | Yb | Lu |
|---|---|---|---|---|---|---|---|
| ***BCR-1 values*** *(Raczek et al., 2001)* | **1.07** | **6.43** | **1.27** | **3.68** | **0.54** | **3.40** | **0.50** |
| **Mean** *(n=36) (ppm)* | 1.06 | 6.38 | 1.27 | 3.65 | 0.56 | 3.41 | 0.52 |
| **Standard Deviation** *(ppm)* | 0.04 | 0.29 | 0.06 | 0.17 | 0.03 | 0.18 | 0.03 |

**Table 5.1 Table of mean values for 36 analyses of BCR-1 for rare earth elements with standard deviations, indicating the precision of the data. For a measure of accuracy, the data are compared to the published data for BCR-1 (Raczek *et al.*, 2001). These data all lie with the standard deviation of the data from the current study.**

### *5.4.2. Institute F. - A. Forel*

Rare-earth element and trace element concentrations of whole-rock powders were determined by inductively coupled plasma mass spectrometry (ICP-MS) using a Hewlett Packard 4500 at the Institute F. - A. Forel, Versoix, Switzerland (http://www.unige.ch/forel/index.html).

## 5.5. Whole-rock isotope geochemistry

Whole-rock strontium, neodymium and lead isotope ratios were analysed at the Scottish Universities Environmental Research Centre (SUERC) (http://www.gla.ac.uk/surrc/) and at the Department of Mineralogy, University of Geneva, Switzerland (http://www.unige.ch/sciences/terre/mineral/isotopes/min_isotopes_labo.html).

All data were corrected to time of crystallisation using the trace element concentrations of parent and daughter elements. Therefore errors in the XRF data are incorporated into the age-corrected data. These errors can have a particularly strong effect in the age correction of strontium isotope ratios. In samples where the ratio of parent to daughter concentrations is low (e.g. Rb ppm < Sr ppm) these introduced errors are low (often less than the error in measuring the isotope ratio in the first place). Higher relative concentrations of parent elements to daughter elements (e.g. Rb ppm > Sr ppm) introduce higher errors into the age-correction. High levels of Rb mean large amounts of radioactive decay has occurred since the time of intrusion and the correction from $ratio_{measured}$ to $ratio_{initial}$ is greater.

### *5.5.1. Strontium isotope ratios*

#### *5.5.1.1. Scottish Universities Environmental Research Centre*

Sr was separated using standard cation exchange techniques (see Appendix 1) with a single pass through Bio-Rad AG50W X8 200-400 resin. It was then loaded on single Ta filaments with 1M phosphoric acid. Isotope ratios were measured on a VG Sector 54–30 thermal ionisation mass spectrometer (TIMS) (Figure 5.2) in dynamic multi-collection mode and corrected for instrumental mass fractionation

using an exponential law and $^{87}Sr/^{86}Sr = 0.1194$. Total procedure blanks are <300 pg. The internal laboratory Sr Standard (NBS987) was analysed at 0.710254 ± 0.000018 (2SD) for the period of the study.



**Figure 5.2 Thermal ionisation mass spectrometer at SUERC, Scotland.**

### *5.5.1.2. Department of Mineralogy, University of Geneva*

Sr was isolated using the method of Deniel and Pin (2001). Sr isotope ratios were measured using a seven-collector Finnigan MAT 262 thermal ionization mass spectrometer with extended geometry and stigmatic focusing using double Re filaments. The $^{87}Sr$ / $^{86}Sr$ ratios were measured in semi-dynamic mode and were mass fractionation corrected to a $^{88}Sr$ / $^{86}Sr$ ratio of 8.375209, and normalized to the $^{87}Sr$ / $^{86}Sr$ ratio of 0.708000 for the Eimer and Amend $SrCO_3$ standard. Measured values of this standard during the period of this study were 0.708019 (2 S.E., n =82).

### *5.5.2. Neodymium isotopes*

#### *5.5.2.1. Scottish Universities Environmental Research Centre*

A rare earth element fraction was collected by cation exchange from the same samples as the Sr fraction. Nd was then separated using standard anion exchange chemistry (see Appendix 1) (Figure 5.3) and analysed using a VG Sector 54–30 thermal ionisation mass spectrometer (TIMS) (Figure 5.2). The internal laboratory Nd Standard (Johnson Matthey, J&M, http://www.matthey.com) was analysed with values of 0.511504 ± 0.000009 (2SD) for the period of the study.

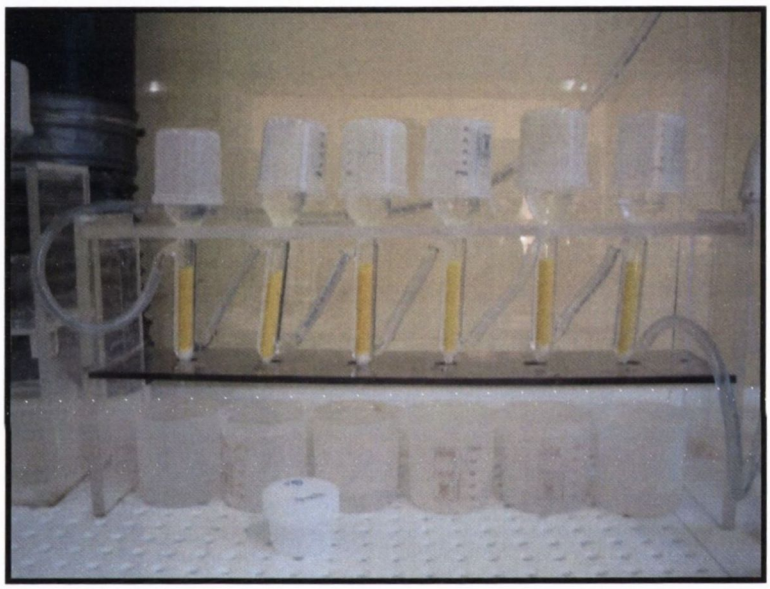

**Figure 5.3 Cation exchange columns for the separation of Nd from a REE solution, at SUERC, Scotland.**

#### *5.5.2.2. Department of Mineralogy, University of Geneva*

Neodymium isotope analyses were carried out at the Department of Mineralogy, University of Geneva, Switzerland. Sm and Nd concentrations for age-correcting the isotopic data used the values determined by ICP-MS. Neodymium isotope ratios were measured on a seven-collector Finnigan MAT 262 thermal

ionisation mass spectrometer with extended geometry and stigmatic focussing, using double Re filaments. $^{143}Nd/^{144}Nd$ was measured in a semi-dynamic mode (quadruple collectors, measurement jumping mode), mass fractionation corrected to $^{146}Nd/^{144}Nd = 0.721903$, and normalised to the La Jolla standard (0.511837). The mean of 101 replicated analyses of this standard is $0.511837 \pm 2(2\sigma)$ (over the lifetime of the lab).

#### *5.5.3. Lead isotopes*

##### *5.5.3.1. Scottish Universities Environmental Research Centre*

Lead chemistry was performed separately and was analysed by a Micromass Isoprobe MC-ICP-MS, using the techniques detailed in Ellam (2006). Total procedural blank was 352 pg. Measurements of NIST SRM981 were used to correct the data for inaccuracies. Uncorrected NIST SRM981 gave values of $^{206}Pb/^{204}Pb = 16.939 \pm 31$, $^{207}Pb/^{204}Pb = 15.497 \pm 19$, $^{208}Pb/^{204}Pb = 36.719 \pm 64$ (2 s.d. N= 12).

## 5.6. Electron microprobe

Feldspar major element compositions were determined using a JEOL JCXA 733 electron microprobe at the University of St. Andrews, Scotland. Analytical conditions included an acceleration voltage of 15 kV, a beam current of 8–20 nA, and counting times of between 20 and 60 s on peaks. A rastered beam was used (ca. 12 $\mu m^2$) and calibration was performed using natural and synthetic minerals as standards. Backscattered electron (BSE) images of feldspars were also collected.

## 5.7. Microdrilling and micro-Sr isotope analysis

Microdrilling for the Sr isotope ratios of individual feldspar zones was carried out using a Merchantek Micromill at the University of Durham, UK (Figure 5.4). Firstly, zones were identified both optically and in backscattered electron images (see section 5.6) of polished thick sections. Using the microdrill software, drill paths within zones were chosen, taking care to avoid inclusions and fractures within the crystals (Figure 5.5). The zones chosen for drilling were greater than ~60 μm to be sure they could be drilled without the danger of contamination from adjacent zones (Figure 5.6). Wide zones also afforded larger sample yields, as 3 ng of Sr was recommended for analysis. Paths were then automatically drilled and powder was collected in a drop of ultra-pure water for micro-analysis of $^{87}Sr/^{86}Sr$ isotope ratios. The milling technique and subsequent micro-chemistry are described in more detail in Charlier *et al.* (2006). The Carlingford sample set yielded between 1.9 and 13 ng of Sr per zone drilled and all samples were analysed successfully for $^{87}Sr/^{86}Sr$ isotope ratios. The internal laboratory Sr Standard (NBS987) was analysed at 0.710259 ± 0.000012 (2SD) for the period of the study (June-July 2006).

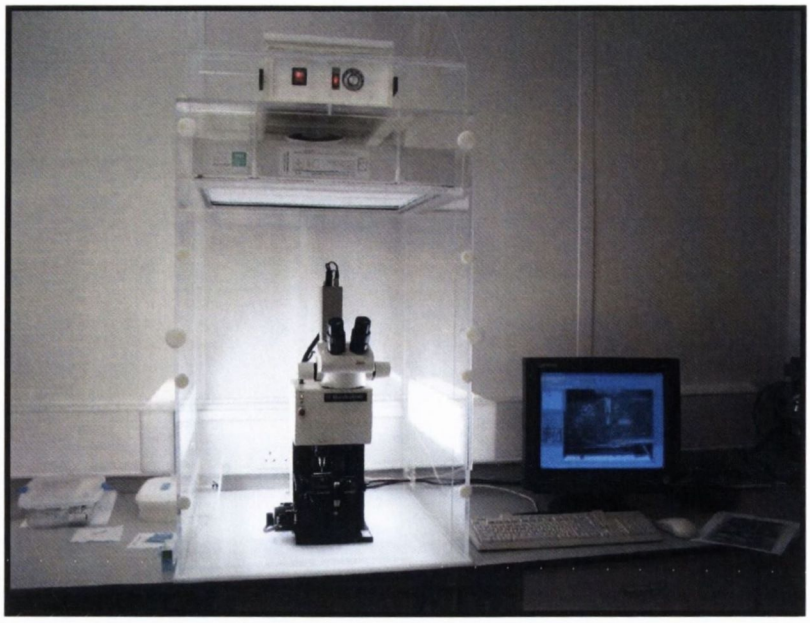

**Figure 5.4 Microdrilling setup at University of Durham, including drill within an over-pressured Perspex clean box and attached computer monitor.**

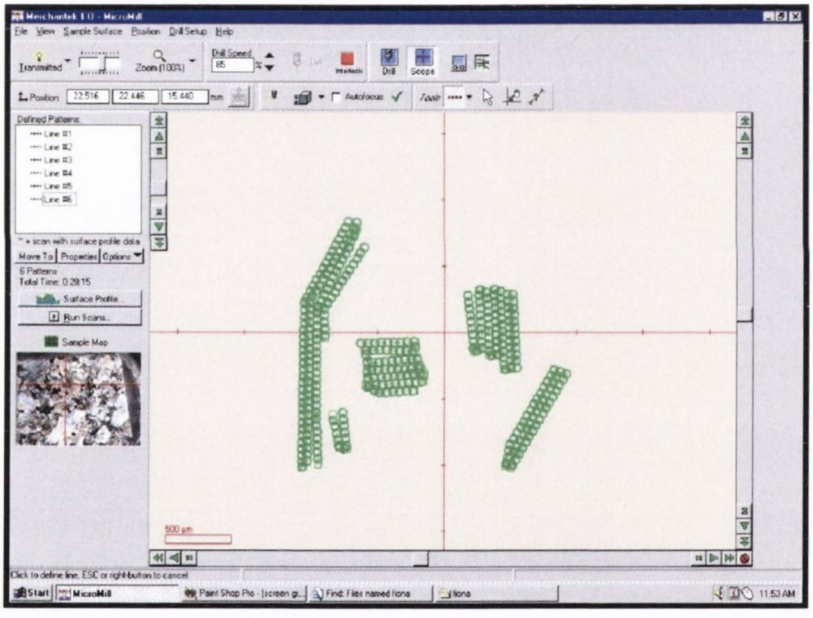


**Figure 5.5 Screen grab of Merchantek Micromill software showing chosen drill paths. The live video image of the crystal does not copy with the screen grab.**

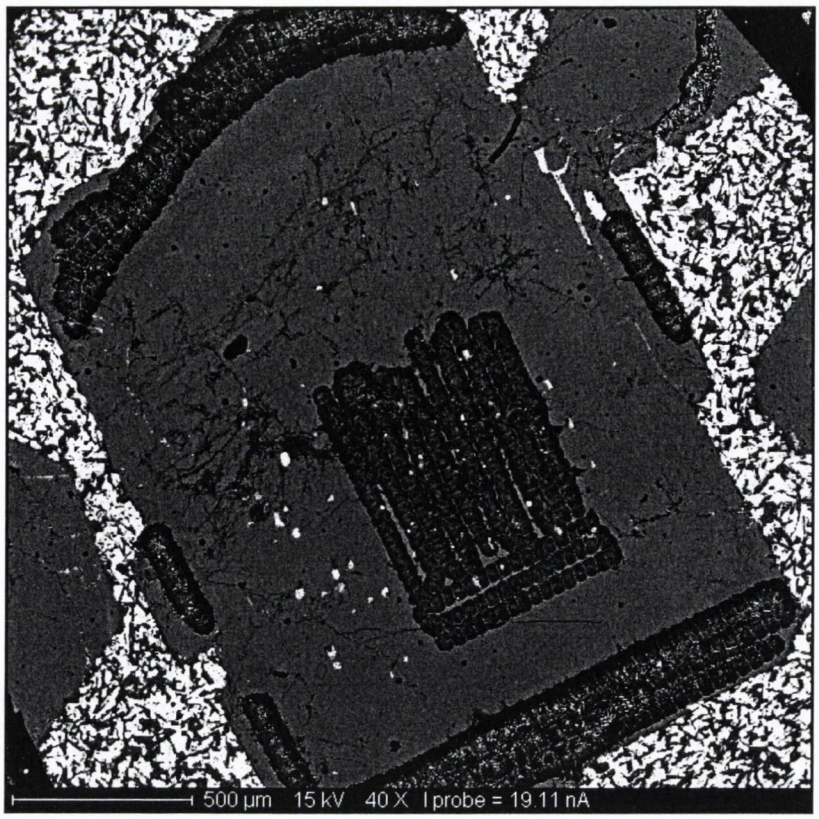


**Figure 5.6 A back scattered electron image of a feldspar that has been micro-drilled. Note the drill paths, showing the collection of two samples, the first from an outer zone and the second from the centre of the crystal.**

## 5.8. Age dating

Two large (5 mm) potassium feldspar crystals were dated at the $^{40}Ar$–$^{39}Ar$ geochronology laboratory at the University of Lund, Sweden. The crystals were loosely crushed in a pestle and mortar and a sieved fraction of 250-500 µm was picked for $^{40}Ar$–$^{39}Ar$ dating. One sample (DD-U) was leached in a dilute HF (5%) solution at room temperature for ten minutes to remove any loosely bound isotopes from alteration on the crystal rims. Both samples were washed several times in deionised water in an ultrasonic bath.

The crushed potassium feldspar crystals were analysed, using a Micromass 5400 mass spectrometer with a Faraday detector and an electron multiplier, a metal

extraction line, containing two SAES C50-ST101 Zr–Al getters and a cold finger cooled to ca. –155°C by a Polycold P100 cryogenic refrigeration unit. The samples were step-heated using a defocused 50W $CO_2$ laser rastered over the samples to provide even heating. Samples were measured on the electron multiplier and time zero regressions were fitted to data collected from 10 scans over the mass range of 40–36. Peak heights and backgrounds were corrected for mass discrimination, isotopic decay and interfering nucleogenic Ca-, K-, and Cl-derived isotopes. $^{40}Ar$ blanks were calculated before every new sample and after every three unknown steps. $^{40}Ar$ blanks were between 4.0 and $2x10^{-16}$ moles. Blank values for masses 39–36 were all less than $7x10^{-18}$ moles. Blank values were subtracted for all incremental steps from the sample signal. Age plateaus were determined using the criteria of Dalrymple & Lamphere (1972), which specify the presence of at least three contiguous incremental heating steps with statistically indistinguishable ages (within 2 sigma error) that constitute >50% of the total $^{39}Ar$ released during the experiment. For further details on analytical procedures see Chew *et al.* (2008).

## 5.9. Experimental Petrology

Melting experiments were run at the HP-HT Laboratory of Experimental Volcanology and Geophysics at the Istituto Nazionale i Geofisica e Vulcanologia (INGV) Rome using the piston cylinder apparatus and a Voggenreiter uniaxial hydraulic press (Figure 5.7). For details on the laboratory see http://www.ingv.it/resources/labs/high-pressure-high-temperature-laboratory.




**Figure 5.7 The Voggenreiter Press and piston cylinder apparatus (yellow) at the Istituto Nazionale i Geofisica e Vulcanologia (INGV) Rome (photo from Deegan, F.M.)**

Samples were ground down to rods c. 2 mm in diameter were placed in platinum capsules. These capsules were loaded in to the piston cylinder assembly and heated to 1000˚C and pressures of 5 Kbar for one hour. For further details on the assembly and techniques see Freda *et al.* (2008).

## 5.10. Data reproducibility

### *5.10.1.Major and trace element data*

#### *5.10.1.1. Comparison of XRF major trace element data from different labs*

Major element values for the Drumadoon (Arran) rocks were analysed at both the Centre d'Analyses Minérale, University of Lausanne and GEOMAR (see sections 5.2.1 and 5.2.3). When compared the data are very similar, however the $Fe_2O_3$ and $Na_2O$ values from the GEOMAR lab are consistently higher than those from Lausanne. MnO shows some inconsistency, however $P_2O_5$ shows the most deviation, most likely because the values are near the detection limit of the machines. $SiO_2$ is the most consistent measurement amongst the data (Figure 5.8, Figure 5.9).

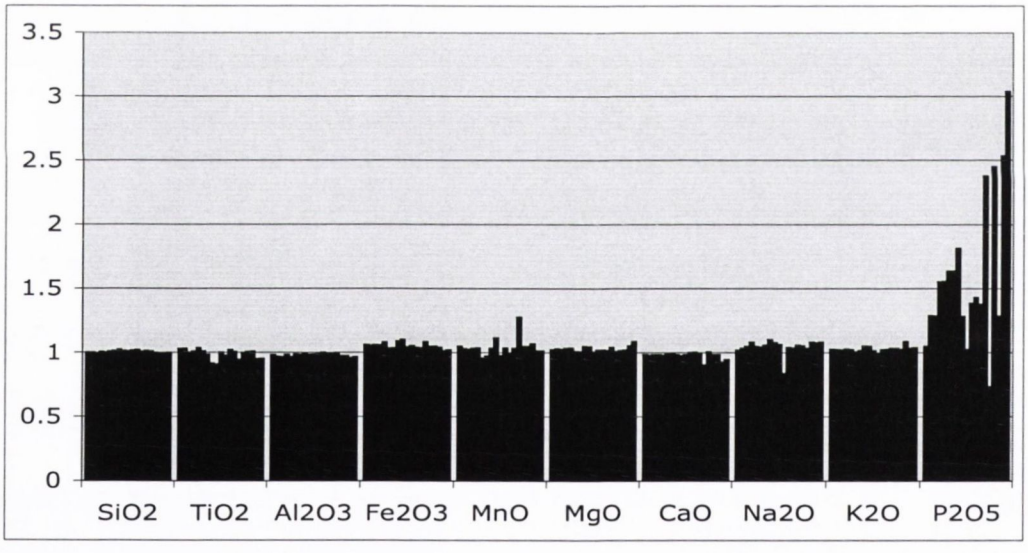


**Figure 5.8 Plot of the ratio of GEOMAR data divided by Lausanne data for all samples. A ratio of 1 means the analysed values are identical. Values above one indicate the Lausanne data are lower than that of GEOMAR, and below one indicate the Lausanne measurements are higher.**

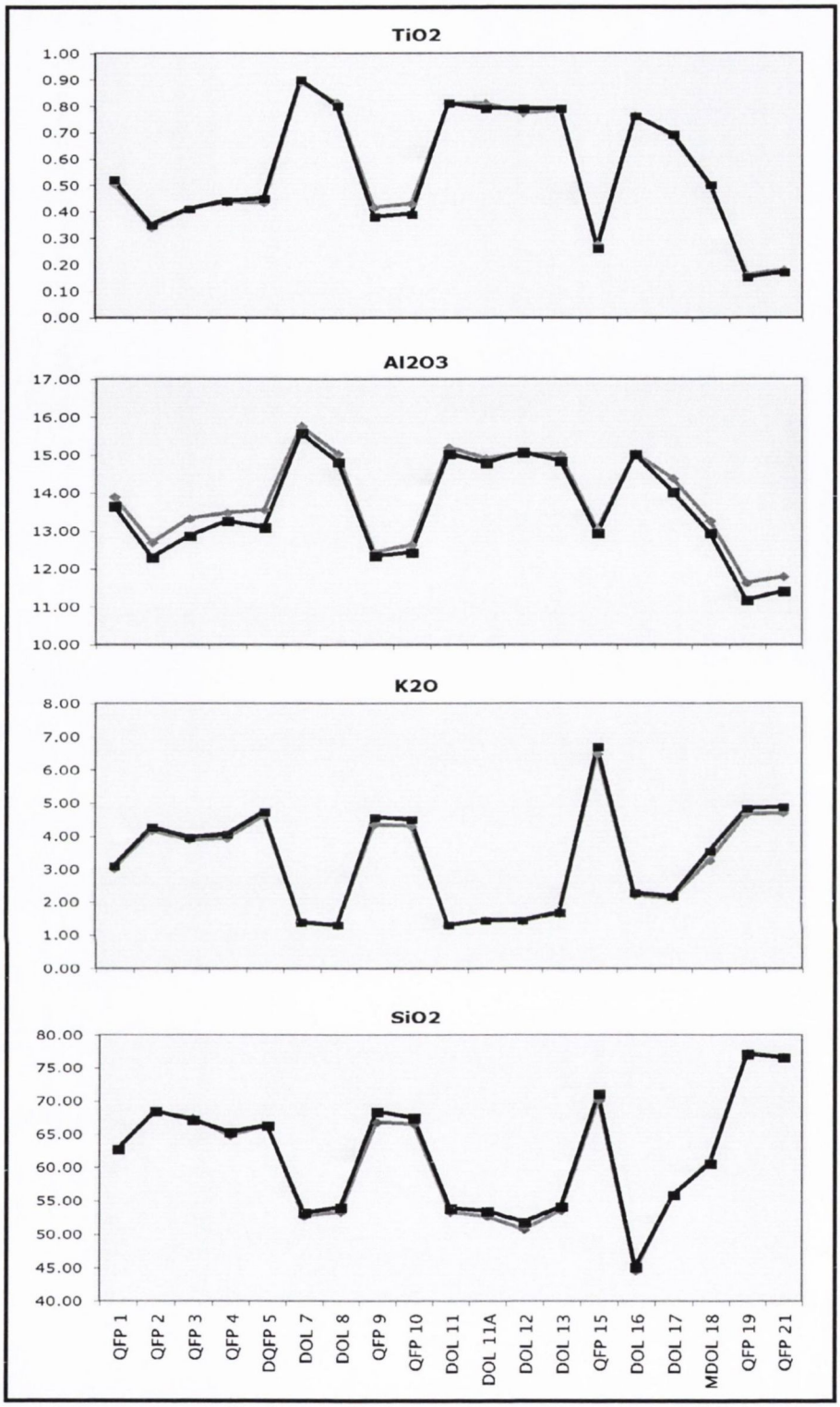


**Figure 5.9 Plots of selected XRF major element data for both the GEOMAR (black) and Lausanne (grey) labs, showing consistency of the data from both labs. Y-axis is weight % oxide.**

*5.10.1.2. Institute F. - A. Forel ICP-MS trace element data*

Trace element concentrations (non-REE) for the Drumadoon (Arran) rocks were determined by inductively coupled plasma mass spectrometry (ICP-MS) at the Institute F. - A. Forel, Versoix, Switzerland. These data were found to be inaccurate, with some samples showing anomalous enrichment/depletion in elements of ionic radius 0.8-1.0 x $10^{-10}$ m (Co, Dy, Hf, Lu, Y, Zn and Zr). The reason for these anomalous values is unknown, though the differences are most apparent in the Zr ppm (Figure 5.10). This suggests incomplete zircon dissolution during sample preparation for ICP-MS. Trace elements were re-run by XRF at GEOMAR (section 5.2.1). It was these XRF data that were used for interpretation.

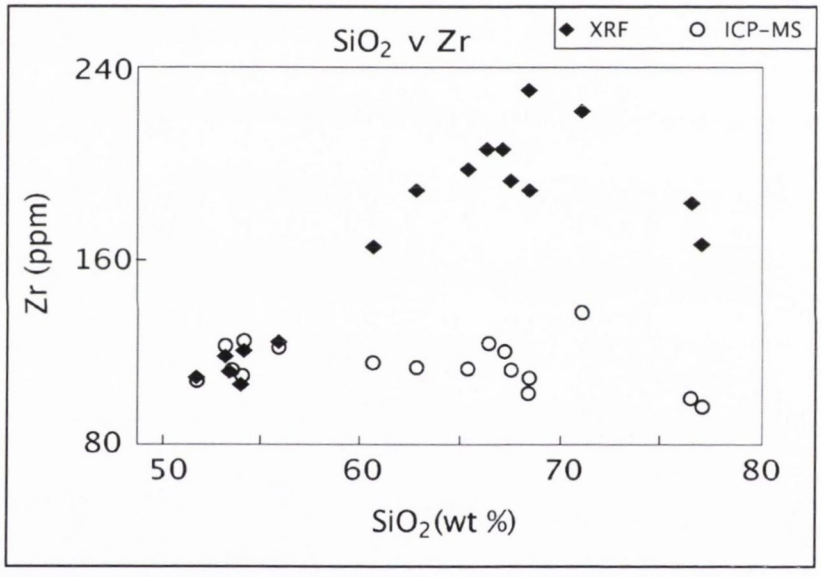


**Figure 5.10 Plot showing Zr ppm as analysed by XRF (diamonds) and ICP-MS (circles). Values for both techniques are similar in the low-silica range, but diverge as silica and Zr concentration increases. In these low-silica samples zirconium would be hosted in pyroxene, which would dissolve more readily during ICP-MS preparation.**

### *5.10.2.Rare earth element data*

#### *5.10.2.1. SUERC ICP-MS rare earth element data*

Eight samples (CSB2, LWG-1, B4, ANG-1, C-CS12-GM, C-CS1-SH, 284-8C, GM1) were run twice for rare earth elements, and one (CS4C) was run three times. Throughout 252 analyses (covering 14 elements) 94.44% of the data lay within a 10% range of the mean value for that sample. 54.76% of values lie within 5% of their mean. All values lay within 14.5% their individual means. Lanthanum was the only element to always lie within 5% of the mean. Published values for geological reference standard BCR-1 lie within standard deviation of values measured in this study (n=36) (Figure 5.1 and Table 5.1) (Raczek *et al.*, 2001).

### *5.10.3.Isotope data*

#### *5.10.3.1. Strontium data repeats*

Several samples were analysed repeatedly for strontium isotope ratios throughout the course of the project, allowing comparison of values within different lab sessions between 2004 and 2007. Data was consistent, and while all points did not overlap within machine error, differences only existed on the fifth (and in some cases fourth) decimal place (Figure 5.11). These errors are on the same order of magnitude as the machine error.

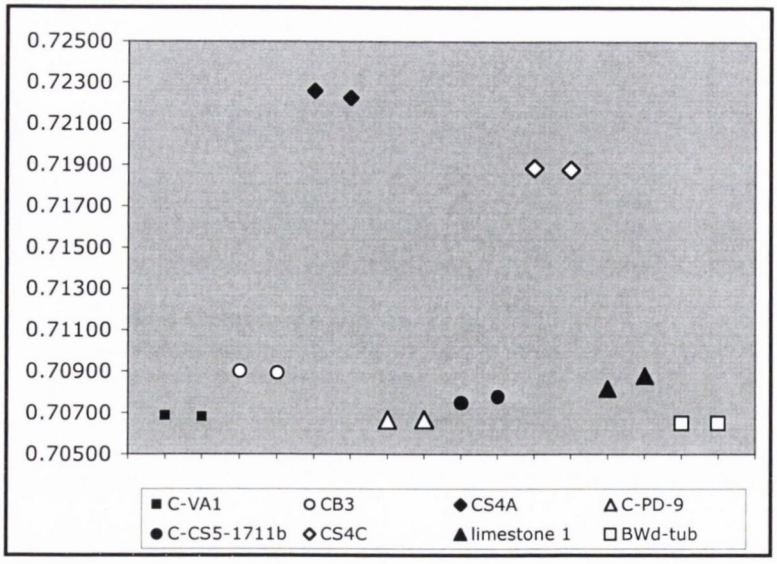


**Figure 5.11 Plot of repeat analyses for strontium isotope ratio (8 samples). Machine errors on the data are not greater than 0.000044 (2 S.E.).**

### *5.10.3.2. Leached versus un-leached strontium isotope analysis*

The majority of samples for strontium analysis were all leached in 20% cold nitric acid ($HNO_3$) overnight before digestion. Some samples were leached in hot $HNO_3$ for one hour. Leaching removes the loosely bound strontium from the sample, including that lying within clay mineral alteration that was not removed during picking. This is performed as weathered material can have a strongly different strontium isotope signature from that of the un-weathered rock, particularly that resulting from interaction with seawater.

Three samples were analysed for both their leached and un-leached strontium isotope ratios, to see if there was a consistent difference in values. Two of these samples (C-VA1 and CB3) yielded results. Both samples were analysed twice leached (one hot and one cold) and once un-leached. The un-leached samples consistently gave a more radiogenic value than the leached samples (Figure 5.12).

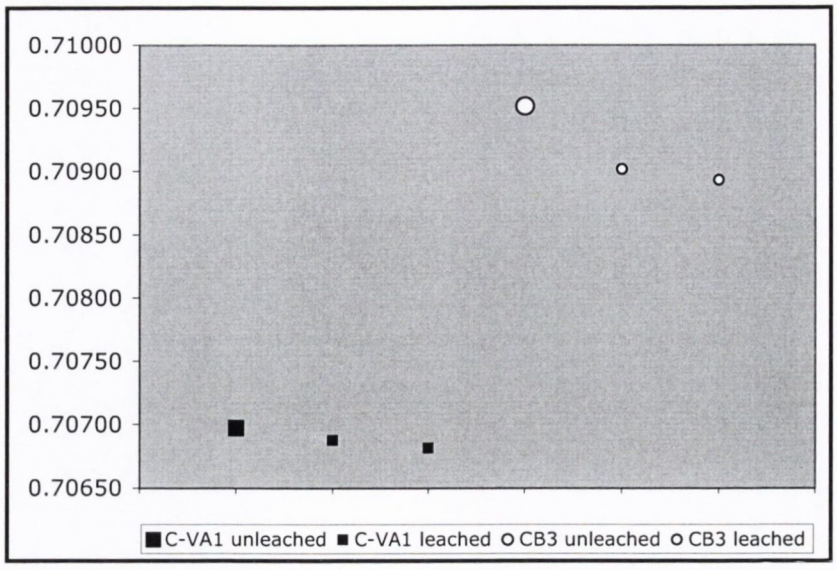


**Figure 5.12 Leached and un-leached strontium isotope ratios for samples C-VA1 and CB3. Large points are un-leached, smaller ones are leached. Errors on the data are smaller than the size of the data points.**

The leached data are consistent with each other, despite being leached using different techniques. However, the un-leached samples are more radiogenic in both cases, but not by the same amount. This suggests all the loosely bound strontium has been removed, rather than a continual leaching process stopped after a certain time – which would result in similar losses from both samples. Therefore sample CB3 appears to have been more weathered, supported by the loss on ignition values for the samples, whereby C-VA1 has a LOI of 1.37%, while CB3 has a total LOI of 2.23% (see Appendix 2.3).

### *5.10.3.3. Difficulties with neodymium isotope ratio analysis*

There was a very high rate of failure amongst samples analysed for neodymium isotope ratios at the Scottish Universities Environmental Research

Centre, with 28% of all neodymium isotope analyses failing. Of the samples that failed (n=14), 93% (n=13) had Nd concentrations below 35 ppm (Figure 5.13).

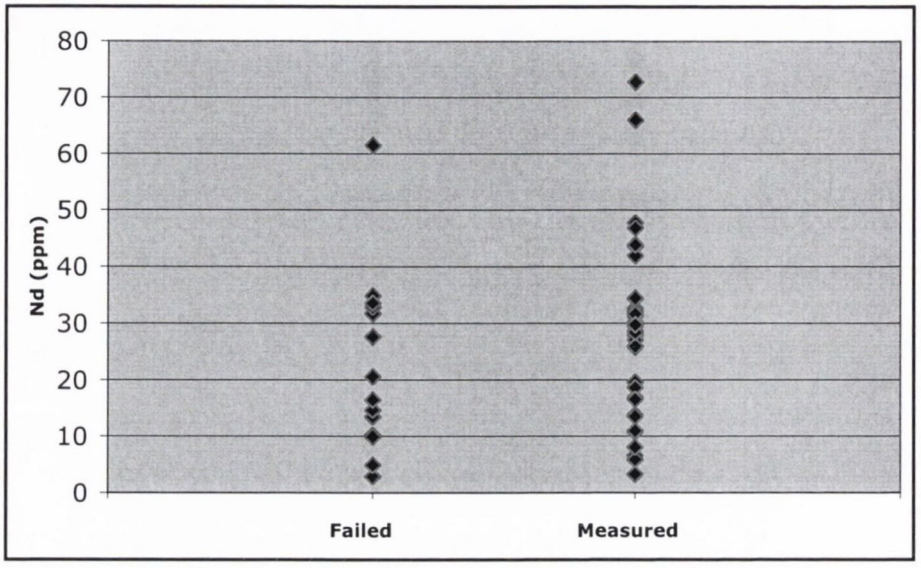


**Figure 5.13 Graph showing neodymium concentration (ppm) and whether the samples were measured for isotope ratio or failed.**

These low Nd concentrations could be significant if the calibration of the anion columns had drifted. A drift in column calibration would mean the Nd separate could have been collected off-peak, and since concentrations were low to begin with, off-peak collection would result in very low yields for the separate, making them more likely to fail when analysed in the mass spectrometer. However, many samples with concentrations of less than 35 ppm did yield results, suggesting that perhaps not all the columns had drifted and some did yield Nd separates capable of being analysed. Several students at the lab experienced this problem at SUERC, and the columns have since been re-calibrated.

# 6. CARLINGFORD

*The geochemical evolution of the Carlingford Igneous Centre, Republic of Ireland: a study of the relative timing of progressive differentiation progresses and the origin of bimodal magmatism.*

## 6.1. Abstract

Magmatism at the Palaeogene Carlingford Igneous Centre is represented by a major gabbro intrusion and a microgranite ring-dyke, both of which are crosscut by a series of aphyric to highly porphyritic basaltic cone-sheets with subordinate rhyolite, basaltic-andesite and trachy-andesite components. These lithologies, plus local crust, were analysed for major and trace elements and whole-rock Sr, Nd and Pb isotopes to assess the petrogenetic processes through these three main magmatic episodes.

All samples ($^{87}Sr/^{86}Sr = 0.7057\text{-}0.7201_{(60Ma)}$) deviate markedly from mantle values towards local Silurian siltstones ($^{87}Sr/^{86}Sr = 0.7144\text{-}0.7276_{(60Ma)}$). The earlier microgranite ring-dyke ($^{87}Sr/^{86}Sr = 0.7067\text{-}0.7127_{(60Ma)}$) seems to have incorporated partial melts of the Silurian crust, rather than bulk material. In contrast, the majority of trends for basaltic samples can be explained by bulk contamination. The highly evolved cone-sheet rhyolites ($^{87}Sr/^{86}Sr = 0.7098\text{-}0.7100_{(60Ma)}$) lie within the range of the basalt/basaltic-andesite, suggesting fractionation after initial contamination of basaltic parental magmas. K-rich trachy-andesites from cone-sheet intrusions ($^{87}Sr/^{86}Sr = 0.7198\text{-}0.7201_{(60Ma)}$) appear to be sedimentary derived, representing the (high-K) melt of hornfelsed xenoliths (*S-type basalts!*). The xenoliths themselves represent the restite remaining after partial melt loss from the local Longford-Down meta-siltstone.

Plagioclase phenocrysts from the late porphyritic basalt cone-sheets show that An generally decreases with crystal growth ($An_{91\text{-}24}$), with resorption surfaces marking distinct compositional steps. Convection and re-equilibration in a heterogeneous magma chamber may therefore be an important process affecting these phenocrysts. This is consistent with groundmass values, which are also highly variable and range in $^{87}Sr/^{86}Sr$ from 0.7064 to 0.7092, with matrix feldspar values of

$An_{62-46}$. Micro-drilled Sr isotope analyses of individual zones of large plagioclase phenocrysts show strong variation, with high-An cores yielding both high (0.7070-0.7077) and low (0.7063-0.7067) Sr ratios compared with low An rims. This observation may be attributed to the presence of some inherited xenocrystic cores from the contact aureole, as well as classical replenishment and magma mixing processes.

Despite the involvement of just a single crustal contaminant, our data imply petrogenetic evolution was not straightforward. Rather, we see a succession of variably overprinting processes that form a time sequence of contamination; from initial contamination of microgranite by crustal partial melts to bulk contamination of gabbro and basalt as the system heats up, and subsequent melting of the remaining restites during late cone-sheet emplacement to form a melt of trachy-andesite-type composition.

## 6.2. Introduction

The Carlingford Igneous Centre is situated in the Southern Uplands Terrane in Northeast Co. Louth, Ireland (Figure 6.1), and was first investigated by Hamilton (1839). It was regularly studied throughout the mid-nineteenth century, including Griffith (1840) and Haughton (1856; 1858; 1876). However, it was not until 1878 that Traill compiled the first geological map of the area. While the Palaeogene age of the Carlingford Igneous Centre was determined by Richey (1932), it was not radiometrically dated until the 1970's (Evans *et al.*, 1973). This whole rock K-Ar analysis gave a minimum age of 60.0 Ma for a late basaltic sheet, supported by an Ar-Ar date of 60.9 ± 0.5 Ma for the Carlingford microgranite (Thompson, 1986). Le

Bas (1960; 1965b; 1967) carried out the last comprehensive study of the entire complex, while Halsall (1974) worked specifically on the minor intrusions.

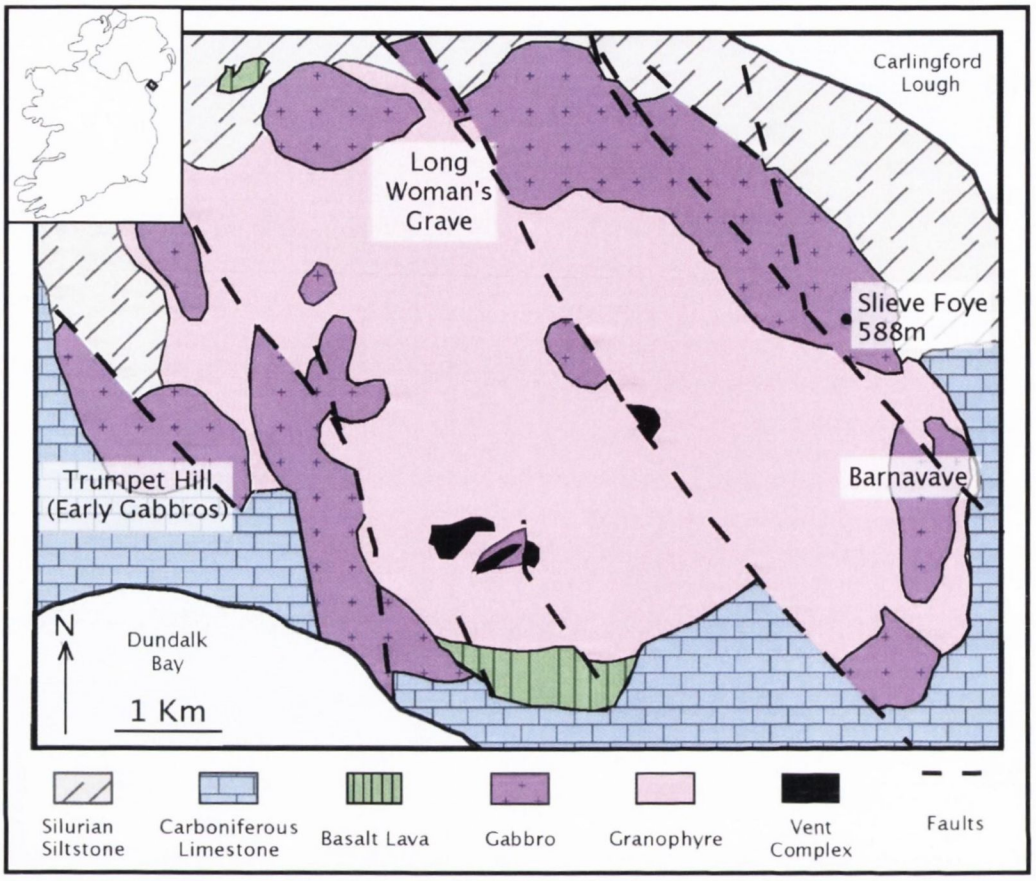


**Figure 6.1 Schematic geological map of the Carlingford Igneous Centre, modified from Le Bas (1967).**

The pre-Palaeogene geology exposed on the Carlingford Peninsula mainly comprises the siltstones and mudstones of the Silurian Longford-Down Basin (Holland, 2001). These rocks were isoclinally folded about a northeast-southwest axis during the Caledonian Orogeny (Phillips, 2001) and gently metamorphosed to greenschist facies. They are unconformably overlain by the basal conglomerate and lowermost members of the Carboniferous Carlingford Limestone succession (mid. - late Arundian, (Mitchell, 2004) (Figure 6.1). Little is known of the terrane basement, however, xenolith suites from within Carboniferous lamprophyres show mylonitised

meta-sediments, meta-diorites and meta-tonalites that most likely represent an under-thrust meta-igneous succession of Lake District type (island arc) (Anderson and Oliver, 1996).

During the Palaeogene, a large central volcanic complex formed, of which only the roots remain today (Richey, 1932). The intrusions were emplaced ~3 km below an extrusive volcanic edifice (Gamble *et al.*, 1992; Allen *et al.*, 2002). Magmatism was bimodal, with large volumes of mafic and felsic magmas and little of intermediate composition. The oldest major Palaeogene intrusion recorded in Carlingford is proposed to be the Early Gabbros at Trumpet Hill to the west of the centre, while an early granophyre is recorded as clasts in vent agglomerates (Figure 6.1) (Le Bas, 1960). The major intrusions seen at the centre are a gabbro loppolith (known as the Later Gabbro) (Le Bas, 1960) and a microgranite ring dyke (Le Bas, 1967). Le Bas (1967) proposed the microgranite was younger than the gabbro, however recent work by O'Driscoll (2006) suggests that this may not be the case and the microgranite may in fact pre-date the Later Gabbro (Figure 6.2). Mixed magmas, seen at Clondike Quarry (J 1823 1021), indicate the main microgranite and Later Gabbro occurred in close temporal succession.

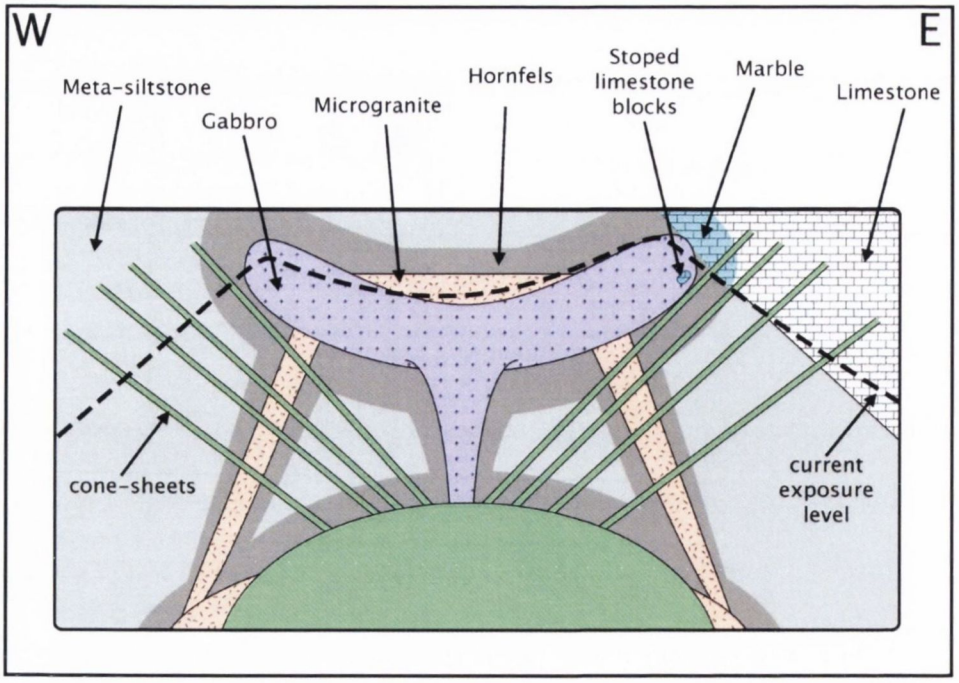


**Figure 6.2 Schematic cross-section of the Carlingford Igneous Centre. Compiled after Le Bas (1960; 1967) and O'Driscoll (2006).**

Both intrusions are in turn crosscut by a series of basaltic cone-sheets, representing the final phase of intrusive activity preserved at the Carlingford Centre. Mapping revealed an overall distribution pattern for the cone-sheets, whereby the frequency of porphyritic cone-sheets increases with altitude, with phenocryst-poor basaltic cone-sheets more prevalent at lower levels in the complex. Significantly, sheets at intermediate altitudes are composite in nature. This vertical zoning suggests a compositional gradient in the cone-sheet source chamber, with porphyritic basalt in the upper levels and hotter, aphyric basalt at the bottom.

Overall, the centre has a bimodal composition, with large amounts of both mafic and felsic compositions, but very few intermediate ones. This paucity of intermediate rocks, known as the Bunsen-Daly Gap (Bunsen, 1851; Daly, 1925), has been a matter of debate for more than 150 years and a number of causes have been suggested. Besides sample bias and trapping of intermediate compositions (on density grounds), crustal contamination is the main process held responsible. Herein

we evaluate the time-integrated changes preserved at the Carlingford Igneous Centre, which shed light on the origin of bimodal igneous suites and the temporal variations recorded in the remnants of a maturing volcanic complex.

## 6.3. Petrography of major lithologies

### *6.3.1. Longford-Down meta-siltstone*

The Longford-Down meta-siltstones form a series of distal turbidites, representing the C (thinly bedded silts), D (cross bedded silts) and E (laminar muds) facies of a Bouma sequence (Figure 6.3). Paleo-current data measured from flute marks suggests that material was originally transported in an east-north-easterly direction.

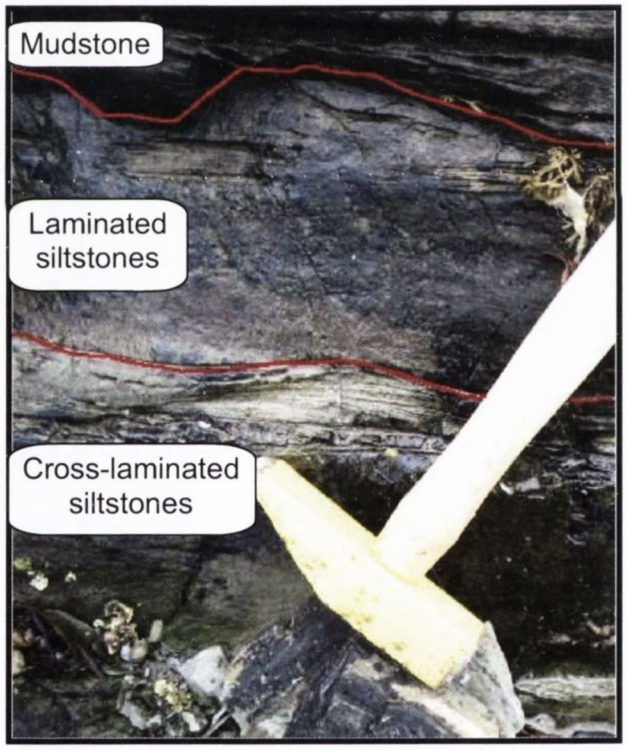


**Figure 6.3 Interbedded siltstones and mudstones showing the upper members of a Bouma sequence.**

The siltstones are gently metamorphosed to greenschist facies. Dark layers contain mostly mica, both biotite (70%) and muscovite (15%), with small amounts of quartz and feldspar, while the pale layers contain no biotite and equal amounts of muscovite (50%) and quartz/feldspar (50%) (Figure 6.4).




**Figure 6.4 Thin section of Longford-Down metasediment (PPL). Note the presence of large amounts of biotite in the darker layers (right), while the paler layers are richer in muscovite and quartz (left).**

### *6.3.2. Hornfels*

The hornfels occurs as a 100-200 m wide metamorphic aureole where the gabbro has intruded the local Longford-Down metasediments. It is a hard, fine-grained rock, normally black in colour but ranging from pale grey/green to black. These colour changes suggest differences in original mineralogy, now metamorphosed to diopside and biotite respectively. The original bedding is only determined by differential weathering of layers, presumably due to a difference in composition or grain size between beds, and shows evidence of ductile deformation.

In thin section the rock is very fine grained and appears to be mainly composed of biotite (normally ~ 50%). Quartz (10%), plagioclase and potassium feldspar (up to 50%) are also present. Diopside also occurs in small quantities, with somewhat greater volumes in the greener layers.

Hornfelsed xenoliths also occur within late cone-sheet intrusions on the slopes of Slieve Foye. These xenoliths are richer in $K_2O$ than their aureole equivalents, suggesting they have interacted with K-rich metamorphic fluids, and perhaps represent aureole rocks from deeper within the complex.

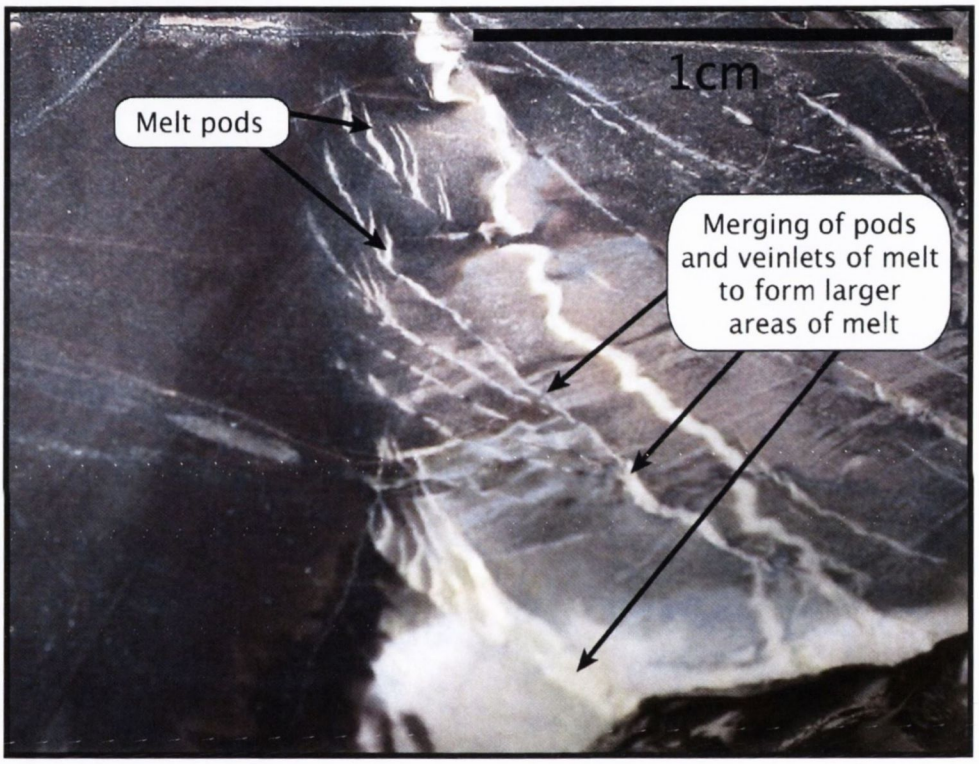


**Figure 6.5 Zoom in to a hand sample of a metasedimentary xenolith from the Slate Rock cone-sheet (IJ 17799 11754). Note the occurrence of in-situ partial melting and the formation of a vein network along which melt can be transported.**

In thin section these xenoliths are fine-grained in nature, similar to their aureole equivalents and contain mainly biotite, quartz, plagioclase and potassium feldspar. However, they also show melting textures, with wisp-like areas of coarse

plagioclase representing partial melting of the xenoliths by the surrounding hot basalt. In some cases these melt pods merge to form veins and patches of pale re-crystallised melt (Figure 6.5, Figure 6.6). In thin section the edges of the xenoliths contain very little biotite, and are mostly quartz and feldspar (~ 65%) with muscovite (30%) and opaques (2%).

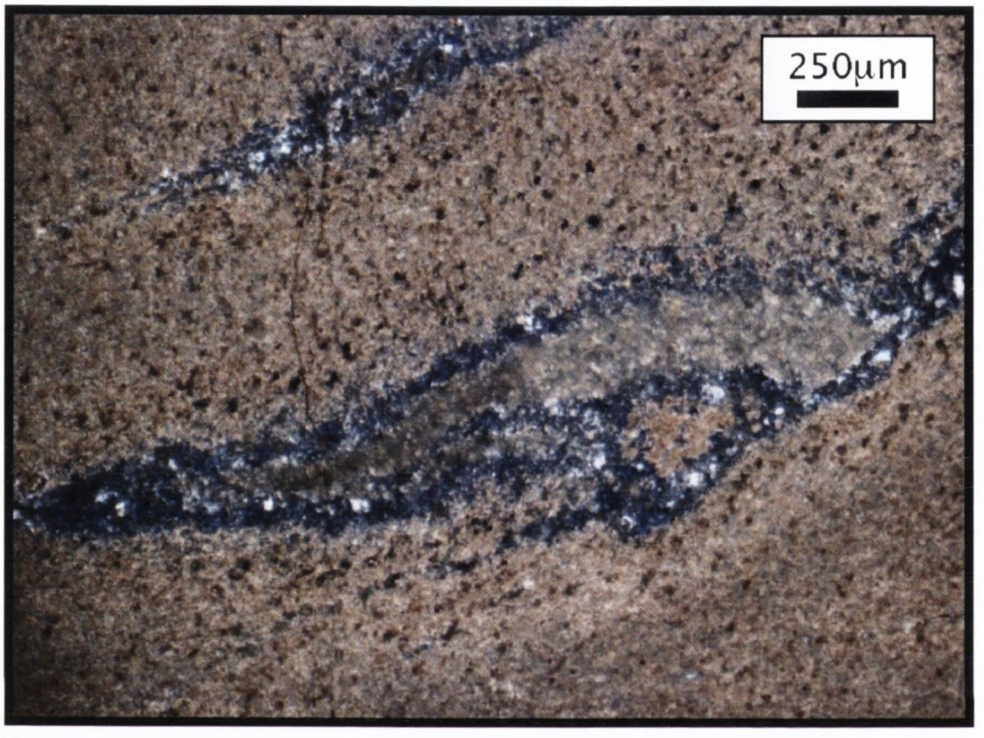


**Figure 6.6 Thin section of hornfels xenolith in XPL. The majority of the rock is biotite, with coarse pockets of frozen melt that are rich in plagioclase. See Figure 6.5 for hand sample image.**

### *6.3.3. Limestone*

The Carboniferous limestone adjacent to the Carlingford Centre is muddy and bedded on a metre scale. It contains isolated dolomite beds. It is poor in macrofossils, except for thin layers of disaggregated crinoidal material and isolated rugose and colonial corals. Microscopically it is heterogeneous in composition. Layers of bioclastic material are mainly surrounded by calcite cement though peloids

and mud are also common. On average it is ~15% micrite, 40% calcite and 45% grains. The grains are mainly peloids (45%) and larger skeletal grains (55%) (Figure 6.7). The skeletal grains include foraminifera (e.g. *Endothyra sp., Paraarchaediscus sp.)*, brachiopod spines and shell fragments, echinoid plates, bryozoans, sponges, algae (e.g. *Koninckopora*) and "pseudoalgae" (Aoujgaliids) (Devuyst, F.X. *pers. comm.)*. The presence of algae suggests deposition in the photic zone (less than 90 m water depth), while the muddy matrix and detrital lithic grains suggest a near shore environment.

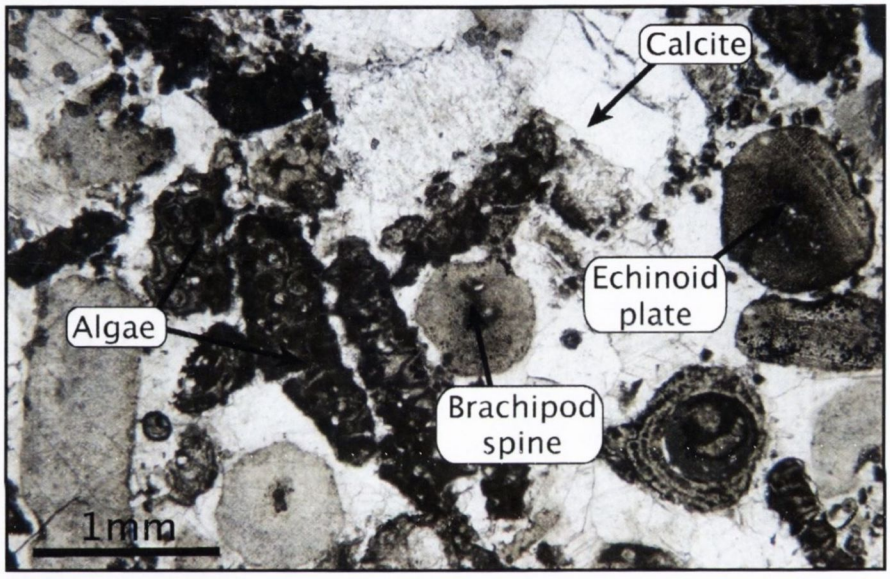


**Figure 6.7 Thin section of the Carlingford Limestone in plane polarised light, showing skeletal grains in a calcitic matrix.**

### *6.3.4. Marble*

Marble was formed where the gabbro intruded the Carlingford limestone. The limestone becomes gradually more crystalline towards the intrusion, eventually forming a pale grey marble with greener diopside-rich layers. The original limestone bedding can still be differentiated as different beds form slightly different coloured

domains. Megablocks of limestone stoped within the gabbro have also been metamorphosed to a coarse marble (Figure 6.8).

Much of the marble is quite fine grained, but near the intrusion grain sizes increase to ~0.7 cm. XRD analysis (see section 5.3) revealed the presence of wollastonite, muscovite and diopside in addition to calcite and dolomite.

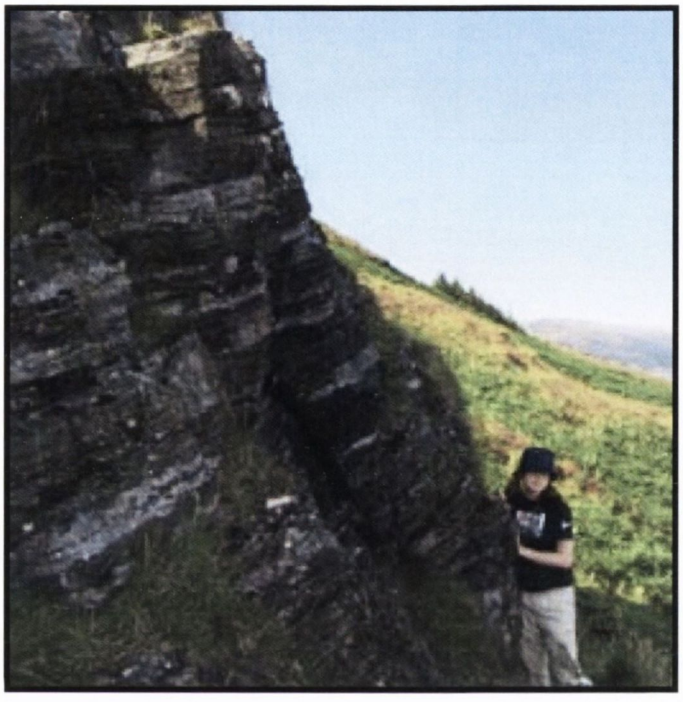

**Figure 6.8 A large block of marble within the main gabbro body at IJ 17842 09073, southeast of Barnavave. The block is ~100m long and is entirely crystalline, with recognisable, but sometimes deformed, bedding.**

### *6.3.5. Microgranite*

The microgranite analysed was collected from the Long Woman's Grave region of the Carlingford Complex (J 12 13) (Figure 6.1) and is a purple hued equigranular microgranite composed almost entirely of feldspar and quartz (50% Quartz, 45% feldspar and 5% hornblende) (Figure 6.9). The feldspar is mainly of

alkali-type and frequently forms a granophyric texture with quartz. The hornblende shows clear pleochroism.

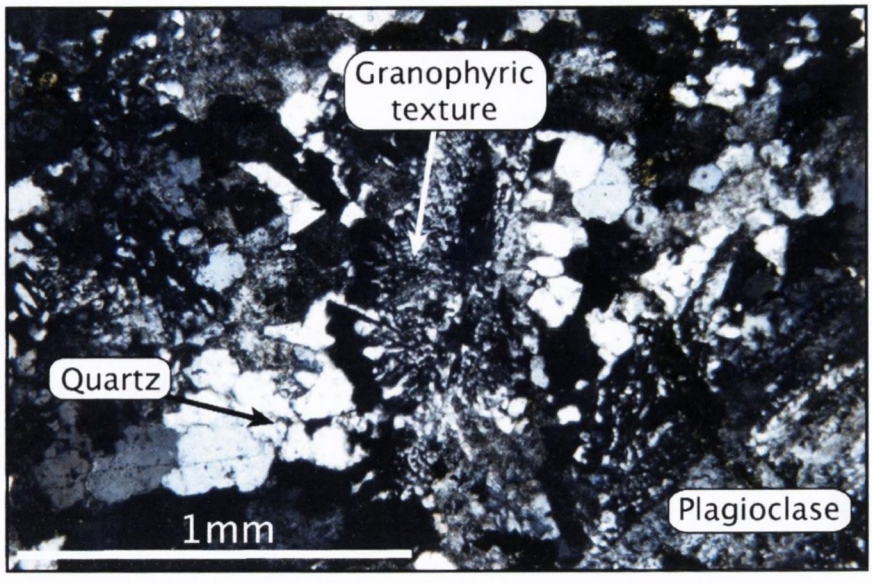


**Figure 6.9 Microgranite thin section in cross polarised light, exhibiting granophyric texture.**

### *6.3.6. Gabbro*

The Carlingford Gabbro is medium to coarse-grained with up to ~90% plagioclase, though typically it contains plagioclase (60%), clinopyroxene (20%), orthopyroxene (15%) and olivine (5%) (Figure 6.10). It has an inequigranular texture with large plagioclases (5-8 mm) and smaller olivines (0.8 mm). The plagioclases are euhedral to subhedral, while olivine is subhedral. The pyroxenes are anhedral and fill the interstices of the olivine and plagioclase cumulate (see also Le Bas, 1960). The gabbro is much more resistant to weathering than any other lithology at the centre and forms all the topographic highs in the area.

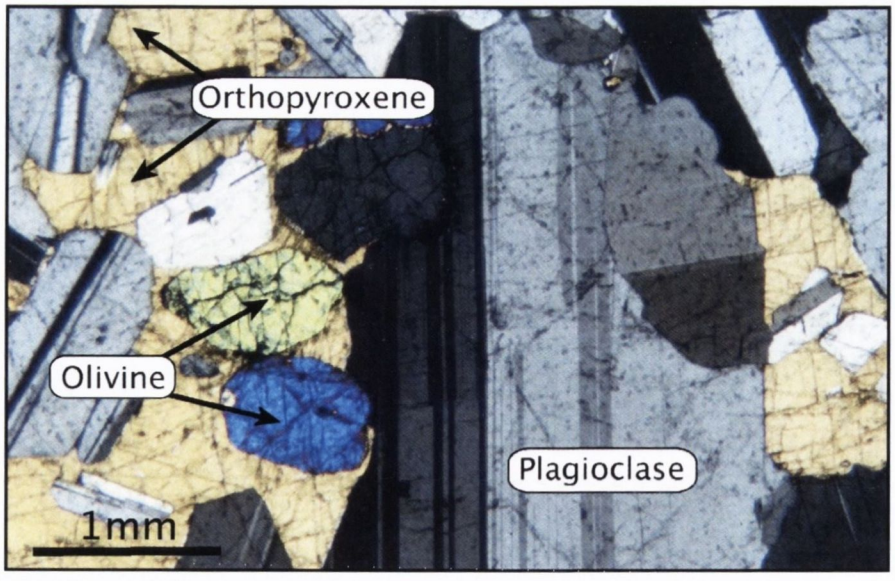


**Figure 6.10 Gabbro thin section in cross polarised light. Note large plagioclase crystals and considerably smaller olivines and orthopyroxenes.**

### *6.3.7. Plagioclase-phyric Basalt (cone-sheets)*

The plagioclase-phyric basalt has a basaltic to doleritic matrix with lath-shaped feldspars, with phenocryst proportions varying from ~10%, to as much as 80%. The plagioclase phenocrysts are large (up to 2 cm) and are compositionally zoned, containing a compositional range of $An_{83-63}$. The majority of feldspar phenocrysts occur as glomerocrysts of euhedral morphology. The matrix is largely micro-crystalline and contains plagioclase (55%), pyroxene (40)% and Fe-Ti oxides (5%) (Figure 6.11).

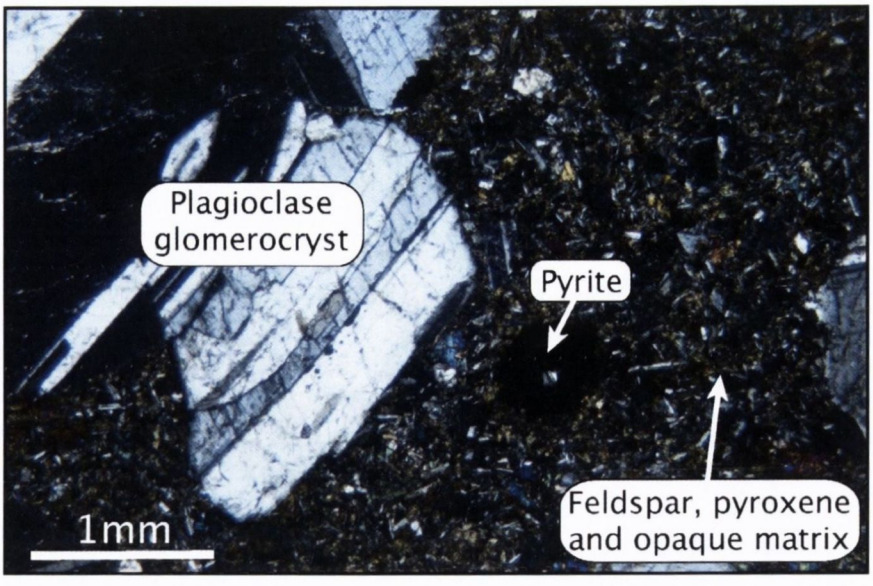


**Figure 6.11 Porphyritic basalt from the cone-sheet swarm. Thin section is in cross-polarised light and shows a large plagioclase glomerocryst in a fine-grained feldspar, pyroxene and Fe-Ti oxide matrix.**

### *6.3.8. Basalt (cone-sheets)*

Cone-sheets of basaltic composition are well exposed on the shores of Carlingford Lough (Figure 6.12), but occur only rarely at higher altitudes. The basalt closely resembles the porphyry matrix (Figure 6.11) in mineralogy and contains plagioclase laths, anhedral pyroxene and Fe-Ti oxides. Accessory pyrite occurs locally.



**Figure 6.12 Basaltic cone-sheet on the Carlingford foreshore, below King John's Castle.**

### *6.3.9. Trachy-andesite (cone-sheets)*

Trachy andesite occurs in the vicinity of large hornfels xenoliths within the Slate Rock cone-sheet. These samples have the same physical appearance as the basaltic samples in hand specimen, though often appear finer grained in thin section. Chemically, however, they plot in the trachy-andesite field of the TAS diagram, *see* Figure 6.14. The trachy-andesites are crystalline in nature and contain mainly plagioclase (50%), with large amounts of quartz xenocrysts in places (20%). There are also muscovite (15%), biotite (5%) and opaques (5%) present (Figure 6.13). These melts appear to be the product of partial melting within the hornfels xenoliths (Figure 6.5, Figure 6.6, Figure 6.13).

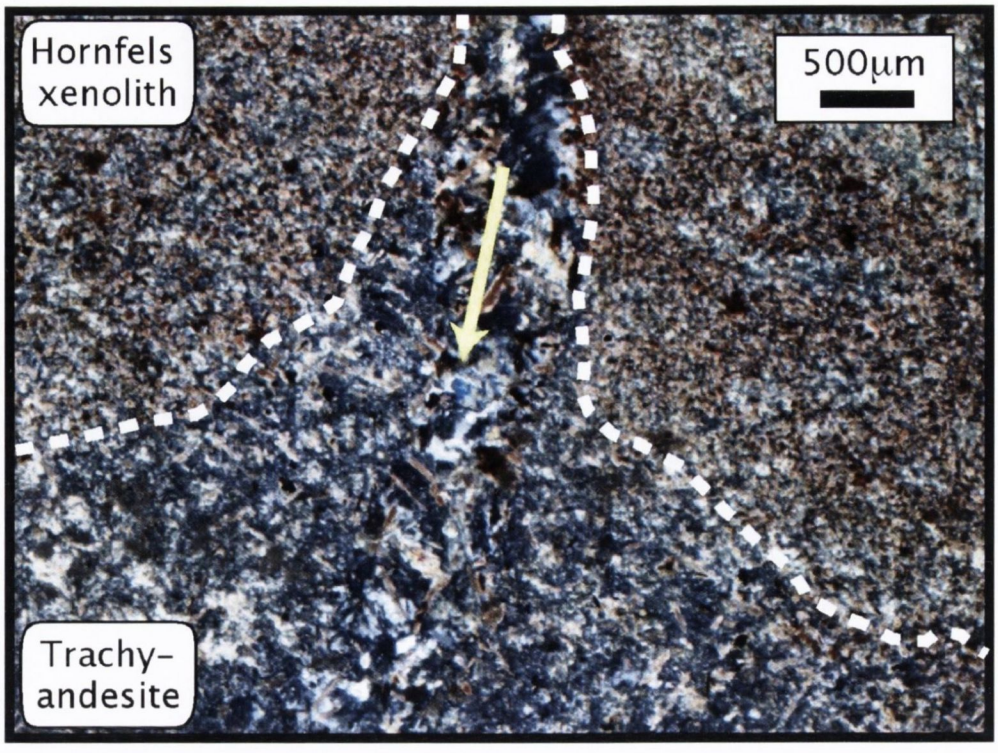


**Figure 6.13 Thin section image (XPL) of the margin of a hornfels xenolith. The margins of the xenolith show enrichment in opaques and lower proportions of biotite. Melt appears to be sourced from the xenolith, collecting through a small vein (centre) and forming the trachy-andesite.**

#### *6.3.10.Rhyolite*

The cone-sheet rhyolites are pale in colour and mostly contain plagioclase feldspar (~80%) with small amounts of quartz (5-10%) and chlorite (5-10%). The rock is fine to medium grained and mostly equigranular, though the quartz crystals are slightly smaller (0.5 mm).

## 6.4. Intrusion sequence of the Carlingford cone-sheets

Work by Halsall (1974) has suggested three cycles of cone-sheet intrusion. Cycle one occurred pre-Later Gabbro, cycle two between the Later Gabbro and the

granophyre, while cycle three was post-granophyre. These cycles were based on Le Bas' overall sequence of intrusion for the centre, whereby the Later Gabbro was older than the microgranite (granophyre) (Le Bas, 1960; 1965b; 1967). However, in light of this work, and that of O'Driscoll (2006), the sequence of major intrusion at the centre has be reinterpreted, with the gabbro most probably post-dating the microgranite. This means these cycles must be re-considered as they were based on invalid assumptions.

Interestingly, while Halsall (1974) considered the porphyritic basalts and 'high-alumina basalts' ($Al_2O_3 > 16.5\%$) as part of the same series, the aphyric basalts that occur coevally with porphyritic members within composite intrusions do not seem to have elevated $Al_2O_3$ values. Therefore this study focuses on the petrology and chemical composition of individual dyke intrusions, rather than on their cycle as defined by Halsall (1974).

## 6.5. Sample selection and preparation

Representative samples (n=43) of the main lithologies exposed at the centre were collected, including gabbro, granophyric microgranite, limestone, marble, siltstone and hornfels (Appendices 2.1 and 3.1). The cone-sheet swarm was sampled in more detail, with traverses through individual sheets. Samples were sliced and weathered edges removed. Samples were then crushed in a jaw-crusher and powdered in a tungsten carbide TEMA mill. All powders were analysed for major and trace elements and a selected sample set were analysed for rare earth elements and strontium, neodymium and lead isotopes.

## 6.6. Geochemical analysis

### *6.6.1. X-Ray fluorescence*

Whole-rock samples were analyzed for major element oxides and trace element concentrations at GEOMAR Research Centre, Kiel, Germany (see section 5.2.1) (Appendices 2.2, 2.3, 2.4, 3.2, 3.3 and 3.4). Major element data had initial totals ranging from 98.75% to 100.63% and were corrected for loss on ignition and normalised to 100% for plotting.

Complementary XRF analyses on Gabbros *C4, C7*; Microgranite *LWG1, LWG2*; Rhyolites *284-8c, 288-8a*; Lower-crustal metasediments *BWA, BWB, BWC, BWD* and Carboniferous carbonates *Limestone 1, Marble 1* were carried at the University of St. Andrews, Scotland (see section 5.2.2) (Appendices 2.2, 2.3, 2.4, 3.2, 3.3 and 3.4). Major element data had initial totals ranging from 99.20% to 99.99% and were also corrected for loss on ignition and normalised to 100% for plotting.

### *6.6.2. X-Ray diffraction*

Powders *Marble 1* and *Silt 1* were analysed by X-ray diffraction at the Department of Geology, Trinity College Dublin (see section 5.3). Results were compared to the "Traces" database (Hiltonbrooks Ltd, http://www.xrays.u-net.com/Software.htm) for mineral identification.

### *6.6.3. ICP-MS*

Rare earth elements and U, Th and Pb concentrations were determined by inductively coupled plasma mass spectrometry (ICP-MS) at the Scottish Universities Environmental Research Centre (SUERC), East Kilbride, Scotland (see section 5.4.1) (Appendices 2.5, 2.6, 3.5 and 3.6).

### *6.6.4. Isotope geochemistry*

Strontium, neodymium and lead isotopes were analysed at the Scottish Universities Environmental Research Centre (SUERC) (see sections 5.5.1.1, 5.5.2.1 and 5.5.3.1 for analytical details) (Appendices 2.7, 2.8, 3.7, and 3.8).

### *6.6.5. Electron microprobe*

Feldspar major element compositions were analysed on a JEOL JCXA 733 electron microprobe at the University of St. Andrews, Scotland. Backscattered electron (BSE) images of feldspars were also collected (see section 5.6 and Appendix 2.10).

### *6.6.6. Microdrilling and micro-Sr isotope analysis*

Microdrilling for the Sr isotope ratios of individual feldspar zones was carried out using a Merchantek Micromill at the University of Durham, UK. The milling technique and subsequent micro-chemistry are described in more detail in Charlier *et al.* (2006) and in section 5.7. See Appendix 2.9 for data tables.

## 6.7. Experimental petrology

A sample of the Longford-Down metasediment was heated to 1000° C at a pressure of 5 Kbar using the piston cylinder facilities at the HP-HT Laboratory of Experimental Volcanology and Geophysics at the Istituto Nazionale i Geofisica e Vulcanologia (INGV) Rome. This experiment simulated a xenolith of metasediment being heated to magma chamber temperatures and pressures. For further experimental details see section 5.9, Samples were cooled, mounted in resin and viewed as back-scattered electron images.

## 6.8. Major and trace element geochemistry

### *6.8.1. Major elements*

Major and trace element data define the gabbro as the most primitive composition seen at Carlingford, while the microgranite is the most evolved. The cone-sheet samples span the intermediate compositions, with the majority of samples lying within the basalt and basaltic-andesite fields of the TAS diagram (Figure 6.14). Three cone-sheet samples, which appeared to be basaltic in the field, are chemically classified as andesite (n=1) and dacite (n=2). In addition, two rhyolitic cone sheet samples were analysed.

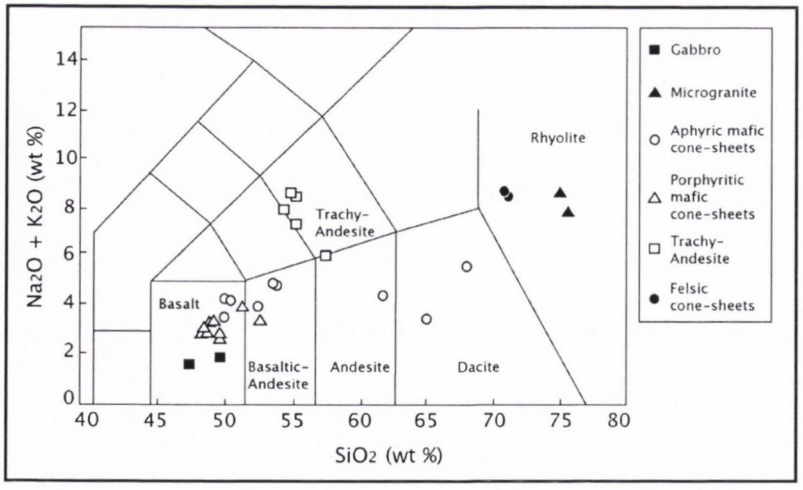


**Figure 6.14 Total Alkali v Silica diagram. Data span much of the spectrum from mafic to felsic with an excursion to higher alkalinities in the mid 50% $SiO_2$ range.**

The majority of samples are sub-alkaline, apart from a distinct set of cone-sheet samples that were collected in the vicinity of large (>1 m) hornfels xenoliths. These are alkaline and plot as trachy-andesites (Figure 6.15). The alkaline nature of these samples is largely due to their elevated $K_2O$ wt% values (Figure 6.16). Conversely, the andesite and dacite samples have $Na_2O$ concentrations that are lower than "normal" Carlingford basalts (Figure 6.17).

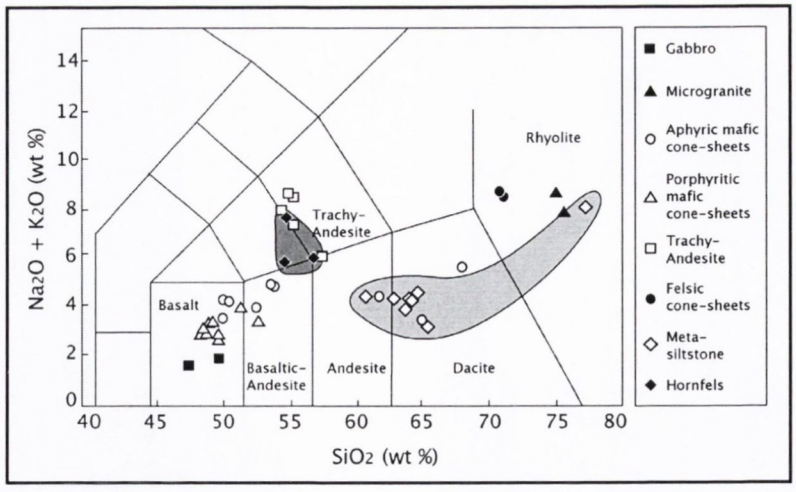


**Figure 6.15 TAS diagram with sedimentary country rocks plotted. Note the hornfelsed metasediments (dark grey field) plot within the trachy-andesite range and low-grade metamorphosed siltstones (pale grey field) within the andesite, dacite and rhyolite ranges. The hornfelsed xenoliths are richer in $K_2O$ than their low grade equivalents, suggesting they have interacted with K-rich metamorphic fluids, and perhaps represent aureole rocks from deeper within the complex.**

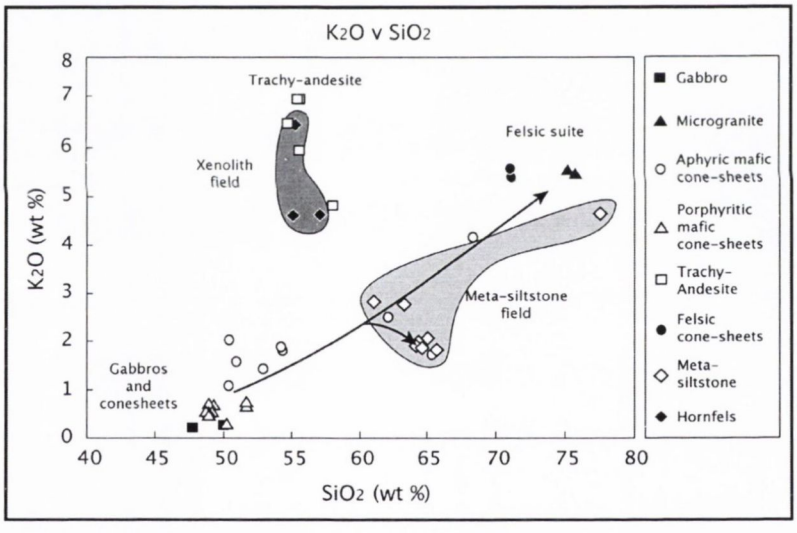


**Figure 6.16 Plot of $K_2O$ v $SiO_2$ showing the chemical relationships of intermediate igneous rocks to local country rocks. Country rock fields in grey. The trachy-andesites show high-$K_2O$, similar to the values of the hornfels xenoliths. Arrows show evolution of the magma from basalt to rhyolite, with diversion to low $K_2O$ in the intermediate range, similar to values of the local meta-siltstones.**

When the andesite and dacite samples were compared to the local low-grade Silurian metasediments (siltstones) it was found that they had similar $SiO_2$ and low $Na_2O$ values (Figure 6.17). In contrast, the trachy-andesite was found to lie in the same compositional range as the $K_2O$-rich hornfels xenoliths (Figure 6.16) suggesting local crust may have had a strong influence on their composition. This is apparent through all the major element plots (see also Figure 6.18 and Figure 6.19).

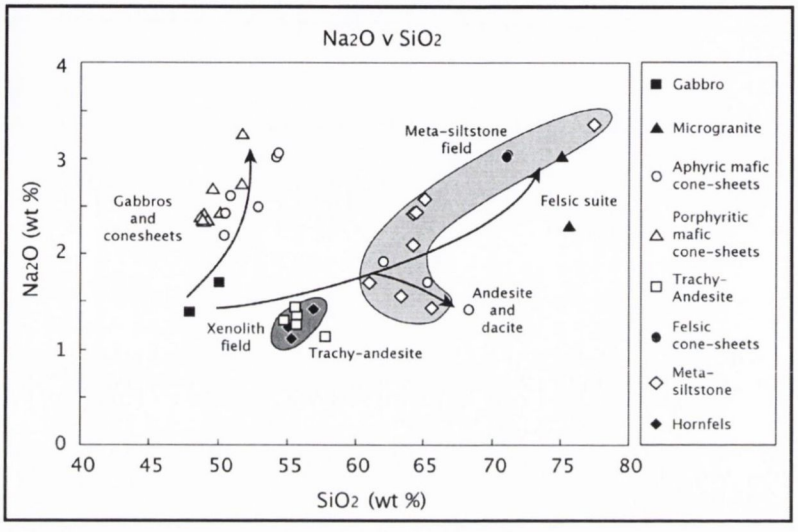


**Figure 6.17 Plot of $Na_2O$ v $SiO_2$ showing trend of increasing $Na_2O$ for the gabbros and cone-sheet gabbros. There are low levels of $Na_2O$ within the intermediate range, echoing $Na_2O$ levels within the local crust. The felsic rocks also lie within the meta-siltstone field, while once again, the trachy-andesites plot with the hornfels xenoliths. Arrows represent general evolutionary trends.**

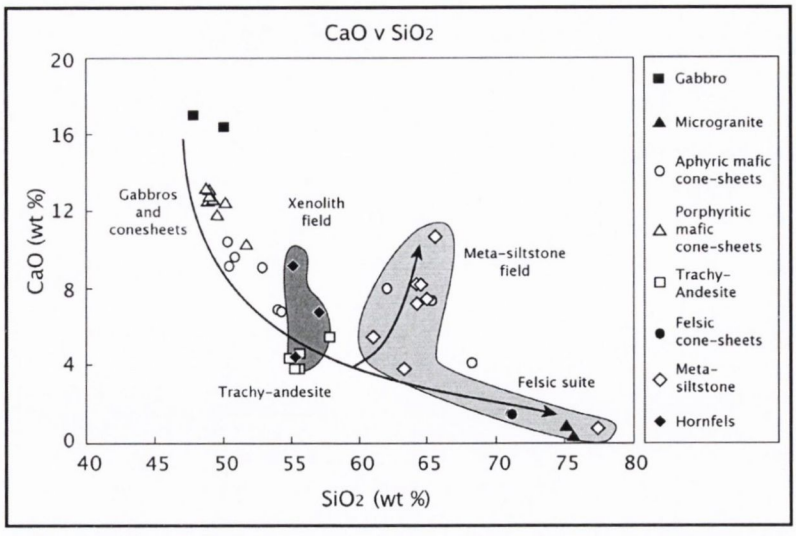


**Figure 6.18 Plot of CaO v $SiO_2$, showing overall trend of decreasing CaO. Once again the intermediate rocks are displaced towards local crustal values. The rhyolites and microgranites lie within the meta-siltstone field, while the trachy-andesites are again consistently within the hornfels xenolith field.**

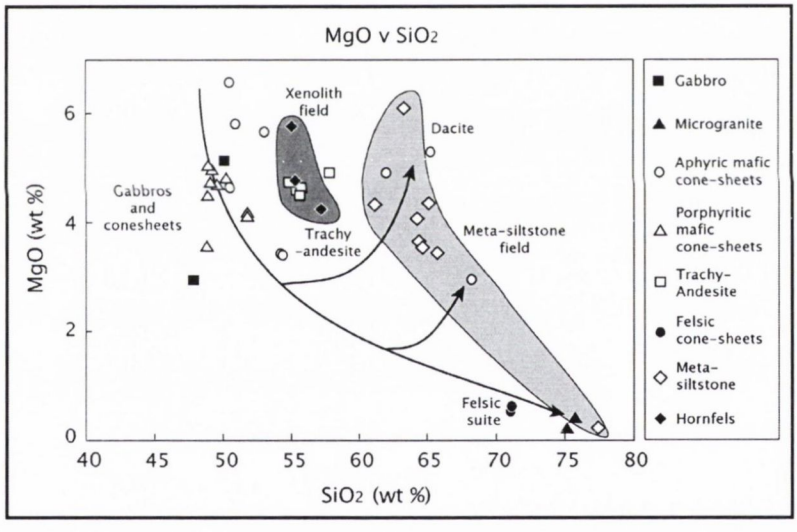


**Figure 6.19 Plot of MgO v $SiO_2$ showing overall decrease in MgO, with excursions to anomalously high MgO values within the mid-$SiO_2$ range. These high intermediate MgO values are similar those of the local crust. Again the trachy-andesites lie within the xenolith field. Arrows suggest possible evolutionary trends for intermediate and evolved samples.**

### *6.8.2. Trace elements*

Trace element data show similar trends to major element data, with several distinct lithological groups. Once again, the intermediate samples plot within (or near) the field of the local metasedimentary siltstones for both incompatible (e.g. Rb, Figure 6.20) and compatible elements (e.g. Sr, Figure 6.21). This points towards a significant component of crustal contamination in their formation.

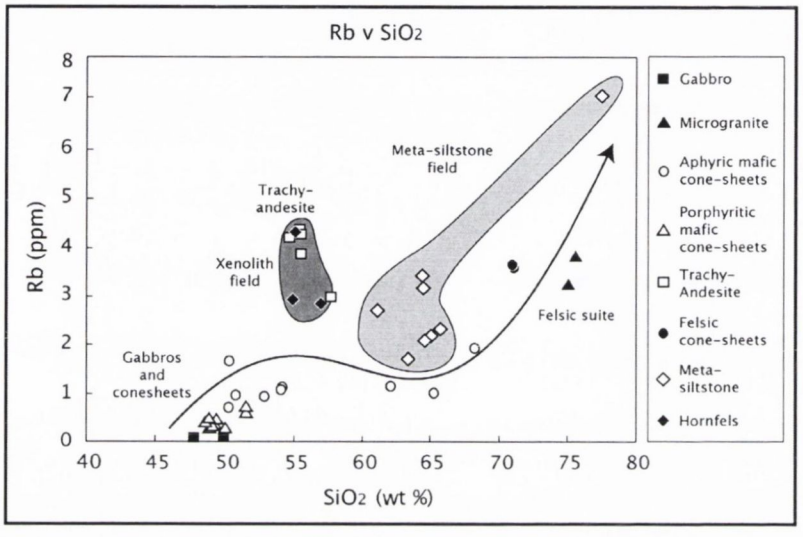


**Figure 6.20 Plot of Rb v $SiO_2$ showing general increase in Rb concentration. There is, however, a dip to lower Rb concentrations at mid-silica ranges, echoing the Rb concentrations of the local crust. While andesite and dacite samples plot near the meta-siltstone, the trachy-andesite plots within the hornfelsed xenolith field.**

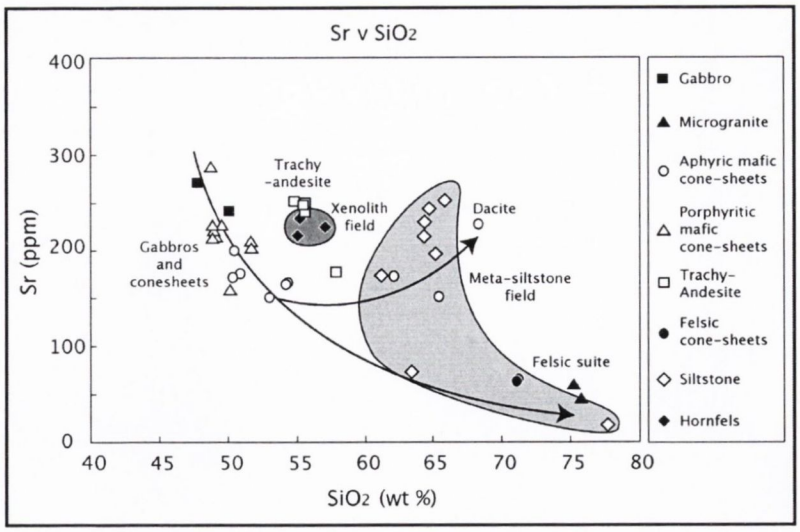


**Figure 6.21 Plot of Sr v $SiO_2$ showing a general decrease in Sr concentration. Note the relatively Sr-rich intermediate rocks, which lie within the meta-siltstone field. The trachy-andesites lie close to the hornfels xenoliths.**

A plot of Zr v $SiO_2$ shows an enrichment trend as expected from an incompatible element (see also Rb, Figure 6.20). Previous major and trace element plots have suggested the influence of the local crust on the felsic rocks of the centre (e.g. Figure 6.17, Figure 6.20). In this case, however, the felsic rocks show much higher Zr levels than the local crust. This may be the result of concentration of Zr by fractional crystallisation, or contamination by a Zr-rich partial melt of the meta-siltstones.

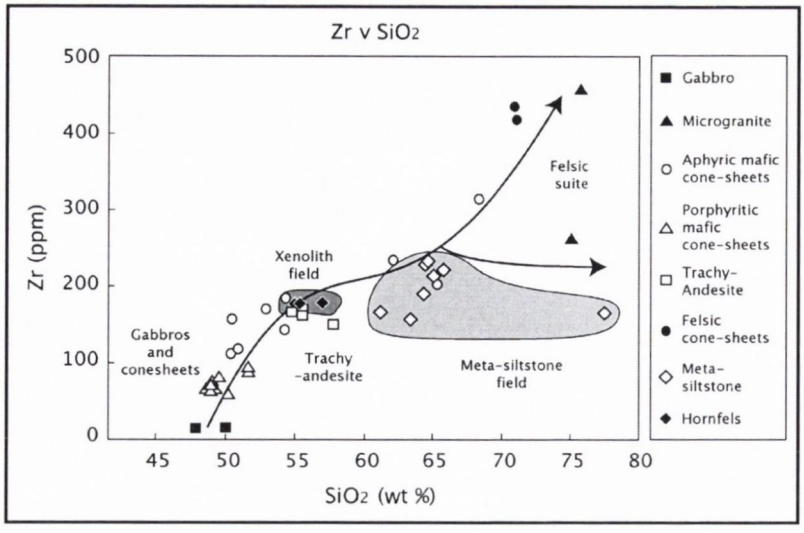


**Figure 6.22 Plot of Zr v $SiO_2$ showing a general trend of enrichment similar to that of Rb (Figure 6.20). There is a slight dip to lower Zr concentrations at mid-silica ranges, suggesting the influence of the local crust. While andesite and dacite samples plot near the meta-siltstone, the trachy-andesite plots within the hornfelsed xenolith field. Arrows indicate the general evolutionary trends of the suite, leading to high and low Zr rhyolites.**

A plot of Zr v Nb (Figure 6.23) shows that while the less evolved gabbros and basalts appear to have been more strongly influenced by fractional crystallisation, the spread of crustal values has had a strong effect on the composition of the more-evolved products.

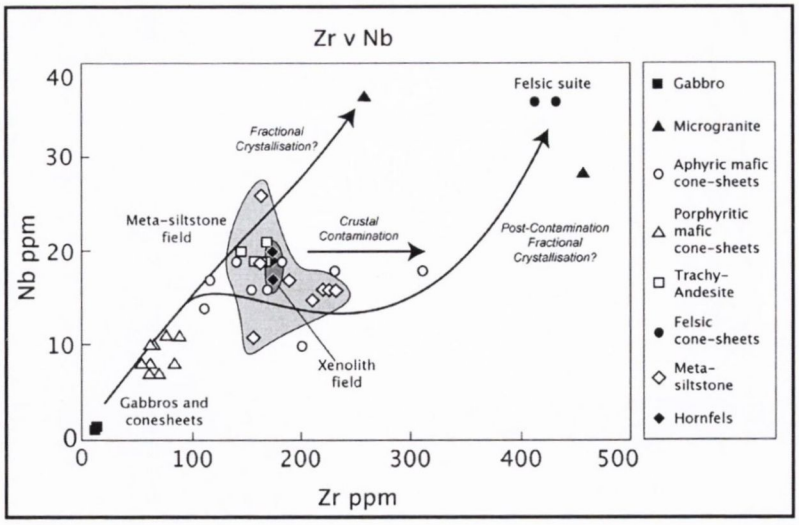


**Figure 6.23 Plot of Zr ppm v Nb ppm. Note decoupling of Zr from Nb at ~Nb=20 ppm, implying addition of Zr by an outside source. This trend is mirrored in the Zr composition of the siltstones, suggesting they may be such a source. The high $SiO_2$ igneous rocks appear to have evolved beyond the composition of the crust, again this may be the result of post-contamination fractional crystallisation, or indeed contamination by a incompatible-rich partial melt of the meta-sedimentary rocks.**

The trachy-andesite again lies within the field of hornfelsed metasediment and the andesite and dacite echo the trend of Zr enrichment seen within the siltstone metasediments (*see also* Figure 6.22). The cone-sheet rhyolites, in turn, appear to be the result of post-contamination fractionation as they have evolved beyond the most Zr-enriched crustal end member. This trend may also be the result of contamination by an incompatible-rich partial melt of the metasediments. The microgranite samples are likely to be the product of a similar combination of fractionation and crustal contamination, but by a more compositionally variable contaminant. Although it is not impossible that one sample of microgranite is the product of pure fractionation (as it sits on the basalt fractionation trend) while the other sample shows a distinct crustal influence. For elements like Zr (56-85 ppm) and Nd (3-6 ppm), the limestone

and marble values are lower than those of the igneous rocks, so any influence these lithologies may have had is not apparent.

### *6.8.3. Rare earth elements*

The strong crustal component of the trachy-andesites is furthermore mirrored in its rare earth element profile, whereby the Longford-Down metasedimentary rocks (both the meta-siltstone and hornfels samples) match the trachy-andesite for virtually all samples and all elements (Figure 6.24). This rare earth element data, combined with the major and trace element data (see sections 6.8.1 and 6.8.2) and the petrology of the hornfels xenoliths (which show partial melting textures, Figure 6.5) suggest the trachy-andesite "magma" is in fact a partial melt of the hornfelsed crust, rather than a primary magma. This melt coincidentally has an igneous-type composition and formed an "*s-type*" basalt, haloing the xenoliths within the surrounding hot basaltic magma.

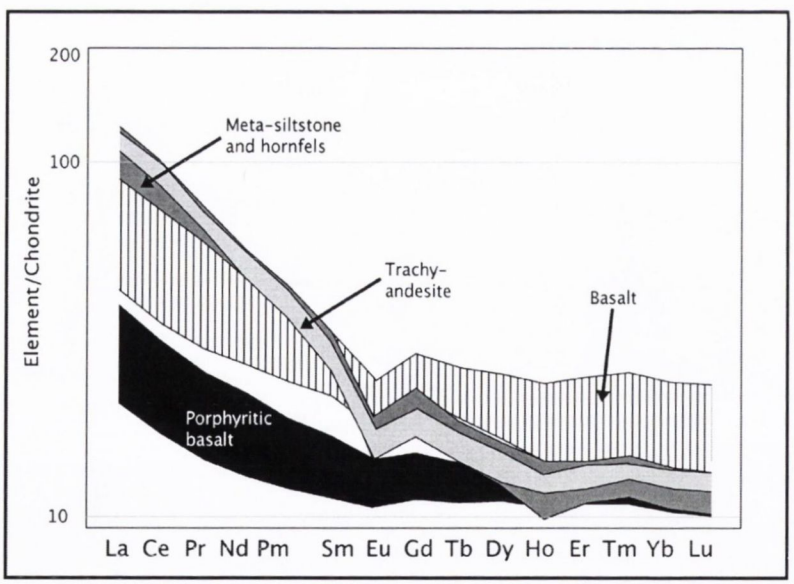


**Figure 6.24 Chondrite normalised rare earth element plot showing the main cone-sheet lithologies and the local crust.**

### *6.8.4. Least-squares mixing calculations*

Least-squares mixing analysis of both major and trace elements was used to compare a calculated mixed composition to that of the trachy-andesite samples. This allows a test of the hypothesis that the trachy-andesite is crustal melt rather than contaminated primary magma (section 6.8.3).

This method produces a best-fit binary mixing ratio for the data using basalt CS4E (the basaltic member of the composite cone-sheet in which the trachy-andesite occurs) and hornfels xenolith C-SB1 as end members. Major element data suggests the trachy-andesite is ~99% hornfels, while the trace element data gives a value of ~88%, indicating the trachy-andesite is almost entirely crustal melt. The trachy-andesite is enriched in Sr and Ba compared to both the basalt and the hornfels, suggesting there has been incorporation of an enriched partial melt from the hornfels, most likely due to melting of feldspar (Figure 6.5, Figure 6.21).

The lower percentage value for trace elements suggests there may have been some mixing of this crustal melt with the surrounding basalt, perhaps by means of trace element diffusion, accounting for why the major elements don't show the change in composition.

The crustal melting hypothesis is supported by the results of experimental petrology, whereby a sample of Longford-Down metasediment was heated to magma chamber temperatures and pressures (1000°C, 5 Kbar) for one hour (See sections 5.9 and 6.7). At these experimental conditions the metasediment melted completely, indicating the potential for xenoliths to form a crustal melt (Figure 6.25).




**Figure 6.25 Back scattered electron image of glass resulting from complete melting of Longford-Down metasediment at 1000°C and 5 Kbar. Plagioclase microlites represent areas of recrystallisation.**

## 6.9. Isotope geochemistry

Using a typical Atlantic MORB basalt composition (Saunders *et al.*, 1988) and the various crustal compositions as end members, geochemical models for both assimilation during fractional crystallisation (AFC) (DePaolo, 1981) and bulk isotope mixing (Langmuir *et al.*, 1978) were run. MORB values were used as the mantle end member as other work within the wider study of which this project is part has shown that even the most primitive samples within the BIPIP (e.g. McClurg's Dyke on Rum) have been significantly contaminated by the crust (Nicoll, G.R., Troll, V.R. *pers. comm.*).

AFC modelling used the *AFC.isotopes* programme of J. Entenmann (http://www.geologynet.com/afc.isotopes.zip). Modelling was run over a range of r-values, to consider the effect of various amounts of assimilation. The r-value

represents the ratio of assimilation to fractional crystallisation, with high r-values representing high levels of assimilation.

### *6.9.1. Strontium and neodymium isotopes*

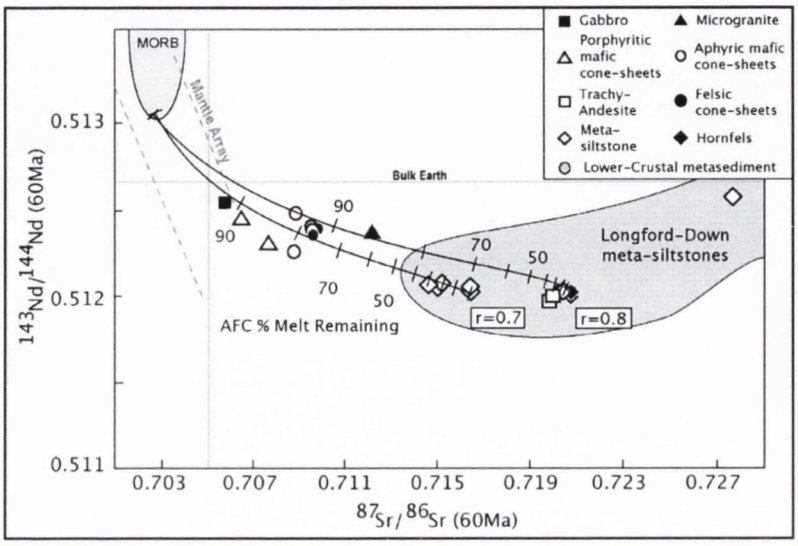


**Figure 6.26 $^{87}Sr/^{86}Sr$ v $^{143}Nd/^{144}Nd$ isotope ratios for major lithologies in the Carlingford Igneous Centre, including local metasedimentary crust. The upper curve represents AFC processes using a hornfels end member and r = 0.8, while the lower curve represents AFC processes involving a meta-siltstone end member with r = 0.7. Lower r-values did not fit the dataset, however, the high values used can be justified as the contaminants are highly fusible (See sections 6.7 and 6.8.4).**

On a plot of strontium versus neodymium isotope ratio (Figure 6.26, Figure 6.27) the substantial involvement of the Silurian siltstones and hornfels is apparent. All data deviate strongly from mantle (MORB) values towards this crustal composition. Geochemical modelling suggests that the contamination processes reflected by the major and trace element systematics are likely to be assimilation during fractional crystallisation. High rates of contamination are proposed, with r-

values of 0.7 - 0.8, which is feasible considering the fusible nature of the mica-rich siltstones.

The cone-sheet rhyolites have a similar isotopic composition to the cone-sheet basalts, implying that they are likely to have fractionated to rhyolite after initial contamination of the basaltic parental magma. The earlier microgranite, although similar in many ways to the cone-sheet rhyolites, has a more radiogenic isotope signature, suggesting it formed by a combination of prolonged assimilation and mineral fractionation. While a r-value of 0.8 appears accurate (Figure 6.26), modelling suggests unusually low levels of fractionation would be needed to form the microgranite (to as much as ~85% melt remaining), this raises questions on the suitability of the end member composition used.

Samples of lower-crustal mylonitic meta-volcanic xenoliths (see Anderson and Oliver, 1996) were also analysed. However, these xenoliths range from $^{87}Sr/^{86}Sr$ = 0.706506(11) to 0.709966(14) and like the Carlingford Limestone/Marble ($^{87}Sr/^{86}Sr$ = 0.708165(13) – 0.712608(12)), these samples do not have significantly radiogenic Sr isotope ratios for their influence to be recognised using the Sr and Nd isotope system.

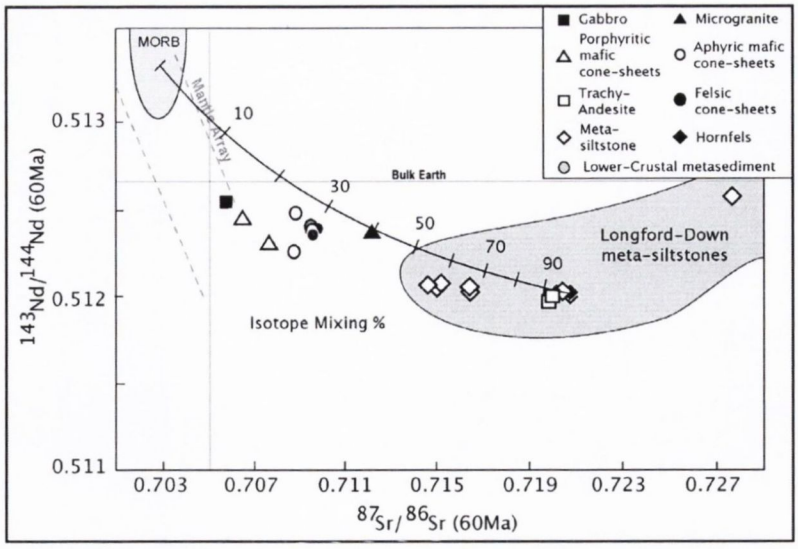


**Figure 6.27 $^{87}Sr/^{86}Sr$ v $^{143}Nd/^{144}Nd$ isotope ratios for major lithologies in the Carlingford Igneous Centre, including local metasedimentary crust. The plot shows the trachy-andesites have a very similar isotopic signature to the hornfelsed xenoliths. The curve represents binary mixing of MORB and hornfelsed metasediment end members.**

The trachy-andesites are isotopically similar to the hornfels xenoliths, however this composition is beyond the physical limitations of AFC processes (Figure 6.26) (e.g. Reiners *et al.*, 1995). Therefore the trachy-andesites are likely to result from the addition of a large volume of hornfels melt (>90%) to a small volume of basaltic magma by bulk mixing (Figure 6.27). This is consistent with results form major, trace and rare earth elements (Section 6.8).

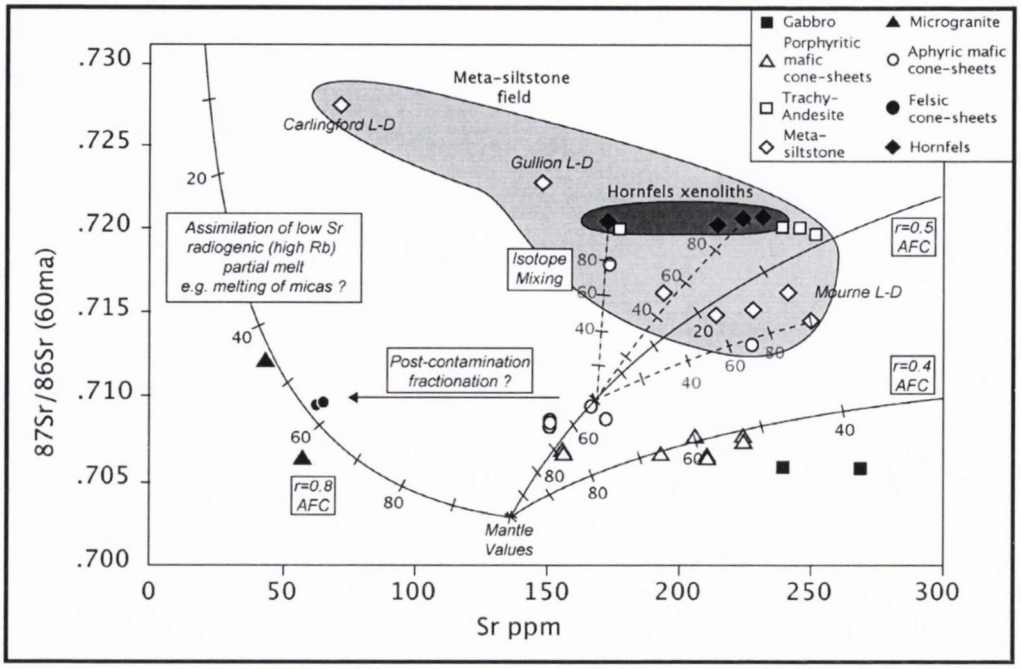


**Figure 6.28 $^{87}Sr/^{86}Sr$ v Sr ppm, showing potential petrogenetic paths. AFC models are in full lines, with bulk mixing models in dashed lines. Meta-siltstones are labelled by location. Note Carlingford hornfels xenoliths are richer in Sr, and less radiogenic, than their meta-siltstone equivalents. The Slieve Gullion value is from Troll *et al.* (2005).**

Assimilation processes are further constrained when $^{87}Sr/^{86}Sr$ is plotted against Sr concentrations (Figure 6.28). Several trends are evident, with all samples displaying contamination by local siltstone. The lesser evolved samples, the gabbro and porphyritic basalts, which plot off the r = 0.7 line in Figure 6.26, are a better fit to an r = 0.4 AFC model using the same crustal end member ($^{87}Sr/^{86}Sr = 0.71629$).

The aphyric basaltic samples, in turn, fit to a modelling curve that represents the assimilation of the $^{87}Sr/^{86}Sr = 0.72750$ end member with an r-value of 0.5. The more evolved "basalts" as seen in Figure 6.14 and Figure 6.23 appear to fit model calculations using r-values of ~0.4 – 0.6, however, they would sit too far along these lines to be physically feasible (see Reiners *et al.*, 1995). It is more likely they are the result of a two-step contamination as implied by Figure 6.23 and Figure 6.28. This

second stage is likely to be late-stage bulk mixing with crustal melt, probably derived from the conduit walls. One sample appears to have dominantly mixed with hornfels (CS4C), while another mixed with meta-siltstone (C-CS-SR). Significantly, the more radiogenic sample (andesite CS4C) was emplaced further into the metamorphic aureole of the gabbro than the less radiogenic sample (dacite C-CS-SR) and would therefore have traversed a more hornfelsed crust (Figure 6.2). The trachy-andesites again appear to be crustal melts with similar isotope values to the hornfels xenoliths (*see also* sections 6.8.2 and 6.8.4). They are slightly enriched in Sr relative to the xenoliths, but this may be the effect of partial melting, resulting in a Sr rich melt (e.g. due to melting of feldspars).

The microgranites are, in comparison, the result of AFC with an r-value of ~0.8, as suggested by Figure 6.26. However, their Sr concentrations do not support contamination by a known whole-rock siltstone, but rather by a low Sr, more radiogenic, end member. In this case, modelling gives more realistic values of fractionation for granite formation (~45-60% melt remaining). Considering the hornfels restite is less radiogenic and has higher Sr ppm than the siltstone protolith, it has most probably lost a highly radiogenic, low Sr ppm partial melt. Such a partial melt is the most likely end-member contaminant for the microgranite (Figure 6.28).

### *6.9.2. Lead isotopes*

A plot of $^{206}Pb/^{204}Pb$ v $^{208}Pb/^{204}Pb$ shows two main crustal fields, one for the Longford-Down Silurian metasediments and the other, with more radiogenic $^{206}Pb/^{204}Pb$ ratios, for the Carboniferous carbonates. The majority of samples from the Carlingford Igneous Centre plot close to or within the Silurian metasediments

field, but one sample, the highly contaminated CS4C, lies within the carbonate field (Figure 6.29).

This sample was collected from a cone-sheet dyke within the Silurian siltstones, but just north of the boundary between the siltstone and the local Carboniferous limestone, near the Slate Rock (IJ 17 11). The limestone rests above a shallow dipping unconformity with the siltstones and therefore the magmas could not have come into contact with the main limestone. However, large (~100 m long) stoped blocks of marbleised limestone are seen in this area of the complex within both the main gabbro body and the microgranite ring-dyke (Figure 6.8) (Le Bas, 1965a). It is therefore conceivable that the magma has come in contact with one of these stoped limestone blocks; either within the cone-sheet magma chamber, or during intrusion as a stoped block frozen within the earlier gabbro/microgranite.

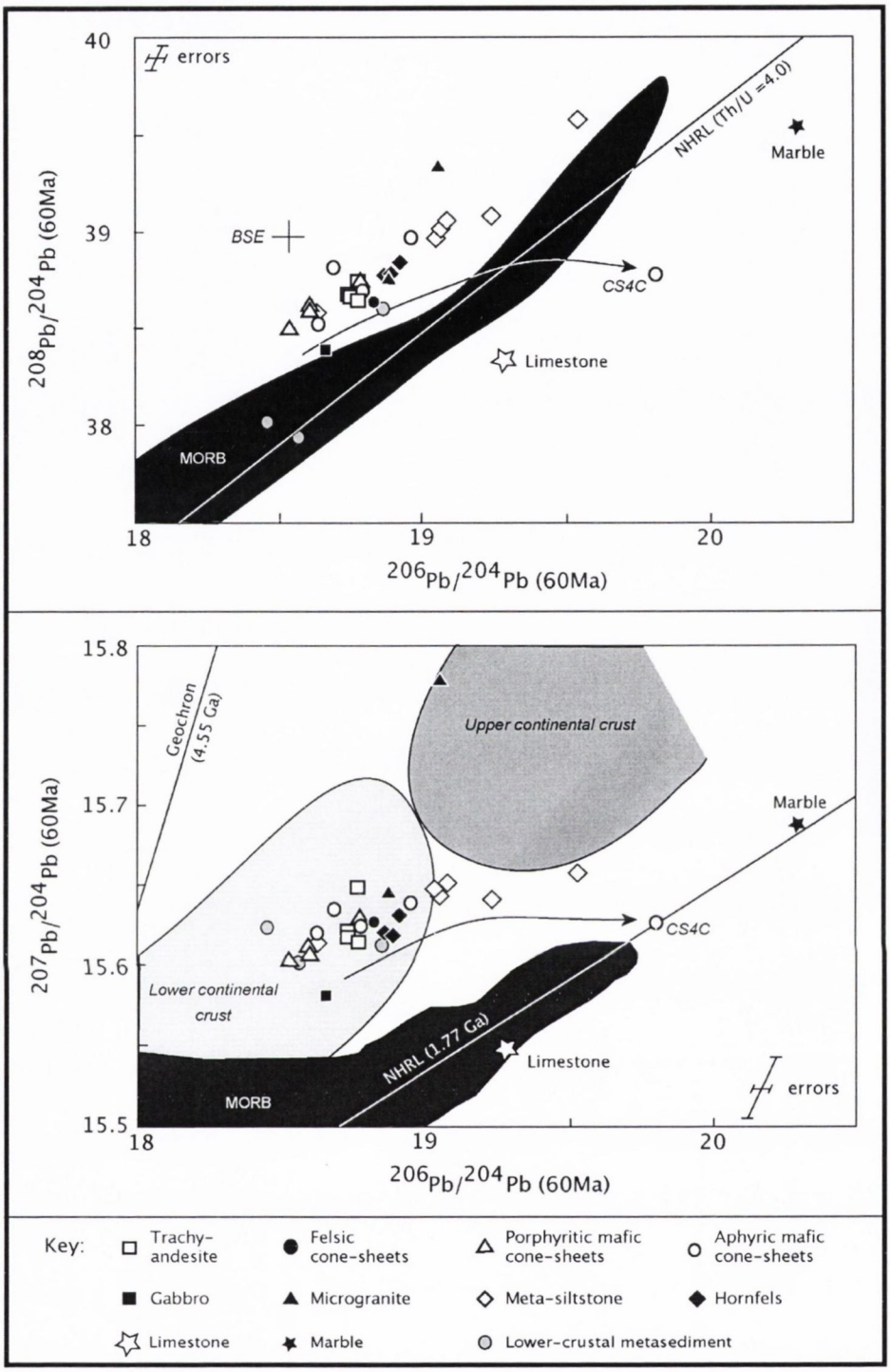


**Figure 6.29 Pb isotope plots showing a single point (CS4C) plotting towards the limestone field. The majority of samples plot towards the local Longford-Down crust. BSE values from Allegre et al (1988). MORB and upper and lower crustal fields from Rollinson (1993) (Figure 6.11).**

## 6.10. Microprobe analysis of zoned plagioclase feldspars

Zoned feldspars from three separate thick sections were analysed with the electron microprobe for their chemical composition. These thick sections (CSRB, CPD9, CPB were all from the Slate Rock locality (J 178 116) and represent the range of phenocryst size and abundance variations within the cone-sheet porphyritic basalt.

Zoned phenocrysts were first identified using a petrological microscope and were then imaged using back-scattered electron microscopy (Figure 6.30), before being systematically investigated through spot analyses with the electron microprobe (see section 5.6).

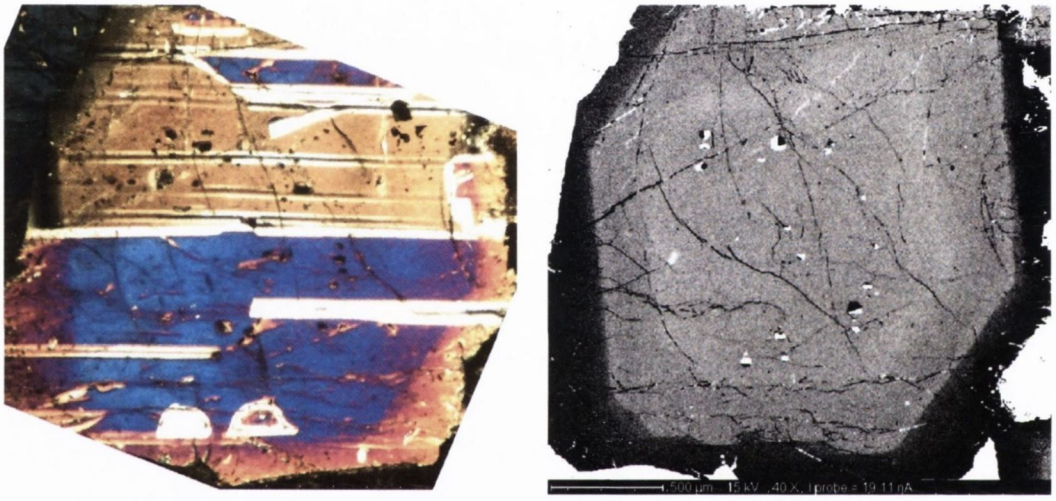

**Figure 6.30 Feldspar CSRB 1, showing zones in cross-polarised light (left) and back-scattered electron (BSE) image. Bright interference colours in the cross-polarised image are the result of viewing a thick-section (~140μm) rather than thin section (~30μm).**

### *6.10.1. Thick section CPD9*

The feldspars in thin section CPD9 have large cores with a composition of $An_{90-75}$ (*average* = $An_{82}$, *mode* = $An_{83}$, *median* = $An_{82}$). Many of these cores show irregular boundaries, suggesting they have been resorbed. They have thin rims

ranging from ~10-80 μm with lower anorthite values ($An_{69-51}$). Five of the six crystals probed show this simple zoning with a high-An core and a thin low-An rim. Feldspar PD9 16 has a more complex zoning pattern, appearing to have two high-An cores in this section, it is most likely a function of the slice through the crystal, cutting through a resorbed core with an irregular shape in three dimensions (Figure 6.31). Groundmass feldspars in this sample take the form of twin-zoned microlites ~40 μm in length. They have lower An values of $An_{62-46}$.

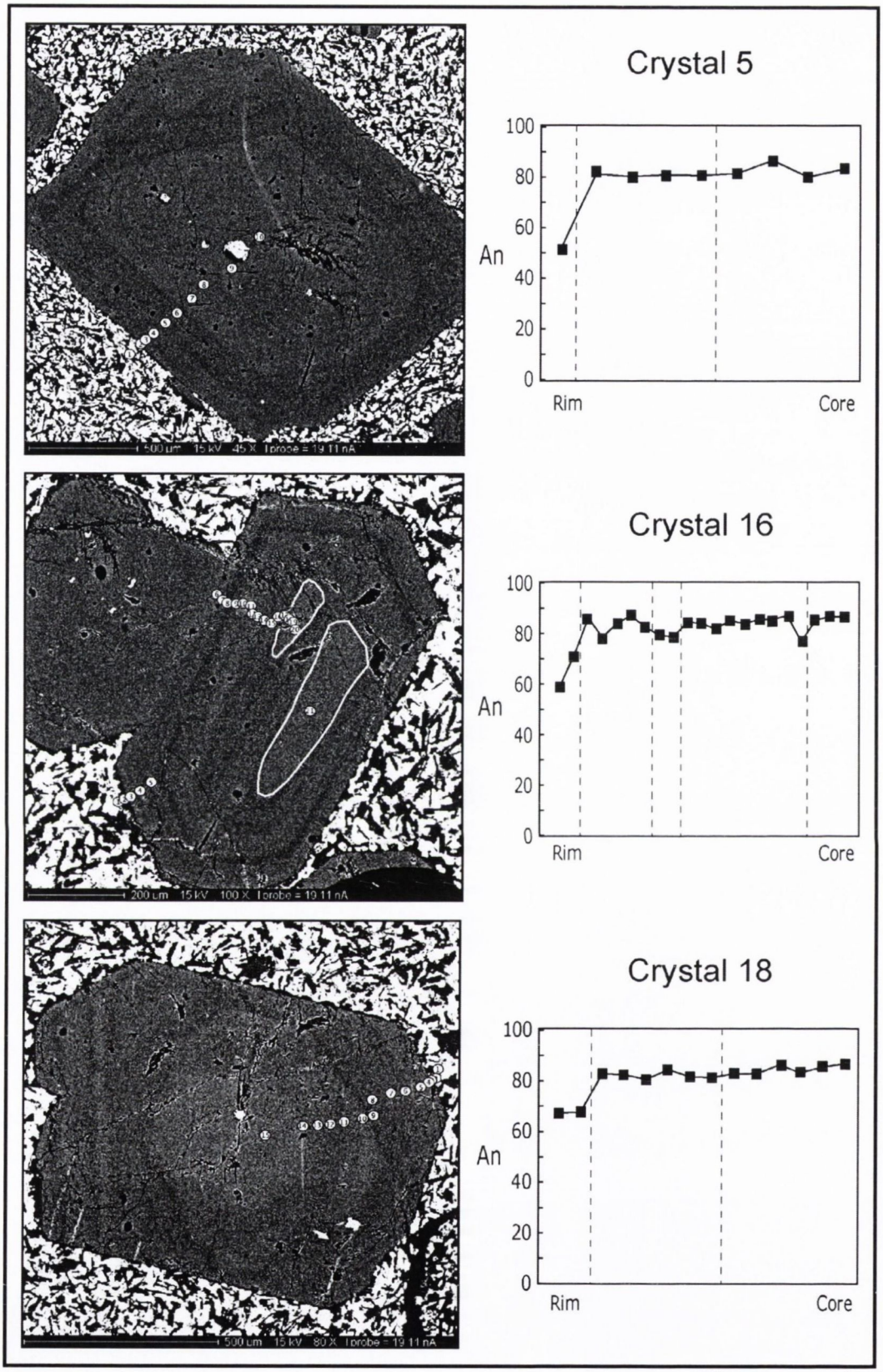


*Caption overleaf*

**Figure 6.31 Feldspars from thin section CPD9, showing microprobe spots and An values for the traverses from rim to core of each crystal. X-axis is not to scale, see spots on BSE image for true sampling density. Dashed lines represent the main zone boundaries. Note crystal 16 shows two high-An cores (delineated in white), this may represent a section of the irregular surface of a single resorbed core. Points that lie outside the crystal are groundmass feldspar analyses (see Appendix 2.10).**

### *6.10.2. Thick section CPB*

The feldspars in CPB are much larger than those within CPD9, but the zoning pattern remains broadly similar. Plagioclase shows high-An cores ($An_{91-86}$), with an *average* = $An_{88}$, *mode* = $An_{86}$ and *median* = $An_{88}$. They have, however, more obvious, thicker, outer rims (95-157 μm), but with similar An values ($An_{76-58}$) (Figure 6.32).

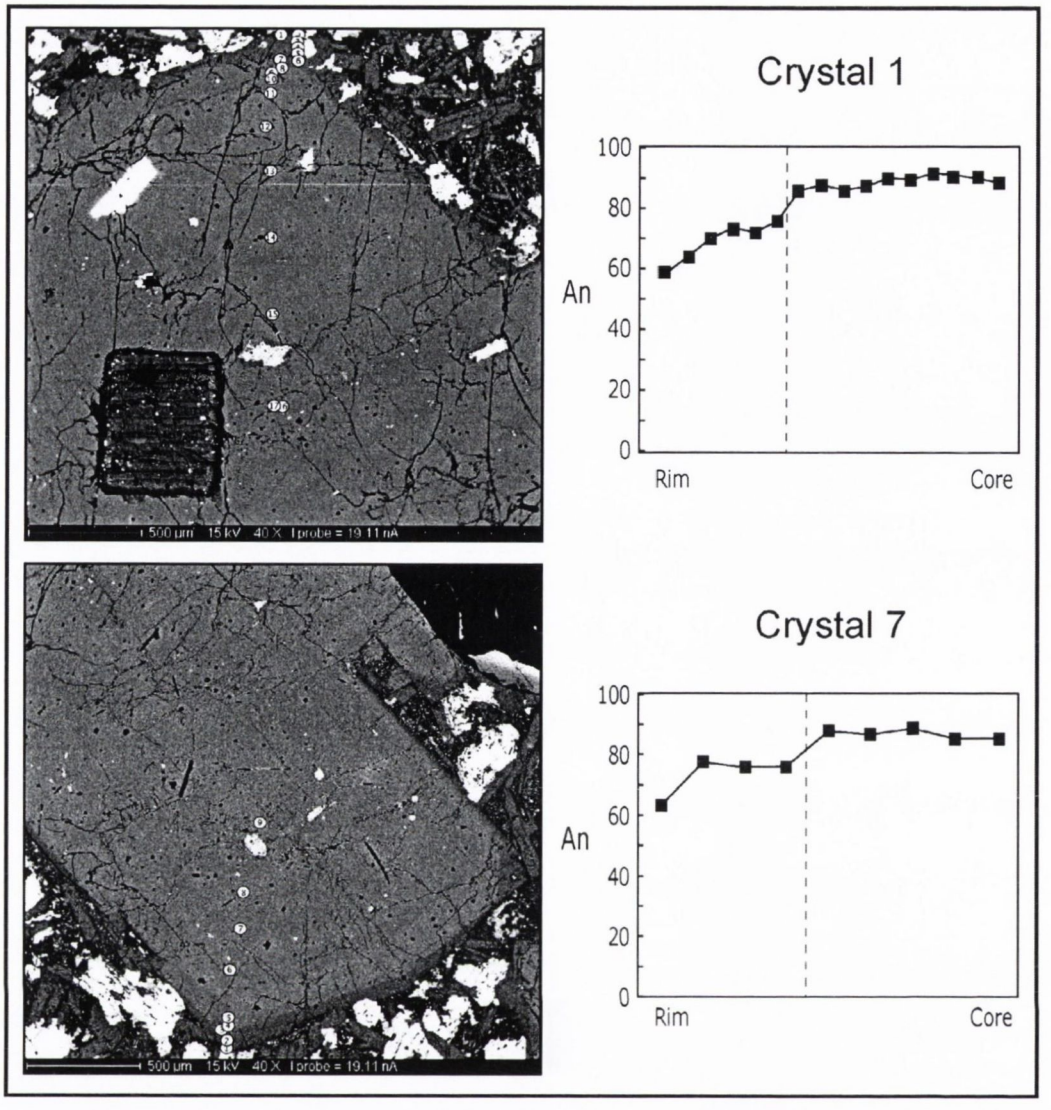


**Figure 6.32 Feldspars from thin section CPB, showing microprobe spots and An values for the traverses from rim to core of each crystal. X-axis is not to scale, see spots on BSE image for true sampling density. Dashed lines represent zone boundaries. Note the drilled area in lower left of the BSE image of crystal 1.**

### *6.10.3. Thick section CSRB*

The feldspars of thin section CSRB are similar in size to those of CPB, but the sample as a whole is coarser grained. Many of the feldspars have obvious

resorbed cores (CSRB 1, CSRB 4 and CSRB 10). Zoning patterns are more complex and the majority of crystals have at least three well-developed zones (Figure 6.33).

The cores range $An_{86-79}$ (*average* = $An_{83}$, *mode* = $An_{83}$, *median* = $An_{83}$), almost exactly the same as CPD9. The next rim ranges $An_{74-52}$ (*average* = $An_{64}$, *mode* = $An_{67}$, *median* = $An_{67}$). Together, these two zones are very similar to the zoning seen in CPB and CPD9, though with this first rim being thicker than in either of the two previous samples (~200-500 μm). Crystals from section CSRB also, however, consistently have a third outer zone, with $An_{50-24}$ (*average* = $An_{39}$, *mode* = $An_{39}$, *median* = $An_{39}$). These crystals must have experienced their final phase of growth in a more evolved melt than either of the previous two batches of crystals. There are no groundmass feldspar microlites in this sample, in fact the section is quite equigranular. However the feldspars' outer rims are similar in composition to the groundmass feldspars of CPD9. Perhaps in the case of this sample, new groundmass microlites did not nucleate, but rather lower An rims grew onto the existing feldspars as the magma cooled. This may indicate a slower cooling regime than that experienced by CPD9, where the groundmass quenched to form a porphyritic texture, rather than the medium to coarse-grained texture of CSRB. This is consistent with cooling in the insulated core of the wide dyke (up to 8 m thick) rather than at the more readily cooled edges. See Appendix 2.10 for the complete microprobe dataset.

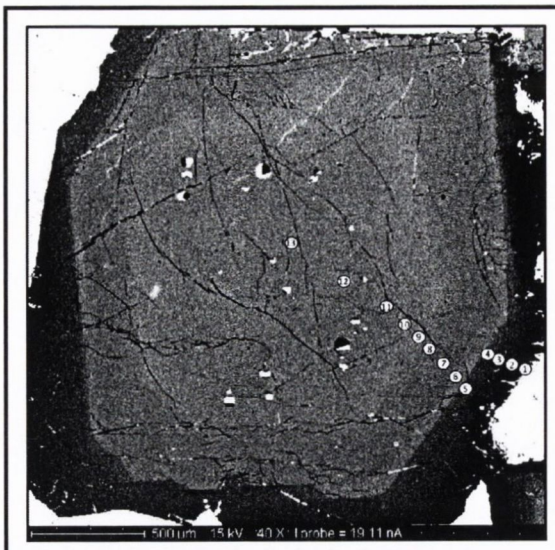


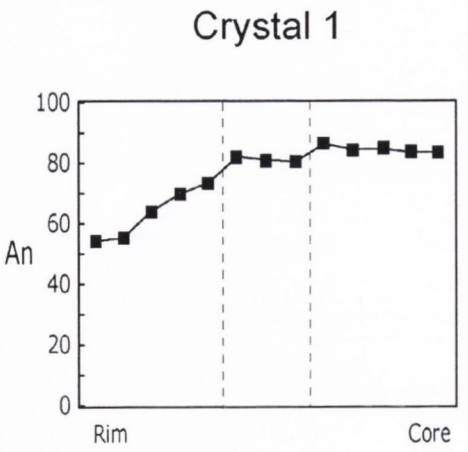


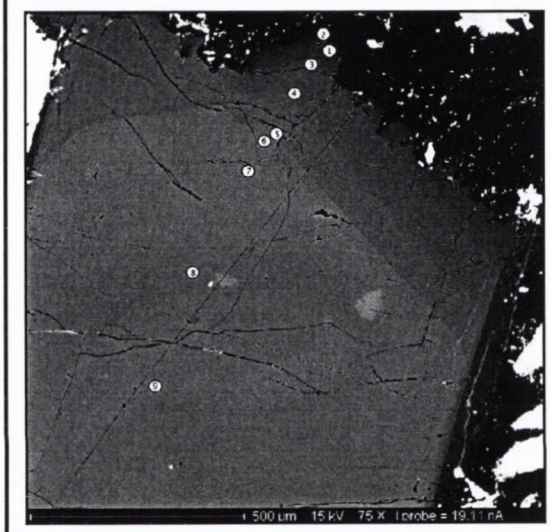


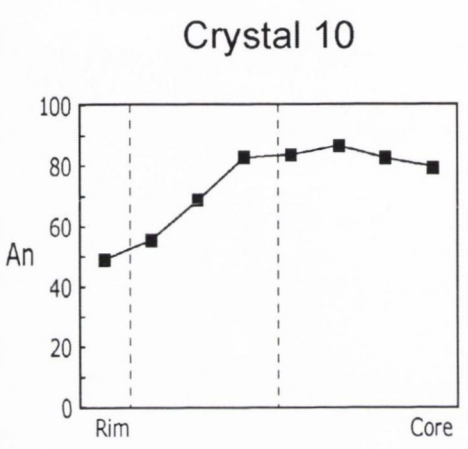


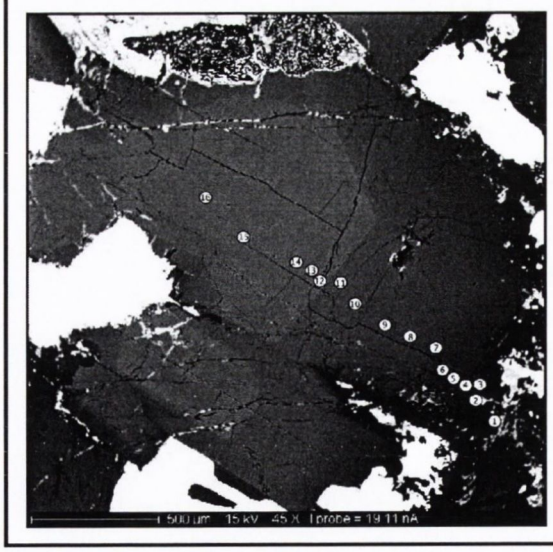


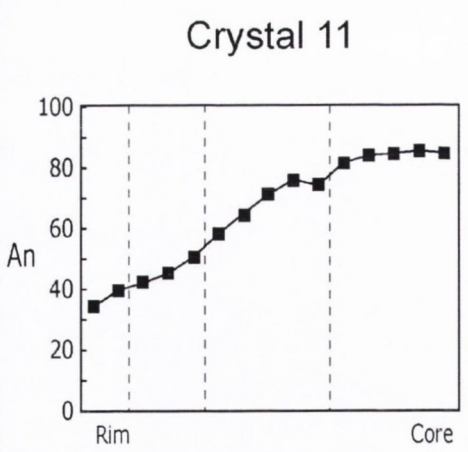


*Caption overleaf*

**Figure 6.33 Feldspars from thin section CSRB, showing microprobe spots and An values for the traverses from rim to core of each crystal. X-axis is not to scale, see spots on BSE image for true sampling density. Dashed lines represent the main zone boundaries. Points that lie outside the crystal are groundmass feldspar analyses (see Appendix 2.10).**

## 6.11. Microdrilling of zoned plagioclase feldspars

Three zoned phenocrysts from the cone-sheet porphyritic basalt were selected for Sr-isotope microanalysis, in the hope that successive zones would preserve isotopic information on the magma's evolutionary history (cf. Davidson and Tepley, 1997; Davidson *et al.*, 2001; Chadwick *et al.*, 2007). Anorthite values decrease from core to rim in all crystals, broadly consistent with prolonged fractional crystallisation. However, while $^{87}Sr/^{86}Sr$ ratios show strong variation with each successive crystal zone, there is no consistent pattern to the isotopic zonation. A constant $^{87}Sr/^{86}Sr$ ratio would be expected throughout a crystal if fractional crystallisation were the sole process as work. Similarly, assimilation during fractional crystallisation would produce a gradually decreasing anorthite trend while showing simultaneously increasing $^{87}Sr/^{86}Sr$ ratio.

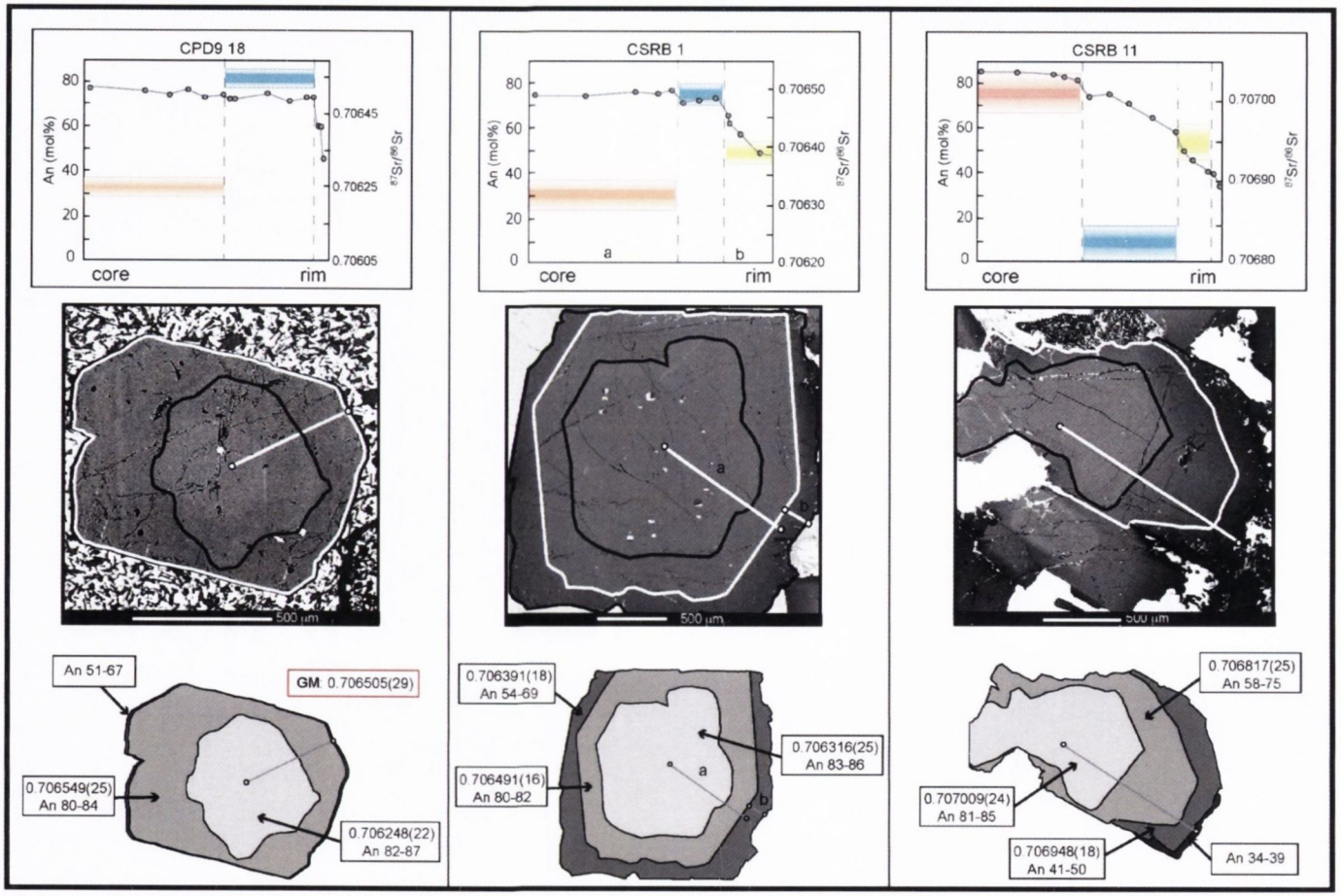


**Figure 6.34 Zoned crystals from porphyritic basalt were analysed for An value and micro-drilled for Sr isotopes. The upper graphs show $^{87}Sr/^{86}Sr$ (blocks) and An composition (lines) for the various zones. The central images show back-scattered election (BSE) images of the zoned crystals prior to drilling. The cartoons show zones marked in grey-scale and annotated with chemical composition. Straight lines represent the microprobe traverse for An.**

### *6.11.1.CPD9 18*

Crystal CPD9 18 shows a pattern that is broadly consistent with assimilation during fractional crystallisation zonation, i.e. decreasing An values ($An_{87-51}$) are coupled with increasing Sr isotope ratios from core to rim. The core shows a distinctly anhedral shape, overgrown by more euhedral outer rims, suggesting it has been resorbed and is thus not a true reflection of a pure AFC evolution, i.e. it has experienced a lost history prior to growth of the outer rims.

### *6.11.2.CSRB 1*

This crystal has similar An ranges and Sr isotope ratios to that of crystal CPB9 18 for both the core and first rims, suggesting these two crystals belong to the same population. However, crystal CSRB 1 preserves a well-developed second rim compared to the narrow second rim in PD9 18, which has very similar An-values. This second rim has lower Sr isotope ratios than the first rim, but higher ratios than the crystal's core, implying growth from a more evolved (low An), but slightly less contaminated (lower Sr isotope ratio), liquid than the previous rim.

### *6.11.3.CSRB 11*

Crystal CSRB 11 has consistently higher Sr-isotope ratios than either of the other two crystals. The core is particularly radiogenic (0.707009(24)) and has very high An values ($An_{85-81}$). This core may be inherited, perhaps from the local marble, explaining its very calcic and radiogenic nature (see Chadwick *et al.*, 2007). The subsequent rims appear to be the result of assimilation during fractional crystallisation, but in a more contaminated liquid than the one that gave rise to

crystals CPD9 18 and CSRB 1, perhaps within more contaminated zones near the walls or roof of the chamber.

## 6.12. Discussion

Major and trace element data and radiogenic isotope ratios indicate the Carlingford magmas have been variably contaminated by the crust through which they have passed (See section 6.8). Even the least evolved lithologies, gabbro and porphyritic basalt, have been contaminated to a small degree. This is supported by trace element data, as well strontium, neodymium and lead isotope ratios, which show the majority of contamination was by various fractions of the local Silurian sedimentary crust (meta-siltstone). This assimilation includes whole rock, partial melt and the assimilation of the remaining hornfelsed restite (Section 6.9). Isotope data also confirm the majority of contamination was by assimilation during fractional crystallisation processes rather than bulk isotope mixing (which formed some of the late stage intermediate rocks). Lead isotope data and crystal isotope stratigraphy (Section 6.11) suggest that the Carlingford limestone and marble may also have had an influence on certain samples, supplying xenocrystic material to parts of the Carlingford magmatic system.

The intermediate rock types seem to be the result of further, though variable, crustal contamination rather than pure crystal fractionation processes. This explains why many of the chemically intermediate rocks do not show obviously intermediate mineralogy but rather appear to be basalt in the field (Sections 6.3.8 and 6.3.9 and Figure 6.14). This evolution of intermediate compositions is likely to be a late-stage process (affecting the already contaminated basaltic magma) within the plumbing system. There, magma is likely to have mixed with melts derived from the conduit

and reservoir walls, as well as successive melts from xenoliths entrained within the flowing magma. This is further supported by the involvement of a limestone end-member contaminant, which is only likely to exist at the uppermost levels of the complex. Indeed the trachy-andesite appears to be almost entirely crustal melt, representing an "s-type basalt" formed within a cone-sheet by melting of hornfels xenoliths by the surrounding hot basaltic magma. The continued flow of basalt (>1000° C) around the xenoliths would have supplied the heat for fusion.

The cone-sheet rhyolite has similar isotopic ratios to the basaltic cone-sheet samples, suggesting it may be the result of post-contamination fractionation, whereas the earlier microgranite ring-dyke system appears to be the result of large amounts of contamination of a low-Sr, highly radiogenic partial melt of the local siltstones (see Duffield and Ruiz, 1998). Indeed, Duffield and Ruiz (1998) (*and references therein*) discuss how magmas can be initially contaminated by highly radiogenic partial melts due to melting of hydrous phases, such as biotite, within the country rocks. As the system heats up and melting continues, the biotite is exhausted as a source of Sr and feldspar begins to melt. This is evident in the trachy-andesites, whereby the melt is enriched in Sr and Ba, the feldspar compatible elements. In this case the micas had already been lost during earlier partial melting of the crust (contaminating the microgranite and forming the initial hornfels restite) and the system has now heated sufficiently to melt feldspar within the restite.

Electron microprobe analysis and crystal isotope stratigraphy reveal many more subtle processes that occurred within the late cone-sheet magma chamber. Crystals CPD9 18 and CSRB 1 record a resorption event and growth within liquids of differing composition. This argues in favour of convection in the magma chamber, e.g. moving crystals from more contaminated regions (near the walls) to less

contaminated ones (towards the centre of the chamber) (Couch *et al.*, 2001). In turn, crystal CSRB 11 appears to have a xenocrystic core and more contaminated rims than those seen in the other crystals, perhaps having formed entirely in the wall region of the chamber. However, crystals CSRB 1 and CSRB 11 are from the same thin section, showing that these various crystal populations had either mixed together already in the magma chamber or on evacuation from the magma chamber during cone-sheet intrusion. The various processes at work in the Carlingford magmatic system are represented schematically in Figure 6.35. A zoned magma chamber is assumed on the basis of field evidence (see section 6.2), whereby the concentration of porphyritic intrusions increase with altitude, and aphyric sheets are more common at lower altitudes. Consequently, it is envisaged that plagioclase would have crystallised in the roof zone, where heat loss was most effective.

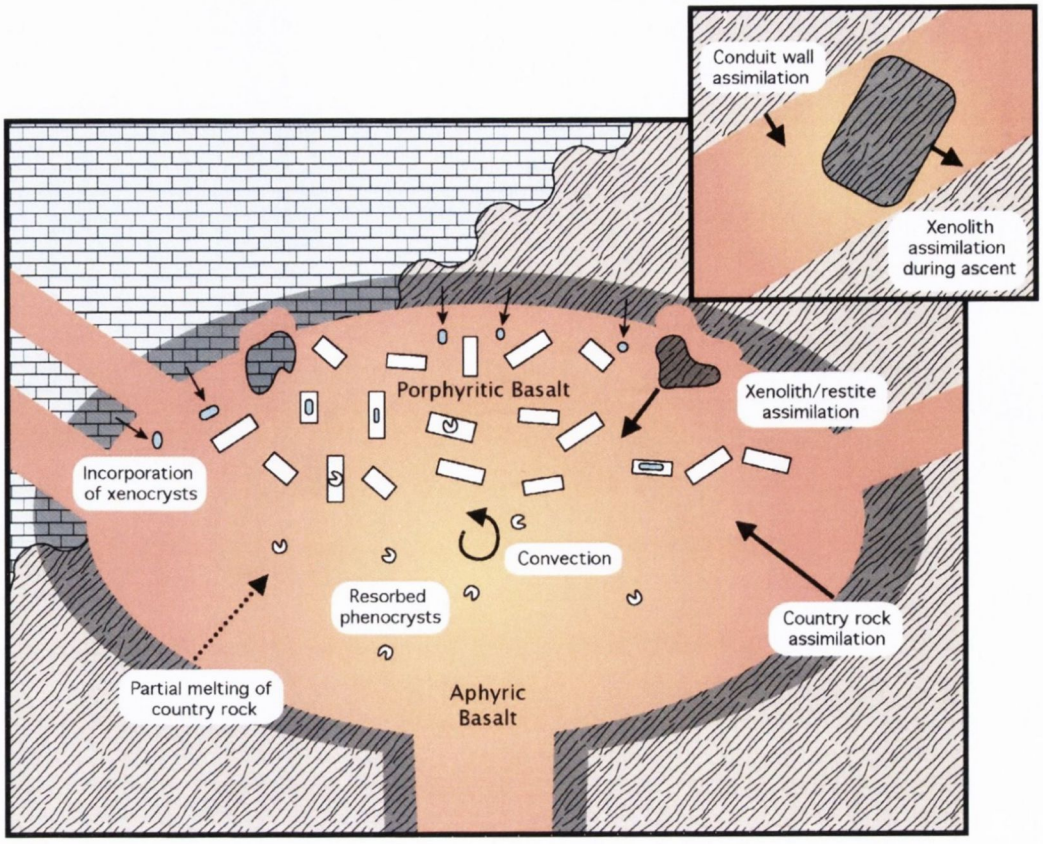


**Figure 6.35 Summary of processes occurring within the Carlingford cone-sheet magma system. These processes include assimilation of both whole-rock melts and partial melts of local crust, as well as restite assimilation. Xenocryst incorporation also occurs; these xenocrysts may form cores to some large magmatic phenocrysts. Convection is apparent from the presence of resorbed phenocrysts and zonation with phenocrysts. Large xenoliths (>1 m) are also present and have contaminated the magma during transport and intrusion.**

When the various processes detailed above are considered in a temporal sequence there is a clear pattern of progressive contamination (*cf.* Annen and Sparks, 2002). Initial assimilation of fertile partial melts formed the early microgranites as the magmatic system warmed up. As the local crust heated with time, bulk rock assimilation pervaded, forming the gabbro. This contamination regime continued in the cone-sheet magma chamber forming the basalt and porphyritic basalt. Finally,

late stage melting of remaining restite occurred on transport and intrusion of the cone-sheets, forming the trachy-andesite-type melt and the "evolved" basalts.

Significantly, the processes seen at Carlingford imply that, at least for this igneous centre, the "Bunsen-Daly Gap" is the product of intense contamination by fertile crust to form large volumes of granitic magma. The intermediate samples, which occur in low volumes and bridge this gap, are the product of contamination that has been restricted by both composition (infertile restites) and/or short interaction times (late-stage contamination during intrusion).

## 6.13. Conclusions

There is a long and complex history of magma-crust interaction recorded at the Carlingford Igneous Centre. As the developing volcanic plumbing system heated the local crust, there were high levels of contamination with a high-Rb, radiogenic, partial melt of the local Longford-Down metasediments (meta-siltstone). This initial melt was assimilated by the rising magma to form the Carlingford microgranite. Magmatism continued and with the arrival of a large body of hot mafic magma the system heated further, contaminating the subsequent Carlingford Later Gabbro with a whole-rock melt of the metasediments. This regime continued with the development of the final phase of magmatism at the Carlingford Igneous Centre, the cone-sheet magma chamber. Both the aphyric and porphyritic basaltic members of the Carlingford cone-sheet swarm were contaminated by these whole-rock crustal melts. This magma chamber was convecting, bringing more contaminated magma from the chamber walls/roof and circulating it within the chamber. Xenocrysts from the chamber walls were incorporated, forming radiogenic cores to magmatic phenocrysts. These xenocrysts indicate interaction with the Carlingford Limestone.

Late-stage magma-crust interaction occurred during cone-sheet emplacement. The intruding magmas picked up hornfelsed xenoliths of meta-siltstones and limestone. Melts of these crustal rocks contaminated the basalts to form intermediate compositions, including andesite and dacite. The hornfels at the edge of the xenoliths was also melted completely by the hot basalt, forming a melt that solidified to form an s-type magma of trachy-andesitic composition surrounding the remaining xenolith.

---

# 7. ARRAN

*A study of magma ascent along a major terrane boundary, focussing on crustal contamination and magma mixing at the Drumadoon Intrusive Complex, Isle of Arran, Scotland*

## 7.1. Abstract

The composite intrusions of Drumadoon Point and An Cumhann occur on the southeast coast of the Isle of Arran, Scotland. The intrusions (shallow level dykes and sills) comprise a central quartz-feldspar-phyric rhyolite flanked by xenocryst-bearing dolerite, with an intermediate zone of dark quartz-feldspar-phyric dacite. New geochemical data reveals information on the evolution of the component magmas and their relationships with each other, and their interaction with the crust through which they have travelled.

During shallow-crustal emplacement, they formed a mixing sequence. Isotopic evidence shows both magmas are contaminated by the crust; the dolerite magma preserves some evidence of contamination within the lower crust, while the rhyolite mainly records upper-crustal contamination. The Highland Boundary Fault divides Arran into two distinct terranes, the Grampian Terrane to the north and the Midland Valley Terrane to the south. The Drumadoon Complex lies within the Midland Valley Terrane but isotopic signatures indicate involvement of Grampian Terrane crust, therefore, while the magmas originated at depth on the northern side of the Highland Boundary Fault, they have crossed this boundary during their evolution, probably just prior to emplacement.

## 7.2. Introduction

The Isle of Arran, in southwest Scotland, was a site of intense igneous activity during the Palaeogene, is bisected by the Highland Boundary Fault, and thus affords the opportunity to investigate magmatism and magma transport mechanisms at a major terrane boundary. The Highland Boundary Fault is a major crustal-scale

discontinuity and forms the boundary between the chemically distinct Neoproterozoic to Lower Palaeozoic Grampian Terrane to the north, and the Palaeozoic to Mesozoic Midland Valley Terranes to the south.

Palaeogene igneous activity on Arran focussed on two main centres, the Northern Granite (Flett, 1942; England, 1992; Goulty *et al.*, 2001) and the Central Complex (King, 1954; King, 1955; Emeleus and Sutherland, 1982) (Figure 7.1). Arran is also characterised by several pulses of minor intrusions, including a well-developed regional N-S basaltic dyke swarm (Speight *et al.*, 1982).

Igneous activity is suggested to have spanned approximately 3 million years, from 61.7-57.4 Ma. This is based on palaeomagnetic constraints and geochronology. Palaeomagnetic studies place magmatism within chrons 26r, 26n and 25r (Hodgson *et al.*, 1990; dates were recalculated using the palaeomagnetic timescale of Gradstein *et al.*, 2004). This palaeomagnetic data is supported by recent Ar-Ar radiometric dates for the Northern Granite (57.85± 0.15 Ma) (Chambers, 2000) and the Drumadoon Sill (58.5 ± 0.8 Ma, (Mussett *et al.*, 1987), 59.04 ± 0.13 Ma and 59.16 ± 0.17 Ma (this study). The central complex has not yet been radiometrically dated.

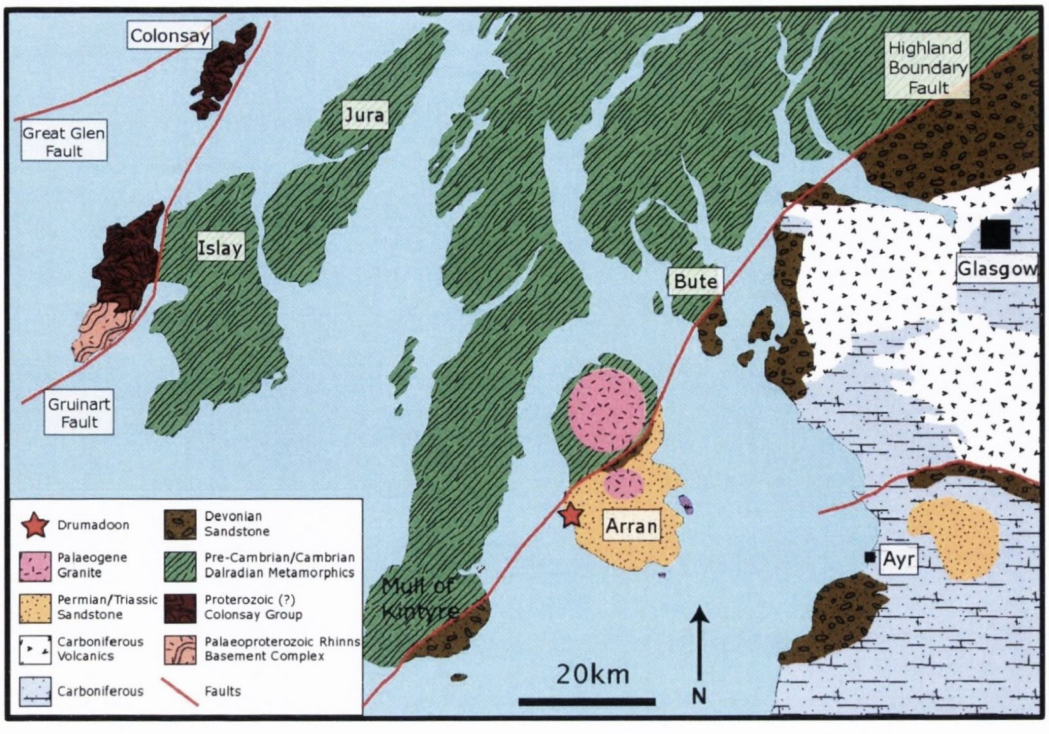


**Figure 7.1 Detailed geology of the Arran region.**

One of the more distinctive minor intrusive events on Arran comprises a series of quartz and feldspar-phyric rhyolites. These rhyolites are seen both as large single intrusions (e.g. Brown Head) and as composite dykes and sills with basaltic-andesite margins e.g. Drumadoon Point, the Doon sill and Beannan Head (Judd, 1893; Harrison, 1925; Kanaris-Sotiriou and Gibb, 1985) (Figure 7.2). Petrologically, these intrusions have been considered to be part of the same intrusive event, examples of which are seen throughout Arran and the Isle of Bute (Smellie, 1914; Brown, 1929; Buist, 1952). Palaeomagnetic studies also suggest these intrusions are members of the same phase of regional rhyolitic magmatism, relating to a normal magnetic reversal, Chron 26n (58.7-58.2 Ma) (Dagley *et al.*, 1978; Mussett *et al.*, 1984; Mussett *et al.*, 1987; Mussett *et al.*, 1989; Hodgson *et al.*, 1990; Gradstein *et al.*, 2004).

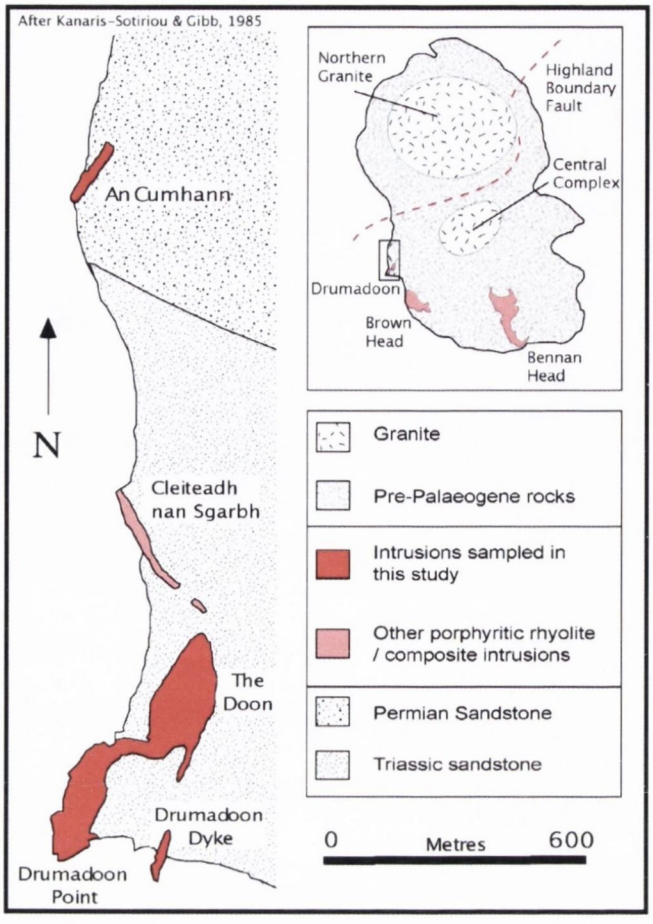


**Figure 7.2 Map of the Drumadoon Intrusive Complex (after Kanaris-Sotiriou and Gibb, 1985) with inset showing an overview of the porphyritic rhyolite sill complexes of Arran.**

## 7.3. The Drumadoon Intrusive Complex

The Drumadoon Intrusive Complex in south-east Arran is one such site of rhyolitic magmatism, and lies approximately 8 km to the south of the surface expression of the Highland Boundary Fault, within the Midland Valley Terrane (Figure 7.1, Figure 7.2). It comprises the composite intrusions (from north to south) of An Cumhann dyke, the Cleiteadh nan Sgarbh dyke, the Doon sill, the Drumadoon dyke and the Drumadoon Point sill (Figure 7.3). The dykes of Cleiteadh nan Sgarbh and An Cumhann generally comprise a central porphyritic rhyolite member flanked by xenocryst-bearing basaltic-andesite, often with a zone of porphyritic dacite

between them. The main Doon sill and the lower level sill at Drumadoon Point predominantly comprise an enclave-bearing porphyritic rhyolite with associated rhyolite, dacite and xenocrystic basaltic-andesite at the margins of the intrusion. The main Doon sill is capped by a quartz and feldspar-phyric rhyolite that does not contain basaltic enclaves. In the case of the feeder dykes, this pristine rhyolite fills the centre of the dykes, implying it was the last magma intruded.

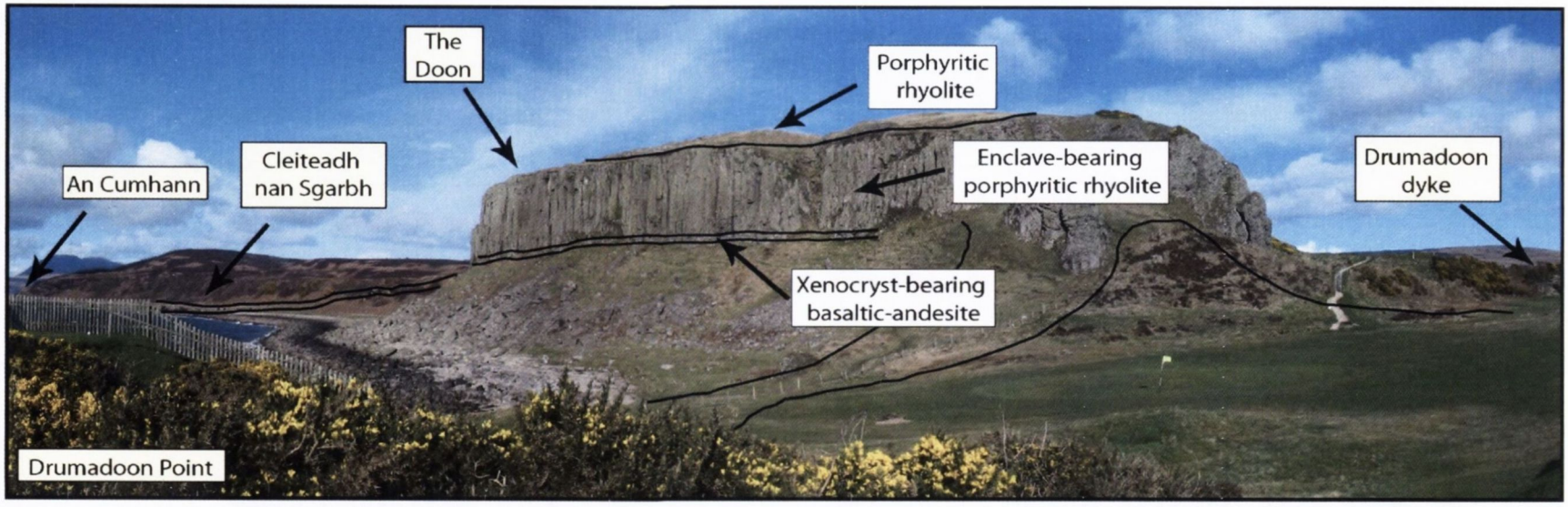


**Figure 7.3 Annotated photograph (looking northeast) of the Drumadoon Intrusive Complex. Cliff is approximately 30 m high.**

## 7.4. Petrology and petrography

### *7.4.1. Xenocrystic dolerite/basalt*

This xenocrystic dolerite (Figure 7.4) ranges in grain size from medium (dolerite) to fine-grained (basalt) and has a matrix mostly comprised of plagioclase laths and altered pyroxene, as well as some olivine. It has approximately 5% xenocrysts, including 3% embayed quartz with fine-grained reaction rims and 2% rounded alkali feldspar (up to 8 mm in size). These feldspars have been heavily resorbed and show thin new equilibrium rims. The matrix comprises 45% plagioclase laths, 5% opaques and ~50% pyroxene, which has decayed to hornblende. Chemically, this magma is of a basaltic-andesite composition (see section 7.8).

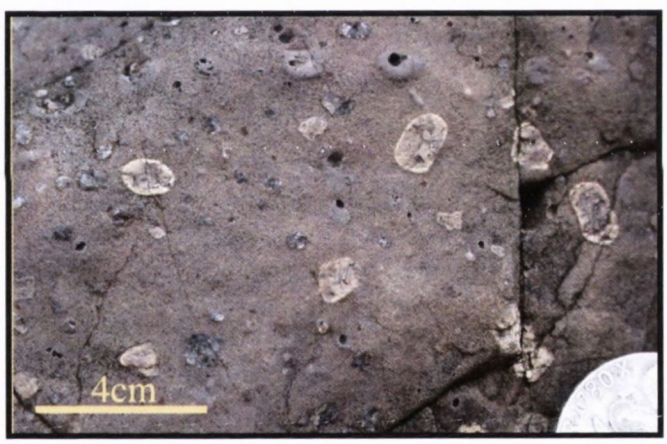


**Figure 7.4 Xenocrystic dolerite with rounded quartz and potassium feldspar xenocrysts.**

Rounded groups of calcite crystals, surrounded by thin chilled rims are also present. They most likely represent cross-sections through calcitic amygdales that have grown within vesicles. The presence of vesicles in the basalt indicate this dyke was intruded at high levels within the crust, most likely < 3 km (Paquet *et al.*, 2007 *and references therein*).

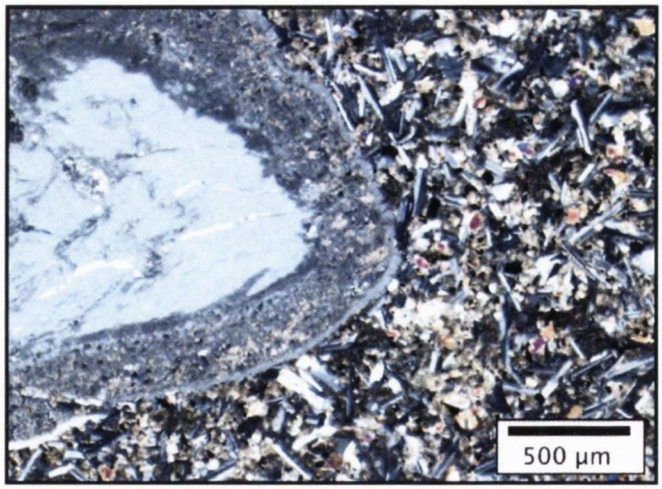


**Figure 7.5 Thin section of xenocrystic basalt, showing chemically eroded xenocrysts of K-feldspar, indicating they were not in equilibrium with the melt.**

### *7.4.2. Porphyritic dacite*

The porphyritic dacite (Figure 7.6) has a fine-grained matrix rich in feldspar. It also contains mafic minerals that are too altered to identify, though they are likely to have been hornblende. It contains approximately 10-20% phenocrysts, which include embayed quartz (40%) and rounded, resorbed alkali feldspar phenocrysts (60%). The dacite also contains ~ 2% unchilled basaltic enclaves. Small micro-enclaves and glomerocrysts of basaltic minerals are also seen within the matrix.



**Figure 7.6 Polished outcrop of porphyritic dacite, showing its dark matrix and quartz and feldspar phenocrysts. Note the presence of basaltic enclaves up to 5 cm in size.**

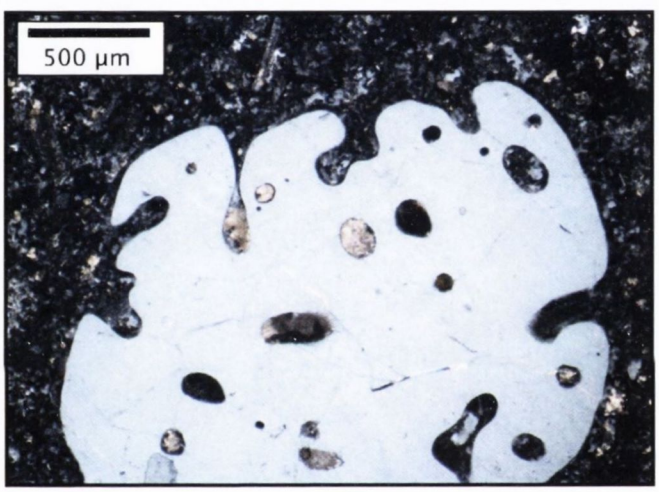


**Figure 7.7 Thin section of porphyritic dacite, showing embayed quartz phenocrysts.**

### *7.4.3. Porphyritic rhyolite*

The porphyritic rhyolite (Figure 7.8) has a fine-grained matrix of mostly feldspar with some (~ 10%) quartz. It contains approximately 35% phenocrysts, which include embayed quartz (25%), and zoned potassium feldspar (75%). The feldspar phenocrysts show resorbed edges in some cases, and minor plagioclase is

present. Perthite, a plagioclase-potassium feldspar exsolution texture is also present, indicating subsolidus crystallisation in places. Some feldspars are altered to calcite.

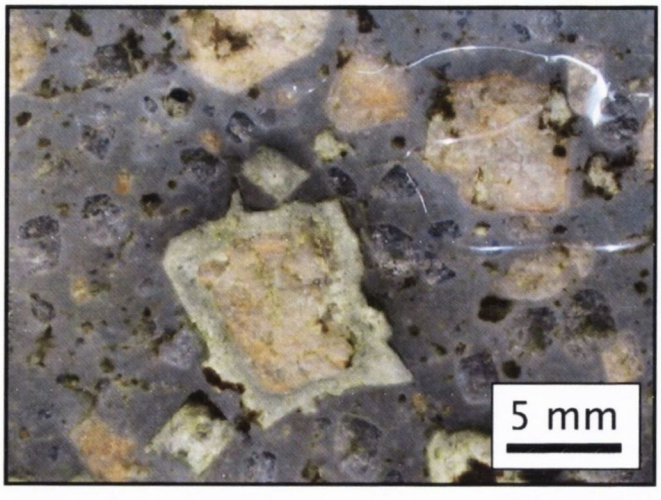


**Figure 7.8 Field photograph of polished rhyolite, showing zoned alkali feldspars and smaller quartz phenocrysts. The feldspar in the centre of the image shows a clear plagioclase rim, while many others do not.**

## 7.5. Contact relationships

The internal contacts within the intrusions exhibit textures indicative of liquid-liquid interaction with no chilled margins. Lobate contacts are ubiquitous, as are enclaves of basaltic-andesite within the rhyolite, and obvious phenocryst transfer from the porphyritic rhyolite to the porphyritic dacite (Figure 7.9, Figure 7.10). This suggests that both magmas were intruded contemporaneously and interacted both in the conduit during transport and *in situ* on final emplacement.

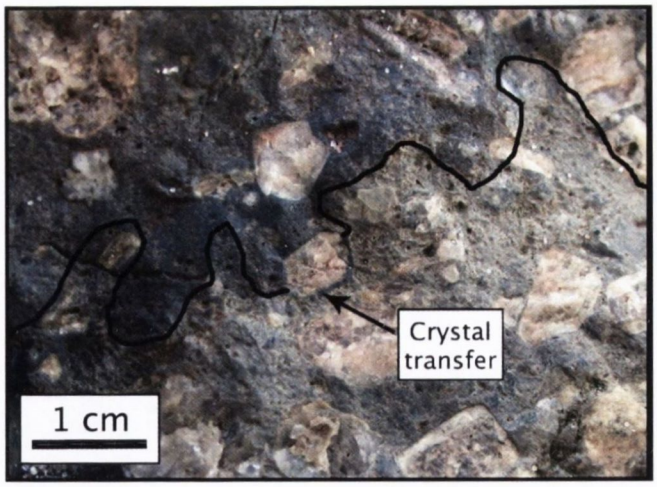


**Figure 7.9 Unchilled lobate contact and crystal transfer between the porphyritic rhyolite and porphyritic dacite.**



**Figure 7.10 Unchilled but distinct contact between the porphyritic dacite (top) and the xenocrystic basaltic-andesite (bottom). Coin for scale has a diameter of 22 mm.**

The basaltic-andesite is nearly always xenocrystic, containing resorbed crystals of both quartz and K-feldspar (Figure 7.10). Assuming these crystals have been sourced from the rhyolite, this suggests the basaltic-andesite and rhyolite have also interacted ***prior*** to intrusion (Kanaris-Sotiriou and Gibb, 1985). Other evidence for interaction prior to intrusion includes the mixing front between basaltic-andesite and dacite, which is marked by an extremely clear (though unchilled) contact.

Entrained xenocrysts would not be expected beyond the limit of the mixing front if all interaction was occurring in the conduit.

A narrow zone of darker dacite often marks the contact between basaltic-andesite and rhyolite, with an obvious, unchilled boundary with the basaltic-andesite, but grading inwards to a less obvious, lobate contact with the lighter-coloured rhyolite, probably representing the zone of interaction during intrusion (Figure 7.9). Previous work on hybridisation at the Drumadoon Intrusive Complex was carried out by Kanaris-Sotiriou and Gibb (1985) at the An Cumhann dyke.

## 7.6. Sample selection and preparation

Samples of basaltic-andesite, dacite, enclave-bearing rhyolite, and rhyolite from An Cumhann, the Doon sill, Drumadoon dyke and Drumadoon Point were analysed for major and trace elements and Sr and Nd isotopes, with the aim of elucidating the petrogenesis of these magmas, including quantification of their relationships with each other and also with the crust through which the magma passed (Appendices 4.1 and 5.1). Previous work by Dickin (1994), based on four samples from the entire Drumadoon suite of intrusions, has suggested the involvement of Grampian Terrane crust in the formation of the porphyry magmas. Kanaris-Sotiriou and Gibb (1985) analysed 44 samples for major and trace elements by XRF. They did not consider a parental basic magma, but rather used the least evolved (yet still mixed) basic sample as their mixing end member. The data set (n=20) focuses on the Drumadoon Intrusive Complex with the intention of looking at crustal contamination in more detail and quantifying the involvement of varying crustal end members, as well as a more detailed look at magma mixing at the

complex. These data will then allow the constraint of magma pathways along this major crustal discontinuity.

### *7.6.1. Sample preparation*

Samples were sliced and weathered edges removed. Xenocrysts were excluded from the basaltic-andesites and were not analysed. Mafic enclaves were also excluded from the enclave-bearing quartz and feldspar-phyric rhyolite. Samples were crushed in a jaw-crusher and powdered in a tungsten carbide TEMA mill.

## 7.7. Geochemical analysis

### *7.7.1. X-ray fluorescence*

Whole-rock samples were analyzed for major oxides by X-ray fluorescence (XRF) at the Centre d'Analyses Minérale, University of Lausanne, Switzerland (see section 5.2.3). Major and trace elements on all samples were also determined by XRF at GEOMAR Research Centre, Kiel, Germany (Section 5.2.1). Major element data had initial totals ranging from 98.48% to 100.32% and were corrected for loss on ignition and normalised to 100% (Appendices 4.2, 4.3, 4.4, 5.2, 5.3 and 5.4).

### *7.7.2. ICP-MS*

Rare-earth element concentrations for the Drumadoon samples were determined by inductively coupled plasma mass spectrometry (ICP-MS) using a Hewlett Packard 4500 at the Institute F. - A. Forel, Versoix, Switzerland (Section 5.4.2) (Appendix 4.5).

Rare earth elements and U, Th and Pb concentrations of other igneous samples, and local crustal samples were determined by inductively coupled plasma mass spectrometry (ICP-MS) at the Scottish Universities Environmental Research Centre (SUERC), East Kilbride, Scotland (see section 5.4.1) (Appendices 4.5, 4.6, 5.5 and 5.6).

### *7.7.3. Isotope geochemistry*

#### *7.7.3.1. Whole rock isotope ratios for Drumadoon samples*

Both strontium and neodymium isotope ratios for the samples from the Drumadoon Intrusive Complex were analysed at the Department of Mineralogy, University of Geneva, Switzerland (Appendices 4.7 and 4.9).

##### 7.7.3.1.1. Strontium isotopes

Strontium isotope ratios were measured using on a seven-collector Finnigan MAT 262 thermal ionization mass spectrometer with extended geometry and stigmatic focusing using double Re filaments. For details on standards see section 5.5.1.2.

##### 7.7.3.1.2. Neodymium isotopes

Neodymium isotope analyses were carried out using a seven-collector Finnigan MAT 262 thermal ionization mass spectrometer with extended geometry and stigmatic focusing using double Re filaments (see section 5.5.2.2).

#### *7.7.3.2. Whole rock isotope ratios for other Arran samples*

All other samples from Arran (Northern Granite, Central Complex and all crustal samples) were analysed for strontium and neodymium isotope ratios at the Scottish Universities Environmental Research Centre, using a VG Sector 54–30 thermal ionisation mass spectrometer (TIMS) (Appendices 4.8, 4.9, 5.7 and 5.8). For analytical details and standards see sections 5.5.1.1 and 5.5.2.1).

#### *7.7.3.3. Age dating*

Two large (5 mm) K-feldspar crystals were loosely crushed in a pestle and mortar and a sieved fraction of 250-500 μm was picked for $^{40}Ar$–$^{39}Ar$ dating. One sample (DD-U) was leached in a dilute HF (5%) solution at room temperature for ten minutes. Both samples were washed several times in deionised water in an ultrasonic bath. They were analysed at the $^{40}Ar$–$^{39}Ar$ geochronology laboratory at the University of Lund (see section 5.8).

## 7.8. Major and trace element geochemistry

### *7.8.1. Major element geochemistry*

A plot of total alkali v. silica (TAS) (Figure 7.11) gives a wide range of compositions at the Drumadoon Igneous Complex. The most primitive samples analysed were basaltic-andesite, ranging through to rhyolite with nearly 80% $SiO_2$. Volumetrically, however, the suite is distinctly bimodal, with only small volumes of intermediate (andesite/dacite) magma. This represents a typical British and Irish Palaeogene Igneous Province Bunsen-Daly Gap (Bunsen, 1851; Daly, 1925).

Harker plots of major element v. silica all show distinctly linear trends, rather than typical curved trends indicative of fractional crystallisation. This suggests that the range of compositions may be the result of binary mixing; whereby two end members have mixed to form a range of intermediate compositions (Figure 7.12, Figure 7.13).

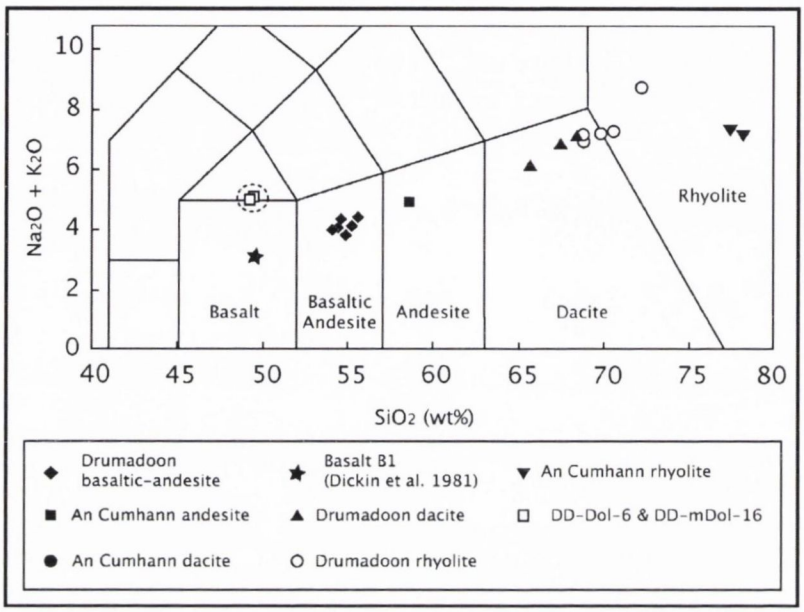


**Figure 7.11 Total alkali v silica plot, classifying the Drumadoon rock suite. The suite is sub-alkaline, with the majority of the samples being basaltic andesite and rhyolite/dacite. Small volumes of andesite and low silica dacite represent the Bunsen-Daly gap. Basalt B1 represents a 'normal' Arran basalt, containing no xenocrysts or evidence of mixing (Dickin *et al.*, 1981).**

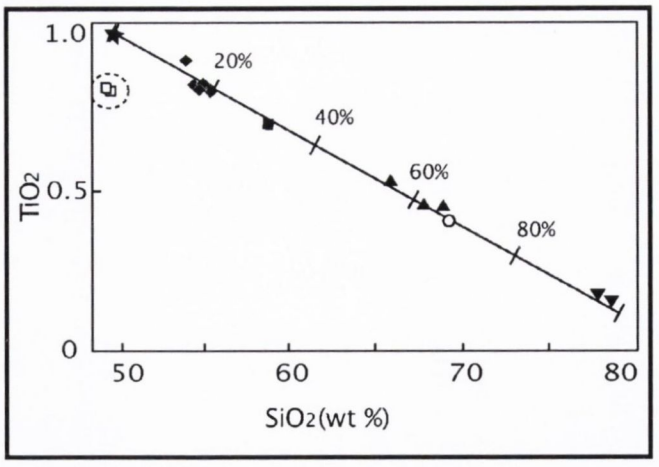


**Figure 7.12 $TiO_2$ v $SiO_2$ showing mixing line. Key as in Figure 7.11. Basalt B1 was used as the basaltic end member as the most mafic composition seen at Drumadoon, the basaltic andesites, show clear evidence of being the product of mixing themselves (presence of xenocrysts).**

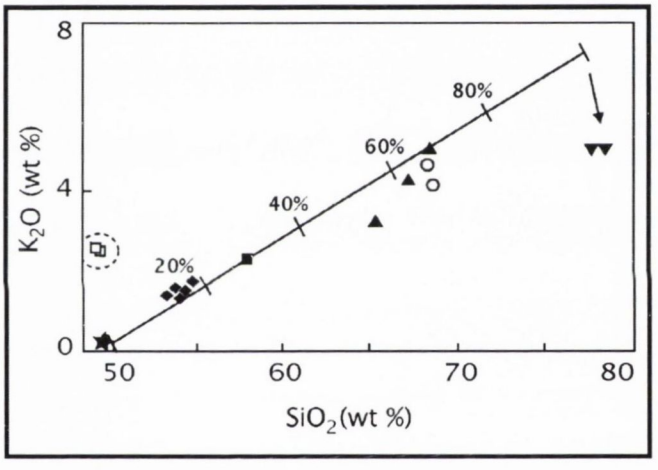


**Figure 7.13 $K_2O$ v $SiO_2$ showing mixing line. Note the distinct drop in $K_2O$ concentrations at high $SiO_2$ concentrations, indicative of potassium feldspar fractionation. Key as in Figure 7.11.**

### *7.8.2. Trace element geochemistry*

The majority of trace element plots show similar linear trends to the major elements when plotted against $SiO_2$ (Figure 7.14). This once again suggests that binary mixing rather than crystal fractionation was the principal mechanism.

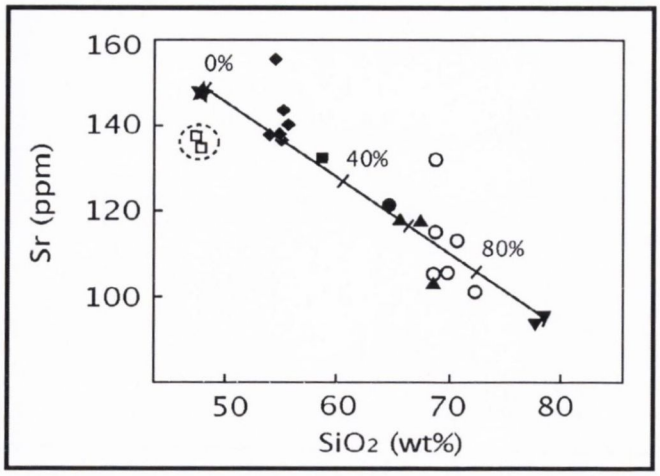


**Figure 7.14 Plot of Sr v $SiO_2$, once again showing a binary mixing line. More scatter is seen than within the major element data (Figure 7.12 and Figure 7.13), this is most likely due to variations in phenocryst/xenocryst density. Key as in Figure 7.11.**

The feldspar-compatible elements Ba and Ce show a significant downturn in the most evolved samples (the An Cumhann rhyolites) (Figure 7.15). This, together with a similar downturn in $K_2O$ (Figure 7.13), suggests the continued crystallisation of potassium feldspar in the magma reservoir after mixing had occurred. Zirconium also shows a significant downturn at high silica values, indicating zircon has also crystallised post-mixing (Figure 7.16).

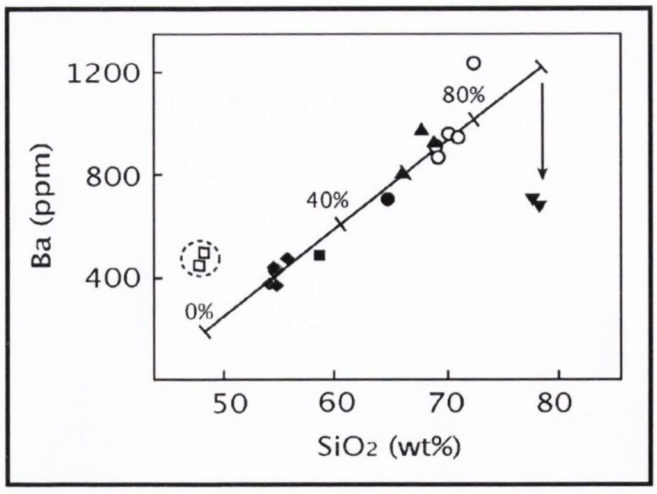


**Figure 7.15 Plot of Ba v $SiO_2$. Note the distinct downturn in barium concentration at high levels of $SiO_2$; this is in agreement with Figure 7.13, which shows a decrease in $K_2O$, together suggesting fractionation of potassium feldspar. Key as in Figure 7.11.**

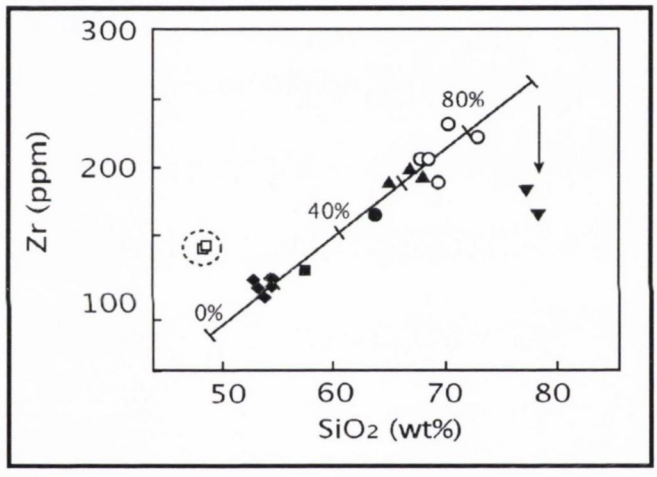


**Figure 7.16 Plot of Zr v SiO2. The drop in Zr concentrations is due to late-stage zircon fractionation. Key as in Figure 7.11.**

Rare earth element profiles of the least and most evolved Drumadoon samples are shown in Figure 7.17, along with the profiles from the Northern Granite. The Northern Granite has previously been suggested to belong to the same period of magmatism as the porphyritic rhyolites seen at Drumadoon (Kanaris-Sotiriou and Gibb, 1985).

The Drumadoon samples show profiles that are relatively enriched in light rare earth elements (LREEs), in fact they are significantly enriched in LREEs compared to the Northern Granite, with only Dy to Lu showing enrichment (Figure 7.17). This may be due to fractionation of LREE minerals from the granite. Evidence for progressive fractionation is indicated by the increasingly deep europium anomaly from basaltic andesite, to rhyolite and granite. This trend indicates the fractionation of plagioclase feldspar.

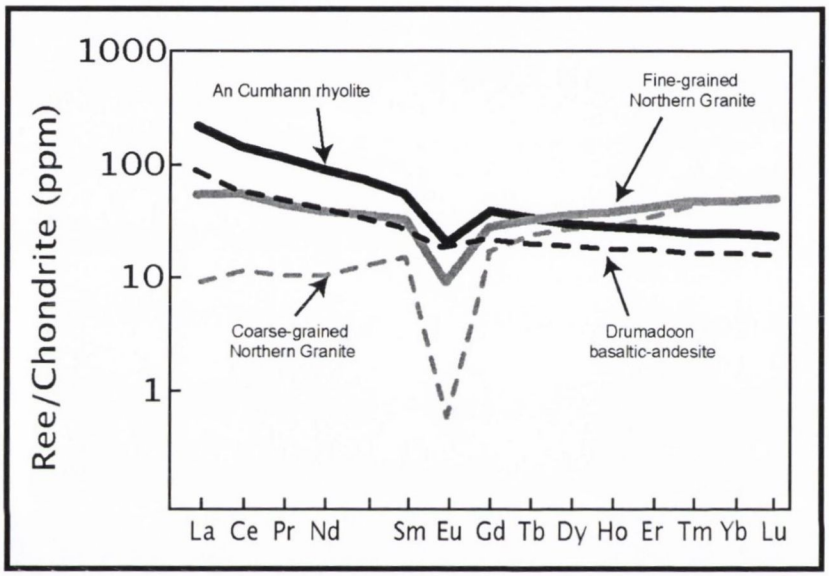


**Figure 7.17 Chondrite-normalised rare-earth element plot. Rhyolite (*solid black*), basaltic-andesite (*dashed black*), fine-grained Northern Granite (*solid grey*) and coarse-grained Northern Granite (*dashed grey*). Note the granites show enrichment in HREE, while the sill samples are enriched in LREE.**

### *7.8.3. Samples DD-Dol-6 and DD-mDol-16*

Two samples, DD-Dol-6 and DD-mDol-16 sat off all the main trends on the graphs above. These samples are samples taken from the very edges of the sill, in contact with the country rocks. They show loss on ignition values (LOI) (total $H_2O$ plus $CO_2$ weight percent) of 9.57% and 9.05%, which is very high for igneous rocks,

suggesting they may be excessively weathered. Unusually for weathered rocks however, these samples contains a very high proportion of $CO_2$ (5.96% and 6.04%). This is only surpassed by the LOI values of the Triassic sandstones within which the sill lies. These sandstones again have high loss on ignition values, 10.68% for unbaked sands from below the sill (sample A-TS) and 10.27% for baked sands and muds directly at the base of the sill (sample A-BTS), with $CO_2$ values of 9.99% and 7.93% respectively. Lower LOI values within the metamorphic aureole of the sill suggest the sediments have lost some fluids during heating by the intrusion. The samples also appear to have been leached, losing elements including Ti, Cr and V (Figure 7.12, Figure 7.18 and Figure 7.19).

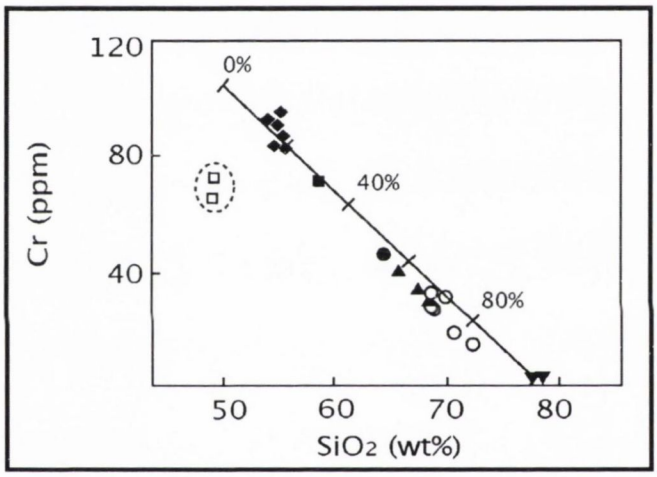


**Figure 7.18 Graph showing depletion in Cr for samples DD-Dol-6 and DD-mDol-16.**

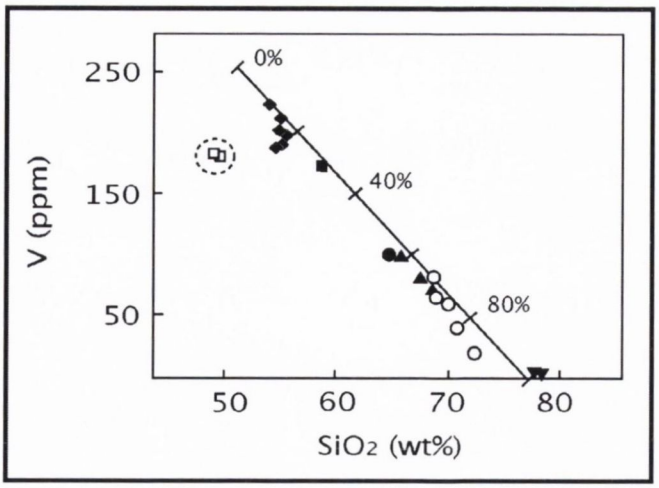


**Figure 7.19 Plot of V v $SiO_2$. Samples DD-dol-6 and DD-mDol-16 show strong depletion in this transition metals.**

This suggests the outer basalts of the sill have interacted with the surrounding sandstones. These fluids may not have been derived from the sandstones themselves, however they are very porous and the fluids may have migrated through them from elsewhere within the stratigraphy. Work by Parnell (2004) on basaltic sills intruded into Carboniferous sediments in Scotland has indicated the leaching of transition metal elements from igneous rocks by hydrocarbon-rich fluids. DD-Dol-6 and DD-mDol-16 show depletion in the elements considered mobile in hydrocarbon-rich fluids including $TiO_2$, Cr and V (Parnell, 2004). $K_2O$, Ba and Zr show enrichment, but this is most likely an artefact of depletion of the other elements (Figure 7.13, Figure 7.15 and Figure 7.16).

The hydrocarbon rich-fluids may not have been derived from the sandstones themselves, as these strata show no indication of significant local hydrocarbon deposits. However they are very porous and the fluids may have migrated through them from elsewhere within the stratigraphy, and indeed the Permo-Trias of the

southern Firth of Clyde has been previously explored for hydrocarbons (Pye and Brown, 2002).

## 7.9. Calculation of the initial composition of the mafic end member

Based on phenocryst-distribution densities, its is possible to estimate a rough minimum (considering that some phenocrysts may have been entirely resorbed) of how much of a typical rhyolite would be required to make a typical Drumadoon xenocrystic basaltic-andesite (see Takeuchi and Nakamura, 2001). A value of ~21% by volume was calculated (Table 7.1). This was achieved by analysing photographs of a typical rhyolite (from Cleiteadh nan Sgarbh) and comparing phenocryst densities with photographs of a Drumadoon Dyke xenocrystic dolerite. These sites were chosen as they afforded large, flat, polished outcrop areas for analysis.

| | | Max per $10cm^2$ | Min per $10cm^2$ | Average per $10cm^2$ | % rhyolite needed |
|---|---|---|---|---|---|
| **Xenocrystic dolerite** | *<15cm from dacite* | 25 | 16 | 21 | 57% |
| | *>15cm from dacite* | 11 | 8 | 9 | 21% |
| **Porphyritic rhyolite** | | 53 | 32 | 42 | |

**Table 7.1 Table of density of xenocryst/phenocryst occurrence in porphyritic rhyolite and xenocrystic dolerite (basaltic-andesite).**

A 21% by volume addition of the most evolved rhyolitic composition (~78% $SiO_2$) would significantly affect the composition of a mafic magma. Samples from closer to the basaltic-andesite/dacite and dacite/rhyolite margins show a much stronger rhyolite influence. While the boundary between the basaltic-andesite and dacite is very distinct, there is a concentration of xenocrysts in the basaltic-andesite within 15 cm of the boundary. This may be due to the rhyolite skimming off basaltic-andesite liquid at the interface (to form dacite), therefore maintaining the distinct unchilled margin while concentrating the xenocrysts below the boundary.

The change in composition can then be approximated using the equation below, whereby the proportion of porphyritic magma ($M_p$) mixed with the original magma ($M_o$) to make the xenocrystic magma ($M_x$) is represented by the ratio of xenocrysts ($C_x$) (per area or volume) in the mixed magma to phenocrysts ($C_p$) (per area or volume) in the parental porphyry. Hence 1 minus the xenocryst/phenocryst ratio represents the proportion of the original aphyric magma.

$$M_x = \left(\frac{C_x}{C_p}\right) M_p + \left(1 - \frac{C_x}{C_p}\right) M_o$$

This can be rearranged to:

$$M_o = \frac{M_x - \left[M_p \left(\frac{C_x}{C_p}\right)\right]}{1 - \left(\frac{C_x}{C_p}\right)}$$

Whereby "$M_x$" and "$M_p$" can be substituted by major element wt%, trace element ppm etc. to calculate the geochemical properties of the original magma ($M_o$).

Therefore, a 21% addition of rhyolite (~78% $SiO_2$) would equate to a ~6% rise in silica in the original magma. Since mixing resulted in a basaltic-andesite (~54% $SiO_2$), the original magma, prior to mixing, can be assumed to be a basalt of ~48% $SiO_2$. Compositionally, this value is comparable to other less-evolved basaltic samples analysed from Arran, e.g. samples B1 and B8 (47.92%, 46.79%) from Dickin *et al.* (1981). Similarly the calculated values for MgO and $Fe_2O_3$ (7.4% and 11.4% respectively) correlate well with the published B1 and B8 values (7.17%, 8.05% for MgO and 11.56%, 11.4% for recalculated FeO and $Fe_2O_3$ to $Fe_2O_{3\,Tot}$).

### *7.9.1. Least-squares mixing analysis*

Least-squares mixing analysis of both major and trace elements was used to compare a calculated mixed composition to that of the dacitic samples. This method produces a best-fit mixing ratio for the data using the B1 basalt (Dickin *et al.*, 1981) and An Cumhann Rhyolite QFP19 as end members. As we preferentially avoided analysing feldspar xenocrysts when measuring major elements by XRF, only the $TiO_2$, MgO, CaO, MnO and $Fe_2O_3$ values of B1 basalt (as they are not K-feldspar compatible) were used for least-squares mixing analysis, making B1 directly comparable to our basaltic-andesite values. This is particularly important, as evidence for late-stage potassium feldspar fractionation has been seen in both major and trace element data (see section 7.8).

Using these major element values, least-squares mixing analysis suggests a mix of 76:24 B1 basalt to rhyolite was required to form the basaltic andesite, which is very similar to our xenocryst-based ratio of 79:21. The extra 3% rhyolite needed for the least-squares model is most likely due to xenocrysts that were entirely resorbed within the basaltic-andesite hybrid.

Maximum and minimum mixing ratios for the formation of the dacitic magma were calculated at 45:55 and 29:71, with a sum of $r^2$ values at 2.3 and 4.6 respectively. These calculations used the An Cumhann rhyolite as the felsic end member and compared basalt B1 to dacites MDOL18 (64.93% $SiO_2$) and DQFP5 (69.78% $SiO_2$).

## 7.10. Isotope geochemistry

### *7.10.1. Age dating*

Ar-Ar step heating yielded two dates of 59.04 ± 0.13 Ma (leached) and 59.16 ± 0.17 Ma (unleached) for a K-feldspar separate from the porphyritic rhyolite (Table 7.2). The data have strong plateaux and low errors (Figure 7.20).

This date correlates well with other dating work on the region, detailed in Table 7.4 and Figure 7.25 and discussed in further detail in section 7.12.2.

| Power (Watts) equivalent to T | Ca/K | $^{36}Ar/^{39}Ar$ | $^{40*}Ar/^{39}Ar$ | Mol $^{39}Ar$ x $10^{-14}$ | $\%^{39}Ar$ in step | cumulative $\%^{39}Ar$ | % rad. $^{40}Ar$ | Age (Ma) | ± Age |
|---|---|---|---|---|---|---|---|---|---|
| *DD-U K-feldspar, J = 0.0183 ± 0.000012* | | | | | | | | | |
| 2 | 0.020 | 0.0011 | 1.781 | 0.51 | 8.3 | 8.3 | 84.4 | 57.86 | 0.26 |
| **0** | **0.023** | **0.0015** | **1.821** | **2.4526** | **39.9** | **48.1** | **81** | **59.15** | **0.13** |
| **2.3** | **0.018** | **0.0017** | **1.817** | **0.5831** | **9.5** | **57.6** | **78.5** | **59.03** | **0.26** |
| **2.5** | **0.021** | **0.0011** | **1.826** | **1.5115** | **24.6** | **82.2** | **85.4** | **59.29** | **0.13** |
| **2.9** | **0.036** | **0.0006** | **1.818** | **0.9713** | **15.8** | **98** | **91.7** | **59.03** | **0.14** |
| **4** | **0.068** | **0.0004** | **1.874** | **0.1246** | **2** | **100** | **93.7** | **60.84** | **1.12** |
| Integrated age | | | | | | | | 59.10 | 0.20 |
| **Plateau Age** | | | | | **91.7** | | | **59.16** | **0.17** |
| *DD-T K-feldspar, J = 0.01835 ± 0.000012* | | | | | | | | | |
| **2** | **0.023** | **0.0003** | **1.813** | **0.874** | **12.7** | **12.7** | **95.2** | **58.87** | **0.12** |
| **2.1** | **0.021** | **0.0009** | **1.817** | **0.4909** | **7.2** | **19.9** | **87.5** | **59.01** | **0.16** |
| **2.2** | **0.023** | **0.0010** | **1.820** | **1.648** | **24** | **43.9** | **85.6** | **59.11** | **0.12** |
| **2.3** | **0.033** | **0.0012** | **1.820** | **0.6666** | **9.7** | **53.7** | **84.2** | **59.10** | **0.16** |
| **2.5** | **0.027** | **0.0007** | **1.818** | **1.3028** | **19** | **72.7** | **89.6** | **59.06** | **0.12** |
| **3.5** | **0.026** | **0.0007** | **1.819** | **1.875** | **27.3** | **100** | **90.1** | **59.08** | **0.10** |
| Integrated age | | | | | | | | 59.21 | 0.18 |
| **Plateau Age** | | | | | **100** | | | **59.04** | **0.13** |

**Table 7.2 $^{40}Ar$-$^{39}Ar$ data from the Drumadoon Igneous Complex. Steps used in calculation of plateau age are in bold. Data is corrected for machine blank, correction factors and $^{37}Ar/^{36}Ar$ post irradiation decay**

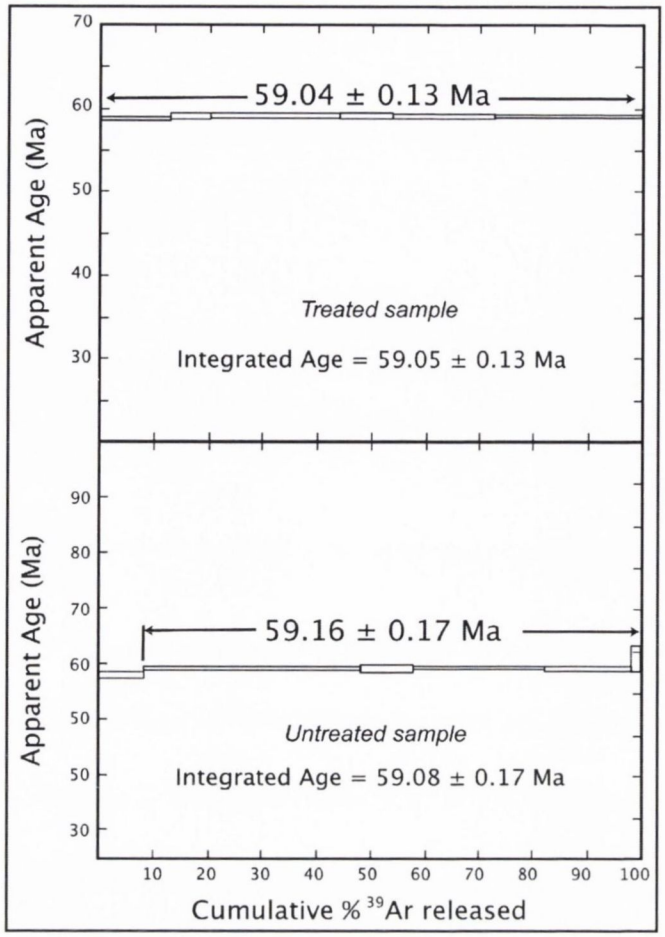


Figure 7.20 Plateaux diagrams for dated K-feldspar samples. The upper sample (DD-T) has been treated in Hf, whereas the lower sample (DD-U) is untreated.

### *7.10.2.Strontium and neodymium isotope geochemistry*

The magmas show strong variation in Sr-isotope ratios, with ranges of 0.70620-0.70797(7), 0.70963-0.71048(1) and 0.71006-0.71202(1) for basaltic-andesite, dacite and porphyritic rhyolite respectively (See Appendix 4.9). These values are significantly displaced from mantle values towards those of the crust (Figure 7.21). Combined with Nd isotope ratios, these data provide strong evidence for crustal contamination.

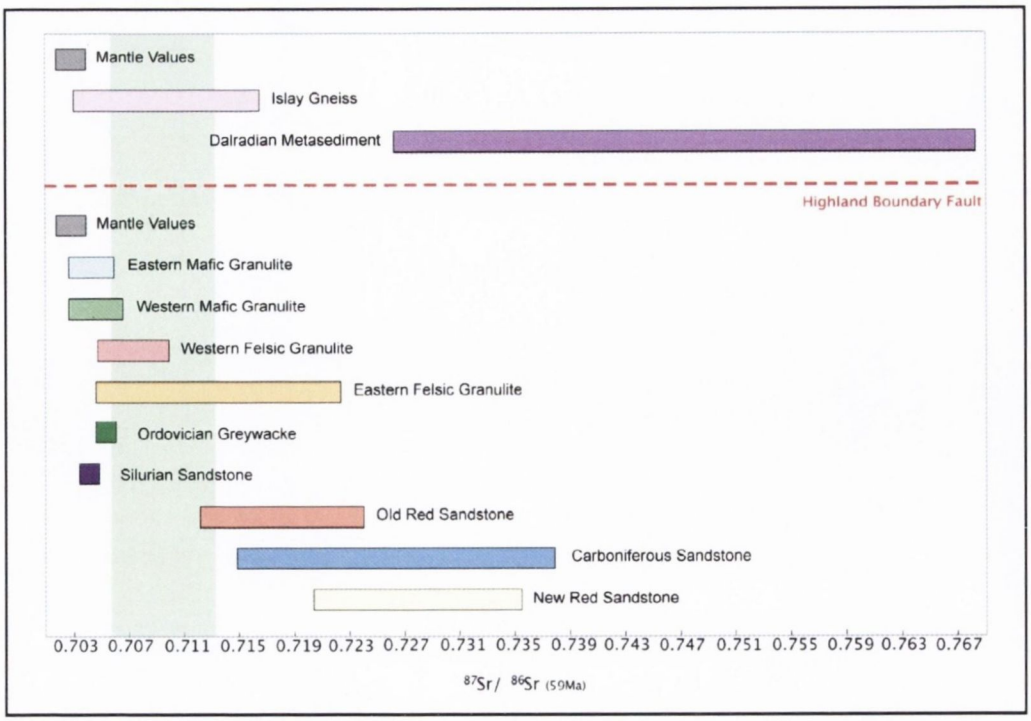


**Figure 7.21 Bar chart of strontium isotope ratios, showing the ranges of crustal values in the Arran region and the strontium isotope range of igneous samples from the Drumadoon Intrusive Complex (green shading). Note how the igneous samples are displaced from mantle values (grey) towards the crustal realm. (Crustal data fields are from this study and Dickin *et al.*, 1981; Dickin and Bowes, 1991; Halliday *et al.*, 1993; Dickin, 1994).**

### *7.10.3. The effect of late-stage magma mixing on the isotope ratios of the basaltic and rhyolitic components of the composite intrusion*

As shown earlier, both the basaltic andesite and dacite contain significant volumes of rhyolite (sections 7.9, 7.9.1). Therefore, to better understand the initial isotopic composition of the two end-member magmas, samples must be "un-mixed" to give their isotope ratios prior to magma mixing. To do this, the basalt to rhyolite ratio of each sample was calculated from their major and trace element geochemistry

(see section 7.9.1), using this ratio, the effect of magma mixing could be removed from the isotope data. The following equation was used:

$$M_m = x(B_i) + (1-x)(R_i)$$

Whereby $x$ represents the proportion of basalt to rhyolite in the mixed magma. $M_m$ is the isotope ratio of the mixed magma (*known*), $B_i$ is the isotope ratio of the original basalt (*unknown*) and $R_i$ is the isotope ratio of the most evolved rhyolite seen at Drumadoon (DD-QFP-19) (*assumed to represent the rhyolitic isotopic endmember*). This equation can be rearranged to two forms:

$$B_i = \frac{M_m - R_i + x(R_i)}{x} \quad where \quad x > 0.5$$

$$R_i = \frac{M_m - x(B_i)}{1-x} \quad where \quad x < 0.5$$

In the case of a magma that contained more basalt than rhyolite ($x > 0.5$), the rhyolitic component was removed, giving an estimation of the pre-mixing basaltic isotope ratio ($B_i$). The samples that contained more rhyolite than basalt ($x < 0.5$) had the basaltic component removed. This step could only be estimated, as there was no pristine basaltic endmember in the dataset, instead the recalculated initial values of the least-mixed basaltic andesite sample (DD-Dol-11) were used (Table 7.3). This appears to be an accurate choice of endmember as all re-corrected rhyolites have similar isotopic values to sample DD-QFP-19. These estimated $B_i$ values are also

very similar to Sr and Nd values published for other Arran basalts (Dickin *et al.*, 1981; Dickin, 1994).

| Sample name | | Proportion of basalt in mixed magma | Sr isotope ratio of mixed magma | Sr isotope ratio of rhyolitic endmember | Calculated initial Sr ratio of basaltic endmember | Nd isotope ratio of mixed magma | Nd isotope ratio of rhyolitic endmember | Calculated initial Nd ratio of basaltic endmember |
|---|---|---|---|---|---|---|---|---|
| | | *x* | *Mm* | *Ri* | *Bi* | *Mm* | *Ri* | *Bi* |
| **DD-Dol-11** | | 0.79 | 0.706329 | 0.712021 | **0.704816** | 0.512283 | 0.512109 | **0.512329** |
| DD-Dol-8 | | 0.77 | 0.706200 | 0.712021 | 0.704461 | 0.512273 | 0.512109 | 0.512321 |
| DD-Dol-11a | $x > 0.5$ | 0.76 | 0.706631 | 0.712021 | 0.704929 | 0.512268 | 0.512109 | 0.512319 |
| DD-Dol-12 | | 0.76 | 0.707641 | 0.712021 | 0.706257 | 0.512257 | 0.512109 | 0.512303 |
| DD-Dol-13 | | 0.75 | 0.706777 | 0.712021 | 0.705028 | 0.512098 | 0.512109 | 0.512095 |
| DD-mDol-17 | | 0.62 | 0.707074 | 0.712021 | 0.704042 | 0.512195 | 0.512109 | 0.512247 |

| Sample name | | Proportion of basalt in mixed magma | Sr isotope ratio of mixed magma | Sr isotope ratio of basaltic endmember | Calculated initial Sr ratio of rhyolitic endmember | Nd isotope ratio of mixed magma | Nd isotope ratio of basaltic endmember | Calculated initial Nd ratio of rhyolitic endmember |
|---|---|---|---|---|---|---|---|---|
| | | *x* | *Mm* | *Bi* | *Ri* | *Mm* | *Bi* | *Ri* |
| DD-mDol-18 | | 0.41 | 0.709631 | 0.704816 | 0.712977 | 0.512152 | 0.512329 | 0.512029 |
| DD-QFP-1 | | 0.37 | 0.709881 | 0.704816 | 0.712856 | 0.512140 | 0.512329 | 0.512029 |
| DD-QFP-10 | | 0.31 | 0.710765 | 0.704816 | 0.713438 | 0.512125 | 0.512329 | 0.512034 |
| DD-dQFP-4 | | 0.3 | 0.710481 | 0.704816 | 0.712908 | 0.512129 | 0.512329 | 0.512044 |
| DD-QFP-3 | | 0.28 | 0.710064 | 0.704816 | 0.712105 | 0.512130 | 0.512329 | 0.512053 |
| DD-dQFP-5 | $x < 0.5$ | 0.28 | 0.710405 | 0.704816 | 0.712578 | 0.512165 | 0.512329 | 0.512102 |
| DD-QFP-9 | | 0.24 | 0.710853 | 0.704816 | 0.712759 | 0.512140 | 0.512329 | 0.512080 |
| DD-QFP-2 | | 0.22 | 0.711074 | 0.704816 | 0.712839 | 0.512129 | 0.512329 | 0.512073 |
| DD-QFP-15 | | 0.08 | 0.711884 | 0.704816 | 0.712499 | 0.512128 | 0.512329 | 0.512111 |
| DD-QFP-21 | | 0.01 | 0.712243 | 0.704816 | 0.712318 | 0.512095 | 0.512329 | 0.512093 |
| **DD-QFP-19** | | 0 | 0.712021 | 0.704816 | **0.712021** | 0.512109 | 0.512329 | **0.512109** |

**Table 7.3 Re-calculated isotopic values for samples from the Drumadoon Igneous Complex. The effects of binary magma mixing have been removed. Values in bold represent those samples used as the basaltic ($B_i$) and rhyolitic ($R_i$) endmembers.**

These calculations give isotope ratios that are more representative of magma prior to mixing. This is important since the two magmas may not be genetically related and therefore may have had significantly different contamination histories.

## 7.11. Modelling of crustal contamination

Considering the proximity to a terrane boundary (Figure 7.1), our data was compared to published data fields for the local crustal lithologies from both the Midland Valley and Grampian Terranes of western Scotland (Figure 7.23, Figure 7.22).

The Drumadoon samples were compared to published data for the crustal lithologies mentioned above (Dickin *et al.*, 1981; Marcantonio *et al.*, 1988; Dickin and Bowes, 1991; Halliday *et al.*, 1993; Dickin, 1994), and newly analysed data from Midland Valley Palaeozoic sediments collected from Arran and the Ayrshire region of south-western Scotland.

Using a typical Atlantic MORB basalt composition (Saunders *et al.*, 1988) and the various crustal compositions as end members, geochemical models for both assimilation during fractional crystallisation (AFC) (DePaolo, 1981) and bulk isotope mixing (Langmuir *et al.*, 1978) were run. MORB values were used as the mantle end member as other work within the wider study of which this project is part has shown that even the most primitive samples within the BIPIP (e.g. McClurg's Dyke) have been significantly contaminated by the crust (Nicoll, G.R., Troll, V.R. *pers. comm.*).

AFC modelling used the *AFC.isotopes* programme of J. Entenmann (http://www.geologynet.com/afc.isotopes.zip). Samples were modelled for both mixing and AFC, and the process that best fit the data was chosen. AFC modelling was run over a range of r-values, to consider the effect of various amounts of assimilation. The r-value represents the ratio of assimilation to fractional crystallisation.

### *7.11.1. Geochemical modelling of contamination by Midland Valley Terrane crust*

As the Drumadoon Intrusive Complex lies within the Midland Valley Terrane, those crustal lithologies were initially considered as a contamination source. The Midland Valley Terrane basement is known from Carboniferous xenolith suites and comprises both mafic and felsic granulites up to a depth of 7 - 8 km (Bamford *et al.*, 1977; Graham and Upton, 1978; Halliday *et al.*, 1993). The xenoliths come from vents across the Midland Valley Terrane (MVT), and for the purpose of this study they were divided into four groups (using Halliday *et al.*, 1993):

1. Mafic granulite xenoliths from the western MVT (Ashentree Glen, Heads of Ayr, Baidland Hill, Hawk's Nib).
2. Felsic granulite xenoliths from the western MVT (Dunaskin Glen, Holmbyre, Baidland Hill).
3. Mafic granulite xenoliths from the eastern MVT (Fidra, Partan Craig).
4. Felsic granulite xenoliths form the eastern MVT (Briggs of Fidra, Partan Craig, Coalyard Hill).

Xenolith samples from the western part of the Midland Valley Terrane are from two distinct regions, one in the north-western part of the terrane and one in the south-western part. However these two sub-groups are isotopically similar and were plotted together, only divided by mafic/felsic composition Figure 7.22.

This granulite basement is overlain by both Upper and Lower Palaeozoic sediments, which filled basins throughout the Ordovician, Silurian and Devonian. Carboniferous sandstones represent deltaic sequences, while the Permo-Trias of the

Arran area comprises aeolian and fluvial sandstones (Trewin, 2002) (see also section 4.5.4 for further details on the geological history of the Midland Valley Terrane).

When modelled as potential geochemical end members, the granulites sampled from western Scotland (mafic and felsic) (Halliday *et al.*, 1993) are not radiogenic enough to contribute significantly to the radiogenic strontium and neodymium signature of the Drumadoon magmas (Figure 7.21).

Similarly, even the most extreme values for the eastern granulites could not produce the magma values without unrealistic levels of assimilation. Modelled results show AFC of eastern MVT felsic granulite (sample PC347, Halliday *et al.*, (1993)) of up to 15% melt remaining would be needed to form the Drumadoon rhyolites (at r = 0.4). Typically, the physical limit of AFC models at r = 0.4 is approximately 50% melt remaining, considering an assimilant of granitic composition (Reiners *et al.*, 1995).

Bulk mixing of up to 87% mafic granulite (sample FD287, Halliday *et al.* (1993)) would be needed to form the radiogenic signature of the Drumadoon basalts (Figure 7.22). Therefore it appears the Midland Valley Terrane lower crust/basement has not been involved in the contamination of the Drumadoon magmas.

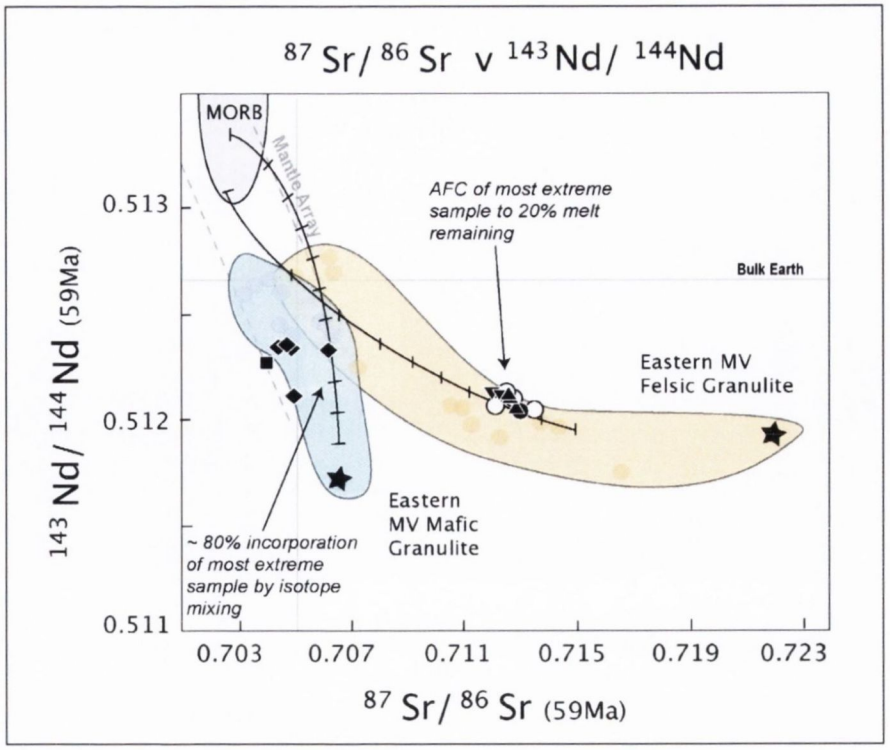


**Figure 7.22 Crustal data fields for the Midland Valley Terrane. Crustal data fields from Halliday *et al.* (1993)**

A similar situation occurs when the Upper Palaeozoic lithologies of the Midland Valley Terrane upper crust are considered. The Ordovician and Silurian greywackes are not sufficiently radiogenic to have contributed to any of the $^{87}Sr/^{86}Sr$ values observed at Drumadoon (Figure 7.21). When the Devonian sandstones were geochemically modelled, it was found they would require assimilation during fractional crystallisation at approximately 15-20% melt remaining to make the rhyolites, once again making them an unrealistic end-member contaminant. Only the Triassic sandstones within which the sills lie shows any indication of having influenced the magmas. However, this influence is not apparent in the isotope signature of the rocks, but rather from major, trace and volatile element data (section 7.8.3).

### *7.11.2.Geochemical modelling of contamination by Grampian Terrane crust*

Despite lying within the Midland Valley Terrane, it appears the majority of crustal influence on the magmas must have been produced by Grampian Terrane lithologies.

The Grampian Terrane upper crust comprises the metasediments of the Dalradian Basin (Anderton, 1982). The basement to the Dalradian has not been directly observed in Scotland, but has been recognised both geophysically (Hall *et al.*, 1984) and geochemically (Frost and O'Nions, 1985; Dickin and Bowes, 1991; Hitchen *et al.*, 1997; Dickin and Durant, 2002). These studies show igneous rocks (from both BIPIP and Caledonian magmatism) have been influenced by a composition similar to a Rhinns Complex-type composition (gneiss), as seen on the island of Islay, and suggest this may compose the underlying basement in the Scottish Grampian Highlands (see section 4.5.3) Therefore these Dalradian metapelite and lower crustal gneisses (Marcantonio *et al.*, 1988) compositions were modelled as potential end members.

Incorporation of between 7 and 10% lower crustal gneiss by bulk mixing could potentially form the basalts seen at Drumadoon, with one sample yielding mixing values of up to ~13% crust. The gneisses do not have enough radiogenic strontium to have been the sole influence on the rhyolitic magma. Similarly, the Dalradian metasediments require AFC to unrealistic levels if they were the sole contaminant forming the rhyolitic magma. However it seems the rhyolites have undergone two step contamination, with initial mixing with ~7.5% lower crust (Sample ph2, Marcantonio *et al.* (1988)) followed by assimilation of Dalradian upper crust during fractional crystallisation to ~60% melt remaining at r = 0.7 (Figure

7.23). Such high r-values are valid considering the fertility of this kind of metasedimentary crust, with a large proportion of fusible, hydrous, K- (and Rb) bearing phases such as biotite and muscovite. Assimilation of a partial melt solely sourced from these fusible components, would yield a more radiogenic contaminant, than the whole rock isotope ratio. If this was the case for the Dalradian metasediments the Drumadoon values could be reached by AFC sooner, with more melt remaining (i.e. > 60% melt remaining).

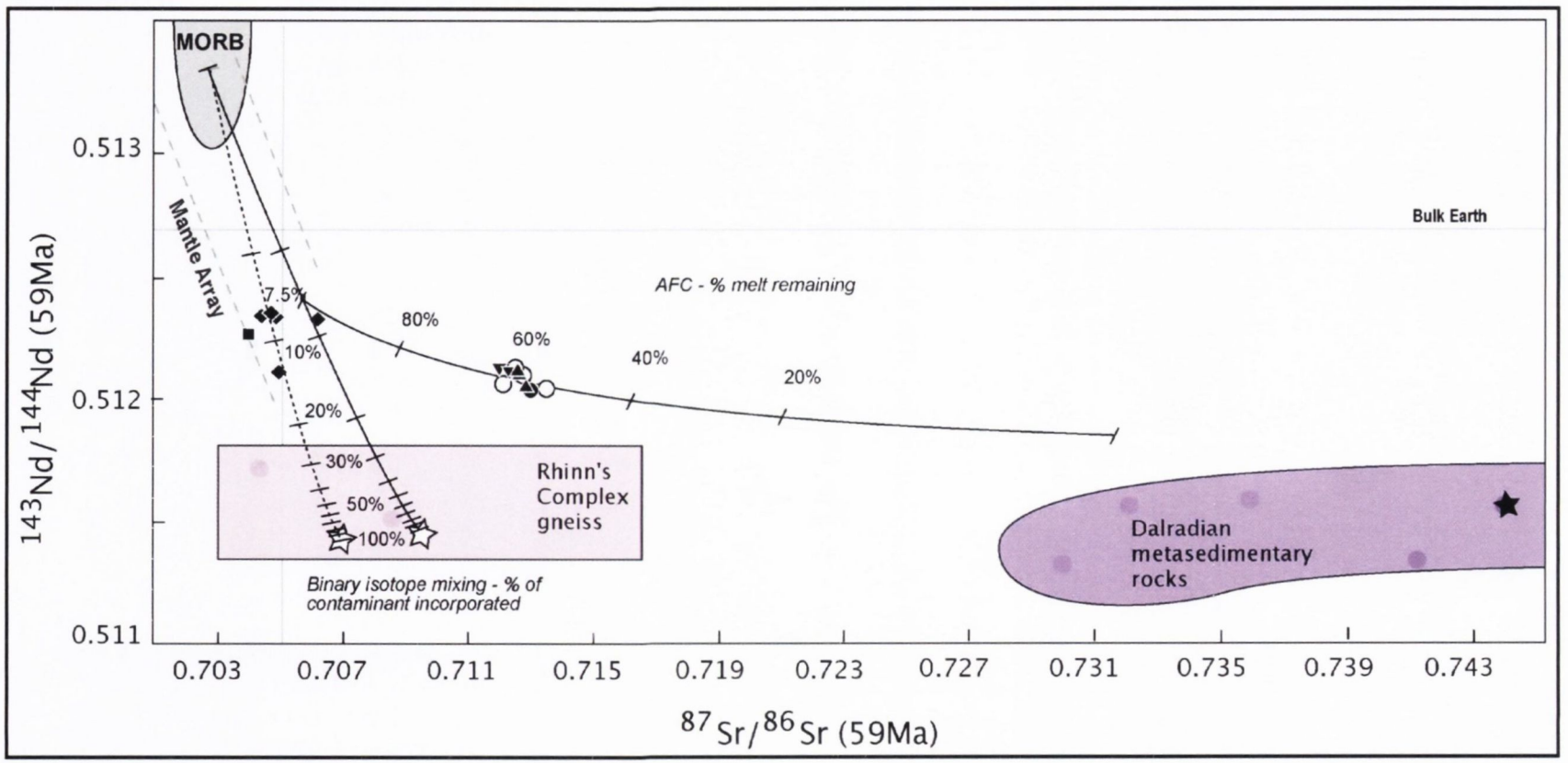


**Figure 7.23 Assimilation and fractional crystallisation (AFC) and binary isotope mixing modelling of crustal contamination in the Drumadoon magma suite. Samples have had the effects of magma mixing "un-mixed" to estimate initial *pre-mixing* isotope ratios. A partial melt of Dalradian metasediment (containing just a fusible mica component, would have a more radiogenic Sr isotope ratio and plot to the right of its whole rock value. Crustal data fields from Dickin *et al.* (1981), Marcantonio *et al.* (1988), Dickin and Bowes (1991) and Dickin (1994).**

## 7.12. Discussion

### *7.12.1.Major and trace element data*

Major and trace element data clearly show binary mixing between two end-member magmas, a porphyritic rhyolite and a basalt. Phenocryst/xenocryst and least-squares mixing analysis suggest mixing ratios of 79%: 21% and 76%: 24% respectively, to form the xenocrystic basaltic-andesite, with the 3% difference probably representing phenocrysts which have been completely resorbed. The dacites were formed by mixing in the ratio range of 45%: 55% to 30%: 70%.

Several elements (e.g. $K_2O$, Ba, Ce, Eu) exhibit evidence of post-mixing K-feldspar removal. Therefore, physical mixing must have occurred within the magma chamber, as crystallisation of feldspar post-intrusion (*in situ*) would not have changed the bulk composition of the rhyolitic samples. This removal of feldspar compatible elements may be due to the fractionation of potassium feldspar or indeed liquid-crystal separation as the viscous porphyritic rhyolite was intruded. Similarly, the presence of phenocrysts in the basaltic–andesite, below the dacite-mixing front, suggests mixing before intrusion.

Using this information an intrusion sequence can be envisaged (Figure 7.24) whereby a basalt magma mixed with a rhyolite magma to form the xenocrystic dolerite, mingled to form the enclave-bearing rhyolite and intruded together to form a composite intrusion. During intrusion, the dacitic magma formed at the interface between the dolerite and rhyolite magmas in the conduit. Finally the rhyolite itself entered the conduit, forming the top of the main Drumadoon sill and the centre of the An Cumhann feeder dyke.

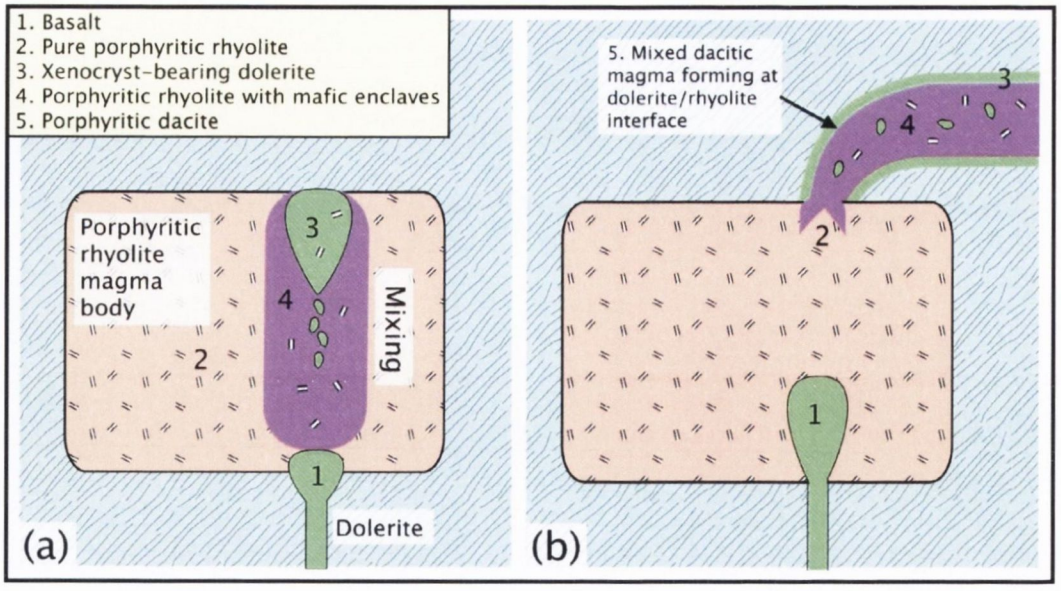


**Figure 7.24 Schematic diagram showing the intrusion sequence of magmas at Drumadoon.**

**(a). The doleritic magma (1) meets a porphyritic rhyolite (2) in the crust and mixes to form the xenocrystic dolerite (3). It mingles to form the enclave-bearing rhyolite (4).**

**(b). The xenocrystic dolerite (3) enters the conduit first, lubricating the way for the enclave-bearing rhyolite (4) which forms the majority of the sill. They interact in the conduit to form the porphyritic dacite (5). The rhyolite with no mafic enclaves enters the conduit last (1) and is seen at the centre of the feeder dykes and at the top of the main sill.**

Kanaris-Sotiriou and Gibb (1985) have previously suggested the porphyritic rhyolites and the Northern Granite magmatic episodes may be related. Rare earth element plots comparing the porphyritic rhyolite to the granite show the granite is significantly depleted in LREEs, with only Dy to Lu showing enrichment (see Figure 7.17). This does not discount a genetic relationship, as such depletion may be due to the fractionation of late-stage REE minerals in the granitic magma, some of which (e.g. fergusonite (a REE oxide) and gadolinite (a REE silicate)) have been recorded in the Northern Granite by Hyslop *et al.* (1999).

### *7.12.2.Significance of age date*

The most recent $^{40}Ar$-$^{39}Ar$ date for the Northern Granite, on a biotite separate dated by Chambers (2000), is 57.85 ± 0.15 Ma (weighted mean average) and does not overlap with our dates for the Drumadoon porphyritic rhyolite. This suggests that the chemical similarities mentioned in 7.12.1 may be the result of distinct batches of similar parental magmas passing through and assimilating identical crustal lithologies.

Previous palaeomagnetic work on the both the quartz and feldspar-phyric rhyolite suite and the Northern Granite, suggested all intrusions were considered to have formed within the same period of normal polarity (chron 26n) (Mussett *et al.*, 1987; Mussett *et al.*, 1989; Hodgson *et al.*, 1990). However, in light of the more precise radiometric dates from both this study and that of Chambers (2000), it seems that while the Northern Granite may lie within chron 26n (based on the palaeomagnetic chronology of Berggren *et al.* (1995)), the Drumadoon sill does not, and is in fact likely to lie within a period of normal polarity within chron 26r.

This data provides further evidence for normal polarity subchrons within chron 26r, as inferred on the Isle of Mull by Chambers and Pringle (2001). The work of Hodgson *et al.* (1990) had previously suggested a magnetostratigraphy of 26r-26n-25r for the Palaeogene igneous rocks of Arran, placing both the Northern Granite and the porphyritic sills within the same normal anomaly (chron 26n), lying between the older Ailsa Craig/Holy Island (chron 26r) and younger Central Complex (chron 25r). This study shows that this is not the case and igneous activity must now span at least two periods of normal polarity.

| Study | Site dated | Method of dating | Date |
|---|---|---|---|
| This study | K-spar separate from Drumadoon sill | $^{40}Ar$-$^{39}Ar$ step heating | 59.05 ± 0.13 Ma<br>59.16 ± 0.17 Ma<br>plateau age |
| (Mussett et al., 1987) | Whole rock (?) from Drumadoon dyke | $^{40}Ar$-$^{39}Ar$ step heating | 58.5 ± 0.8 Ma |
| (Buist et al., 1979) | Bute composite sill | K-Ar dating | Minimum age of 56.3 ± 1.0 Ma |
| (Chambers, 2000; Emeleus and Bell, 2005) | Northern Granite - biotite separate | $^{40}Ar$-$^{39}Ar$ step heating | 57.35 ± 0.22 Ma<br>58.64 ± 0.34 Ma<br>58.07 ± 0.25 Ma<br>57.85 ± 0.15 Ma (WMA) |
| (Dickin et al., 1981) | Northern Granite - whole-rock | Rb-Sr isochron | 60.3 ± 1.6 Ma |
| (Evans et al., 1973) | Feldspar-quartz concentrate from Northern Granite | $^{40}Ar$-$^{39}Ar$ age spectrum | 58.8 ± 0.6 Ma corrected to 60.3 ± 0.6 Ma in (Hodgson et al., 1990) |
| (Hodgson et al., 1990) | Northern Granite<br>Drumadoon sill<br>Brown Head sill<br>Bennan Head sill | Palaeomagnetic polarity | N. Granite and Porphyry sills suggested to have formed in same period of N polarity - Chron 26, from 58.7-58.4 ± 0.2Ma (Gradstein et al., 2004). |
| (Mussett et al., 1989) | Dun Dubh plug,<br>Bute composite sill | Palaeomagnetic polarity | N polarity, attributed to same period of N polarity as the other porphyries |
| (Mussett et al., 1987) | Judd 4 dyke<br>Cleiteadh Nan Sgarbh dyke<br>Drumadoon sill<br>Drumadoon dyke<br>Brown Head sill<br>Bennan Head Sill | Palaeomagnetic polarity | Activity on Arran spans a R-N-R period. All porphyries are N. Attributed to ~58.5 Ma |

**Table 7.4 Available radiometric and palaeomagnetic dates for the Arran (and surrounding areas) porphyritic rhyolite sills and the Northern Granite. WMA – weighted mean average.**

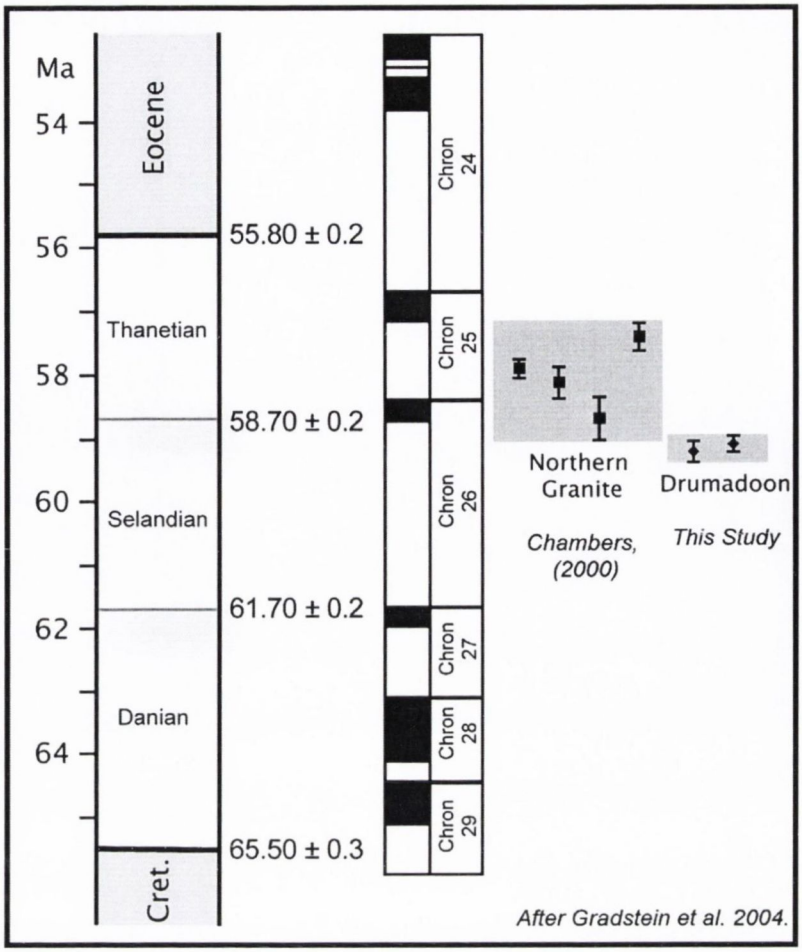


**Figure 7.25 Palaeomagnetic stratigraphy of the Paleocene (Gradstein *et al.*, 2004), with recent radiometric dates for the Arran porphyritic rhyolite intrusions and the Northern Granite. Black intervals are periods of normal polarity, while white intervals are reverse polarity. Palaeomagnetic data previously suggested these intrusions all lay within chron 26n (Mussett *et al.*, 1987; Mussett *et al.*, 1989; Hodgson *et al.*, 1990).**

### *7.12.3.Structure of the crust and the magma pathway*

The isotope data point towards major involvement of the Grampian terrane, despite the Drumadoon Igneous Complex being located within the Midland Valley Terrane crustal block. Therefore, while the magmas originated at depth on the northern side of the Highland Boundary Fault, they have crossed this boundary at

some point during their evolution and ascent, most likely during shallow-level emplacement, as all data suggest the Grampian Terrane as the sole crustal influence.

Gravimetric studies on the Highland Boundary Fault suggest a sub-vertical orientation, dipping very steeply to the northwest (Dentith *et al.*, 1992). Given this geometry, the magma is unlikely to have taken a direct vertical traverse through the crust, but rather experienced an element of horizontal movement, not least during final shallow-level emplacement. As a suite, the Arran porphyries (Harrison, 1925; Kanaris-Sotiriou and Gibb, 1985), and those from Bute (Smellie, 1914, 1916; Buist, 1952), all crop out just south of the Highland Boundary Fault, despite being ~35 km apart and the Bute sills being ~30 km further north. This suggests that the fault plane may have acted as an intrusion pathway along which the magma travelled, followed by intrusion into the footwall (Midland Valley Terrane) (Figure 7.26). Intrusion into the footwall of faults has also been noted at the Skye igneous centre (Butler and Hutton, 1994). Indeed work by Grosfils (2007) has shown that high level magma chambers are more likely to form laterally propagating sills, such as those seen at Arran (rather than vertical dykes).

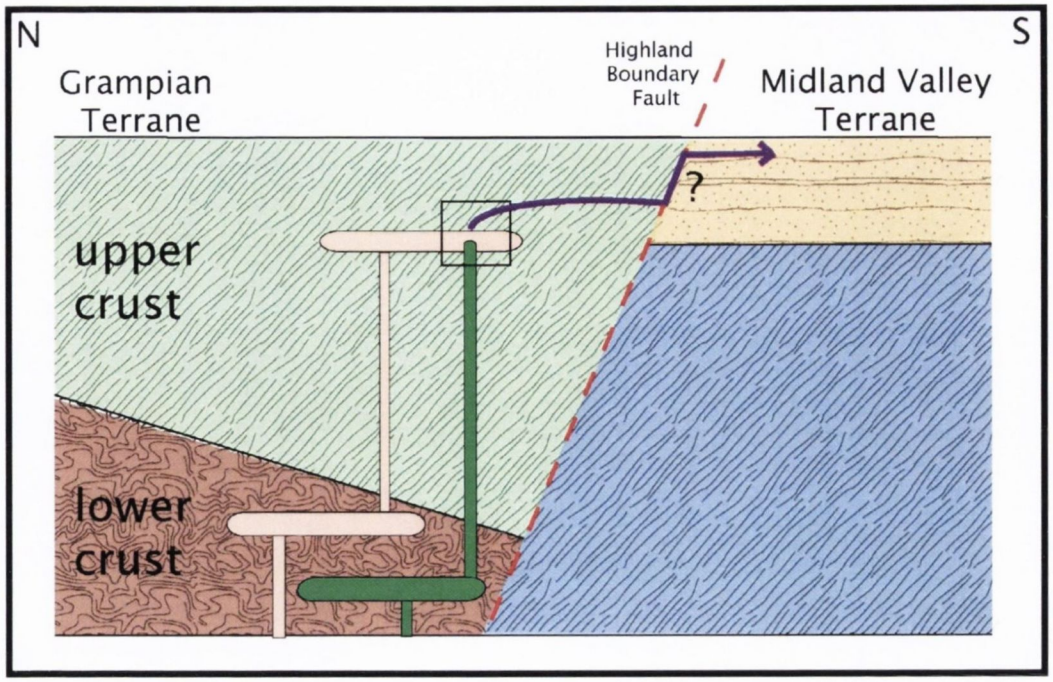


**Figure 7.26 Schematic diagram showing the intrusion pathways of both the rhyolitic (pink) and basaltic (green) magmas. The rhyolite was contaminated in both the upper and lower crust, while the basalt just shows lower crustal influences. The magmas met in the upper crust and mixed and mingled (black square) (see Figure 7.24). They then intruded across the terrane boundary, most likely exploiting the Highland Boundary Fault (purple arrow).**

An alternative crustal structure has been proposed in Strachan (2000), whereby some Grampian crust may have under-thrust the Midland Valley Terrane during the Grampian Orogeny. This would result in a stratigraphy whereby Dalradian rocks lie stratigraphically below the rocks of the Midland Valley, meaning magma could be contaminated by Grampian Terrane lithologies and still make a direct vertical traverse through the crust. While this may seem like a simpler emplacement scenario, we must consider how likely this underlying thrust slice is to contain a significant thickness of Dalradian rock as well as the southward-thinning Rhinns Complex-type lower crust. Similarly, if the magmas were to take this route through the crust then they would have had to travel through a significant portion of Midland

Valley Terrane basement and Mesozoic/Palaeozoic sediments. However we see no isotopic evidence of their involvement through crustal contamination. While the Midland Valley crust has a less radiogenic Sr isotopic signature than its Grampian equivalent; it might seem possible that the stronger Dalradian signature may have masked its influence, as assimilation of less radiogenic Midland Valley crust would simply reverse the trend (see Troll *et al.*, 2005). However we have seen from geochemical modelling of assimilation during fractional crystallisation (AFC) that the current isotopic ratio of the rhyolites suggests they have neared the physical limit of assimilation of Dalradian crust (Reiners *et al.*, 1995). This implies they have achieved the most radiogenic signature possible, inferring therefore, that their signature could not have been retrogressed due to incorporation of a third, less radiogenic, crustal end member.

The only Midland Valley Terrane influence evident is interaction of the margins of the sill with the fluids within the sandstone country rocks (Section 7.8.3 and Figure 7.18). Here, the hydrocarbon-rich fluids, most likely heated by the sill, are inferred to have leached several elements ($TiO_2$, V, Cr etc.) from these marginal zones.

## 7.13. Conclusions

Across the complex, the rock-types show a typical BIPIP "Bunsen-Daly Gap" distribution (Bunsen, 1851; Daly, 1925), with strongly bimodal (basalt-rhyolite) compositions. Significantly, the intermediate compositions, while seemingly bridging the Bunsen-Daly Gap, are not the product of pure fractional crystallisation but rather these magmas seem to be the result of mixing of end-member compositions (Section 7.8). The comparatively large volumes of felsic magma

(porphyritic rhyolite) at Drumadoon appear to be the result of high levels of crustal contamination during fractionation of a basaltic parent (Section 7.11).

It appears the basalt and rhyolite magmas had separate paths through the crust, and only met in the upper crust. The basaltic-andesite shows lower crustal contamination, but no upper crustal contamination. The porphyritic rhyolite is also likely to have been contaminated to low degrees in the lower crust, but this was followed by large-scale assimilation during fractional crystallisation in the upper crust. Crustal contamination occurred by both bulk isotope mixing and assimilation during fractional crystallisation (AFC) (Section 7.11).

Within the upper crust, the basalt is likely to have encroached upon the crystallising rhyolite body. On passing through the rhyolitic crystal mush, the basaltic magma mixed and mingled, forming the xenocryst-bearing basaltic-andesite, possibly some mixed dacite and the enclave-bearing rhyolite (Figure 7.24). The basaltic-andesite, being less viscous, would have flowed faster and formed the initial intrusion, lubricating the way for the viscous rhyolite. Work by Rubin (1995) suggests that it is difficult for granitic dykes to escape the source region, so lubrication by basaltic magma in the conduit (by both heat and volatiles released from the cooling mafic magma) may be crucial for transport of such magmas over large distances (see Takeuchi and Nakamura (2001)).

The magmas have crossed a major crustal boundary on emplacement and bearing in mind the inclined nature of the Highland Boundary Fault, it is likely they travelled laterally for a significant distance, maybe as much at 30 - 40 km. Indeed the fault zone itself may have been an important magma pathway (Figure 7.26).

# 8. MOURNE

*Geochemical and field evidence for magma mixing and crustal contamination within the Mourne Intrusive Complex, Northern Ireland.*

## 8.1. Abstract

The Mourne Intrusive Complex lies within the Longford-Down Terrane, the Irish correlative of the Southern Uplands Terrane, in south-eastern Northern Ireland. The complex formed at ca. 56 Ma and comprises five main granite bodies (termed G1-G5) with several suites of minor intrusions, including a regional mafic/intermediate dyke swarm and a series of composite basalt/rhyolite cone-sheets. The granites are highly fractionated and therefore rich in incompatible elements; this, coupled with a large crustal component, means they are significantly enriched in Rb. Hence they yield imprecise Rb-Sr isotopic data due to the uncertainty in correcting for ingrowth of radiogenic Sr. Therefore work has focussed on the Glasdrumman cone-sheet, which is composite in nature (rhyolite/basalt) and contains much lower Rb levels. The rhyolites show a strong influence by the Longford-Down metasedimentary crust and have mixed with a less-contaminated basalt to form a hybrid rhyolite, with a dark groundmass. The intrusion records many late-stage physical processes, including magma mixing and mingling, phenocryst transferral, flow differentiation, and the transition from laminar to turbulent flow as the intrusion conduit narrowed.

The regional dyke swarm contains abundant mafic cumulate enclaves, indicating the presence of a large volume of mafic magma at depth below the centre, which is likely to have been a source of magma for the Mourne Intrusive Complex, and a heat source to (partially) melt local metasedimentary country rock.

## 8.2. Introduction

### *8.2.1. The Mourne granite complex*

The Mourne granite complex is situated in the Longford Down (Southern Uplands) Terrane. The terrane comprises the siltstones and mudstones of the Silurian Longford-Down Basin (Holland, 2001) (see sections 4.5.5 and 6.3.1). These rocks metamorphosed to greenschist facies during the Caledonian Orogeny (Phillips, 2001). Little is known of the terrane basement, however, xenolith suites from within Carboniferous lamprophyres show mylonitised meta-sediments, meta-diorites and meta-tonalites that most likely represent an under-thrust meta-igneous succession of Lake District type (island arc) (Anderson and Oliver, 1996).

The complex comprises a series of five granites, divided into two centres – the Eastern (G1-G2) and Western Mournes (G3-G5) (Richey, 1928). Work by Hood (1981) and Gibson (1984) further sub-divided these granites into various facies based on grain size and mineralogy (Figure 8.1). The centres were intruded at approximately 56 Ma (Meighan *et al.*, 1984; Gibson *et al.*, 1987; Gamble *et al.*, 1999). They were considered by Richey (1928) and Hood (1981) to be a series of stacked ring-dykes emplaced due to cauldron subsidence, however recent work by Stevenson et al (2007) envisages them to be a series of laccolithic intrusions.

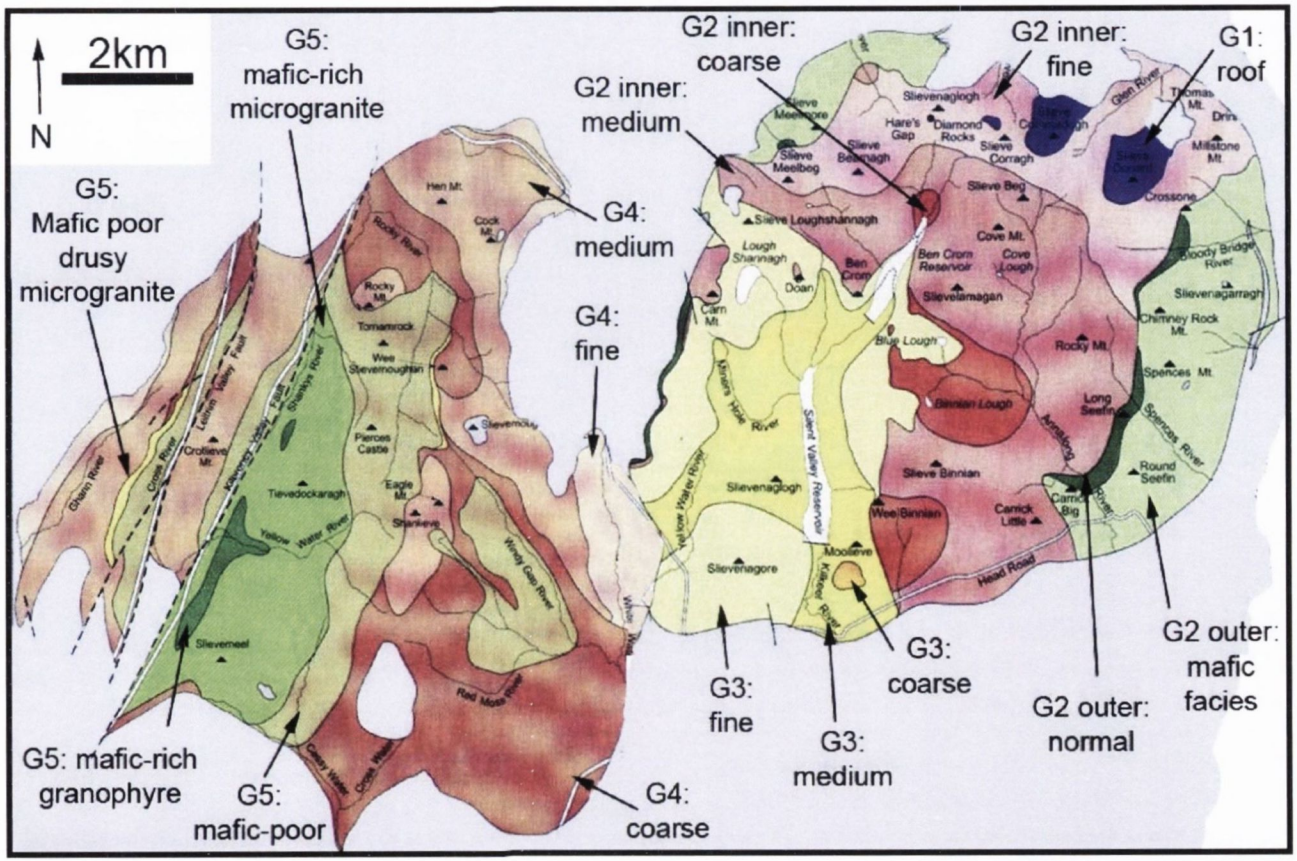


**Figure 8.1 Map of the Mourne granite complex, showing the various granites (G1-5). Facies within the granites are indicated. Grey background represents the Longford-Down metasediments (country rock). Map after figures 15.3 and 15.4 of Cooper and Johnston (2004),. These figures use the data of Hood (1981) and Gibson (1984).**

### *8.2.2. The Mourne dyke swarm*

Minor intrusions occur frequently within the vicinity of the Mourne intrusive complex. The majority of these dykes appear to be early. They are cross-cut by the granites and form part of the regional (NW-SE) Palaeogene dyke swarm, though most likely intensified by the presence of an igneous centre. These dykes range in composition from mafic through to felsic (Tomkeieff and Marshall, 1935; Akiman, 1971). Throughout the Eastern Mourne centre, a series of thick composite cone-sheets, 20 – 30 m thick in places, is also exposed sporadically around the north and east of the granites (Akiman, 1973).

#### *8.2.2.1. Dunmore Head dykes*

Numerous members of the Mourne dyke swarm are exposed in the coastal section between Dunmore Head and Green Harbour. These dykes were numbered and described in detail by Tomkeieff and Marshall (1935). Of particular interest to this study are dykes 60, 61 and 63, which crop out at Dunmore Head. These andesitic dykes contain enclaves of anorthosite and large (>5 cm) phenocrysts of plagioclase, indicating cumulate development in the source magma chamber of these dykes (Figure 8.2, Figure 8.3). This suggests the presence of a large volume of fractionated basaltic magma at depth beneath the granitic Mourne Intrusive Complex.



**Figure 8.2 Large enclaves of cumulate anorthosite within dyke 60 at Dunmore Head.**



**Figure 8.3 Two large plagioclase phenocrysts within dyke 61 at Dunmore Head.**

#### *8.2.2.2. The Mourne cone-sheet*

The Mourne cone-sheets are comprised of thin, outer basaltic margins, narrow intermediate zones of dark, hybridised rhyolite with large feldspar

phenocrysts and enclaves of basalt and a thick, inner pink quartz and feldspar-phyric rhyolite member which forms most of the intrusion (Figure 8.4).



**Figure 8.4 The composite cone-sheet at Glasdrumman Port, showing the basaltic margin (left) and large basaltic enclaves (centre) lying within the central porphyritic rhyolite member. Photograph taken looking south. The dyke dips west beneath the main granite bodies.**

At Grugandoo (IJ 201 256), a member of the swarm appears to be truncated by the G4 granite of the Western Centre (Emeleus and Preston, 1969). Further outcrops are seen at Annalong, Knockchree, Knockshee Hill, Formal Hill, Bloody Bridge, and in the Glen River. While there are many outcrops, they are sparsely distributed. On many previously published maps they are joined together, implying a single cone-sheet. It is, however, likely that the outcrops represent several members of the same cone-sheet swarm, rather than outcrops of one single intrusion (D. Hood,

*pers. comm.*). The best exposure of the sheet is seen at Glasdrumman Port (IJ 380 222), with *c.* 200 m of almost complete exposure. The Glasdrumman cone-sheet is discussed further in section 8.4.

## 8.3. Geochemical Analysis

Major, trace and rare earth element data and Sr, Nd and Pb isotope ratios were obtained for the Mourne Intrusive Centre, as well as the surrounding Mourne cone-sheet and Longford-Down metasedimentary country rocks.

### *8.3.1. Sample selection and preparation*

Representative samples (n=26) of the main lithologies exposed at the Mourne Intrusive Complex were collected, including samples of the G1, G2, G3, and G4 granites (Appendices 6.1, 7.1 and 8.1). A detailed sample traverse was taken through the Mourne cone-sheet at Glasdrumman. Country rock samples, including a traverse through a large screen of metasediment lying within the G2 outer granite at Bloody Bridge were collected. Four lower crustal xenoliths were also analysed (see also Anderson and Oliver, 1996).

Samples were sliced and weathered edges removed. Samples were then crushed in a jaw-crusher and powdered in a tungsten carbide TEMA mill. All powders were analysed for major and trace elements and a selected sample set were analysed for rare earth element concentrations and strontium, neodymium and lead isotopes.

### *8.3.2. X-Ray fluorescence*

The majority of whole-rock samples were analyzed for major element oxide and trace element concentrations at GEOMAR Research Centre, Kiel, Germany (see section 5.2.1). Major element data had initial totals ranging from 98.75% to 100.48% and were corrected for loss on ignition and normalised to 100% for plotting.

Complementary XRF analyses on granites *M-G2-outer, M-G3, M-G4* and lower-crustal metasediments *BWA, BWB, BWC, BWD* were carried at the University of St. Andrews, Scotland (see section 5.2.2). Major element data had initial totals ranging from 99.20% to 99.83% and were also corrected for loss on ignition and normalised to 100% for plotting.

For complete data tables see Appendices 6.2, 6.3, 6.4, 7.2, 7.3, 7.4, 8.2, 8.3 and 8.4)

### *8.3.3. ICP-MS*

Rare earth elements and U, Th and Pb concentrations were determined by inductively coupled plasma mass spectrometry (ICP-MS) at the Scottish Universities Environmental Research Centre (SUERC), East Kilbride, Scotland (see section 5.4.1 and Appendices 6.5, 6.6, 7.5, 7.6, 8.5 and 8.6).

### *8.3.4. Isotope geochemistry*

Strontium, neodymium and lead isotopes were analysed at the Scottish Universities Environmental Research Centre (SUERC) (see sections 5.5.1.1, 5.5.2.1 and 5.5.3.1 for analytical details). See Appendices 6.7, 6.8, 7.7, 7.8, 8.7 and 8.8 for the complete data set.

### *8.3.5. Age correction of strontium isotope ratios for the Mourne granites*

As mentioned in section 5.5, high Rb/Sr ratios in a sample can have a strong effect on the age correction of strontium isotope ratios. This is the case with the Mourne granites, which can have maximum Rb/Sr ratios > 100 (500 ppm Rb and 5 ppm Sr). The average Rb value is 470 ppm, with the average Sr concentration measured at 8 ppm. This approximates to an average Rb/Sr ratio of ~ 60. These high values are likely due to the effects of concentration of incompatible Rb and depletion of compatible Sr due to feldspar fractionation combined with significant input of Rb-rich crustal material. The high Rb/Sr ratios result in very unreliable age correction of Sr isotope data as evident in Figure 8.5, whereby the error propagation on the age-corrected strontium initial ratio increase significantly with increasing Rb/Sr ratio.

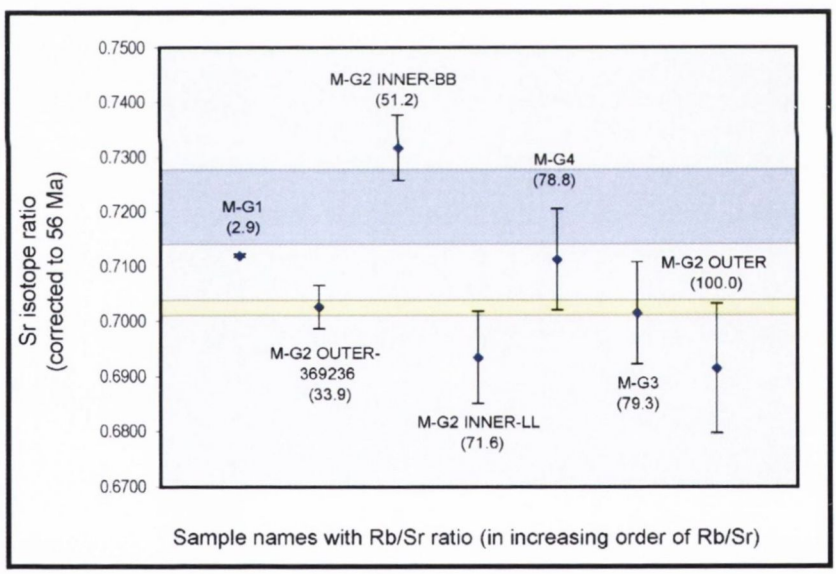


**Figure 8.5 Plot of strontium isotope ratios for the Mourne granites, with error bars representing the propagated error in the age-corrected Sr data using a ± 5 % analytical uncertainty in Rb/Sr ratio. The data shows that the higher the Rb/Sr ratio, the greater the uncertainty in the data. The yellow box shows the typical range of strontium isotope ratio for the mantle (Saunders *et al.*, 1988). The blue box represents typical crustal ranges within the region.**

The problem in determining Sr initial ratios in high Rb/Sr samples can be compounded by Rb contamination in the Sr fraction during the chemical separation of the elements by ion chromatography. Incomplete separation of Rb from Sr would result in higher Sr initial ratios, as $^{87}Rb$ gets included in the $^{87}Sr$ analysis. This problem is far more relevant in Sr analysis by ICP-MS, as the Sr (and the contaminating Rb) both enter the plasma. In TIMS analysis, Rb ionizes at lower filament currents than Sr, and so is typically quickly burnt off quickly during a Sr analysis and does not significantly affect the final Sr isotopic ratio.

The range for mantle and local crustal strontium isotopic ratios has also been plotted in Figure 8.5. Some broad conclusions can be gleaned from the data. Sample M-G1, shows the lowest propagated errors and can be deemed a reliable analysis. This suggests that G1, the first granite of the Mourne Intrusive Complex, has had a significant crustal input, as the strontium isotopic ratio has deviated from the mantle field towards that of the local Longford-Down metasedimentary crust. For the remaining sampled granites, G2, G3 and G4, it is clear that the uncertainties on the data are so large that they span the entire mantle and crust range for the region, and the data are thus too vague to draw any conclusions on magma petrogenesis. Similarly many data points have been age-corrected to values that are less radiogenic (but within error) of the strontium isotopic ratio of the mantle, resulting in very unrealistic ranges.

Therefore further work on the Mourne Intrusive centre was focussed on the Glasdrumman section of the Mourne cone-sheet, where detailed geochemical traverses could be performed and Rb/Sr ratios within the evolved members were more favourable for accurate and precise age corrected Sr isotope data as Rb/Sr ratios range from 1.5 to 6.8 for the rhyolites.

## 8.4. The Glasdrumman cone-sheet

### *8.4.1. Fieldwork*

Initial fieldwork involved detailed mapping, logging and sampling of the Glasdrumman composite sheet, exposed at Glasdrumman Port, south of Newcastle, County Down (IJ 380 222). The Glasdrumman cone-sheet ranges from 12 - 30 m thick and generally dips between 35 and 55 degrees to the west beneath the main granite bodies (Figure 8.6).

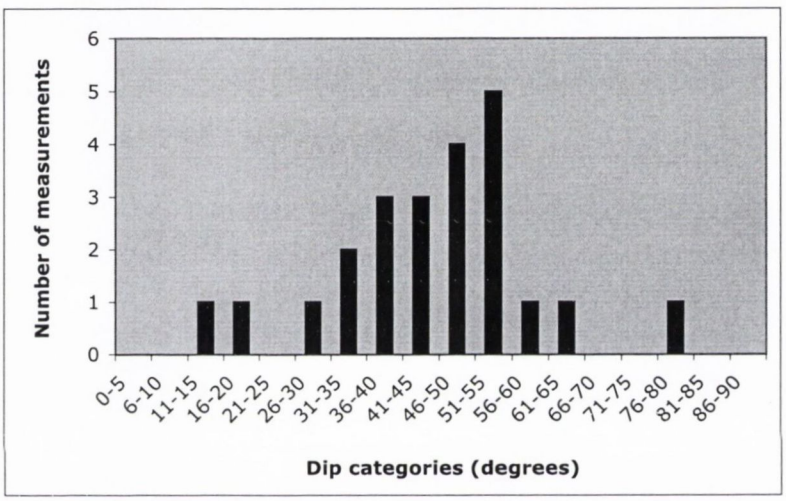


**Figure 8.6 Distribution of dip values for the Glasdrumman section of the Mourne cone-sheet. All measurements dip west. The data represent measurements from internal and external boundaries of the dyke.**

The dyke is comprised of thin basaltic outer margins and a thick inner zone of quartz and K-feldspar-phyric pink rhyolite, which forms the majority of the intrusion. Narrow zones of a darker, hybridised, porphyritic rhyolite, with large feldspar phenocrysts and enclaves of basalt lie between the basalt and the main rhyolite. A solitary outcrop along strike to the north (at the back of the beach) shows the mafic and felsic magmas commingled together (Figure 8.7).

The area was mapped and seven traverses of the dyke were logged, noting petrological differences, including the nature of internal and external boundaries, xenocryst/phenocryst types and the density of enclaves present. The results of this survey are presented in Figure 8.7 and Figure 8.8.

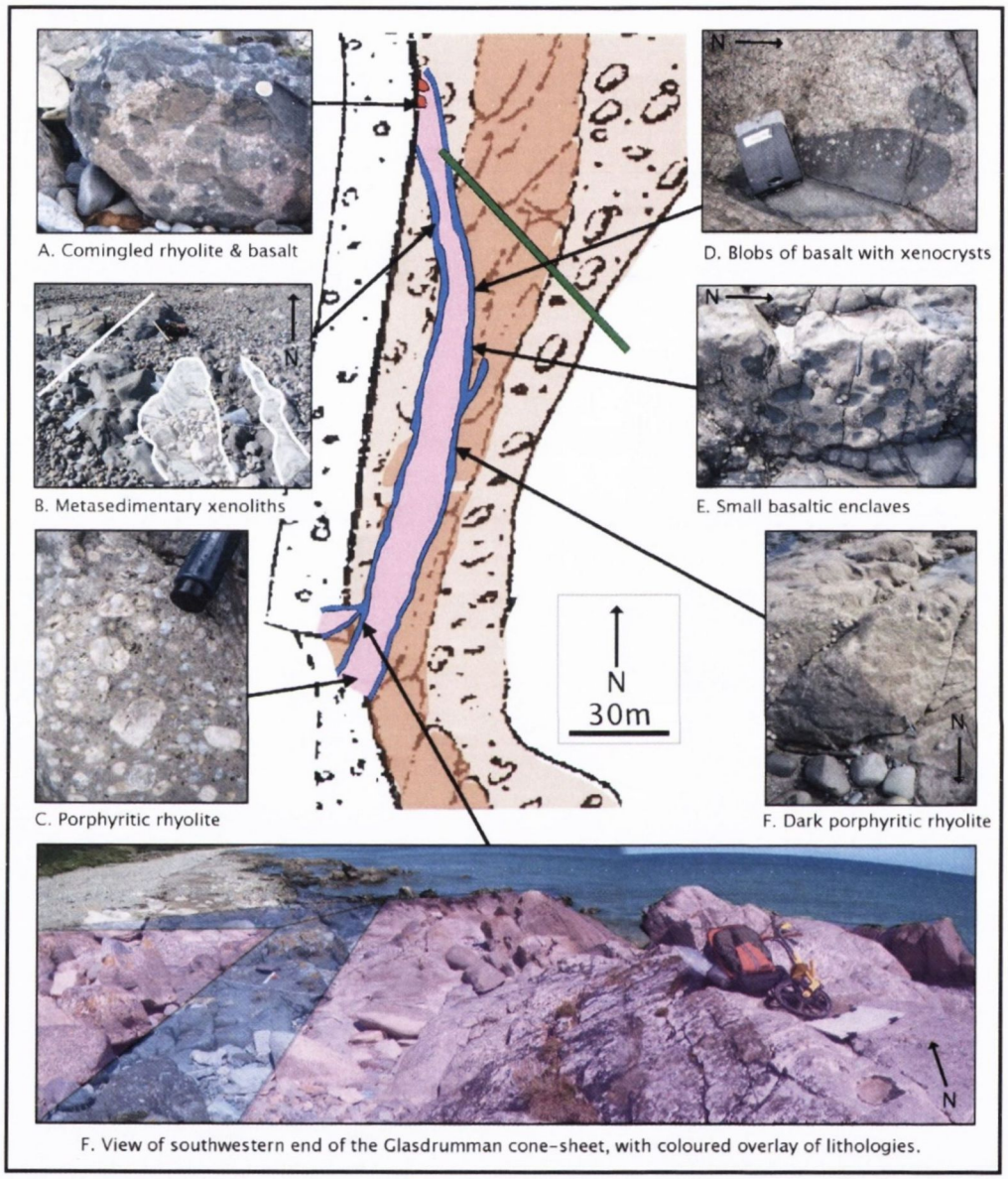


**Figure 8.7 Map of the Glasdrumman composite sheet, with photographs of features as seen along the intrusion. Note, the dark rhyolite (photograph F) occurs all along the intrusion between the basalt and rhyolite, but is too narrow to be seen in map view. See logged section for more lithological detail and key (Figure 8.8).**

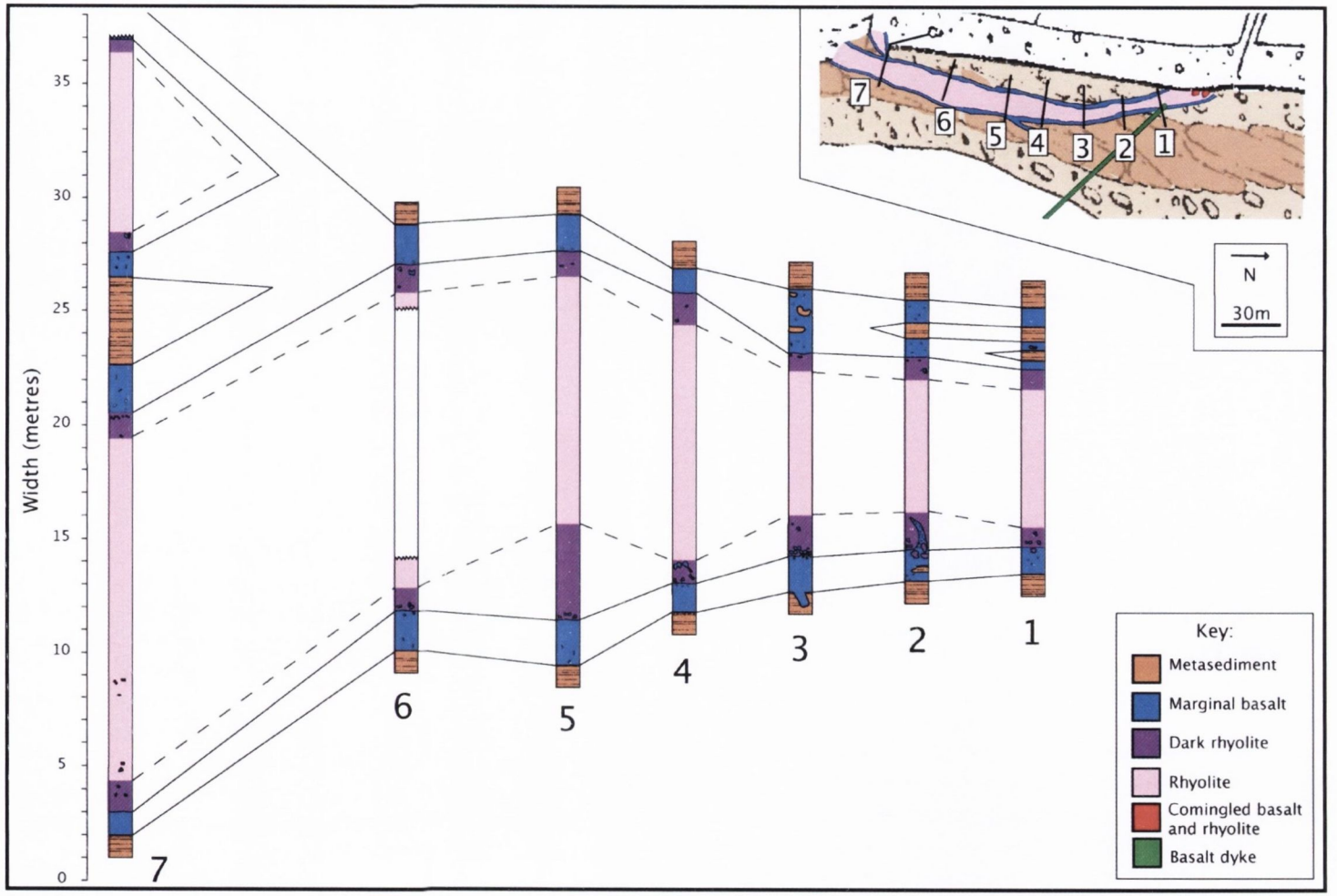


**Figure 8.8 Seven logged traverses of the Glasdrumman composite intrusion. Traverses are marked on the map (inset).**

### *8.4.2. Petrology and petrography*

#### *8.4.2.1. Xenocrystic basalt*

The xenocrystic basalt in fine to medium-grained (dolerite) and contains numerous xenocrysts of quartz and alkali feldspar. These xenocrysts appear to be sourced from disaggregated enclaves of the adjacent porphyritic rhyolite (Figure 8.9, Figure 8.10).



**Figure 8.9 The marginal basalt of the Glasdrumman cone-sheet, showing K-feldspar xenocrysts, most likely originating from a disaggregated enclave of the adjacent porhyritic rhyolite. In some regions these xenocrysts are abundant, though less so in others (see Figure 4.11).**



**Figure 8.10 A purer section of marginal basalt than that seen in Figure 8.9. Note the presence of a small, quartz-rich disaggregated rhyolite enclave.**

In thin section the basalt contains 35 - 40% plagioclase laths (~ 1 mm in length), and 55% pyroxene, much of which has been altered to amphibole. There is ~ 1% chlorite and 5% opaques present (Figure 8.11).

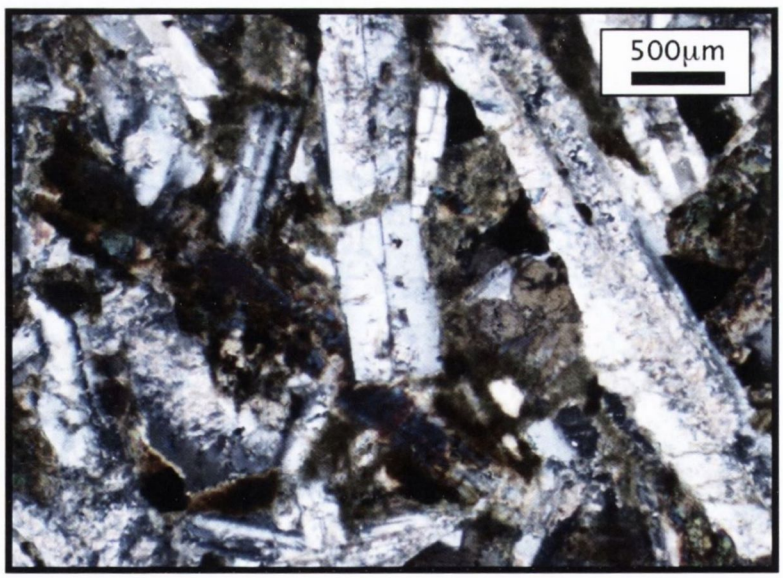


**Figure 8.11 Thin section of Glasdrumman basalt, showing plagioclase laths, with amphibole and chlorite representing weathered mafic minerals.**

### *8.4.2.2. Quartz and feldspar-phyric rhyolite*

The Glasdrumman rhyolite is a pink, fine-grained rhyolite, with abundant quartz and feldspar phenocrysts (Figure 8.12). The groundmass is composed of quartz and feldspar, often showing graphic texture. There is also ~ 2% biotite and chlorite. It contains 35 – 40% phenocrysts of which ~ 65% are alkali feldspar and 35 % are quartz (Figure 8.13). The feldspar phenocrysts are often > 1 cm in diameter, while the quartz is usually ~ 5 mm.



**Figure 8.12 Close-up of quartz and K-feldspar phenocrysts within the Glasdrumman porphyritic rhyolite. The feldspars show very obvious zoning.**

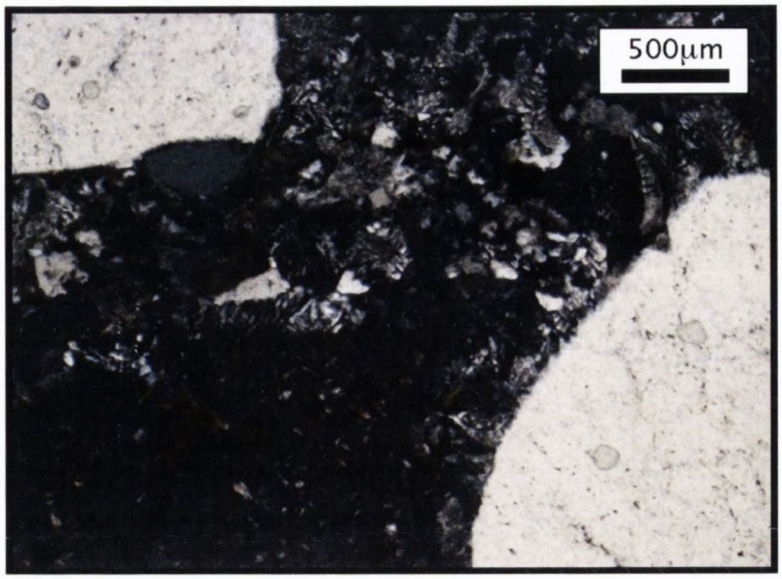


**Figure 8.13 Thin section of rhyolite, showing quartz and alkali feldspar phenocrysts in a quartz and feldspar groundmass exhibiting graphic texture.**

#### *8.4.2.3. Hybridised rhyolite*

A hybridised rhyolite lies between the xenocrystic basalt and the pale porphyritic rhyolite on both margins of the dyke (Figure 8.7). It is also porphyritic, but has a darker groundmass than the rhyolite and contains abundant mafic enclaves (Figure 8.8, Figure 8.14).



**Figure 8.14 Porphyritic rhyolite (left) and dark porphyritic rhyolite (right). The dark rhyolite has a darker groundmass and larger K-feldspar phenocrysts than the adjacent rhyolite.**

This darker rhyolite appears to be the product of mixing and mingling of the central pale rhyolite and the marginal basalt. It contains megacrysts of alkali feldspar (2 – 3 cm in size), often with obvious zoning and very pink K-feldspar rims (Figure 8.15).



**Figure 8.15 Close-up view of phenocrysts within the dark rhyolite. K-feldspar megacrysts show clear zoning with distinct dark pink rims.**

In thin section (Figure 8.16), the hybridised rhyolite has a groundmass of fine-grained quartz and feldspar, similar to that of the pale central rhyolite (section 8.4.2.2). However it contains ~ 5% chlorite, most likely representing altered hornblende. It also contains ~ 3% opaques, which are not as abundant within the central rhyolite. The hybridised rhyolite contains ~ 30% phenocrysts, of which ~75% are alkali feldspar and 25% are quartz. The quartz is rounded and resorbed in places. The alkali feldspars are also rounded, and show clear reaction rims. There are rare rounded plagioclase phenocrysts. The rounded nature of all the phenocrysts indicates that they were not in equilibrium with the melt.

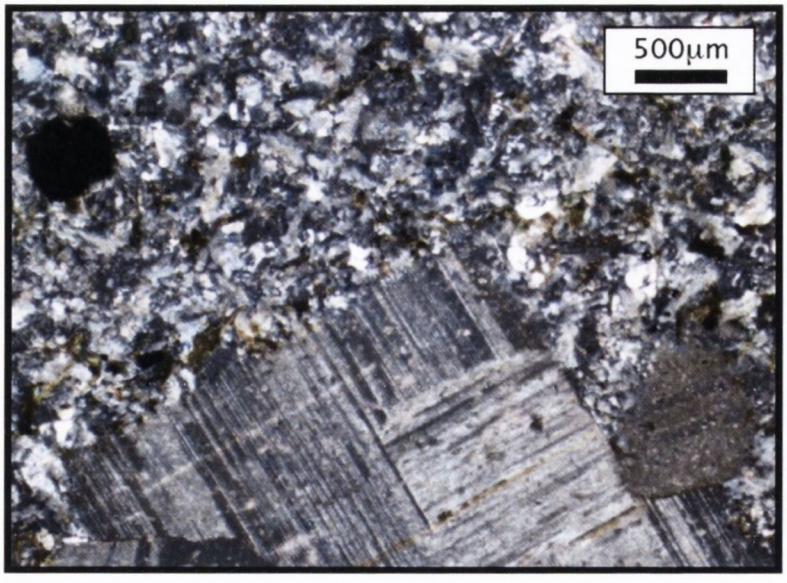


**Figure 8.16 Thin section image of the hybridised rhyolite, showing a large plagioclase phenocryst in a quartz, feldspar and chlorite groundmass.**

#### *8.4.2.4. Mingled rhyolite and basalt*

An outcrop of mingled basalt and rhyolite is exposed at the northernmost end of the Glasdrumman cone-sheet, denoted as the purple outcrops in Figure 8.7. In this segment of the dyke, the compositional zoning appears to have broken down, mingling rhyolite with basaltic enclaves (Figure 8.17). This is due to the immiscibility of the two magmas because of their viscosity differences, and is most likely the result of turbulence in the dyke. The dyke appears to be significantly narrower in this section (~ 11 m) than further south (~ 20 m) (Figure 8.7 and Figure 8.8). If the volume of magma travelling through the dyke was similar along the whole length of the Glasdrumman exposure then it is possible the narrower conduit caused the magma to become turbulent, mingling the magmas, rather than flowing in a distinctly zoned dyke.



**Figure 8.17 An outcrop of mingled basalt and rhyolite exposed at the northernmost end of the Glasdrumman cone-sheet. Note the density of basalt enclaves and the large feldspar phenocrysts within the rhyolitic groundmass.**

### *8.4.3. Contact relationships*

The internal contacts within the Glasdrumman cone-sheet intrusion exhibit textures indicative of liquid-liquid interaction. There are no internal chilled margins. Lobate contacts are ubiquitous, as are enclaves of basaltic within the rhyolite, and of rhyolite within the basalt (Figure 8.18). There is obvious phenocryst transfer between the host rhyolite and the basaltic enclaves (Figure 8.19). There is a distinct zone of dark, hybridised rhyolite between the marginal basalt and central rhyolite. This suggests that both magmas were intruded contemporaneously and interacted both in the conduit during transport and *in situ* on final emplacement (Figure 8.14, Figure 8.15).

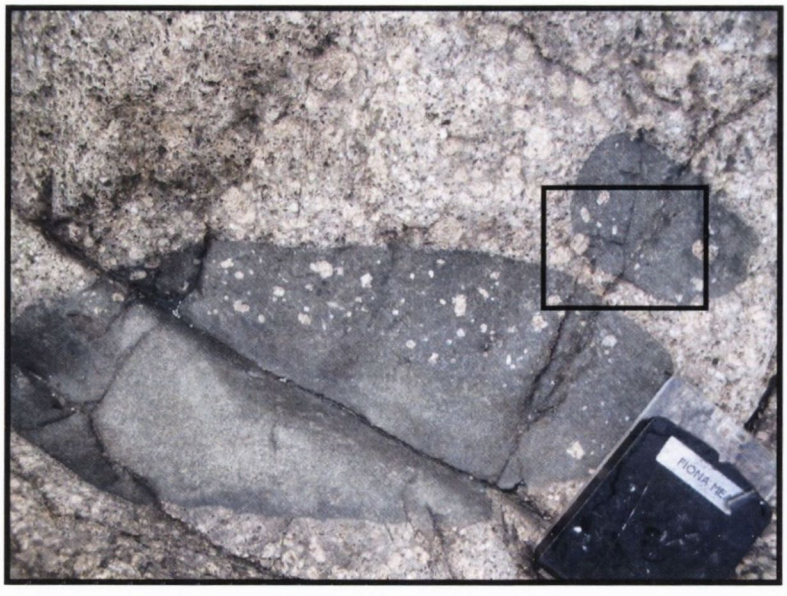

**Figure 8.18 Enclaves of basalt within the dark rhyolite. These enclaves indicate both magmas were liquid at the same time. Note the lack of chilled margins and the presence of xenocrysts of K-feldspar (derived from the rhyolite) within the basaltic enclave. For a close-up view of the area marked by the black box, see Figure 8.19.**

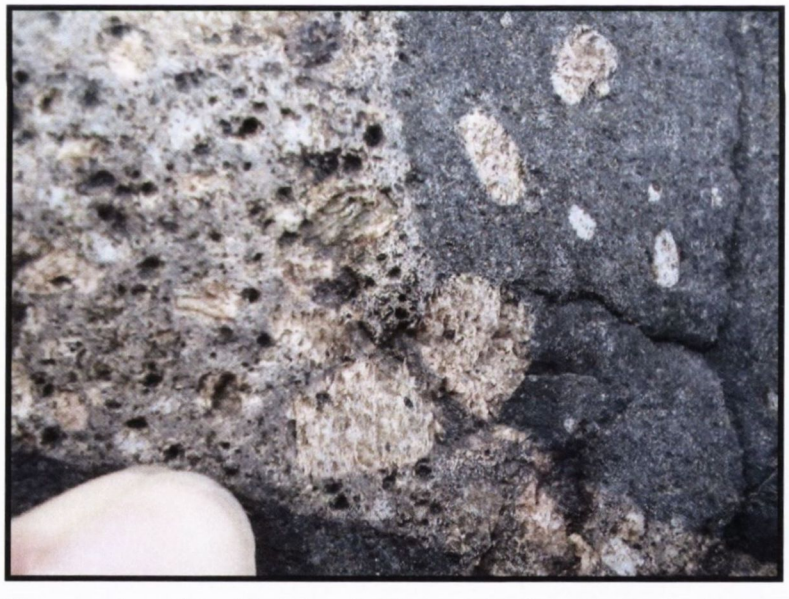

**Figure 8.19 Close-up view of the black box in Figure 8.18. Crystal transfer is clear between the dark rhyolite and the basalt (centre). There is also an obvious absense of chilled margins.**

The basalt is often xenocrystic, containing resorbed crystals of both quartz and K-feldspar. These xenocrysts are often concentrated in zones, representing the disaggregated remains of rhyolite enclaves that had been incorporated into the basaltic margins of the dyke (Figure 8.9, Figure 8.10). The boundary between the marginal basalt and the dark rhyolite is often irregular, with wispy boundaries and frequent enclaves (Figure 8.8, Figure 8.20). This indicates active mixing and mingling during intrusion, suggesting the majority of interaction may have occurred during intrusion, rather than within the magma chamber



**Figure 8.20 The lower boundary between the basalt and hybridised rhyolite, showing 'flames" of basalt injecting into the hybridised rhyolite. Interaction is greater within this structure, with a higher concentration of xenocrysts. The segment of the white measuring tape in the top left corner is 25cm in length. See also Figure 8.8 for an overview of the structure of the boundary between the basalt and dark, hybridised rhyolite, especially at the lower margins, where interaction appears greater.**

### *8.4.4. Sample selection*

Samples for geochemical analysis were collected at intervals across a section of the dyke (Traverse 1 in Figure 8.8) to ensure that samples were representative. Sample names, lithologies and locations are detailed in Table 8.1.

| Sample Name | Distance from lower dyke margin (cm) | Lithology | |
|---|---|---|---|
| G-T1-S23 | 1130 | Longford-Down Metasediment | *Boundary at 1120 cm* |
| G-T1-S22 | 1115 | Basalt | |
| G-T1-S21 | 1055 | | |
| G-T1-S20 | 1010 | | *Boundary at 1005 cm* |
| G-T1-S19 | 1000 | Longford-Down Metasediment | |
| G-T1-S18 | 910 | Basalt | *Boundary at 925 cm* |
| G-T1-S17 | 860 | Longford-Down Metasediment | *Boundary at 880 cm* |
| G-T1-S16 | 810 | Basalt | *Boundary at 845 cm* |
| G-T1-S15 | 800 | Dark Porphyritic Rhyolite | *Boundary at 805 cm* |
| G-T1-S14 | 750-760 | | *Boundary at 730 cm* |
| G-T1-S13 | 730 | Porphyritic Rhyolite | |
| G-T1-S12 | 690 | | |
| G-T1-S11 | 560 | | |
| G-T1-S10 | 415 | | |
| G-T1-S9 | 345 | | |
| G-T1-S8 | 240 | | |
| G-T1-S7 | 125 | Dark Porphyritic Rhyolite | *Boundary at 220 cm* |
| G-T1-S6 | 120 | | |
| G-T1-S5 | 85 | | |
| G-T1-S4 | 80 | Basalt | *Boundary at 82 cm* |
| G-T1-S3 | 35 | | |
| G-T1-S2 | 0-5 | | |
| G-T1-S1 | -5 | Longford-Down Metasediment | *Boundary at 0 cm* |

**Table 8.1 Table of relative sample locations for traverse 1 (see Figure 8.8) of the Glasdrumman cone-sheet, with lithological boundaries marked. Coloured blocks are not representative of actual thicknesses.**

### *8.4.5. Major and trace element geochemistry*

#### *8.4.5.1. Major element data*

A total alkali versus silica (TAS) plot indicates both the central member of the dyke and the hybridised intermediate member are both rhyolitic in composition, despite the groundmass of the hybrid being significantly darker (see Figure 8.14).

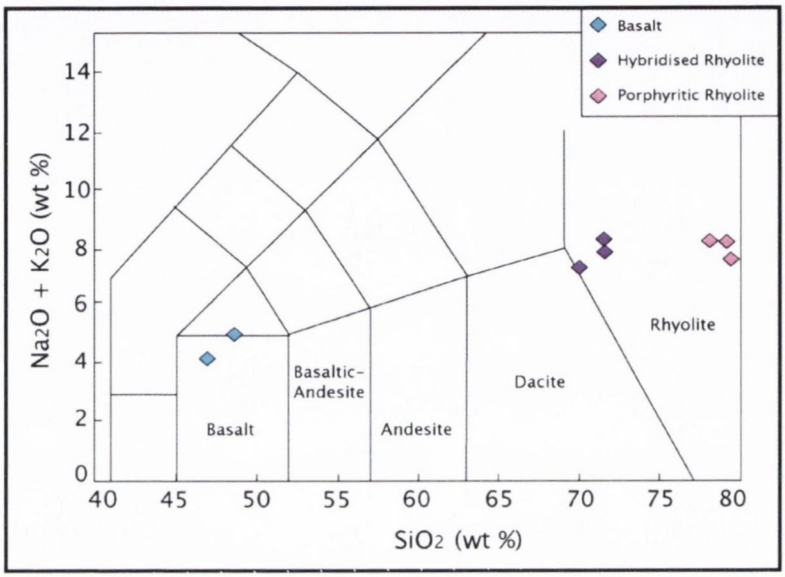


**Figure 8.21 Total alkali versus silica plot for the Glasdrumman sample suite, with chemical classification of the various lithologies.**

When major elements are plotted against distance across the dyke it is clear the hybridised rhyolite has a chemical composition intermediate to that of the basalt and rhyolite. One hybrid sample, G-$T_1$-$S_7$, at 125 cm, was sampled near a basaltic enclave, and shows a chemical composition that appears to have a more mafic influence. It is this effect that causes the kink in the U-shaped trends in Figure 8.22.

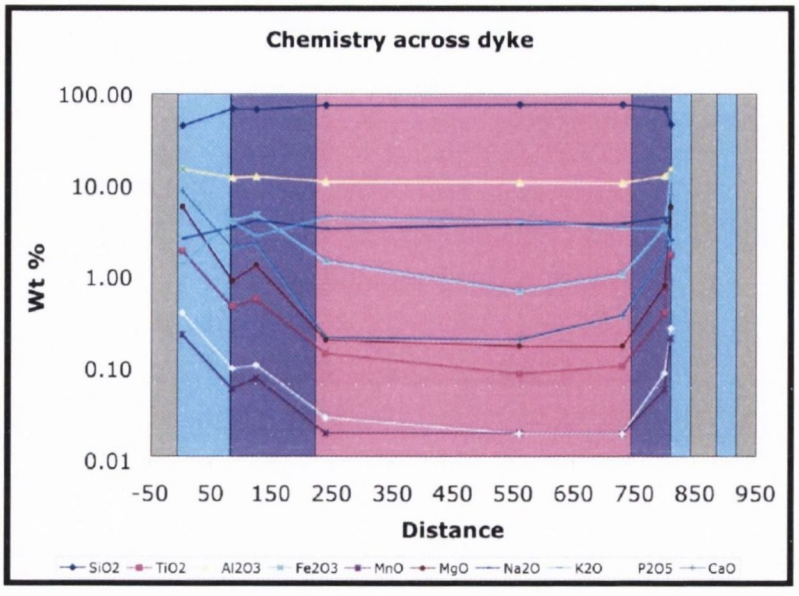


**Figure 8.22 Plot of major elements against distance across the dyke. Coloured stripes represent lithologies detailed in Table 8.1.**

The hybrid nature of the dark rhyolite is further confirmed by major element versus silica (Harker) plots. MgO shows a distinct linear trend, with the dark (hybridised) rhyolite showing increased MgO concentrations compared to the central rhyolite (Figure 8.23). This straight-line trend is interpreted as bimodal mixing, whereby the basalt and rhyolite have mixed to form a dark hybridised rhyolite. This mixing trend is echoed by almost all of the other major elements (e.g. CaO, Figure 8.24)

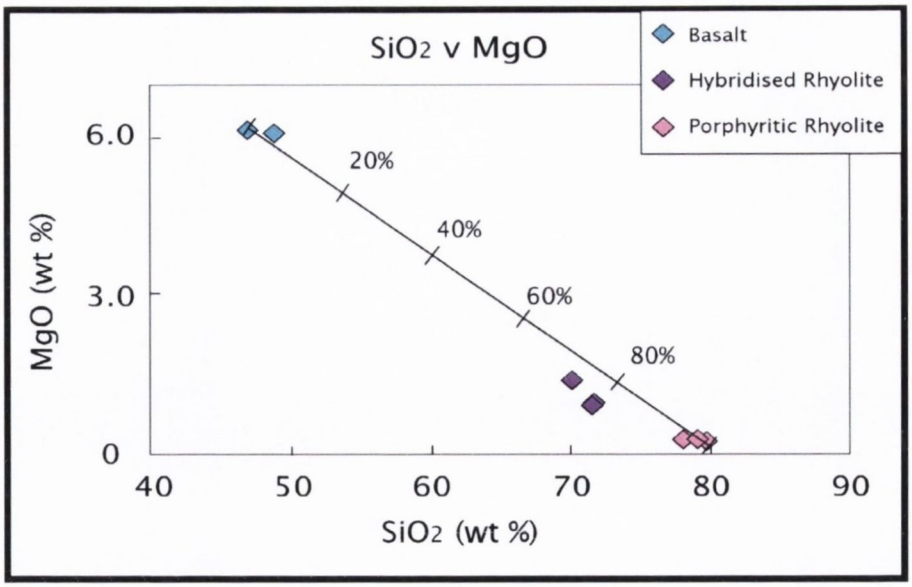


**Figure 8.23 Plot of $SiO_2$ vs. MgO, showing a linear relationship, indicating mixing of basalt and rhyolite to form a hybridised rhyolite.**

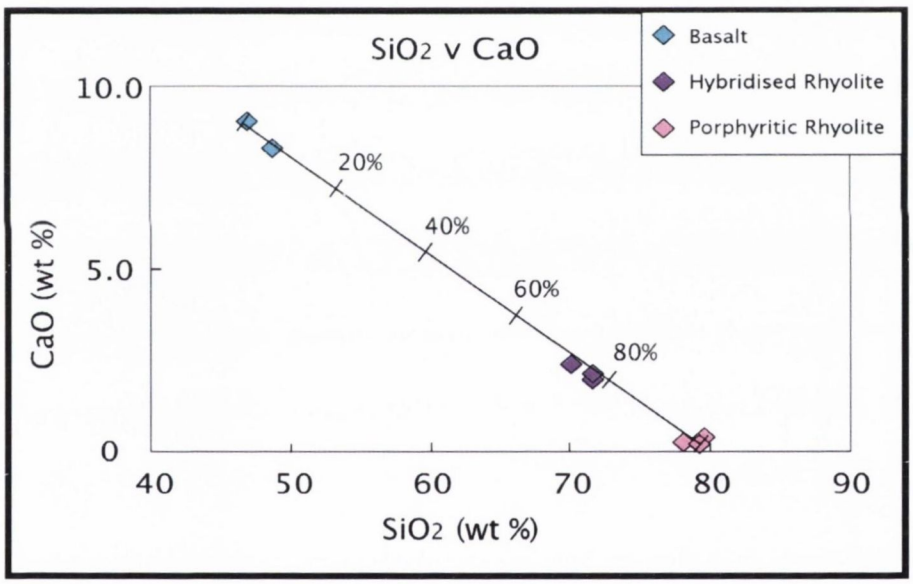


**Figure 8.24 plot of $SiO_2$ vs. CaO, again showing a linear relationship between samples, indicating magma mixing between basalt and rhyolite to form hybridised rhyolite. The mixing line indicates a mix of ~25:75.**

Only one element, $Na_2O$, does not show a clear mixing trend. In fact, the hybrid samples show higher $Na_2O$ concentrations than either of the end-member magmas, suggesting $Na_2O$ concentration has occurred (Figure 8.25). The hybridised

rhyolites are rich in large alkali feldspar phenocrysts, and are perhaps the source of elevated $Na_2O$ (Figure 8.35 and Figure 8.36)

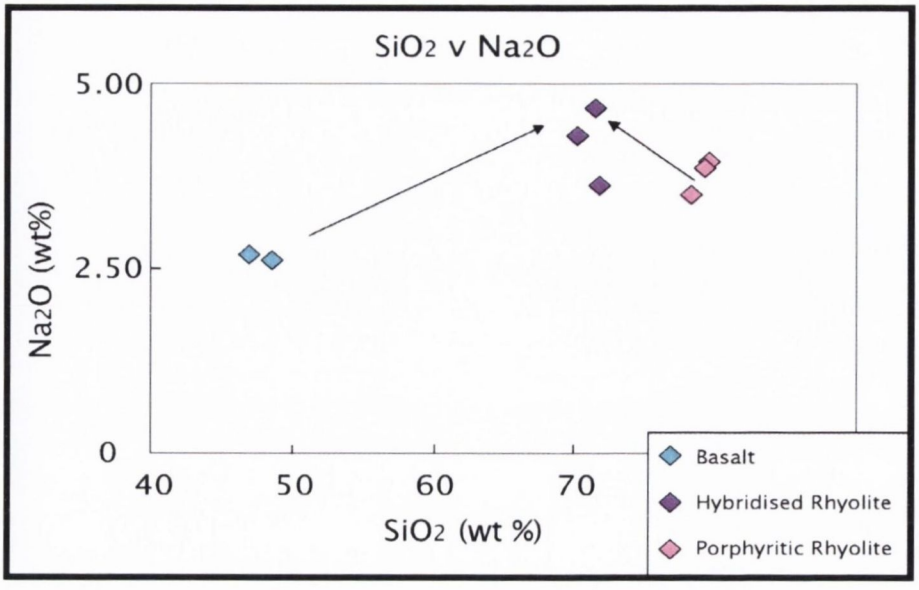


**Figure 8.25 Plot of $SiO_2$ v $Na_2O$. Note that the hybridised rhyolites are more enriched in $Na_2O$ than either the basalt or rhyolite.**

### *8.4.5.2. Trace element data*

Trace element data for the Glasdrumman cone-sheet are plotted against distance in Figure 8.26. Unlike the majority of the major elements, only Sr, Th, Zn and Rb show a simple mixing trend, with the dark, hybridised rhyolite lying between the basalt and rhyolite values (Figure 8.27).

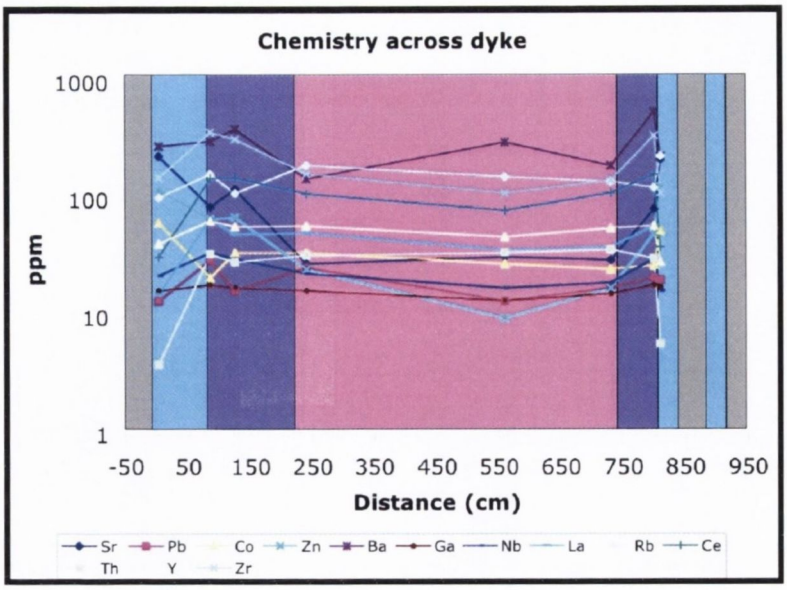


**Figure 8.26 Plot of trace element vs. distance across the dyke. Coloured stripes represent lithologies detailed in Table 8.1. For many of the trace elements the hybridised samples show enrichment/depletion beyond the limits of either of the end members (basalt/rhyolite).**

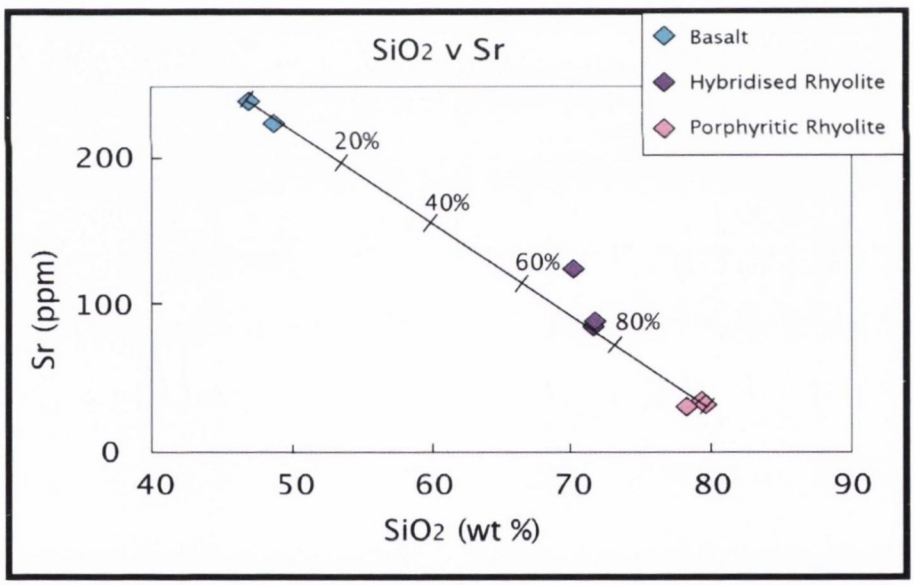


**Figure 8.27 Plot of $SiO_2$ vs. Sr, once again showing a linear relationship, explained by magma mixing. One hybrid sample is slightly enriched, representing the sample from the centre of the hybridised zone. Unlike many of the trace elements, Sr does not show higher concentrations within the hybridised zone than in either of the adjacent zones.**

The majority of trace elements, however, show an M-shaped geometry in Figure 8.26. In this case both the upper and lower dark hybridised rhyolites are more enriched in certain elements than either of the end members (Ba, Pb, Ce, La, Y, Ga, Zr and Nb) (Figure 8.28 and Figure 8.29). These enrichments suggest concentration of minerals within the margins of the dyke, such as alkali feldspar ($Na_2O$, Ba, Pb), allanite (Ce, La, Y) and zircon (Zr).

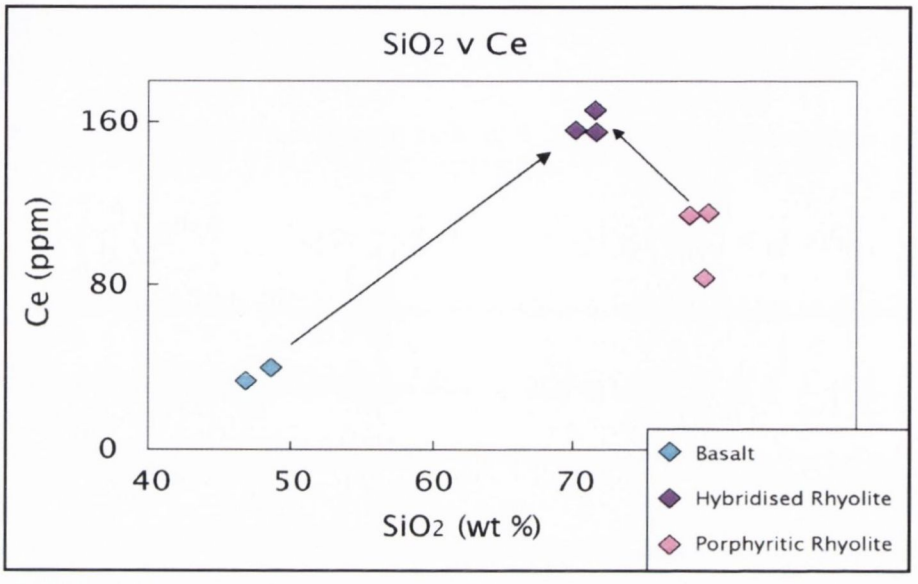


**Figure 8.28 Plot of $SiO_2$ vs. Ce, showing clearly that the hybridised rhyolite has higher Ce concentrations than either the basalt or the central rhyolite.**

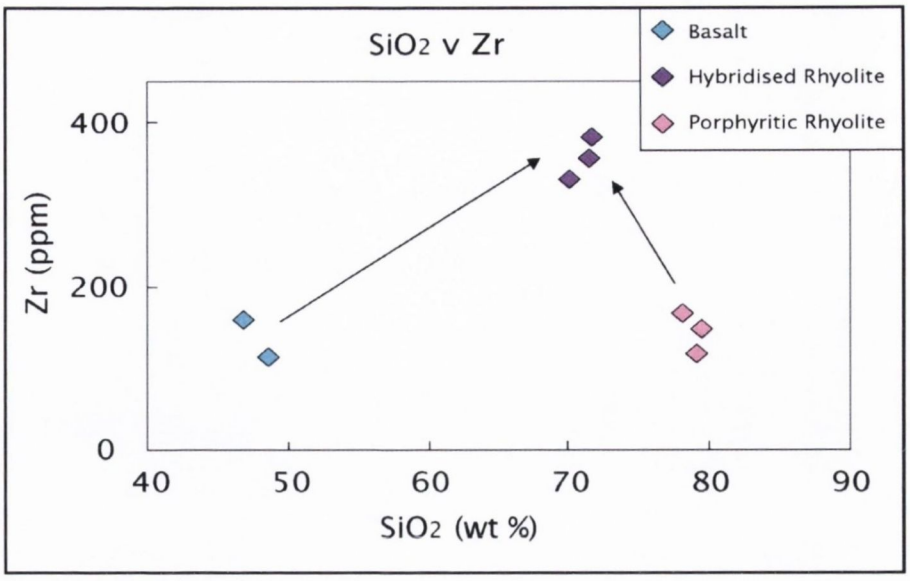


**Figure 8.29 Plot of $SiO_2$ vs. Zr. The hybridised rhyolites have Zr concentrations over twice that of either the basalt or rhyolite. Such high levels of zirconium suggest zircon was concentrated within the hybridised magma, perhaps due to flow differentiation, whereby denser phases were partitioned into the marginal zones of the dyke.**

#### *8.4.5.3. Least-squares mixing analysis*

Major-element data was modelled using least-squares mixing analysis to calculate the proportions of rhyolite and basalt in the dark rhyolite. $NaO_2$ was not used as it shows enrichment within the hybridised rhyolites (see sections 8.4.5.1). This analysis suggests the dark quartz-feldspar-phyric rhyolite at the lower margin is the product of a ~21:79 mix of basalt and quartz-feldspar-phyric rhyolite, whereas the upper margin hybrid is a ~25:75 mix. A similar ratio was calculated by Akiman (1971) (24:76) as part of a less detailed major and trace element study of the intrusion.



**Figure 8.30 Abundant mafic enclaves at the lower basalt/dark rhyolite contact (bottom right). The enclaves are irregular in shape and often contain xenocrysts of quartz and alkali feldspar (note the pen in the centre for scale).**

#### *8.4.5.4. Rare earth element data*

A plot of chondrite-normalised rare earth elements (Figure 8.31) once again shows the hybridised rhyolites to be enriched in rare earth elements when compared to the basalt and rhyolite end members. The green line in Figure 8.31 indicates the expected REE profile resulting from a 21:79 basalt: rhyolite mix. Both the rhyolite and the hybrid rhyolite are particularly enriched in the light rare earth elements and have strongly negative europium anomalies. The hybrid rhyolite shows a deeper europium trough than the rhyolite.

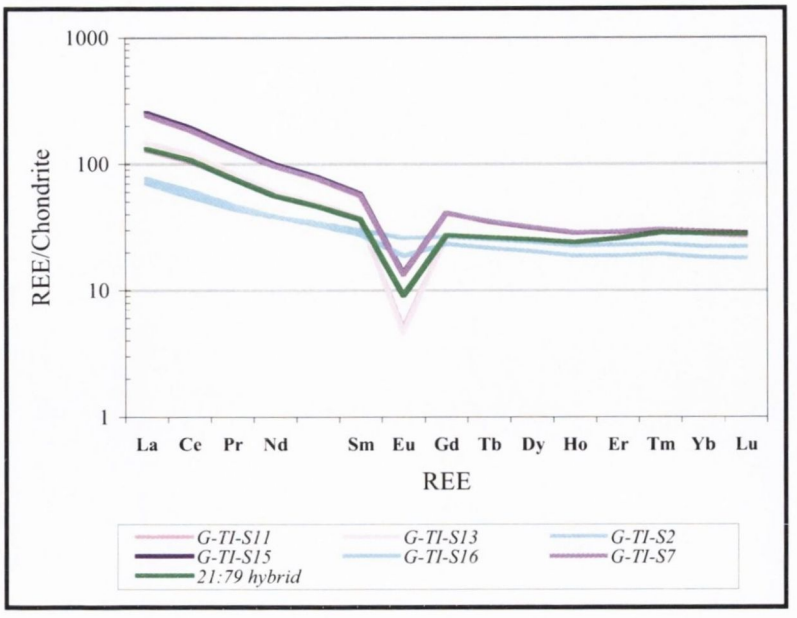


**Figure 8.31 Chondrite-normalised rare earth element concentrations for the rhyolite (pink), basalt (blue) and the hybridised rhyolite (purple). Once again the hybrid magma appears to be enriched in REEs compared to the parent end members. It is particularly enriched in the light rare earth elements (LREEs) compared to both the basalt and rhyolite. Typically a hybrid would be expected to have values intermediate to the two end members. Note the presence of a europium anomaly in both the hybrid and the rhyolite. The rhyolite trough appears more pronounced, however this is a function of the logarithmic scale on the y-axis of the graph.**

The depth of the europium trough was calculated as Eu*, whereby:

$$Eu^* \approx \frac{(Sm + Gd)}{2} - Eu_{measured}$$

Using this equation the europium anomaly for the rhyolite was calculated as being 27 ppm deep, while the expected (modelled) hybrid anomaly was 22 ppm deep, having been "filled in" by the Eu-rich basalt. The actual hybrid anomaly is 36 ppm deep, indicating not only has enrichment occurred, but the Eu anomaly has deepened relative to the adjacent REEs. While the hybrid magma must show overall

enrichment in minerals that contain the REEs, especially the LREE, the deeper europium trough means that Eu has also been relatively depleted. Europium is commonly accommodated within plagioclase and the depth of the anomaly may relate to the proportion of plagioclase within the magmas. While larger alkali feldspar may be concentrated in the dyke margins due to their size, and REE-rich minerals due to their density, smaller plagioclases may not have been concentrated to the same degree. This would result in a marginal hybrid with a bigger negative Eu anomaly than both the hypothesised mixed composition and the rhyolite.

### *8.4.6. Isotope geochemistry*

#### *8.4.6.1. Whole rock strontium isotope ratios*

Many of the Mourne granites exhibited high Rb/Sr ratios that resulted in large propagated errors on strontium isotope ratios (Section 8.3.5 and Figure 8.5). While all but one of the Glasdrumman rhyolites have Rb/Sr values of > 1, these ratios are not high enough to create significant uncertainties on the age-corrected data (Figure 8.32).

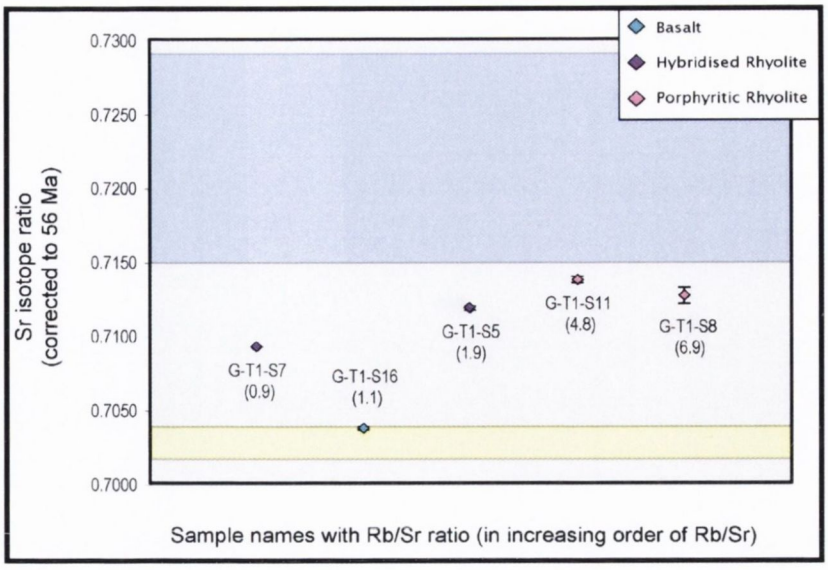


**Figure 8.32 Plot of age-corrected strontium isotope ratios for the Glasdrumman cone-sheet, showing the errors introduced by a 5% error on Rb/Sr ratio. Compare to Figure 8.5, where the propagated errors are much higher. Yellow box represents mantle values (Saunders *et al.*, 1988), blue box represents the range for the local Longford-Down crust.**

The data detailed in Figure 8.32 indicate the basalt lies within the mantle range, suggesting it has had limited interaction with the crust. The rhyolites, in contrast, show isotope ratios skewed towards the local Longford-Down crust, suggesting they have undergone significant crustal contamination.

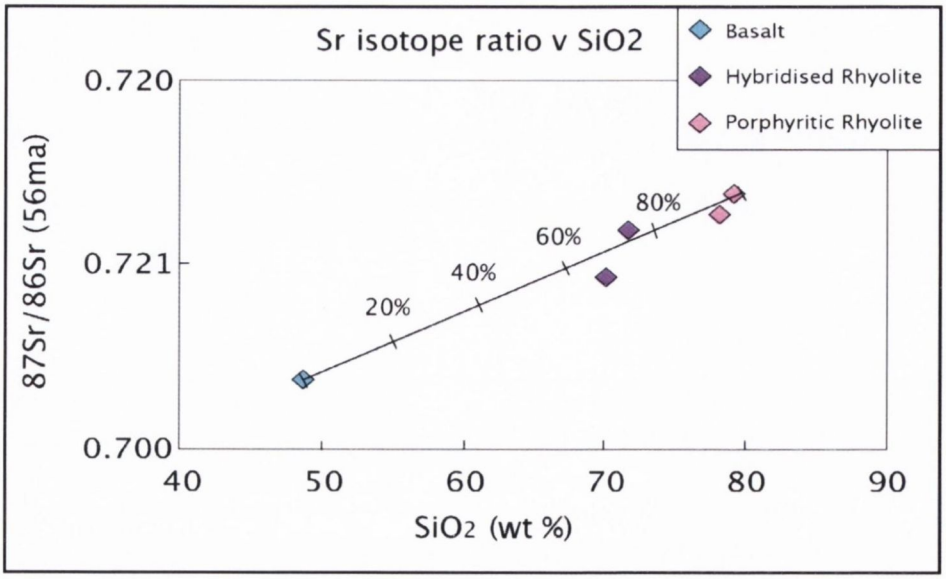


**Figure 8.33 Plot of strontium isotope ratio versus silica. Note the mixing ratios calculated in section 8.4.5.3 are similar, indicating that the hybrid rhyolite is a mix of ~ 75:25 rhyolite to basalt. Also note that the higher silica rhyolites have higher (more radiogenic) strontium ratios than the lower silica basalts.**

When strontium isotope ratio is plotted against silica (Figure 8.33) it is clear the higher silica rhyolites have more radiogenic isotope ratios than the lower silica basalts. The data in Figure 8.32 show that the rhyolites contain a significant crustal component; this plot suggests that contamination may have occurred by the process of assimilation during fractional crystallisation (AFC), whereby the most evolved samples are those with the most radiogenic strontium ratios.

*8.4.6.2. Whole rock lead isotope ratios*

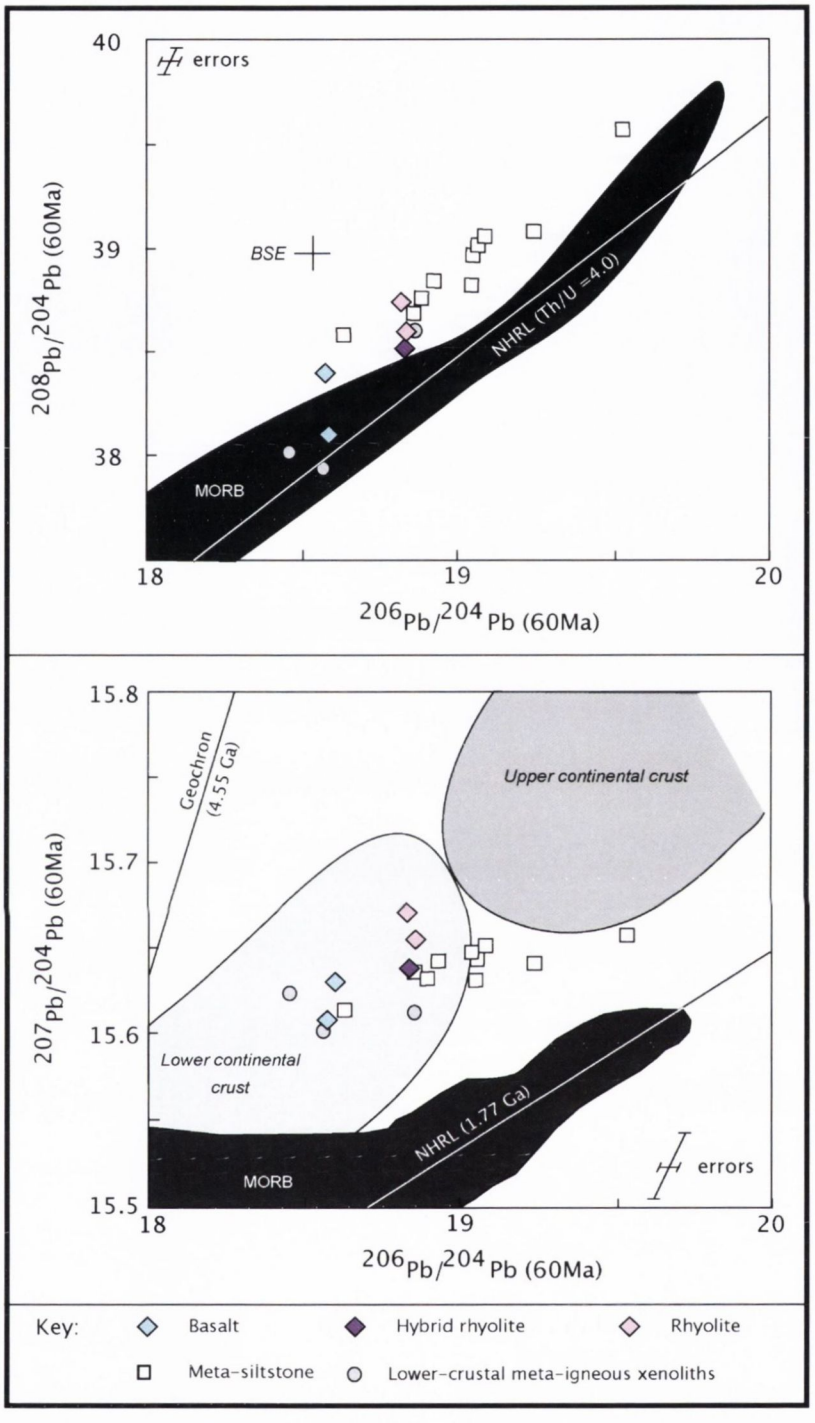


**Figure 8.34 Pb isotope plots showing Glasdrumman samples and local crust. All samples plot towards the local Longford-Down crust. BSE values from Allegre et al (1988). MORB and upper and lower crustal fields from Figure 6.11 of Rollinson (1993)**

The rhyolitic samples lie within the lead isotope ratio range of the least radiogenic Longford-Down crustal end-members (Figure 8.34). This may indicate that these felsic magmas are crustal melts. However they may also be magmas contaminated by a more radiogenic crustal samples, or indeed radiogenic partial melts of the Longford-Down metasediments. This mode of contamination has been seen at the nearby Carlingford Igneous Centre (see sections 6.9 and 6.12).

A partial melt can be more radiogenic than the whole-rock protolith as the first phases to melt (those forming the partial melt) can contain higher proportions of the parent isotopes than the protolith as a whole. When partial melting occurs, the various isotopic systems can also become decoupled, depending on which isotopes the melted phases contain. This means one system may suggest large amounts of contamination, while others may not. Conversely, a complete crustal melt would be expected to have the same isotopic signature as the crust, for all isotope systems.

Therefore, assimilation during fractional crystallisation of a radiogenic partial melt is supported by strontium isotope ratios, as the rhyolite values do not fall within the crustal range for strontium isotopes, but do for lead isotopes (Figure 8.33).

When $^{208}Pb/^{204}Pb$ and $^{207}Pb/^{204}Pb$ are plotted against $^{206}Pb/^{204}Pb$, the Glasdrumman samples form a clear trend away from the mantle towards the crust (Figure 8.34). The lower crustal xenolith samples, denoted as grey circles in Figure 8.34, are not sufficiently radiogenic to have had a recognisable influence.

On a plot of $^{207}Pb/^{204}Pb$ v $^{206}Pb/^{204}Pb$ the basaltic samples lie outside the mantle field, indicating they have had significant crustal interaction, despite this influence not being so apparent in $^{208}Pb/^{204}Pb$ and $^{87}Sr/^{86}Sr$ plots (Figure 8.32, Figure 8.34). This is likely due to assimilation of a $^{207}Pb/^{204}Pb$ rich contaminant that did not

have a significant $^{208}Pb/^{204}Pb$ or $^{87}Sr/^{86}Sr$ component. The lack of an obviously radiogenic strontium component as seen in the rhyolites, suggests contamination by a metasediment that has already lost an initial mica-rich fraction, and Pb-rich, Rb-poor K-feldspar and epidote are now contributing to partial melt formation. This is feasible as the crust in the area has been repeatedly intruded and had most likely contributed significant volumes of partial melt to the formation of granites G1-G3 (Section 8.3.5). Basalt, being significantly hotter than granite, could partially melt this crustal restite, melting components the granite could not.

### *8.4.7. Discussion*

#### *8.4.7.1. Major and trace element data*

Major and trace element data indicate magma mixing has occurred, forming the dark rhyolite hybrid magma (Sections 8.4.5.1 and 8.4.5.2). Least-squares mixing analyses demonstrate the lower margin is the product of a ~21:79 mix of basalt and the central quartz-feldspar-phyric rhyolite, whereas the upper margin hybrid is a ~25:75 mix (Section 8.4.5.3).

The upper hybrid has a higher proportion of basalt; this is likely to be the result of more efficient mixing at the top of the intrusion. The upper hybrid clearly contains a lower concentration of mafic enclaves (Figure 8.8) and the basalt has been incorporated fully to form a more homogenised mixed (rather than mingled) magma. This may be due to the unstable density structure of basalt overlying rhyolite. In this situation the basalt would sink downwards, getting mixed with the rhyolite to form a hybrid magma (see also Snyder *et al.*, 1997).

In the case of the lower margin of the sheet, rhyolite overlies basalt. This is a more stable density stratification and the basalt and rhyolite could flow

independently with less interaction. In fact, the lower margin basalts have a different spatial relationship with the rhyolite and show large amounts of wisps and blobs incorporated into the rhyolite (Figure 8.8, Figure 8.30). This is most likely because the rhyolite is skimming off basalt as it flows by, mixing and mingling to form the lower dark rhyolite hybrid.

Harker plots show enrichment of several elements ($Na_2O$, Ba, Pb, Ce, La, Y and Zr) within the hybrid member of the dyke, showing higher concentrations than either end-member (Section 8.4.5.2). These data suggest the accumulation of minerals such as alkali feldspar ($Na_2O$, Ba, Pb), allanite (Ce, La, Y) and zircon (Zr) in the hybridised marginal zone of the quartz and feldspar-phyric rhyolite member. This may be due to flow differentiation, whereby large and/or dense phenocryst phases have concentrated near the intrusion's edge. This correlates well with field observations where larger feldspars (> 2 cm) are certainly concentrated in these zones (Figure 8.35 and Figure 8.36).



**Figure 8.35 Close-up of the margin between the marginal basalt and the dark rhyolite, showing a large concentration of phenocrysts at the interface.**



**Figure 8.36 Concentration of phenocrysts at the interface between the basalt and dark rhyolite at the margin of the intrusion. Once again, note the clear boundary, but the lack of a chilled margin, indicating the composite nature of the intrusion.**

### *8.4.7.2. Strontium and lead isotope ratio data*

Strontium and lead isotope ratios indicate a strong crustal influence on the magmas of the Glasdrumman cone-sheet. Even the least evolved members of the suite, the basalts, show significant contamination on a plot of $^{207}Pb/^{204}Pb$ v $^{206}Pb/^{204}Pb$ (see sections 8.4.6.1 and 8.4.6.2).

The rhyolites show evidence of contamination by the fusible Rb-rich components (micas) of the Longford-Down metasediments. This partial melt appears to have been incorporated by assimilation during fractional crystallisation. The $^{207}Pb/^{204}Pb$ signature of the Glasdrumman basalts suggests they too have been contaminated by a partial melt, but one of an already depleted end member (i.e. one that had already lost its mica fraction). This indicates late-stage contamination by a crust that has already contributed significantly to contamination of the Glasdrumman rhyolites or indeed the Mourne Granites (G1-G3).

The heat source driving the magmatic system and crustal assimilation may be a large body of mafic magma beneath the high-level granitic bodies. Its existence is hinted at by the cumulate xenoliths within the Dunmore Head dykes (see section 8.2.2.1). Geophysical surveys of Bouguer gravity anomaly data (Figure 8.37) confirm the presence of a large body of mafic magma off the coast of northeast Ireland, approximately 10km thick and at a depth of approximately 2-3km, (see Reay (2004) for further details on gravity surveys of Northern Ireland).

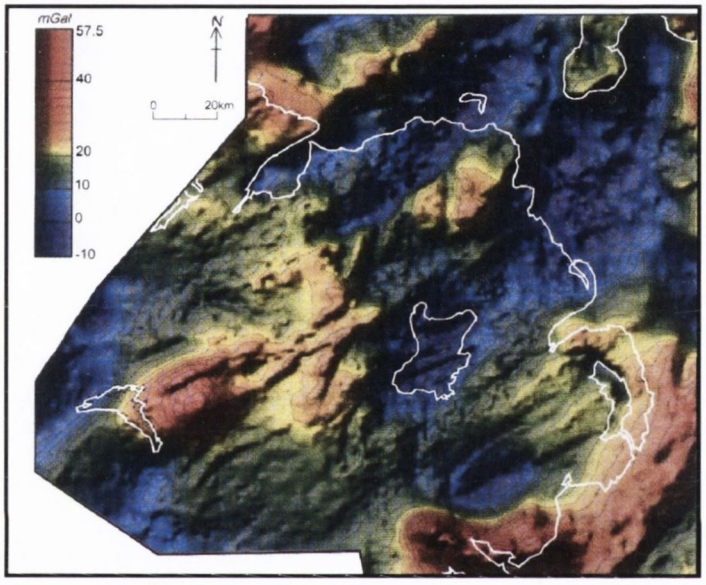


**Figure 8.37 Bouguer gravity anomaly map for Northern Ireland. Note the gravity high off the eastern coast, representing a large (~10km thick) mafic body. This body may have been the magma reservoir for magmatism across the region, including the Mourne, Carlingford and Slieve Gullion igneous centres. From Figure 19.2 in Reay (2004).**

### *8.4.8. Conclusions*

Magmatism at the Mourne intrusive centre may have been fed from a large body of mafic magma deep beneath the centre. This magma would have been the source of the parental magmas for the main granites (G1-G5) and the Glasdrumman intrusion, and would have provided the heat to drive crustal melting and assimilation.

Granites G2-G5 are all highly fractionated and did not yield usable isotopic data for quantitative analysis of crustal influences due to the large errors on age corrected values introduced by high Rb/Sr ratios.

The Glasdrumman cone-sheet yielded much more favourable Rb/Sr ratios for analysis of crustal contamination. It is comprised of a central rhyolite member, flanked by xenocrystic basalt. These magmas have interacted with partial melts of the crust through which they have passed, the meta-sediments of the Longford-Down inlier. The rhyolite was contaminated by a partial melt of the micaceous components of these metasediments, while the basalt appears to have been contaminated by a partial melt of the subsequent restite, indicating late-stage interaction with the crust. The two magmas were emplaced together to form a composite intrusion. On intrusion, they mixed and mingled to form an enclave-bearing hybrid rhyolite with a dark groundmass. Mixing was more complete at the upper margin and upper hybrid shows a mixing ratio of 25:75 (basalt to rhyolite). The lower margin shows more evidence of mingling. The lower hybrid contains frequent mafic enclaves and the shows a mixing ratio of 21:79.

Flow differentiation within the sheet resulted in the concentration of dense REE-rich minerals and large K-feldspar phenocrysts at the edge of the rhyolite, within the hybrid. The conduit narrowed in thickness to the north and flow became turbulent as large volumes of magma flowed through a smaller space, breaking down the zoned basalt and rhyolite into a single commingled unit, with a rhyolitic matrix and ubiquitous mafic enclaves.

# 9. SLIEVE GULLION

*A study of a new exposure of a caldera fault segment at the Slieve Gullion Igneous Centre and its implications for the emplacement of the early ring-complex.*

*This chapter forms part of a study completed with Prof. V.R. Troll (TCD, University of Uppsala), Dr. D.M. Chew (TCD) and Dr. C.H. Emeleus (University of Durham),*

## 9.1. Abstract

A contact zone between porphyritic microgranite of the early ring-complex of the Paleocene Slieve Gullion igneous centre and Lower Palaeozoic metasedimentary rocks of the Longford-Down inlier was exposed along a section excavated during construction of the new M1 motorway. The outcrop displays a thin sliver of Longford-Down metasediment in contact with porphyritic microgranite in a steep, and locally intensely crushed, contact zone that dips away from the ring-complex. This outcrop pattern is reminiscent of a "caldera-superfault" (cf Kokelaar, 2007). Given the recent discussion on sheet versus ring-dyke emplacement of the early ring-complex at Slieve Gullion (Stevenson *et al.*, 2008), this new evidence argues in favour of the traditional ring-dyke model with magma ascending along an active ring fracture associated with caldera subsidence.

## 9.2. Introduction

We report herein on a new outcrop section along the M1 motorway about 8 km north of Dundalk (Loc. IJ 07981 14632), at Ravensdale (Figure 9.1). The outcrop section was exposed in May 2007 and was accessible prior to opening of the motorway (August 2nd, 2007) for a limited period of time only. It is unclear at the time of writing if the outcrop will remain exposed, but there is a possibility it may be covered by steel mesh to increase slope stability at a later date (D. Murphy, *pers. comm.*, www.siac.ie). The section was inspected on the 24th and 27th of June and on the 16th of July 2007.

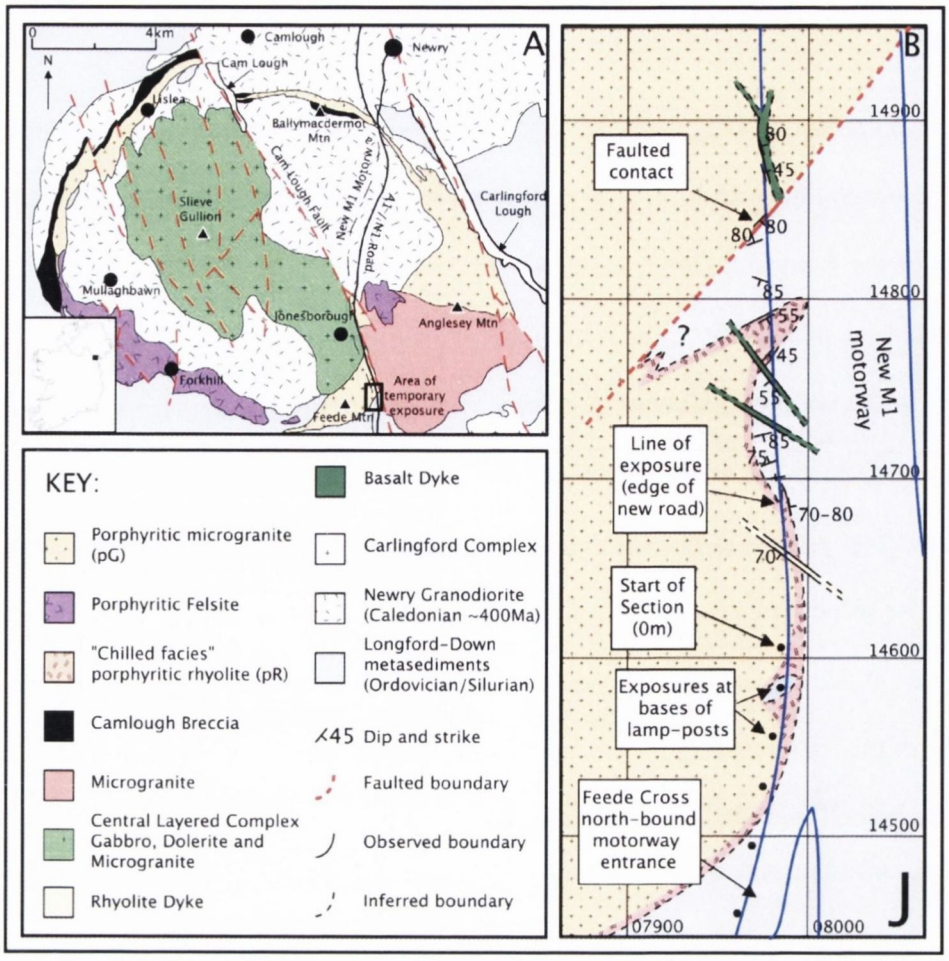


**Figure 9.1 Maps of the Slieve Gullion Igneous Centre. Fig 1a: Generalised Geology of the Slieve Gullion Centre after Cooper and Johnston, (2004), showing region of new exposure at Feede Mountain (black box). Fig 1b: Detailed map of the Feede Mountain exposure**

The outcrop extends for approximately 300 m on a 6-7 m high, steeply inclined (70°) rock-face orientated almost perfectly N-S. A schematic section profile is illustrated in Figure 9.2. At the southern end of this section, a thick body of porphyritic, feldspar-rich, microgranite crops out. It closely resembles the "Porphyritic Granophyre" of the early ring-dyke of Richey and Thomas (1932) and Emeleus (1962), but is much fresher in appearance. Additionally, zoned phenocrysts are seen in both Richey's "Porphyritic Microgranite" (see plate 34B and accompanying text in Emeleus (1957)) and the porphyritic microgranite exposed

here. A contact zone between Longford-Down metasediment and microgranite is exposed further north along the section and is locally intensely crushed. This damage zone extends for more than 2 m into both lithologies, indicating a major fault at this junction. This discovery is significant for the current discussion on the emplacement of the early Slieve Gullion ring-complex, where the classic ring-dyke interpretation (Richey and Thomas, 1932; Emeleus, 1962; McDonnell *et al.*, 2004) is challenged by a model based on a combination of anisotropy of magnetic susceptibility (AMS) measurements and field data (Stevenson *et al.*, 2008). These authors suggest the early ring-complex represents a flat-lying, laterally extensive sheet, which was subsequently domed by the emplacement of the central layered intrusion resulting in a ring-like outcrop pattern.

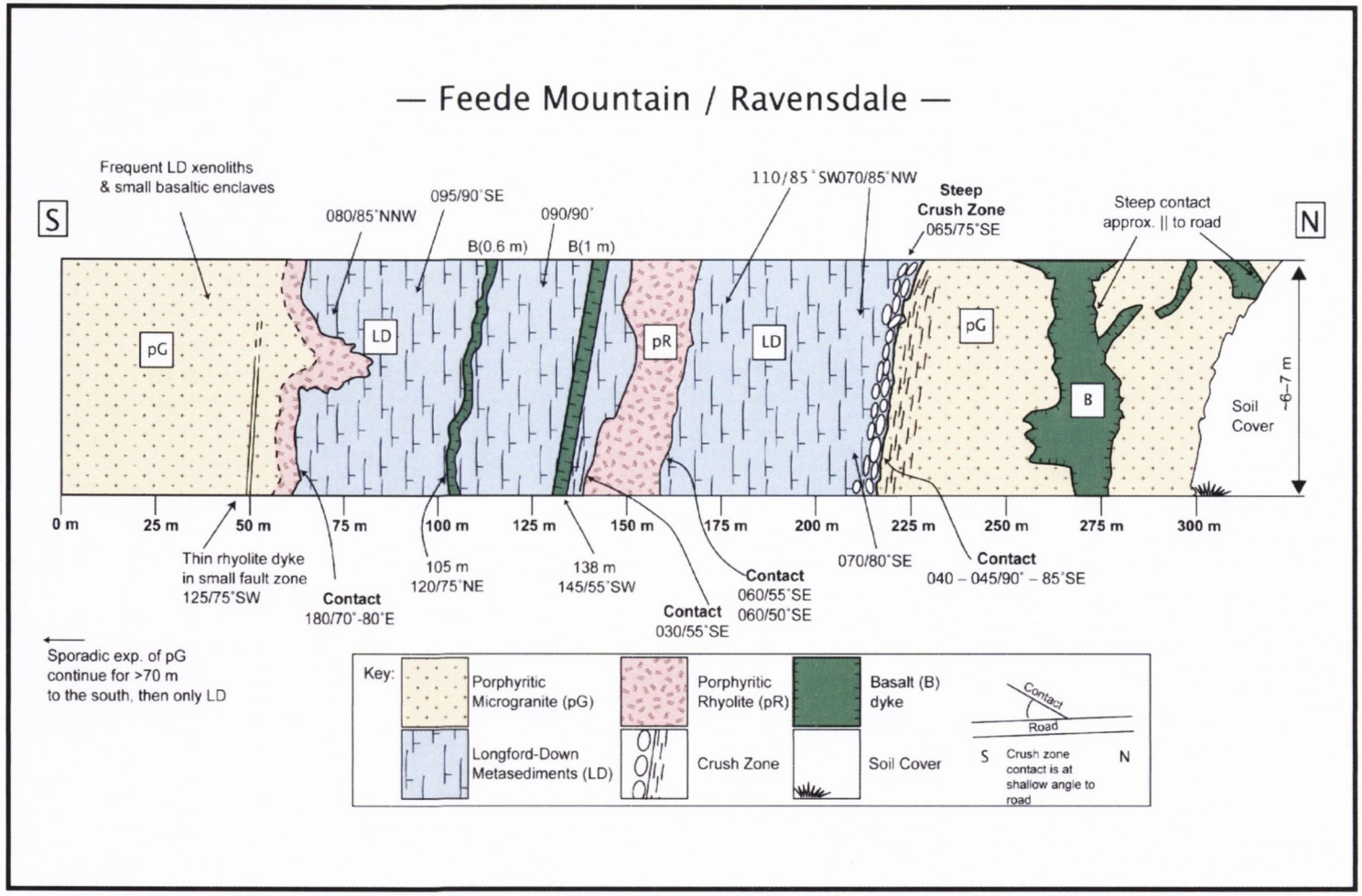


**Figure 9.2 Log of the newly exposed road section at Feede Mountain**

## 9.3. Description of exposure

The engineering staff of Siac (www.siac.ie) informed us that explosives were used at a minimum of 2 m away from the currently exposed rock face. More than twenty oriented and non-oriented samples were taken along the section and a representative set of rocks has been deposited in the collection of the Geological Museum at Trinity College Dublin (Appendix 9.1).

**Start of section** (IJ 07981 14632); **0 m.** Pinkish-grey porphyritic microgranite (pG) contains potassium feldspar and plagioclase phenocrysts of 3 mm - 15 mm. The feldspars show strong zonation, often with pink potassium feldspar cores and white plagioclase rims or vice versa. Similarly zoned feldspars are commonly found elsewhere in the porphyritic microgranite ring-dyke (see Plate 34B in Emeleus (1957) and Troll et al (2005)). Dark green and grey mylonitic tuffisite[1] bands are present, and small mafic enclaves of up to 5 cm across, often with embayed, lobate contacts, occur. Phenocrysts are less obvious on fresh surfaces, but are very prominent on weathered and/or fracture surfaces (Figure 9.3, Figure 9.4, Figure 9.5).

[1] Tuffisite is defined herein as a rock resulting from fracturing of viscous magma with material being transported and deposited by a migrating fluid phase, such as magmatic volatiles.



**Figure 9.3 Mafic enclaves in porphyritic microgranite (pG). Coin is 2.5 cm across Inset: Mafic enclave with microgranite xenocryst trace (right) and zoned feldspar in microgranite (left). Coin is 1.7 cm across.**

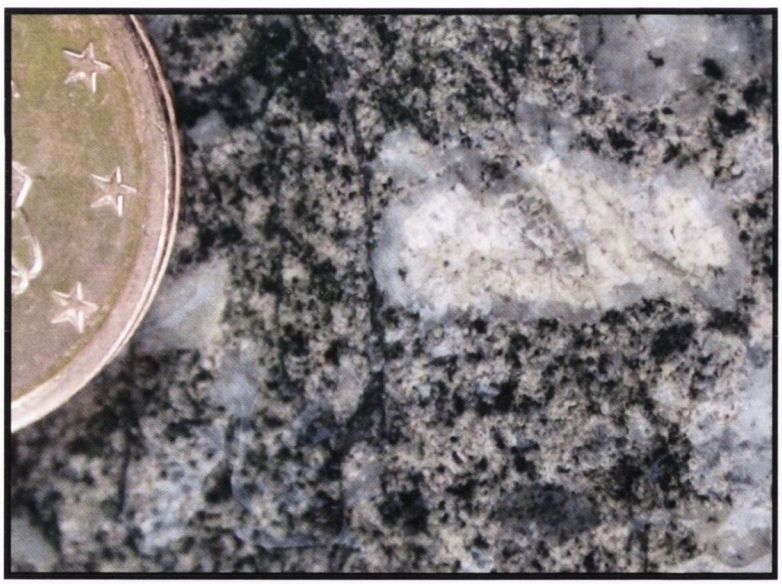

**Figure 9.4 K-feldspar with plagioclase rim (rapakivi texture) in porphyritic microgranite (pG). Coin is 1.7 cm across.**

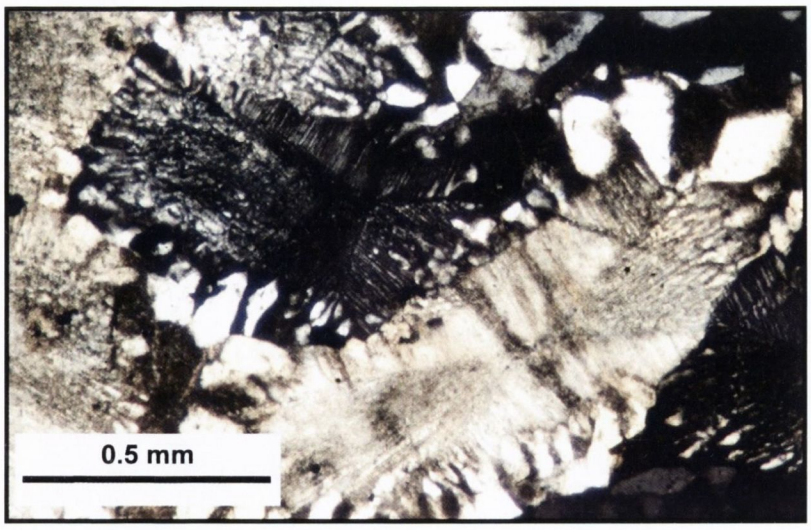


**Figure 9.5 Porphyritic microgranite (pG) with granophyric texture at start of section (thin section in XPL).**

South of "0 m" on the logged section, small exposures were revealed at the bases of six lampposts, which were subsequently covered by topsoil. Lampposts #1 (at "0 m"), #3 and #4 all exhibited porphyritic microgranite, while lampposts #2, 5 and 6 south of 0 m exposed Longford-Down metasedimentary rock. The distance between the lampposts is approximately 35 m.

**At 21 m,** the porphyritic microgranite (pG) is slightly darker in appearance and contains a higher proportion of plagioclase phenocrysts together with small mafic enclaves. Xenoliths of metasedimentary rock are also present, ranging in size from 1 - 10 cm.

**At 35 m**, outcrop of porphyritic microgranite (pG) with elongate mafic enclaves and occasional tuffisite bands continues. Small xenoliths (1 - 3 cm) of Newry Granodiorite are common, with some xenoliths displaying with pink potassium-feldspar or white plagioclase rims, (e.g. Figure 9.6).



**Figure 9.6 Porphyritic rhyolite (pR) showing zoned feldspars (at pencil tip) and Newry Granodiorite fragments (e.g. centre right) with plagioclase overgrowths.**

**At 50 m** (IJ 07976 14686) a thin rhyolite dyke with orientation 125/075° SW cuts the porphyritic microgranite (Figure 9.2). The porphyritic microgranite once again has potassium-feldspar cores with plagioclase rims, but the reverse of this zoning pattern also occurs. The phenocrysts are up to 15 mm across. Zoning is visible with the naked eye and the modal content of phenocrysts is between 30-40%. No obvious crystal alignment was detected. Tuffisite veins are present again, as are small basaltic enclaves up to several cm in length (Figure 9.7). Crystal transfer, whereby phenocrysts from microgranite have migrated into the mafic enclaves, is frequently observed.

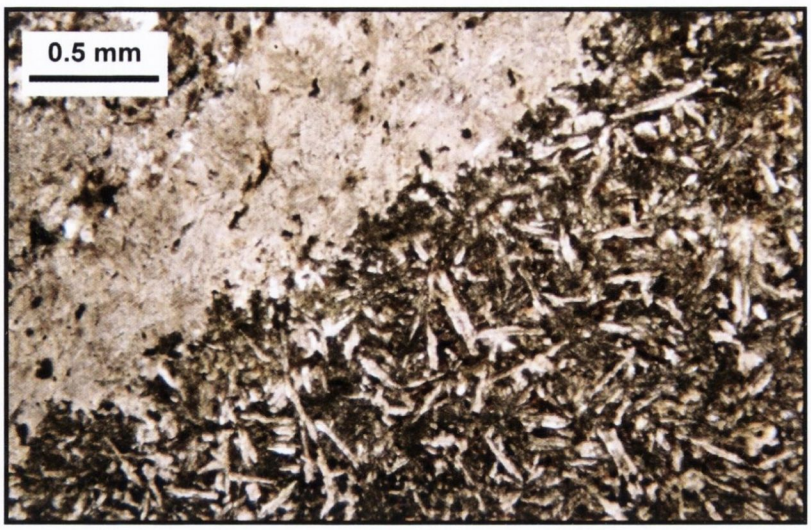


**Figure 9.7 Mafic enclave in porphyritic microgranite (thin section in PPL).**

**At 63 m** (J07986 14688), the first major contact of granophyre with Longford-Down metasedimentary rock occurs (Figure 9.2). To the south of the contact the phenocryst-rich, pink potassium feldspar and white plagioclase-bearing microgranite (pG), with phenocrysts up to 15 mm in size is encountered. Both zoning types are present in the feldspars and no clear alignment is obvious. At, and near, the contact the groundmass of the microgranite becomes much more fine-grained, forming a chilled marginal facies of porphyritic rhyolite (pR). Abundant sub-angular fragments of metasediment are observed in the porphyritic microgranite. Locally, intense tuffisite veining occurs within the microgranite, and especially in the marginal rhyolite. The northern side of the contact shows Longford-Down metasediment with bedding orientation 080/90° to 85° NNW. The overall contact dips steeply (70° - 80°) to the east and strikes approximately parallel to the road (north-south), thus implying that the microgranite is actually lying behind a thin veneer of Longford-Down metasediment. A finger (protrusion) of microgranite (*ca.* 2 m wide) breaks through this screen of Longford-Down metasediment about 3 m above the road (Figure 9.2, Figure 9.8).

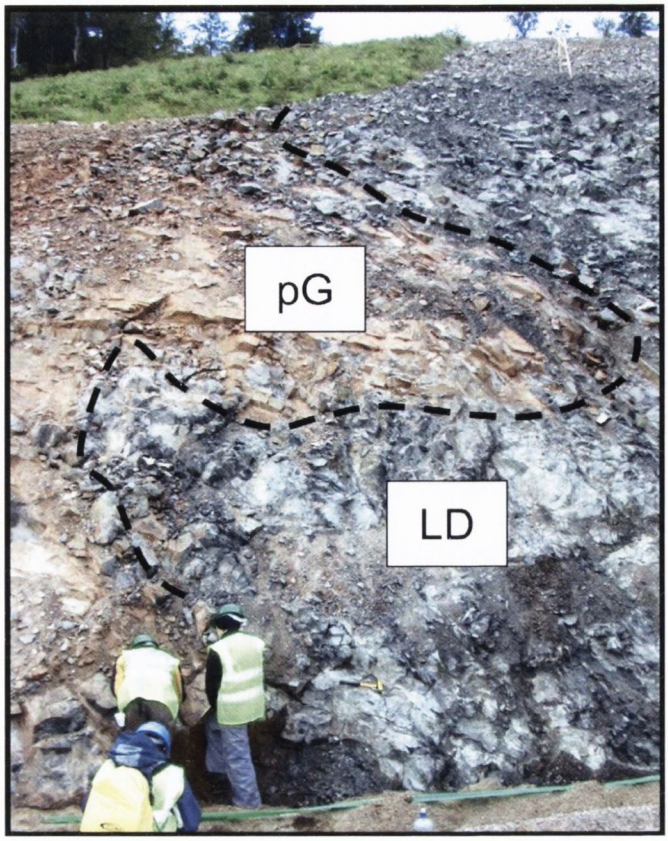


**Figure 9.8 Porphyritic microgranite (pG) finger (protrusion) in Longford-Down metasediments at 63 m.**

**At 72 m** (J 07968 14699), the strike of the Longford-Down metasediments is 070/75° NW. The bedding is locally highly irregular, but generally steep in dip. The metasedimentary rocks appear highly hornfelsed, showing intense green and black colouration, representing mineralogies rich in diopside and biotite, respectively (Figure 9.9, Figure 9.10)



**Figure 9.9 Hornfelsed Longford-Down metasediments striking at approximately 90° to the road.**

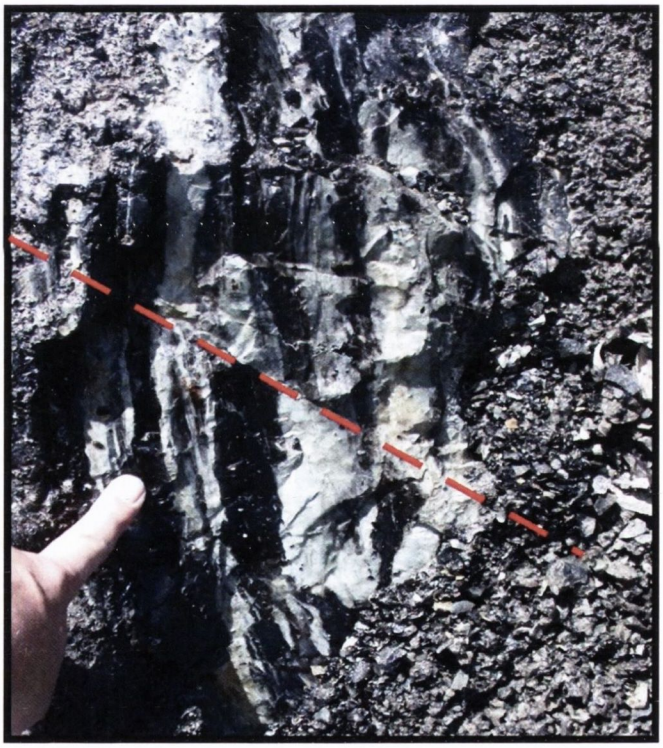

**Figure 9.10 Micro-faulting in metasediments. Note the strong colouration in the bands, indicating high-temperature overprint (hornfelsing).**

**At 80 m** the overall orientation of bedding in metasediment is approximately 100/90°, and **at 90 m** (IJ07974 14726), the "stripy" green and black metasediment is of similar orientation (095/90°). However, irregular bands with microfractures locally exhibit offsets of up to 10 cm (Figure 9.10).

**At 100 m** (J07974 14740), the metasediment strikes 080/85-90° SE, consistent with the regional trend of the Longford-Down metasediments of about 060 – 070 (see Anderson, 2004).

**At 105 m**, a thin, near vertical but sinuous, basaltic dyke (0.6 m wide) intrudes Longford-Down metasediment (Figure 9.2). It trends approximately 120 with local dips of 75° NE. The dyke is feldspar-phyric with phenocryst-poor margins. The baked country rock shows minor folding, but the general trend remains consistent.

**At 136 m** (J07977 14763), the metasediments strike approximately 090/90° - 80° SE. **At 138 m**, another small basaltic dyke (about 1 m wide) cuts through the metasediments and is inclined 145/55° SW.

**At 145 m** (J07969 14780), a contact is exposed between porphyritic rhyolite (pR on Figure 9.2), and a veneer of metasediment higher up on the rock face. The porphyritic rhyolite is again characterised by a significantly finer-grained groundmass than the porphyritic microgranite. The contact is locally irregular, but has an overall orientation striking approximately 030-025 and dipping 55° SE (Figure 9.11).

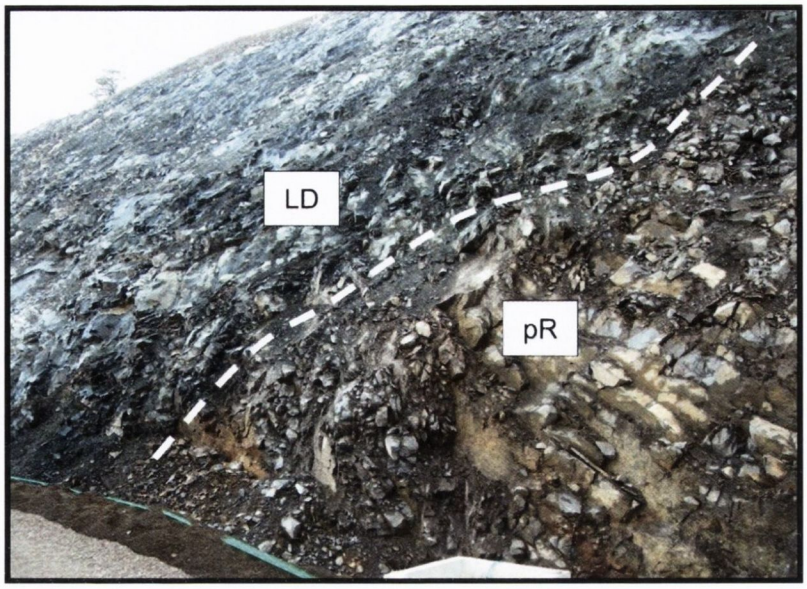


**Figure 9.11 Southern contact between Longford-Down (LD) metasediments and porphyritic rhyolite (pR) apophysis at 145 m.**

**At 155 m** (IJ07968 14786), the porphyritic rhyolite (pR) still shows a finer-grained groundmass than the porphyritic microgranite (pG) first encountered at around 0 m. However, similar mafic enclaves occur and the zoning is identical in the large phenocrysts of both the rhyolite and microgranite, suggesting that the two rock types are closely related (Figure 9.3, Figure 9.4, Figure 9.5, Figure 9.6, Figure 9.12, Figure 9.13). This hypothesis is supported by the similarity to the marginal fine-grained facies seen at 63 m, suggesting that the porphyritic rhyolite (pR) lithology here at 155 m represents a narrow microgranite apophysis that cooled quickly against the local country rock.



**Figure 9.12 Zoned feldspars and xenocryst-bearing enclaves in porphyritic rhyolite (pR) at ~150 m. Coin is 1.7 cm across.**

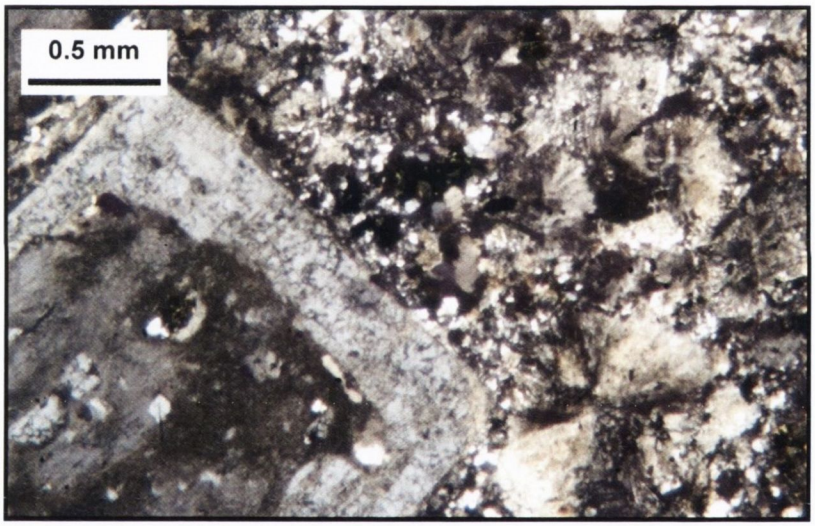


**Figure 9.13 Porphyritic rhyolite (pR) at offshoot (145 m) (thin section in XPL). Compare groundmass to that of the porphyritic microgranite (Figure 9.5).**

**At 163 m** (J07961 14809) another, locally irregular, contact of overall orientation 060/55° SE separates porphyritic rhyolite (pR) from the metasediments (Figure 9.14). This geometry supports the hypothesis that the finer-grained porphyritic rhyolite from 145 - 163 m is indeed an offshoot, or apophysis, of the

main body and is probably a chilled facies of the microgranite. The bedding in the Longford-Down metasediments on the northern side of this contact is 110/85° SW.

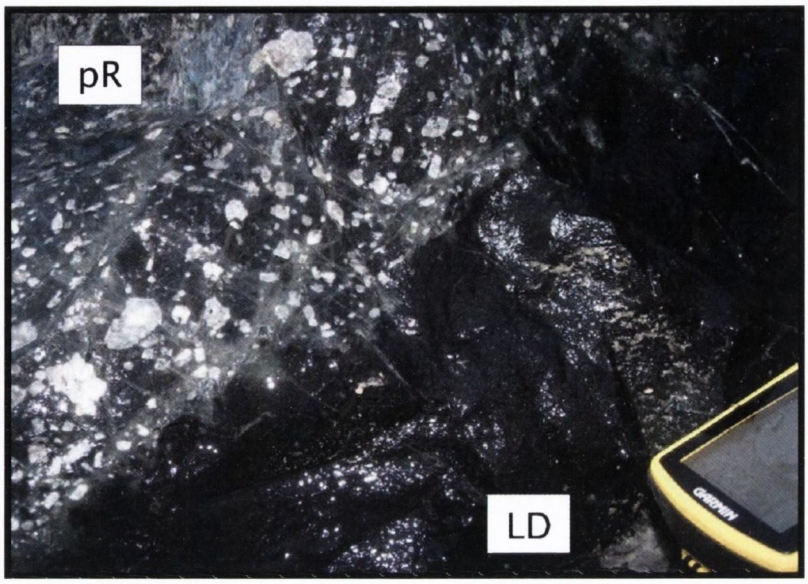


**Figure 9.14 Northern contact of porphyritic rhyolite (pR) apophysis and Longford-Down metasediment at 163 m. GPS instrument for scale.**

**At 200 m** (J07967 14836) metasediments show bedding orientations of 070/80° NW and at **220 m** (J07965 14849), bedding in the metasediments is 070/90°.

**At 218 m** (J07967 14850), a major contact is exposed between Longford-Down metasediments and porphyritic microgranite (pG), with an overall orientation of approximately 045/80° - 85° SE (Figure 9.2**,** Figure 9.15**)**. Extensive brecciation occurs in the metasediments close to this contact (Figure 9.16).

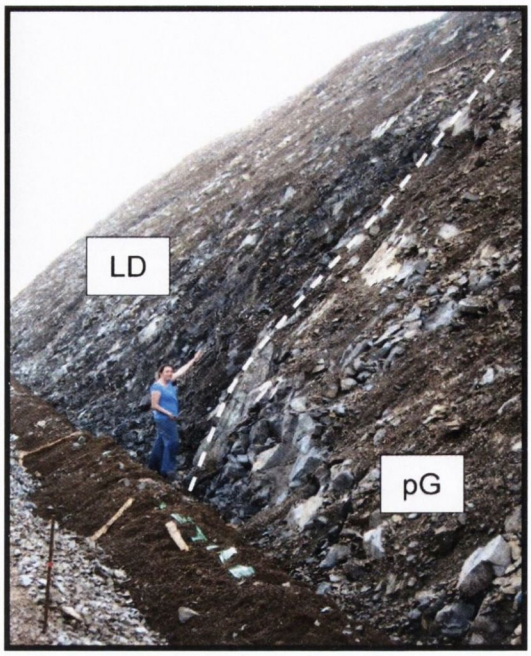


**Figure 9.15 Main contact (at 225 m) between Longford-Down metasediments (LD) and porphyritic microgranite (pG), which is steeply inclined and at its base dips at ~80° to the SE.**

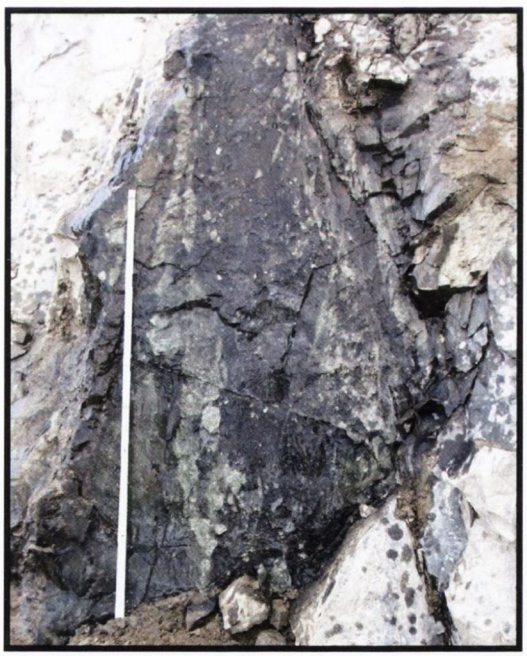

**Figure 9.16 Crushed zone in Longford-Down metasediments at the main contact at 225 m. Metre stick for scale.**

Within this intense brecciation zone, a mixture of metasediment and igneous fragments occurs locally (Figure 9.16, Figure 9.17, Figure 9.18, Figure 9.19). The igneous clasts are frequently aligned in the crush zone in a plane that strikes approximately 055-065 and dips from 90°-75° SE, thus broadly parallel to the contact in the core of the crush zone.



**Figure 9.17 Crushed zone in Longford-Down metasediments at 225 m, ca 1 m south of contact (in "damage zone"). Note the presence of angular and strung-out igneous clasts. Coin is 2.5 cm across.**

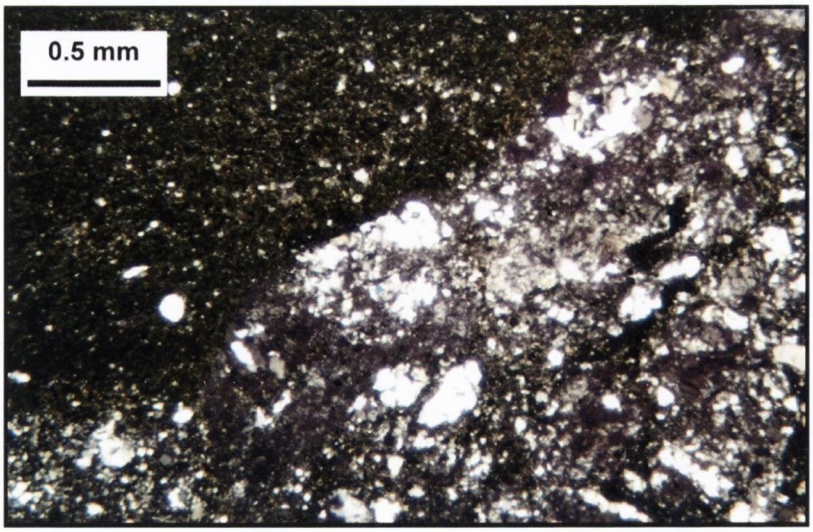


**Figure 9.18 Crushing at contact in Longford-Down metasediments and porphyritic microgranite (at ~218 m). (Thin section in XPL). Compare grain size of the porphyritic microgranite (lower right) to that in Figure 9.5 and Figure 9.7.**

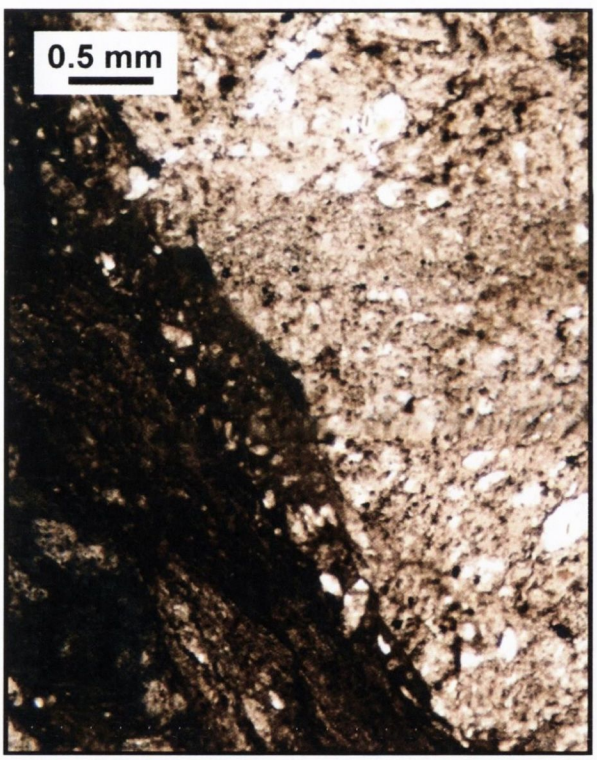


**Figure 9.19 Thin section in PPL of crush zone rocks at ~218 m, showing fine-grained cataclastic groundmass and igneous fragments.**

On the northern side of the steep contact, porphyritic microgranite is exposed but shows unusually small phenocrysts and no regular phenocryst zoning is visible (only relict fragments of zoned crystals), suggesting extensive shearing and crushing in the porphyritic microgranite as well (Figure 9.20).



**Figure 9.20 Crushed porphyritic microgranite at contact. Note the very small grain-size and the absence of unbroken zoned phenocrysts and enclaves, implying severe physical crushing and inter-mingling. Samples taken from 2 m north of the contact show regular grain-size again. Coin is 2.5 cm across.**

Crystal size in the porphyritic microgranite increases again (to a maximum phenocryst size of ~ 20 mm) approximately 2 m from the core of the crush zone, indicating a damage zone of about 5 m in total width. Mafic enclaves are present several metres north of the contact, but they are conspicuously absent close to the contact, implying intense physical mingling and shearing of the magma in the crush

zone. Numerous thick mylonitic tuffisite and cataclastic veins are present in the damage zone (Figure 9.21, Figure 9.22, Figure 9.23), reaching thicknesses of up to tens of centimetres, but also forming pervasive networks between thicker veins. Although irregular in nature, their overall trend is sub-vertical. These veins are similar to those considered characteristic for highly viscous flow regimes in steep to vertical conduits and silicic feeder dykes elsewhere (e.g. Tuffen *et al.*, 2003; e.g. Tuffen and Dingwell, 2005).



**Figure 9.21 Wide and extensive mylonitic tuffisite veins in porphyritic microgranite near contact (226/7 m). Inset: Pervasive tuffisite veins near contact (226 m).**

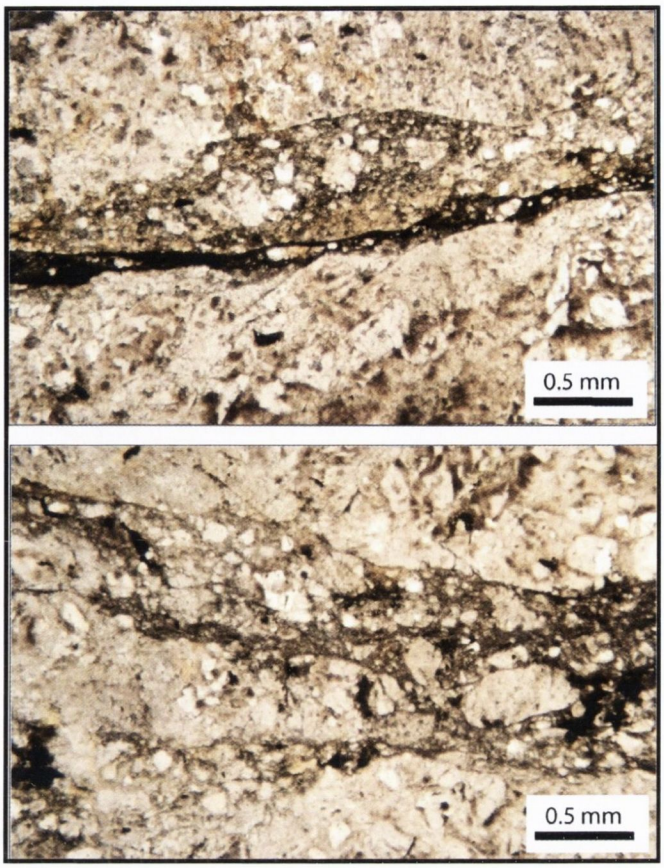


**Figure 9.22 Mylonitic tuffisite veins at contact (218 m) in porphyritic microgranite (thin section in PPL).**

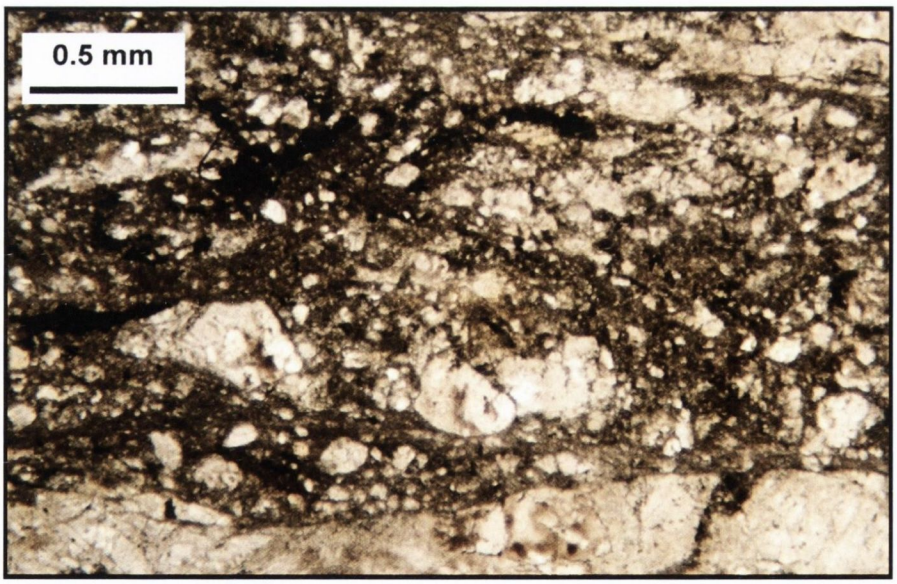


**Figure 9.23 Pervasive tuffisite veining with cataclastic crushing in damage zone near main contact (~218 m) (thin section in PPL).**

**Between 258 and 278 m**, basalt is found in contact with porphyritic microgranite. The steep contact dips towards the road and strikes approximately parallel to it (Figure 9.24). Windows of microgranite occur within the basalt, so that the basalt appears as a veneer over the microgranite, due to the near road-parallel strike of the dyke. At the base of the outcrop, both contacts of this dyke can be observed, suggesting a feeder to the dyke up to 2 m wide that flares out towards the top of the outcrop. A thin dyke (0.3 m) extends upward from the intrusion at its northern end. The main dyke also contains numerous angular xenoliths of microgranite from 20 cm to 70 cm across (Figure 9.25), implying that the basalt intruded after the microgranite had solidified. The microgranite is again holocrystalline with abundant zoned feldspar phenocrysts up to 20 mm across and a crystalline groundmass.



**Figure 9.24 Contact of basaltic dyke with microgranite at 276 m. Notebook for scale.**



**Figure 9.25 Basaltic dyke at 270 m, containing large angular microgranite xenoliths, suggesting that dyke intrusion postdates the solidification of the porphyritic microgranite (pG).**

**At 300 m**, the outcrop of porphyritic microgranite is lost underneath a cover of soil that extends for the rest of the valley.

## 9.4. Discussion

The Slieve Gullion Igneous Centre has been the subject of much research in the past ninety years, including work on the central Layered Complex (Reynolds, 1951; Gamble, 1979b; Gamble *et al.*, 1992) and the earlier ring-complex (Richey, 1932; Richey and Thomas, 1932; Emeleus, 1962). A number of mechanisms for emplacement of the Slieve Gullion ring centre have been proposed, with Richey's ring-dyke model being widely accepted for most of the 20$^{th}$ century (Richey, 1932; Richey and Thomas, 1932; Emeleus, 1962). A recent re-investigation by Stevenson

*et al.* (2008), however, proposes a different mode of emplacement. These authors suggest that an early caldera-like volcanic vent complex was intruded by a sub-horizontal sheet of porphyritic microgranite, prior to emplacement of the central layered intrusion. In the Stevenson *et al.* (2008) model, the layered intrusion is thought to have domed the porphyritic microgranite sheet, causing preferential erosion of the central uplifted part of the sheet and resulting in a ring-like outcrop pattern. Although faulted outer contacts have been reported by Richey and Thomas (1932) and Emeleus (1962), Stevenson *et al.* (2008), point out that none are available for inspection at Slieve Gullion at present, depriving us of clear field relationships. However, dyke-like bodies of porphyritic rhyolite and microgranite are reported from the southwest of the ring-complex (e.g. NE Glendesha and Forkhill quarry, (Emeleus, 1962; McDonnell *et al.*, 2004)) and are likely to represent magma that ascended (in a partly fragmental fashion) through annular caldera-related conduit systems (cf. Walter and Troll, 2001) Stevenson *et al.* (2008)regard these as accidental offshoots and do not consider them in detail in their paper. Moreover, steep-sided contacts of porphyritic granophyre (pG) that show intense crushing and evidence for multiple episodes of movement and injection were reported from Camlough Mountain to the north, Ballymacdermot Mountain to the northeast and Anglesey Mountain in the east-south-east of the complex (Richey and Thomas, 1932). Referring to outcrops near Camlough Mountain and Ballymacdermot Mountain, Richey and Thomas (1932) state that it is "self-evident that the granophyre (pG) hereabouts forms a dyke-like intrusion".

The field evidence from this new outcrop demonstrates that another marginal contact of the ring-complex's porphyritic microgranite is present, forming a steep crush zone (at 225 m in Figure 9.2), that curves along the outer margin of the ring

intrusion (see Figure 9.1). The curved nature of the contact was also mapped by Richey (1932) and Emeleus (1957). Richey's field maps (6" Louth 4NE) trace this SW-NE trending outer contact for *ca.* 1 km across the southern slopes of Feede Mountain, with the last exposure of porphyritic granophyre appearing ~100 m west of the current exposure. The contact was then extrapolated across the main road at J081 163. This is somewhat north of the current exposures, suggesting the contact may have been offset by one of the many NNW-SSE faults mapped in the area, probably the continuation of the Cam Lough Fault (Figure 9.1). At this point the ring-dyke is also much wider than at any other point in its annular outcrop. This may in part be due to multiple intrusion (see Richey, 1932), however downthrow to the east of a near-normal fault with some right-lateral movement would expose part of the flat-lying top of the intrusion as well as explain the offsets seen along the Cam Lough Fault to the Northwest of the centre. Richey also records a fine-grained chilled facies to the porphyritic microgranite near its contact with metasediments in this area, similar to that seen in our logged section.

The extensive crushing at the contact (at 218 m in Figure 9.2) is thus akin to descriptions from other localities at Slieve Gullion, though much more severe, (cf. Richey and Thomas, 1932; cf. Emeleus, 1957; Emeleus, 1962), and also to other typical caldera-bounding ring-faults in classic caldera complexes such as Glencoe (Moore and Kokelaar, 1997, 1998; Kokelaar and Moore, 2006; Kokelaar, 2007). Moreover, internal textures in the porphyritic microgranite are extremely similar to those reported from silicic feeder dykes from Iceland, showing abundant tuffisite and cataclastic veins filling in micro-fractures (cf. Tuffen *et al.*, 2003; cf. Tuffen and Dingwell, 2005), thus building up an integrated picture of upward-directed caldera-related magma transport within Slieve Gullion's early ring-complex. As this new

evidence is *a)* consistent with earlier descriptions of faulted outer contacts elsewhere by e.g. Richey (*op. cit.*), and *b)* because dyke-like masses of "ring-complex" rocks occur at several other locations (Emeleus, 1962; McDonnell *et al.*, 2004), we suggest that these features are probably typical of the ring's outer contact. This, coupled with the new evidence presented here, strongly supports the more traditional view of a ring-dyke and is not consistent with an extensive lateral sheet as proposed by Stevenson and co-workers (2008). Although the emplacement mechanism is perhaps not exactly as originally envisaged by Richey and Thomas (1932) (cf. Walter and Troll, 2001; McDonnell *et al.*, 2004), our new field data show a striking resemblance with the key features of their ring-dyke model. New outcrop information, combined with modern views on caldera faulting and fissure flow, therefore creates a picture that supports the more traditional model of ring-dyke emplacement and accompanying caldera collapse, rather than the recent re-interpretation of substantial lateral magma emplacement.

---

# 10. DISCUSSION AND CONCLUSIONS

Modern geochemical analysis allows us to trace magmatic processes across the dissected magma plumbing systems of the British and Irish Palaeogene Igneous Province. Work at the Drumadoon, Carlingford and Mourne intrusive centres has shown magma evolution within the BIPIP to be the result of a complex interplay of deep crustal fractionation of primary basaltic magmas with additional shallow crustal fractionation within sub-volcanic magma chambers and reservoirs. Large bodies of mafic rock have been geophysically imaged beneath these centres (Tantrigoda, 1999; Reay, 2004). These magma bodies (see Figure 8.37) would have fed volcanism and heated the crust to allow assimilation to form granitic rocks. Theses chambers were not closed systems and were continually fed by new magma, over long periods of time, promoting interaction with local country rocks as the magma made its way through the crust. Indeed, crustal contamination has proven to be a particularly important process for the formation of evolved magmas in the province (Dickin *et al.*, 1981; Dickin *et al.*, 1984; Kerr and Kempton, 1995; Geldmacher *et al.*, 2002; Troll *et al.*, 2004; Troll *et al.*, 2005).

The notion of crustal provincialism within the British and Irish Palaeogene Igneous Province has long been discussed (Meighan, 1979; Dickin *et al.*, 1984; Meighan *et al.*, 1984; Thompson *et al.*, 1986; Gamble *et al.*, 1992; Geldmacher *et al.*, 1998; Kerr *et al.*, 1999; Geldmacher *et al.*, 2002). The BIPIP, as part of the larger North Atlantic Igneous province (Section 4.2), is an essentially basaltic province, and therefore we might expect large volumes of relatively pristine basaltic magma with mantle-like isotopic signatures. However, the crust in the British and Irish segments of the NAIP is thick, fertile and variable. Therefore, the theory of crustal provincialism would suggest that this variable crust has influenced the primary basaltic magmas, with crustal influences changing as terrane boundaries are

traversed. Hence, the magmas should show the isotopic signature of the terrane in which they lie. In fact, Dickin *et al.* (1984) stated *"It is therefore concluded that the small degree of isotopic heterogeneity that may have been inherited from the mantle by the Tertiary* [Palaeogene] *magmas was far exceeded by the over-whelming influence of the continental crust".*

Nowhere should this influence be more apparent than at the central volcanoes of the BIPIP, where long-lived magma storage and supply systems had time to develop and heat the crust through repeated intrusion (Annen and Sparks, 2002; Troll *et al.*, 2004). Indeed, the local crust had a strong part to play in magma evolution at all of the centres studied, from incorporation of partial melts (Chapters 6 and 8) and whole rock melts (Chapters 6 and 7) to the inclusion of xenocrysts and xenoliths (Chapters 6, 8 and 9).

While there are approximately 50,000 $km^3$ of mafic rocks within the province, there is only 500 $km^3$ of rock of felsic composition (Dickin *et al.*, 1984). These felsic rocks are mostly intrusive granites and rhyolites (e.g. Mourne, Carlingford, Arran) (Emeleus, 1962; Thompson, 1969; Sparks, 1988; England, 1992; Meighan *et al.*, 1992; McDonnell *et al.*, 2004), though some extrusive rhyolitic lavas and ignimbrites do exist (e.g. Tardree, Rum, Eigg, Donald's Hill) (Old, 1975; Gould, 2004; Troll *et al.*, 2004). They occur almost exclusively at the volcanic centres, where magma suites are often bimodal in composition, with little or no intermediate magmatism. This compositional distribution is known as the "Bunsen-Daly Gap" (Bunsen, 1851; Daly, 1925) (see Section 4.4.2). It appears that felsic magmatism in the province is restricted to locations where crustal contamination should be most active. In fact, work at Carlingford, Mourne and Arran (Chapters 6, 7 and 8) has shown that the felsic magmas result from high levels of contamination during ascent,

with temporal storage and fractionation providing latent heat for the assimilation of crust throughout the upper and lower crust (DePaolo, 1981).

It must be noted that there is a broad trend of increasing proportion of granite at the central complexes as the crustal terranes are traversed from north to south (Figure 10.1). The southern terranes are younger, and have suffered less metamorphic overprint (up to greenschist facies). These southern terranes (Grampian, Midland Valley and Southern Upland terranes) are therefore rich in fusible hydrous minerals, such as micas, making the crust a very fertile contaminant. This appears to have lead to increased production of felsic melts in the southern sectors of the British and Irish Palaeogene Igneous Province.

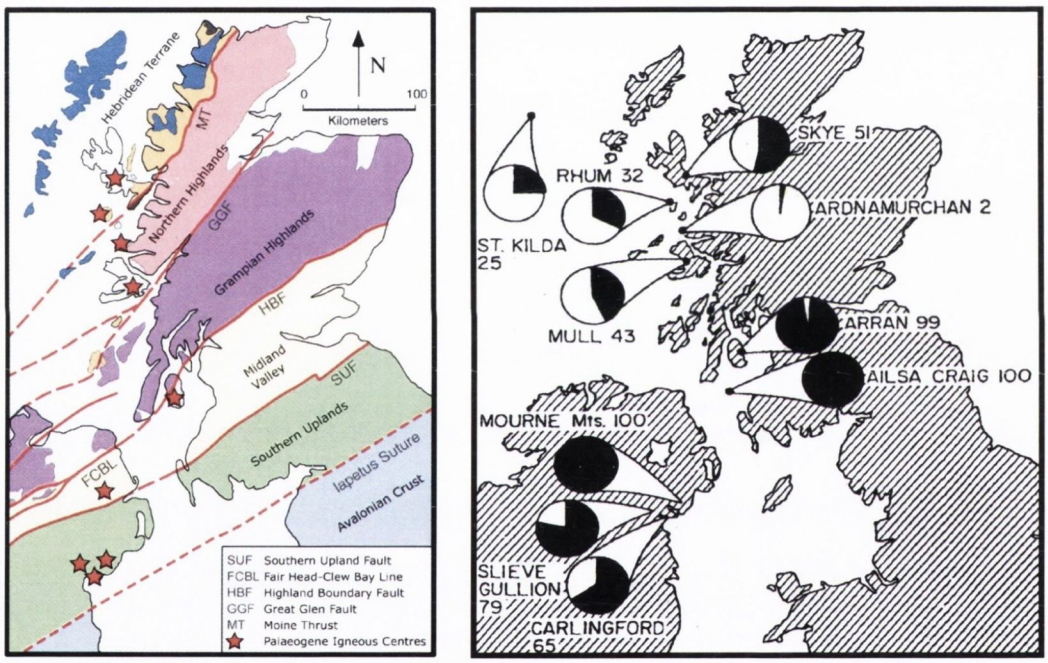


**Figure 10.1 Map of crustal terranes throughout the northern British Isles (left). The terranes get younger as boundaries are traversed to the south, and their metamorphic grade generally decreases. The map, right, shows the proportions of mafic (white) and felsic (black) magmas at each of the main igneous centres (from Bell, 1982, Figure 31.1). Note how the granite-rich centres mostly occur in the younger, less metamorphosed terranes. Similarly Lundy, which lies within the Bristol Channel, is 100% felsic rocks.**

Therefore it is hypothesised that basaltic magmas are more common in situations where they travelled through the crust quickly, perhaps along well-developed pathways, such as crustal fissures, and thus did not have significant residence time to interact with the crust (see Font *et al.*, 2008). Similarly, they may occur where the crust is infertile and could not provide large enough volumes of partial melt to form felsic magmas by assimilation during fractional crystallisation (Hebridean and Northern Highlands Terranes) (Figure 10.1). Indeed, work by Nicoll (2008), has shown that the felsic magmas of the northern terranes are almost exclusively the product of crustal melting in the vicinity of large volumes of hot mafic magma, rather than the result of protracted magma-crust interaction.

Where basaltic magmas stalled within the crust, they had the opportunity to fractionate and interact with the surrounding crust. If stalled within a fertile crust (e.g. Grampian, Midland Valley and Southern Upland Terranes), ample partial melts were available for assimilation during crystallisation, thus rapidly forming evolved magmas of felsic composition. The crust across the British Isles is so thick (>20km) it is likely large volumes of magma were stalled, either structurally or physically (due to neutral buoyancy). Many of these bodies solidified, forming the large mafic bodies that have been imaged geophysically (Tantrigoda, 1999; Reay, 2004), though not before feeding smaller rising bodies of magma which rapidly differentiated by incorporating crust, thus forming granites, microgranites and rhyolite intrusions. It is these upper crustal intrusions that are exposed today, representing a small fraction of Palaeogene magmas that have made it to the near surface environment. Most of the rocks have not survived this journey unscathed, and show significant crustal influence, even those of apparently primitive compositions. Intrusions such as those at Drumadoon demonstrate to us that there has also been significant lateral transport

in some cases, and care must be taken when assuming magmas have been contaminated by the crust in which they lie, or that directly below them (Hildreth and Fierstein, 2000; Wolff *et al.*, 2008).

Significantly, this work shows that the (low volumes of) intermediate magmas that seemingly bridge the Bunsen-Daly gap are not the products of fractional crystallisation, but rather appear to be the result of both mixing of end-member compositions, and variable amounts of crustal contamination of basaltic magmas during late-stage storage, transport and emplacement. It must be noted that larger volumes of intermediate magmas may exist in the lower crust, where stalled mafic bodies fractionally crystallised or suffered minimal crustal contamination. However erosion has not been sufficiently high to expose such bodies to our investigation.

Continued research into the British and Irish Palaeogene Igneous Province is providing insight into felsic and intermediate magmatism within flood basalt provinces (Bryan *et al.*, 2002). The extensive back-catalogue of research on the province provides an excellent starting point for testing and applying new techniques, as field relationships are not only well constrained, but there are large geochemical datasets for almost all of the centres (Dickin *et al.*, 1981; Hood, 1981; O'Connor, 1988; Sparks, 1988; Meighan *et al.*, 1991; Dickin, 1994; Geldmacher *et al.*, 1998; Kerr *et al.*, 1999; Ellam and Stuart, 2000; Geldmacher *et al.*, 2002; McDonnell *et al.*, 2004; Troll *et al.*, 2004; Chambers *et al.*, 2005; Troll *et al.*, 2005; Font *et al.*, 2008), and the surrounding crust (O'Nions *et al.*, 1983; Frost and O'Nions, 1985; Thirlwall, 1986; Marcantonio *et al.*, 1988; Dickin and Bowes, 1991; Halliday *et al.*, 1993).

Differing erosion levels amongst the various centres provide snapshots of the magma plumbing systems of large central volcanoes, allowing us to evaluate a wide range of magmatic processes in the field (e.g. Chapter 9). However it is detailed geochemical analysis that allows us to model that which is not exposed; from magma storage and transport, to high-level differentiation processes occurring during eruption (Chapters 6, 7 and 8). The geochemical analyses presented in this thesis thus permit us to recognise the subtleties of these magmatic processes, and to uncover information on the magmas' journey through the lower crust. These data provide a detailed glimpse into the temporal evolution of magmatic processes within the sub-volcanic magma chambers of the southern BIPIP, revealing evidence of processes that could not have been elucidated through petrology or fieldwork. Careful interpretation of these geochemical data allow us to unravel a time sequence of variably overprinted processes for many of these centres; from initial contamination by crustal partial melts, to bulk contamination, and final assimilation of the remaining restite during transport and emplacement.

---

# 11. FURTHER WORK

*A suggestion of further work that could add to, and be based on, the findings of this research.*

Bulk rock analysis of Nd, Sr and Pb isotopic compositions of whole rock samples is a well established as a geochemical technique. The isotopic composition of a rock or a mineral serves as a kind of petrological "DNA", directly reflecting the influences of any chemical components involved (e.g. source composition, assimilation of crustal country-rock), but insensitive to changing physical conditions such as temperature, pressure and crystallisation conditions. However, information locked in crystals that have experienced protracted crystallisation, such as zoned feldspar, becomes blurred by this conventional method (See sections 6.11 and 6.12, where xenocrystic cores from marbles were recognised within drilled phenocrysts at Carlingford).

Due to the general problem of interpreting whole-rock and groundmass chemical data derived from igneous rocks (which often suffered post-emplacement modification), magmatic crystals (phenocrysts) may be the only reliable indicators that help us to understand the petrogenetic processes that magma underwent prior to eruption.

Recognising that the crystalline components within the rock *do* preserve individual records of differentiation we can apply modern in situ trace element and isotopic analytical techniques to unravel their differentiation history. This not only gives us a means of accounting for the effects of differentiation and constraining the nature of the original source, but also allows quantification of the mechanisms of differentiation. *In-situ* chemical analysis is a new and powerful tool in geochemistry and igneous petrology that allows us to make meaningful isotopic measurements at a crystal-zone scale (μm). Techniques for the analysis of Sr-isotopes in feldspar have recently been established using micro-drilling and TIMS (Davidson and Tepley, 1997; Davidson *et al.*, 2001; Charlier *et al.*, 2006) and have proven successful during

this study (Chapter 6). Furthermore, laser ablation multi-collector inductively coupled mass spectrometry (LA-MC-ICP-MS) permits analysis of Pb isotopes and trace elements at a spatial resolution of < 100 μm scale and combined with the inherent low detection limits (routinely ppb level). The high precision and rapidity of LA-MC-ICP-MS analysis offers entirely novel ways of studying magma petrogenesis at the scale of single crystals (Gagnevin *et al.*, 2005; Tyrrell *et al.*, 2006; Tyrrell *et al.*, 2007). This technique could be particularly useful when applied to the large, zoned, K-feldspars seen at Arran (Chapter 7), Glasdrumman (Chapter 7) and Slieve Gullion (Chapter 9).

Through this study (and that of Nicoll (2008)), together with the work of others (Dickin *et al.*, 1981; Hood, 1981; O'Connor, 1988; Sparks, 1988; Meighan *et al.*, 1991; Dickin, 1994; Geldmacher *et al.*, 1998; Kerr *et al.*, 1999; Ellam and Stuart, 2000; Geldmacher *et al.*, 2002; McDonnell *et al.*, 2004; Troll *et al.*, 2004; Chambers *et al.*, 2005; Troll *et al.*, 2005; Font *et al.*, 2008), there is now an in depth back-catalogue of whole rock strontium, neodymium and lead isotope ratio data for the BIPIP and the surrounding crust. This study has shown a broad sequence of contamination across the province, with initial contamination of magmas within the lower crust, followed by subsequent contamination within the upper crust (cf. Geldmacher *et al.*, 1998; Geldmacher *et al.*, 2002; Troll *et al.*, 2004; Troll *et al.*, 2005). These data provide an excellent starting point, from which the BIPIP can be used as a testing ground for detailed crystal isotope stratigraphy, providing a crystal-scale record of crustal contamination. There is strong evidence for incorporation of sedimentary/metamorphic xenocrysts into BIPIP magmas forming radiogenic cores to magmatic phenocrysts (e.g. as hypothesised at Carlingford (Chapter 6)). Often these xenocrysts are the only evidence of interaction with an individual end-member,

and therefore, crustal feldspars will have to be analysed, so their influence can be constrained.

While the large whole-rock dataset has shown strong general trends of contamination, often modelling of whole-rock crustal end-members cannot recreate differentiation trends accurately. In fact, incorporation of crustal partial melts from selective fusion appears to be the most important feature of magma-crust interaction within the province (Chapter 6). Therefore, crustal contamination models should be refined by comparing our crystal-scale study to experimentally generated crustal partial melts. Such experiments would use a piston cylinder apparatus and a uniaxial hydraulic press (such as those at INGV, Rome, http://www.ingv.it/) to melt actual crustal samples at various temperatures and pressures. A pilot experiment (Section 6.8.4, Figure 6.25) has shown that the glasses generated can then be analysed using the same in-situ techniques as the magmatic phenocrysts, giving more accurate end-member compositions for geochemical modelling, with the added advantage of providing accurate temperature and pressure constraints to crustal contamination. This approach could be particularly valuable for clarifying whether whole-rock or partial melts of the local Dalradian metasediments were the main contributor to contamination at Arran (Chapter 7).

Therefore, further in-situ analysis of phenocrysts from Carlingford, Arran, Mourne and Slieve Gullion, coupled with experimental petrology, could ultimately quantify the role the crust has played in the petrogenesis of magmas within the British and Irish Palaeogene Igneous Province.

# 12. ACKNOWLEDGEMENTS

I would like to express my sincerest thanks to everyone who has helped me throughout my Ph.D. studies, to all my friends and colleagues, but most importantly to those mentioned below:

To my father whose encouragement to excel has got me to where I am today, and to my mother, whose belief in doing what makes you happy has kept me there. And to my sisters, who regularly remind me that they're only *stones*…

To Carl Elliott, for his love and support and for always making me remember that there's more to life, the most important thing I've learned in the last four years.

To Mark Collery, for being my best friend, for making the unbearable bearable, for being there, no matter what, and for always being on hand for an emergency cup of tea. It's been a bumpy road, but we've made it.

To Aoife O'Halloran, for being there when this journey started and sticking it out to the end, 5 houses and several manic episodes later…

To the VAMP group, past and present, (especially Graeme Nicoll and Marc-Antoine Longpré) for their friendship and feedback and for keeping me sane when work was driving me crazy.

To the staff and students of the Department of Geology (2000-2008), in particular John Graham, for making my time at Trinity so enjoyable, for supporting

and encouraging me throughout my studies and giving me the opportunity to fulfil my potential.

To Valentin Troll and David Chew, thank you for your support, inspiration and encouragement throughout my years at Trinity College. Without them, this study would not have been possible. Their friendship and guidance has pushed me further than I could ever have imagined and I will be forever grateful for the time and effort they have invested in me, and I can only hope that I have done them proud.

---

I would also like to thank the following people, institutes, societies and governmental bodies for their help, both technical and financial throughout the course of this project:

Neil Kearney, Maura Morgan, Frank Hendron, Declan Burke and Noel McGinley (TCD) for all their technical help. Rob Ellam, Anne Kelly, Vincent Gallagher, Valerie Olive and all the staff of the Scottish Universities Environmental Research Centre (SUERC) (Sr, Nd, and Pb isotopes, REEs); Dagmar Rau (GEOMAR) and Angus Calder (University of St. Andrew's) for XRF analysis; Stephen Daly (UCD) for detailed discussion; Laura Font and Victoria Martin, for help with microdrilling (University of Durham); Donald Herd for EMP training (University of St. Andrew's); Lili Freda (INGV, Rome) for experimental petrology; Siac engineering staff, especially D. Murphy, for access to Slieve Gullion outcrops. V.R.T acknowledges a Science Foundation Ireland (SFI) basic research grant, while Trinity College Dublin, the Volcanic and Magmatic Studies Group, the European Science Foundation and the Mineralogical Society of Great Britain and Ireland are thanked for support for travel to conferences and workshops.

The Irish Research Council for Science Engineering and Technology (IRSCET) are sincerely thanked for awarding me the postgraduate scholarship that allowed me to undertake these studies.

I would also like to thank my examiners, Prof. John Gamble (UCC) and Dr. Quentin Crowley (TCD), for their insightful reviews and encouraging comments during their examination of this thesis.

# 13. PUBLISHED CONTRIBUTIONS

## 13.1. Papers

**Meade, F.C.**, Chew, D.M., Troll, V.R., Ellam, R.M, Page, L.M. Magma ascent at a major terrane boundary: crustal contamination at the Drumadoon Intrusive Complex, Isle of Arran, Scotland. *Journal of Petrology. (submitted)*

Troll, V.R., **Meade, F.C.**, Chew, D.M., Emeleus, C.H., (2008). A new caldera fault segment exposed at Slieve Gullion: implications for the emplacement of the early ring-complex. *Irish Journal of Earth Sciences,* **26,** 1-16.

## 13.2. Conference abstracts

**Meade, F.C.**, Troll, V.R., Chew, D.M., Ellam, R.M. (2008). Magma ascent at a major terrane boundary: crustal contamination at the Drumadoon Intrusive Complex, Isle of Arran, Scotland. *33rd International Geological Congress,* conference abstracts.

**Meade, F.C.**, Troll, V.R., Chew, D.M., Ellam, R.M., Font, L., Chadwick, J.P. (2008). Crustal contamination in the British and Irish Palaeogene Igneous Province: mechanisms, timing and implications for petrogenesis. *Volcanic and Magmatic Studies Group Meeting, Dublin.*

Kerrigan, M., McDonnell, G., **Meade, F.**, Troll, V., Chew, D. (2008). Multiple versus composite intrusion: revisiting Judd's Dykes on the Isle of Arran, Scotland. *Volcanic and Magmatic Studies Group Meeting, Dublin*, conference abstracts.

**Meade, F.C.**, Troll, V.R., Chew, D.M., Ellam, R.M., Font, L., Chadwick, J.P. (2007). Crustal contamination in the British and Irish Palaeogene Igneous Province: mechanisms, timing and implications for the formation of granitic magmas. *Geochimica et Cosmochimica Acta*, 71 (15), supplement 1, p A648.

**Meade, F.C.**, Troll, V.R., Chew, D.M., Ellam, R.M., Font, L., Chadwick, J.P. (2007). Crustal contamination in the British and Irish Palaeogene Igneous Province: mechanisms, timing and implications. *Golden Rum – Past, Present and Future research in the North Atlantic Igneous Province: a celebration of 50 years of Rum research*, Conference Abstracts. **Invited contribution.**

**Meade, F.C.**, Troll, V.R., Ellam, R.M., Font, L., Chadwick, J.P. (2007) Relative timing of crustal contamination processes: Carlingford Igneous Centre, Republic of Ireland. EGU 2007, Vienna, *Geophysical Research Abstracts*, Vol. 9, 02998, 2007

**Meade, F.C.**, Chew, D.M., Troll, V.R. (2007). Magma ascent at a major terrane boundary: crustal contamination at the Drumadoon Intrusive Complex, Isle of Arran, Scotland. EGU 2007, Vienna, *Geophysical Research Abstracts*, Vol. 9, 03904, 2007

Troll, V.R., Nicoll, G.R., **Meade, F.C.**, Ellam, R.M., Emeleus, H., Font, L., Donaldson, C.H., Meighan, I.M., Gamble, J.A. (2006). The British-Irish Palaeocene Igneous Province Revisited: Influence of Crustal Composition on

Differentiation Processes Across Five Major Crustal Terranes, *EGU 2007*, Vienna, Geophysical Research Abstracts, Vol. 9, 03870, 2007

**Meade, F.C.**, Troll, V.R., Ellam, R.M., Font, L., Chadwick, J.P. (2007). Late-stage cone-sheet intrusions at the Carlingford Igneous Centre, Ireland: Variable styles of contamination by a single crustal endmember. *Volcanic and Magmatic Studies Group Meeting, Oxford*, conference abstracts.

Deegan, F., **Meade, F.**, Troll, V. (2007). Hornfelsed country rock megablocks in the Mourne Mountains, NE Ireland: element diffusion and brittle shearing. *Volcanic and Magmatic Studies Group Meeting, Oxford*, conference abstracts.

**Meade, F.C.**, Troll, V.R., Ellam, R.M., Font. L., Chadwick, J.P. (2006). Variable Styles of Magma-Crust Interaction recorded in Cone-Sheets at the Carlingford Igneous Centre, Republic of Ireland, *Eos Trans.* AGU, 87(52), Fall Meet. Suppl., Abstract V22A-07

Troll, V.R., Nicoll, G.R., **Meade, F.C.**, Ellam, R.M., Emeleus, H., Font, L., Donaldson, C.H., Meighan, I.M., Gamble, J.A. (2006). The British-Irish Palaeocene Igneous Province Revisited: Influence of Crustal Composition on Differentiation Processes Across Four Major Crustal Terranes, *Eos Trans.* AGU, 87(52), Fall Meet. Suppl., Abstract V11A-0552

**Meade, F.C.**, Chew, D.M., Troll, V.R. (2006). Magma ascent at a major terrane boundary: crustal contamination at the Drumadoon Intrusive Complex, Isle of Arran, Scotland. *Fermor meeting 2006, Minerals, Magmas and Megastructures, London,* conference abstracts.

**Meade, F.**, Chew, D.M., Troll, V. (2006). The geochemistry of the Drumadoon Intrusive Complex, Isle of Arran. *Irish Geological Research Meeting (IGRM), Cork.* Conference Abstracts, p.p. 49.

**Meade, F.**, Chew, D.M., Troll, V.R. & Nicholas, C. (2006). Geochemistry of the Drumadoon Intrusive Complex, Isle of Arran, Scotland, *Volcanic and Magmatic Studies Group Meeting, Leeds,* conference abstracts.

**Meade, F.**, Troll, V.R., O'Halloran, A & Chadwick, J. (2005). Emplacement relationships of cone-sheet magmas at the Carlingford Igneous Centre, Ireland. *Volcanic and Magmatic Studies Group Meeting, Milton Keynes,* conference abstracts.

---

# 14. BIBLIOGRAPHY

Abratis, M., Schmincke, H.-U., and Hansteen, T.H., 2002, Composition and evolution of submarine volcanic rocks from the central and western Canary Islands. *International Journal of Earth Sciences*, **91**, 562-582.

Akiman, O., 1971, *The petrology and geochemistry of the Tertiary dyke swarm associated with the Mourne Mountain granites, Northern Ireland* [PhD thesis]: University of Durham.

—, 1973, Kuzeydogu Irlanda kompozit intruezyonlarinin olusumu; Genesis of the composite intrusions of northeastern Ireland. *Bulletin of the Geological Society of Turkey*, **16**, 1-21.

Allegre, C.J., Lewin, E., and Dupre, B., 1988, A coherent crust-mantle model for the uranium-thorium-lead isotopic system. *Chemical Geology*, **70**, 211-234.

Allen, P.A., Bennett, S.D., Cunningham, M.J.M., Carter, A., Gallagher, K., Lazzaretti, E., Galewsky, J., Densmore, A.L., Phillips, W.E.A., Naylor, D., and Solla Hach, C., 2002, *The post-Variscan thermal and denudational history of Ireland*, In Doré, A.G., Cartwright, J.A., Turner, J.P. & White, N., ed., *Exhumation of the North Atlantic Margin: Timing, Mechanisms and Implications for Petroleum Exploration*, Volume 196: Geological Society Special Publications: Geological Society, London, p. 371-399.

Anderson, T.B., 2004, *Southern Uplands-Down-Longford Terrane*, In Mitchell, W.I., ed., *The Geology of Northern Ireland, Our Natural Foundation*: Geological Survey of Northern Ireland, Belfast, p. 41-60.

Anderson, T.B., and Oliver, G.J.H., 1996, Xenoliths of Iapetus Suture mylonites in County Down lamprophyres, Northern Ireland. *Journal of the Geological Society of London*, **153**, 403-407.

Anderton, R., 1982, Dalradian deposition and the late Precambrian-Cambrian history of the N. Atlantic region: a review of the early evolution of the Iapetus Ocean. *Journal of the Geological Society, London*, **139**.

—, 2000, *Tertiary events: the North Atlantic plume and Alpine pulses*, In Woodcock, N., and Strachan, R., eds., *Geological History of Britain and Ireland*: Blackwell Science, London, p. 374-391.

Annen, C., and Sparks, R.S.J., 2002, Effects of repetitive emplacement of basaltic intrusions on thermal evolution and melt generation in the crust. *Earth and Planetary Science Letters*, **203**, 937-955.

Bamford, D., Nunn, K., Prodehl, C., and Jacob, B., 1977, LISPB; III, Upper crustal structure of northern Britain. *Journal of the Geological Society, London*, **133**, 481-488.

Bell, B.R., and Williamson, I.T., 2002, *Tertiary igneous activity*, In Trewin, N.H., ed., *The Geology of Scotland (4th ed.)*: The Geological Society, London, p. 371-407.

Bell, J.D., 1982, *Tertiary Acid Intrusions*, In Sutherland, D.S., ed., *Igneous Rocks of the British Isles*: John Wiley & Sons, Chichester, p. 427-440.

Berggren, W.A., Kent, D.V., Swisher, C.C., and Aubry, M.P., 1995, *A revised Cenozoic geochronology and chronostratigraphy, geochronology, time scales and global stratigraphic correlation*, In Berggren, W.A., Kent, D.V., Aubry, M.P., and Hardenbol, J., eds., *Geochronology, time scales and global stratigraphic correlation*, Volume 54: Special Publication - Society for Sedimentary Geology, p. 129-212.

Bluck, B.J., Dempster, T.J., and Rogers, G., 1997, Allochthonous metamorphic blocks on the Hebridean passive margin. *Journal of Geological Society, London*, **154**, 921-924.

Brown, J.W., 1929, Dykes and associated intrusions of the Island of Bute. *Transactions of the Geological Society of Glasgow*, **18**, 388-419.

Bryan, S.E., Riley, T.R., Jerram, D.A., Stephens, C.J., and Leat, P.T., 2002, *Silicic volcanism: An undervalued component of large igneous provinces and volcanic rifted margins*, In Menzies, M.A., Klemperer, S.L., Ebinger, C.J., and Baker, J., eds., *Volcanic Rifted Margins*: Special Paper: Geological Society of America, Boulder, Colorado, p. 97-118.

Buist, D.S., 1952, A contribution to the petrochemistry and petrogenesis of the composite sill of South Bute. *Transactions of the Edinburgh Geological Society*, **15**, 52-68.

Bunsen, R.W., 1851, Úber die Processe der vulkanischen Gesteinsbildungen Islands. *Annalen der Physik und Chemie*, **83**, 197-272.

Butler, R.W.H., and Hutton, D.H.W., 1994, Basin Structure and Tertiary magmatism on Skye, NW Scotland. *Journal of the Geological Society, London*, **151**, 931-944.

Campbell, I.H., and Griffiths, R.W., 1990, Implications of mante plume structure for the evolution of flood basalts. *Earth and Planetary Science Letters*, **99**, 79-93.

Chadwick, J.P., Troll, V.R., Ginibre, C., Morgan, D., Gertisser, R., Waight, T.E., and Davidson, J.P., 2007, Carbonate Assimilation at Merapi Volcano, Java, Indonesia: Insights from Crystal Isotope Stratigraphy. *Journal of Petrology*, **48**, 1793-1812.

Chambers, L.M., 2000, *Age and duration of the British Tertiary Igneous Province: implications for the development of the ancestral Iceland plume* [PhD thesis]: University of Edinburgh.

Chambers, L.M., and Pringle, M.S., 2001, Age and duration of activity at the Isle of Mull Tertiary igneous centre, Scotland, and confirmation of the existence of subchrons during Anomaly 26r. *Earth and Planetary Science Letters*, **193**, 333-345.

Chambers, L.M., Pringle, M.S., and Parrish, R.R., 2005, Rapid formation of the Small Isles Tertiary centre constrained by precise $^{40}Ar/^{39}Ar$ and U/Pb ages. *Lithos*, **79**, 367-384.

Charlier, B.L.A., Ginibre, C., Morgan, D., Nowell, G.M., Pearson, D.G., Davidson, J.P., and Ottley, C.J., 2006, Methods for the microsampling and high-precision analysis of strontium and rubidium isotopes at single crystal scale for petrological and geochronological applications. *Chemical Geology*, **232**, 114-133.

Chew, D.M., Flowerdew, M.J., Page, L.M., Crowley, Q.G., J.S., D., and Cooper, M.J., 2008, The tectonothermal evolution and provenance of the Tyrone Central Inlier, Ireland: Grampian imbrication of an outboard Laurentian microcontinent? *Journal of the Geological Society, London*, **165**, 675-685.

Cooper, M.R., 2004, *Palaeogene Extrusive Igneous Rocks*, In Mitchell, W.I., ed., *The Geology of Northern Ireland - Our Natural Foundation*: Geological Survey of Northern Ireland, Belfast, p. 167-178.

Cooper, M.R., and Johnston, T.P., 2004, *Palaeogene Intrusive Igneous Rocks*, In Mitchell, W.I., ed., *The Geology of Northern Ireland - Our Natural Foundation*: Geological Survey of Northern Ireland, Belfast, p. 179-198.

Couch, S., Sparks, R.S.J., and Carroll, M.R., 2001, Mineral disequilibrium in lavas explained by convective self-mixing in open magma chambers. *Nature*, **411**, 1037-1039.

Dagley, P., Mussett, A.E., Wilson, R.L., and Hall, J.M., 1978, The British Tertiary igneous province; palaeomagnetism of the Arran dykes. *Geophysical Journal of the Royal Astronomical Society*, **54**, 75-91.

Dalrymple, G.B., and Lamphere, M.A., 1972, 40Ar/39Ar technique of K-Ar dating: a comparison with the conventional technique. *Earth and Planetary Science Letters*, **12**, 300-308.

Daly, J.S., Muir, R.J., and Cliff, R.A., 1991, A precise U-Pb zircon age for the Inishtrahull syenite gneiss, County Donegal, Ireland. *Journal of the Geological Society, London*, **148**, 639-642.

Daly, R.A., 1925, The Geology of Ascension Island. *Proceedings of the American Academy of Arts and Science*, **60**, 1-80.

Dalziel, I.W.D., and Soper, N.J., 2001, Neoproterozoic extension on the Scottish promontory of Laurentia: paleogeographic and tectonic implications. *Journal of Geology*, **109**, 299-317.

Davidson, J.P., and Tepley, F.I., 1997, Recharge in volcanic systems; evidence from isotope profiles of phenocrysts. *Science*, **275**, 825-829.

Davidson, J.P., Tepley, F.J.I., Palacz, Z., and Main, S., 2001, Magma recharge, contamination and residence times revealed by in-situ laser ablation isotopic analysis of feldspar in volcanic rocks. *Contributions to Mineralogy and Petrology*, **131**, 196-209.

Deniel, C., and Pin, C., 2001, Single-stage method for the simultaneous isolation of lead and strontium from silicate samples for isotopic measurements. *Analytica Chimica Acta*, **426**, 95-103.

Dentith, M.C., Trench, A., and Bluck, B.J., 1992, Geophysical constraints on the nature of the Highland Boundary Fault Zone in western Scotland. *Geological Magazine*, **129**, 411-419.

DePaolo, D.J., 1981, Trace element and isotopic effects of combined wallrock assimilation and fractional crystallisation. *Earth and Planetary Science Letters*, **53**, 189-202.

Dickin, A.P., 1992, Evidence for an Early Proterozoic crustal province in the North Atlantic region. *Journal of the Geological Society, London*, **149**, 483-486.

—, 1994, Nd isotope chemistry of Tertiary igneous rocks from Arran, Scotland; implications for magma evolution and crustal structure. *Geological Magazine*, **131**, 329-333.

Dickin, A.P., and Bowes, D.R., 1991, Isotopic evidence for the extent of early Proterozoic basement in Scotland and Northwest Ireland. *Geological Magazine*, **128**, 385-388.

Dickin, A.P., Brown, J.L., Thompson, R.N., Halliday, A.N., Morrison, M.A., Hutchison, R., and O'Hara, M.J., 1984, Crustal Contamination and the Granite Problem in the British Tertiary Volcanic Province. *Philosophical Transactions of the Royal Society of London. Series A, Mathematical and Physical Sciences*, **310**, 755-780.

Dickin, A.P., and Durant, G.P., 2002, The Blackstones Bank igneous complex: geochemistry and crustal context of a submerged Tertiary igneous centre in the Scottish Hebrides. *Geological Magazine*, **139**, 199-207.

Dickin, A.P., Moorbath, S., and Welke, H.J., 1981, Isotope, trace element and major element geochemistry of Tertiary igneous rocks, Isle of Arran, Scotland. *Transactions of the Royal Society of Edinburgh: Earth Sciences*, **72**, 159-170.

Duffield, W.A., and Ruiz, J., 1998, A model that helps explain Sr-isotope disequilibrium between feldspar phenocrysts and melt in large-volume silicic magma systems. *Journal of Volcanology and Geothermal Research*, **87**, 7-13.

Eldholm, O., and Grue, K., 1994, North Atlantic volcanic margins: dimensions and production rates. *Journal of Geophysical Research*, **99**, 2955-2968.

Ellam, R.M., 2006, New constraints on the petrogenesis of the Nuanetsi picrite basalts from Pb and Hf isotope data. *Earth and Planetary Science Letters*, **245**, 153-161.

Ellam, R.M., and Stuart, F.M., 2000, The sub-lithospheric source of North Atlantic basalts; evidence for, and significance of, a common end-member. *Journal of Petrology*, **41**, 919-932.

Emeleus, C.H., 1957, *Studies of the granophyres and related rocks of the Slieve Gullion Tertiary igneous complex, Ireland* [Unpublished D. Phil thesis thesis]: University of Oxford.

—, 1962, The porphyritic felsite of the Tertiary ring complex of Slieve Gullion, Co. Armagh. *Proceedings of the Royal Irish Academy*, **62**, 55-76.

Emeleus, C.H., and Bell, B.R., 2005, *British regional geology: the Palaeogene volcanic districts of Scotland:* British Geological Survey, Nottingham. pp. 214.

Emeleus, C.H., and Preston, J., 1969, *The Tertiary volcanic rocks of Ireland:* Queen's University, Belfast. pp. 70.

Emeleus, C.H., and Sutherland, D.S., 1982, *The central complexes, Igneous rocks of the British Isles*, p. 369-414.

England, R.W., 1992, The genesis, ascent, and emplacement of the Northern Arran Granite, Scotland; implications for granitic diapirism. *Geological Society of America Bulletin*, **104**, 606-614.

Evans, A.L., Fitch, F.J., and Miller, J.A., 1973, Potassium-argon age determinations on some British Tertiary igneous rocks. *Journal of the Geological Society, London*, **129**, 419-443.

Flett, W.R., 1942, The contact between the granites of North Arran. *Transactions of the Geological Society of Glasgow*, **20**, 180-204.

Font, L., Davidson, J.P., Pearson, D.G., Nowell, G.M., Jerram, D.A., and Ottley, C.J., 2008, Sr and Pb Isotope Micro-analysis of Plagioclase Crystals from Skye Lavas: an Insight into Open-system Processes in a Flood Basalt Province. *Journal of Petrology*, **49**, 1449-1471.

Freda, C., Gaeta, M., Misiti, V., Mollo, S., and Scarlato, P., 2008, Magma-carbonate interaction: an experimental study on ultapotassic rocks from Alban Hills (Central Italy). *Lithos*, **101**, 397-415.

Frost, C.D., and O'Nions, R.K., 1985, Caledonian magma genesis and crustal recycling. *Journal of Petrology*, **26**, 515-544.

Gagnevin, D., Daly, J.S., Waight, T.E., Morgan, D., and Poli, G., 2005, Pb isotopic zoning of K-feldspar megacrysts determined by laser ablation multiple-collector ICP-MS: insights into granite petrogenesis. *Geochimica et Cosmochimica Acta*, **69**, 1899-1915.

Gamble, J.A., 1979a, The geochemistry and petrogenesis of dolerites and gabbros from the Tertiary central volcanic complex of Slieve Gullion, North East Ireland. *Contributions to Mineralogy and Petrology*, **69**, 5-19.

—, 1979b, Some relationships between coexisting granitic and basaltic magmas and the genesis of hybrid rocks in the Tertiary Central Complex of Slieve Gullion, Northeast Ireland. *Journal of Volcanology and Geothermal Research*, **5**, 297-316.

Gamble, J.A., Meighan, I.G., and McCormick, A.G., 1992, The petrogenesis of Tertiary microgranites and granophyres from the Slieve Gullion central complex, NE Ireland. *Journal of the Geological Society, London*, **149, Part 1**, 93-106.

Gamble, J.A., Wysoczanski, R.J., and Meighan, I.G., 1999, Constraints on the age of the British Tertiary volcanic province from ion microprobe U-Pb (SHRIMP) ages for acid igneous rocks from NE Ireland. *Journal of the Geological Society, London*, **156**, 291-299.

Geldmacher, J., Haase, K.M., Devey, C.W., and Garbe-Schoenberg, C.D., 1998, The petrogenesis of Tertiary cone-sheets in Ardnamurchan, NW Scotland; petrological and geochemical constraints on crustal contamination and partial melting. *Contributions to Mineralogy and Petrology*, **131**, 196-209.

Geldmacher, J., Troll, V.R., Emeleus, C.H., and Donaldson, C.H., 2002, Pb-isotope evidence for contrasting crustal contamination of primitive to evolved magmas from Ardnamurchan and Rum; implications for the structure of the underlying crust. *Scottish Journal of Geology*, **38, Part 1**, 55-61.

Gibson, D., 1984, *The petrology and geochemistry of the western Mournes granites, Co. Down* [Ph.D. thesis]: Queen's University, Belfast.

Gibson, D., McCormick, A.G., Meighan, I.G., and Halliday, A.N., 1987, The British Tertiary igneous province; young Rb-Sr ages for the Mourne Mountains granites. *Scottish Journal of Geology*, **23, Part 2**, 221-225.

Glennie, K.W., 2002, *Permian and Triassic*, In Trewin, N.H., ed., *The Geology of Scotland*: The Geological Society, London, p. 301-322.

Gould, R.J., 2004, *Antrim Lava Field: flow patterns and provence of interbasaltic zircons* [Ph.D. thesis]: University of Dublin, Trinity College.

Goulty, N.R., Dobson, A.J., Jones, G.D., Al-Kindi, S.A., and Holland, J.G., 2001, Gravity evidence for diapiric ascent of the northern Arran Granite. *Journal of the Geological Society, London*, **158, Part 5**, 869-876.

Gradstein, F.M., Ogg, J.G., and Smith, A.G., eds., 2004, *A Geological Time Scale:* Cambridge University Press Cambridge. pp. 610.

Graham, A.M., and Upton, B.G.J., 1978, Gneisses in diatremes, Scottish Midland Valley; petrology and tectonic implications. *Journal of the Geological Society, London*, **135, Part 2**, 219-228.

Griffith, R., 1840, Presidential Address. *Journal of the Geological Society of Dublin*, **1843**, 95-130.

Grosfils, E.B., 2007, Magma reservoir failure on the terrestrial planets: Assessing the importance of graviational loading in simple elastic models. *Journal of Volcanology and Geothermal Research*, **166**, 47-75.

Hall, J., Brewer, J.A., Matthews, D.H., Warner, M.R., and Bowes, D.R., 1984, Crustal structure across the Caledonides from the "WINCH" seismic reflection profile; influences on the evolution of the Midland Valley of Scotland, Deep geology of the Midland Valley of Scotland and adjacent regions; symposium, Volume 75, Part 2, Edinburgh, United Kingdom, p. 97-109.

Halliday, A.N., 1984, Coupled Sm-Nd and U-Pb systematics in late Caledonian granites and the basement under northern Britain. *Nature*, **307**, 229-233.

Halliday, A.N., Dickin, A.P., Hunter, R.N., Davies, G.R., Dempster, T.J., Hamilton, P.J., and Upton, B.G.J., 1993, Formation and composition of the lower continental crust; evidence from Scottish xenolith suites. *Journal of Geophysical Research*, **98**, 581-607.

Halsall, T.J., 1974, *The minor intrusions and structure of the Carlingford complex, Eire* [PhD thesis]: University of Leicester.

Hamilton, C.W., 1839, Observations and sections made in the district lying between the Mourne and Dublin Mountains. *Journal of the Geological Society of Dublin*, **1843**, 51-69.

Hamilton, M.A., Pearson, D.G., Thompson, R.N., Kelley, S.P., and Emeleus, C.H., 1998, Rapid eruption of Skye lavas inferred from precise U-Pb and Ar-Ar dating of the Rum and Cuillin plutonic complexes. *Nature*, **394**, 260-263.

Harker, S., 2002, *Cretaceous*, In Trewin, N.H., ed., *The Geology of Scotland*: Geological Society, London, p. 351-360.

Harrison, J.V., 1925, The Geology of a Composite Intrusion at Bennan, South Arran. *Transactions of the Geological Society of Glasgow*, **17**, 173-180.

Haughton, S., 1856, Experimental researches on the granites of Ireland. *Quarterly Journal of the Geological Society of London*, **12**, 171-202.

—, 1858, Experimental researches on the granites of Ireland. *Quarterly Journal of the Geological Society of London*, **14**, 300-305.

—, 1876, On the trap dykes that penetrate the granites, metamorphic slates and Carboniferous Limestones of the district of Mourne in the north east of Ireland. *Journal of the Royal Geological Society of Ireland*, **4**, 91-104.

Hildreth, W., and Fierstein, J., 2000, Katmai volcanic cluster and the great eruption of 1912. *GSA Bulletin*, **112**, 1594-1620.

Hitchen, K., Morton, A.C., Mearns, E.W., Whitehouse, M., and Stoker, M.S., 1997, Geological implications from geochemical and isotopic studies of Upper Cretaceous and Lower Tertiary igneous rocks around the northern Rockall Trough. *Journal of the Geological Society, London*, **154**, 517-521.

Hodgson, B.D., Dagley, P., and Mussett, A.E., 1990, Magnetostratigrahy of the Tertiary igneous rocks of Arran. *Scottish Journal of Geology*, **26**, 99-118.

Holbrook, W.S., Larsen, H.C., Korenaga, J., Dahl-Jensen, T., Reid, I.D., Kelemen, P.H., Hopper, P.R., Kent, G.M., Lizzaralde, D., Bernstein, S., and Detrick, R.S., 2001, Mantle thermal structure and active upwelling during continental breakup in the North Atlantic. *Earth and Planetary Science Letters*, **190**, 251-266.

Holland, C.H., 2001, *Silurian*, In Holland, C.H., ed., *The Geology of Ireland*: Dunedin Academic Press, Edinburgh, p. 117-144.

Hood, D.N., 1981, *Geochemical, petrological and structural studies on the Tertiary granites and associated rocks of the eastern Mourne Mountains, Co. Down, Northern Ireland.* [Ph.D. thesis]: Queen's University, Belfast.

Hudson, J.D., and Trewin, N.H., 2002, *Jurassic*, In Trewin, N.H., ed., *The Geology of Scotland*: Geological Society, London, p. 323-350.

Hyslop, E.K., Gillanders, R.J., Hill, P.G., and Fakes, R.D., 1999, Rare-earth-bearing minerals fergusonite and gadolinite from the Arran granite. *Scottish Journal of Geology*, **35**, 65-69.

Judd, J.W., 1893, On composite dykes in Arran. *Quarterly Journal of the Geological Society of London*, **49**, 536-565.

Kanaris-Sotiriou, R., and Gibb, F.G.F., 1985, Hybridization and the petrogenesis of composite intrusions; the dyke at An Cumhann, Isle of Arran, Scotland. *Geological Magazine*, **122**, 361-372.

Kent, R.W., and Fitton, J.G., 2000, Mantle Sources and Melting Dynamics in the British Palaeogene Igneous Province. *Journal of Petrology*, **41**, 1023-1040.

Kerr, A.C., and Kempton, P.D., 1995, Crustal assimilation during turbulent magma ascent (ATA); new isotopic evidence from Mull Tertiary lava succession, N.W. Scotland. *Contributions to Mineralogy and Petrology*, **119**, 142-154.

Kerr, A.C., Kent, R.W., Thomson, B.A., Seedhouse, J.K., and Donaldson, C.H., 1999, Geochemical Evolution of the Tertiary Mull Volcano, Western Scotland. *Journal of Petrology*, **40**, 873-908.

King, B.C., 1954, Gabbro tuff in the central volcanic complex of Arran. *Transactions of the Geological Society of Glasgow*, **21, Part 3**, 440-446.

—, 1955, The Ard Bheinn area of the central igneous complex of Arran. *Quarterly Journal of the Geological Society of London*, **110, Part 4**, 323-355.

—, 1959, Age of the Granites of the Ard Bheinn area, Arran. *Proceedings of the Geological Society of London*, **1569**, 134.

Kokelaar, P., 2007, Friction melting, catastrophic dilation and breccia formation along caldera superfaults. *Journal of the Geological Society of London*, **164**, 751-754.

Kokelaar, P., and Moore, I.D., 2006, *Classic area of British geology: Glencoe caldera volcano, Scotland:* British Geological Survey, Keyworth. pp. 127.

Langmuir, C.H., Vocke, R.D., Hansan, G.N., and Hart, S.R., 1978, A general mixing equation with applications to Icelandic basalts. *Earth and Planetary Science Letters*, **37**, 380-392.

Le Bas, M.J., 1960, The petrology of the layered basic rocks of the Carlingford complex, County Louth. *Transactions - Royal Society of Edinburgh*, **64**, 169-200.

—, 1965a, The contamination of a gabbro by Carboniferous limestone at Carlingford, County Louth. *Mineralogical Magazine*, **34**, 292-302.

—, 1965b, On the origin of the Tertiary granophyres of the Carlingford complex, Ireland. *Proceedings of the Geological Society of London*, **1621**, 65.

—, 1967, On the origin of the Tertiary granophyres of the Carlingford complex, Ireland. *Proceedings of the Royal Irish Academy*, **65**, 325-337.

Lyle, P., 2000, The eruption environment of multi-tiered columnar basalt lava flows. *Journal of the Geological Society*, **157**, 715-722.

Macdonald, R., and Fettes, D.J., 2007, The tectonomagmatic evolution of Scotland. *Transactions of the Royal Society of Edinburgh: Earth Sciences*, **97**, 213-295.

Marcantonio, F., Dickin, A.P., McNutt, R.H., and Heaman, L.M., 1988, A 1,800-million-year-old Proterozoic gneiss terrane in Islay with implications for the crustal structure and evolution of Britain. *Nature*, **335**, 62-64.

Marshall, L.A., and Sparks, R.S.J., 1984, Origin of some mixed-magma and net-veined ring intrusions. *Journal of the Geological Society*, **141**, 171-182.

McDonnell, S., Troll, V.R., Emeleus, C.H., Meighan, I.G., Brock, D., and Gould, R.J., 2004, Intrusive history of the Slieve Gullion ring dyke, Ireland: implications for the internal structure of silicic sub-caldera magma chambers. *Mineralogical Magazine*, **68**, 725-738.

Meighan, I.G., 1979, The acid igneous rocks of the British Tertiary province. *Bulletin of the Geological Survey of Great Britain*, **70**, 7-8 and 10-22.

Meighan, I.G., Fallick, A.E., and McCormick, A.G., 1992, Anorogenic granite magma genesis: new isotopic data for the southern sector of the British Tertiary Igneous Province. *Transactions of the Royal Society of Edinburgh: Earth Sciences*, **83**, 227-233.

Meighan, I.G., Gibson, D., and Hood, D.N., 1984, Some aspects of Tertiary acid magmatism in NE Ireland. *Mineralogical Magazine*, **48**, 351-363.

Meighan, I.G., McCormick, A.G., Fallick, A.E., and Chappell, B.W., 1991, Granite magmatism in the British Tertiary igneous province, Second Hutton symposium on Granites and related rocks, Canberra, Australia, p. 67.

Meighan, I.G., McCormick, A.G., Gibson, D., Gamble, J.A., and Graham, I.J., 1988, *Rb-Sr isotopic determinations and the timing of Tertiary central complex magmatism in NE Ireland*, In Morton, A.C., and Parson, L.M., eds., *Early Tertiary volcanism and the opening of the NE Atlantic*, Volume 39, London, United Kingdom, p. 349-360.

Meyer, R., van Wijk, J., and Gernigon, L., 2007, *North Atlantic Igneous Province: A Review of Models for its Formation*, In Foulger, G.R., and Jurdy, D.M., eds., *Plates, Plumes, and Planetary processes*, Volume 430: Special Papers: Geological Society of America, p. 525-552.

Mitchell, W.I., 2004, *Carboniferous*, In Mitchell, W.I., ed., *The Geology of Northern Ireland: Our Natural Foundation*: Geological Survey of Northern Ireland, Belfast, p. 79-116.

Moore, I., and Kokelaar, P., 1997, Tectonic influences in piecemeal caldera collapse at Glencoe Volcano, Scotland. *Journal of the Geological Society*, **154**, 765-768.

—, 1998, Tectonically controlled piecemeal caldera collapse: A case study of Glencoe volcano, Scotland. *Geological Society of America Bulletin*, **110**, 1448-1466.

Mussett, A.E., Dagley, P., Hodgson, B., and Skelhorn, R.R., 1987, Palaeomagnetism and age of the quartz-porphyry intrusions, Isle of Arran. *Scottish Journal of Geology*, **23**, 9-22.

Mussett, A.E., Dagley, P., and Skelhorn, R.R., 1988, *Time and duration of activity in the British Tertiary igneous province*, In Morton, A.C., and Parson, L.M., eds., *Early Tertiary volcanism and the opening of the NE Atlantic*, Volume 39: Geological Society Special Publications: Geological Society of London, London, p. 337-348.

—, 1989, Further evidence for a single polarity and a common source for the quartz-porphyry intrusions of the Arran area. *Scottish Journal of Geology*, **25**, 353-359.

Mussett, A.E., Dagley, P., Skelhorn, R.R., and Wilkinson, I., 1984, Mixed polarities in a composite dyke, Arran, The Eighth U. K. geophysical assembly, Volume 77, Newcastle upon Tyne, United Kingdom, p. 303.

Nicoll, G.R., 2008, *Evolution and crustal contamination of igneous rocks from the Palaeocene Volcanic District of North-West Scotland* [Ph.D. thesis]: University of Dublin, Trinity College Dublin.

O'Connor, P.J., 1988, *Strontium isotope geochemistry of Tertiary igneous rocks, NE Ireland*, In Morton, A.C., and Parson, L.M., eds., *Early Tertiary volcanism and the opening of the NE Atlantic*, Volume 39: Geological Society Special Publications: Geological Society of London, London, p. 361-363.

O'Driscoll, B., 2006, Magmatic layering and magnetic fabrics in the Palaeogene Carlingford Later Gabbros, Co. Louth, Ireland. *Irish Journal of Earth Science*, **24**, 37-50.

O'Nions, R.K., Hamilton, P.J., and Hooker, P.J., 1983, A Nd isotope investigation of sediments related to crustal development in the British Isles. *Earth and Planetary Science Letters*, **63**, 229-240.

Old, R.A., 1975, The age and field relationships of the Tardree Tertiary rhyolite complex, County Antrim, Northern Ireland. *Bulletin of the Geological Survey of Great Britain*, 21-40.

Olive, V., Ellam, R.M., and Wilson, L., 2001, A Protocol for the Determination of the Rare Earth Elements at Picomole Level in Rocks by ICP-MS: Results on Geological Reference Materials USGS PCC-1 and DTS-1. *Geostandards Newsletter*, **25**, 219-228.

Paquet, F., Dauteuil, O., Hallot, E., and Moreau, F., 2007, Tectonics and magma dynamics coupling in a dyke swarm of Iceland. *Journal of Structural Geology*, **29**, 1477-1493.

Parnell, J., 2004, Titanium mobilization by hydrocarbon fluids related to sill intrusion in a sedimentary sequence, Scotland. *Ore Geology Reviews*, **24**, 155-167.

Phillips, W.E.A., 2001, *Caledonian Deformation*, In Holland, C.H., ed., *The Geology of Ireland*: Dunedin Academic Press, Edinburgh, p. 179-199.

Pye, M., and Brown, S., 2002, *Hydrocarbons*, In Trewin, N.H., ed., *The Geology of Scotland*: The Geological Society, London, p. 461-471.

Raczek, I., Stoll, B., Hofmann, A.W., and Jochum, K.P., 2001, High-Precision Trace Element Data for the USGS Reference Materials BCR-1, BCR-2, BHVO-1, AGV-1, AGV-2, DTS-1, DTS-2, GSP-1 and GPS-2 by ID-TIMS and MIC-SSMS. *Geostandards Newsletter*, **25**, 77-86.

Reay, D.M., 2004, *Geophysics and Concealed Geology*, In Mitchell, W.I., ed., *The Geology of Northern Ireland - Our Natural Foundation*: Geological Survey of Northern Ireland, Belfast, p. 227-248.

Reiners, P.W., Nelson, B.K., and Ghiorso, M.S., 1995, Assimilation of felsic crust by basaltic magma: thermal limits and extents of crustal contamination of mantle-derived magmas. *Geology*, **23**, 563-566.

Reynolds, D.L., 1951, The Geology of Slieve Gullion, Foughill, and Carrickarnan: an actualistic interpretation of a Tertiary gabbro-granophyre complex. *Transactions of the Royal Society of Edinburgh*, **62**, 85-143.

Richards, M.A., Duncan, R.A., and Courtillot, V.E., 1989, Flood Basalts and Hot-Spot Tracks: Plume Heads and Tails. *Science*, **246**, 103-107.

Richey, J.E., 1927, The structural relations of the Mourne Mountains (Northern Ireland). *Quarterly Journal of the Geological Society of London*, **83**, 653-688.

—, 1928, The structural relations of the Mourne Mountains (Northern Ireland). *Quarterly Journal of the Geological Society of London*, **83**, 653-688.

—, 1932, Tertiary Ring Structures in Britain. *Transactions of the Geological Society, Glasgow*, **19**, 42-140.

Richey, J.E., and Thomas, H.H., 1932, The Tertiary Ring Complex of Slieve Gullion, Ireland. *Quarterly Journal of the Geological Society of London*, **88**, 653-688.

Rollinson, H.R., 1993, *Using Geochemical Data:* Pearson Education, Harlow. pp. 352.

Rubin, A.M., 1995, Getting granite dikes out of the source region. *Journal of Geophysical Research*, **100**, 5911-5929.

Saunders, A.D., Fitton, J.G., Kerr, A.C., Norry, M.J., and Kent, R.W., 1997, *The North Atlantic igneous province*, In Mahoney, J.J., and Coffin, M.F., eds., *Large igneous provinces; continental, oceanic, and planetary flood volcanism*, Volume 100: Geophysical Monograph, p. 45-93.

Saunders, A.D., Jones, S.M., Morgan, L.A., Pierce, K.L., Widdowson, M., and Xu, Y.G., 2007, Regional uplift associated with continental large igneous provinces: The roles of mantle plumes and the lithosphere. *Chemical Geology*, **241**, 282-318.

Saunders, A.D., Norry, M.J., and Tarney, J., 1988, Origin of MORB and chemically-depleted mantle reservoirs; trace element constraints. *Journal of Petrology*, **1988**, 415-445.

Sevastopulo, G.D., and Wyse Jackson, P.N., 2001, *Carboniferous (Dinantian)*, In Holland, C.H., ed., *The Geology of Ireland*: Dunedin Academic Press, Edinburgh, p. 241-312.

Smallwood, J.R., and White, R.S., 2002, *Ridge-plume interaction in the North Atlantic and its influence on continental breakup and seafloor spreading*, In Jolley, D.W., and Bell, B.R., eds., *The North Atlantic Igneous Province: Stratigraphy, Tectonic, Volcanic and Magmatic Processes*, Volume 197: Special Publications: Geological Society, London, p. 15-37.

Smellie, W.R., 1914, The Tertiary Composite Sill of South Bute. *Transactions of the Geological Society of Glasgow*, **15**, 121-139.

—, 1916, The Igneous Rocks of Bute. *Transactions of the Geological Society of Glasgow*, **15**, 334-373.

Snyder, D., Crambes, C., Tait, S., and Wiebe, R.A., 1997, Magma mingling in dykes and sills. *The Journal of Geology*, **105**, 75-86.

Sparks, R.S.J., 1988, Petrology and geochemistry of the Loch Ba ring-dyke, Mull (N.W.) Scotland: an example of the extreme differentiation of tholeiitic magmas. *Contributions to Mineralogy and Petrology*, **100**, 446-461.

Speight, J.M., Skelhorn, R.R., Sloan, T., and Knaap, R.J., 1982, *The dyke swarms of Scotland*, In Sutherland, D.S., ed., *Igneous Rocks of the British Isles*: Wylie, Chicester, p. 449-459.

Stevenson, C.T.E., Owens, W.H., Hutton, D.H.W., Hood, D.N., and Meighan, I.G., 2007, Laccolithic, as opposed to cauldron subsidence, emplacement of the Eastern Mourne Pluton, N. Ireland; evidence from anisotropy of magnetic susceptibility. *Journal of the Geological Society of London*, **164**, 99-110.

Stevenson, C.T.E., O'Driscoll, B., Holohan, E.P., Couchman, R., Reavy, R.J., and Andrews, G.M.D., 2008, *The structure, fabrics and AMS of the Slieve Gullion ring-complex, N. Ireland: testing the ring-dyke emplacement model*, In Thompson, K., and Petford, N., eds., *Structure and Emplacement of High-Level Magmatic Systems*: Geological Society of London Special Publications (302): Geological Society of London, London, p. 159-184.

Stone, P., Plant, J.A., Mendum, J.R., and Green, P.M., 1999, A regional geochemical assessment of some terrane relationships in the British Caledonides. *Scottish Journal of Geology*, **35, Part 2**, 145-156.

Storey, M., Duncan, R.A., and Tegner, C., 2007, Timing and duration of volcanism in the North Atlantic Igneous Province: Implications for geodynamics and links to the Iceland hotspot. *Chemical Geology*, **241**, 264-281.

Strachan, R.A., 2000, *The Grampian Orogeny: Mid-Ordovician arc-continent collision along the Laurentian margin of Iapetus*, In Woodcock, N.H., and Strachan, R.A., eds., *Geological History of Britain and Ireland*: Blackwell Publishing Limited, p. 88-106.

Strachan, R.A., Smith, M., Harris, A.L., and Fettes, D.J., 2002, *The Northern Highland and Grampian terranes*, In Trewin, N.H., ed., *The Geology of Scotland*: The Geological Society, London, p. 81-147.

Takeuchi, S., and Nakamura, M., 2001, Role of precursary less-viscous mixed magma in the eruption of phenocryst-rich magma: evidence from the Hokkaido-Komagatake 1929 eruption. *Bulletin of Volcanology*, **63**, 365-376.

Tantrigoda, D.A., 1999, Interpretation of magnetic anomalies over the Isle of Arran. *Scottish Journal of Geology*, **35, Part 1**, 51-55.

Thirlwall, M.F., 1986, Lead isotope evidence for the nature of the mantle beneath Caledonian Scotland. *Earth and Planetary Science Letters*, **80**, 55-70.

Thompson, P., 1986, *Dating the British Tertiary Igneous Province in Ireland by the $^{40}Ar$-$^{39}Ar$ stepwise degassing method* [PhD thesis]: University of Liverpool.

Thompson, R.N., 1969, Tertiary granites and associated rocks of the Marsco area, Isle of Skye. *Quarterly Journal of the Geological Society of London*, **124**, 349-385.

Thompson, R.N., and Gibson, S.A., 1991, Subcontinental mantle plumes, hotspots and pre-existing thinspots. *Journal of the Geological Society, London*, **148**, 973-977.

Thompson, R.N., Morrison, M.A., Dickin, A.P., Gibson, I.L., Harmon, R.S., Hildreth, W., Grove, T.L., and Dungan, M.A., 1986, Two contrasting styles of interaction between basic magmas and continental crust in the British Tertiary volcanic province, Conference on Open magmatic systems, Volume 91, Taos, NM, United States, p. 5985-5997.

Tomkeieff, S.I., and Marshall, C.E., 1935, The Mourne dike swarm. *Quarterly Journal of the Geological Society of London*, **91**, 251-292.

Traill, W.A., 1878, Explanatory memoir to accompany part of sheets 60 and 71: Memoirs of the Geological Survey of Ireland.

Trewin, N.H., ed., 2002, *The Geology of Scotland:* The Geological Society of London London. pp. 576.

Trewin, N.H., and Rollin, K.E., 2002, *Geological history and structure of Scotland*, In Trewin, N.H., ed., *The Geology of Scotland*: The Geological Society, London, p. 1-25.

Troll, V.R., Chadwick, J.P., Ellam, R.M., McDonnell, S., Emeleus, C.H., and Meighan, I.G., 2005, Sr and Nd isotope evidence for successive crustal contamination of Slieve Gullion ring-dyke magmas, Co. Armagh, Ireland. *Geological Magazine*, **142**, 659-668.

Troll, V.R., Donaldson, C.H., and Emeleus, C.H., 2004, Pre-eruptive magma mixing in ash-flow deposits of the Tertiary Rum igneous centre, Scotland. *Contributions to Mineralogy and Petrology*, **147**, 722-739.

Troll, V.R., Nicoll, G.R., Donaldson, C.H., and Emeleus, C.H., 2008, Dating the onset of volcanism at the Rum Igneous Centre, NW Scotland. *Journal of the Geological Society, London*, **165**, 651-659.

Tuffen, H., and Dingwell, D., 2005, Fault textures in volcanic conduits: evidence for seismic trigger mechanisms during silicic eruptions. *Bulletin of Volcanology*, **67**, 370-387.

Tuffen, H., Dingwell, D.B., and Pinkerton, H., 2003, Repeated fracture and healing of silicic magma generates flow banding and earth-quakes? *Geology*, **31**, 1089-1092.

Tyrrell, S., Haughton, P.D.W., and Daly, J.S., 2007, Drainage reorganization during breakup of Pangea revealed by in-situ Pb isotopic analysis of detrital K-feldspar. *Geology*, **35**, 971-974.

Tyrrell, S., Haughton, P.D.W., Daly, J.S., Kokfelt, T.F., and Gagnevin, D., 2006, The use of the common Pb isotope composition of detrital K-feldspar grains as a provenance tool and its application to Upper Carboniferous paleodrainage, northern England. *Journal of Sedimentary Research*, **76**, 324-345.

Upton, B.G.J., 1988, *History of Tertiary igneous activity in the N Atlantic borderlands*, In Morton, A.C., and Parson, L.M., eds., *Early Tertiary volcanism and the opening of the NE Atlantic*, Volume 39: Geological Society Special Publications: Geological Society, London, p. 429-453.

Walter, T.R., and Troll, V.R., 2001, Formation of caldera periphery faults, an experimental study. *Bulletin of Volcanology*, **63**, 191-203.

White, R.S., 1988, *A hot-spot model for early Tertiary volcanism in the N Atlantic*, In Morton, A.C., and Parson, L.M., eds., *Early Tertiary Volcanism and the Opening of the NE Atlantic*, Volume 39: Special Publication: Geological Society, London, p. 3-13.

White, R.S., and McKenzie, D.P., 1989, Magmatism at rift zones: the generation of volcanic continental margins and flood basalts. *Journal of Geophysical Research*, **94**, 7685-7729.

White, R.S., Smith, L.K., Roberts, A.W., Christie, P.A.F., Kusznir, N.J., and iSIMM TEAM, 2008, Lower-crustal intrusion on the North Atlantic continental margin. *Nature*, **452**, 460-465.

Wolff, J.A., Ramos, F.C., Hart, G.L., Patterson, J.D., and Brandon, A.D., 2008, Columbia River flood basalts from a centralized crustal magmatic system. *Nature Geoscience*, **1**, 177-180.

# APPENDICES 1-9

*Geochemical data tables for igneous and crustal samples from Carlingford, Arran, Mourne and Slieve Gullion.*

**APPENDIX 1. ISOTOPE SEPARATION PROCEDURES (SUERC) 294**

1.1. LEACHING 295
1.2. DISSOLUTION 295
1.3. CATION EXCHANGE PROCEDURE FOR STRONTIUM SEPARATION 295
1.4. ANION EXCHANGE PROCEDURE FOR NEODYMIUM SEPARATION 296

**APPENDIX 2. CARLINGFORD 298**

2.1. SAMPLE LOCATIONS 299
2.2. MAJOR ELEMENTS 301
2.3. LOSS ON IGNITION 304
2.4. TRACE ELEMENTS 306
2.5. RARE EARTH ELEMENTS 310
2.6. U, TH AND PB PPM 313
2.7. RAW ISOTOPE RATIO DATA 314
*2.7.1. Strontium 314*
*2.7.2. Neodymium 316*
*2.7.3. Lead 318*
2.8. AGE CORRECTED ISOTOPE DATA 320
*2.8.1. Strontium 320*
*2.8.2. Neodymium 322*
*2.8.3. Lead 324*
2.9. MICRODRILLED STRONTIUM DATA 326
*2.9.1. Raw strontium isotope ratios 326*
*2.9.2. Age-corrected strontium isotope ratios 327*
2.10. MICROPROBE DATA 328
*2.10.1. Sample CSRB – feldspar 1 328*
*2.10.2. Sample CSRB – feldspar 2 331*
*2.10.3. Sample CSRB – feldspar 10 334*
*2.10.4. Sample CSRB – feldspar 11 337*
*2.10.5. Sample CSRB – feldspar 15 340*
*2.10.6. Sample PD9 – feldspar 1 343*
*2.10.7. Sample PD9 – feldspar 2 346*
*2.10.8. Sample PD9 – feldspar 5 348*
*2.10.9. Sample PD9 – feldspar 11 350*
*2.10.10. Sample PD9 – feldspar 16 353*
*2.10.11. Sample PD9 – feldspar 18 357*
*2.10.12. Sample CPB – feldspar 1 360*
*2.10.13. Sample CPB – feldspar 7 363*

**APPENDIX 3. CARLINGFORD CRUST 365**

3.1. SAMPLE LOCATIONS 366
3.2. MAJOR ELEMENTS 367
3.3. LOSS ON IGNITION 368
3.4. TRACE ELEMENTS 369
3.5. RARE EARTH ELEMENTS 371
3.6. U, TH AND PB PPM 372
3.7. RAW ISOTOPE RATIO DATA 373
*3.7.1. Strontium 373*
*3.7.2. Neodymium 374*
*3.7.3. Lead 375*

3.8. AGE CORRECTED ISOTOPE DATA 376
*3.8.1. Strontium* *376*
*3.8.2. Neodymium* *377*
*3.8.3. Lead* *378*

**APPENDIX 4. ARRAN** **379**

4.1. SAMPLE LOCATIONS 380
*4.1.1. Drumadoon* *380*
*4.1.2. Other igneous samples* *381*
4.2. MAJOR ELEMENTS 382
*4.2.1. Drumadoon* *382*
*4.2.2. Other igneous samples* *386*
4.3. LOSS ON IGNITION 387
*4.3.1. Drumadoon* *387*
*4.3.2. Other igneous samples* *389*
4.4. TRACE ELEMENTS 389
*4.4.1. Drumadoon* *389*
*4.4.2. Other igneous samples (XRF)* *394*
4.5. RARE EARTH ELEMENTS 395
*4.5.1. Drumadoon (Institute F. - A. Forel, Versoix)* *395*
*4.5.2. Other igneous samples (SUERC)* *397*
4.6. U, TH AND PB PPM 397
4.7. RAW ISOTOPE RATIO DATA 398
*4.7.1. Drumadoon (Department of Mineralogy, Uni. of Geneva)* *398*
4.8. OTHER IGNEOUS SAMPLES (SUERC) 400
*4.8.1. Strontium* *400*
*4.8.2. Neodymium* *400*
4.9. AGE CORRECTED ISOTOPE DATA 401
*4.9.1. Strontium* *401*
*4.9.2. Neodymium* *402*

**APPENDIX 5. ARRAN CRUST** **403**

5.1. SAMPLE LOCATIONS 404
5.2. MAJOR ELEMENTS 405
5.3. LOSS ON IGNITION 406
5.4. TRACE ELEMENTS 407
5.5. RARE EARTH ELEMENTS 408
5.6. U, TH AND PB PPM 409
5.7. RAW ISOTOPE RATIO DATA 409
*5.7.1. Strontium* *409*
5.8. AGE CORRECTED ISOTOPE DATA 410
*5.8.1. Strontium* *410*

**APPENDIX 6. MOURNE** **411**

6.1. SAMPLE LOCATIONS 412
6.2. MAJOR ELEMENTS 413
6.3. LOSS ON IGNITION 414
6.4. TRACE ELEMENTS 415
6.5. RARE EARTH ELEMENTS 416
6.6. U, TH AND PB PPM 416
6.7. RAW ISOTOPE RATIO DATA 417

*6.7.1. Strontium* 417
*6.7.2. Neodymium* 417
*6.7.3. Lead* 418
6.8. AGE CORRECTED ISOTOPE DATA 418
*6.8.1. Strontium* 418
*6.8.2. Neodymium* 419
*6.8.3. Lead* 419

**APPENDIX 7. GLASDRUMMAN** **420**

7.1. SAMPLE LOCATIONS 421
7.2. MAJOR ELEMENTS 422
7.3. LOSS ON IGNITION 423
7.4. TRACE ELEMENTS 424
7.5. RARE EARTH ELEMENTS 425
7.6. U, TH AND PB PPM 426
7.7. RAW ISOTOPE RATIO DATA 426
*7.7.1. Strontium* 426
*7.7.2. Lead* 427
7.8. AGE CORRECTED ISOTOPE DATA 427
*7.8.1. Strontium* 427
*7.8.2. Lead* 428

**APPENDIX 8. MOURNE / GLASDRUMMAN CRUST** **429**

*8.1. SAMPLE LOCATIONS* 430
*8.2. MAJOR ELEMENTS* 431
*8.3. LOSS ON IGNITION* 432
*8.4. TRACE ELEMENTS* 433
8.5. RARE EARTH ELEMENTS 434
*8.6. U, TH AND PB PPM* 435
8.7. RAW ISOTOPE RATIO DATA 436
*8.7.1. Strontium* 436
*8.7.2. Lead* 437
8.8. AGE CORRECTED ISOTOPE DATA 438
*8.8.1. Strontium* 438
*8.8.2. Lead* 439

**APPENDIX 9. SLIEVE GULLION** **440**

9.1. SAMPLE LOCATIONS 441

# Appendix 1. ISOTOPE SEPARATION PROCEDURES (SUERC)

Throughout all the following techniques, samples were collected, heated and stored in Savillex PFA beakers.

## 1.1. Leaching

- 0.2 g of sample was leached in 20% cold nitric acid ($HNO_3$) overnight (or $HNO_3$ on the hotplate at 150° C for one hour) before digestion.
- It was then washed in de-ionised Milli-Q water and centrifuged (repeated three times) and finally dried by evaporation.

## 1.2. Dissolution

- Addition of 2 ml of twice distilled concentrated $HNO_3$ and 5 ml of 40% HF. Heated to 150° – 160° C overnight and then dried by evaporation.
- Addition of 2 mls of twice distilled concentrated $HNO_3$. Heated to 150° – 160° C overnight and then dried by evaporation.
- Addition of 6 ml of 6M HCl. Heated to (150° – 160° C) overnight and then dried by evaporation.

## 1.3. Cation exchange procedure for strontium separation

- The cation columns (Bio-Rad AG50W X8 200-400 resin) were pre-treated twice with 5 ml of 2.5M HCl
- The sample was loaded in 2 ml of 2.5M HCl and washed through with 2 x 1 ml of 2.5M HCl.
- 68 ml of 2.5M HCl was added to the column and allowed to filter through the resin.

- All acids that passed through the column were discarded to this point.
- Clean beakers were placed beneath the columns and 14 ml of 2.5M HCl added to collect the Sr fraction. These samples were then dried by evaporation. A further drop of concentrated $HNO_3$ was added and dried and the samples were then ready for analysis.

The elutions were continued after collection of the Sr fraction to separate a REE fraction.

- 18 ml of 2.5M HCl was added to the columns and discarded.
- 37 ml of 3M $HNO_3$ was also added and discarded.
- A further 28 ml of $HNO_3$ was added to the columns and the REE fraction collected. It was then dried by evaporation.

## 1.4. Anion exchange procedure for neodymium separation

Neodymium was then separated out with the use of constant temperature anion exchange columns using Bio-Rad AG1 X8 200 - 400 mesh anion exchange resin.

- The REE isolate was dissolved in 1ml of orange cocktail (OC) (2L orange cocktail concentrate = 1336mls of ultra pure $H_2O$, 408mls of acetic acid and 256mls of 5M $HNO_3$. This is then diluted 1 part OC to 3 parts methanol as required)
- The columns were pre-treated with 5mls of OC.
- The sample (dissolved in 1ml of OC) was loaded into the column and washed through with 2 x 1 ml of OC.

- This was followed by 20mls of OC and all eluents were discarded.
- Clean beakers were placed under the columns and 15 ml of yellow cocktail (YC) was added and collected. (2L yellow cocktail concentrate = 1464mls of ultra pure $H_2O$, 408mls of acetic acid and 128mls of 5M $HNO_3$. This is then diluted 1 part YC to 3 parts methanol as required)
- These neodymium samples were dried by evaporation.
- A drop of concentrated $HNO_3$ was added and dried.
- The sample was now ready for analysis.

# Appendix 2. CARLINGFORD

## 2.1. Sample locations

| Sample name | Lithology | Locality | Grid Reference |
|---|---|---|---|
| **C4** | Gabbro | *Slieve Foye* | IJ 170 118 |
| **C7** | Gabbro | *Slieve Foye* | IJ 173 120 |
| **LWG1** | Microgranite | *Windy Gap* | IJ 131 137 |
| **LWG2** | Microgranite | *Windy Gap* | IJ 131 137 |
| **288-8a** | Cone-sheet rhyolite | *Glenmore* | IJ 15808 12031 |
| **284-8c** | Cone-sheet rhyolite | *Glenmore* | IJ 15808 12031 |
| **C-CS4-1711a** | Cone-sheet trachy-andesite | *Slate Rock* | IJ 17827 11701 |
| **C-CS4-1711a 2** | Cone-sheet trachy-andesite | *Slate Rock* | IJ 17827 11701 |
| **CS4B2** | Cone-sheet trachy-andesite | *Slate Rock* | IJ 17799 11754 |
| **CS4A** | Cone-sheet trachy-andesite | *Slate Rock* | IJ 17799 11754 |
| **CS4B** | Cone-sheet trachy-andesite | *Slate Rock* | IJ 17799 11754 |
| **C-PD-9** | Porphyritic mafic cone sheet | *Slate Rock* | IJ 178 113 |
| **C-P-CP** | Porphyritic mafic cone sheet | *Slate Rock* | IJ 178 113 |
| **CP-CR** | Porphyritic mafic cone sheet | *Slate Rock* | IJ 178 113 |

| Sample name | Lithology | Locality | Grid Reference |
|---|---|---|---|
| **C-CS-Segm** | Porphyritic mafic cone-sheet | *Glenmore* | IJ 15808 12031 |
| **C-CS3-1711b** | Porphyritic mafic cone-sheet | *Slate Rock* | IJ 17875 11610 |
| **C-CS3-1711a** | Porphyritic mafic cone-sheet | *Slate Rock* | IJ 17827 11701 |
| **C-Cs12-GM** | Porphyritic mafic cone-sheet | *Glenmore* | IJ 15808 12031 |
| **C-CS5-1711b** | Porphyritic mafic cone-sheet | *Slate Rock* | IJ 17875 11610 |
| **C-VA1** | Porphyritic mafic cone-sheet | *South of the Split Rock* | IJ 147 129 |
| **GM1** | Porphyry groundmass | *Slate Rock* | IJ 179 116 |
| **GM2** | Porphyritic mafic cone-sheet | *Slate Rock* | IJ 179 116 |
| **C-CS7-1711b** | Aphyric mafic cone-sheet | *Slate Rock* | IJ 17875 11610 |
| **C-CS1-SH** | Aphyric mafic cone-sheet | *Shore near King John's Castle* | IJ 18790 12084 |
| **CB3** | Aphyric mafic cone-sheet | *Slate Rock??* | |
| **B4** | Aphyric mafic cone-sheet | *Slate Rock??* | |
| **B5** | Aphyric mafic cone-sheet | *Slate Rock??* | |
| **C-CS-SR** | Aphyric mafic cone-sheet | *Slate Rock* | IJ 17875 11610 |
| **CS4E** | Aphyric mafic cone-sheet | *Slate Rock* | IJ 17799 11754 |
| **C-CS-road** | Aphyric mafic cone-sheet | *Road cut near King John's Castle* | IJ 1875 1200 |
| **CS4C** | Aphyric mafic cone-sheet | *Slate Rock* | IJ 17799 11754 |

## 2.2. Major elements

| Sample | C4 | C7 | LWG1 | LWG2 | 288-8a |
|---|---|---|---|---|---|
| **Rock type** | *Gabbro* | *Gabbro* | *Microgranite* | *Microgranite* | *Cone-sheet rhyolite* |
| **$SiO_2$** | 47.22 | 49.79 | 73.25 | 74.35 | 69.60 |
| **$TiO_2$** | 0.31 | 0.35 | 0.29 | 0.21 | 0.46 |
| **$AL_2O_3$** | 27.11 | 21.27 | 12.90 | 12.77 | 12.63 |
| **$Fe_2O_3$** | 2.82 | 4.64 | 2.24 | 2.17 | 4.63 |
| **MnO** | 0.04 | 0.09 | 0.00 | 0.02 | 0.10 |
| **MgO** | 2.92 | 5.11 | 0.35 | 0.20 | 0.49 |
| **CaO** | 16.74 | 16.24 | 0.20 | 0.73 | 1.43 |
| **$Na_2O$** | 1.37 | 1.69 | 2.21 | 2.98 | 2.96 |
| **$K_2O$** | 0.17 | 0.22 | 5.33 | 5.50 | 5.50 |
| **$P_2O_5$** | 0.01 | 0.01 | 0.02 | 0.02 | 0.09 |
| **LOI** | 1.30 | 0.60 | 3.03 | 0.96 | 1.62 |
| **Total** | 100.02 | 100.01 | 99.81 | 99.89 | 99.51 |

| Sample | 284-8c | C-CS4-1711a | C-CS4-1711a 2 | CS4B2 | CS4A |
|---|---|---|---|---|---|
| **Rock type** | *Cone-sheet rhyolite* | *Cone-sheet trachy-andesite* | *Cone-sheet trachy-andesite* | *Cone-sheet trachy-andesite* | *Cone-sheet trachy-andesite* |
| **$SiO_2$** | 69.47 | 54.17 | 54.18 | 55.97 | 54.35 |
| **$TiO_2$** | 0.46 | 0.95 | 0.95 | 0.92 | 0.98 |
| **$AL_2O_3$** | 12.68 | 18.66 | 18.65 | 17.29 | 18.43 |
| **$Fe_2O_3$** | 4.55 | 7.16 | 7.09 | 6.51 | 7.54 |
| **MnO** | 0.09 | 0.06 | 0.06 | 0.08 | 0.07 |
| **MgO** | 0.60 | 4.49 | 4.40 | 4.75 | 4.54 |
| **CaO** | 1.41 | 3.68 | 3.69 | 5.28 | 4.47 |
| **$Na_2O$** | 2.97 | 1.40 | 1.32 | 1.10 | 1.23 |
| **$K_2O$** | 5.32 | 6.92 | 6.90 | 4.70 | 5.86 |
| **$P_2O_5$** | 0.09 | 0.19 | 0.19 | 0.18 | 0.20 |
| **LOI** | 1.93 | 2.12 | 2.12 | 2.68 | 2.35 |
| **Total** | 99.57 | 99.80 | 99.55 | 99.46 | 100.02 |

| Sample | CS4B | C-PD-9 | C-P-CP | CP-CR | C-CS-Segm |
|---|---|---|---|---|---|
| Rock type | *Cone-sheet trachy-andesite* | *Porphyritic mafic cone-sheet* | *Porphyritic mafic cone-sheet* | *Porphyritic mafic cone-sheet* | *Porphyritic mafic cone-sheet* |
| $SiO_2$ | 53.34 | 47.98 | 48.31 | 48.47 | 50.51 |
| $TiO_2$ | 0.98 | 0.85 | 0.85 | 0.75 | 0.96 |
| $AL_2O_3$ | 18.75 | 19.28 | 19.94 | 21.02 | 18.89 |
| $Fe_2O_3$ | 7.41 | 9.46 | 9.22 | 8.50 | 9.75 |
| MnO | 0.07 | 0.17 | 0.17 | 0.16 | 0.20 |
| MgO | 4.61 | 4.92 | 4.64 | 4.43 | 4.07 |
| CaO | 4.21 | 12.21 | 12.50 | 12.90 | 9.91 |
| $Na_2O$ | 1.26 | 2.36 | 2.31 | 2.34 | 2.66 |
| $K_2O$ | 6.41 | 0.64 | 0.47 | 0.41 | 0.60 |
| $P_2O_5$ | 0.19 | 0.12 | 0.12 | 0.10 | 0.14 |
| LOI | 2.74 | 1.19 | 1.60 | 1.24 | 2.33 |
| Total | 99.97 | 99.18 | 100.13 | 100.32 | 100.02 |

| Sample | C-CS3-1711b | C-CS3-1711a | C-Cs12-GM | C-CS5-1711b | C-VA1 |
|---|---|---|---|---|---|
| Rock type | *Porphyritic mafic cone-sheet* | *Porphyritic mafic cone-sheet* | *Porphyritic mafic cone-sheet* | *Porphyritic mafic cone-sheet* | *Porphyritic mafic cone-sheet* |
| $SiO_2$ | 48.64 | 48.43 | 50.76 | 48.57 | 49.93 |
| $TiO_2$ | 0.81 | 0.68 | 0.91 | 0.82 | 0.78 |
| $AL_2O_3$ | 19.85 | 23.50 | 18.99 | 19.89 | 19.21 |
| $Fe_2O_3$ | 9.21 | 7.11 | 9.34 | 9.03 | 9.52 |
| MnO | 0.16 | 0.12 | 0.16 | 0.16 | 0.16 |
| MgO | 4.87 | 3.52 | 3.99 | 4.60 | 4.78 |
| CaO | 12.41 | 12.99 | 10.00 | 11.55 | 12.34 |
| $Na_2O$ | 2.32 | 2.37 | 3.19 | 2.61 | 2.41 |
| $K_2O$ | 0.47 | 0.48 | 0.66 | 0.60 | 0.23 |
| $P_2O_5$ | 0.11 | 0.11 | 0.14 | 0.11 | 0.09 |
| LOI | 1.20 | 1.03 | 1.77 | 1.68 | 1.37 |
| Total | 100.05 | 100.34 | 99.91 | 99.62 | 100.82 |

| Sample | GM1 | GM2 | c-cs7-1711b | C-CS1-SH | CB3 |
|---|---|---|---|---|---|
| Rock type | *Porphyry groundmass* | *Porphyritic mafic cone-sheet* | *Aphyric mafic cone-sheet* | *Aphyric mafic cone-sheet* | *Aphyric mafic cone-sheet* |
| $SiO_2$ | 48.10 | 48.65 | 63.89 | 49.19 | 51.82 |
| $TiO_2$ | 1.39 | 1.54 | 0.75 | 1.35 | 1.22 |
| $AL_2O_3$ | 14.89 | 14.09 | 11.30 | 13.81 | 14.46 |
| $Fe_2O_3$ | 12.90 | 13.97 | 5.91 | 12.86 | 11.70 |
| MnO | 0.21 | 0.23 | 0.17 | 0.22 | 0.22 |
| MgO | 5.85 | 6.01 | 5.20 | 6.44 | 5.55 |
| CaO | 10.72 | 9.87 | 7.17 | 10.15 | 8.89 |
| $Na_2O$ | 2.63 | 2.63 | 1.65 | 2.36 | 2.44 |
| $K_2O$ | 0.60 | 0.66 | 1.67 | 1.06 | 1.38 |
| $P_2O_5$ | 0.20 | 0.22 | 0.16 | 0.19 | 0.18 |
| LOI | 2.51 | 2.26 | 1.45 | 2.33 | 2.23 |
| Total | 100.00 | 100.13 | 99.32 | 99.96 | 100.09 |

| Sample | B4 | B5 | C-CS-SR | CS4E | C-CS-road |
|---|---|---|---|---|---|
| Rock type | *Aphyric mafic cone-sheet* | *Aphyric mafic cone-sheet* | *Aphyric mafic cone-sheet* | *Aphyric mafic cone-sheet* | *Aphyric mafic cone-sheet* |
| $SiO_2$ | 53.45 | 53.31 | 66.22 | 49.37 | 50.22 |
| $TiO_2$ | 1.83 | 1.82 | 0.79 | 1.58 | 1.24 |
| $AL_2O_3$ | 13.26 | 13.28 | 13.45 | 15.33 | 15.43 |
| $Fe_2O_3$ | 14.51 | 14.52 | 4.13 | 13.44 | 12.02 |
| MnO | 0.19 | 0.20 | 0.04 | 0.21 | 0.20 |
| MgO | 3.32 | 3.35 | 2.87 | 4.55 | 5.76 |
| CaO | 6.68 | 6.71 | 4.05 | 8.97 | 9.50 |
| $Na_2O$ | 3.00 | 2.94 | 1.37 | 2.14 | 2.57 |
| $K_2O$ | 1.78 | 1.84 | 4.04 | 1.99 | 1.55 |
| $P_2O_5$ | 0.33 | 0.33 | 0.11 | 0.25 | 0.17 |
| LOI | 2.06 | 2.00 | 1.93 | 2.79 | 1.97 |
| Total | 100.41 | 100.30 | 99.00 | 100.62 | 100.63 |

| Sample | CS4C |
|---|---|
| Rock type | *Aphyric mafic cone-sheet* |
| $SiO_2$ | 60.81 |
| $TiO_2$ | 0.85 |
| $AL_2O_3$ | 13.04 |
| $Fe_2O_3$ | 5.93 |
| MnO | 0.19 |
| MgO | 4.81 |
| CaO | 7.82 |
| $Na_2O$ | 1.87 |
| $K_2O$ | 2.46 |
| $P_2O_5$ | 0.18 |
| LOI | 1.53 |
| Total | 99.49 |

## 2.3. Loss on ignition

| Sample | C4 | C7 | LWG1 | LWG2 | 288-8a |
|---|---|---|---|---|---|
| Rock type | *Gabbro* | *Gabbro* | *Microgranite* | *Microgranite* | *Cone-sheet rhyolite* |
| $H_2O$ | - | - | - | - | - |
| $CO_2$ | - | - | - | - | - |
| $SO_3$ | 0.05 | 0.02 | 0.01 | 0.01 | 0.95 |
| LOI | 1.25 | 0.58 | 3.02 | 0.95 | 0.67 |
| Total LOI | 1.30 | 0.60 | 3.03 | 0.96 | 1.62 |

| Sample | 284-8c | C-CS4-1711a | C-CS4-1711a 2 | CS4B2 | CS4A |
|---|---|---|---|---|---|
| Rock type | *Cone-sheet rhyolite* | *Cone-sheet trachy-andesite* | *Cone-sheet trachy-andesite* | *Cone-sheet trachy-andesite* | *Cone-sheet trachy-andesite* |
| $H_2O$ | - | 1.97 | 1.97 | 2.36 | 2.13 |
| $CO_2$ | - | 0.15 | 0.15 | 0.32 | 0.22 |
| $SO_3$ | 1.16 | - | - | - | - |
| LOI | 0.77 | - | - | - | - |
| Total LOI | 1.93 | 2.12 | 2.12 | 2.68 | 2.35 |

| Sample | CS4B | C-PD-9 | C-P-CP | CP-CR | C-CS-Segm |
|---|---|---|---|---|---|
| Rock type | *Cone-sheet trachy-andesite* | *Porphyritic mafic cone-sheet* | *Porphyritic mafic cone-sheet* | *Porphyritic mafic cone-sheet* | *Porphyritic mafic cone-sheet* |
| $H_2O$ | 2.55 | 1.04 | 1.03 | 0.88 | 2.06 |
| $CO_2$ | 0.19 | 0.15 | 0.57 | 0.36 | 0.27 |
| $SO_3$ | - | - | - | - | - |
| LOI | - | - | - | - | - |
| Total LOI | 2.74 | 1.19 | 1.60 | 1.24 | 2.33 |

| Sample | C-CS3-1711b | C-CS3-1711a | C-Cs12-GM | C-CS5-1711b | C-VA1 |
|---|---|---|---|---|---|
| Rock type | *Porphyritic mafic cone-sheet* | *Porphyritic mafic cone-sheet* | *Porphyritic mafic cone-sheet* | *Porphyritic mafic cone-sheet* | *Porphyritic mafic cone-sheet* |
| $H_2O$ | 1.17 | 1.02 | 1.57 | 1.65 | 1.34 |
| $CO_2$ | 0.03 | 0.01 | 0.20 | 0.03 | 0.03 |
| $SO_3$ | - | - | - | - | - |
| LOI | - | - | - | - | - |
| Total LOI | 1.20 | 1.03 | 1.77 | 1.68 | 1.37 |

| Rock type | *Porphyry groundmass* | *Porphyritic mafic cone-sheet* | *Aphyric mafic cone-sheet* | *Aphyric mafic cone-sheet* | *Aphyric mafic cone-sheet* |
|---|---|---|---|---|---|
| $H_2O$ | 1.40 | 1.40 | 1.35 | 1.45 | 1.89 |
| $CO_2$ | 1.11 | 0.86 | 0.10 | 0.88 | 0.34 |
| $SO_3$ | - | - | - | - | - |
| LOI | - | - | - | - | - |
| **Total LOI** | 2.51 | 2.26 | 1.45 | 2.33 | 2.23 |

| Sample | B4 | B5 | C-CS-SR | CS4E | C-CS-road |
|---|---|---|---|---|---|
| Rock type | *Aphyric mafic cone-sheet* | *Aphyric mafic cone-sheet* | *Aphyric mafic cone-sheet* | *Aphyric mafic cone-sheet* | *Aphyric mafic cone-sheet* |
| $H_2O$ | 1.95 | 1.90 | 1.47 | 2.53 | 1.77 |
| $CO_2$ | 0.11 | 0.10 | 0.46 | 0.26 | 0.20 |
| $SO_3$ | - | - | - | - | - |
| LOI | - | - | - | - | - |
| **Total LOI** | 2.06 | 2.00 | 1.93 | 2.79 | 1.97 |

| Sample | CS4C |
|---|---|
| Rock type | *Aphyric mafic cone-sheet* |
| $H_2O$ | 1.40 |
| $CO_2$ | 0.13 |
| $SO_3$ | - |
| LOI | - |
| **Total LOI** | 1.53 |

## 2.4. Trace elements

| Sample | C4 | C7 | LWG1 | LWG2 | 288-8a |
|---|---|---|---|---|---|
| Rock type | *Gabbro* | *Gabbro* | *Microgranite* | *Microgranite* | *Cone-sheet rhyolite* |
| Co | - | - | - | - | 15 |
| Cr | 45 | 231 | 8 | 6 | <18 |
| Ni | 88 | 37 | < 1 | < 1 | <2 |
| V | 104 | 145 | 3 | 6 | 17 |
| Zn | 17 | 25 | 47 | 19 | 44 |
| Ce | 5 | 4 | 33 | 153 | 119 |
| La | 2 | 2 | 50 | 76 | 35 |
| Nb | 1 | 1 | 28 | 37 | 36 |
| Ga | 13 | 14 | 18 | 19 | 19 |
| Pb | 1 | < 1 | 25 | 15 | 28 |
| Pr | < 5 | < 5 | < 5 | 10 | <4 |
| Rb | 4 | 4 | 216 | 184 | 208 |
| Ba | 71 | 78 | 944 | 338 | 746 |
| Sr | 270 | 241 | 44 | 57 | 64 |
| Th | < 1 | < 1 | 22 | 33 | 20 |
| Y | 8 | 10 | 50 | 80 | 75 |
| Zr | 12 | 13 | 459 | 259 | 435 |

| Sample | 284-8c | C-CS4-1711a | C-CS4-1711a 2 | CS4B2 | CS4A |
|---|---|---|---|---|---|
| Rock type | *Cone-sheet rhyolite* | *Cone-sheet trachy-andesite* | *Cone-sheet trachy-andesite* | *Cone-sheet trachy-andesite* | *Cone-sheet trachy-andesite* |
| Co | 10 | 19 | 23 | 22 | 25 |
| Cr | <18 | 135 | 145 | 121 | 136 |
| Ni | <2 | 89 | 91 | 73 | 80 |
| V | 12 | 147 | 151 | 162 | 167 |
| Zn | 38 | 89 | 89 | 81 | 92 |
| Ce | 99 | 67 | 69 | 50 | 83 |
| La | 18 | - | - | - | - |
| Nb | 36 | 21 | 19 | 20 | 19 |
| Ga | 17 | 21 | 22 | 25 | 25 |
| Pb | 20 | 53 | 48 | 15 | 31 |
| Pr | 14 | <4 | 6 | 5 | <4 |
| Rb | 206 | 245 | 247 | 169 | 219 |
| Ba | 717 | 791 | 786 | 474 | 685 |
| Sr | 66 | 246 | 248 | 177 | 239 |
| Th | 24 | 9 | 16 | 10 | 13 |
| Y | 67 | 33 | 35 | 26 | 33 |
| Zr | 416 | 170 | 168 | 147 | 159 |

| Sample | CS4B | C-PD-9 | C-P-CP | CP-CR | C-CS-Segm |
|---|---|---|---|---|---|
| Rock type | *Cone-sheet trachy-andesite* | *Porphyritic mafic cone-sheet* | *Porphyritic mafic cone-sheet* | *Porphyritic mafic cone-sheet* | *Porphyritic mafic cone-sheet* |
| **Co** | 21 | 43 | 49 | 39 | 48 |
| **Cr** | 137 | 115 | 87 | 104 | 67 |
| **Ni** | 87 | 32 | 25 | 33 | 23 |
| **V** | 176 | 222 | 207 | 183 | 246 |
| **Zn** | 92 | 72 | 68 | 64 | 166 |
| **Ce** | 82 | 32 | 34 | - | 31 |
| **La** | - | <14 | - | - | - |
| **Nb** | 19 | 10 | 7 | 8 | 11 |
| **Ga** | 27 | 19 | 16 | 18 | 19 |
| **Pb** | 48 | 18 | | 5 | 31 |
| **Pr** | 7 | <4 | - | - | - |
| **Rb** | 240 | 25 | 15 | 14 | 40 |
| **Ba** | 751 | 167 | 151 | 133 | 221 |
| **Sr** | 251 | 211 | 220 | 224 | 201 |
| **Th** | 12 | 6 | - | - | 5 |
| **Y** | 32 | 25 | 22 | 24 | 35 |
| **Zr** | 164 | 65 | 70 | 63 | 89 |

| Sample | C-CS3-1711b | C-CS3-1711a | C-Cs12-GM | C-CS5-1711b | C-VA1 |
|---|---|---|---|---|---|
| Rock type | *Porphyritic mafic cone-sheet* | *Porphyritic mafic cone-sheet* | *Porphyritic mafic cone-sheet* | *Porphyritic mafic cone-sheet* | *Porphyritic mafic cone-sheet* |
| **Co** | 45 | 35 | 33 | 39 | 42 |
| **Cr** | 127 | 121 | 62 | 101 | 175 |
| **Ni** | 36 | 24 | 26 | 26 | 35 |
| **V** | 215 | 159 | 230 | 198 | 237 |
| **Zn** | 65 | 56 | 154 | 70 | 70 |
| **Ce** | - | 17 | 12 | 14 | 21 |
| **La** | - | - | <14 | 15 | <14 |
| **Nb** | 10 | 7 | 8 | 11 | 8 |
| **Ga** | 15 | 18 | 17 | 20 | 18 |
| **Pb** | 6 | 7 | 20 | 9 | 10 |
| **Pr** | - | - | <4 | <4 | <4 |
| **Rb** | 16 | 21 | 33 | 24 | 15 |
| **Ba** | 126 | 181 | 450 | 147 | 59 |
| **Sr** | 213 | 284 | 207 | 225 | 157 |
| **Th** | - | 5 | <4 | <4 | <4 |
| **Y** | 25 | 19 | 28 | 28 | 24 |
| **Zr** | 63 | 62 | 85 | 77 | 55 |

| Sample | GM1 | GM2 | c-cs7-1711b | C-CS1-SH | CB3 |
|---|---|---|---|---|---|
| Rock type | *Porphyry groundmass* | *Porphyritic mafic cone-sheet* | *Aphyric mafic cone-sheet* | *Aphyric mafic cone-sheet* | *Aphyric mafic cone-sheet* |
| Co | 74 | 71 | 36 | 59 | 61 |
| Cr | 73 | 52 | 131 | 97 | 244 |
| Ni | 35 | 34 | 38 | 44 | 28 |
| V | 283 | 310 | 93 | 333 | 206 |
| Zn | 103 | 113 | 103 | 95 | 101 |
| Ce | 31 | 30 | 61 | 39 | 45 |
| La | - | - | <14 | <14 | <14 |
| Nb | 16 | 13 | 10 | 14 | 16 |
| Ga | 16 | 17 | 15 | 18 | 16 |
| Pb | 13 | 11 | 30 | <4 | 11 |
| Pr | <4 | <4 | <4 | <4 | <4 |
| Rb | 21 | 23 | 57 | 41 | 55 |
| Ba | 236 | 244 | 170 | 227 | 365 |
| Sr | 194 | 188 | 152 | 172 | 151 |
| Th | <4 | 5 | 8 | <4 | 9 |
| Y | 41 | 47 | 27 | 37 | 48 |
| Zr | 123 | 133 | 201 | 111 | 169 |

| Sample | B4 | B5 | C-CS-SR | CS4E | C-CS-road |
|---|---|---|---|---|---|
| Rock type | *Aphyric mafic cone-sheet* | *Aphyric mafic cone-sheet* | *Aphyric mafic cone-sheet* | *Aphyric mafic cone-sheet* | *Aphyric mafic cone-sheet* |
| Co | 46 | 45 | 35 | 53 | 50 |
| Cr | <18 | <18 | 83 | 74 | 83 |
| Ni | 4 | 9 | 26 | 19 | 43 |
| V | 334 | 330 | 121 | 323 | 288 |
| Zn | 129 | 372 | 71 | 101 | 95 |
| Ce | 59 | 58 | 63 | 52 | 24 |
| La | <14 | <14 | <14 | 19 | <14 |
| Nb | 19 | 19 | 18 | 16 | 17 |
| Ga | 20 | 18 | 16 | 18 | 19 |
| Pb | 26 | 48 | 65 | 12 | 5 |
| Pr | <4 | <4 | <4 | <4 | <4 |
| Rb | 65 | 62 | 110 | 96 | 55 |
| Ba | 386 | 439 | 652 | 368 | 270 |
| Sr | 167 | 166 | 227 | 200 | 176 |
| Th | 9 | 4 | 10 | <4 | <4 |
| Y | 49 | 48 | 24 | 44 | 38 |
| Zr | 183 | 141 | 312 | 155 | 117 |

| Sample | CS4C |
|---|---|
| **Rock type** | *Aphyric mafic cone-sheet* |
| **Co** | 27 |
| **Cr** | 135 |
| **Ni** | 54 |
| **V** | 114 |
| **Zn** | 71 |
| **Ce** | 88 |
| **La** | 17 |
| **Nb** | 18 |
| **Ga** | 16 |
| **Pb** | 11 |
| **Pr** | 7 |
| **Rb** | 65 |
| **Ba** | 353 |
| **Sr** | 173 |
| **Th** | 8 |
| **Y** | 33 |
| **Zr** | 232 |

## 2.5. Rare earth elements

| Sample | C4 | C7 | LWG1 | LWG2 | 288-8a |
|---|---|---|---|---|---|
| Rock type | *Gabbro* | *Gabbro* | *Microgranite* | *Microgranite* | *Cone-sheet rhyolite* |
| La | 2.3 | 2.3 | 53.7 | 31.9 | 57.0 |
| Ce | 4.8 | 5.1 | 37.5 | 66.8 | 106.7 |
| Pr | 0.6 | 0.7 | 9.0 | 7.8 | 12.6 |
| Nd | 2.9 | 3.3 | 28.4 | 29.4 | 46.8 |
| Sm | 0.9 | 1.1 | 4.0 | 6.4 | 9.9 |
| Eu | 0.5 | 0.5 | 0.6 | 0.4 | 1.6 |
| Gd | 1.2 | 1.5 | 4.8 | 6.9 | 10.4 |
| Tb | 0.2 | 0.3 | 0.9 | 1.3 | 1.8 |
| Dy | 1.4 | 1.8 | 6.6 | 8.7 | 11.1 |
| Ho | 0.3 | 0.4 | 1.6 | 1.9 | 2.3 |
| Er | 0.8 | 1.1 | 5.2 | 5.9 | 6.9 |
| Tm | 0.1 | 0.2 | 0.9 | 1.0 | 1.1 |
| Yb | 0.7 | 1.0 | 5.7 | 6.4 | 6.8 |
| Lu | 0.1 | 0.2 | 0.9 | 0.9 | 1.0 |

| Sample | 284-8c | 284-8c re-run | C-CS4-1711a | CS4B2 | CS4A |
|---|---|---|---|---|---|
| Rock type | *Cone-sheet rhyolite* | *Cone-sheet rhyolite* | *Cone-sheet trachy-andesite* | *Cone-sheet trachy-andesite* | *Cone-sheet trachy-andesite* |
| La | 57.3 | 53.3 | 37.6 | 35.3 | 36.3 |
| Ce | 108.7 | 100.5 | 78.4 | 70.8 | 76.2 |
| Pr | 12.6 | 11.6 | 9.0 | 7.9 | 8.7 |
| Nd | 47.7 | 43.6 | 33.6 | 28.6 | 32.6 |
| Sm | 10.0 | 9.1 | 6.1 | 5.2 | 5.9 |
| Eu | 1.7 | 1.5 | 1.2 | 1.1 | 1.2 |
| Gd | 10.6 | 9.4 | 5.1 | 4.5 | 5.0 |
| Tb | 1.8 | 1.6 | 0.8 | 0.7 | 0.8 |
| Dy | 11.6 | 10.1 | 4.6 | 4.3 | 4.6 |
| Ho | 2.4 | 2.1 | 0.9 | 0.9 | 0.9 |
| Er | 7.3 | 6.3 | 2.8 | 2.7 | 2.8 |
| Tm | 1.2 | 1.0 | 0.4 | 0.4 | 0.5 |
| Yb | 7.3 | 6.4 | 2.8 | 2.7 | 2.8 |
| Lu | 1.1 | 1.0 | 0.4 | 0.4 | 0.4 |

| Sample | CS4B | C-PD-9 | C-Cs12-GM | C-Cs12-GM re-run | C-CS5-1711b |
|---|---|---|---|---|---|
| Rock type | *Cone-sheet trachy-andesite* | *Porphyritic mafic cone-sheet* | *Porphyritic mafic cone-sheet* | *Porphyritic mafic cone-sheet* | *Porphyritic mafic cone-sheet* |
| **La** | 38.3 | 8.4 | 12.7 | 12.2 | 9.7 |
| **Ce** | 79.5 | 18.2 | 26.4 | 26.2 | 20.6 |
| **Pr** | 9.1 | 2.3 | 3.3 | 3.2 | 2.6 |
| **Nd** | 34.3 | 10.2 | 13.8 | 13.5 | 11.2 |
| **Sm** | 6.3 | 2.8 | 3.4 | 3.4 | 3.0 |
| **Eu** | 1.3 | 1.0 | 1.1 | 1.1 | 1.0 |
| **Gd** | 5.4 | 3.5 | 4.1 | 4.1 | 3.7 |
| **Tb** | 0.8 | 0.6 | 0.7 | 0.7 | 0.6 |
| **Dy** | 4.9 | 4.1 | 4.6 | 4.6 | 4.2 |
| **Ho** | 1.0 | 0.9 | 0.9 | 1.0 | 0.9 |
| **Er** | 3.0 | 2.6 | 2.8 | 2.8 | 2.6 |
| **Tm** | 0.5 | 0.4 | 0.4 | 0.4 | 0.4 |
| **Yb** | 2.9 | 2.5 | 2.6 | 2.7 | 2.4 |
| **Lu** | 0.5 | 0.4 | 0.4 | 0.4 | 0.4 |

| Sample | C-VA1 | GM1 | GM1 re-run | GM1 re-run | C-CS1-SH |
|---|---|---|---|---|---|
| Rock type | *Porphyritic mafic cone-sheet* | *Porphyry groundmass* | *Porphyry groundmass* | *Porphyry groundmass* | *Aphyric mafic cone-sheet* |
| **La** | 6.8 | 15.7 | 16.4 | 15.9 | 14.1 |
| **Ce** | 14.6 | 34.3 | 35.6 | 34.6 | 29.8 |
| **Pr** | 1.8 | 4.3 | 4.5 | 4.4 | 3.7 |
| **Nd** | 8.1 | 18.7 | 19.4 | 18.9 | 16.5 |
| **Sm** | 2.3 | 5.0 | 5.1 | 5.0 | 4.4 |
| **Eu** | 0.8 | 1.5 | 1.6 | 1.5 | 1.4 |
| **Gd** | 3.1 | 6.1 | 6.2 | 6.1 | 5.5 |
| **Tb** | 0.6 | 1.0 | 1.1 | 1.1 | 1.0 |
| **Dy** | 3.8 | 6.8 | 7.1 | 6.9 | 6.4 |
| **Ho** | 0.8 | 1.4 | 1.5 | 1.4 | 1.3 |
| **Er** | 2.4 | 4.1 | 4.3 | 4.1 | 3.9 |
| **Tm** | 0.4 | 0.6 | 0.7 | 0.6 | 0.6 |
| **Yb** | 2.3 | 3.8 | 4.1 | 3.8 | 3.8 |
| **Lu** | 0.3 | 0.6 | 0.6 | 0.6 | 0.6 |

| Sample | C-CS1-SH re-run | CB3 | B4 | B4 re-run | C-CS-SR |
|---|---|---|---|---|---|
| **Rock type** | *Aphyric mafic cone-sheet* | *Aphyric mafic cone-sheet* | *Aphyric mafic cone-sheet* | *Aphyric mafic cone-sheet* | *Aphyric mafic cone-sheet* |
| **La** | 14.4 | 27.8 | 26.3 | 28.0 | 26.2 |
| **Ce** | 31.0 | 57.3 | 55.5 | 59.2 | 51.0 |
| **Pr** | 3.9 | 6.7 | 6.8 | 7.2 | 5.7 |
| **Nd** | 16.9 | 27.0 | 27.8 | 30.3 | 21.1 |
| **Sm** | 4.5 | 6.5 | 6.7 | 7.2 | 4.0 |
| **Eu** | 1.4 | 1.5 | 1.8 | 2.0 | 1.0 |
| **Gd** | 5.7 | 7.4 | 7.6 | 8.6 | 3.7 |
| **Tb** | 1.0 | 1.3 | 1.3 | 1.4 | 0.6 |
| **Dy** | 6.5 | 8.4 | 8.3 | 9.4 | 3.2 |
| **Ho** | 1.4 | 1.8 | 1.7 | 1.9 | 0.6 |
| **Er** | 4.0 | 5.3 | 5.1 | 5.9 | 1.9 |
| **Tm** | 0.6 | 0.8 | 0.8 | 0.9 | 0.3 |
| **Yb** | 3.9 | 5.1 | 4.9 | 5.7 | 1.8 |
| **Lu** | 0.6 | 0.8 | 0.7 | 0.9 | 0.3 |

| Sample | CS4C | CS4C re-run | CS4C re-run |
|---|---|---|---|
| **Rock type** | *Aphyric mafic cone-sheet* | *Aphyric mafic cone-sheet* | *Aphyric mafic cone-sheet* |
| **La** | 32.5 | 33.2 | 35.0 |
| **Ce** | 68.9 | 70.1 | 74.0 |
| **Pr** | 8.2 | 8.4 | 8.9 |
| **Nd** | 31.7 | 32.9 | 34.8 |
| **Sm** | 6.2 | 6.5 | 7.0 |
| **Eu** | 1.3 | 1.3 | 1.4 |
| **Gd** | 5.8 | 5.9 | 6.6 |
| **Tb** | 0.9 | 0.9 | 1.0 |
| **Dy** | 5.2 | 5.5 | 6.0 |
| **Ho** | 1.0 | 1.1 | 1.2 |
| **Er** | 2.8 | 3.1 | 3.4 |
| **Tm** | 0.4 | 0.5 | 0.5 |
| **Yb** | 2.7 | 2.9 | 3.3 |
| **Lu** | 0.4 | 0.4 | 0.5 |

## 2.6. U, Th and Pb ppm

| Sample | C4 | C7 | LWG1 | LWG2 |
|---|---|---|---|---|
| Rock type | *Gabbro* | *Gabbro* | *Microgranite* | *Microgranite* |
| U | 0.1 | 0.2 | 3.5 | 4.3 |
| Th | 0.3 | 0.4 | 20.3 | 30.4 |
| Pb | 4.9 | 2.6 | 25.8 | 17.5 |

| Sample | 288-8a | 284-8c | C-CS4-1711a | CS4B2 |
|---|---|---|---|---|
| Rock type | *Cone-sheet rhyolite* | *Cone-sheet rhyolite* | *Cone-sheet trachy-andesite* | *Cone-sheet trachy-andesite* |
| U | 4.6 | 4.2 | 3.0 | 2.8 |
| Th | 21.5 | 20.9 | 11.2 | 10.8 |
| Pb | 19.1 | 17.1 | 43.0 | 12.4 |

| Sample | CS4A | CS4B | C-PD-9 | C-Cs12-GM |
|---|---|---|---|---|
| Rock type | *Cone-sheet trachy-andesite* | *Cone-sheet trachy-andesite* | *Porphyritic mafic cone-sheet* | *Porphyritic mafic cone-sheet* |
| U | 3.0 | 3.0 | 0.2 | 0.4 |
| Th | 11.6 | 11.5 | 1.4 | 2.2 |
| Pb | 31.1 | 34.1 | 9.5 | 21.0 |

| Sample | C-Cs12-GM re-run | C-CS5-1711b | C-VA1 | GM1 |
|---|---|---|---|---|
| Rock type | *Porphyritic mafic cone-sheet* | *Porphyritic mafic cone-sheet* | *Porphyritic mafic cone-sheet* | *Porphyry groundmass* |
| U | 0.2 | 0.5 | 0.8 | 0.5 |
| Th | 2.0 | 1.9 | 3.3 | 2.8 |
| Pb | 18.5 | 8.7 | 6.1 | 22.2 |

| Sample | GM1 re-run | C-CS1-SH | C-CS1-SH re-run | CB3 |
|---|---|---|---|---|
| Rock type | *Porphyry groundmass* | *Aphyric mafic cone-sheet* | *Aphyric mafic cone-sheet* | *Aphyric mafic cone-sheet* |
| U | 0.5 | 0.7 | 0.7 | 1.3 |
| Th | 2.9 | 2.8 | 2.9 | 6.9 |
| Pb | 5.2 | 6.1 | 8.9 | 10.9 |

| Sample | B4 | C-CS-SR | CS4C | CS4C re-run |
|---|---|---|---|---|
| Rock type | *Aphyric mafic cone-sheet* | *Aphyric mafic cone-sheet* | *Aphyric mafic cone-sheet* | *Aphyric mafic cone-sheet* |
| U | 1.8 | 3.5 | 2.5 | 2.5 |
| Th | 6.8 | 9.3 | 9.6 | 10.0 |
| Pb | 22.5 | 56.3 | 10.0 | 11.8 |

## 2.7. Raw isotope ratio data

### *2.7.1. Strontium*

| Sample | Rock type | Lab Number | $^{87}Sr/^{86}Sr$ measured | % S.E. | 2 S.E. | 2S.D. |
|---|---|---|---|---|---|---|
| **C4** | *Gabbro* | *D831* | 0.705709 | 0.0013 | 0.000026 | 0.000026 |
| **C7** | *Gabbro* | *D830* | 0.705788 | 0.0013 | 0.000026 | 0.000026 |
| **LWG1** | *Microgranite* | *D832* | 0.724407 | 0.0015 | 0.000030 | 0.000030 |
| **LWG2** | *Microgranite* | *D925* | 0.714334 | 0.0012 | 0.000024 | 0.000024 |
| **288-8a** | *Cone-sheet rhyolite* | *D834* | 0.717505 | 0.0011 | 0.000022 | 0.000022 |
| **284-8c** | *Cone-sheet rhyolite* | *D833* | 0.717366 | 0.0012 | 0.000024 | 0.000024 |
| **C-CS4-1711a** | *Cone-sheet trachy-andesite* | *D852* | 0.722428 | 0.0014 | 0.000028 | 0.000028 |
| **CS4B2** | *Cone-sheet trachy-andesite* | *D853* | 0.722264 | 0.0011 | 0.000022 | 0.000022 |
| **CS4B2** *unleached* | *Cone-sheet trachy-andesite* | *E439* | Failed | | | |
| **CS4A** | *Cone-sheet trachy-andesite* | *E442* | 0.722601 | 0.0013 | 0.000026 | 0.000026 |
| **CS4A *re-run*** | *Cone-sheet trachy-andesite* | *D854* | 0.722266 | 0.0013 | 0.000026 | 0.000026 |
| **CS4B** | *Cone-sheet trachy-andesite* | *D855* | 0.722048 | 0.0012 | 0.000024 | 0.000024 |
| **C-PD-9** | *Porphyritic mafic cone-sheet* | *E444* | 0.706668 | 0.0014 | 0.000028 | 0.000028 |
| **C-PD-9 *re-run*** | *Porphyritic mafic cone-sheet* | *D856* | 0.706678 | 0.0012 | 0.000024 | 0.000024 |
| **C-Cs12-GM** | *Porphyritic mafic cone-sheet* | *D919* | 0.707921 | 0.0011 | 0.000022 | 0.000022 |
| **C-Cs12-GM** *re-run* | *Porphyritic mafic cone-sheet* | *D857* | Failed | | | |

| Sample | Rock type | Lab Number | $^{87}Sr/^{86}Sr$ measured | % S.E. | 2 S.E. | 2S.D. |
|---|---|---|---|---|---|---|
| **C-CS5-1711b** | *Porphyritic mafic cone-sheet* | *E443* | 0.707495 | 0.0013 | 0.000026 | 0.000026 |
| **C-CS5-1711b *re-run*** | *Porphyritic mafic cone-sheet* | *D858* | 0.707791 | 0.0021 | 0.000042 | 0.000042 |
| **C-VA1 *unleached*** | *Porphyritic mafic cone-sheet* | *E438* | 0.706974 | 0.0015 | 0.000030 | 0.000030 |
| **C-VA1** | *Porphyritic mafic cone-sheet* | *E450* | 0.706876 | 0.0012 | 0.000024 | 0.000024 |
| **C-VA1 re-run** | *Porphyritic mafic cone-sheet* | *D859* | 0.706818 | 0.0013 | 0.000026 | 0.000026 |
| **GM1** | *Groundmass of porphyry* | *D917* | 0.706684 | 0.0014 | 0.000028 | 0.000028 |
| **GM1 *Re-run*** | *Groundmass of porphyry* | *D841* | Failed | | | |
| **C-pdfsp** | *Feldspar separate from porphyry* | *E109* | 0.706294 | 0.0012 | 0.000024 | 0.000024 |
| **C-CS1-SH** | *Aphyric mafic cone-sheet* | *D918* | 0.709253 | 0.0013 | 0.000026 | 0.000026 |
| **C-cs-sr** | *Aphyric mafic cone-sheet* | *E865* | 0.714303 | 0.0014 | 0.000028 | 0.000028 |
| **CB3 *unleached*** | *Aphyric mafic cone-sheet* | *E440* | 0.709515 | 0.0012 | 0.000024 | 0.000024 |
| **CB3** | *Aphyric mafic cone-sheet* | *E464* | 0.709019 | 0.0012 | 0.000024 | 0.000024 |
| **CB3 *re-run*** | *Aphyric mafic cone-sheet* | *D861* | 0.708933 | 0.0012 | 0.000024 | 0.000024 |
| **B4** | *Aphyric mafic cone-sheet* | *D862* | 0.710356 | 0.0013 | 0.000026 | 0.000026 |
| **CS4C** | *Aphyric mafic cone-sheet* | *E465* | 0.718876 | 0.0013 | 0.000026 | 0.000026 |
| **CS4C** *re-run* | *Aphyric mafic cone-sheet* | *D863* | 0.718792 | 0.0012 | 0.000024 | 0.000024 |

### *2.7.2. Neodymium*

| Sample | Rock type | Lab Number | $^{143}Nd/^{144}Nd$ Measured | % S.E. | 2 S.E. | 2S.D. |
|---|---|---|---|---|---|---|
| **C4** | *Gabbro* | *D831* | Failed | | | |
| **C7** | *Gabbro* | *D830* | 0.512606 | 0.0021 | 0.000042 | 0.000042 |
| **LWG1** | *Microgranite* | *D832* | 0.512377 | 0.0046 | 0.000092 | 0.000092 |
| **LWG2** | *Microgranite* | *D925* | *Not Analysed* | | | |
| **288-8a** | *Cone-sheet rhyolite* | *D834* | 0.512400 | 0.0022 | 0.000044 | 0.000044 |
| **284-8c** | *Cone-sheet rhyolite* | *D833* | 0.512425 | 0.0012 | 0.000024 | 0.000024 |
| **C-CS4-1711a** | *Cone-sheet trachy-andesite* | *D852* | *Not Analysed* | | | |
| **CS4B2** | *Cone-sheet trachy-andesite* | *D853* | Failed | | | |
| **CS4B2** *unleached* | *Cone-sheet trachy-andesite* | *E439* | 0.512062 | 0.0007 | 0.000014 | 0.000014 |
| **CS4A** | *Cone-sheet trachy-andesite* | *E442* | *Not Analysed* | | | |
| **CS4A *re-run*** | *Cone-sheet trachy-andesite* | *D854* | 0.512044 | 0.0014 | 0.000028 | 0.000028 |
| **CS4B** | *Cone-sheet trachy-andesite* | *D855* | 0.511986 | 0.0006 | 0.000012 | 0.000012 |
| **C-PD-9** | *Porphyritic mafic cone-sheet* | *E444* | *Not Analysed* | | | |
| **C-PD-9 *re-run*** | *Porphyritic mafic cone-sheet* | *D856* | Failed | | | |
| **C-Cs12-GM** | *Porphyritic mafic cone-sheet* | *D919* | 0.512448 | 0.0005 | 0.000010 | 0.000010 |
| **C-Cs12-GM** *re-run* | *Porphyritic mafic cone-sheet* | *D857* | 0.512359 | 0.0007 | 0.000014 | 0.000014 |

| Sample | Rock type | Lab Number | $^{143}Nd/^{144}Nd$ Measured | % S.E. | 2 S.E. | 2S.D. |
|---|---|---|---|---|---|---|
| **C-CS5-1711b** | *Porphyritic mafic cone-sheet* | *E443* | *Not Analysed* | | | |
| **C-CS5-1711b *re-run*** | *Porphyritic mafic cone-sheet* | *D858* | *Not Analysed* | | | |
| **C-VA1 *unleached*** | *Porphyritic mafic cone-sheet* | *E438* | 0.512482 | 0.0009 | 0.000018 | 0.000018 |
| **C-VA1** | *Porphyritic mafic cone-sheet* | *E450* | *Not Analysed* | | | |
| **C-VA1 *re-run*** | *Porphyritic mafic cone-sheet* | *D859* | *Not Analysed* | | | |
| **GM1** | *Groundmass of porphyry* | *D917* | 0.512496 | 0.0033 | 0.000066 | 0.000066 |
| **GM1 *Re-run*** | *Groundmass of porphyry* | *D841* | 0.512049 | 0.0007 | 0.000014 | 0.000014 |
| **C-pdfsp** | *Feldspar separate from porphyry* | *E109* | Failed | | | |
| **C-CS1-SH** | *Aphyric mafic cone-sheet* | *D918* | 0.512535 | 0.0009 | 0.000018 | 0.000018 |
| **C-cs-sr** | *Aphyric mafic cone-sheet* | *E865* | *Not Analysed* | | | |
| **CB3 *unleached*** | *Aphyric mafic cone-sheet* | *E440* | 0.512298 | 0.0016 | 0.000032 | 0.000032 |
| **CB3** | *Aphyric mafic cone-sheet* | *E464* | *Not Analysed* | | | |
| **CB3 *re-run*** | *Aphyric mafic cone-sheet* | *D861* | *Not Analysed* | | | |
| **B4** | *Aphyric mafic cone-sheet* | *D862* | 0.512419 | 0.0026 | 0.000052 | 0.000052 |
| **CS4C** | *Aphyric mafic cone-sheet* | *E465* | *Not Analysed* | | | |
| **CS4C** *re-run* | *Aphyric mafic cone-sheet* | *D863* | Failed | | | |

### *2.7.3. Lead*

| Sample | Rock Type | Lab Number | $^{206}Pb/^{204}Pb$ | 2 S.E. | $^{207}Pb/^{204}Pb$ | 2 S.E. | $^{208}Pb/^{204}Pb$ | 2 S.E. |
|---|---|---|---|---|---|---|---|---|
| **C7** | *Gabbro* | N476 | 18.708 | 0.019 | 15.583 | 0.019 | 38.423 | 0.020 |
| **LWG1** | *Microgranite* | N480 | 18.967 | 0.010 | 15.648 | 0.010 | 38.905 | 0.011 |
| **LWG2** | *Microgranite* | D925 | 19.216 | 0.002 | 15.785 | 0.002 | 39.683 | 0.003 |
| **288-8a** | *Cone-sheet rhyolite* | N479 | 18.982 | 0.011 | 15.633 | 0.011 | 38.852 | 0.011 |
| **C-CS4-1711a** | *Cone-sheet trachy-andesite* | N458 | 18.783 | 0.010 | 15.622 | 0.010 | 38.733 | 0.011 |
| **CS4B2** | *Cone-sheet trachy-andesite* | N452 | 18.909 | 0.014 | 15.620 | 0.014 | 38.819 | 0.015 |
| **CS4A** | *Cone-sheet trachy-andesite* | N455 | 18.802 | 0.010 | 15.618 | 0.010 | 38.741 | 0.010 |
| **CS4B** | *Cone-sheet trachy-andesite* | N477 | 18.833 | 0.021 | 15.651 | 0.020 | 38.810 | 0.021 |
| **C-PD-9** | *Porphyritic mafic cone-sheet* | N457 | 18.553 | 0.011 | 15.603 | 0.011 | 38.520 | 0.011 |
| **C-Cs12-GM** | *Porphyritic mafic cone-sheet* | D919 | 18.800 | 0.002 | 15.629 | 0.002 | 38.750 | 0.003 |
| **C-CS5-1711b** | *Porphyritic mafic cone-sheet* | N456 | 18.645 | 0.026 | 15.613 | 0.026 | 38.652 | 0.026 |
| **C-VA1** | *Porphyritic mafic cone-sheet* | N451 | 18.693 | 0.014 | 15.610 | 0.014 | 38.687 | 0.015 |
| **GM1** | *Groundmass of porphyry* | D917 | 18.689 | 0.002 | 15.650 | 0.002 | 38.742 | 0.003 |
| **C-pdfsp** | *Feldspar separate from porphyry* | E128 | 18.466 | 0.005 | 15.513 | 0.004 | 38.382 | 0.011 |

| Sample | Rock Type | Lab Number | $^{206}Pb/^{204}Pb$ | 2 S.E. | $^{207}Pb/^{204}Pb$ | 2 S.E. | $^{208}Pb/^{204}Pb$ | 2 S.E. |
|---|---|---|---|---|---|---|---|---|
| **C-CS1-SH** | *Aphyric mafic cone-sheet* | D918 | 19.015 | 0.002 | 15.642 | 0.002 | 39.034 | 0.002 |
| **C-cs-sr** | *Aphyric mafic cone-sheet* | E877 | 18.675 | 0.005 | 15.622 | 0.007 | 38.545 | 0.009 |
| **CB3** | *Aphyric mafic cone-sheet* | N453 | 18.767 | 0.020 | 15.638 | 0.020 | 38.944 | 0.020 |
| **B4** | *Aphyric mafic cone-sheet* | N478 | 18.844 | 0.013 | 15.629 | 0.013 | 38.743 | 0.013 |
| **CS4C** | *Aphyric mafic cone-sheet* | E878 | 19.962 | 0.005 | 15.634 | 0.006 | 38.966 | 0.008 |
| **CS4C** *re-run* | *Aphyric mafic cone-sheet* | N454 | 19.001 | 0.014 | 15.638 | 0.014 | 38.944 | 0.014 |

## 2.8. Age corrected isotope data

### *2.8.1. Strontium*

| Sample | Rock type | Lab Number | Age (Ma) | Rb ppm | Sr ppm | $^{87}Sr/^{86}Sr$ measured | $^{87}Sr/^{86}Sr$ age-corrected |
|---|---|---|---|---|---|---|---|
| **C4** | *Gabbro* | *D831* | 61.4 | 4 | 270 | 0.705709 | 0.705675 |
| **C7** | *Gabbro* | *D830* | 61.4 | 4 | 241 | 0.705788 | 0.705743 |
| **LWG1** | *Microgranite* | *D832* | 61.4 | 216 | 44 | 0.724407 | 0.712026 |
| **LWG2** | *Microgranite* | *D925* | 61.4 | 184 | 57 | 0.714334 | 0.706248 |
| **288-8a** | *Cone-sheet rhyolite* | *D834* | 60 | 208 | 64 | 0.717505 | 0.709482 |
| **284-8c** | *Cone-sheet rhyolite* | *D833* | 60 | 206 | 66 | 0.717366 | 0.709662 |
| **C-CS4-1711a** | *Cone-sheet trachy-andesite* | *D852* | 60 | 245 | 246 | 0.722428 | 0.719968 |
| **CS4B2** | *Cone-sheet trachy-andesite* | *D853* | 60 | 169 | 177 | 0.722264 | 0.719906 |
| **CS4B2** *unleached* | *Cone-sheet trachy-andesite* | *E439* | | | | Failed | |
| **CS4A** | *Cone-sheet trachy-andesite* | *E442* | 60 | 219 | 239 | 0.722601 | 0.720338 |
| **CS4A** ***re-run*** | *Cone-sheet trachy-andesite* | *D854* | 60 | 219 | 239 | 0.722266 | 0.720003 |
| **CS4B** | *Cone-sheet trachy-andesite* | *D855* | 60 | 240 | 251 | 0.722048 | 0.719687 |
| **C-PD-9** | *Porphyritic mafic cone-sheet* | *E444* | 60 | 25 | 211 | 0.706678 | 0.706386 |
| **C-PD-9** ***re-run*** | *Porphyritic mafic cone-sheet* | *D856* | 60 | 25 | 211 | 0.706668 | 0.706376 |
| **C-Cs12-GM** | *Porphyritic mafic cone-sheet* | *D919* | 60 | 33 | 207 | 0.707921 | 0.707527 |
| **C-Cs12-GM** *re-run* | *Porphyritic mafic cone-sheet* | *D857* | | | | Failed | |

| Sample | Rock type | Lab Number | Age (Ma) | Rb ppm | Sr ppm | $^{87}Sr/^{86}Sr$ measured | $^{87}Sr/^{86}Sr$ age-corrected |
|---|---|---|---|---|---|---|---|
| **C-CS5-1711b** | *Porphyritic mafic cone-sheet* | *E443* | 60 | 24 | 225 | 0.707495 | 0.707232 |
| **C-CS5-1711b *re-run*** | *Porphyritic mafic cone-sheet* | *D858* | 60 | 24 | 225 | 0.707791 | 0.707528 |
| **C-VA1 *unleached*** | *Porphyritic mafic cone-sheet* | *E438* | 60 | 15 | 157 | 0.706974 | 0.706738 |
| **C-VA1** | *Porphyritic mafic cone-sheet* | *E450* | 60 | 15 | 157 | 0.706876 | 0.706640 |
| **C-VA1 re-run** | *Porphyritic mafic cone-sheet* | *D859* | 60 | 15 | 157 | 0.706818 | 0.706583 |
| **GM1** | *Groundmass of porphyry* | *D917* | 60 | 21 | 194 | 0.706684 | 0.706417 |
| **GM1 *Re-run*** | *Groundmass of porphyry* | *D841* | | | | Failed | |
| **C-pdfsp** | *Feldspar separate from porphyry* | *E109* | | | | 0.706294 | |
| **C-CS1-SH** | *Aphyric mafic cone-sheet* | *D918* | 60 | 41 | 172 | 0.709253 | 0.708665 |
| **C-cs-sr** | *Aphyric mafic cone-sheet* | *E865* | 60 | 110 | 227 | 0.714303 | 0.713107 |
| **CB3 *unleached*** | *Aphyric mafic cone-sheet* | *E440* | 60 | 55 | 151 | 0.709515 | 0.708617 |
| **CB3** | *Aphyric mafic cone-sheet* | *E464* | 60 | 55 | 151 | 0.709019 | 0.708121 |
| **CB3 *re-run*** | *Aphyric mafic cone-sheet* | *D861* | 60 | 55 | 151 | 0.708933 | 0.708034 |
| **B4** | *Aphyric mafic cone-sheet* | *D862* | 60 | 65 | 167 | 0.710356 | 0.709396 |
| **CS4C** | *Aphyric mafic cone-sheet* | *E465* | 60 | 65 | 173 | 0.718876 | 0.717948 |
| **CS4C** *re-run* | *Aphyric mafic cone-sheet* | *D863* | 60 | 65 | 173 | 0.718792 | 0.717865 |

### *2.8.2. Neodymium*

| Sample | Rock type | Lab Number | Age (Ma) | Sm ppm | Nd ppm | $^{143}Nd/^{144}Nd$ Measured | $^{143}Nd/^{144}Nd$ age-corrected |
|---|---|---|---|---|---|---|---|
| **C4** | *Gabbro* | *D831* | | | | Failed | |
| **C7** | *Gabbro* | *D830* | 61.4 | 1 | 3 | 0.512606 | 0.512528 |
| **LWG1** | *Microgranite* | *D832* | 61.4 | 4 | 28 | 0.512377 | 0.512343 |
| **LWG2** | *Microgranite* | *D925* | | | | *Not Analysed* | |
| **288-8a** | *Cone-sheet rhyolite* | *D834* | 60 | 10 | 47 | 0.512400 | 0.512350 |
| **284-8c** | *Cone-sheet rhyolite* | *D833* | 60 | 9 | 44 | 0.512425 | 0.512376 |
| **C-CS4-1711a** | *Cone-sheet trachy-andesite* | *D852* | | | | *Not Analysed* | |
| **CS4B2** | *Cone-sheet trachy-andesite* | *D853* | | | | Failed | |
| **CS4B2** *unleached* | *Cone-sheet trachy-andesite* | *E439* | 60 | 5 | 29 | 0.512062 | 0.512019 |
| **CS4A** | *Cone-sheet trachy-andesite* | *E442* | | | | *Not Analysed* | |
| **CS4A** ***re-run*** | *Cone-sheet trachy-andesite* | *D854* | 60 | *6* | *33* | 0.512044 | 0.512001 |
| **CS4B** | *Cone-sheet trachy-andesite* | *D855* | 60 | 6 | 34 | 0.511986 | 0.511943 |
| **C-PD-9** | *Porphyritic mafic cone-sheet* | *E444* | | | | *Not Analysed* | |
| **C-PD-9** ***re-run*** | *Porphyritic mafic cone-sheet* | *D856* | | | | Failed | |
| **C-Cs12-GM** | *Porphyritic mafic cone-sheet* | *D919* | 60 | *3* | *14* | 0.512448 | 0.512389 |
| **C-Cs12-GM** *re-run* | *Porphyritic mafic cone-sheet* | *D857* | 60 | 3 | 14 | 0.512359 | 0.512300 |

| Sample | Rock type | Lab Number | Age (Ma) | Sm ppm | Nd ppm | $^{143}Nd/^{144}Nd$ Measured | $^{143}Nd/^{144}Nd$ age-corrected |
|---|---|---|---|---|---|---|---|
| **C-CS5-1711b** | *Porphyritic mafic cone-sheet* | *E443* | | | | *Not Analysed* | |
| **C-CS5-1711b *re-run*** | *Porphyritic mafic cone-sheet* | *D858* | | | | *Not Analysed* | |
| **C-VA1 *unleached*** | *Porphyritic mafic cone-sheet* | *E438* | 60 | 2 | 8 | 0.512482 | 0.512413 |
| **C-VA1** | *Porphyritic mafic cone-sheet* | *E450* | | | | *Not Analysed* | |
| **C-VA1 *re-run*** | *Porphyritic mafic cone-sheet* | *D859* | | | | *Not Analysed* | |
| **GM1** | *Groundmass of porphyry* | *D917* | 60 | 5 | 19 | 0.512496 | 0.512434 |
| **GM1 *Re-run*** | *Groundmass of porphyry* | *D841* | 60 | 5 | 19 | 0.512049 | 0.5120 |
| **C-pdfsp** | *Feldspar separate from porphyry* | *E109* | | | | Failed | |
| **C-CS1-SH** | *Aphyric mafic cone-sheet* | *D918* | 60 | 5 | 17 | 0.512535 | 0.512472 |
| **C-cs-sr** | *Aphyric mafic cone-sheet* | *E865* | | | | *Not Analysed* | |
| **CB3 *unleached*** | *Aphyric mafic cone-sheet* | *E440* | 60 | 6 | 27 | 0.512298 | 0.512241 |
| **CB3** | *Aphyric mafic cone-sheet* | *E464* | | | | *Not Analysed* | |
| **CB3 *re-run*** | *Aphyric mafic cone-sheet* | *D861* | | | | *Not Analysed* | |
| **B4** | *Aphyric mafic cone-sheet* | *D862* | 60 | 7 | 30 | 0.512419 | 0.512363 |
| **CS4C** | *Aphyric mafic cone-sheet* | *E465* | | | | *Not Analysed* | |
| **CS4C** *re-run* | *Aphyric mafic cone-sheet* | *D863* | | | | Failed | |

### *2.8.3. Lead*

| Sample | Rock Type | Lab Number | Age (Ma) | U (ppm) | Th (ppm) | Pb (ppm) | $^{206}Pb/^{204}Pb$ age-corrected | $^{207}Pb/^{204}Pb$ age-corrected | $^{208}Pb/^{204}Pb$ age-corrected |
|---|---|---|---|---|---|---|---|---|---|
| **C7** | *Gabbro* | N476 | 61.4 | 0.2 | 0.4 | 2.6 | 18.660 | 15.581 | 38.390 |
| **LWG1** | *Microgranite* | N480 | 61.4 | 3.5 | 20.3 | 25.8 | 18.885 | 15.644 | 38.745 |
| **LWG2** | *Microgranite* | D925 | 61.4 | 4.3 | 30.4 | 17.5 | 19.063 | 15.778 | 39.325 |
| **288-8a** | *Cone-sheet rhyolite* | N479 | 60 | 4.6 | 21.5 | 19.1 | 18.837 | 15.626 | 38.629 |
| **C-CS4-1711a** | *Cone-sheet trachy-andesite* | N458 | 60 | 3.0 | 11.2 | 43.0 | 18.742 | 15.620 | 38.682 |
| **CS4B2** | *Cone-sheet trachy-andesite* | N452 | 60 | 2.8 | 10.8 | 12.4 | 18.774 | 15.614 | 38.648 |
| **CS4A** | *Cone-sheet trachy-andesite* | N455 | 60 | 3.0 | 11.6 | 31.1 | 18.744 | 15.616 | 38.668 |
| **CS4B** | *Cone-sheet trachy-andesite* | N477 | 60 | 3.0 | 11.5 | 34.1 | 18.780 | 15.648 | 38.743 |
| **C-PD-9** | *Porphyritic mafic cone-sheet* | N457 | 60 | 0.2 | 1.4 | 9.5 | 18.537 | 15.602 | 38.492 |
| **C-Cs12-GM** | *Porphyritic mafic cone-sheet* | D919 | 60 | 0.4 | 2.2 | 21.0 | 18.789 | 15.629 | 38.730 |
| **C-CS5-1711b** | *Porphyritic mafic cone-sheet* | N456 | 60 | 0.5 | 1.9 | 8.7 | 18.609 | 15.611 | 38.608 |
| **C-VA1** | *Porphyritic mafic cone-sheet* | N451 | 60 | 0.8 | 3.3 | 6.1 | 18.613 | 15.606 | 38.580 |
| **GM1** | *Groundmass of porphyry* | D917 | 60 | 0.5 | 2.9 | 5.2 | 18.629 | 15.647 | 38.635 |

| Sample | Rock Type | Lab Number | Age (Ma) | U (ppm) | Th (ppm) | Pb (ppm) | $^{206}Pb/^{204}Pb$ age-corrected | $^{207}Pb/^{204}Pb$ age-corrected | $^{208}Pb/^{204}Pb$ age-corrected |
|---|---|---|---|---|---|---|---|---|---|
| **C-CS1-SH** | *Aphyric mafic cone-sheet* | D918 | 60 | 0.7 | 2.9 | 8.9 | 18.966 | 15.640 | 38.971 |
| **C-cs-sr** | *Aphyric mafic cone-sheet* | E877 | 60 | 3.5 | 9.3 | 56.3 | 18.637 | 15.620 | 38.513 |
| **CB3** | *Aphyric mafic cone-sheet* | N453 | 60 | 1.3 | 6.9 | 10.9 | 18.696 | 15.635 | 38.818 |
| **B4** | *Aphyric mafic cone-sheet* | N478 | 60 | 1.8 | 6.8 | 22.5 | 18.796 | 15.627 | 38.683 |
| **CS4C** | *Aphyric mafic cone-sheet* | E878 | 60 | 2.5 | 9.6 | 10.0 | 19.811 | 15.627 | 38.774 |
| **CS4C** *re-run* | *Aphyric mafic cone-sheet* | N454 | 60 | 2.5 | 10.0 | 11.8 | 18.873 | 15.632 | 38.777 |

## 2.9. Microdrilled strontium data

### *2.9.1. Raw strontium isotope ratios*

| Sample | Rock type | Lab Number | $^{87}Sr/^{86}Sr$ measured | 87Sr/86Sr corrected for standards * | % S.E. | 2 S.E. | 2S.D. |
|---|---|---|---|---|---|---|---|
| **CSRB 11** | *Feldspar core* | **M23-8** | 0.707183 | 0.707164 | 0.000010 | 0.000020 | 0.000020 |
| **CSRB 11** | *Feldspar rim* | **M23-10** | 0.706938 | 0.706919 | 0.000008 | 0.000016 | 0.000016 |
| **CSRB 11** | *Feldspar rim* | **M23-14** | 0.706996 | 0.706977 | 0.000006 | 0.000013 | 0.000013 |
| **CSRB 1** | *Feldspar core* | **M23-11** | 0.706366 | 0.706347 | 0.000011 | 0.000022 | 0.000022 |
| **CSRB 1** | *Feldspar middle zone* | **M23-12** | 0.706563 | 0.706544 | 0.000005 | 0.000011 | 0.000011 |
| **CSRB 1** | *Feldspar rim* | **M23-13** | 0.706469 | 0.706450 | 0.000006 | 0.000013 | 0.000013 |
| **PD9** | *Feldspar core* | **M23-20** | 0.706300 | 0.706281 | 0.000009 | 0.000019 | 0.000019 |
| **PD9** | *Feldspar rim* | **M23-21** | 0.706621 | 0.706602 | 0.000011 | 0.000022 | 0.000022 |
| **PD9** | *Groundmass* | **M23-22** | 0.706966 | 0.706947 | 0.000013 | 0.000027 | 0.000027 |

*** Data normalised to an NBS 987 87Sr/86Sr value of 0.710240**

### *2.9.2. Age-corrected strontium isotope ratios*

| Sample | Rock type | Lab Number | Age (Ma) | Rb ppm | Sr ppm | $^{87}Sr/^{86}Sr$ measured | $^{87}Sr/^{86}Sr$ age-corrected |
|---|---|---|---|---|---|---|---|
| **CSRB 11** | *Feldspar core* | **M23-8** | 60 | 5 | 84 | 0.707164 | 0.707003 |
| **CSRB 11** | *Feldspar rim* | **M23-10** | 60 | 5 | 124 | 0.706919 | 0.706813 |
| **CSRB 11** | *Feldspar rim* | **M23-14** | 60 | 4 | 157 | 0.706977 | 0.706389 |
| **CSRB 1** | *Feldspar core* | **M23-11** | 60 | 3 | 232 | 0.706347 | 0.706947 |
| **CSRB 1** | *Feldspar middle zone* | **M23-12** | 60 | 1 | 114 | 0.706544 | 0.706315 |
| **CSRB 1** | *Feldspar rim* | **M23-13** | 60 | 4 | 167 | 0.706450 | 0.706489 |
| **PD9** | *Feldspar core* | **M23-20** | 60 | 2 | 123 | 0.706281 | 0.706247 |
| **PD9** | *Feldspar rim* | **M23-21** | 60 | 2 | 74 | 0.706602 | 0.706548 |
| **PD9** | *Groundmass* | **M23-22** | 60 | 13 | 70 | 0.706947 | 0.706490 |

## 2.10. Microprobe data

### *2.10.1.Sample CSRB – feldspar 1*

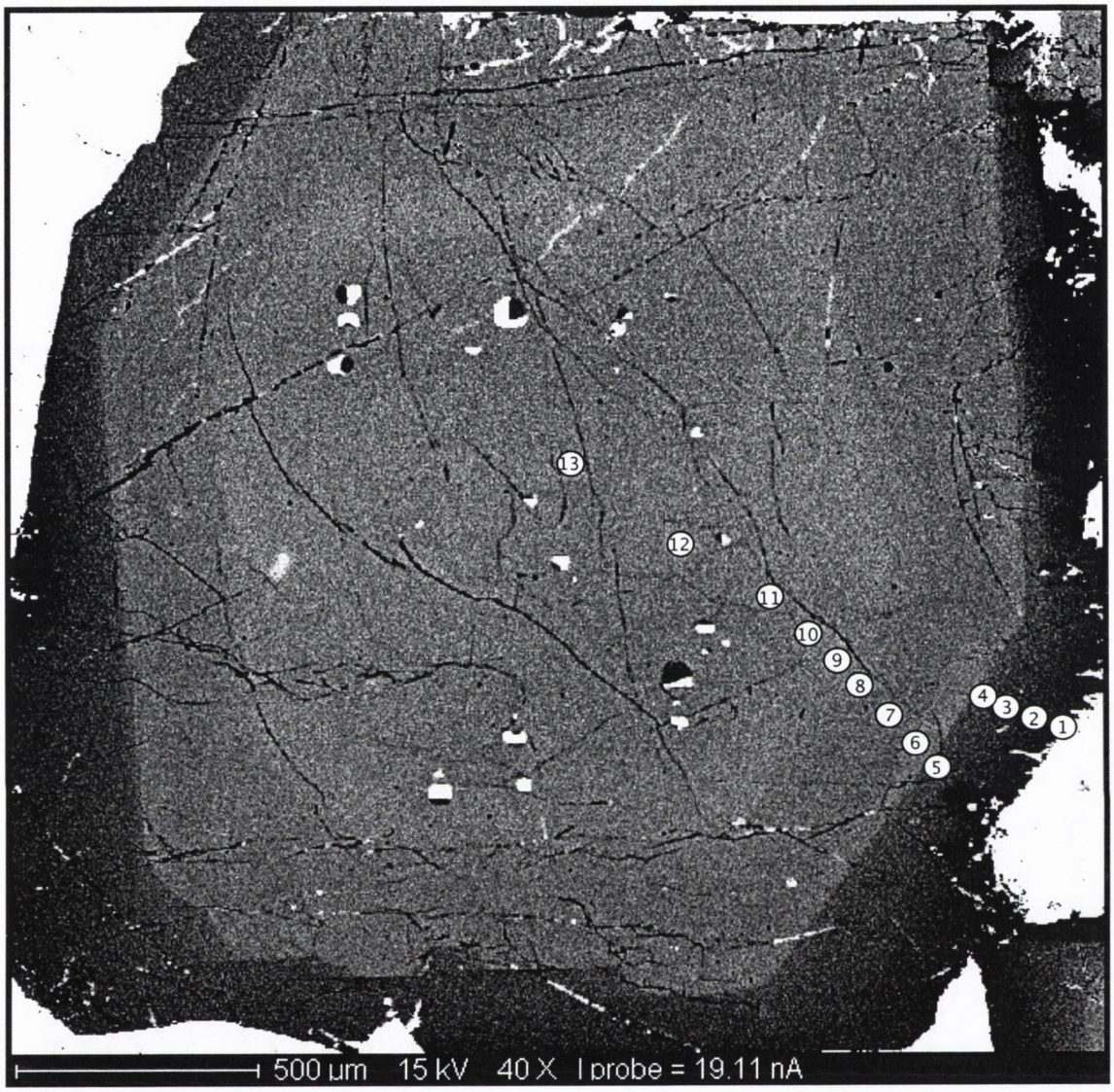

| Sample Name | CSRB | CSRB | CSRB | CSRB | CSRB |
|---|---|---|---|---|---|
| **Feldspar number** | *1* | *1* | *1* | *1* | *1* |
| **Point Number** | *1* | *2* | *3* | *4* | *5* |
| **Analysis number** | *144* | *145* | *146* | *147* | *148* |
| **SiO2** | 55.08 | 53.91 | 52.64 | 50.87 | 49.47 |
| **Al2O3** | 27.62 | 28.23 | 29.76 | 29.42 | 31.38 |
| **FeO** | 1.26 | 0.75 | 0.55 | 0.75 | 0.69 |
| **CaO** | 10.93 | 11.64 | 13.07 | 13.86 | 15.46 |
| **Na2O** | 4.88 | 5.02 | 3.89 | 3.18 | 2.98 |
| **K2O** | 0.28 | 0.25 | 0.20 | 0.16 | 0.11 |
| **BaO** | 0.00 | 0.01 | 0.09 | 0.09 | 0.00 |
| **TOTAL** | 100.05 | 99.81 | 100.20 | 98.33 | 100.09 |
| **Or** | *1.66* | *1.42* | *1.17* | *0.96* | *0.62* |
| **Ab** | *43.95* | *43.21* | *34.60* | *29.06* | *25.70* |
| **An** | *54.39* | *55.37* | *64.23* | *69.98* | *73.68* |

| Sample Name | CSRB | CSRB | CSRB | CSRB | CSRB |
|---|---|---|---|---|---|
| **Feldspar number** | *1* | *1* | *1* | *1* | *1* |
| **Point Number** | *6* | *7* | *8* | *9* | *10* |
| **Analysis number** | *149* | *150* | *151* | *152* | *153* |
| **SiO2** | 48.00 | 48.01 | 46.98 | 47.72 | 47.09 |
| **Al2O3** | 32.57 | 32.19 | 33.15 | 32.88 | 32.46 |
| **FeO** | 0.57 | 0.42 | 0.50 | 0.60 | 0.54 |
| **CaO** | 16.63 | 16.29 | 16.88 | 17.28 | 17.15 |
| **Na2O** | 1.93 | 2.04 | 2.20 | 1.46 | 1.68 |
| **K2O** | 0.06 | 0.06 | 0.07 | 0.05 | 0.06 |
| **BaO** | 0.02 | 0.05 | 0.06 | 0.00 | 0.01 |
| **TOTAL** | 99.78 | 99.06 | 99.84 | 99.99 | 98.99 |
| **Or** | *0.35* | *0.36* | *0.40* | *0.30* | *0.35* |
| **Ab** | *17.30* | *18.41* | *19.01* | *13.22* | *15.00* |
| **An** | *82.35* | *81.23* | *80.59* | *86.48* | *84.64* |

| Sample Name | CSRB | CSRB | CSRB |
|---|---|---|---|
| **Feldspar number** | *1* | *1* | *1* |
| **Point Number** | *11* | *12* | *13* |
| **Analysis number** | *154* | *155* | *156* |
| **SiO2** | 47.63 | 46.53 | 47.56 |
| **Al2O3** | 33.31 | 33.43 | 33.34 |
| **FeO** | 0.36 | 0.35 | 0.55 |
| **CaO** | 16.99 | 17.08 | 17.37 |
| **Na2O** | 1.65 | 1.79 | 1.83 |
| **K2O** | 0.05 | 0.05 | 0.06 |
| **BaO** | 0.02 | 0.00 | 0.00 |
| **TOTAL** | 100.01 | 99.23 | 100.71 |
| **Or** | *0.30* | *0.29* | *0.34* |
| **Ab** | *14.90* | *15.90* | *15.96* |
| **An** | *84.80* | *83.81* | *83.70* |

### *2.10.2.Sample CSRB – feldspar 2*

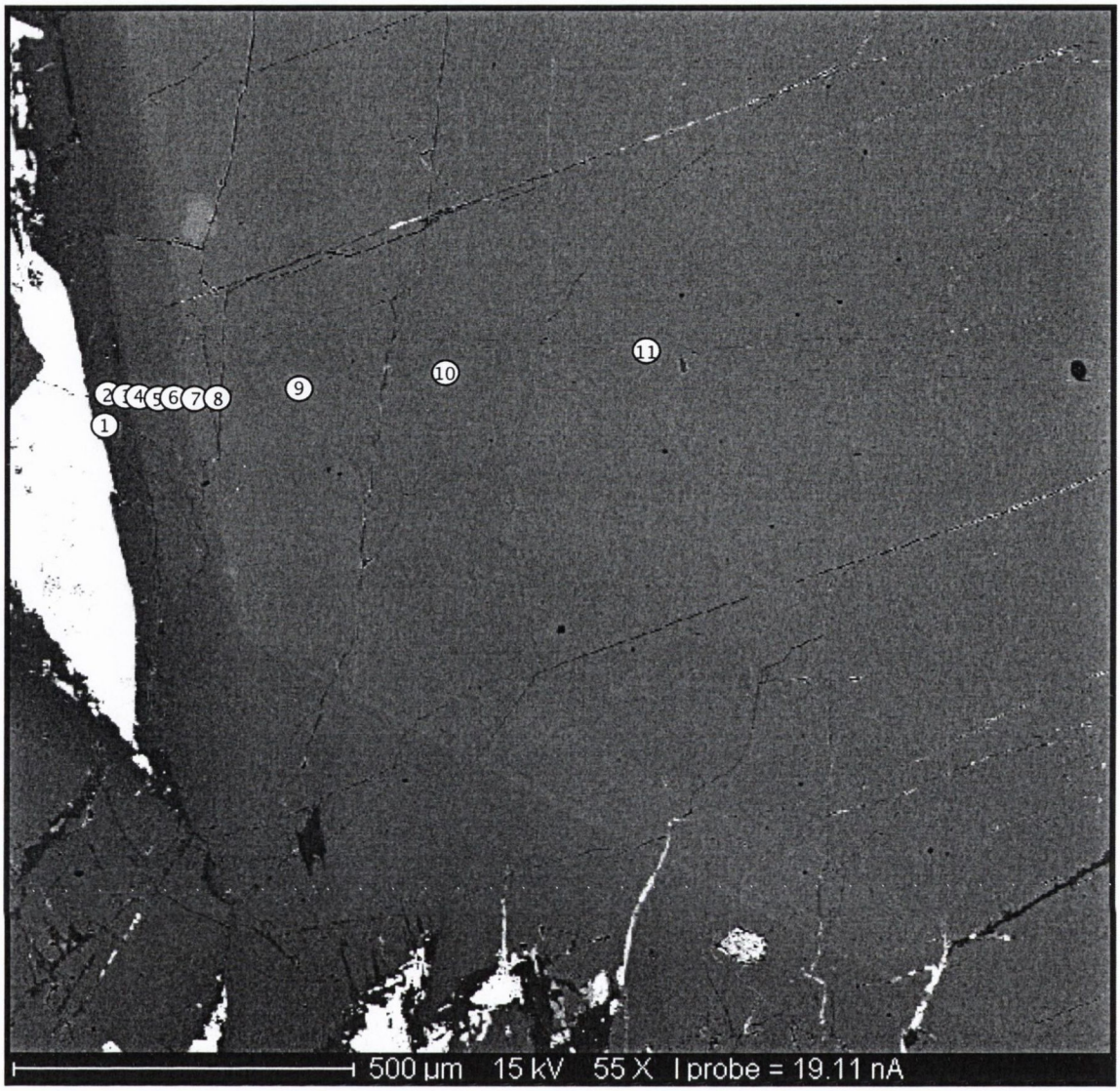

| Sample Name | CSRB | CSRB | CSRB | CSRB | CSRB |
|---|---|---|---|---|---|
| **Feldspar number** | *2* | *2* | *2* | *2* | *2* |
| **Point Number** | *1* | *2* | *3* | *4* | *5* |
| **Analysis number** | *109* | *110* | *111* | *112* | *113* |
| **SiO2** | 60.08 | 58.67 | 55.80 | 56.26 | 51.49 |
| **Al2O3** | 25.30 | 25.93 | 25.41 | 28.19 | 29.27 |
| **FeO** | 0.48 | 0.56 | 2.84 | 0.63 | 0.69 |
| **CaO** | 7.32 | 8.14 | 8.42 | 10.53 | 13.50 |
| **Na2O** | 6.83 | 6.08 | 5.58 | 4.98 | 3.52 |
| **K2O** | 0.32 | 1.12 | 0.44 | 0.30 | 0.19 |
| **BaO** | 0.06 | 0.03 | 0.07 | 0.03 | 0.00 |
| **TOTAL** | 100.39 | 100.53 | 98.56 | 100.92 | 98.66 |
| **Or** | *1.90* | *6.51* | *2.75* | *1.80* | *1.13* |
| **Ab** | *61.61* | *53.73* | *53.03* | *45.29* | *31.70* |
| **An** | *36.49* | *39.75* | *44.22* | *52.92* | *67.18* |

| Sample Name | CSRB | CSRB | CSRB | CSRB | CSRB |
|---|---|---|---|---|---|
| **Feldspar number** | *2* | *2* | *2* | *2* | *2* |
| **Point Number** | *6* | *7* | *8* | *9* | *10* |
| **Analysis number** | *114* | *115* | *116* | *117* | *118* |
| **SiO2** | 52.52 | 50.02 | 47.81 | 47.11 | 47.62 |
| **Al2O3** | 30.00 | 31.06 | 32.71 | 32.56 | 33.34 |
| **FeO** | 0.79 | 0.45 | 0.46 | 0.55 | 0.40 |
| **CaO** | 13.61 | 15.11 | 16.77 | 16.62 | 16.77 |
| **Na2O** | 3.40 | 2.81 | 1.90 | 2.22 | 1.76 |
| **K2O** | 0.18 | 0.11 | 0.05 | 0.09 | 0.07 |
| **BaO** | 0.00 | 0.00 | 0.06 | 0.00 | 0.01 |
| **TOTAL** | 100.50 | 99.56 | 99.76 | 99.15 | 99.97 |
| **Or** | *1.07* | *0.64* | *0.29* | *0.52* | *0.42* |
| **Ab** | *30.80* | *25.02* | *16.96* | *19.37* | *15.89* |
| **An** | *68.13* | *74.34* | *82.74* | *80.12* | *83.69* |

| Sample Name | CSRB |
|---|---|
| **Feldspar number** | *2* |
| **Point Number** | *11* |
| **Analysis number** | *119* |
| **SiO2** | 47.19 |
| **Al2O3** | 33.02 |
| **FeO** | 0.51 |
| **CaO** | 17.26 |
| **Na2O** | 1.39 |
| **K2O** | 0.05 |
| **BaO** | 0.00 |
| **TOTAL** | 99.42 |
| **Or** | *0.30* |
| **Ab** | *12.68* |
| **An** | *87.02* |

### *2.10.3.Sample CSRB – feldspar 10*

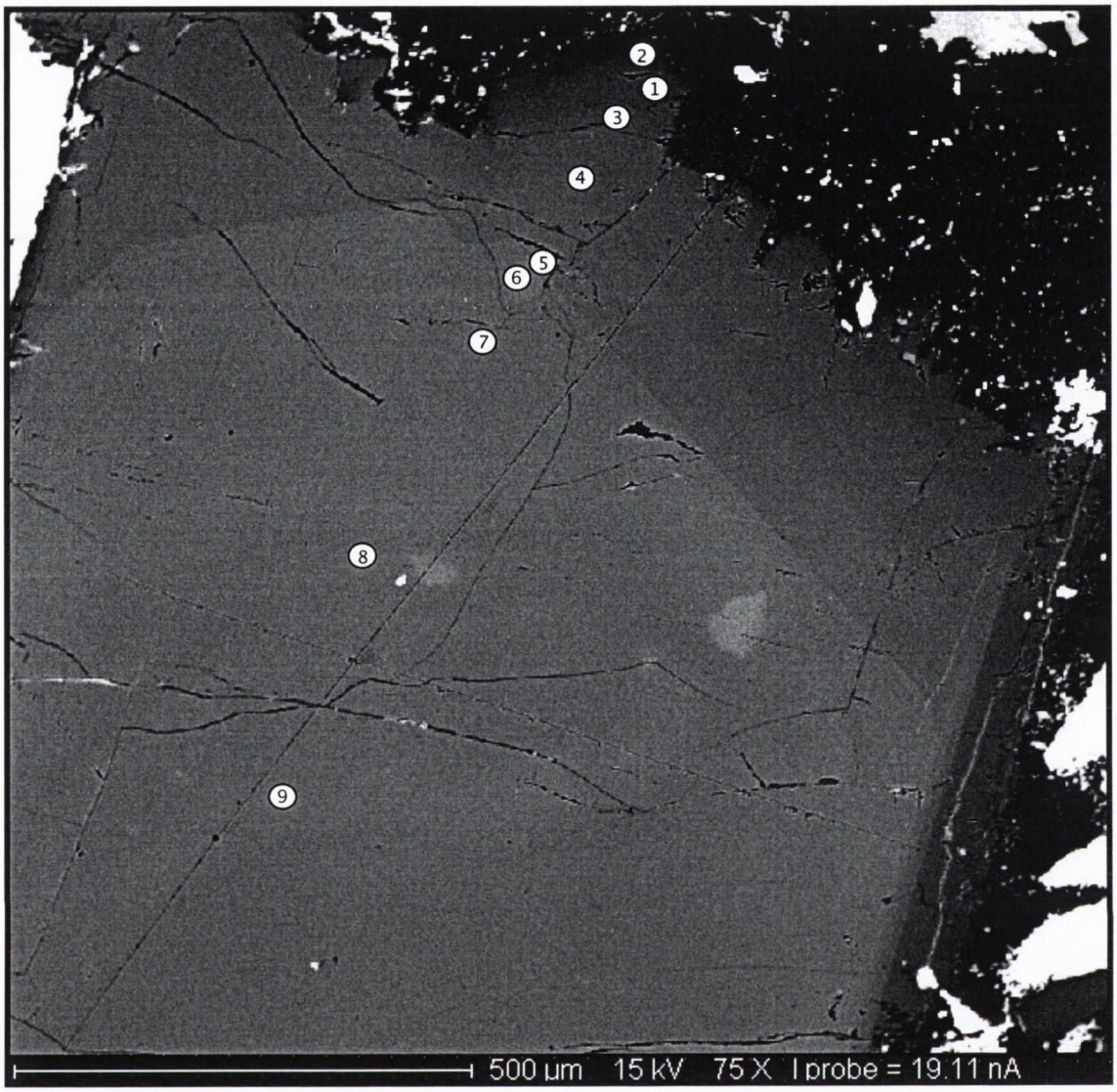

| Sample Name | CSRB | CSRB | CSRB | CSRB | CSRB |
|---|---|---|---|---|---|
| **Feldspar number** | *10* | *10* | *10* | *10* | *10* |
| **Point Number** | *1* | *2* | *3* | *4* | *5* |
| **Analysis number** | *54* | *55* | *56* | *57* | *58* |
| **SiO2** | 58.82 | 65.33 | 55.56 | 51.69 | 49.94 |
| **Al2O3** | 27.15 | 23.92 | 28.57 | 30.81 | 31.65 |
| **FeO** | 0.59 | 0.27 | 0.58 | 0.67 | 0.65 |
| **CaO** | 8.89 | 4.58 | 11.36 | 14.17 | 15.36 |
| **Na2O** | 4.74 | 6.39 | 4.83 | 3.45 | 1.66 |
| **K2O** | 0.45 | 0.46 | 0.26 | 0.17 | 0.10 |
| **BaO** | 0.03 | 0.16 | 0.08 | 0.01 | 0.00 |
| **TOTAL** | 100.67 | 101.11 | 101.24 | 100.97 | 99.36 |
| **Or** | *2.98* | *3.28* | *1.52* | *0.98* | *0.64* |
| **Ab** | *47.64* | *69.28* | *42.82* | *30.28* | *16.25* |
| **An** | *49.38* | *27.44* | *55.66* | *68.73* | *83.10* |

| Sample Name | CSRB | CSRB | CSRB | CSRB | CSRB |
|---|---|---|---|---|---|
| **Feldspar number** | *10* | *10* | *10* | *10* | *10* |
| **Point Number** | *6* | *7* | *8* | *9* | *10* |
| **Analysis number** | *59* | *60* | *61* | *62* | *63* |
| **SiO2** | 47.98 | 47.95 | 48.45 | 48.82 | 60.01 |
| **Al2O3** | 33.38 | 33.65 | 32.40 | 32.51 | 26.01 |
| **FeO** | 0.53 | 0.43 | 0.64 | 0.51 | 0.52 |
| **CaO** | 17.07 | 17.38 | 16.66 | 16.38 | 7.69 |
| **Na2O** | 1.75 | 1.39 | 1.85 | 2.21 | 6.54 |
| **K2O** | 0.07 | 0.06 | 0.08 | 0.07 | 0.52 |
| **BaO** | 0.03 | 0.02 | 0.05 | 0.02 | 0.06 |
| **TOTAL** | 100.81 | 100.88 | 100.13 | 100.52 | 101.35 |
| **Or** | *0.41* | *0.36* | *0.47* | *0.41* | *3.07* |
| **Ab** | *15.58* | *12.60* | *16.65* | *19.54* | *58.75* |
| **An** | *84.01* | *87.04* | *82.87* | *80.05* | *38.18* |

| Sample Name | CSRB |
|---|---|
| **Feldspar number** | *10* |
| **Point Number** | *11* |
| **Analysis number** | *64* |
| **SiO2** | 63.67 |
| **Al2O3** | 23.94 |
| **FeO** | 0.66 |
| **CaO** | 4.65 |
| **Na2O** | 5.22 |
| **K2O** | 0.40 |
| **BaO** | 0.01 |
| **TOTAL** | 98.55 |
| **Or** | *3.27* |
| **Ab** | *64.82* |
| **An** | *31.91* |

### *2.10.4.Sample CSRB – feldspar 11*

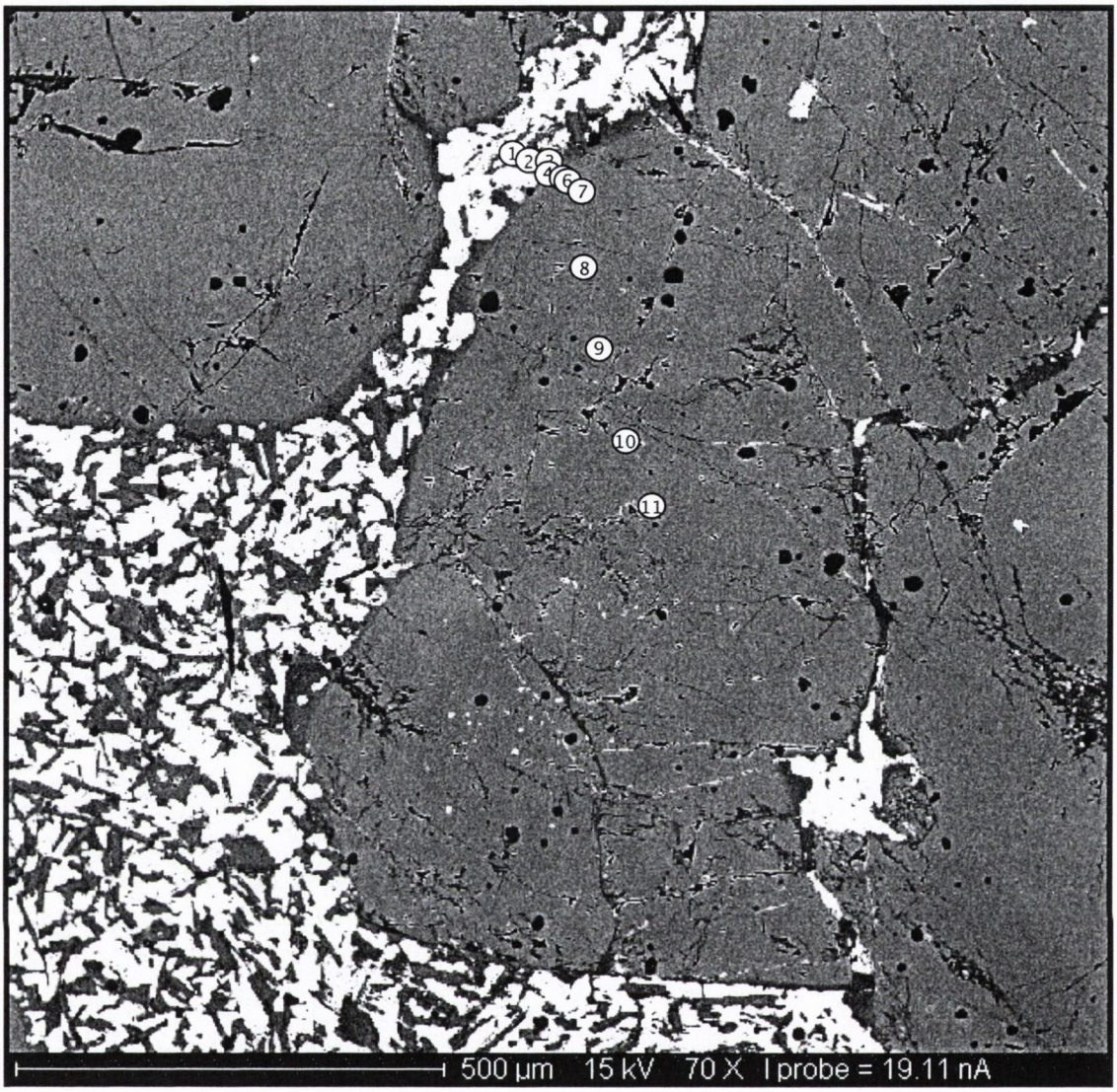

| Sample Name | CSRB | CSRB | CSRB | CSRB | CSRB |
|---|---|---|---|---|---|
| **Feldspar number** | *11* | *11* | *11* | *11* | *11* |
| **Point Number** | *1* | *2* | *3* | *4* | *5* |
| **Analysis number** | *93* | *94* | *95* | *96* | *97* |
| **SiO2** | 71.09 | 63.23 | 61.22 | 60.69 | 58.58 |
| **Al2O3** | 21.28 | 24.79 | 25.66 | 26.09 | 26.90 |
| **FeO** | 0.15 | 0.35 | 0.42 | 0.52 | 0.55 |
| **CaO** | 0.70 | 5.61 | 7.14 | 7.78 | 8.89 |
| **Na2O** | 5.56 | 5.70 | 5.64 | 5.62 | 5.74 |
| **K2O** | 0.06 | 0.37 | 0.56 | 0.50 | 0.35 |
| **BaO** | 0.07 | 0.11 | 0.12 | 0.01 | 0.10 |
| **TOTAL** | 98.91 | 100.16 | 100.76 | 101.21 | 101.11 |
| **Or** | *0.66* | *2.69* | *3.70* | *3.21* | *2.12* |
| **Ab** | *92.88* | *63.03* | *56.66* | *54.84* | *52.74* |
| **An** | *6.46* | *34.28* | *39.64* | *41.95* | *45.14* |

| Sample Name | CSRB | CSRB | CSRB | CSRB | CSRB |
|---|---|---|---|---|---|
| **Feldspar number** | *11* | *11* | *11* | *11* | *11* |
| **Point Number** | *6* | *7* | *8* | *9* | *10* |
| **Analysis number** | *98* | *99* | *100* | *101* | *102* |
| **SiO2** | 57.18 | 54.68 | 53.33 | 51.55 | 50.29 |
| **Al2O3** | 27.26 | 28.58 | 29.53 | 30.09 | 31.14 |
| **FeO** | 0.62 | 0.68 | 0.65 | 0.67 | 0.63 |
| **CaO** | 9.86 | 11.47 | 12.50 | 13.96 | 14.81 |
| **Na2O** | 5.16 | 4.42 | 3.62 | 3.04 | 2.50 |
| **K2O** | 0.33 | 0.27 | 0.22 | 0.15 | 0.13 |
| **BaO** | 0.03 | 0.00 | 0.01 | 0.08 | 0.06 |
| **TOTAL** | 100.44 | 100.10 | 99.86 | 99.54 | 99.56 |
| **Or** | *2.01* | *1.62* | *1.36* | *0.91* | *0.79* |
| **Ab** | *47.66* | *40.42* | *33.92* | *28.01* | *23.21* |
| **An** | *50.33* | *57.96* | *64.72* | *71.08* | *75.99* |

| Sample Name | CSRB | CSRB | CSRB | CSRB | CSRB |
|---|---|---|---|---|---|
| **Feldspar number** | *11* | *11* | *11* | *11* | *11* |
| **Point Number** | *11* | *12* | *13* | *14* | *15* |
| **Analysis number** | *103* | *104* | *105* | *106* | *107* |
| **SiO2** | 49.42 | 47.88 | 48.17 | 47.44 | 47.09 |
| **Al2O3** | 31.79 | 32.76 | 32.80 | 33.27 | 33.40 |
| **FeO** | 0.51 | 0.47 | 0.53 | 0.55 | 0.52 |
| **CaO** | 15.31 | 16.59 | 16.55 | 17.07 | 17.19 |
| **Na2O** | 2.88 | 2.02 | 1.70 | 1.66 | 1.57 |
| **K2O** | 0.10 | 0.07 | 0.06 | 0.06 | 0.08 |
| **BaO** | 0.01 | 0.03 | 0.02 | 0.03 | 0.00 |
| **TOTAL** | 100.02 | 99.82 | 99.83 | 100.08 | 99.85 |
| **Or** | *0.58* | *0.41* | *0.36* | *0.35* | *0.47* |
| **Ab** | *25.25* | *17.98* | *15.62* | *14.91* | *14.12* |
| **An** | *74.17* | *81.61* | *84.02* | *84.73* | *85.41* |

| Sample Name | CSRB |
|---|---|
| **Feldspar number** | *11* |
| **Point Number** | *16* |
| **Analysis number** | *108* |
| **SiO2** | 46.30 |
| **Al2O3** | 33.09 |
| **FeO** | 0.60 |
| **CaO** | 17.35 |
| **Na2O** | 1.68 |
| **K2O** | 0.06 |
| **BaO** | 0.01 |
| **TOTAL** | 99.09 |
| **Or** | *0.35* |
| **Ab** | *14.86* |
| **An** | *84.79* |

### *2.10.5.Sample CSRB – feldspar 15*

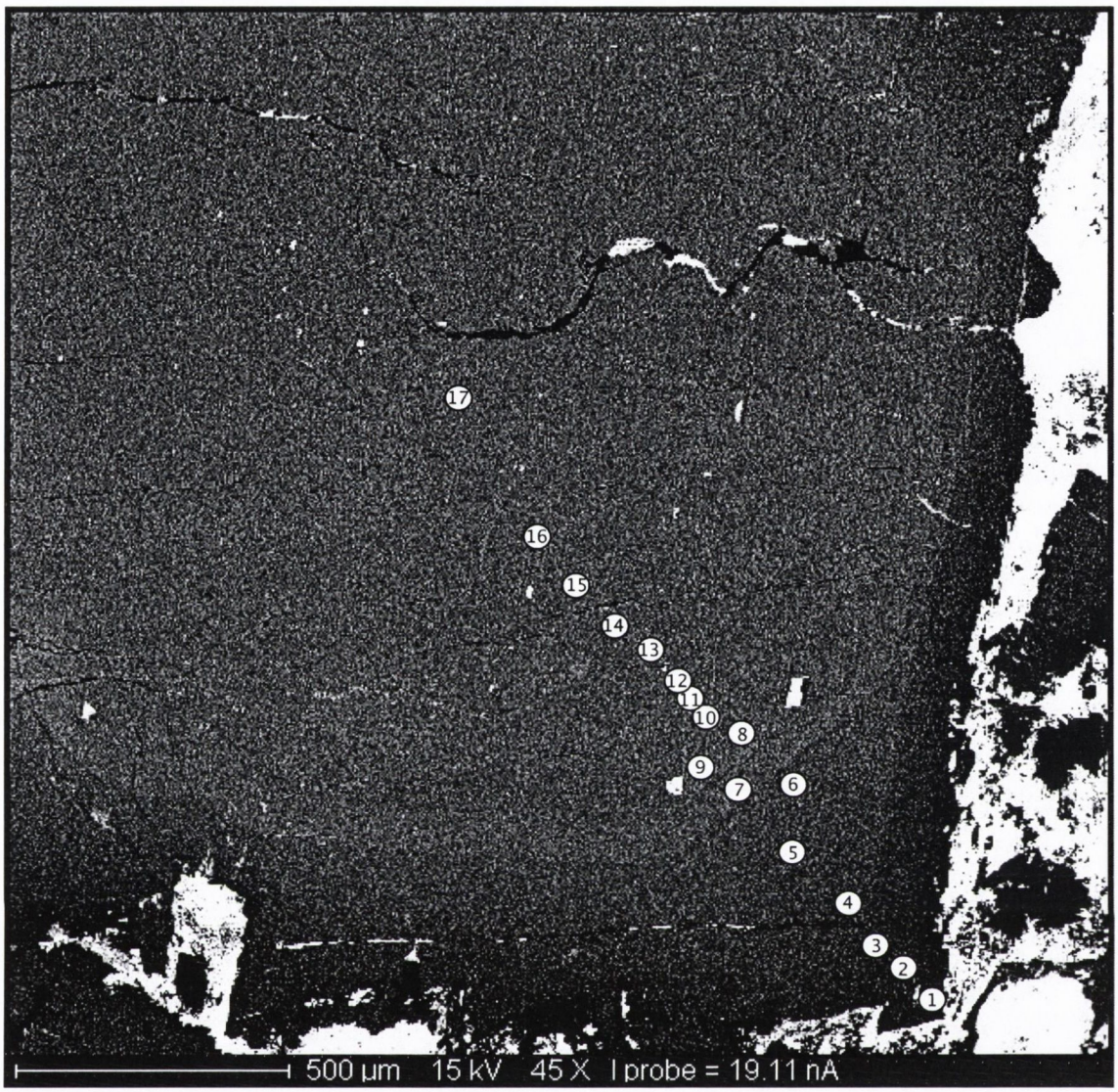

| Sample Name | CSRB | CSRB | CSRB | CSRB | CSRB |
|---|---|---|---|---|---|
| **Feldspar number** | *15* | *15* | *15* | *15* | *15* |
| **Point Number** | *1* | *2* | *3* | *4* | *5* |
| **Analysis number** | *37* | *38* | *39* | *40* | *41* |
| **SiO2** | 63.75 | 57.30 | 56.85 | 54.49 | 51.94 |
| **Al2O3** | 23.57 | 26.42 | 26.93 | 28.73 | 30.40 |
| **FeO** | 0.62 | 0.71 | 0.67 | 0.81 | 0.66 |
| **CaO** | 4.48 | 8.87 | 9.50 | 11.68 | 14.02 |
| **Na2O** | 7.41 | 6.24 | 5.68 | 4.52 | 3.61 |
| **K2O** | 0.42 | 0.41 | 0.33 | 0.26 | 0.14 |
| **BaO** | 0.19 | 0.03 | 0.01 | 0.00 | 0.00 |
| **TOTAL** | 100.44 | 99.98 | 99.97 | 100.49 | 100.77 |
| **Or** | *2.72* | *2.36* | *1.95* | *1.53* | *0.80* |
| **Ab** | *72.92* | *54.68* | *50.96* | *40.55* | *31.53* |
| **An** | *24.36* | *42.95* | *47.10* | *57.91* | *67.67* |

| Sample Name | CSRB | CSRB | CSRB | CSRB | CSRB |
|---|---|---|---|---|---|
| **Feldspar number** | *15* | *15* | *15* | *15* | *15* |
| **Point Number** | *6* | *7* | *8* | *9* | *10* |
| **Analysis number** | *42* | *43* | *44* | *45* | *46* |
| **SiO2** | 50.59 | 47.80 | 19.88 | 47.11 | 48.08 |
| **Al2O3** | 31.23 | 33.16 | 16.97 | 33.28 | 33.47 |
| **FeO** | 0.76 | 0.52 | 0.22 | 0.36 | 0.47 |
| **CaO** | 14.63 | 16.65 | 7.39 | 17.22 | 17.30 |
| **Na2O** | 3.14 | 2.07 | 2.01 | 1.44 | 1.83 |
| **K2O** | 0.15 | 0.08 | 0.05 | 0.04 | 0.04 |
| **BaO** | 0.00 | 0.01 | 0.05 | 0.04 | 0.06 |
| **TOTAL** | 100.50 | 100.29 | 46.57 | 99.49 | 101.25 |
| **Or** | *0.87* | *0.46* | *0.54* | *0.24* | *0.23* |
| **Ab** | *27.73* | *18.28* | *32.81* | *13.11* | *16.03* |
| **An** | *71.40* | *81.25* | *66.66* | *86.65* | *83.74* |

| Sample Name | CSRB | CSRB | CSRB | CSRB | CSRB |
|---|---|---|---|---|---|
| **Feldspar number** | *15* | *15* | *15* | *15* | *15* |
| **Point Number** | *11* | *12* | *13* | *14* | *15* |
| **Analysis number** | *47* | *48* | *49* | *50* | *51* |
| **SiO2** | 47.71 | 47.08 | 47.12 | 46.39 | 47.49 |
| **Al2O3** | 33.05 | 33.95 | 33.63 | 33.83 | 33.46 |
| **FeO** | 0.61 | 0.32 | 0.45 | 0.45 | 0.48 |
| **CaO** | 16.85 | 16.98 | 17.14 | 17.46 | 17.22 |
| **Na2O** | 1.67 | 1.96 | 1.78 | 1.56 | 1.91 |
| **K2O** | 0.05 | 0.07 | 0.08 | 0.05 | 0.08 |
| **BaO** | 0.00 | 0.08 | 0.00 | 0.02 | 0.06 |
| **TOTAL** | 99.94 | 100.44 | 100.20 | 99.76 | 100.70 |
| **Or** | *0.30* | *0.40* | *0.47* | *0.29* | *0.46* |
| **Ab** | *15.16* | *17.21* | *15.75* | *13.88* | *16.64* |
| **An** | *84.54* | *82.39* | *83.79* | *85.83* | *82.90* |

| Sample Name | CSRB | CSRB |
|---|---|---|
| **Feldspar number** | *15* | *15* |
| **Point Number** | *16* | *17* |
| **Analysis number** | *52* | *53* |
| **SiO2** | 47.60 | 47.30 |
| **Al2O3** | 33.34 | 33.60 |
| **FeO** | 0.39 | 0.49 |
| **CaO** | 17.42 | 17.21 |
| **Na2O** | 1.61 | 1.62 |
| **K2O** | 0.06 | 0.06 |
| **BaO** | 0.04 | 0.00 |
| **TOTAL** | 100.46 | 100.28 |
| **Or** | *0.35* | *0.35* |
| **Ab** | *14.28* | *14.50* |
| **An** | *85.37* | *85.14* |

### *2.10.6.Sample PD9 – feldspar 1*

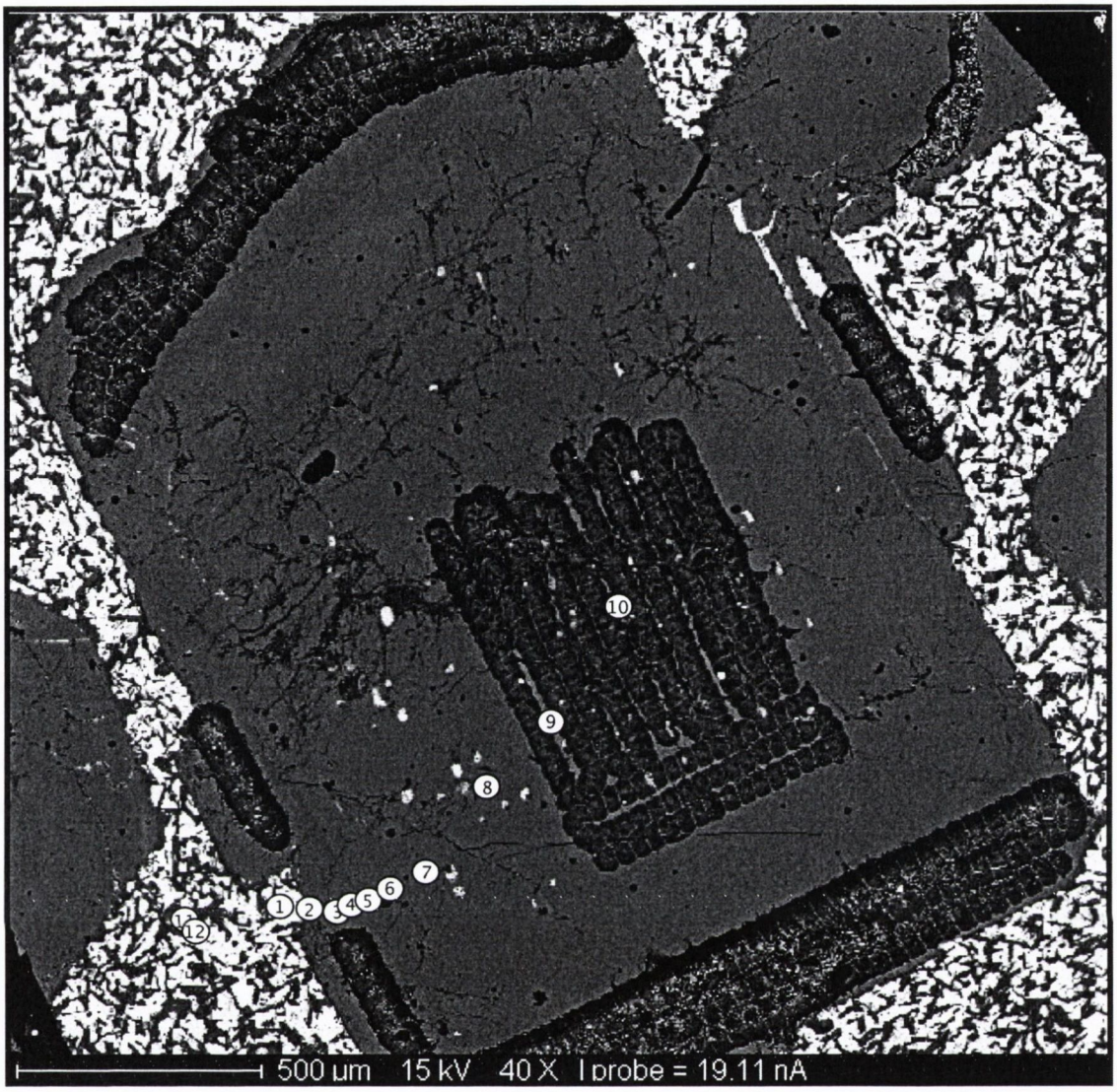

| Sample Name | PD9 | PD9 | PD9 | PD9 | PD9 |
|---|---|---|---|---|---|
| **Feldspar number** | *1* | *1* | *1* | *1* | *1* |
| **Point Number** | *1* | *2* | *3* | *4* | *5* |
| **Analysis number** | *196* | *197* | *198* | *199* | *200* |
| **SiO2** | 54.26 | 53.06 | 48.55 | 48.52 | 48.23 |
| **Al2O3** | 28.88 | 30.35 | 32.86 | 33.05 | 33.26 |
| **FeO** | 0.85 | 0.67 | 0.51 | 0.52 | 0.62 |
| **CaO** | 11.92 | 13.59 | 16.59 | 16.60 | 16.69 |
| **Na2O** | 4.65 | 3.53 | 2.11 | 1.75 | 1.21 |
| **K2O** | 0.13 | 0.15 | 0.09 | 0.04 | 0.08 |
| **BaO** | 0.07 | 0.00 | 0.00 | 0.00 | 0.00 |
| **TOTAL** | 100.76 | 101.35 | 100.71 | 100.48 | 100.09 |
| **Or** | *0.76* | *0.89* | *0.52* | *0.24* | *0.50* |
| **Ab** | *41.07* | *31.69* | *18.61* | *15.98* | *11.54* |
| **An** | *58.18* | *67.42* | *80.87* | *83.78* | *87.96* |

| Sample Name | PD9 | PD9 | PD9 | PD9 | PD9 |
|---|---|---|---|---|---|
| **Feldspar number** | *1* | *1* | *1* | *1* | *1* |
| **Point Number** | *6* | *7* | *8* | *9* | *10* |
| **Analysis number** | *201* | *202* | *203* | *204* | *205* |
| **SiO2** | 47.60 | 48.12 | 47.55 | 48.76 | 50.57 |
| **Al2O3** | 33.56 | 32.02 | 33.29 | 32.40 | 33.46 |
| **FeO** | 0.60 | 0.36 | 0.41 | 0.34 | 0.65 |
| **CaO** | 17.04 | 17.01 | 17.02 | 16.35 | 16.16 |
| **Na2O** | 1.97 | 1.96 | 2.40 | 2.16 | 2.25 |
| **K2O** | 0.10 | 0.06 | 0.12 | 0.08 | 0.04 |
| **BaO** | 0.07 | 0.02 | 0.04 | 0.01 | 0.05 |
| **TOTAL** | 100.94 | 99.55 | 100.83 | 100.10 | 103.18 |
| **Or** | *0.57* | *0.35* | *0.66* | *0.47* | *0.23* |
| **Ab** | *17.20* | *17.19* | *20.19* | *19.20* | *20.08* |
| **An** | *82.22* | *82.46* | *79.14* | *80.33* | *79.69* |

| Sample Name | PD9 groundmass | PD9 groundmass |
|---|---|---|
| **Feldspar number** | *1* | *1* |
| **Point Number** | *1* | *2* |
| **Analysis number** | *206* | *207* |
| **SiO2** | 57.20 | 53.21 |
| **Al2O3** | 26.58 | 30.51 |
| **FeO** | 0.91 | 1.03 |
| **CaO** | 9.36 | 13.17 |
| **Na2O** | 5.77 | 4.36 |
| **K2O** | 0.22 | 0.10 |
| **BaO** | 0.02 | 0.06 |
| **TOTAL** | 100.06 | 102.44 |
| **Or** | *1.31* | *0.56* |
| **Ab** | *52.04* | *37.25* |
| **An** | *46.65* | *62.18* |

### *2.10.7.Sample PD9 – feldspar 2*

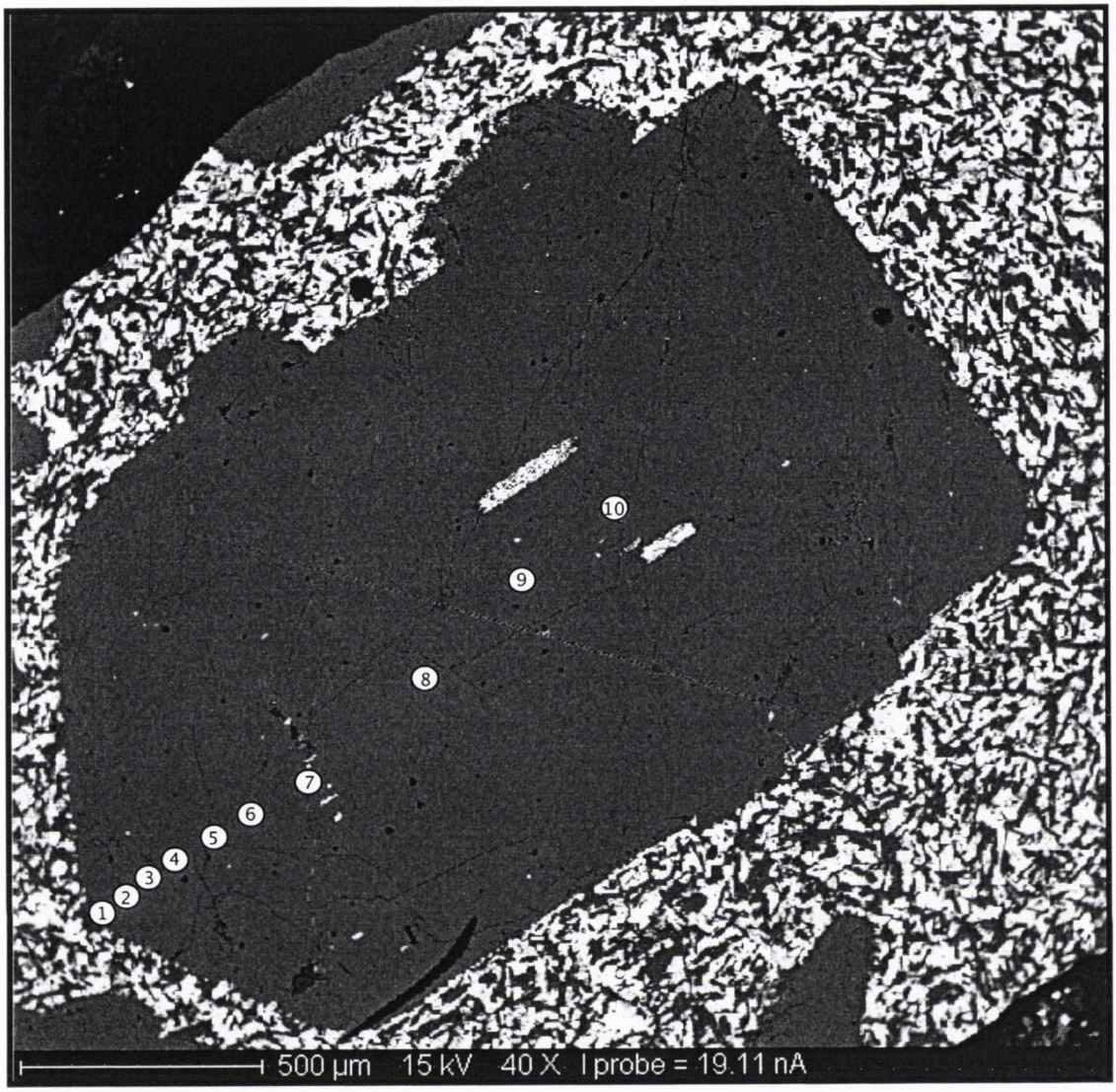

| Sample Name | PD9 | PD9 | PD9 | PD9 | PD9 |
|---|---|---|---|---|---|
| **Feldspar number** | *2* | *2* | *2* | *2* | *2* |
| **Point Number** | *1* | *2* | *3* | *4* | *5* |
| **Analysis number** | *208* | *209* | *210* | *211* | *212* |
| **SiO2** | 51.88 | 48.64 | 48.09 | 48.23 | 49.11 |
| **Al2O3** | 30.98 | 34.91 | 33.69 | 33.20 | 32.20 |
| **FeO** | 1.05 | 0.42 | 0.41 | 0.44 | 0.54 |
| **CaO** | 13.89 | 16.39 | 17.02 | 16.82 | 16.29 |
| **Na2O** | 3.46 | 2.18 | 1.94 | 1.85 | 1.94 |
| **K2O** | 0.22 | 0.09 | 0.06 | 0.06 | 0.07 |
| **BaO** | 0.00 | 0.00 | 0.01 | 0.00 | 0.00 |
| **TOTAL** | 101.48 | 102.63 | 101.22 | 100.60 | 100.15 |
| **Or** | *1.28* | *0.52* | *0.35* | *0.35* | *0.42* |
| **Ab** | *30.67* | *19.30* | *17.04* | *16.54* | *17.66* |
| **An** | *68.04* | *80.18* | *82.61* | *83.11* | *81.93* |

| Sample Name | PD9 | PD9 | PD9 | PD9 | PD9 |
|---|---|---|---|---|---|
| **Feldspar number** | *2* | *2* | *2* | *2* | *2* |
| **Point Number** | *6* | *7* | *8* | *9* | *10* |
| **Analysis number** | *213* | *214* | *215* | *216* | *217* |
| **SiO2** | 49.25 | 47.91 | 48.77 | 48.64 | 48.75 |
| **Al2O3** | 32.19 | 32.16 | 32.98 | 33.12 | 32.79 |
| **FeO** | 0.59 | 0.66 | 0.43 | 0.44 | 0.43 |
| **CaO** | 16.08 | 16.54 | 16.75 | 16.62 | 16.93 |
| **Na2O** | 2.33 | 1.78 | 1.83 | 2.45 | 1.48 |
| **K2O** | 0.08 | 0.08 | 0.08 | 0.07 | 0.08 |
| **BaO** | 0.03 | 0.00 | 0.08 | 0.06 | 0.03 |
| **TOTAL** | 100.55 | 99.13 | 100.92 | 101.40 | 100.49 |
| **Or** | *0.47* | *0.48* | *0.47* | *0.39* | *0.48* |
| **Ab** | *20.68* | *16.22* | *16.43* | *20.98* | *13.59* |
| **An** | *78.86* | *83.30* | *83.10* | *78.63* | *85.92* |

### *2.10.8.Sample PD9 – feldspar 5*

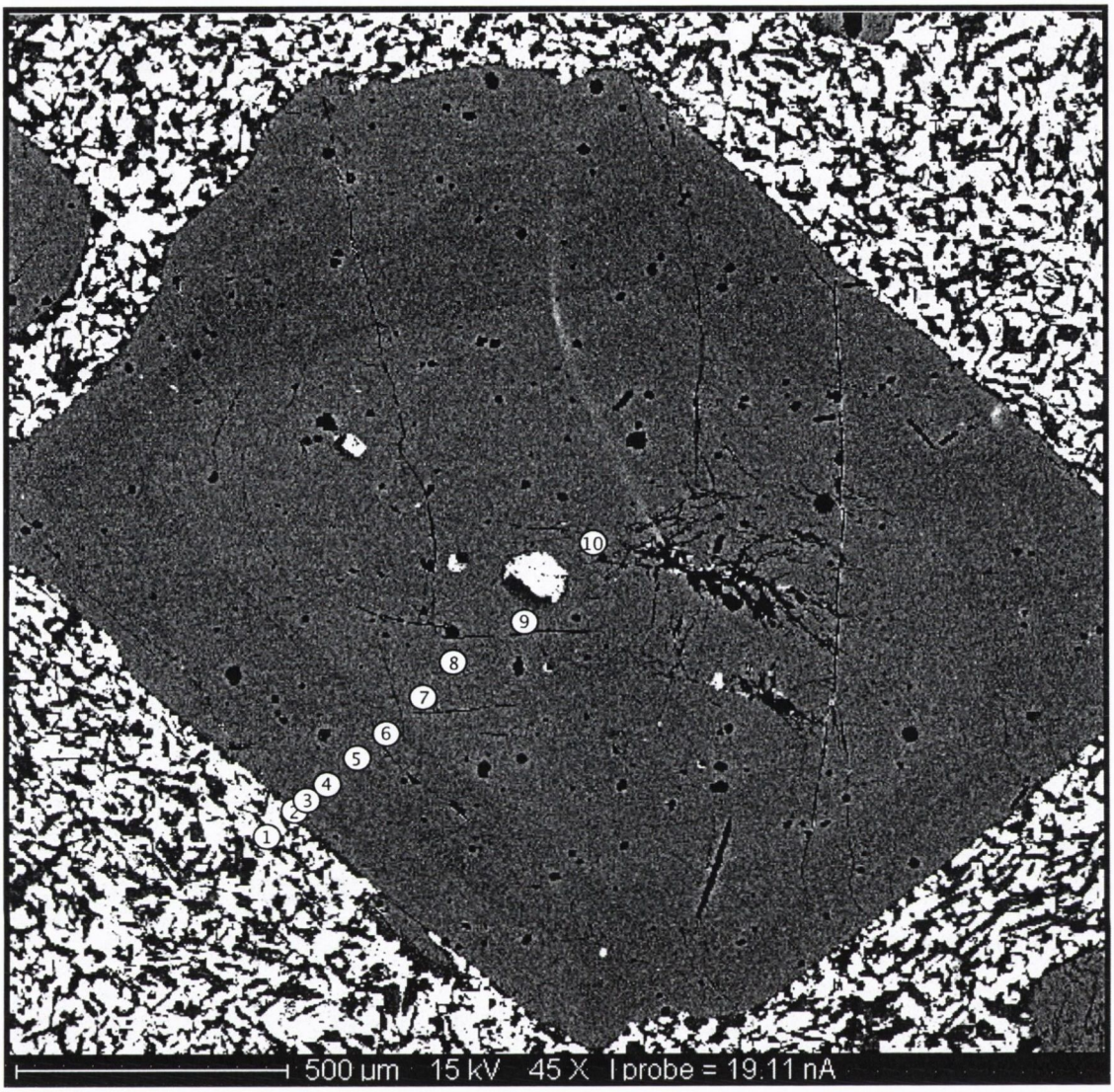

| Sample Name | PD9 | PD9 | PD9 | PD9 | PD9 |
|---|---|---|---|---|---|
| **Feldspar number** | *5* | *5* | *5* | *5* | *5* |
| **Point Number** | *1* | *2* | *3* | *4* | *5* |
| **Analysis number** | *157* | *158* | *159* | *160* | *161* |
| **SiO2** | 54.71 | 56.64 | 48.94 | 48.98 | 49.45 |
| **Al2O3** | 28.59 | 27.63 | 33.21 | 32.99 | 32.62 |
| **FeO** | 0.94 | 0.67 | 0.66 | 0.43 | 0.36 |
| **CaO** | 11.01 | 10.38 | 16.32 | 16.42 | 16.19 |
| **Na2O** | 5.00 | 5.41 | 2.03 | 2.21 | 2.06 |
| **K2O** | 0.20 | 0.08 | 0.10 | 0.08 | 0.09 |
| **BaO** | 0.07 | 0.11 | 0.00 | 0.00 | 0.05 |
| **TOTAL** | 100.52 | 100.92 | 101.26 | 101.11 | 100.82 |
| **Or** | *1.17* | *0.47* | *0.59* | *0.46* | *0.54* |
| **Ab** | *44.58* | *48.31* | *18.26* | *19.49* | *18.62* |
| **An** | *54.25* | *51.22* | *81.14* | *80.04* | *80.85* |

| Sample Name | PD9 | PD9 | PD9 | PD9 | PD9 |
|---|---|---|---|---|---|
| **Feldspar number** | *5* | *5* | *5* | *5* | *5* |
| **Point Number** | *6* | *7* | *8* | *9* | *10* |
| **Analysis number** | *162* | *163* | *164* | *165* | *166* |
| **SiO2** | 48.72 | 48.20 | 48.69 | 48.00 | 47.23 |
| **Al2O3** | 32.63 | 33.27 | 33.78 | 32.98 | 33.37 |
| **FeO** | 0.41 | 0.40 | 0.56 | 0.55 | 0.61 |
| **CaO** | 16.45 | 16.97 | 17.17 | 16.85 | 17.02 |
| **Na2O** | 2.14 | 2.09 | 1.42 | 2.27 | 1.87 |
| **K2O** | 0.08 | 0.08 | 0.07 | 0.09 | 0.06 |
| **BaO** | 0.03 | 0.08 | 0.00 | 0.01 | 0.08 |
| **TOTAL** | 100.46 | 101.09 | 101.69 | 100.75 | 100.24 |
| **Or** | *0.47* | *0.46* | *0.42* | *0.51* | *0.35* |
| **Ab** | *18.97* | *18.14* | *12.96* | *19.50* | *16.53* |
| **An** | *80.57* | *81.40* | *86.62* | *79.99* | *83.12* |

### *2.10.9.Sample PD9 – feldspar 11*

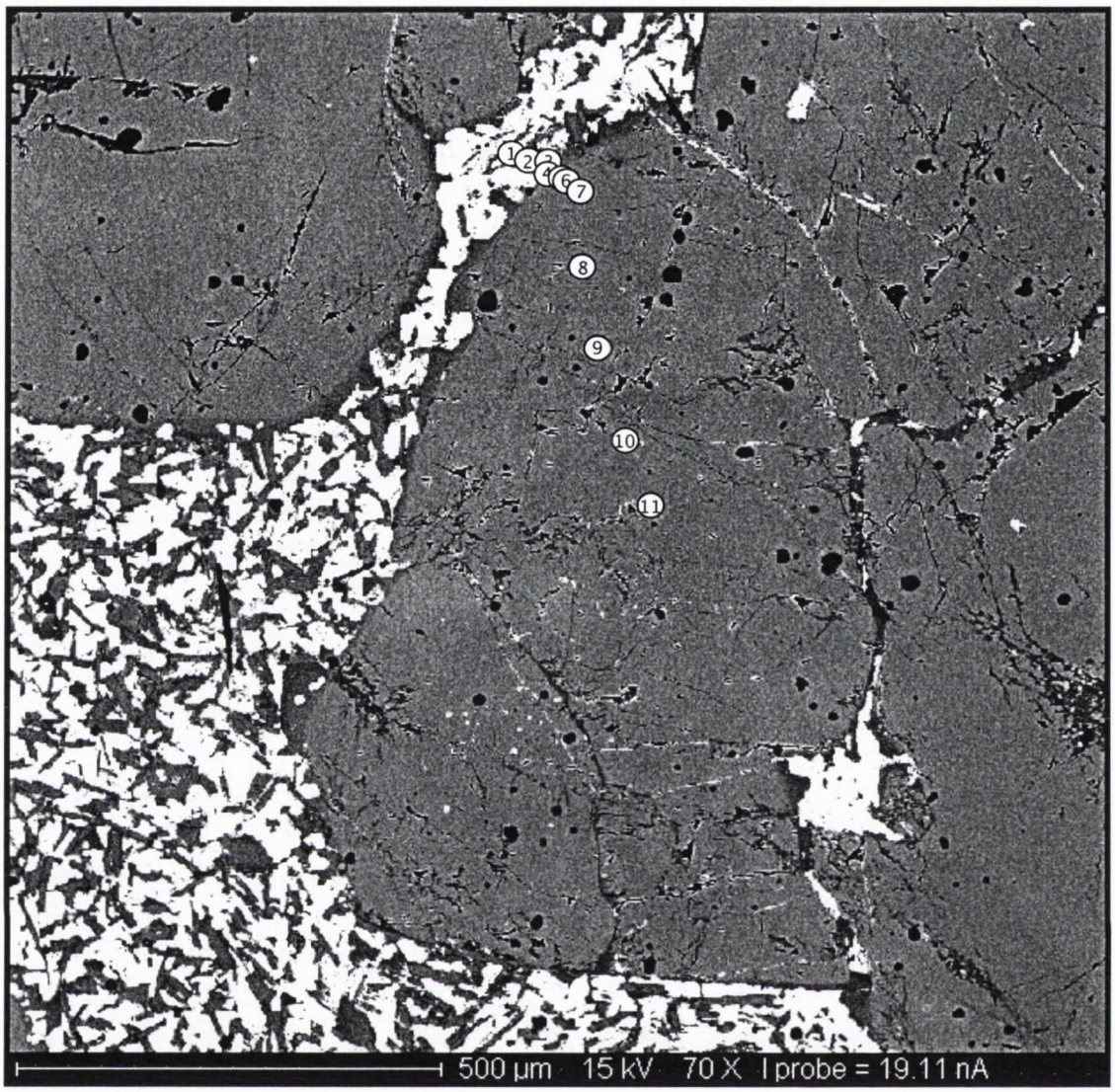

| Sample Name | PD9 | PD9 | PD9 | PD9 | PD9 |
|---|---|---|---|---|---|
| **Feldspar number** | *11* | *11* | *11* | *11* | *11* |
| **Point Number** | *1* | *2* | *3* | *4* | *5* |
| **Analysis number** | *254* | *255* | *256* | *257* | *258* |
| **SiO2** | 53.77 | 59.06 | 55.00 | 52.35 | 48.62 |
| **Al2O3** | 29.04 | 26.78 | 28.10 | 30.48 | 32.85 |
| **FeO** | 1.12 | 0.68 | 0.80 | 0.77 | 0.64 |
| **CaO** | 12.23 | 8.57 | 11.48 | 13.72 | 16.47 |
| **Na2O** | 3.63 | 6.09 | 4.90 | 3.17 | 1.33 |
| **K2O** | 0.13 | 0.26 | 0.27 | 0.21 | 0.09 |
| **BaO** | 0.04 | 0.08 | 0.02 | 0.00 | 0.04 |
| **TOTAL** | 99.96 | 101.52 | 100.57 | 100.70 | 100.04 |
| **Or** | *0.82* | *1.56* | *1.56* | *1.27* | *0.56* |
| **Ab** | *34.66* | *55.38* | *42.90* | *29.11* | *12.68* |
| **An** | *64.53* | *43.07* | *55.54* | *69.62* | *86.76* |

| Sample Name | PD9 | PD9 | PD9 | PD9 | PD9 |
|---|---|---|---|---|---|
| **Feldspar number** | *11* | *11* | *11* | *11* | *11* |
| **Point Number** | *6* | *7* | *8* | *9* | *10* |
| **Analysis number** | *259* | *260* | *261* | *262* | *263* |
| **SiO2** | 48.30 | 48.07 | 48.17 | 48.26 | 48.38 |
| **Al2O3** | 33.22 | 32.71 | 33.55 | 33.66 | 33.11 |
| **FeO** | 0.76 | 0.58 | 0.57 | 0.53 | 0.49 |
| **CaO** | 16.73 | 16.51 | 17.13 | 17.07 | 16.65 |
| **Na2O** | 1.81 | 1.83 | 1.49 | 0.96 | 1.88 |
| **K2O** | 0.07 | 0.15 | 0.08 | 0.07 | 0.06 |
| **BaO** | 0.00 | 0.00 | 0.00 | 0.00 | 0.03 |
| **TOTAL** | 100.89 | 99.85 | 100.99 | 100.55 | 100.60 |
| **Or** | *0.41* | *0.89* | *0.48* | *0.44* | *0.36* |
| **Ab** | *16.30* | *16.56* | *13.53* | *9.20* | *16.91* |
| **An** | *83.28* | *82.55* | *85.99* | *90.36* | *82.74* |

| Sample Name | PD9 |
|---|---|
| **Feldspar number** | *11* |
| **Point Number** | *11* |
| **Analysis number** | *264* |
| **SiO2** | 48.52 |
| **Al2O3** | 32.13 |
| **FeO** | 0.36 |
| **CaO** | 16.59 |
| **Na2O** | 1.72 |
| **K2O** | 0.08 |
| **BaO** | 0.03 |
| **TOTAL** | 99.43 |
| **Or** | *0.48* |
| **Ab** | *15.72* |
| **An** | *83.80* |

### *2.10.10. Sample PD9 – feldspar 16*

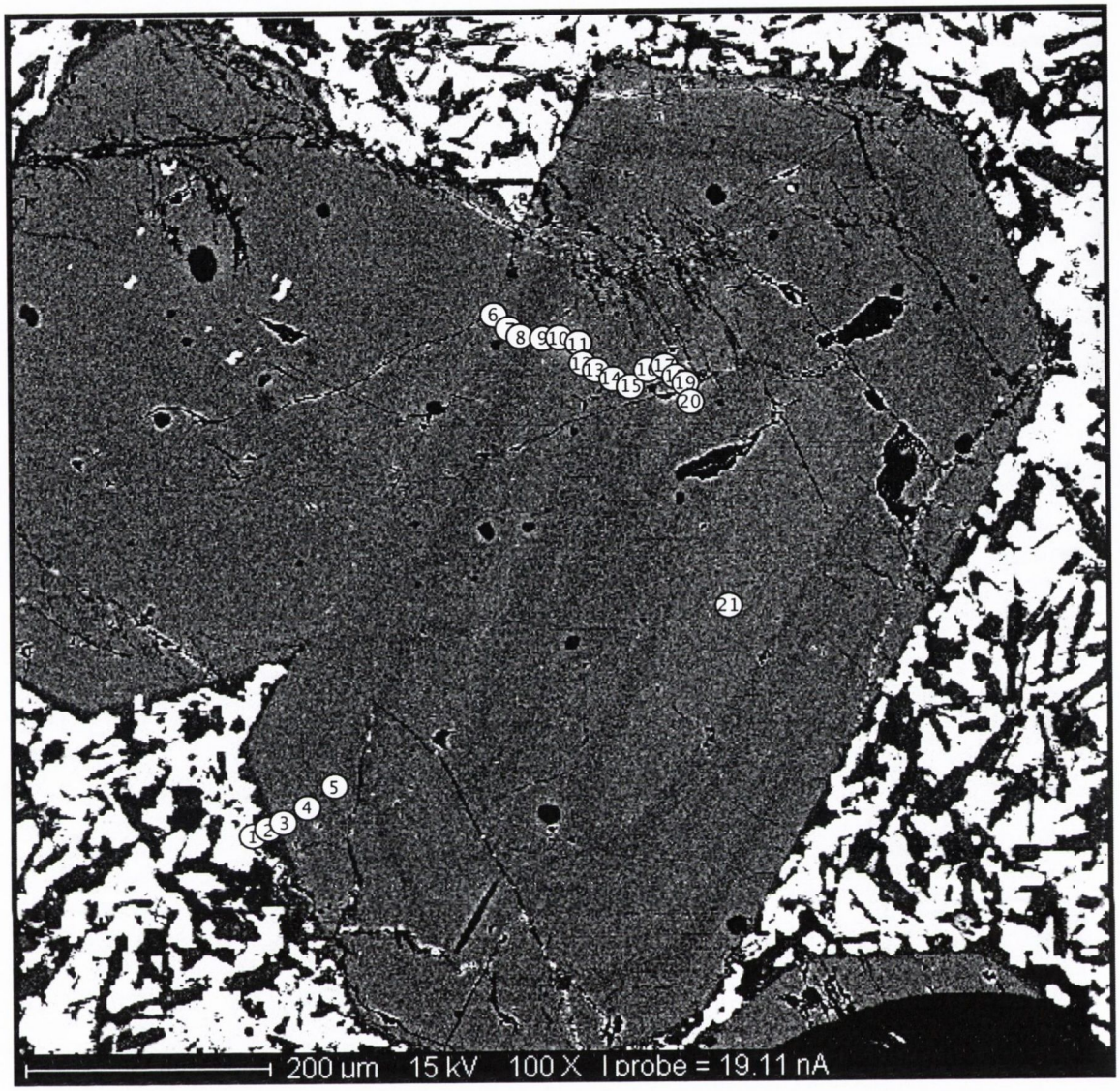

| Sample Name | PD9 | PD9 | PD9 | PD9 | PD9 |
|---|---|---|---|---|---|
| **Feldspar number** | *16* | *16* | *16* | *16* | *16* |
| **Point Number** | *1* | *2* | *3* | *4* | *5* |
| **Analysis number** | *218* | *219* | *220* | *221* | *222* |
| **SiO2** | 51.30 | 53.20 | 48.64 | 48.61 | 48.88 |
| **Al2O3** | 28.65 | 30.91 | 32.92 | 30.26 | 32.91 |
| **FeO** | 5.31 | 0.85 | 0.80 | 4.48 | 0.50 |
| **CaO** | 10.67 | 13.55 | 16.72 | 13.92 | 16.53 |
| **Na2O** | 4.26 | 3.19 | 1.62 | 2.16 | 1.91 |
| **K2O** | 0.18 | 0.12 | 0.10 | 0.22 | 0.09 |
| **BaO** | 0.00 | 0.00 | 0.11 | 0.00 | 0.00 |
| **TOTAL** | 100.37 | 101.82 | 100.91 | 99.65 | 100.82 |
| **Or** | *1.15* | *0.73* | *0.60* | *1.45* | *0.53* |
| **Ab** | *41.46* | *29.66* | *14.83* | *21.61* | *17.20* |
| **An** | *57.39* | *69.61* | *84.57* | *76.95* | *82.27* |

| Sample Name | PD9 | PD9 | PD9 | PD9 | PD9 |
|---|---|---|---|---|---|
| **Feldspar number** | *16* | *16* | *16* | *16* | *16* |
| **Point Number** | *6* | *7* | *8* | *9* | *10* |
| **Analysis number** | *223* | *224* | *225* | *226* | *227* |
| **SiO2** | 48.26 | 48.21 | 50.05 | 49.61 | 48.12 |
| **Al2O3** | 33.64 | 33.33 | 32.37 | 32.11 | 33.25 |
| **FeO** | 0.48 | 0.50 | 0.85 | 0.55 | 0.54 |
| **CaO** | 17.25 | 16.58 | 15.85 | 15.83 | 17.04 |
| **Na2O** | 1.57 | 2.08 | 2.40 | 2.55 | 1.90 |
| **K2O** | 0.06 | 0.09 | 0.13 | 0.08 | 0.05 |
| **BaO** | 0.00 | 0.03 | 0.02 | 0.00 | 0.01 |
| **TOTAL** | 101.26 | 100.82 | 101.67 | 100.73 | 100.91 |
| **Or** | *0.35* | *0.52* | *0.76* | *0.46* | *0.29* |
| **Ab** | *14.09* | *18.40* | *21.34* | *22.47* | *16.74* |
| **An** | *85.55* | *81.07* | *77.90* | *77.07* | *82.97* |

| Sample Name | PD9 | PD9 | PD9 | PD9 | PD9 |
|---|---|---|---|---|---|
| **Feldspar number** | *16* | *16* | *16* | *16* | *16* |
| **Point Number** | *11* | *12* | *13* | *14* | *15* |
| **Analysis number** | *228* | *229* | *230* | *231* | *232* |
| **SiO2** | 48.91 | 48.73 | 48.26 | 49.33 | 49.37 |
| **Al2O3** | 33.57 | 33.22 | 33.60 | 33.10 | 33.03 |
| **FeO** | 0.39 | 0.58 | 0.61 | 0.53 | 0.52 |
| **CaO** | 16.92 | 16.70 | 17.35 | 16.65 | 16.50 |
| **Na2O** | 1.95 | 2.23 | 1.83 | 1.94 | 1.67 |
| **K2O** | 0.07 | 0.06 | 0.06 | 0.06 | 0.08 |
| **BaO** | 0.00 | 0.00 | 0.00 | 0.00 | 0.00 |
| **TOTAL** | 101.81 | 101.52 | 101.71 | 101.61 | 101.17 |
| **Or** | *0.41* | *0.34* | *0.34* | *0.35* | *0.49* |
| **Ab** | *17.19* | *19.39* | *15.97* | *17.35* | *15.41* |
| **An** | *82.41* | *80.26* | *83.68* | *82.29* | *84.11* |

| Sample Name | PD9 | PD9 | PD9 | PD9 | PD9 |
|---|---|---|---|---|---|
| **Feldspar number** | *16* | *16* | *16* | *16* | *16* |
| **Point Number** | *16* | *17* | *18* | *19* | *20* |
| **Analysis number** | *233* | *234* | *235* | *236* | *237* |
| **SiO2** | 48.27 | 49.11 | 50.34 | 48.58 | 47.33 |
| **Al2O3** | 33.13 | 32.67 | 31.83 | 33.39 | 33.62 |
| **FeO** | 0.41 | 0.53 | 0.33 | 0.26 | 0.64 |
| **CaO** | 17.00 | 16.55 | 15.79 | 16.82 | 17.64 |
| **Na2O** | 1.73 | 1.50 | 2.80 | 1.75 | 1.65 |
| **K2O** | 0.08 | 0.08 | 0.10 | 0.08 | 0.05 |
| **BaO** | 0.06 | 0.05 | 0.02 | 0.00 | 0.00 |
| **TOTAL** | 100.68 | 100.49 | 101.21 | 100.88 | 100.93 |
| **Or** | *0.47* | *0.49* | *0.57* | *0.47* | *0.29* |
| **Ab** | *15.48* | *14.02* | *24.16* | *15.77* | *14.43* |
| **An** | *84.05* | *85.49* | *75.28* | *83.76* | *85.28* |

| Sample Name | PD9 |
|---|---|
| **Feldspar number** | *16* |
| **Point Number** | *21* |
| **Analysis number** | *238* |
| **SiO2** | 47.41 |
| **Al2O3** | 33.52 |
| **FeO** | 0.55 |
| **CaO** | 17.65 |
| **Na2O** | 1.69 |
| **K2O** | 0.05 |
| **BaO** | 0.00 |
| **TOTAL** | 100.87 |
| **Or** | *0.29* |
| **Ab** | *14.73* |
| **An** | *84.99* |

### *2.10.11. Sample PD9 – feldspar 18*

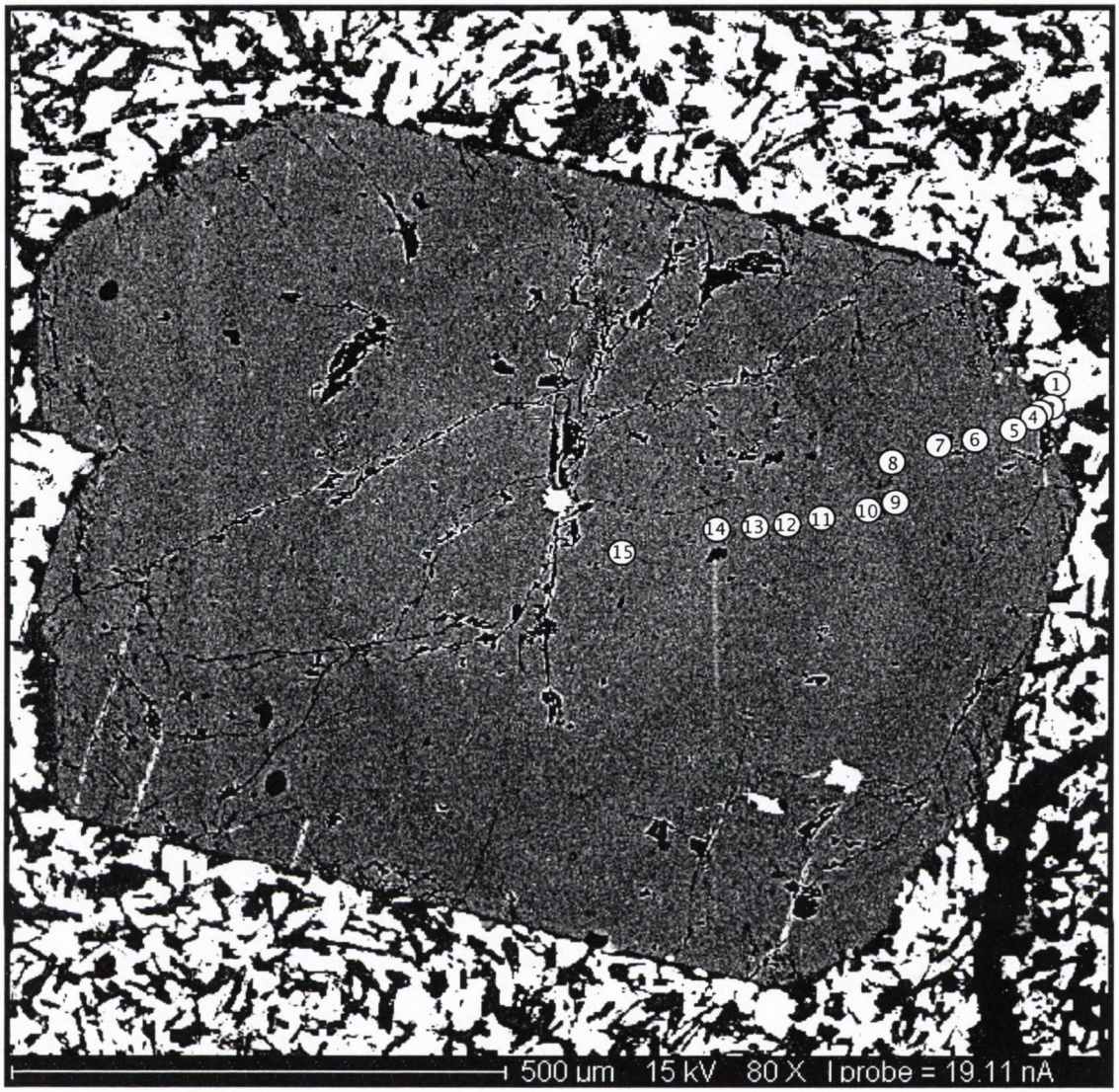

| Sample Name | PD9 | PD9 | PD9 | PD9 | PD9 |
|---|---|---|---|---|---|
| **Feldspar number** | *18* | *18* | *18* | *18* | *18* |
| **Point Number** | *1* | *2* | *3* | *4* | *5* |
| **Analysis number** | *239* | *240* | *241* | *242* | *243* |
| **SiO2** | 56.65 | 52.95 | 52.05 | 48.56 | 47.54 |
| **Al2O3** | 28.34 | 29.74 | 30.40 | 33.42 | 33.16 |
| **FeO** | 1.04 | 0.93 | 0.68 | 0.54 | 0.70 |
| **CaO** | 10.37 | 13.61 | 13.96 | 16.82 | 16.69 |
| **Na2O** | 5.33 | 3.59 | 3.62 | 1.91 | 1.94 |
| **K2O** | 0.13 | 0.14 | 0.16 | 0.06 | 0.09 |
| **BaO** | 0.02 | 0.00 | 0.01 | 0.00 | 0.04 |
| **TOTAL** | 101.88 | 100.96 | 100.88 | 101.31 | 100.16 |
| **Or** | *0.77* | *0.82* | *0.92* | *0.35* | *0.53* |
| **Ab** | *47.82* | *32.04* | *31.64* | *16.99* | *17.29* |
| **An** | *51.41* | *67.13* | *67.44* | *82.66* | *82.19* |

| Sample Name | PD9 | PD9 | PD9 | PD9 | PD9 |
|---|---|---|---|---|---|
| **Feldspar number** | *18* | *18* | *18* | *18* | *18* |
| **Point Number** | *6* | *7* | *8* | *9* | *10* |
| **Analysis number** | *244* | *245* | *246* | *247* | *248* |
| **SiO2** | 47.84 | 47.87 | 48.75 | 48.98 | 48.16 |
| **Al2O3** | 33.32 | 32.59 | 33.02 | 32.89 | 33.44 |
| **FeO** | 0.61 | 0.72 | 0.42 | 0.46 | 0.51 |
| **CaO** | 16.52 | 16.80 | 16.52 | 16.27 | 17.21 |
| **Na2O** | 2.17 | 1.65 | 2.04 | 2.03 | 1.95 |
| **K2O** | 0.08 | 0.12 | 0.07 | 0.08 | 0.06 |
| **BaO** | 0.00 | 0.00 | 0.02 | 0.06 | 0.00 |
| **TOTAL** | 100.54 | 99.75 | 100.84 | 100.77 | 101.33 |
| **Or** | *0.46* | *0.72* | *0.41* | *0.48* | *0.34* |
| **Ab** | *19.12* | *14.98* | *18.19* | *18.33* | *16.96* |
| **An** | *80.42* | *84.30* | *81.40* | *81.19* | *82.70* |

| Sample Name | PD9 | PD9 | PD9 | PD9 | PD9 |
|---|---|---|---|---|---|
| **Feldspar number** | *18* | *18* | *18* | *18* | *18* |
| **Point Number** | *11* | *12* | *13* | *14* | *15* |
| **Analysis number** | *249* | *250* | *251* | *252* | *253* |
| **SiO2** | 47.96 | 47.91 | 47.89 | 48.24 | 48.30 |
| **Al2O3** | 33.30 | 32.79 | 33.35 | 33.47 | 33.68 |
| **FeO** | 0.40 | 0.40 | 0.49 | 0.51 | 0.49 |
| **CaO** | 17.07 | 16.77 | 16.75 | 17.27 | 17.32 |
| **Na2O** | 1.94 | 1.48 | 1.82 | 1.62 | 1.44 |
| **K2O** | 0.06 | 0.03 | 0.06 | 0.05 | 0.05 |
| **BaO** | 0.07 | 0.02 | 0.00 | 0.07 | 0.02 |
| **TOTAL** | 100.80 | 99.40 | 100.36 | 101.23 | 101.30 |
| **Or** | *0.35* | *0.18* | *0.36* | *0.29* | *0.30* |
| **Ab** | *17.00* | *13.75* | *16.37* | *14.47* | *13.04* |
| **An** | *82.66* | *86.07* | *83.27* | *85.24* | *86.66* |

### *2.10.12. Sample CPB – feldspar 1*

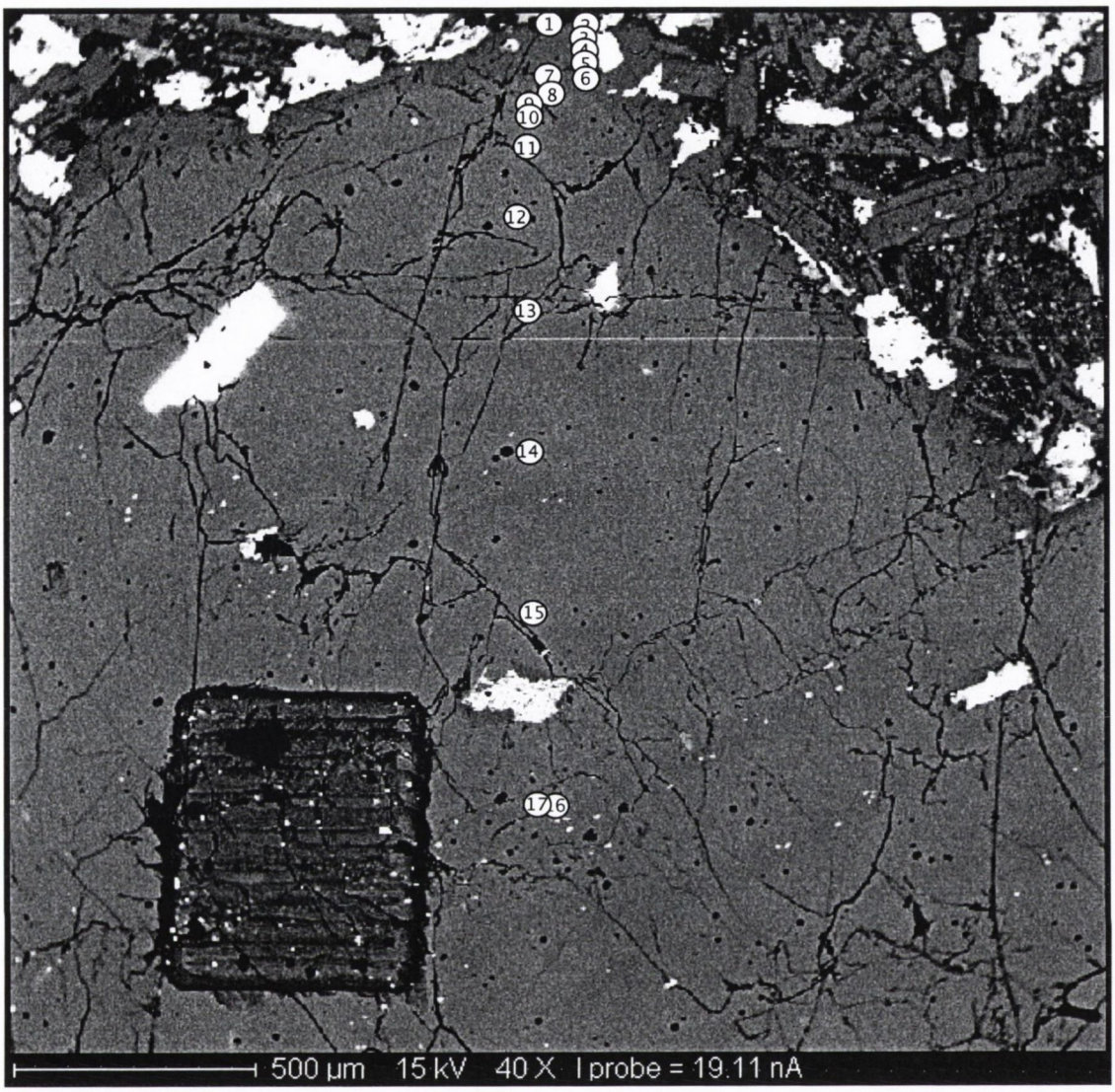

| Sample Name | CPB | CPB | CPB | CPB | CPB |
|---|---|---|---|---|---|
| **Feldspar number** | *1* | *1* | *1* | *1* | *1* |
| **Point Number** | *1* | *2* | *3* | *4* | *5* |
| **Analysis number** | *304* | *305* | *306* | *307* | *308* |
| **SiO2** | 99.32 | 54.70 | 52.72 | 52.81 | 51.94 |
| **Al2O3** | 0.00 | 29.10 | 29.78 | 30.13 | 30.26 |
| **FeO** | 0.67 | 0.57 | 0.75 | 0.73 | 0.91 |
| **CaO** | 0.06 | 11.52 | 13.31 | 13.66 | 14.21 |
| **Na2O** | 0.00 | 4.36 | 3.85 | 3.10 | 2.73 |
| **K2O** | 0.05 | 0.21 | 0.40 | 0.23 | 0.18 |
| **BaO** | 0.00 | 0.12 | 0.00 | 0.06 | 0.00 |
| **TOTAL** | 100.10 | 100.58 | 100.81 | 100.72 | 100.23 |
| **Or** | *49.80* | *1.27* | *2.29* | *1.40* | *1.11* |
| **Ab** | *0.00* | *40.13* | *33.57* | *28.70* | *25.51* |
| **An** | *50.20* | *58.60* | *64.13* | *69.89* | *73.38* |

| Sample Name | CPB | CPB | CPB | CPB | CPB |
|---|---|---|---|---|---|
| **Feldspar number** | *1* | *1* | *1* | *1* | *1* |
| **Point Number** | *6* | *7* | *8* | *9* | *10* |
| **Analysis number** | *309* | *310* | *311* | *312* | *313* |
| **SiO2** | 51.08 | 52.15 | 48.55 | 48.49 | 48.42 |
| **Al2O3** | 30.46 | 31.67 | 32.99 | 32.77 | 33.02 |
| **FeO** | 0.63 | 0.57 | 0.69 | 0.52 | 0.53 |
| **CaO** | 14.58 | 14.73 | 16.95 | 16.62 | 17.04 |
| **Na2O** | 3.05 | 2.56 | 1.53 | 1.26 | 1.52 |
| **K2O** | 0.14 | 0.10 | 0.06 | 0.10 | 0.06 |
| **BaO** | 0.00 | 0.00 | 0.01 | 0.00 | 0.05 |
| **TOTAL** | 99.94 | 101.78 | 100.78 | 99.76 | 100.64 |
| **Or** | *0.82* | *0.61* | *0.36* | *0.63* | *0.36* |
| **Ab** | *27.23* | *23.78* | *13.99* | *11.99* | *13.85* |
| **An** | *71.94* | *75.61* | *85.65* | *87.39* | *85.79* |

| Sample Name | CPB | CPB | CPB | CPB | CPB |
|---|---|---|---|---|---|
| **Feldspar number** | *1* | *1* | *1* | *1* | *1* |
| **Point Number** | *11* | *12* | *13* | *14* | *15* |
| **Analysis number** | *314* | *315* | *316* | *317* | *318* |
| **SiO2** | 47.83 | 47.43 | 47.52 | 47.84 | 48.32 |
| **Al2O3** | 34.00 | 32.89 | 33.09 | 32.92 | 33.29 |
| **FeO** | 0.48 | 0.42 | 0.58 | 0.53 | 0.40 |
| **CaO** | 17.42 | 17.62 | 17.44 | 16.80 | 17.35 |
| **Na2O** | 1.41 | 1.07 | 1.12 | 0.86 | 0.93 |
| **K2O** | 0.07 | 0.06 | 0.06 | 0.05 | 0.07 |
| **BaO** | 0.00 | 0.02 | 0.05 | 0.00 | 0.02 |
| **TOTAL** | 101.21 | 99.51 | 99.86 | 99.00 | 100.38 |
| **Or** | *0.42* | *0.36* | *0.37* | *0.32* | *0.44* |
| **Ab** | *12.72* | *9.87* | *10.37* | *8.45* | *8.80* |
| **An** | *86.86* | *89.77* | *89.26* | *91.23* | *90.76* |

| Sample Name | CPB | CPB |
|---|---|---|
| **Feldspar number** | *1* | *1* |
| **Point Number** | *16* | *17* |
| **Analysis number** | *319* | *320* |
| **SiO2** | 40.25 | 48.44 |
| **Al2O3** | 28.71 | 33.42 |
| **FeO** | 0.64 | 0.22 |
| **CaO** | 14.36 | 17.21 |
| **Na2O** | 0.81 | 1.23 |
| **K2O** | 0.17 | 0.06 |
| **BaO** | 0.00 | 0.00 |
| **TOTAL** | 84.94 | 100.58 |
| **Or** | *1.26* | *0.37* |
| **Ab** | *9.15* | *11.41* |
| **An** | *89.59* | *88.22* |

### *2.10.13. Sample CPB – feldspar 7*

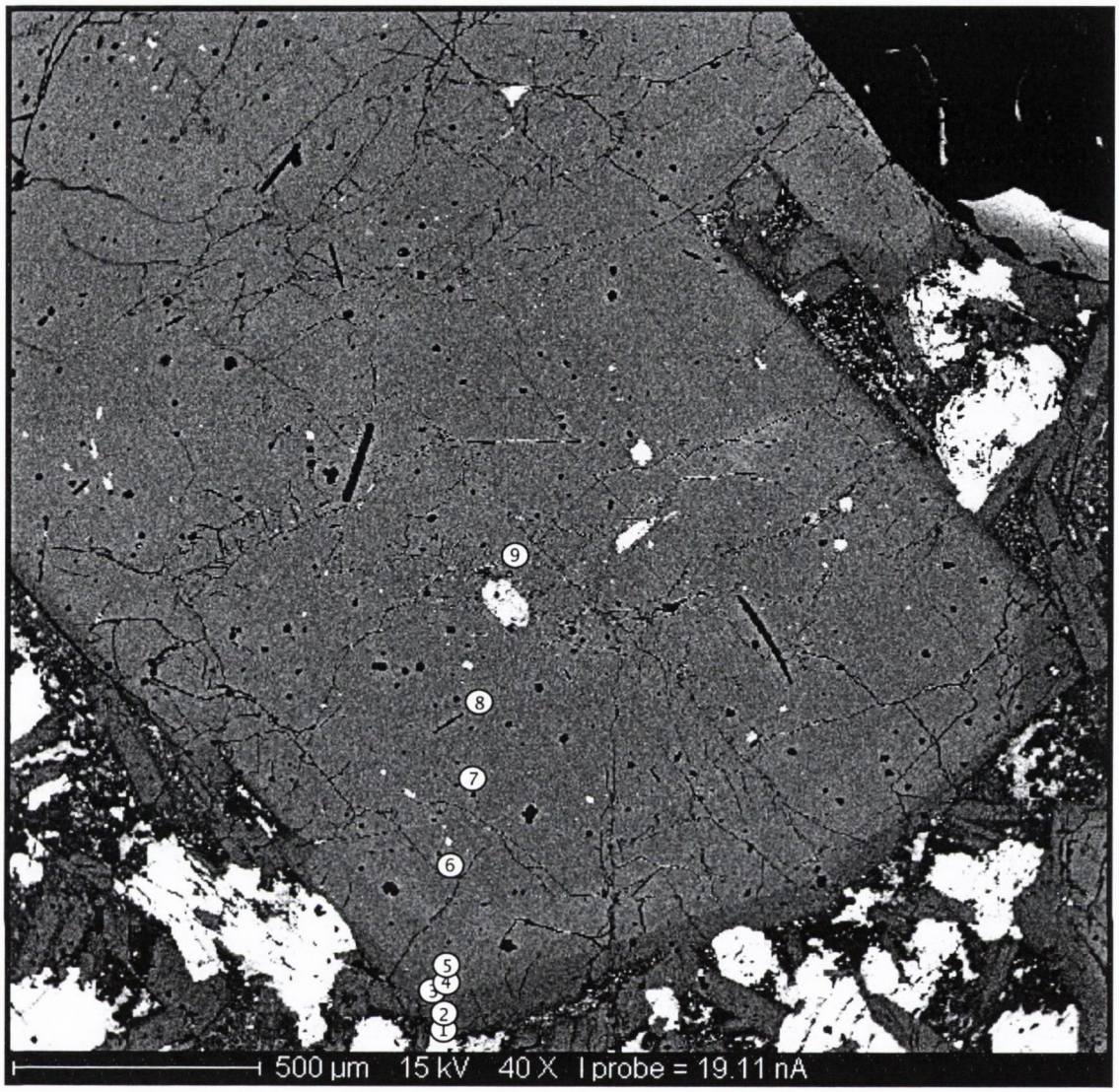

| Sample Name | CPB | CPB | CPB | CPB | CPB |
|---|---|---|---|---|---|
| **Feldspar number** | *7* | *7* | *7* | *7* | *7* |
| **Point Number** | *1* | *2* | *3* | *4* | *5* |
| **Analysis number** | *321* | *322* | *323* | *324* | *325* |
| **SiO2** | 55.10 | 52.12 | 51.33 | 50.22 | 47.77 |
| **Al2O3** | 28.47 | 30.65 | 30.39 | 30.89 | 33.36 |
| **FeO** | 0.74 | 0.68 | 0.57 | 0.70 | 0.63 |
| **CaO** | 11.40 | 14.18 | 14.49 | 15.06 | 17.16 |
| **Na2O** | 3.52 | 2.15 | 2.47 | 2.55 | 1.28 |
| **K2O** | 0.25 | 0.20 | 0.15 | 0.12 | 0.07 |
| **BaO** | 0.05 | 0.04 | 0.00 | 0.00 | 0.00 |
| **TOTAL** | 99.53 | 100.02 | 99.40 | 99.54 | 100.27 |
| **Or** | *1.65* | *1.30* | *0.93* | *0.72* | *0.43* |
| **Ab** | *35.26* | *21.25* | *23.35* | *23.29* | *11.84* |
| **An** | *63.10* | *77.45* | *75.71* | *75.99* | *87.73* |

| Sample Name | CPB | CPB | CPB | CPB |
|---|---|---|---|---|
| **Feldspar number** | *7* | *7* | *7* | *7* |
| **Point Number** | *6* | *7* | *8* | *9* |
| **Analysis number** | *326* | *327* | *328* | *329* |
| **SiO2** | 47.32 | 47.29 | 47.46 | 47.59 |
| **Al2O3** | 33.84 | 33.34 | 33.02 | 33.04 |
| **FeO** | 0.56 | 0.41 | 0.49 | 0.65 |
| **CaO** | 17.46 | 17.39 | 17.34 | 17.03 |
| **Na2O** | 1.46 | 1.21 | 1.60 | 1.57 |
| **K2O** | 0.05 | 0.04 | 0.08 | 0.05 |
| **BaO** | 0.03 | 0.00 | 0.00 | 0.00 |
| **TOTAL** | 100.72 | 99.68 | 99.99 | 99.93 |
| **Or** | *0.30* | *0.24* | *0.47* | *0.30* |
| **Ab** | *13.10* | *11.16* | *14.24* | *14.25* |
| **An** | *86.60* | *88.60* | *85.29* | *85.45* |

# Appendix 3. CARLINGFORD CRUST

## 3.1. Sample locations

| Sample | limestone 1 | marble 1 | BWa | BWb |
|---|---|---|---|---|
| Rock type | *Limestone* | *Marble* | *Meta-igneous xenolith* | *Meta-igneous xenolith* |
| La | 10.9 | 6.2 | 12.0 | 13.0 |
| Ce | 22.4 | 12.8 | 24.5 | 27.0 |
| Pr | 2.6 | 1.6 | 3.1 | 3.4 |
| Nd | 9.9 | 6.3 | 13.5 | 14.6 |
| Sm | 1.9 | 1.3 | 3.1 | 3.4 |
| Eu | 0.4 | 0.3 | 0.6 | 0.7 |
| Gd | 1.7 | 1.4 | 3.2 | 3.5 |
| Tb | 0.3 | 0.2 | 0.5 | 0.6 |
| Dy | 1.5 | 1.4 | 3.2 | 3.4 |
| Ho | 0.3 | 0.3 | 0.6 | 0.6 |
| Er | 0.9 | 0.9 | 1.8 | 1.7 |
| Tm | 0.1 | 0.1 | 0.3 | 0.3 |
| Yb | 0.8 | 0.9 | 1.6 | 1.4 |
| Lu | 0.1 | 0.1 | 0.2 | 0.2 |

| Sample | BWc | BWd-tub | C-SB1 | C-SB2 |
|---|---|---|---|---|
| Rock type | *Meta-igneous xenolith* | *Meta-igneous xenolith* | *Hornfels xenolith* | *Hornfels xenolith* |
| La | 10.1 | 27.2 | 37.3 | 37.6 |
| Ce | 20.2 | 56.0 | 79.5 | 79.0 |
| Pr | 2.6 | 6.8 | 8.7 | 8.9 |
| Nd | 11.0 | 27.6 | 32.0 | 33.6 |
| Sm | 2.5 | 5.7 | 5.6 | 6.5 |
| Eu | 0.5 | 1.8 | 1.2 | 1.5 |
| Gd | 2.6 | 5.3 | 4.9 | 6.0 |
| Tb | 0.4 | 0.8 | 0.7 | 0.9 |
| Dy | 2.4 | 4.8 | 4.1 | 5.3 |
| Ho | 0.5 | 0.9 | 0.7 | 1.1 |
| Er | 1.3 | 2.6 | 2.4 | 3.1 |
| Tm | 0.2 | 0.4 | 0.4 | 0.5 |
| Yb | 1.1 | 2.4 | 2.3 | 2.9 |
| Lu | 0.2 | 0.4 | 0.3 | 0.4 |

| Sample | C-SB3 | C-LD1 | silt1 |
|---|---|---|---|
| Rock type | *Hornfels xenolith* | *Hornfelsed meta-siltstone* | *Meta-siltstone* |
| La | 38.6 | 36.2 | 31.0 |
| Ce | 81.8 | 78.4 | 65.4 |
| Pr | 9.2 | 8.9 | 7.7 |
| Nd | 34.3 | 33.5 | 29.7 |
| Sm | 6.4 | 6.3 | 5.9 |
| Eu | 1.3 | 1.2 | 1.1 |
| Gd | 5.7 | 5.6 | 5.2 |
| Tb | 0.9 | 0.8 | 0.8 |
| Dy | 5.0 | 4.7 | 4.7 |
| Ho | 1.0 | 0.9 | 0.9 |
| Er | 3.0 | 2.6 | 2.7 |
| Tm | 0.5 | 0.4 | 0.4 |
| Yb | 2.9 | 2.4 | 2.6 |
| Lu | 0.4 | 0.3 | 0.4 |

## 3.2. Major elements

| Sample | limestone 1 | marble 1 | BWa | BWb | BWc |
|---|---|---|---|---|---|
| Rock type | *Limestone* | *Marble* | *Meta-igneous xenolith* | *Meta-igneous xenolith* | *Meta-igneous xenolith* |
| $SiO_2$ | 22.20 | 44.64 | 49.27 | 49.93 | 48.53 |
| $TiO_2$ | 0.24 | 0.12 | 1.10 | 1.05 | 1.17 |
| $AL_2O_3$ | 4.25 | 5.96 | 20.17 | 19.72 | 21.38 |
| $Fe_2O_3$ | 1.54 | 0.54 | 6.80 | 7.02 | 6.53 |
| MnO | 0.01 | 0.01 | 0.15 | 0.17 | 0.10 |
| MgO | 1.90 | 6.41 | 5.37 | 5.56 | 5.18 |
| CaO | 38.53 | 35.22 | 2.34 | 2.42 | 1.65 |
| $Na_2O$ | 0.83 | 2.04 | 2.53 | 2.49 | 1.80 |
| $K_2O$ | 0.92 | 1.80 | 6.26 | 5.86 | 7.54 |
| $P_2O_5$ | 0.01 | 0.02 | 0.13 | 0.17 | 0.11 |
| LOI | 29.57 | 3.07 | 5.09 | 4.99 | 5.29 |
| Total | 99.99 | 99.82 | 99.20 | 99.37 | 99.27 |

| Sample | BWd-tub | C-SB1 | C-SB2 | C-SB3 | C-LD1 |
|---|---|---|---|---|---|
| Rock type | *Meta-igneous xenolith* | *Hornfels xenolith* | *Hornfels xenolith* | *Hornfels xenolith* | *Hornfelsed meta-siltstone* |
| $SiO_2$ | 51.24 | 54.37 | 54.50 | 56.27 | 60.12 |
| $TiO_2$ | 1.35 | 0.93 | 0.91 | 0.98 | 0.91 |
| $AL_2O_3$ | 16.20 | 18.52 | 16.46 | 18.41 | 16.29 |
| $Fe_2O_3$ | 9.02 | 7.77 | 6.17 | 5.79 | 6.81 |
| MnO | 0.11 | 0.06 | 0.15 | 0.08 | 0.09 |
| MgO | 5.92 | 4.67 | 5.71 | 4.19 | 4.26 |
| CaO | 4.07 | 4.33 | 9.07 | 6.66 | 5.34 |
| $Na_2O$ | 4.23 | 1.08 | 1.21 | 1.39 | 1.67 |
| $K_2O$ | 2.02 | 6.45 | 4.58 | 4.57 | 2.77 |
| $P_2O_5$ | 0.30 | 0.17 | 0.19 | 0.20 | 0.19 |
| LOI | 5.29 | 2.10 | 1.17 | 1.63 | 1.49 |
| Total | 99.75 | 100.45 | 100.12 | 100.17 | 99.94 |

| Sample | silt1 |
|---|---|
| Rock type | *Meta-siltstone* |
| $SiO_2$ | 60.59 |
| $TiO_2$ | 0.80 |
| $AL_2O_3$ | 13.99 |
| $Fe_2O_3$ | 6.45 |
| MnO | 0.11 |
| MgO | 5.84 |
| CaO | 3.66 |
| $Na_2O$ | 1.49 |
| $K_2O$ | 2.65 |
| $P_2O_5$ | 0.17 |
| LOI | 4.21 |
| Total | 99.95 |

## 3.3. Loss on ignition

| Sample | limestone 1 | marble 1 | BWa | BWb | BWc |
|---|---|---|---|---|---|
| Rock type | *Limestone* | *Marble* | *Meta-igneous xenolith* | *Meta-igneous xenolith* | *Meta-igneous xenolith* |
| $H_2O$ | - | - | - | - | - |
| $CO_2$ | - | - | - | - | - |
| $SO_3$ | 0.78 | 0.01 | 1.22 | 0.75 | 1.32 |
| LOI | 28.79 | 3.06 | 3.87 | 4.24 | 3.97 |
| Total LOI | 29.57 | 3.07 | 5.09 | 4.99 | 5.29 |

| Sample | BWd-tub | C-SB1 | C-SB2 | C-SB3 | C-LD1 |
|---|---|---|---|---|---|
| Rock type | *Meta-igneous xenolith* | *Hornfels xenolith* | *Hornfels xenolith* | *Hornfels xenolith* | *Hornfelsed meta-siltstone* |
| $H_2O$ | - | 1.86 | 1.14 | 1.56 | 1.46 |
| $CO_2$ | - | 0.24 | 0.03 | 0.07 | 0.03 |
| $SO_3$ | 1.65 | - | - | - | - |
| LOI | 3.64 | - | - | - | - |
| Total LOI | 5.29 | 2.10 | 1.17 | 1.63 | 1.49 |

| Sample | silt1 |
|---|---|
| Rock type | *Meta-siltstone* |
| $H_2O$ | - |
| $CO_2$ | - |
| $SO_3$ | 0.01 |
| LOI | 4.20 |
| Total LOI | 4.21 |

## 3.4. Trace elements

| Sample | limestone 1 | marble 1 | BWa | BWb | BWc |
|---|---|---|---|---|---|
| Rock type | *Limestone* | *Marble* | *Meta-igneous xenolith* | *Meta-igneous xenolith* | *Meta-igneous xenolith* |
| Co | - | - | - | - | - |
| Cr | 71 | 26 | 485 | 382 | 542 |
| Ni | 23 | 2 | 156 | 131 | 165 |
| V | 43 | 49 | 185 | 178 | 198 |
| Zn | 46 | 17 | 93 | 141 | 88 |
| Ce | 22 | 11 | 49 | 47 | 45 |
| La | 11 | 7 | 21 | 20 | 10 |
| Nb | 6 | 3 | 4 | 4 | 4 |
| Ga | 6 | 6 | 13 | 13 | 15 |
| Pb | 19 | 3 | 39 | 73 | 66 |
| Pr | < 5 | < 5 | < 5 | < 5 | 40 |
| Rb | 43 | 49 | 178 | 173 | 237 |
| Ba | 88 | 74 | 6152 | 5597 | 6247 |
| Sr | 978 | 161 | 1169 | 1153 | 1140 |
| Th | 6 | 3 | 3 | 3 | 2 |
| Y | 12 | 14 | 17 | 16 | 13 |
| Zr | 85 | 56 | 75 | 82 | 66 |

| Sample | BWd-tub | C-SB1 | C-SB2 | C-SB3 | C-LD1 |
|---|---|---|---|---|---|
| Rock type | *Meta-igneous xenolith* | *Hornfels xenolith* | *Hornfels xenolith* | *Hornfels xenolith* | *Hornfelsed meta-siltstone* |
| Co | - | 31 | 29 | 33 | 38 |
| Cr | 194 | 118 | 120 | 135 | 129 |
| Ni | 65 | 90 | 55 | 64 | 88 |
| V | 180 | 164 | 142 | 162 | 145 |
| Zn | 78 | 90 | 95 | 90 | 126 |
| Ce | 49 | 83 | 85 | 72 | 78 |
| La | 19 | 29 | 47 | 51 | 33 |
| Nb | 9 | 19 | 20 | 17 | 19 |
| Ga | 11 | 23 | 20 | 20 | 18 |
| Pb | 5 | 25 | 24 | 25 | 33 |
| Pr | < 5 | <4 | 8 | 6 | <4 |
| Rb | 23 | 247 | 166 | 160 | 154 |
| Ba | 1342 | 662 | 488 | 559 | 166 |
| Sr | 1118 | 232 | 215 | 224 | 173 |
| Th | 3 | 23 | 13 | 12 | 16 |
| Y | 24 | 22 | 31 | 30 | 23 |
| Zr | 136 | 174 | 175 | 176 | 163 |

| **Sample** | **silt1** |
|---|---|
| **Rock type** | *Meta-siltstone* |
| **Co** | - |
| **Cr** | 143 |
| **Ni** | 75 |
| **V** | 131 |
| **Zn** | 94 |
| **Ce** | 62 |
| **La** | 26 |
| **Nb** | 11 |
| **Ga** | 14 |
| **Pb** | 7 |
| **Pr** | <5 |
| **Rb** | 97 |
| **Ba** | 262 |
| **Sr** | 73 |
| **Th** | <1 |
| **Y** | 24 |
| **Zr** | 155 |

## 3.5. Rare earth elements

| Sample | limestone 1 | marble 1 | BWa | BWb |
|---|---|---|---|---|
| Rock type | *Limestone* | *Marble* | *Meta-igneous xenolith* | *Meta-igneous xenolith* |
| La | 10.9 | 6.2 | 12.0 | 13.0 |
| Ce | 22.4 | 12.8 | 24.5 | 27.0 |
| Pr | 2.6 | 1.6 | 3.1 | 3.4 |
| Nd | 9.9 | 6.3 | 13.5 | 14.6 |
| Sm | 1.9 | 1.3 | 3.1 | 3.4 |
| Eu | 0.4 | 0.3 | 0.6 | 0.7 |
| Gd | 1.7 | 1.4 | 3.2 | 3.5 |
| Tb | 0.3 | 0.2 | 0.5 | 0.6 |
| Dy | 1.5 | 1.4 | 3.2 | 3.4 |
| Ho | 0.3 | 0.3 | 0.6 | 0.6 |
| Er | 0.9 | 0.9 | 1.8 | 1.7 |
| Tm | 0.1 | 0.1 | 0.3 | 0.3 |
| Yb | 0.8 | 0.9 | 1.6 | 1.4 |
| Lu | 0.1 | 0.1 | 0.2 | 0.2 |

| Sample | BWc | BWd-tub | C-SB1 | C-SB2 |
|---|---|---|---|---|
| Rock type | *Meta-igneous xenolith* | *Meta-igneous xenolith* | *Hornfels xenolith* | *Hornfels xenolith* |
| La | 10.1 | 27.2 | 37.3 | 37.6 |
| Ce | 20.2 | 56.0 | 79.5 | 79.0 |
| Pr | 2.6 | 6.8 | 8.7 | 8.9 |
| Nd | 11.0 | 27.6 | 32.0 | 33.6 |
| Sm | 2.5 | 5.7 | 5.6 | 6.5 |
| Eu | 0.5 | 1.8 | 1.2 | 1.5 |
| Gd | 2.6 | 5.3 | 4.9 | 6.0 |
| Tb | 0.4 | 0.8 | 0.7 | 0.9 |
| Dy | 2.4 | 4.8 | 4.1 | 5.3 |
| Ho | 0.5 | 0.9 | 0.7 | 1.1 |
| Er | 1.3 | 2.6 | 2.4 | 3.1 |
| Tm | 0.2 | 0.4 | 0.4 | 0.5 |
| Yb | 1.1 | 2.4 | 2.3 | 2.9 |
| Lu | 0.2 | 0.4 | 0.3 | 0.4 |

| Sample | C-SB3 | C-LD1 | silt1 |
|---|---|---|---|
| Rock type | *Hornfels xenolith* | *Hornfelsed meta-siltstone* | *Meta-siltstone* |
| La | 38.6 | 36.2 | 31.0 |
| Ce | 81.8 | 78.4 | 65.4 |
| Pr | 9.2 | 8.9 | 7.7 |
| Nd | 34.3 | 33.5 | 29.7 |
| Sm | 6.4 | 6.3 | 5.9 |
| Eu | 1.3 | 1.2 | 1.1 |
| Gd | 5.7 | 5.6 | 5.2 |
| Tb | 0.9 | 0.8 | 0.8 |
| Dy | 5.0 | 4.7 | 4.7 |
| Ho | 1.0 | 0.9 | 0.9 |
| Er | 3.0 | 2.6 | 2.7 |
| Tm | 0.5 | 0.4 | 0.4 |
| Yb | 2.9 | 2.4 | 2.6 |
| Lu | 0.4 | 0.3 | 0.4 |

## 3.6. U, Th and Pb ppm

| Sample | limestone 1 | marble 1 | BWa | BWb |
|---|---|---|---|---|
| Rock type | *Limestone* | *Marble* | *Meta-igneous xenolith* | *Meta-igneous xenolith* |
| U | 3.2 | 1.2 | 1.8 | 1.2 |
| Th | 3.1 | 2.7 | 1.3 | 1.4 |
| Pb | 15.3 | 6.0 | 35.6 | 68.7 |

| Sample | BWc | BWd-tub | C-SB1 | C-SB2 |
|---|---|---|---|---|
| Rock type | *Meta-igneous xenolith* | *Meta-igneous xenolith* | *Hornfels xenolith* | *Hornfels xenolith* |
| U | 1.7 | 0.9 | 2.7 | 3.0 |
| Th | 0.9 | 3.6 | 12.1 | 11.5 |
| Pb | 59.6 | 6.6 | 24.3 | 14.9 |

| Sample | C-SB3 | C-LD1 | silt1 |
|---|---|---|---|
| Rock type | *Hornfels xenolith* | *Hornfelsed meta-siltstone* | *Meta-siltstone* |
| U | 3.1 | 2.4 | 2.5 |
| Th | 12.0 | 11.2 | 9.3 |
| Pb | 18.3 | 34.5 | 9.8 |

## 3.7. Raw isotope ratio data

### *3.7.1. Strontium*

| Sample | Rock type | Lab Number | $^{87}Sr/^{86}Sr$ measured | % S.E. | 2 S.E. | 2S.D. |
|---|---|---|---|---|---|---|
| **limestone 1** | Limestone | *D920* | 0.708165 | 0.0013 | 0.000026 | 0.000026 |
| **limestone 1** ***re-run*** | Limestone | *E466* | 0.708781 | 0.0013 | 0.000026 | 0.000026 |
| **marble1** | Marble | *E470* | 0.712608 | 0.0012 | 0.000024 | 0.000024 |
| **BWa** | *Meta-igneous xenolith* | *D837* | 0.709245 | 0.0013 | 0.000026 | 0.000026 |
| **BWb** | *Meta-igneous xenolith* | *E468* | 0.709383 | 0.0014 | 0.000028 | 0.000028 |
| **BWb** | *Meta-igneous xenolith* | *D838* | 0.709435 | 0.0015 | 0.000030 | 0.000030 |
| **BWc** | *Meta-igneous xenolith* | *D839* | 0.709966 | 0.0014 | 0.000028 | 0.000028 |
| **BWd-tub** | *Meta-igneous xenolith* | *E469* | 0.706494 | 0.0022 | 0.000044 | 0.000044 |
| **BWd-tub** ***re-run*** | *Meta-igneous xenolith* | *D840* | 0.706506 | 0.0011 | 0.000022 | 0.000022 |
| **C-SB1** | *Hornfels xenolith* | *E102* | 0.723196 | 0.0012 | 0.000024 | 0.000024 |
| **C-SB2** | *Hornfels xenolith* | *E103* | 0.722039 | 0.0012 | 0.000024 | 0.000024 |
| **C-SB3** | *Hornfels xenolith* | *E104* | 0.722327 | 0.0012 | 0.000024 | 0.000024 |
| **C-LD1** | *Hornfelsed Longford-Down meta-siltstone* | *E105* | 0.722519 | 0.0014 | 0.000028 | 0.000028 |
| **Silt1** | *Longford-Down meta-siltstone* | *D836* | 0.730812 | 0.0013 | 0.000026 | 0.000026 |

### *3.7.2. Neodymium*

| Sample | Rock type | Lab Number | $^{143}Nd/^{144}Nd$ Measured | % S.E. | 2 S.E. | 2S.D. |
|---|---|---|---|---|---|---|
| **limestone 1** | Limestone | *D920* | *Not Analysed* | | | |
| **limestone 1** ***re-run*** | Limestone | *E466* | *Not Analysed* | | | |
| **marble1** | Marble | *E470* | *Not Analysed* | | | |
| **BWa** | *Meta-igneous xenolith* | *D837* | Failed | | | |
| **BWb** | *Meta-igneous xenolith* | *E468* | *Not Analysed* | | | |
| **BWb** | *Meta-igneous xenolith* | *D838* | Failed | | | |
| **BWc** | *Meta-igneous xenolith* | *D839* | 0.512433 | 0.0079 | 0.000158 | 0.000158 |
| **BWd-tub** | *Meta-igneous xenolith* | *E469* | *Not Analysed* | | | |
| **BWd-tub** ***re-run*** | *Meta-igneous xenolith* | *D840* | Failed | | | |
| **C-SB1** | *Hornfels xenolith* | *E102* | 0.512031 | 0.0006 | 0.000012 | 0.000012 |
| **C-SB2** | *Hornfels xenolith* | *E103* | 0.51206 | 0.0060 | 0.000120 | 0.000120 |
| **C-SB3** | *Hornfels xenolith* | *E104* | 0.512054 | 0.0007 | 0.000014 | 0.000014 |
| **C-LD1** | *Hornfelsed Longford-Down meta-siltstone* | *E105* | 0.512055 | 0.0007 | 0.000014 | 0.000014 |
| **Silt1** | *Longford-Down meta-siltstone* | *D836* | 0.512606 | 0.0023 | 0.000046 | 0.000046 |

### *3.7.3. Lead*

| Sample | Rock Type | Lab Number | $^{206}Pb/^{204}Pb$ | 2 S.E. | $^{207}Pb/^{204}Pb$ | 2 S.E. | $^{208}Pb/^{204}Pb$ | 2 S.E. |
|---|---|---|---|---|---|---|---|---|
| **limestone 1** | *Limestone* | N481 | 19.414 | 0.109 | 15.554 | 0.108 | 38.377 | 0.109 |
| **marble 1** | *Marble* | N484 | 20.429 | 0.077 | 15.693 | 0.081 | 39.623 | 0.076 |
| **BWb** | *Meta-igneous xenolith* | N482 | 18.476 | 0.050 | 15.622 | 0.050 | 38.012 | 0.050 |
| **BWc** | *Meta-igneous xenolith* | N475 | 18.588 | 0.038 | 15.601 | 0.039 | 37.932 | 0.040 |
| **BWd-tub** | *Meta-igneous xenolith* | N483 | 18.948 | 0.012 | 15.616 | 0.013 | 38.696 | 0.013 |
| **C-SB1** | *Hornfels xenolith* | E121 | 18.931 | 0.002 | 15.623 | 0.002 | 38.862 | 0.004 |
| **C-SB2** | *Hornfels xenolith* | E122 | 19.048 | 0.002 | 15.637 | 0.002 | 38.991 | 0.005 |
| **C-SB3** | *Hornfels xenolith* | E123 | 18.995 | 0.004 | 15.623 | 0.003 | 38.916 | 0.007 |
| **C-LD1** | *Hornfelsed Longford-Down meta-siltstone* | E124 | 18.669 | 0.002 | 15.615 | 0.002 | 38.637 | 0.004 |
| **silt1** | *Longford-Down meta-siltstone* | N459 | 19.694 | 0.006 | 15.665 | 0.006 | 39.767 | 0.007 |

## 3.8. Age corrected isotope data

### *3.8.1. Strontium*

| Sample | Rock type | Lab Number | Age (Ma) | Rb ppm | Sr ppm | $^{87}Sr/^{86}Sr$ measured | $^{87}Sr/^{86}Sr$ age-corrected |
|---|---|---|---|---|---|---|---|
| **limestone 1** | Limestone | *D920* | 60 | 43 | 978 | 0.708165 | 0.708058 |
| **limestone 1** ***re-run*** | Limestone | *E466* | 60 | 43 | 978 | 0.708781 | 0.708674 |
| **marble1** | Marble | *E470* | 60 | 49 | 161 | 0.712608 | 0.711857 |
| **BWa** | *Meta-igneous xenolith* | *D837* | 60 | 178 | 1,169 | 0.709245 | 0.708870 |
| **BWb** | *Meta-igneous xenolith* | *E468* | 60 | 173 | 1,153 | 0.709383 | 0.709014 |
| **BWb** | *Meta-igneous xenolith* | *D838* | 60 | 173 | 1,153 | 0.709435 | 0.709066 |
| **BWc** | *Meta-igneous xenolith* | *D839* | 60 | 237 | 1,140 | 0.709966 | 0.709453 |
| **BWd-tub** | *Meta-igneous xenolith* | *E469* | 60 | 23 | 1,118 | 0.706494 | 0.706443 |
| **BWd-tub** ***re-run*** | *Meta-igneous xenolith* | *D840* | 60 | 23 | 1,118 | 0.706506 | 0.706455 |
| **C-SB1** | *Hornfels xenolith* | *E102* | 60 | 247 | 232 | 0.723196 | 0.720566 |
| **C-SB2** | *Hornfels xenolith* | *E103* | 60 | 166 | 215 | 0.722039 | 0.720133 |
| **C-SB3** | *Hornfels xenolith* | *E104* | 60 | 160 | 224 | 0.722327 | 0.720563 |
| **C-LD1** | *Hornfelsed Longford-Down meta-siltstone* | *E105* | 60 | 154 | 173 | 0.722519 | 0.720320 |
| **Silt1** | *Longford-Down meta-siltstone* | *D836* | 60 | 97 | 73 | 0.730812 | 0.727498 |

### *3.8.2. Neodymium*

| Sample | Rock type | Lab Number | Age (Ma) | Sm ppm | Nd ppm | $^{143}Nd/^{144}Nd$ Measured | $^{143}Nd/^{144}Nd$ age-corrected |
|---|---|---|---|---|---|---|---|
| **limestone 1** | Limestone | *D920* | 60 | | | *Not Analysed* | |
| **limestone 1** ***re-run*** | Limestone | *E466* | 60 | | | *Not Analysed* | |
| **marble1** | Marble | *E470* | 60 | | | *Not Analysed* | |
| **BWa** | *Meta-igneous xenolith* | *D837* | 60 | | | Failed | |
| **BWb** | *Meta-igneous xenolith* | *E468* | 60 | | | *Not Analysed* | |
| **BWb** | *Meta-igneous xenolith* | *D838* | 60 | | | Failed | |
| **BWc** | *Meta-igneous xenolith* | *D839* | 60 | 3 | 11 | 0.512433 | 0.512379 |
| **BWd-tub** | *Meta-igneous xenolith* | *E469* | 60 | | | *Not Analysed* | |
| **BWd-tub** ***re-run*** | *Meta-igneous xenolith* | *D840* | 60 | | | Failed | |
| **C-SB1** | *Hornfels xenolith* | *E102* | 60 | 6 | 32 | 0.512031 | 0.511990 |
| **C-SB2** | *Hornfels xenolith* | *E103* | 60 | 6 | 34 | 0.512060 | 0.512015 |
| **C-SB3** | *Hornfels xenolith* | *E104* | 60 | 6 | 34 | 0.512054 | 0.512010 |
| **C-LD1** | *Hornfelsed Longford-Down meta-siltstone* | *E105* | 60 | 6 | 33 | 0.512055 | 0.512010 |
| **Silt1** | *Longford-Down meta-siltstone* | *D836* | 60 | 6 | 30 | 0.512606 | 0.512559 |

### *3.8.3. Lead*

| Sample | Rock Type | Lab Number | Age (Ma) | U (ppm) | Th (ppm) | Pb (ppm) | $^{206}Pb/^{204}Pb$ age-corrected | $^{207}Pb/^{204}Pb$ age-corrected | $^{208}Pb/^{204}Pb$ age-corrected |
|---|---|---|---|---|---|---|---|---|---|
| **limestone 1** | *Limestone* | N481 | 60 | 3.2 | 3.1 | 19.4 | 19.288 | 15.548 | 38.337 |
| **marble 1** | *Marble* | N484 | 60 | 1.2 | 2.7 | 20.4 | 20.301 | 15.686 | 39.530 |
| **BWb** | *Meta-igneous xenolith* | N482 | 60 | 1.2 | 1.4 | 18.5 | 18.465 | 15.622 | 38.008 |
| **BWc** | *Meta-igneous xenolith* | N475 | 60 | 1.7 | 0.9 | 18.6 | 18.571 | 15.600 | 37.929 |
| **BWd-tub** | *Meta-igneous xenolith* | N483 | 60 | 0.9 | 3.6 | 18.9 | 18.869 | 15.612 | 38.589 |
| **C-SB1** | *Hornfels xenolith* | E121 | 60 | 2.7 | 12.1 | 18.9 | 18.863 | 15.620 | 38.764 |
| **C-SB2** | *Hornfels xenolith* | E122 | 60 | 3.0 | 11.5 | 19.0 | 18.925 | 15.631 | 38.838 |
| **C-SB3** | *Hornfels xenolith* | E123 | 60 | 3.1 | 12.0 | 19.0 | 18.892 | 15.619 | 38.786 |
| **C-LD1** | *Hornfelsed Longford-Down meta-siltstone* | E124 | 60 | 2.4 | 11.2 | 18.7 | 18.627 | 15.613 | 38.574 |
| **silt1** | *Longford-Down meta-siltstone* | N459 | 60 | 2.5 | 9.3 | 19.7 | 19.535 | 15.658 | 39.574 |

# Appendix 4. ARRAN

## 4.1. Sample locations

### *4.1.1. Drumadoon*

| Sample Number | Lithologic description and locality | Grid Reference |
|---|---|---|
| DD-QFP-1 | *Enclave-bearing porphyrytic rhyolite from fallen column* | NR 88513 29350 |
| DD-QFP-2 | *Porphyrytic rhyolite from fallen column, no visible enclaves* | NR 88494 29300 |
| DD-QFP-3 | *Porphyrytic rhyolite from fallen column* | NR 88471 29183 |
| DD-dQFP-4 | *Porphyrytic dacite from dyke interior* | NR 88391 29105 |
| DD-dQFP-5 | *Dacite from dyke interior* | NR 88391 29108 |
| DD-Dol-6 | *Dolerite from base of sill on the Doon, 5cm above base* | NR 88482 29140 |
| DD-Dol-8 | *Dolerite from base of sill on the Doon, 5cm above base* | NR 88482 29140 |
| DD-QFP-9 | *Base of porphyrytic rhyolite sill on the Doon* | NR 88482 29140 |
| DD-QFP-10 | *Base of porphyrytic rhyolite sill on the Doon, 50 m to north of Loc. 1* | NR 88480 29180 |
| DD-Dol-11 | *Dolerite sill, base of the Doon* | NR 88480 29180 |
| DD-Dol-11a | *Dolerite adjacent to dacite on coast* | NR 88278 28803 |
| DD-Dol-12 | *Dolerite adjacent to dacite on coast* | NR 88278 28803 |
| DD-Dol-13 | *Dolerite adjacent to dacite on coast* | NR 88278 28803 |
| DD-QFP-15 | *Pure porphyritic rhyolite dyke* | NR 88485 28715 |
| DD-mDol-16 | *Marginal dolerite, aphyric. At contact* | NR 88392 31155 |
| DD-mDol-17 | *Marginal dolerite, aphyric. 10 cm from SE contact* | NR 88392 31155 |
| DD-mDol-18 | *Marginal dolerite, crystal-bearing. 30 cm from SE contact* | NR 88392 31155 |
| DD-QFP-19 | *Pale rhyolite, 6 m SE of NW margin* | NR 88421 31217 |
| DD-QFP-21 | *Pale rhyolite, 6 m SE of NW margin* | NR 88421 31217 |
| DD-Kspar | *Single euhedral K-spar crystals from quarry* | NR 88625 29145 |

### *4.1.2. Other igneous samples*

| Sample Number | Lithologic description and locality | Grid Reference |
|---|---|---|
| **ACCG1** | *Central Complex microgranite, active quarry at Dereneneach* | NR 93007 33621 |
| **AKIL1** | *Olivine Basalt from dyke trending 146, Kildonan Shore* | NS 02249 20961 |
| **ANG-1** | *Northern Granite, NE Arran* | - |
| **ANG-2** | *Northern Granite, NE Arran* | - |
| **ANG-3** | *Northern Granite, NE Arran* | - |

## 4.2. Major elements

### *4.2.1. Drumadoon*

#### *4.2.1.1. GEOMAR*

| Sample | DD-QFP-1 | DD-QFP-2 | DD-QFP-3 | DD-dQFP-4 | DD-dQFP-5 |
|---|---|---|---|---|---|
| **Rock type** | *Dacite* | *Rhyolite* | *Rhyolite* | *Dacite* | *Dacite* |
| **$SiO_2$** | 62.69 | 68.37 | 67.06 | 65.28 | 66.22 |
| **$TiO_2$** | 0.52 | 0.35 | 0.41 | 0.44 | 0.45 |
| **$AL_2O_3$** | 13.64 | 12.29 | 12.86 | 13.25 | 13.09 |
| **$Fe_2O_3$** | 5.81 | 3.90 | 5.25 | 4.95 | 4.72 |
| **MnO** | 0.11 | 0.10 | 0.13 | 0.11 | 0.11 |
| **MgO** | 2.81 | 1.33 | 2.06 | 2.24 | 2.87 |
| **CaO** | 3.87 | 3.34 | 2.70 | 3.60 | 2.18 |
| **$Na_2O$** | 2.73 | 2.75 | 2.94 | 2.60 | 2.04 |
| **$K_2O$** | 3.08 | 4.25 | 3.96 | 4.04 | 4.72 |
| **$P_2O_5$** | 0.05 | 0.05 | 0.05 | 0.06 | 0.06 |
| **LOI** | 4.96 | 3.51 | 3.13 | 3.69 | 3.90 |
| **Total** | 100.27 | 100.24 | 100.55 | 100.26 | 100.36 |

| Sample | DD-Dol-6 | DD-Dol-7 | DD-Dol-8 | DD-QFP-9 | DD-QFP-10 |
|---|---|---|---|---|---|
| **Rock type** | *Basalt* | *Basaltic-Andesite* | *Basaltic-Andesite* | *Rhyolite* | *Rhyolite* |
| **$SiO_2$** | 44.93 | 53.12 | 53.97 | 68.35 | 67.39 |
| **$TiO_2$** | 0.75 | 0.90 | 0.80 | 0.38 | 0.39 |
| **$AL_2O_3$** | 14.84 | 15.57 | 14.81 | 12.32 | 12.42 |
| **$Fe_2O_3$** | 9.82 | 9.68 | 9.78 | 4.90 | 6.06 |
| **MnO** | 0.18 | 0.15 | 0.20 | 0.08 | 0.13 |
| **MgO** | 4.25 | 6.57 | 6.41 | 2.98 | 3.26 |
| **CaO** | 11.46 | 8.18 | 8.26 | 1.65 | 1.60 |
| **$Na_2O$** | 2.39 | 2.54 | 2.41 | 2.54 | 2.47 |
| **$K_2O$** | 2.27 | 1.37 | 1.29 | 4.56 | 4.49 |
| **$P_2O_5$** | 0.07 | 0.08 | 0.07 | 0.05 | 0.05 |
| **LOI** | 9.57 | 3.17 | 3.08 | 2.81 | 3.19 |
| **Total** | 100.53 | 101.33 | 101.08 | 100.62 | 101.45 |

| Sample | DD-Dol-11 | DD-Dol-11a | DD-Dol-12 | DD-Dol-12wr | DD-Dol-13 |
|---|---|---|---|---|---|
| Rock type | *Basaltic-Andesite* | *Basaltic-Andesite* | *Basaltic-Andesite* | *Basaltic-Andesite including xenocrysts* | *Basaltic-Andesite* |
| $SiO_2$ | 53.83 | 53.42 | 51.77 | 51.04 | 54.05 |
| $TiO_2$ | 0.81 | 0.79 | 0.79 | 0.78 | 0.79 |
| $AL_2O_3$ | 15.02 | 14.78 | 15.06 | 14.47 | 14.84 |
| $Fe_2O_3$ | 9.57 | 9.40 | 9.35 | 9.21 | 9.64 |
| MnO | 0.20 | 0.14 | 0.13 | 0.14 | 0.14 |
| MgO | 6.26 | 5.84 | 5.57 | 5.34 | 5.62 |
| CaO | 8.60 | 8.16 | 7.79 | 8.07 | 7.72 |
| $Na_2O$ | 2.45 | 2.53 | 2.65 | 2.47 | 2.60 |
| $K_2O$ | 1.29 | 1.43 | 1.44 | 1.38 | 1.67 |
| $P_2O_5$ | 0.08 | 0.08 | 0.08 | 0.07 | 0.07 |
| LOI | 3.20 | 3.85 | 6.53 | 6.92 | 3.43 |
| Total | 101.31 | 100.42 | 101.16 | 99.89 | 100.57 |

| Sample | DD-Dol-13wr | DD-QFP-15 | DD-mDol-16 | DD-mDol-17 | DD-mDol-18 |
|---|---|---|---|---|---|
| Rock type | *Basaltic-Andesite including xenocrysts* | *Rhyolite* | *Basalt* | *Andesite* | *Dacite* |
| $SiO_2$ | 55.01 | 71.01 | 45.02 | 55.80 | 60.50 |
| $TiO_2$ | 0.75 | 0.26 | 0.76 | 0.69 | 0.50 |
| $AL_2O_3$ | 14.72 | 12.92 | 15.01 | 14.02 | 12.92 |
| $Fe_2O_3$ | 9.24 | 3.18 | 9.96 | 8.50 | 6.61 |
| MnO | 0.11 | 0.05 | 0.19 | 0.16 | 0.14 |
| MgO | 5.25 | 1.51 | 4.35 | 5.10 | 2.58 |
| CaO | 7.34 | 0.63 | 11.61 | 6.08 | 4.08 |
| $Na_2O$ | 2.77 | 1.91 | 2.34 | 2.56 | 2.84 |
| $K_2O$ | 1.78 | 6.68 | 2.27 | 2.16 | 3.53 |
| $P_2O_5$ | 0.07 | 0.04 | 0.07 | 0.06 | 0.05 |
| LOI | 3.59 | 2.23 | 9.05 | 4.89 | 6.20 |
| Total | 100.63 | 100.42 | 100.63 | 100.02 | 99.95 |

| Sample | DD-QFP-19 | DD-QFP-21 |
|---|---|---|
| Rock type | *Rhyolite* | *Rhyolite* |
| $SiO_2$ | 77.01 | 76.50 |
| $TiO_2$ | 0.15 | 0.17 |
| $AL_2O_3$ | 11.16 | 11.40 |
| $Fe_2O_3$ | 1.83 | 2.14 |
| MnO | 0.03 | 0.06 |
| MgO | 0.51 | 0.44 |
| CaO | 0.54 | 0.57 |
| $Na_2O$ | 2.21 | 2.36 |
| $K_2O$ | 4.82 | 4.87 |
| $P_2O_5$ | 0.03 | 0.03 |
| LOI | 1.39 | 1.39 |
| Total | 99.68 | 99.93 |

*4.2.1.2.Centre d'Analyses Minérale, University of Lausanne*

| Sample | DD-QFP-1 | DD-QFP-2 | DD-QFP-3 | DD-dQFP-4 | DD-dQFP-5 |
|---|---|---|---|---|---|
| **Rock type** | *Dacite* | *Rhyolite* | *Rhyolite* | *Dacite* | *Dacite* |
| **$SiO_2$** | 62.63 | 68.30 | 67.32 | 64.77 | 66.16 |
| **$TiO_2$** | 0.50 | 0.34 | 0.41 | 0.43 | 0.43 |
| **$AL_2O_3$** | 13.88 | 12.68 | 13.31 | 13.47 | 13.54 |
| **$Fe_2O_3$** | 5.48 | 3.69 | 4.94 | 4.68 | 4.36 |
| **MnO** | 0.10 | 0.10 | 0.13 | 0.11 | 0.11 |
| **MgO** | 2.74 | 1.29 | 2.00 | 2.16 | 2.76 |
| **CaO** | 3.93 | 3.41 | 2.74 | 3.66 | 2.22 |
| **$Na_2O$** | 2.68 | 2.65 | 2.80 | 2.41 | 1.95 |
| **$K_2O$** | 3.00 | 4.15 | 3.87 | 3.92 | 4.60 |
| **$P_2O_5$** | 0.05 | 0.04 | 0.04 | 0.04 | 0.04 |
| **$Cr_2O_3$** | 0.01 | 0.00 | 0.00 | 0.01 | 0.01 |
| **NiO** | 0.01 | 0.00 | 0.00 | 0.00 | 0.00 |
| **LOI** | 4.76 | 3.11 | 2.75 | 3.37 | 3.69 |
| **Total** | 99.78 | 99.76 | 100.32 | 99.02 | 99.88 |

| Sample | DD-Dol-7 | DD-Dol-8 | DD-QFP-9 | DD-QFP-10 | DD-Dol-11 |
|---|---|---|---|---|---|
| **Rock type** | *Basaltic-Andesite* | *Basaltic-Andesite* | *Rhyolite* | *Rhyolite* | *Basaltic-Andesite* |
| **$SiO_2$** | 52.61 | 53.26 | 66.72 | 66.46 | 53.22 |
| **$TiO_2$** | 0.89 | 0.81 | 0.41 | 0.43 | 0.81 |
| **$AL_2O_3$** | 15.75 | 15.02 | 12.43 | 12.63 | 15.19 |
| **$Fe_2O_3$** | 9.36 | 9.42 | 4.50 | 5.50 | 9.17 |
| **MnO** | 0.16 | 0.21 | 0.08 | 0.12 | 0.20 |
| **MgO** | 6.50 | 6.35 | 2.84 | 3.12 | 6.21 |
| **CaO** | 8.26 | 8.30 | 1.68 | 1.64 | 8.72 |
| **$Na_2O$** | 2.43 | 2.28 | 2.31 | 2.29 | 2.30 |
| **$K_2O$** | 1.36 | 1.27 | 4.33 | 4.28 | 1.27 |
| **$P_2O_5$** | 0.05 | 0.05 | 0.04 | 0.04 | 0.05 |
| **$Cr_2O_3$** | 0.02 | 0.02 | 0.00 | 0.01 | 0.02 |
| **NiO** | 0.01 | 0.01 | 0.00 | 0.00 | 0.01 |
| **LOI** | 2.27 | 2.30 | 3.49 | 2.63 | 2.52 |
| **Total** | 99.67 | 99.29 | 98.81 | 99.13 | 99.69 |

| Sample | DD-Dol-11a | DD-Dol-12 | DD-Dol-13 | DD-QFP-15 | DD-mDol-16 |
|---|---|---|---|---|---|
| Rock type | *Basaltic-Andesite* | *Basaltic-Andesite* | *Basaltic-Andesite* | *Rhyolite* | *Basalt* |
| $SiO_2$ | 52.61 | 50.65 | 53.50 | 70.02 | 44.44 |
| $TiO_2$ | 0.81 | 0.77 | 0.78 | 0.27 | 0.76 |
| $AL_2O_3$ | 14.90 | 15.03 | 15.00 | 13.03 | 15.02 |
| $Fe_2O_3$ | 8.91 | 8.98 | 9.28 | 2.93 | 9.50 |
| MnO | 0.13 | 0.13 | 0.14 | 0.04 | 0.18 |
| MgO | 5.71 | 5.45 | 5.53 | 1.45 | 4.30 |
| CaO | 8.15 | 7.75 | 7.76 | 0.70 | 11.51 |
| $Na_2O$ | 3.02 | 2.54 | 2.51 | 1.80 | 2.22 |
| $K_2O$ | 1.43 | 1.41 | 1.63 | 6.46 | 2.19 |
| $P_2O_5$ | 0.06 | 0.06 | 0.06 | 0.03 | 0.05 |
| $Cr_2O_3$ | 0.02 | 0.02 | 0.02 | 0.00 | 0.02 |
| NiO | 0.01 | 0.01 | 0.01 | 0.00 | 0.01 |
| LOI | 3.72 | 6.84 | 3.22 | 2.06 | 9.37 |
| Total | 99.49 | 99.63 | 99.42 | 98.79 | 99.59 |

| Sample | DD-mDol-17 | DD-mDol-18 | DD-QFP-19 | DD-QFP-21 | DD-Kspar |
|---|---|---|---|---|---|
| Rock type | *Andesite* | *Dacite* | *Rhyolite* | *Rhyolite* | *K-Feldspar separate* |
| $SiO_2$ | 55.80 | 60.76 | 77.17 | 76.57 | 65.41 |
| $TiO_2$ | 0.69 | 0.50 | 0.16 | 0.18 | 0.04 |
| $AL_2O_3$ | 14.36 | 13.25 | 11.62 | 11.78 | 18.48 |
| $Fe_2O_3$ | 8.09 | 6.34 | 1.80 | 2.09 | 0.46 |
| MnO | 0.15 | 0.13 | 0.03 | 0.06 | 0.00 |
| MgO | 5.02 | 2.52 | 0.48 | 0.40 | 0.09 |
| CaO | 6.16 | 4.15 | 0.58 | 0.60 | 0.36 |
| $Na_2O$ | 2.48 | 2.63 | 2.05 | 2.18 | 3.04 |
| $K_2O$ | 2.10 | 3.24 | 4.65 | 4.68 | 10.21 |
| $P_2O_5$ | 0.03 | 0.05 | 0.02 | 0.01 | 0.01 |
| $Cr_2O_3$ | 0.01 | 0.01 | 0.00 | 0.00 | 0.00 |
| NiO | 0.01 | 0.01 | 0.00 | 0.00 | 0.00 |
| LOI | 4.79 | 6.55 | 1.40 | 1.30 | 0.39 |
| Total | 99.69 | 100.13 | 99.97 | 99.86 | 98.48 |

### *4.2.2. Other igneous samples*

| **Sample** | **AKIL1** | **ANG-1** | **ANG-2** | **ANG-3** |
|---|---|---|---|---|
| **Rock type** | *Basalt* | *Granite* | *Granite* | *Granite* |
| **$SiO_2$** | 47.71 | 77.65 | 77.32 | 77.33 |
| **$TiO_2$** | 1.53 | 0.04 | 0.07 | 0.06 |
| **$AL_2O_3$** | 16.35 | 12.66 | 12.24 | 12.37 |
| **$Fe_2O_3$** | 13.16 | 0.89 | 1.06 | 0.98 |
| **MnO** | 0.19 | 0.01 | 0.02 | 0.01 |
| **MgO** | 8.22 | 0.02 | 0.07 | 0.06 |
| **CaO** | 9.68 | 0.30 | 0.47 | 0.46 |
| **$Na_2O$** | 0.15 | 3.58 | 3.66 | 3.61 |
| **$K_2O$** | 2.09 | 4.47 | 4.62 | 4.77 |
| **$P_2O_5$** | 0.14 | < 0.01 | < 0.01 | < 0.01 |
| **LOI** | 0.36 | 0.32 | 0.42 | 0.32 |
| **Total** | 99.22 | 99.94 | 99.96 | 99.97 |

## 4.3. Loss on ignition

### *4.3.1. Drumadoon*

#### *4.3.1.1. GEOMAR*

| Sample | DD-QFP-1 | DD-QFP-2 | DD-QFP-3 | DD-dQFP-4 | DD-dQFP-5 |
|---|---|---|---|---|---|
| Rock type | *Dacite* | *Rhyolite* | *Rhyolite* | *Dacite* | *Dacite* |
| $H_2O$ | 3.01 | 1.72 | 2.00 | 1.80 | 2.68 |
| $CO_2$ | 1.95 | 1.79 | 1.13 | 1.89 | 1.22 |
| $SO_3$ | - | - | - | - | - |
| LOI | - | - | - | - | - |
| Total LOI | 4.96 | 3.51 | 3.13 | 3.69 | 3.90 |

| Sample | DD-Dol-6 | DD-Dol-7 | DD-Dol-8 | DD-QFP-9 | DD-QFP-10 |
|---|---|---|---|---|---|
| Rock type | *Basalt* | *Basaltic-Andesite* | *Basaltic-Andesite* | *Rhyolite* | *Rhyolite* |
| $H_2O$ | 3.61 | 2.36 | 2.43 | 1.98 | 2.41 |
| $CO_2$ | 5.96 | 0.81 | 0.65 | 0.83 | 0.78 |
| $SO_3$ | - | - | - | - | - |
| LOI | - | - | - | - | - |
| Total LOI | 9.57 | 3.17 | 3.08 | 2.81 | 3.19 |

| Sample | DD-Dol-11 | DD-Dol-11a | DD-Dol-12 | DD-Dol-12wr | DD-Dol-13 |
|---|---|---|---|---|---|
| Rock type | *Basaltic-Andesite* | *Basaltic-Andesite* | *Basaltic-Andesite* | *Basaltic-Andesite incl. xenocrysts* | *Basaltic-Andesite* |
| $H_2O$ | 2.35 | 1.49 | 1.52 | 0.76 | 1.23 |
| $CO_2$ | 0.85 | 2.36 | 5.01 | 6.16 | 2.20 |
| $SO_3$ | - | - | - | - | - |
| LOI | - | - | - | - | - |
| Total LOI | 3.20 | 3.85 | 6.53 | 6.92 | 3.43 |

| Sample | DD-Dol-13wr | DD-QFP-15 | DD-mDol-16 | DD-mDol-17 | DD-mDol-18 |
|---|---|---|---|---|---|
| Rock type | *Basaltic-Andesite incl. xenocrysts* | *Rhyolite* | *Basalt* | *Andesite* | *Dacite* |
| $H_2O$ | 0.96 | 1.82 | 3.01 | 1.97 | 1.48 |
| $CO_2$ | 2.63 | 0.41 | 6.04 | 2.92 | 4.72 |
| $SO_3$ | - | - | - | - | - |
| LOI | - | - | - | - | - |
| Total LOI | 3.59 | 2.23 | 9.05 | 4.89 | 6.20 |

| Sample | DD-QFP-19 | DD-QFP-21 |
|---|---|---|
| Rock type | *Rhyolite* | *Rhyolite* |
| $H_2O$ | 1.13 | 1.13 |
| $CO_2$ | 0.26 | 0.26 |
| $SO_3$ | - | - |
| LOI | - | - |
| Total LOI | 1.39 | 1.39 |

| **Sample** | **DD-QFP-1** | **DD-QFP-2** | **DD-QFP-3** | **DD-dQFP-4** | **DD-dQFP-5** |
|---|---|---|---|---|---|
| **Rock type** | *Dacite* | *Rhyolite* | *Rhyolite* | *Dacite* | *Dacite* |
| **$H_2O$** | - | - | - | - | - |
| **$CO_2$** | - | - | - | - | - |
| **$SO_3$** | - | - | - | - | - |
| **LOI** | 4.76 | 3.11 | 2.75 | 3.37 | 3.69 |
| **Total LOI** | 4.76 | 3.11 | 2.75 | 3.37 | 3.69 |

| **Sample** | **DD-Dol-6** | **DD-Dol-7** | **DD-Dol-8** | **DD-QFP-9** | **DD-QFP-10** |
|---|---|---|---|---|---|
| **Rock type** | *Basalt* | *Basaltic-Andesite* | *Basaltic-Andesite* | *Rhyolite* | *Rhyolite* |
| **$H_2O$** | - | - | - | - | - |
| **$CO_2$** | - | - | - | - | - |
| **$SO_3$** | - | - | - | - | - |
| **LOI** | 9.79 | 2.27 | 2.30 | 3.49 | 2.63 |
| **Total LOI** | 9.79 | 2.27 | 2.30 | 3.49 | 2.63 |

| **Sample** | **DD-Dol-11** | **DD-Dol-11a** | **DD-Dol-12** | **DD-Dol-13** | **DD-QFP-15** |
|---|---|---|---|---|---|
| **Rock type** | *Basaltic-Andesite* | *Basaltic-Andesite* | *Basaltic-Andesite* | *Basaltic-Andesite* | *Rhyolite* |
| **$H_2O$** | - | - | - | - | - |
| **$CO_2$** | - | - | - | - | - |
| **$SO_3$** | - | - | - | - | - |
| **LOI** | 2.52 | 3.72 | 6.84 | 3.22 | 2.06 |
| **Total LOI** | 2.52 | 3.72 | 6.84 | 3.22 | 2.06 |

| **Sample** | **DD-mDol-16** | **DD-mDol-17** | **DD-mDol-18** | **DD-QFP-19** | **DD-QFP-21** |
|---|---|---|---|---|---|
| **Rock type** | *Basalt* | *Andesite* | *Dacite* | *Rhyolite* | *Rhyolite* |
| **$H_2O$** | - | - | - | - | - |
| **$CO_2$** | - | - | - | - | - |
| **$SO_3$** | - | - | - | - | - |
| **LOI** | 9.37 | 4.79 | 6.55 | 1.40 | 1.30 |
| **Total LOI** | 9.37 | 4.79 | 6.55 | 1.40 | 1.30 |

| **Sample** | **DD-Kspar** |
|---|---|
| **Rock type** | *K-Feldspar separate* |
| **$H_2O$** | - |
| **$CO_2$** | - |
| **$SO_3$** | - |
| **LOI** | 0.39 |
| **Total LOI** | 0.39 |

### *4.3.2. Other igneous samples*

| Sample | AKIL1 | ANG-1 | ANG-2 | ANG-3 |
|---|---|---|---|---|
| Rock type | *Basalt* | *Granite* | *Granite* | *Granite* |
| $H_2O$ | - | - | - | - |
| $CO_2$ | - | - | - | - |
| $SO_3$ | 0.36 | 0.01 | 0.01 | 0.01 |
| LOI | - | 0.31 | 0.41 | 0.31 |
| Total LOI | 0.36 | 0.32 | 0.42 | 0.32 |

## 4.4. Trace elements

### *4.4.1. Drumadoon*

#### *4.4.1.1. GEOMAR (XRF)*

| Sample | DD-QFP-1 | DD-QFP-2 | DD-QFP-3 | DD-dQFP-4 | DD-dQFP-5 |
|---|---|---|---|---|---|
| Rock type | *Dacite* | *Rhyolite* | *Rhyolite* | *Dacite* | *Dacite* |
| Co | 43 | 39 | 41 | 27 | 18 |
| Cr | 47 | 23 | 32 | 40 | 38 |
| Ni | 29 | 2 | 13 | 17 | 19 |
| V | 98 | 42 | 65 | 79 | 81 |
| Zn | 64 | 61 | 57 | 57 | 61 |
| Ce | 108 | 142 | 120 | 146 | 108 |
| La | 120 | 69 | 63 | 65 | 57 |
| Nb | 16 | 22 | 20 | 18 | 22 |
| Ga | 20 | 16 | 14 | 18 | 19 |
| Pb | 18 | 19 | 22 | 22 | 24 |
| Pr | 18 | 12 | 13 | 13 | 12 |
| Rb | 73 | 106 | 101 | 82 | 99 |
| Ba | 761 | 877 | 857 | 943 | 896 |
| Sr | 95 | 84 | 88 | 94 | 57 |
| Th | 16 | 14 | 17 | 10 | 17 |
| Y | 57 | 53 | 53 | 49 | 58 |
| Zr | 188 | 231 | 206 | 197 | 206 |

| Sample | DD-Dol-7 | DD-Dol-8 | DD-QFP-9 | DD-QFP-10 | DD-Dol-11 |
|---|---|---|---|---|---|
| **Rock type** | *Basaltic-Andesite* | *Basaltic-Andesite* | *Rhyolite* | *Rhyolite* | *Basaltic-Andesite* |
| **Co** | 48 | 57 | 52 | 37 | 30 |
| **Cr** | 87 | 111 | 113 | 37 | 37 |
| **Ni** | 76 | 89 | 90 | 12 | 13 |
| **V** | 181 | 222 | 209 | 59 | 71 |
| **Zn** | 57 | 86 | 75 | 55 | 51 |
| **Ce** | 74 | 39 | 45 | 117 | 101 |
| **La** | 34 | <4 | 56 | 43 | 110 |
| **Nb** | 11 | 7 | 8 | 19 | 17 |
| **Ga** | 18 | 15 | 15 | 17 | 15 |
| **Pb** | 21 | 10 | 12 | 17 | 21 |
| **Pr** | 5 | <3 | 9 | 9 | 22 |
| **Rb** | 44 | 34 | 29 | 98 | 98 |
| **Ba** | 485 | 313 | 373 | 911 | 885 |
| **Sr** | 137 | 145 | 141 | 64 | 63 |
| **Th** | 11 | 6 | 11 | 14 | 20 |
| **Y** | 36 | 36 | 34 | 48 | 49 |
| **Zr** | 140 | 118 | 106 | 188 | 192 |

| Sample | DD-Dol-11a | DD-Dol-12 | DD-Dol-12wr | DD-Dol-13 | DD-Dol-13wr |
|---|---|---|---|---|---|
| **Rock type** | *Basaltic-Andesite* | *Basaltic-Andesite* | *Basaltic-Andesite including xenocrysts* | *Basaltic-Andesite* | *Basaltic-Andesite including xenocrysts* |
| **Co** | 53 | 49 | 57 | 63 | 57 |
| **Cr** | 109 | 106 | 100 | 102 | 91 |
| **Ni** | 88 | 78 | 78 | 82 | 66 |
| **V** | 201 | 190 | 190 | 186 | 181 |
| **Zn** | 78 | 78 | 69 | 65 | 78 |
| **Ce** | 63 | 55 | 69 | 50 | 59 |
| **La** | 109 | <10 | 143 | 20 | 28 |
| **Nb** | 9 | 7 | 6 | 9 | 11 |
| **Ga** | 19 | 16 | 18 | 18 | 16 |
| **Pb** | 15 | 13 | 9 | 7 | 13 |
| **Pr** | 16 | <4 | 22 | <4 | <5 |
| **Rb** | 32 | 26 | 25 | 29 | 36 |
| **Ba** | 343 | 415 | 387 | 393 | 439 |
| **Sr** | 146 | 160 | 208 | 190 | 157 |
| **Th** | <4 | 6 | 9 | 13 | 10 |
| **Y** | 33 | 35 | 34 | 33 | 38 |
| **Zr** | 109 | 111 | 108 | 109 | 123 |

| Sample | DD-QFP-15 | DD-mDol-16 | DD-mDol-17 | DD-mDol-18 | DD-QFP-19 |
|---|---|---|---|---|---|
| **Rock type** | *Rhyolite* | *Basalt* | *Andesite* | *Dacite* | *Rhyolite* |
| **Co** | 45 | 38 | 40 | 49 | 33 |
| **Cr** | 101 | <18 | 78 | 83 | 55 |
| **Ni** | 74 | - | 74 | 59 | 29 |
| **V** | 195 | 20 | 182 | 171 | 100 |
| **Zn** | 85 | 42 | 59 | 68 | 57 |
| **Ce** | 52 | 138 | 66 | 55 | 92 |
| **La** | <4 | 59 | 94 | 135 | 31 |
| **Nb** | 9 | 21 | 12 | 10 | 16 |
| **Ga** | 16 | 18 | 18 | 16 | 14 |
| **Pb** | 17 | 21 | 13 | 20 | 18 |
| **Pr** | <2 | 13 | 15 | 21 | 6 |
| **Rb** | 37 | 134 | 44 | 45 | 69 |
| **Ba** | 410 | 1193 | 452 | 441 | 673 |
| **Sr** | 152 | 53 | 135 | 132 | 104 |
| **Th** | <5 | 20 | 8 | 12 | 13 |
| **Y** | 37 | 67 | 38 | 39 | 51 |
| **Zr** | 119 | 222 | 145 | 124 | 164 |

| Sample | DD-QFP-21 | DD-Kspar |
|---|---|---|
| **Rock type** | *Rhyolite* | *K-Feldspar separate* |
| **Co** | 44 | 33 |
| **Cr** | <2 | <3 |
| **Ni** | - | - |
| **V** | <8 | <6 |
| **Zn** | 34 | 47 |
| **Ce** | 166 | 117 |
| **La** | 409 | 652 |
| **Nb** | 24 | 23 |
| **Ga** | 16 | 17 |
| **Pb** | 22 | 25 |
| **Pr** | 69 | 104 |
| **Rb** | 145 | 145 |
| **Ba** | 648 | 649 |
| **Sr** | 39 | 34 |
| **Th** | 14 | 21 |
| **Y** | 73 | 67 |
| **Zr** | 166 | 183 |

*4.4.1.2.Institute F. - A. Forel, Versoix (ICP-MS)*

| Sample | DD-QFP-1 | DD-QFP-2 | DD-QFP-3 | DD-dQFP-4 | DD-dQFP-5 |
|---|---|---|---|---|---|
| **Rock type** | *Dacite* | *Rhyolite* | *Rhyolite* | *Dacite* | *Dacite* |
| **Sc** | 18.4 | 11.9 | 14.8 | 16.3 | 16.6 |
| **Ti** | 2928.0 | 2003.0 | 2409.0 | 2564.0 | 2604.0 |
| **V** | 94.7 | 40.2 | 63.9 | 75.0 | 73.6 |
| **Cr** | 46.4 | 19.1 | 33.4 | 36.3 | 36.1 |
| **Co** | 48.4 | 40.7 | 46.2 | 31.1 | 18.5 |
| **Ni** | 36.0 | 15.2 | 26.8 | 28.6 | 27.3 |
| **Cu** | 35.8 | 18.1 | 32.8 | 29.9 | 29.1 |
| **Zn** | 63.4 | 55.0 | 60.0 | 55.7 | 61.5 |
| **Rb** | 69.6 | 102.3 | 96.6 | 81.2 | 95.0 |
| **Sr** | 91.5 | 83.3 | 87.5 | 90.3 | 54.8 |
| **Y** | 48.6 | 46.0 | 46.7 | 41.6 | 48.4 |
| **Zr** | 113.4 | 108.6 | 119.9 | 112.6 | 123.3 |
| **Nb** | 17.6 | 21.4 | 19.8 | 18.4 | 19.5 |
| **Ba** | 798.4 | 946.4 | 884.1 | 974.4 | 933.3 |
| **Hf** | 3.8 | 3.8 | 4.1 | 3.8 | 4.2 |
| **Ta** | 2.6 | 3.0 | 2.8 | 2.6 | 2.8 |
| **Pb** | 16.0 | 18.2 | 17.3 | 16.3 | 17.1 |
| **Th** | 14.6 | 18.2 | 17.2 | 15.7 | 16.8 |
| **U** | 2.3 | 2.8 | 2.7 | 2.4 | 2.7 |

| Sample | DD-Dol-7 | DD-Dol-8 | DD-QFP-9 | DD-QFP-10 | DD-Dol-11 |
|---|---|---|---|---|---|
| **Rock type** | *Basaltic-Andesite* | *Basaltic-Andesite* | *Rhyolite* | *Rhyolite* | *Basaltic-Andesite* |
| **Sc** | 34.2 | 32.2 | 14.2 | 14.4 | 32.7 |
| **Ti** | 5072.0 | 4522.0 | 2244.0 | 2268.0 | 4646.0 |
| **V** | 216.3 | 195.4 | 59.1 | 62.8 | 202.2 |
| **Cr** | 100.7 | 105.9 | 28.1 | 33.3 | 105.3 |
| **Co** | 52.5 | 46.7 | 41.6 | 33.3 | 51.2 |
| **Ni** | 75.9 | 79.6 | 22.7 | 27.2 | 80.8 |
| **Cu** | 70.6 | 73.0 | 24.3 | 35.9 | 72.7 |
| **Zn** | 81.2 | 73.8 | 54.5 | 66.8 | 73.1 |
| **Rb** | 30.5 | 27.6 | 96.9 | 93.8 | 28.8 |
| **Sr** | 145.6 | 138.1 | 61.3 | 60.6 | 145.5 |
| **Y** | 34.5 | 31.3 | 40.6 | 40.0 | 31.2 |
| **Zr** | 122.4 | 110.0 | 101.8 | 111.7 | 109.6 |
| **Nb** | 9.0 | 8.1 | 18.7 | 18.8 | 8.2 |
| **Ba** | 372.8 | 359.3 | 946.5 | 902.3 | 364.5 |
| **Hf** | 3.6 | 3.2 | 3.6 | 3.8 | 3.2 |
| **Ta** | 1.5 | 1.6 | 2.4 | 3.1 | 1.5 |
| **Pb** | 8.1 | 7.4 | 16.2 | 15.4 | 7.3 |
| **Th** | 6.3 | 5.7 | 16.5 | 15.8 | 5.6 |
| **U** | 1.0 | 1.0 | 2.5 | 2.5 | 1.0 |

| Sample | DD-Dol-11a | DD-Dol-12 | DD-Dol-13 | DD-QFP-15 | DD-mDol-16 |
|---|---|---|---|---|---|
| **Rock type** | *Basaltic-Andesite* | *Basaltic-Andesite* | *Basaltic-Andesite* | *Rhyolite* | *Basalt* |
| **Sc** | 31.2 | 30.7 | 31.8 | 10.3 | 31.0 |
| **Ti** | 4465.0 | 4380.0 | 4617.0 | 1563.0 | 4488.0 |
| **V** | 190.6 | 185.5 | 195.6 | 21.4 | 182.9 |
| **Cr** | 96.3 | 95.3 | 95.3 | 17.4 | 90.4 |
| **Co** | 43.9 | 63.3 | 43.2 | 44.4 | 41.3 |
| **Ni** | 74.8 | 74.2 | 72.5 | 11.9 | 70.5 |
| **Cu** | 69.5 | 69.2 | 68.9 | 12.6 | 67.0 |
| **Zn** | 75.1 | 62.9 | 86.0 | 44.7 | 58.2 |
| **Rb** | 26.6 | 24.3 | 33.5 | 131.7 | 39.9 |
| **Sr** | 155.2 | 183.6 | 153.8 | 54.9 | 140.9 |
| **Y** | 30.5 | 28.5 | 34.0 | 52.2 | 33.7 |
| **Zr** | 112.1 | 108.1 | 124.6 | 136.6 | 125.3 |
| **Nb** | 8.4 | 8.2 | 9.5 | 23.5 | 10.3 |
| **Ba** | 430.2 | 440.8 | 468.2 | 1239.5 | 530.9 |
| **Hf** | 3.2 | 3.1 | 3.7 | 4.7 | 3.6 |
| **Ta** | 1.2 | 1.4 | 1.2 | 3.0 | 1.2 |
| **Pb** | 7.3 | 5.5 | 8.4 | 20.6 | 9.6 |
| **Th** | 6.0 | 5.8 | 7.0 | 21.1 | 7.6 |
| **U** | 1.0 | 1.0 | 1.2 | 3.1 | 1.3 |

| Sample | DD-mDol-17 | DD-mDol-18 | DD-QFP-19 | DD-QFP-21 | DD-Kspar |
|---|---|---|---|---|---|
| **Rock type** | *Andesite* | *Dacite* | *Rhyolite* | *Rhyolite* | *K-Feldspar separate* |
| **Sc** | 27.8 | 20.5 | 5.8 | 7.3 | 5.0 |
| **Ti** | 3980.0 | 3031.0 | 889.9 | 1011.0 | 164.2 |
| **V** | 160.7 | 105.8 | 4.2 | 5.5 | 1.7 |
| **Cr** | 81.0 | 54.8 | 2.5 | 3.7 | 1.9 |
| **Co** | 50.3 | 35.0 | 51.5 | 39.0 | 0.5 |
| **Ni** | 62.1 | 43.2 | 1.9 | 3.5 | 0.9 |
| **Cu** | 69.2 | 50.9 | 6.0 | 8.2 | 3.9 |
| **Zn** | 67.5 | 58.6 | 40.2 | 44.2 | 12.2 |
| **Rb** | 42.6 | 68.1 | 142.9 | 141.4 | 108.8 |
| **Sr** | 131.8 | 104.4 | 36.3 | 35.5 | 204.2 |
| **Y** | 36.4 | 42.1 | 64.3 | 56.8 | 3.5 |
| **Zr** | 121.2 | 115.1 | 96.1 | 100.3 | 15.0 |
| **Nb** | 11.9 | 16.4 | 23.3 | 24.4 | 2.1 |
| **Ba** | 482.4 | 698.3 | 681.2 | 696.8 | 6790.5 |
| **Hf** | 3.7 | 3.9 | 4.0 | 4.2 | 0.5 |
| **Ta** | 2.2 | 2.2 | 3.8 | 3.5 | 0.5 |
| **Pb** | 11.2 | 16.4 | 22.4 | 22.8 | 24.5 |
| **Th** | 9.2 | 13.9 | 23.7 | 23.2 | 1.9 |
| **U** | 1.6 | 2.5 | 3.3 | 3.0 | 0.3 |

### *4.4.2. Other igneous samples (XRF)*

| **Sample** | **AKIL1** | **ANG-1** | **ANG-2** | **ANG-3** |
|---|---|---|---|---|
| **Rock type** | *Basalt* | *Granite* | *Granite* | *Granite* |
| **Co** | - | - | - | - |
| **Cr** | - | 1 | 3 | 2 |
| **Ni** | - | 1 | 1 | 1 |
| **V** | - | 1 | 2 | 1 |
| **Zn** | - | 35 | 36 | 32 |
| **Ce** | - | 10 | 38 | 60 |
| **La** | - | 3 | 12 | 21 |
| **Nb** | - | 58 | 26 | 25 |
| **Ga** | - | 26 | 22 | 22 |
| **Pb** | - | 40 | 28 | 28 |
| **Pr** | - | <5 | <5 | 8 |
| **Rb** | - | 313 | 194 | 197 |
| **Ba** | - | 9 | 287 | 355 |
| **Sr** | - | 1 | 17 | 18 |
| **Th** | - | 28 | 17 | 17 |
| **Y** | - | 42 | 61 | 69 |
| **Zr** | - | 161 | 119 | 107 |

## 4.5. Rare earth elements

### *4.5.1. Drumadoon (Institute F. - A. Forel, Versoix)*

| **Sample** | **DD-QFP-1** | **DD-QFP-2** | **DD-QFP-3** | **DD-dQFP-4** | **DD-dQFP-5** |
|---|---|---|---|---|---|
| **Rock type** | *Dacite* | *Rhyolite* | *Rhyolite* | *Dacite* | *Dacite* |
| **La** | 55.0 | 66.3 | 61.5 | 57.7 | 60.1 |
| **Ce** | 99.4 | 120.4 | 112.7 | 107.0 | 110.8 |
| **Pr** | 11.7 | 13.9 | 13.2 | 12.2 | 12.8 |
| **Nd** | 43.9 | 51.6 | 49.2 | 45.3 | 47.0 |
| **Sm** | 8.8 | 9.6 | 9.4 | 8.7 | 9.2 |
| **Eu** | 1.3 | 1.4 | 1.4 | 1.5 | 1.3 |
| **Gd** | 8.6 | 9.2 | 8.9 | 8.3 | 8.8 |
| **Tb** | 1.4 | 1.4 | 1.4 | 1.3 | 1.4 |
| **Dy** | 8.4 | 8.5 | 8.2 | 7.5 | 8.5 |
| **Ho** | 1.7 | 1.7 | 1.7 | 1.5 | 1.7 |
| **Er** | 5.1 | 5.0 | 4.9 | 4.6 | 5.2 |
| **Tm** | 0.7 | 0.7 | 0.7 | 0.7 | 0.7 |
| **Yb** | 4.8 | 4.6 | 4.5 | 4.3 | 4.8 |
| **Lu** | 0.7 | 0.7 | 0.7 | 0.6 | 0.7 |

| **Sample** | **DD-Dol-7** | **DD-Dol-8** | **DD-QFP-9** | **DD-QFP-10** | **DD-Dol-11** |
|---|---|---|---|---|---|
| **Rock type** | *Basaltic-Andesite* | *Basaltic-Andesite* | *Rhyolite* | *Rhyolite* | *Basaltic-Andesite* |
| **La** | 23.7 | 21.5 | 59.4 | 55.5 | 21.5 |
| **Ce** | 44.0 | 39.6 | 110.8 | 103.2 | 39.9 |
| **Pr** | 5.3 | 4.8 | 12.8 | 12.0 | 4.8 |
| **Nd** | 21.3 | 19.4 | 47.5 | 45.0 | 19.6 |
| **Sm** | 4.9 | 4.4 | 9.0 | 8.6 | 4.5 |
| **Eu** | 1.1 | 1.1 | 1.3 | 1.3 | 1.1 |
| **Gd** | 5.6 | 5.1 | 8.5 | 8.1 | 4.9 |
| **Tb** | 0.9 | 0.9 | 1.3 | 1.2 | 0.8 |
| **Dy** | 5.9 | 5.6 | 7.5 | 7.3 | 5.4 |
| **Ho** | 1.2 | 1.2 | 1.5 | 1.5 | 1.1 |
| **Er** | 3.7 | 3.4 | 4.5 | 4.4 | 3.4 |
| **Tm** | 0.6 | 0.5 | 0.6 | 0.6 | 0.5 |
| **Yb** | 3.7 | 3.3 | 4.1 | 4.0 | 3.2 |
| **Lu** | 0.6 | 0.5 | 0.6 | 0.6 | 0.5 |

| Sample | DD-Dol-11a | DD-Dol-12 | DD-Dol-13 | DD-QFP-15 | DD-mDol-16 |
|---|---|---|---|---|---|
| **Rock type** | *Basaltic-Andesite* | *Basaltic-Andesite* | *Basaltic-Andesite* | *Rhyolite* | *Basalt* |
| **La** | 22.6 | 22.1 | 26.1 | 75.7 | 29.4 |
| **Ce** | 41.4 | 40.1 | 48.8 | 134.8 | 53.5 |
| **Pr** | 4.9 | 4.8 | 5.8 | 15.9 | 6.3 |
| **Nd** | 19.9 | 19.2 | 23.1 | 58.9 | 24.6 |
| **Sm** | 4.5 | 4.2 | 5.1 | 11.0 | 5.3 |
| **Eu** | 1.1 | 1.1 | 1.2 | 1.7 | 1.3 |
| **Gd** | 4.9 | 4.8 | 5.7 | 10.3 | 5.8 |
| **Tb** | 0.8 | 0.8 | 0.9 | 1.5 | 0.9 |
| **Dy** | 5.3 | 5.0 | 6.0 | 9.3 | 5.8 |
| **Ho** | 1.1 | 1.1 | 1.3 | 1.9 | 1.2 |
| **Er** | 3.4 | 3.1 | 3.7 | 5.7 | 3.5 |
| **Tm** | 0.5 | 0.4 | 0.5 | 0.8 | 0.5 |
| **Yb** | 3.2 | 2.9 | 3.5 | 5.4 | 3.1 |
| **Lu** | 0.5 | 0.4 | 0.5 | 0.8 | 0.5 |

| Sample | DD-mDol-17 | DD-mDol-18 | DD-QFP-19 | DD-QFP-21 | DD-Kspar |
|---|---|---|---|---|---|
| **Rock type** | *Andesite* | *Dacite* | *Rhyolite* | *Rhyolite* | *K-Feldspar separate* |
| **La** | 30.7 | 45.5 | 74.9 | 61.0 | 9.3 |
| **Ce** | 57.3 | 86.7 | 123.5 | 115.6 | 10.7 |
| **Pr** | 6.8 | 10.2 | 16.2 | 13.6 | 1.0 |
| **Nd** | 26.6 | 38.5 | 61.6 | 51.0 | 3.2 |
| **Sm** | 5.7 | 7.9 | 12.0 | 10.4 | 0.6 |
| **Eu** | 1.0 | 1.2 | 1.2 | 1.0 | 4.5 |
| **Gd** | 6.0 | 7.8 | 11.8 | 10.0 | 0.6 |
| **Tb** | 1.0 | 1.2 | 1.8 | 1.6 | 0.1 |
| **Dy** | 6.4 | 7.6 | 11.1 | 10.0 | 0.6 |
| **Ho** | 1.3 | 1.6 | 2.3 | 2.1 | 0.1 |
| **Er** | 4.0 | 4.7 | 6.8 | 6.1 | 0.5 |
| **Tm** | 0.6 | 0.7 | 1.0 | 0.9 | 0.1 |
| **Yb** | 3.8 | 4.3 | 6.3 | 5.9 | 0.5 |
| **Lu** | 0.6 | 0.7 | 0.9 | 0.9 | 0.1 |

### *4.5.2. Other igneous samples (SUERC)*

| Sample | ACCG1 | ANG-1 | ANG-1 Duplicate | ANG-2 | ANG-3 |
|---|---|---|---|---|---|
| **Rock type** | *Micrgranite* | *Granite* | *Granite* | *Granite* | *Granite* |
| **La** | 43.9 | 3.0 | 2.7 | 15.1 | 18.9 |
| **Ce** | 90.6 | 9.9 | 9.0 | 37.3 | 54.7 |
| **Pr** | 10.6 | 1.3 | 1.2 | 4.7 | 6.2 |
| **Nd** | 41.9 | 6.6 | 5.9 | 19.5 | 25.8 |
| **Sm** | 9.7 | 3.2 | 2.8 | 5.7 | 7.3 |
| **Eu** | 1.7 | 0.0 | 0.0 | 0.7 | 0.7 |
| **Gd** | 10.4 | 4.5 | 3.8 | 7.2 | 8.3 |
| **Tb** | 1.8 | 1.1 | 1.0 | 1.6 | 1.6 |
| **Dy** | 11.3 | 9.2 | 7.9 | 11.8 | 11.8 |
| **Ho** | 2.3 | 2.3 | 1.9 | 2.7 | 2.6 |
| **Er** | 6.8 | 8.2 | 6.9 | 9.3 | 8.8 |
| **Tm** | 1.1 | 1.6 | 1.3 | 1.7 | 1.6 |
| **Yb** | 6.5 | 10.9 | 8.9 | 11.0 | 10.3 |
| **Lu** | 1.0 | 1.7 | 1.4 | 1.7 | 1.6 |

## 4.6. U, Th and Pb ppm

| Sample | ACCG1 | AKIL1 | ANG-1 | ANG-2 | ANG-3 |
|---|---|---|---|---|---|
| **Rock type** | *Microgranite* | *Olivine Basalt* | *Granite* | *Granite* | *Granite* |
| **U** | 3.4 | 0.1 | 10.7 | 5.7 | 4.9 |
| **Th** | 18.0 | 0.4 | 31.6 | 20.3 | 17.8 |
| **Pb** | 11.5 | 0.8 | 36.1 | 26.4 | 29.8 |

## 4.7. Raw isotope ratio data

### *4.7.1. Drumadoon (Department of Mineralogy, Uni. of Geneva)*

#### *4.7.1.1.Strontium*

| Sample | Rock type | Lab Number | $^{87}Sr/^{86}Sr$ measured | % S.E. | 2 S.E. | 2S.D. |
|---|---|---|---|---|---|---|
| DD-QFP-1 | *Dacite* | 3544 (2) | 0.711732 | 0.00035 | 0.000007 | 0.000007 |
| DD-QFP-2 | *Rhyolite* | 3545 (3) | 0.714061 | 0.00040 | 0.000008 | 0.000008 |
| DD-QFP-3 | *Rhyolite* | 3546 (4) | 0.712751 | 0.00060 | 0.000012 | 0.000012 |
| DD-dQFP-4 | *Dacite* | 3547 (5) | 0.712669 | 0.00035 | 0.000007 | 0.000007 |
| DD-dQFP-5 | *Dacite* | 3548 (6) | 0.714621 | 0.00050 | 0.000010 | 0.00001 |
| DD-Dol-6 | *Basalt* | 3594 | 0.708636 | 0.00050 | 0.000010 | 0.00001 |
| DD-Dol-8 | *Basaltic-Andesite* | 3550 (8) | 0.706686 | 0.00040 | 0.000008 | 0.000008 |
| DD-QFP-9 | *Rhyolite* | 3551 (9) | 0.714698 | 0.00035 | 0.000007 | 0.000007 |
| DD-QFP-10 | *Rhyolite* | 3552 (10) | 0.714535 | 0.00035 | 0.000007 | 0.000007 |
| DD-Dol-11 | *Basaltic-Andesite* | 3553 (11) | 0.706811 | 0.00040 | 0.000008 | 0.000008 |
| DD-Dol-11a | *Basaltic-Andesite* | 3554 (12) | 0.707048 | 0.00315 | 0.000063 | 0.000063 |
| DD-Dol-12 | *Basaltic-Andesite* | 3583 | 0.707962 | 0.00025 | 0.000005 | 0.000005 |
| DD-Dol-13 | *Basaltic-Andesite* | 3584 | 0.707306 | 0.00025 | 0.000005 | 0.000005 |
| DD-QFP-15 | *Rhyolite* | 3585 | 0.717721 | 0.00030 | 0.000006 | 0.000006 |
| DD-mDol-16 | *Basalt* | 3586 | 0.708662 | 0.00035 | 0.000007 | 0.000007 |
| DD-mDol-17 | *Andesite* | 3587 | 0.707860 | 0.00035 | 0.000007 | 0.000007 |
| DD-mDol-18 | *Dacite* | 3588 | 0.711216 | 0.00045 | 0.000009 | 0.000009 |
| DD-QFP-19 | *Rhyolite* | 3592 | 0.721596 | 0.00275 | 0.000055 | 0.000055 |
| DD-QFP-21 | *Rhyolite* | 3593 | 0.721948 | 0.00040 | 0.000008 | 0.000008 |
| DD-Kspar | *K-Feldspar separate* | 3543 (1) | 0.714823 | 0.00045 | 0.000009 | 0.000009 |

*4.7.1.2.Neodymium*

| Sample | Rock type | Lab Number | $^{143}Nd/^{144}Nd$ Measured | % S.E. | 2 S.E. | 2S.D. |
|---|---|---|---|---|---|---|
| DD-QFP-1 | *Dacite* | 3544 (2) | 0.512187 | 0.00015 | 0.000003 | 0.000003 |
| DD-QFP-2 | *Rhyolite* | 3545 (3) | 0.512173 | 0.00020 | 0.000004 | 0.000004 |
| DD-QFP-3 | *Rhyolite* | 3546 (4) | 0.512175 | 0.00025 | 0.000005 | 0.000005 |
| DD-dQFP-4 | *Dacite* | 3547 (5) | 0.512174 | 0.00025 | 0.000005 | 0.000005 |
| DD-dQFP-5 | *Dacite* | 3548 (6) | 0.512211 | 0.00020 | 0.000004 | 0.000004 |
| DD-Dol-6 | *Basalt* | 3594 | 0.512264 | 0.00025 | 0.000005 | 0.000005 |
| DD-Dol-8 | *Basaltic-Andesite* | 3550 (8) | 0.512326 | 0.00020 | 0.000004 | 0.000004 |
| DD-QFP-9 | *Rhyolite* | 3551 (9) | 0.512184 | 0.00020 | 0.000004 | 0.000004 |
| DD-QFP-10 | *Rhyolite* | 3552 (10) | 0.512170 | 0.00020 | 0.000004 | 0.000004 |
| DD-Dol-11 | *Basaltic-Andesite* | 3553 (11) | 0.512336 | 0.00035 | 0.000007 | 0.000007 |
| DD-Dol-11a | *Basaltic-Andesite* | 3554 (12) | 0.512321 | 0.00025 | 0.000005 | 0.000005 |
| DD-Dol-12 | *Basaltic-Andesite* | 3583 | 0.512308 | 0.00030 | 0.000006 | 0.000006 |
| DD-Dol-13 | *Basaltic-Andesite* | 3584 | 0.512150 | 0.00040 | 0.000008 | 0.000008 |
| DD-QFP-15 | *Rhyolite* | 3585 | 0.512172 | 0.00020 | 0.000004 | 0.000004 |
| DD-mDol-16 | *Basalt* | 3586 | 0.512281 | 0.00020 | 0.000004 | 0.000004 |
| DD-mDol-17 | *Andesite* | 3587 | 0.512245 | 0.00025 | 0.000005 | 0.000005 |
| DD-mDol-18 | *Dacite* | 3588 | 0.512200 | 0.00025 | 0.000005 | 0.000005 |
| DD-QFP-19 | *Rhyolite* | 3592 | 0.512155 | 0.00020 | 0.000004 | 0.000004 |
| DD-QFP-21 | *Rhyolite* | 3593 | 0.512143 | 0.00025 | 0.000005 | 0.000005 |
| DD-Kspar | *K-Feldspar separate* | 3543 (1) | 0.512182 | 0.00035 | 0.000007 | 0.000007 |

## 4.8. Other igneous samples (SUERC)

### *4.8.1. Strontium*

| Sample | Rock type | Lab Number | $^{87}Sr/^{86}Sr$ measured | % S.E. | 2 S.E. | 2S.D. |
|---|---|---|---|---|---|---|
| **ACCG1** | *Micrgranite* | E107 | 0.711711 | 0.00130 | 0.000026 | 0.000026 |
| **AKIL1** | *Basalt* | E108 | 0.703607 | 0.00110 | 0.000022 | 0.000022 |
| **ANG-1** | *Granite* | D909 | 1.661396 | 0.00080 | 0.000016 | 0.000016 |
| **ANG-2** | *Granite* | D910 | 0.741864 | 0.00120 | 0.000024 | 0.000024 |
| **ANG-3** | *Granite* | D911 | 0.741135 | 0.00130 | 0.000026 | 0.000026 |

### *4.8.2. Neodymium*

| Sample | Rock type | Lab Number | $^{143}Nd/^{144}Nd$ Measured | % S.E. | 2 S.E. | 2S.D. |
|---|---|---|---|---|---|---|
| **ACCG1** | *Micrgranite* | E107 | 0.512385 | 0.00150 | 0.000030 | 0.000030 |
| **AKIL1** | *Basalt* | E108 | 0.513004 | 0.00070 | 0.000014 | 0.000014 |
| **ANG-1** | *Granite* | D909 | 0.512255 | 0.00150 | 0.000030 | 0.000030 |
| **ANG-2** | *Granite* | D910 | 0.512168 | 0.00060 | 0.000012 | 0.000012 |
| **ANG-3** | *Granite* | D911 | 0.512140 | 0.00060 | 0.000012 | 0.000012 |

## 4.9. Age corrected isotope data

### *4.9.1. Strontium*

| Sample | Rock type | Estimated age (Ma) | Rb ppm | Sr ppm | 87Sr/86Sr (Measured) | 87Sr/86Sr (59.16Ma) |
|---|---|---|---|---|---|---|
| DD-QFP-1 | *Dacite* | 59.16 | *73* | *95* | 0.711732 | 0.709863 |
| DD-QFP-2 | *Rhyolite* | 59.16 | *106* | *84* | 0.714061 | 0.710991 |
| DD-QFP-3 | *Rhyolite* | 59.16 | *101* | *88* | 0.712751 | 0.709959 |
| DD-dQFP-4 | *Dacite* | 59.16 | *82* | *94* | 0.712669 | 0.710547 |
| DD-dQFP-5 | *Dacite* | 59.16 | *99* | *57* | 0.714621 | 0.710395 |
| DD-Dol-6 | *Basalt* | 59.16 | *44* | *137* | 0.708636 | 0.707855 |
| DD-Dol-8 | *Basaltic-Andesite* | 59.16 | *29* | *141* | 0.706686 | 0.706186 |
| DD-QFP-9 | *Rhyolite* | 59.16 | *98* | *64* | 0.714698 | 0.710972 |
| DD-QFP-10 | *Rhyolite* | 59.16 | *98* | *63* | 0.714535 | 0.710750 |
| DD-Dol-11 | *Basaltic-Andesite* | 59.16 | *32* | *146* | 0.706811 | 0.706278 |
| DD-Dol-11a | *Basaltic-Andesite* | 59.16 | *26* | *160* | 0.707048 | 0.706653 |
| DD-Dol-12 | *Basaltic-Andesite* | 59.16 | *29* | *190* | 0.707962 | 0.707591 |
| DD-Dol-13 | *Basaltic-Andesite* | 59.16 | *37* | *152* | 0.707306 | 0.706714 |
| DD-QFP-15 | *Rhyolite* | 59.16 | *134* | *53* | 0.717721 | 0.711567 |
| DD-mDol-16 | *Basalt* | 59.16 | *44* | *135* | 0.708662 | 0.707869 |
| DD-mDol-17 | *Andesite* | 59.16 | *45* | *132* | 0.707860 | 0.707031 |
| DD-mDol-18 | *Dacite* | 59.16 | *69* | *104* | 0.711216 | 0.709602 |
| DD-QFP-19 | *Rhyolite* | 59.16 | *145* | *39* | 0.721596 | 0.712543 |
| DD-QFP-21 | *Rhyolite* | 59.16 | *145* | *34* | 0.721948 | 0.711564 |
| DD-Kspar | *K-Feldspar separate* | 59.16 | *109* | *204* | 0.714823 | 0.713527 |

### *4.9.2. Neodymium*

| Sample | Rock type | Estimated age (Ma) | Sm ppm | Nd ppm | 143Nd/144Nd (measured) | 143Nd/144Nd (59.16Ma) |
|---|---|---|---|---|---|---|
| DD-QFP-1 | *Dacite* | 59.16 | *9* | *44* | 0.512187 | 0.512140 |
| DD-QFP-2 | *Rhyolite* | 59.16 | *10* | *52* | 0.512173 | 0.512129 |
| DD-QFP-3 | *Rhyolite* | 59.16 | *9* | *49* | 0.512175 | 0.512130 |
| DD-dQFP-4 | *Dacite* | 59.16 | *9* | *45* | 0.512174 | 0.512129 |
| DD-dQFP-5 | *Dacite* | 59.16 | *9* | *47* | 0.512211 | 0.512165 |
| DD-Dol-6 | *Basalt* | 59.16 | *5* | *25* | 0.512264 | 0.512213 |
| DD-Dol-8 | *Basaltic-Andesite* | 59.16 | *4* | *19* | 0.512326 | 0.512273 |
| DD-QFP-9 | *Rhyolite* | 59.16 | *9* | *47* | 0.512184 | 0.512140 |
| DD-QFP-10 | *Rhyolite* | 59.16 | *9* | *45* | 0.512170 | 0.512125 |
| DD-Dol-11 | *Basaltic-Andesite* | 59.16 | *4* | *20* | 0.512336 | 0.512283 |
| DD-Dol-11a | *Basaltic-Andesite* | 59.16 | *4* | *20* | 0.512321 | 0.512268 |
| DD-Dol-12 | *Basaltic-Andesite* | 59.16 | *4* | *19* | 0.512308 | 0.512257 |
| DD-Dol-13 | *Basaltic-Andesite* | 59.16 | *5* | *23* | 0.512150 | 0.512098 |
| DD-QFP-15 | *Rhyolite* | 59.16 | *11* | *59* | 0.512172 | 0.512128 |
| DD-mDol-16 | *Basalt* | 59.16 | *5* | *25* | 0.512281 | 0.512231 |
| DD-mDol-17 | *Andesite* | 59.16 | *6* | *27* | 0.512245 | 0.512195 |
| DD-mDol-18 | *Dacite* | 59.16 | *8* | *38* | 0.512200 | 0.512152 |
| DD-QFP-19 | *Rhyolite* | 59.16 | *12* | *62* | 0.512155 | 0.512109 |
| DD-QFP-21 | *Rhyolite* | 59.16 | *10* | *51* | 0.512143 | 0.512095 |
| DD-Kspar | *K-Feldspar separate* | 59.16 | *1* | *3* | 0.512182 | 0.512141 |

# Appendix 5. ARRAN CRUST

## 5.1. Sample locations

| Sample Number | Lithologic description and locality | Grid Reference |
|---|---|---|
| *Midland Valley* | | |
| MV-Ord | *Ordovician greywacke, South of Girvan* | NX 15285 93585 |
| MV-Sil | *Silurian Sandstone, near Muirkirk* | NS 65667 36687 |
| MV-Dev-WK | *Devonian Sandstone, West Kilbride* | NS 21148 45321 |
| A-Dev | *Devonian Sandstone, North of Corrie* | NS 01458 47003 |
| MV-Carb-T | *Carboniferous Sandstone, Troon* | NS 31613 30632 |
| MV-Carb-SC | *Carboniferous Sandstone, Saltcoats* | NS 24294 41041 |
| A-Ps | *Permian Sandstone, Tormore Shore* | NR 889 325 |
| A-Ts | *Triassic Sandstone from shore below the Doon* | NR 88590 29644 |
| A-BTs | *Baked Triassic Sandstone from base of the Doon* | NR 88658 24971 |
| *Grampian Highlands* | | |
| A-Dal | *Dalradian schist, Glen Catacol, Arran* | NR 91708 48642 |

## 5.2. Major elements

| Sample | MV-Ord | MV-Sil | MV-Dev-WK | Mv-Carb-T |
|---|---|---|---|---|
| **Rock type** | *Greywacke* | *Sandstone* | *Sandstone* | *Sandstone* |
| **$SiO_2$** | 54.51 | 64.19 | 75.87 | 71.03 |
| **$TiO_2$** | 1.59 | 0.65 | 0.16 | 0.95 |
| **$AL_2O_3$** | 14.47 | 10.01 | 4.17 | 11.49 |
| **$Fe_2O_3$** | 9.98 | 5.19 | 1.40 | 10.30 |
| **MnO** | 0.12 | 0.07 | 0.14 | 0.03 |
| **MgO** | 5.44 | 2.85 | 0.64 | 1.24 |
| **CaO** | 5.12 | 6.82 | 7.79 | 0.34 |
| **$Na_2O$** | 3.24 | 1.97 | 0.03 | 1.17 |
| **$K_2O$** | 1.22 | 1.39 | 1.68 | 0.63 |
| **$P_2O_5$** | 0.16 | 0.15 | 0.04 | 0.18 |
| **LOI** | 5.01 | 6.92 | 7.23 | 3.47 |
| **Total** | 100.86 | 100.21 | 99.15 | 100.83 |

| Sample | MV-Carb-SC | A-Ps | A-Ts | A-BTs |
|---|---|---|---|---|
| **Rock type** | *Sandstone* | *Sandstone* | *Sandstone* | *Sandstone* |
| **$SiO_2$** | 53.92 | 86.33 | 66.98 | 53.98 |
| **$TiO_2$** | 0.79 | 0.18 | 0.27 | 0.64 |
| **$AL_2O_3$** | 24.69 | 6.59 | 5.05 | 12.25 |
| **$Fe_2O_3$** | 2.15 | 0.76 | 1.34 | 5.95 |
| **MnO** | 0.02 | 0.00 | 0.12 | 0.12 |
| **MgO** | 1.14 | 0.23 | 4.86 | 5.03 |
| **CaO** | 2.95 | 0.08 | 7.21 | 6.51 |
| **$Na_2O$** | 0.96 | 0.61 | 0.34 | 0.75 |
| **$K_2O$** | 5.38 | 3.90 | 2.64 | 4.57 |
| **$P_2O_5$** | 0.09 | 0.03 | 0.04 | 0.14 |
| **LOI** | 6.95 | 0.57 | 10.68 | 10.27 |
| **Total** | 99.04 | 99.28 | 99.53 | 100.21 |

## 5.3. Loss on ignition

| Sample | MV-Ord | MV-Sil | MV-Dev-WK | Mv-Carb-T |
|---|---|---|---|---|
| **Rock type** | *Greywacke* | *Sandstone* | *Sandstone* | *Sandstone* |
| $H_2O$ | 3.69 | 2.33 | 0.91 | 3.45 |
| $CO_2$ | 1.32 | 4.59 | 6.32 | 0.02 |
| **Total LOI** | 5.01 | 6.92 | 7.23 | 3.47 |

| Sample | MV-Carb-SC | A-Ps | A-Ts | A-BTs |
|---|---|---|---|---|
| **Rock type** | *Sandstone* | *Sandstone* | *Sandstone* | *Sandstone* |
| $H_2O$ | 4.88 | 0.52 | 0.69 | 2.34 |
| $CO_2$ | 2.07 | 0.05 | 9.99 | 7.93 |
| **Total LOI** | 6.95 | 0.57 | 10.68 | 10.27 |

## 5.4. Trace elements

| Sample | MV-Ord | MV-Sil | MV-Dev-WK | Mv-Carb-T |
|---|---|---|---|---|
| **Rock type** | *Greywacke* | *Sandstone* | *Sandstone* | *Sandstone* |
| **Co** | 43 | 31 | 45 | 51 |
| **Cr** | 186 | 168 | <14 | 102 |
| **Ni** | 60 | 59 | below detection limit | 45 |
| **V** | 256 | 85 | 22 | 105 |
| **Zn** | 85 | 44 | <2 | 16 |
| **Ce** | 37 | 48 | <6 | 184 |
| **La** | 236 | 415 | <8 | 99 |
| **Nb** | 10 | 16 | 5 | 15 |
| **Ga** | 19 | 14 | <5 | 17 |
| **Pb** | 19 | 19 | below detection limit | <5 |
| **Pr** | 34 | 62 | <4 | 18 |
| **Rb** | 16 | 50 | 41 | 25 |
| **Ba** | 257 | 211 | 645 | 434 |
| **Sr** | 204 | 197 | 152 | 45 |
| **Th** | 8 | 12 | <4 | 19 |
| **Y** | 39 | 15 | 13 | 349 |
| **Zr** | 145 | 253 | 77 | 766 |

| Sample | MV-Carb-SC | A-Ps | A-Ts | A-BTs |
|---|---|---|---|---|
| **Rock type** | *Sandstone* | *Sandstone* | *Sandstone* | *Sandstone* |
| **Co** | 17 | 32 | 31 | 24 |
| **Cr** | 136 | <17 | 19 | 68 |
| **Ni** | below detection limit | below dectection limit | 5 | 23 |
| **V** | 171 | 23 | 25 | 75 |
| **Zn** | 87 | 9 | 41 | 74 |
| **Ce** | 97 | 45 | <8 | 75 |
| **La** | 43 | 111 | 25 | 36 |
| **Nb** | below detection limit | 8 | 18 | 19 |
| **Ga** | 23 | 9 | <6 | 18 |
| **Pb** | 19 | 10 | 13 | 21 |
| **Pr** | 11 | 21 | <4 | 7 |
| **Rb** | 207 | 73 | 50 | 115 |
| **Ba** | 1639 | 637 | 424 | 530 |
| **Sr** | 1648 | 85 | 90 | 148 |
| **Th** | 18 | <3 | 8 | 13 |
| **Y** | 30 | 6 | 15 | 26 |
| **Zr** | 123 | 95 | 328 | 184 |

## 5.5. Rare earth elements

| Sample | MV-Ord | MV-Sil | MV-Dev-WK | Mv-Carb-T |
|---|---|---|---|---|
| Rock type | *Greywacke* | *Sandstone* | *Sandstone* | *Sandstone* |
| **La** | 13.5 | 23.9 | 10.5 | 140.4 |
| **Ce** | 30.7 | 49.0 | 20.6 | 284.1 |
| **Pr** | 4.1 | 5.9 | 2.6 | 33.7 |
| **Nd** | 17.9 | 22.4 | 10.0 | 132.4 |
| **Sm** | 4.6 | 4.1 | 2.1 | 24.4 |
| **Eu** | 1.4 | 0.9 | 0.6 | 3.5 |
| **Gd** | 5.2 | 3.5 | 2.2 | 23.6 |
| **Tb** | 0.9 | 0.5 | 0.3 | 3.6 |
| **Dy** | 5.5 | 2.8 | 2.1 | 22.2 |
| **Ho** | 1.1 | 0.5 | 0.4 | 4.6 |
| **Er** | 3.3 | 1.6 | 1.2 | 13.4 |
| **Tm** | 0.5 | 0.3 | 0.2 | 2.0 |
| **Yb** | 3.1 | 1.7 | 1.1 | 11.8 |
| **Lu** | 0.5 | 0.3 | 0.2 | 1.7 |

| Sample | MV-Carb-SC | A-Ps | A-Ts | A-BTs |
|---|---|---|---|---|
| Rock type | *Sandstone* | *Sandstone* | *Sandstone* | *Sandstone* |
| **La** | 49.4 | 7.4 | 7.8 | 29.4 |
| **Ce** | 103.6 | 16.4 | 16.4 | 59.9 |
| **Pr** | 11.8 | 1.7 | 2.0 | 7.0 |
| **Nd** | 44.8 | 6.5 | 8.0 | 26.5 |
| **Sm** | 8.6 | 1.2 | 1.7 | 5.0 |
| **Eu** | 1.9 | 0.4 | 0.5 | 1.1 |
| **Gd** | 7.3 | 1.0 | 1.7 | 4.4 |
| **Tb** | 1.0 | 0.1 | 0.3 | 0.6 |
| **Dy** | 5.8 | 0.8 | 1.7 | 3.5 |
| **Ho** | 1.1 | 0.2 | 0.3 | 0.7 |
| **Er** | 3.3 | 0.4 | 1.0 | 1.9 |
| **Tm** | 0.5 | 0.1 | 0.2 | 0.3 |
| **Yb** | 3.3 | 0.5 | 1.1 | 1.8 |
| **Lu** | 0.5 | 0.1 | 0.2 | 0.3 |

## 5.6. U, Th and Pb ppm

| Sample | MV-Ord | MV-Sil | MV-Dev-WK | A-Dev |
|---|---|---|---|---|
| Rock type | *Greywacke* | *Sandstone* | *Sandstone* | *Sandstone* |
| U | 1.0 | 1.8 | 0.4 | 1.3 |
| Th | 2.0 | 7.4 | 2.2 | 5.6 |
| Pb | 7.2 | 8.3 | 5.9 | 21.6 |

| Sample | MV-Carb-SC | A-Ps | A-Ts | A-BTs |
|---|---|---|---|---|
| Rock type | *Sandstone* | *Sandstone* | *Sandstone* | *Sandstone* |
| U | 2.9 | 0.6 | 0.6 | 1.8 |
| Th | 14.6 | 2.1 | 2.3 | 7.5 |
| Pb | 31.8 | 10.7 | 11.8 | 18.7 |

## 5.7. Raw isotope ratio data

### *5.7.1. Strontium*

| Sample | Rock type | Lab Number | $^{87}Sr/^{86}Sr$ measured | % S.E. | 2 S.E. | 2 S.D. |
|---|---|---|---|---|---|---|
| **MV-Ord** | *Greywacke* | E855 | 0.706090 | 0.00130 | 0.000026 | 0.000026 |
| **MV-Sil** | *Sandstone* | E858 | 0.714750 | 0.00140 | 0.000028 | 0.000028 |
| **MV-Dev-WK** | *Sandstone* | E856 | 0.720040 | 0.00210 | 0.000042 | 0.000042 |
| **MV-Carb-T** | *Sandstone* | E860 | 0.716290 | 0.00170 | 0.000034 | 0.000034 |
| **MV-Carb-SC** | *Sandstone* | E862 | 0.735050 | 0.00150 | 0.000030 | 0.000030 |
| **A-Ps** | *Sandstone* | E448 | 0.737470 | 0.00130 | 0.000026 | 0.000026 |
| **A-Ts** | *Sandstone* | E449 | 0.733690 | 0.00130 | 0.000026 | 0.000026 |
| **A-BTs** | *Sandstone* | E447 | 0.730250 | 0.00150 | 0.000030 | 0.000030 |
| **A-Dal** | *Shist* | E448 | 0.736046 | 0.00140 | 0.000028 | 0.000028 |

## 5.8. Age corrected isotope data

### *5.8.1. Strontium*

| Sample Number | Rb | Sr | 87Sr/86Sr | Estimated age (Ma) | 87Sr/86Sr (59.16Ma) |
|---|---|---|---|---|---|
| MV-Ord | 16 | 204 | 0.706087 | 59.16 | 0.705896 |
| MV-Sil | 50 | 12 | 0.714753 | 59.16 | 0.704614 |
| MV-Dev-WK | 41 | 152 | 0.720041 | 59.16 | 0.719385 |
| MV-Carb-T | 25 | 45 | 0.716288 | 59.16 | 0.714936 |
| MV-Carb-SC | 207 | 1648 | 0.735053 | 59.16 | 0.734746 |
| A-Ps | 73 | 85 | 0.737474 | 59.16 | 0.735380 |
| A-Ts | 50 | 90 | 0.733688 | 59.16 | 0.732334 |
| A-BTs | 115 | 148 | 0.730253 | 59.16 | 0.728359 |

# Appendix 6. MOURNE

## 6.1. Sample locations

| Sample | Lithology | Locality | Grid Reference |
|---|---|---|---|
| **MG-1** | *Granite* | G1 Top of Slieve Donard | IJ 35 27 |
| **MG-2 inner - LL** | *Granite* | G2 inner at Lindsays Leap | IJ 37 29 |
| **MG-2 inner-BB** | *Granite* | G2 inner at Bloody Bridge River | IJ 36 26 |
| **MG-2 OUTER** | *Granite* | G2 outer Eastern Mournes | - |
| **MG-2 OUTER 369 236** | *Granite* | G2 outer | IJ 369 236 |
| **MG-3** | *Granite* | G3 Western Mournes | - |
| **MG4** | *Granite* | G4 Western Mournes | - |

## 6.2. Major elements

| Sample | MG-1 | MG-2 inner -LL | MG-2 inner- BB | MG-2 OUTER |
|---|---|---|---|---|
| **Rock type** | *Granite G1* | *Granite G2* | *Granite G2* | *Granite G2* |
| **$SiO_2$** | 69.51 | 76.71 | 77.43 | 75.09 |
| **$TiO_2$** | 0.45 | 0.09 | 0.09 | 0.06 |
| **$AL_2O_3$** | 13.45 | 11.61 | 11.61 | 12.00 |
| **$Fe_2O_3$** | 4.21 | 1.21 | 1.20 | 0.93 |
| **MnO** | 0.09 | 0.02 | 0.02 | 0.02 |
| **MgO** | 0.38 | 0.15 | 0.15 | 0.03 |
| **CaO** | 1.62 | 0.50 | 0.46 | 0.19 |
| **$Na_2O$** | 3.43 | 3.24 | 3.21 | 3.52 |
| **$K_2O$** | 5.30 | 4.99 | 4.85 | 5.13 |
| **$P_2O_5$** | 0.12 | 0.01 | <0.01 | < 0.01 |
| **LOI** | 0.41 | 0.27 | 0.31 | 2.91 |
| **Total** | **98.97** | **98.80** | **99.33** | **99.87** |

| Sample | MG-2 OUTER 369 236 | MG-3 | MG4 |
|---|---|---|---|
| **Rock type** | *Granite G2* | *Granite G3* | *Granite G4* |
| **$SiO_2$** | 77.47 | 76.55 | 77.30 |
| **$TiO_2$** | 0.09 | 0.08 | 0.07 |
| **$AL_2O_3$** | 11.28 | 12.10 | 11.71 |
| **$Fe_2O_3$** | 1.02 | 1.28 | 0.96 |
| **MnO** | 0.02 | 0.02 | 0.01 |
| **MgO** | 0.15 | 0.10 | 0.05 |
| **CaO** | 0.44 | 0.37 | 0.24 |
| **$Na_2O$** | 2.96 | 3.24 | 3.63 |
| **$K_2O$** | 5.11 | 5.13 | 4.99 |
| **$P_2O_5$** | 0.02 | 0.01 | < 0.01 |
| **LOI** | 0.22 | 0.91 | 0.71 |
| **Total** | **98.78** | **99.79** | **99.67** |

## 6.3. Loss on ignition

| Sample | MG-1 | MG-2 inner -LL | MG-2 inner- BB | MG-2 OUTER |
|---|---|---|---|---|
| **Rock type** | *Granite G1* | *Granite G2* | *Granite G2* | *Granite G2* |
| **$H_2O$** | 0.38 | 0.26 | 0.29 | - |
| **$CO_2$** | 0.03 | 0.01 | 0.02 | - |
| **$SO_3$** | - | - | - | 0.01 |
| **LOI** | - | - | - | 2.90 |
| **Total LOI** | **0.41** | **0.27** | **0.31** | **2.91** |

| Sample | MG-2 OUTER 369 236 | MG-3 | MG4 |
|---|---|---|---|
| **Rock type** | *Granite G2* | *Granite G3* | *Granite G4* |
| **$H_2O$** | 0.21 | - | - |
| **$CO_2$** | 0.01 | - | - |
| **$SO_3$** | - | 0.01 | 0.01 |
| **LOI** | - | 0.90 | 0.70 |
| **Total LOI** | **0.22** | **0.91** | **0.71** |

## 6.4. Trace elements

| Sample | MG-1 | MG-2 inner -LL | MG-2 inner- BB | MG-2 OUTER |
|---|---|---|---|---|
| Rock type | *Granite G1* | *Granite G2* | *Granite G2* | *Granite G2* |
| Co | 37 | 21 | 22 | - |
| Cr | <18 | <18 | <18 | <1 |
| Ni | <2 | <2 | <2 | <1 |
| V | <12 | <12 | <12 | 1 |
| Zn | 109 | 40 | 24 | 42 |
| Ce | 132 | 100 | 90 | 38 |
| La | 50 | 20 | 29 | 15 |
| Nb | 44 | 30 | 24 | 26 |
| Ga | 22 | 22 | 23 | 24 |
| Pb | 56 | 50 | 43 | 43 |
| Pr | 14 | 9 | 5 | <5 |
| Rb | 236 | 501 | 461 | 500 |
| Ba | 1023 | 23 | 50 | 13 |
| Sr | 81 | 7 | 9 | 5 |
| Th | 28 | 50 | 47 | 42 |
| Y | 75 | 64 | 52 | 15 |
| Zr | 503 | 127 | 118 | 97 |

| Sample | MG-2 OUTER 369 236 | MG-3 | MG4 |
|---|---|---|---|
| Rock type | *Granite G2* | *Granite G3* | *Granite G4* |
| Co | 59 | - | - |
| Cr | <18 | 4 | <1 |
| Ni | <2 | <1 | <1 |
| V | <12 | 1 | 2 |
| Zn | 22 | 26 | 51 |
| Ce | 110 | 69 | 49 |
| La | 51 | 27 | 24 |
| Nb | 21 | 24 | 24 |
| Ga | 19 | 22 | 23 |
| Pb | 41 | 42 | 5 |
| Pr | 16 | <5 | <5 |
| Rb | 407 | 476 | 473 |
| Ba | 86 | 23 | 16 |
| Sr | 12 | 6 | 6 |
| Th | 38 | 45 | 52 |
| Y | 39 | 31 | 36 |
| Zr | 134 | 120 | 108 |

## 6.5. Rare earth elements

| Sample | MG-1 | MG-2 OUTER | MG-3 | MG4 |
|---|---|---|---|---|
| **Rock type** | *Granite G1* | *Granite G2* | *Granite G3* | *Granite G4* |
| **La** | 71.1 | 15.9 | 24.4 | 22.3 |
| **Ce** | 149.7 | 38.6 | 64.2 | 45.1 |
| **Pr** | 17.3 | 3.4 | 6.1 | 5.0 |
| **Nd** | 66.0 | 10.5 | 20.6 | 16.6 |
| **Sm** | 13.5 | 2.1 | 4.6 | 3.6 |
| **Eu** | 2.0 | 0.1 | 0.1 | 0.1 |
| **Gd** | 12.7 | 1.9 | 3.9 | 3.5 |
| **Tb** | 2.1 | 0.4 | 0.7 | 0.7 |
| **Dy** | 12.6 | 2.6 | 5.0 | 5.0 |
| **Ho** | 2.5 | 0.6 | 1.0 | 1.1 |
| **Er** | 7.3 | 1.8 | 3.5 | 3.6 |
| **Tm** | 1.2 | 0.3 | 0.6 | 0.6 |
| **Yb** | 7.1 | 2.2 | 4.2 | 4.3 |
| **Lu** | 1.1 | 0.3 | 0.7 | 0.7 |

## 6.6. U, Th and Pb ppm

| Sample | MG-1 | MG-2 OUTER | MG-3 | MG4 |
|---|---|---|---|---|
| **Rock type** | *Granite G1* | *Granite G2* | *Granite G3* | *Granite G4* |
| **U** | 10.3 | 10.9 | 12.3 | 9.7 |
| **Th** | 22.8 | 43.8 | 44.0 | 48.9 |
| **Pb** | 32.5 | 43.1 | 34.7 | 32.4 |

## 6.7. Raw isotope ratio data

### *6.7.1. Strontium*

| Sample | Rock type | Lab Number | $^{87}Sr/^{86}Sr$ measured | % S.E. | 2 S.E. | 2S.D. |
|---|---|---|---|---|---|---|
| **MG-1** | *Granite G1* | E91 | 0.718521 | 0.00130 | 0.000026 | 0.000026 |
| **MG-2 inner -LL** | *Granite G2* | E93 | 0.860483 | 0.00110 | 0.000022 | 0.000022 |
| **MG-2 inner- BB** | *Granite G2* | E94 | 0.851096 | 0.00110 | 0.000022 | 0.000022 |
| **MG-2 OUTER** | *Granite G2* | D921/D930 | 0.926377 | 0.00110 | 0.000022 | 0.000022 |
| **MG-2 OUTER 369 236** | *Granite G2* | E92 | 0.781101 | 0.00120 | 0.000024 | 0.000024 |
| **MG-3** | *Granite G3* | D922 | 0.887175 | 0.00120 | 0.000024 | 0.000024 |
| **MG4** | *Granite G4* | D923 | 0.895918 | 0.00120 | 0.000024 | 0.000024 |

### *6.7.2. Neodymium*

| Sample | Rock type | Lab Number | $^{143}Nd/^{144}Nd$ Measured | % S.E. | 2 S.E. | 2S.D. |
|---|---|---|---|---|---|---|
| **MG-1** | *Granite G1* | E91 | 0.512418 | 0.00070 | 0.000014 | 0.000014 |
| **MG-2 inner -LL** | *Granite G2* | E93 | 0.512405 | 0.00070 | 0.000014 | 0.000014 |
| **MG-2 inner- BB** | *Granite G2* | E94 | 0.512402 | 0.00050 | 0.000010 | 0.000010 |
| **MG-2 OUTER** | *Granite G2* | D921/D930 | 0.512439 | 0.00070 | 0.000014 | 0.000014 |
| **MG-2 OUTER 369 236** | *Granite G2* | E92 | 0.512394 | 0.00070 | 0.000014 | 0.000014 |
| **MG-3** | *Granite G3* | D922 | - | - | - | - |
| **MG4** | *Granite G4* | D923 | 0.512464 | 0.00080 | 0.000016 | 0.000016 |

### *6.7.3. Lead*

| Sample | Rock Type | Lab Number | $^{206}Pb/^{204}Pb$ | 2 S.E. | $^{207}Pb/^{204}Pb$ | 2 S.E. | $^{208}Pb/^{204}Pb$ | 2 S.E. |
|---|---|---|---|---|---|---|---|---|
| **MG-1** | *Granite G1* | E110 | 18.818 | 0.002 | 15.646 | 0.002 | 38.649 | 0.005 |
| **MG-2 inner -LL** | *Granite G2* | E112 | 18.857 | 0.002 | 15.644 | 0.002 | 38.631 | 0.004 |
| **MG-2 inner- BB** | *Granite G2* | E113 | 18.851 | 0.002 | 15.636 | 0.002 | 38.609 | 0.004 |
| **MG-2 OUTER** | *Granite G2* | D921 | 19.171 | 0.001 | 15.858 | 0.002 | 39.321 | 0.002 |
| **MG-2 OUTER 369 236** | *Granite G2* | E111 | 18.832 | 0.002 | 15.636 | 0.002 | 38.605 | 0.005 |
| **MG-3** | *Granite G3* | D922 | 18.932 | 0.002 | 15.693 | 0.002 | 38.794 | 0.003 |
| **MG4** | *Granite G4* | D923 | 19.133 | 0.002 | 15.822 | 0.002 | 39.190 | 0.002 |

## 6.8. Age corrected isotope data

### *6.8.1. Strontium*

| Sample | Rock type | Lab Number | Age (Ma) | Rb ppm | Sr ppm | $^{87}Sr/^{86}Sr$ measured | $^{87}Sr/^{86}Sr$ age-corrected |
|---|---|---|---|---|---|---|---|
| **MG-1** | *Granite G1* | E91 | 56 | 236 | 81 | 0.718521 | 0.711808 |
| **MG-2 inner -LL** | *Granite G2* | E93 | 56 | 501 | 7 | 0.860483 | 0.693289 |
| **MG-2 inner- BB** | *Granite G2* | E94 | 56 | 461 | 9 | 0.851096 | 0.731548 |
| **MG-2 OUTER** | *Granite G2* | D921/D930 | 56 | 500 | 5 | 0.926377 | 0.691290 |
| **MG-2 OUTER 369 236** | *Granite G2* | E92 | 56 | 407 | 12 | 0.781101 | 0.702476 |
| **MG-3** | *Granite G3* | D922 | 56 | 476 | 6 | 0.887175 | 0.701373 |
| **MG4** | *Granite G4* | D923 | 56 | 473 | 6 | 0.895918 | 0.711132 |

### 6.8.2. *Neodymium*

| Sample | Rock type | Lab Number | Age (Ma) | Sm ppm | Nd ppm | $^{143}Nd/^{144}Nd$ Measured | $^{143}Nd/^{144}Nd$ age-corrected |
|---|---|---|---|---|---|---|---|
| **MG-1** | *Granite G1* | E91 | 56 | 14 | 66 | 0.512418 | 0.512373 |
| **MG-2 inner -LL** | *Granite G2* | E93 | 56 | - | - | 0.512405 | - |
| **MG-2 inner- BB** | *Granite G2* | E94 | 56 | - | - | 0.512402 | - |
| **MG-2 OUTER** | *Granite G2* | D921/D930 | 56 | 2 | 0 | 0.512439 | 0.512394 |
| **MG-2 OUTER 369 236** | *Granite G2* | E92 | 56 | - | - | 0.512394 | - |
| **MG-3** | *Granite G3* | D922 | 56 | 5 | 21 | - | - |
| **MG4** | *Granite G4* | D923 | 56 | 4 | 17 | 0.512464 | 0.512416 |

### 6.8.3. *Lead*

| Sample | Rock Type | Lab Number | Age (Ma) | U (ppm) | Th (ppm) | Pb (ppm) | $^{206}Pb/^{204}Pb$ age-corrected | $^{207}Pb/^{204}Pb$ age-corrected | $^{208}Pb/^{204}Pb$ age-corrected |
|---|---|---|---|---|---|---|---|---|---|
| **MG-1** | *Granite G1* | E110 | 56 | 10.3 | 22.8 | 32.5 | 18.640 | 15.638 | 38.520 |
| **MG-2 inner -LL** | *Granite G2* | E112 | 56 | - | - | - | - | - | - |
| **MG-2 inner- BB** | *Granite G2* | E113 | 56 | - | - | - | - | - | - |
| **MG-2 OUTER** | *Granite G2* | D921 | 56 | 10.9 | 43.7 | 43.1 | 19.027 | 15.851 | 39.132 |
| **MG-2 OUTER 369 236** | *Granite G2* | E111 | 56 | - | - | - | - | - | - |
| **MG-3** | *Granite G3* | D922 | 56 | 12.3 | 44.0 | 34.7 | 18.734 | 15.684 | 38.561 |
| **MG4** | *Granite G4* | D923 | 56 | 9.7 | 48.9 | 32.4 | 18.964 | 15.814 | 38.909 |

# Appendix 7. GLASDRUMMAN

## 7.1. Sample locations

| Sample Name | Distance from lower dyke margin (cm) | Lithology | |
|---|---|---|---|
| **G-T1-S23** | 1130 | Longford-Down Metasediment | |
| | | | *Boundary at 1120 cm* |
| **G-T1-S22** | 1115 | | |
| **G-T1-S21** | 1055 | Basalt | |
| **G-T1-S20** | 1010 | | |
| | | | *Boundary at 1005 cm* |
| **G-T1-S19** | 1000 | Longford-Down Metasediment | |
| **G-T1-S18** | 910 | Basalt | *Boundary at 925 cm* |
| **G-T1-S17** | 860 | Longford-Down Metasediment | *Boundary at 880 cm* |
| **G-T1-S16** | 810 | Basalt | *Boundary at 845 cm* |
| **G-T1-S15** | 800 | Dark Porphyritic Rhyolite | *Boundary at 805 cm* |
| **G-T1-S14** | 750-760 | | |
| | | | *Boundary at 730 cm* |
| **G-T1-S13** | 730 | | |
| **G-T1-S12** | 690 | | |
| **G-T1-S11** | 560 | Porphyritic Rhyolite | |
| **G-T1-S10** | 415 | | |
| **G-T1-S9** | 345 | | |
| **G-T1-S8** | 240 | | |
| **G-T1-S7** | 125 | | *Boundary at 220 cm* |
| **G-T1-S6** | 120 | Dark Porphyritic Rhyolite | |
| **G-T1-S5** | 85 | | |
| **G-T1-S4** | 80 | | *Boundary at 82 cm* |
| **G-T1-S3** | 35 | Basalt | |
| **G-T1-S2** | 0-5 | | |
| | | | *Boundary at 0 cm* |
| **G-T1-S1** | -5 | Longford-Down Metasediment | |

## 7.2. Major elements

| Sample | G-T1-S2 | G-T1-S5 | G-T1-S7 | G-T1-S8 |
|---|---|---|---|---|
| **Rock type** | *Basalt* | *Dark porphyritic rhyolite* | *Dark porphyritic rhyolite* | *Porphyritic rhyolite* |
| **$SiO_2$** | 46.43 | 69.88 | 68.59 | 77.33 |
| **$TiO_2$** | 1.99 | 0.48 | 0.58 | 0.15 |
| **$AL_2O_3$** | 15.45 | 12.28 | 12.75 | 11.41 |
| **$Fe_2O_3$** | 15.26 | 4.15 | 4.92 | 1.52 |
| **MnO** | 0.24 | 0.06 | 0.08 | 0.02 |
| **MgO** | 6.04 | 0.91 | 1.36 | 0.21 |
| **CaO** | 8.95 | 2.09 | 2.39 | 0.22 |
| **$Na_2O$** | 2.67 | 3.54 | 4.21 | 3.45 |
| **$K_2O$** | 1.42 | 4.04 | 2.87 | 4.61 |
| **$P_2O_5$** | 0.41 | 0.10 | 0.11 | 0.03 |
| **LOI** | 1.62 | 2.21 | 1.66 | 0.56 |
| **Total** | **100.48** | **99.74** | **99.52** | **99.51** |

| Sample | G-T1-S11 | G-T1-S13 | G-T1-S15 | G-T1-S16 |
|---|---|---|---|---|
| **Rock type** | *Porphyritic rhyolite* | *Porphyritic rhyolite* | *Dark porphyritic rhyolite* | *Basalt* |
| **$SiO_2$** | 78.59 | 79.12 | 69.92 | 48.23 |
| **$TiO_2$** | 0.09 | 0.11 | 0.41 | 1.81 |
| **$AL_2O_3$** | 11.32 | 11.10 | 12.93 | 15.39 |
| **$Fe_2O_3$** | 0.72 | 1.10 | 3.56 | 13.95 |
| **MnO** | 0.02 | 0.02 | 0.06 | 0.22 |
| **MgO** | 0.18 | 0.18 | 0.81 | 6.01 |
| **CaO** | 0.21 | 0.39 | 1.92 | 8.23 |
| **$Na_2O$** | 3.85 | 3.94 | 4.53 | 2.60 |
| **$K_2O$** | 4.22 | 3.59 | 3.55 | 2.33 |
| **$P_2O_5$** | 0.02 | 0.02 | 0.09 | 0.28 |
| **LOI** | 0.49 | 0.63 | 1.96 | 1.36 |
| **Total** | **99.71** | **100.20** | **99.74** | **100.41** |

## 7.3. Loss on ignition

| Sample | G-T1-S2 | G-T1-S5 | G-T1-S7 | G-T1-S8 |
|---|---|---|---|---|
| **Rock type** | *Basalt* | *Dark porphyritic rhyolite* | *Dark porphyritic rhyolite* | *Porphyritic rhyolite* |
| **$H_2O$** | 1.59 | 1.03 | 1.06 | 0.45 |
| **$CO_2$** | 0.03 | 1.18 | 0.60 | 0.11 |
| **$SO_3$** | - | - | - | - |
| **LOI** | - | - | - | - |
| **Total LOI** | **1.62** | **2.21** | **1.66** | **0.56** |

| Sample | G-T1-S11 | G-T1-S13 | G-T1-S15 | G-T1-S16 |
|---|---|---|---|---|
| **Rock type** | *Porphyritic rhyolite* | *Porphyritic rhyolite* | *Dark porphyritic rhyolite* | *Basalt* |
| **$H_2O$** | 0.36 | 0.39 | 0.91 | 1.24 |
| **$CO_2$** | 0.13 | 0.24 | 1.05 | 0.12 |
| **$SO_3$** | - | - | - | - |
| **LOI** | - | - | - | - |
| **Total LOI** | **0.49** | **0.63** | **1.96** | **1.36** |

## 7.4. Trace elements

| Sample | G-T1-S2 | G-T1-S5 | G-T1-S7 | G-T1-S8 |
|---|---|---|---|---|
| Rock type | *Basalt* | *Dark porphyritic rhyolite* | *Dark porphyritic rhyolite* | *Porphyritic rhyolite* |
| Co | 65 | 22 | 36 | 36 |
| Cr | 63 | <18 | <18 | <18 |
| Ni | 53 | <2 | <2 | <2 |
| V | 330 | 43 | 72 | <12 |
| Zn | 122 | 69 | 72 | 26 |
| Ce | 33 | 154 | 156 | 114 |
| La | 16 | 70 | 52 | 53 |
| Nb | 23 | 36 | 32 | 24 |
| Ga | 17 | 19 | 18 | 17 |
| Pb | 14 | 31 | 17 | 27 |
| Pr | <4 | 13 | 6 | 17 |
| Rb | 106 | 167 | 115 | 199 |
| Ba | 290 | 319 | 404 | 153 |
| Sr | 237 | 88 | 125 | 29 |
| Th | 4 | 35 | 30 | 34 |
| Y | 43 | 67 | 60 | 61 |
| Zr | 156 | 381 | 332 | 168 |

| Sample | G-T1-S11 | G-T1-S13 | G-T1-S15 | G-T1-S16 |
|---|---|---|---|---|
| Rock type | *Porphyritic rhyolite* | *Porphyritic rhyolite* | *Dark porphyritic rhyolite* | *Basalt* |
| Co | 29 | 26 | 28 | 55 |
| Cr | <18 | <18 | <18 | 65 |
| Ni | <2 | <2 | <2 | 45 |
| V | <12 | <12 | 27 | 312 |
| Zn | 10 | 18 | 52 | 130 |
| Ce | 82 | 115 | 165 | 40 |
| La | 38 | 40 | 61 | 30 |
| Nb | 18 | 20 | 32 | 17 |
| Ga | 14 | 16 | 19 | 18 |
| Pb | 14 | 18 | 22 | 21 |
| Pr | 10 | <4 | 11 | <4 |
| Rb | 159 | 144 | 128 | 238 |
| Ba | 312 | 196 | 566 | 236 |
| Sr | 33 | 31 | 84 | 223 |
| Th | 36 | 38 | 32 | 6 |
| Y | 49 | 58 | 61 | 30 |
| Zr | 116 | 148 | 353 | 115 |

## 7.5. Rare earth elements

| Sample | G-T1-S2 | G-T1-S5 | G-T1-S7 | G-T1-S8 |
|---|---|---|---|---|
| **Rock type** | *Basalt* | *Dark porphyritic rhyolite* | *Dark porphyritic rhyolite* | *Porphyritic rhyolite* |
| **La** | 22.07 | 90.63 | 76.31 | 64.93 |
| **Ce** | 45.38 | 179.96 | 151.70 | 135.48 |
| **Pr** | 5.44 | 19.36 | 16.29 | 14.39 |
| **Nd** | 23.15 | 69.08 | 57.97 | 50.25 |
| **Sm** | 5.89 | 12.89 | 11.15 | 9.84 |
| **Eu** | 1.93 | 0.92 | 1.00 | 0.42 |
| **Gd** | 6.95 | 12.10 | 10.64 | 9.19 |
| **Tb** | 1.21 | 1.90 | 1.70 | 1.49 |
| **Dy** | 7.86 | 11.52 | 10.32 | 9.27 |
| **Ho** | 1.64 | 2.31 | 2.09 | 1.91 |
| **Er** | 4.84 | 6.85 | 6.20 | 5.89 |
| **Tm** | 0.76 | 1.11 | 1.00 | 0.99 |
| **Yb** | 4.68 | 6.79 | 6.14 | 6.19 |
| **Lu** | 0.72 | 1.04 | 0.91 | 0.93 |

| Sample | G-T1-S11 | G-T1-S13 | G-T1-S15 | G-T1-S16 |
|---|---|---|---|---|
| **Rock type** | *Porphyritic rhyolite* | *Porphyritic rhyolite* | *Dark porphyritic rhyolite* | *Basalt* |
| **La** | 40.37 | 46.31 | 79.64 | 24.01 |
| **Ce** | 86.26 | 98.93 | 158.66 | 50.23 |
| **Pr** | 9.56 | 10.53 | 16.93 | 5.82 |
| **Nd** | 33.73 | 36.62 | 60.28 | 23.19 |
| **Sm** | 7.17 | 7.48 | 11.38 | 5.46 |
| **Eu** | 0.37 | 0.34 | 1.01 | 1.40 |
| **Gd** | 6.99 | 7.21 | 10.71 | 6.11 |
| **Tb** | 1.24 | 1.27 | 1.69 | 1.04 |
| **Dy** | 8.19 | 8.33 | 10.27 | 6.63 |
| **Ho** | 1.73 | 1.77 | 2.08 | 1.36 |
| **Er** | 5.44 | 5.64 | 6.18 | 4.00 |
| **Tm** | 0.93 | 0.98 | 1.00 | 0.63 |
| **Yb** | 5.87 | 6.24 | 6.17 | 3.86 |
| **Lu** | 0.88 | 0.94 | 0.92 | 0.58 |

## 7.6. U, Th and Pb ppm

| Sample | G-TI-S2 | G-TI-S5 | G-TI-S8 | G-TI-S11 |
|---|---|---|---|---|
| **Rock type** | *Basalt* | *Dark Porphyritic Rhyolite* | *Porphyritic Rhyolite* | *Porphyritic Rhyolite* |
| **U** | 1.0 | 7.4 | 6.4 | 6.0 |
| **Th** | 3.5 | 31.3 | 35.3 | 32.8 |
| **Pb** | 7.5 | 22.4 | 8.2 | 20.5 |

| Sample | G-TI-S13 | G-TI-S15 | G-TI-S16 |
|---|---|---|---|
| **Rock type** | *Porphyritic Rhyolite* | *Dark Porphyritic Rhyolite* | *Basalt* |
| **U** | 7.1 | 8.5 | 2.1 |
| **Th** | 36.5 | 30.4 | 7.1 |
| **Pb** | 18.4 | 18.6 | 5.8 |

## 7.7. Raw isotope ratio data

### *7.7.1. Strontium*

| Sample | Rock type | Lab Number | $^{87}Sr/^{86}Sr$ measured | % S.E. | 2 S.E. | 2S.D. |
|---|---|---|---|---|---|---|
| **G-T1-S2** | *Basalt* | - | - | - | - | - |
| **G-T1-S5** | *Dark porphyritic rhyolite* | E472 | 0.716221 | 0.0013 | 0.000026 | 0.000026 |
| **G-T1-S7** | *Dark porphyritic rhyolite* | E861 | 0.711382 | 0.0013 | 0.000026 | 0.000026 |
| **G-T1-S8** | *Porphyritic rhyolite* | E863 | 0.728524 | 0.0014 | 0.000028 | 0.000028 |
| **G-T1-S11** | *Porphyritic rhyolite* | E473 | 0.724892 | 0.0013 | 0.000026 | 0.000026 |
| **G-T1-S16** | *Basalt* | E864 | 0.706216 | 0.0013 | 0.000026 | 0.000026 |

### *7.7.2. Lead*

| Sample | Rock Type | Lab Number | $^{206}Pb/^{204}Pb$ | 2 S.E. | $^{207}Pb/^{204}Pb$ | 2 S.E. | $^{208}Pb/^{204}Pb$ | 2 S.E. |
|---|---|---|---|---|---|---|---|---|
| **G-T1-S2** | *Basalt* | N485 | 18.901 | 0.042 | 15.675 | 0.043 | 38.824 | 0.042 |
| **G-T1-S5** | *Dark porphyritic rhyolite* | N486 | 19.043 | 0.025 | 15.665 | 0.025 | 38.866 | 0.024 |
| **G-T1-S7** | *Dark porphyritic rhyolite* | E873 | 19.000 | 0.005 | 15.644 | 0.006 | 38.865 | 0.007 |
| **G-T1-S8** | *Porphyritic rhyolite* | E875 | 19.035 | 0.006 | 15.652 | 0.007 | 38.897 | 0.008 |
| **G-T1-S11** | *Porphyritic rhyolite* | N487 | 19.006 | 0.011 | 15.647 | 0.012 | 38.802 | 0.012 |
| **G-T1-S16** | *Basalt* | E876 | 18.779 | 0.006 | 15.619 | 0.007 | 38.630 | 0.009 |

## 7.8. Age corrected isotope data

### *7.8.1. Strontium*

| Sample | Rock type | Lab Number | Age (Ma) | Rb ppm | Sr ppm | $^{87}Sr/^{86}Sr$ measured | $^{87}Sr/^{86}Sr$ age-corrected |
|---|---|---|---|---|---|---|---|
| **G-T1-S5** | *Dark porphyritic rhyolite* | E472 | 56 | 167 | 88 | 0.716221 | 0.711849 |
| **G-T1-S7** | *Dark porphyritic rhyolite* | E861 | 56 | 115 | 125 | 0.711382 | 0.709264 |
| **G-T1-S8** | *Porphyritic rhyolite* | E863 | 56 | 199 | 29 | 0.728524 | 0.712697 |
| **G-T1-S11** | *Porphyritic rhyolite* | E473 | 56 | 159 | 33 | 0.724892 | 0.713785 |
| **G-T1-S16** | *Basalt* | E864 | 56 | 238 | 223 | 0.706216 | 0.703760 |

### *7.8.2. Lead*

| Sample | Rock Type | Lab Number | Age (Ma) | U (ppm) | Th (ppm) | Pb (ppm) | $^{206}Pb/^{204}Pb$ age-corrected | $^{207}Pb/^{204}Pb$ age-corrected | $^{208}Pb/^{204}Pb$ age-corrected |
|---|---|---|---|---|---|---|---|---|---|
| **G-T1-S2** | *Basalt* | N485 | 56 | 1.0 | 3.5 | 7.5 | 18.828 | 15.671 | 38.737 |
| **G-T1-S5** | *Dark porphyritic rhyolite* | N486 | 56 | 7.4 | 31.3 | 22.4 | 18.857 | 15.656 | 38.608 |
| **G-T1-S7** | *Dark porphyritic rhyolite* | E873 | 56 | - | - | - | - | - | - |
| **G-T1-S8** | *Porphyritic rhyolite* | E875 | 56 | 6.4 | 35.3 | 8.2 | 18.600 | 15.631 | 38.105 |
| **G-T1-S11** | *Porphyritic rhyolite* | N487 | 56 | 6.0 | 32.8 | 20.5 | 18.841 | 15.639 | 38.506 |
| **G-T1-S16** | *Basalt* | E876 | 56 | 2.1 | 7.1 | 5.8 | 18.577 | 15.609 | 38.406 |

# Appendix 8. Mourne / Glasdrumman crust

## *8.1. Sample locations*

| Sample | Lithology | Locality | Grid Reference |
|---|---|---|---|
| **M-SC1** | *Hornfelsed Longford-Down* | Bloody Bridge River Screen | IJ 37 26 |
| **M-SC2** | *Hornfelsed Longford-Down* | Bloody Bridge River Screen | IJ 37 26 |
| **M-SC3** | *Hornfelsed Longford-Down* | Bloody Bridge River Screen | IJ 37 26 |
| **M-SC4** | *Hornfelsed Longford-Down* | Bloody Bridge River Screen | IJ 37 26 |
| **M-SC5** | *Hornfelsed Longford-Down* | Bloody Bridge River Screen | IJ 37 26 |
| **M-LD-BB** | *Longford-Down* | Bloody Bridge River, east of screen | IJ 37 26 |
| **BWA** | *Meta-igneous xenolith* | Ballywhiskin, Co. Down | IJ 6148 7320 |
| **BWB** | *Meta-igneous xenolith* | Ballywhiskin, Co. Down | IJ 6148 7320 |
| **BWC** | *Meta-igneous xenolith* | Ballywhiskin, Co. Down | IJ 6148 7320 |
| **BWD-TUB** | *Meta-igneous xenolith* | Ballywhiskin, Co. Down | IJ 6148 7320 |

## *8.2. Major elements*

| Sample | M-SC1 | M-SC2 | M-SC3 | M-SC4 | M-SC5 |
|---|---|---|---|---|---|
| Rock type | *Hornfelsed Longford-Down* | *Hornfelsed Longford-Down* | *Hornfelsed Longford-Down* | *Hornfelsed Longford-Down* | *Hornfelsed Longford-Down* |
| $SiO_2$ | 62.96 | 64.78 | 63.04 | 62.70 | 76.22 |
| $TiO_2$ | 0.78 | 0.71 | 0.78 | 0.82 | 0.12 |
| $AL_2O_3$ | 12.58 | 10.52 | 12.10 | 12.53 | 11.65 |
| $Fe_2O_3$ | 6.52 | 5.30 | 5.88 | 5.31 | 1.56 |
| MnO | 0.10 | 0.13 | 0.11 | 0.11 | 0.03 |
| MgO | 3.98 | 3.37 | 3.55 | 3.43 | 0.19 |
| CaO | 7.06 | 10.54 | 8.10 | 7.93 | 0.68 |
| $Na_2O$ | 2.06 | 1.41 | 2.38 | 2.35 | 3.30 |
| $K_2O$ | 1.86 | 1.80 | 1.96 | 1.81 | 4.61 |
| $P_2O_5$ | 0.16 | 0.14 | 0.16 | 0.18 | 0.02 |
| LOI | 0.85 | 0.31 | 0.80 | 1.67 | 0.37 |
| **Total** | **99.27** | **99.27** | **99.27** | **99.27** | **98.75** |

| Sample | M-LD-BB | BWA | BWB | BWC | BWD-TUB |
|---|---|---|---|---|---|
| Rock type | *Longford-Down* | *Meta-igneous xenolith* | *Meta-igneous xenolith* | *Meta-igneous xenolith* | *Meta-igneous xenolith* |
| $SiO_2$ | 64.20 | 49.27 | 49.93 | 48.53 | 51.24 |
| $TiO_2$ | 0.76 | 1.10 | 1.05 | 1.17 | 1.35 |
| $AL_2O_3$ | 12.39 | 20.17 | 19.72 | 21.38 | 16.20 |
| $Fe_2O_3$ | 4.92 | 6.80 | 7.02 | 6.53 | 9.02 |
| MnO | 0.06 | 0.15 | 0.17 | 0.10 | 0.11 |
| MgO | 4.31 | 5.37 | 5.56 | 5.18 | 5.92 |
| CaO | 7.37 | 2.34 | 2.42 | 1.65 | 4.07 |
| $Na_2O$ | 2.54 | 2.53 | 2.49 | 1.80 | 4.23 |
| $K_2O$ | 2.05 | 6.26 | 5.86 | 7.54 | 2.02 |
| $P_2O_5$ | 0.16 | 0.13 | 0.17 | 0.11 | 0.30 |
| LOI | 1.00 | 5.09 | 4.99 | 5.29 | 5.29 |
| **Total** | **99.76** | **99.20** | **99.37** | **99.27** | **99.75** |

## *8.3. Loss on ignition*

| Sample | M-SC1 | M-SC2 | M-SC3 | M-SC4 |
|---|---|---|---|---|
| **Rock type** | *Hornfelsed Longford-Down* | *Hornfelsed Longford-Down* | *Hornfelsed Longford-Down* | *Hornfelsed Longford-Down* |
| **$H_2O$** | 0.84 | 0.30 | 0.77 | 1.64 |
| **$CO_2$** | 0.01 | 0.01 | 0.03 | 0.03 |
| **$SO_3$** | - | - | - | - |
| **LOI** | - | - | - | - |
| **Total LOI** | **0.85** | **0.31** | **0.80** | **1.67** |

| Sample | M-SC5 | M-LD-BB | BWA | BWB |
|---|---|---|---|---|
| **Rock type** | *Hornfelsed Longford-Down* | *Longford-Down* | *Meta-igneous xenolith* | *Meta-igneous xenolith* |
| **$H_2O$** | 0.35 | 0.95 | - | - |
| **$CO_2$** | 0.02 | 0.05 | - | - |
| **$SO_3$** | - | - | 1.22 | 0.75 |
| **LOI** | - | - | 3.87 | 4.24 |
| **Total LOI** | **0.37** | **1.00** | **5.09** | **4.99** |

| Sample | BWC | BWD-TUB |
|---|---|---|
| **Rock type** | *Meta-igneous xenolith* | *Meta-igneous xenolith* |
| **$H_2O$** | - | - |
| **$CO_2$** | - | - |
| **$SO_3$** | 1.32 | 1.65 |
| **LOI** | 3.97 | 3.64 |
| **Total LOI** | **5.29** | **5.29** |

## *8.4. Trace elements*

| Sample | M-SC1 | M-SC2 | M-SC3 | M-SC4 | M-SC5 |
|---|---|---|---|---|---|
| Rock type | *Hornfelsed Longford-Down* | *Hornfelsed Longford-Down* | *Hornfelsed Longford-Down* | *Hornfelsed Longford-Down* | *Hornfelsed Longford-Down* |
| Co | 40 | 56 | 38 | 38 | 41 |
| Cr | 120 | 126 | 136 | 138 | <18 |
| Ni | 61 | 42 | 53 | 49 | <2 |
| V | 105 | 88 | 98 | 102 | 14 |
| Zn | 94 | 95 | 92 | 80 | 37 |
| Ce | 53 | 60 | 74 | 71 | 100 |
| La | <14 | 24 | 25 | 24 | 33 |
| Nb | 17 | 16 | 16 | 16 | 26 |
| Ga | 11 | 12 | 13 | 15 | 22 |
| Pb | 14 | 8 | 14 | 12 | 47 |
| Pr | <4 | <4 | <4 | <4 | 11 |
| Rb | 196 | 131 | 183 | 118 | 405 |
| Ba | 279 | 384 | 302 | 221 | 86 |
| Sr | 215 | 251 | 229 | 242 | 17 |
| Th | 12 | 12 | 12 | 10 | 51 |
| Y | 21 | 25 | 22 | 23 | 65 |
| Zr | 187 | 219 | 224 | 231 | 162 |

| Sample | M-LD-BB | BWA | BWB | BWC | BWD-TUB |
|---|---|---|---|---|---|
| Rock type | *Longford-Down* | *Meta-igneous xenolith* | *Meta-igneous xenolith* | *Meta-igneous xenolith* | *Meta-igneous xenolith* |
| Co | 39 | - | - | - | - |
| Cr | 132 | 485 | 382 | 542 | 194 |
| Ni | 60 | 156 | 131 | 165 | 65 |
| V | 95 | 185 | 178 | 198 | 180 |
| Zn | 37 | 93 | 141 | 88 | 78 |
| Ce | 86 | 49 | 47 | 45 | 49 |
| La | 42 | 21 | 20 | 10 | 19 |
| Nb | 15 | 4 | 4 | 4 | 9 |
| Ga | 15 | 13 | 13 | 15 | 11 |
| Pb | 11 | 39 | 73 | 66 | 5 |
| Pr | <4 | < 5 | < 5 | 40 | < 5 |
| Rb | 123 | 178 | 173 | 237 | 23 |
| Ba | 405 | 6152 | 5597 | 6247 | 1342 |
| Sr | 195 | 1169 | 1153 | 1140 | 1118 |
| Th | 14 | 3 | 3 | 2 | 3 |
| Y | 21 | 17 | 16 | 13 | 24 |
| Zr | 210 | 75 | 82 | 66 | 136 |

## 8.5. Rare earth elements

| Sample | M-SC1 | M-SC2 | M-SC4 | M-LD-BB |
|---|---|---|---|---|
| Rock type | *Hornfelsed Longford-Down* | *Hornfelsed Longford-Down* | *Hornfelsed Longford-Down* | *Longford-Down* |
| La | 30.7 | 28.3 | 35.3 | 31.4 |
| Ce | 64.3 | 60.0 | 72.0 | 65.9 |
| Pr | 7.7 | 7.3 | 8.4 | 7.9 |
| Nd | 29.5 | 28.4 | 31.7 | 30.0 |
| Sm | 5.8 | 5.8 | 5.9 | 5.8 |
| Eu | 1.1 | 1.2 | 1.3 | 1.2 |
| Gd | 5.2 | 5.2 | 5.2 | 5.1 |
| Tb | 0.8 | 0.8 | 0.8 | 0.8 |
| Dy | 4.8 | 4.8 | 4.4 | 4.5 |
| Ho | 1.0 | 0.9 | 0.9 | 0.9 |
| Er | 2.8 | 2.7 | 2.5 | 2.5 |
| Tm | 0.4 | 0.4 | 0.4 | 0.4 |
| Yb | 2.7 | 2.4 | 2.4 | 2.3 |
| Lu | 0.4 | 0.4 | 0.4 | 0.3 |

| Sample | BWA | BWB | BWC | BWD-TUB |
|---|---|---|---|---|
| Rock type | *Meta-igneous xenolith* | *Meta-igneous xenolith* | *Meta-igneous xenolith* | *Meta-igneous xenolith* |
| La | 12.0 | 13.0 | 10.1 | 27.2 |
| Ce | 24.5 | 27.0 | 20.2 | 56.0 |
| Pr | 3.1 | 3.4 | 2.6 | 6.8 |
| Nd | 13.5 | 14.6 | 11.0 | 27.6 |
| Sm | 3.1 | 3.4 | 2.5 | 5.7 |
| Eu | 0.6 | 0.7 | 0.5 | 1.8 |
| Gd | 3.2 | 3.5 | 2.6 | 5.3 |
| Tb | 0.5 | 0.6 | 0.4 | 0.8 |
| Dy | 3.2 | 3.4 | 2.4 | 4.8 |
| Ho | 0.6 | 0.6 | 0.5 | 0.9 |
| Er | 1.8 | 1.7 | 1.3 | 2.6 |
| Tm | 0.3 | 0.3 | 0.2 | 0.4 |
| Yb | 1.6 | 1.4 | 1.1 | 2.4 |
| Lu | 0.2 | 0.2 | 0.2 | 0.4 |

## 8.6. *U, Th and Pb ppm*

| Sample | Bwa | BWb | BWc | BWD-tub |
|---|---|---|---|---|
| Rock type | *Meta-igneous xenolith* | *Meta-igneous xenolith* | *Meta-igneous xenolith* | *Meta-igneous xenolith* |
| U | 1.8 | 1.2 | 1.7 | 0.9 |
| Th | 1.3 | 1.4 | 0.9 | 3.6 |
| Pb | 35.6 | 68.7 | 59.6 | 6.6 |

| Sample | M-LD-BB | MSC1 | MSC2 | MSC4 |
|---|---|---|---|---|
| Rock type | *Siltstone* | *Hornfelsed Siltstone* | *Hornfelsed Siltstone* | *Hornfelsed Siltstone* |
| U | 2.4 | 2.2 | 2.2 | 2.3 |
| Th | 9.5 | 9.5 | 9.0 | 10.3 |
| Pb | 7.2 | 7.0 | 8.0 | 7.8 |

## 8.7. Raw isotope ratio data

### *8.7.1. Strontium*

| Sample | Rock type | Lab Number | $^{87}Sr/^{86}Sr$ measured | % S.E. | 2 S.E. | 2S.D. |
|---|---|---|---|---|---|---|
| **M-SC1** | *Hornfelsed Longford-Down* | E95 | 0.717000 | 0.00110 | 0.000022 | 0.000022 |
| **M-SC2** | *Hornfelsed Longford-Down* | E98 | 0.715737 | 0.00110 | 0.000022 | 0.000022 |
| **M-SC3** | *Hornfelsed Longford-Down* | E96 | 0.716894 | 0.00120 | 0.000024 | 0.000024 |
| **M-SC4** | *Hornfelsed Longford-Down* | E97 | 0.717477 | 0.00120 | 0.000024 | 0.000024 |
| **M-SC5** | *Hornfelsed Longford-Down* | E100 | 0.768654 | 0.00120 | 0.000024 | 0.000024 |
| **M-LD-BB** | *Longford-Down* | E101 | 0.717847 | 0.00130 | 0.000026 | 0.000026 |
| **BWa** | *meta sed xenolith* | D837 | 0.709245 | 0.00130 | 0.000026 | 0.000026 |
| **BWb** | *meta sed xenolith* | E468 | 0.709383 | 0.00140 | 0.000028 | 0.000028 |
| **BWb *re-run*** | *meta sed xenolith* | D838 | 0.709435 | 0.00150 | 0.000030 | 0.000030 |
| **BWc** | *meta sed xenolith* | D839 | 0.709966 | 0.00140 | 0.000028 | 0.000028 |
| **BWd-tub** | *meta sed xenolith* | E469 | 0.706494 | 0.00220 | 0.000044 | 0.000044 |
| **BWd-tub *re-run*** | *meta sed xenolith* | D840 | 0.706506 | 0.00110 | 0.000022 | 0.000022 |

### *8.7.2. Lead*

| Sample | Rock Type | Lab Number | $^{206}Pb/^{204}Pb$ | 2 S.E. | $^{207}Pb/^{204}Pb$ | 2 S.E. | $^{208}Pb/^{204}Pb$ | 2 S.E. |
|---|---|---|---|---|---|---|---|---|
| **M-SC1** | *Hornfelsed Longford-Down* | E114 | 19.040 | 0.002 | 15.646 | 0.002 | 38.958 | 0.004 |
| **M-SC2** | *Hornfelsed Longford-Down* | E117 | 19.081 | 0.001 | 15.651 | 0.001 | 39.056 | 0.004 |
| **M-SC3** | *Hornfelsed Longford-Down* | E115 | 19.038 | 0.001 | 15.648 | 0.001 | 38.978 | 0.004 |
| **M-SC4** | *Hornfelsed Longford-Down* | E116 | 19.059 | 0.001 | 15.643 | 0.001 | 39.009 | 0.003 |
| **M-SC5** | *Hornfelsed Longford-Down* | E115 | 18.830 | 0.002 | 15.628 | 0.001 | 38.626 | 0.004 |
| **M-LD-BB** | *Longford-Down* | E1120 | 19.235 | 0.002 | 15.641 | 0.001 | 39.072 | 0.004 |
| **BWB** | *Meta-igneous xenolith* | N482 | 18.476 | 0.050 | 15.622 | 0.050 | 38.012 | 0.050 |
| **BWC** | *Meta-igneous xenolith* | N475 | 18.588 | 0.038 | 15.601 | 0.039 | 37.932 | 0.040 |
| **BWD-TUB** | *Meta-igneous xenolith* | N483 | 18.948 | 0.012 | 15.616 | 0.013 | 38.696 | 0.013 |

## 8.8. Age corrected isotope data

### *8.8.1. Strontium*

| Sample | Rock type | Lab Number | Age (Ma) | Rb ppm | Sr ppm | $^{87}Sr/^{86}Sr$ measured | $^{87}Sr/^{86}Sr$ age-corrected |
|---|---|---|---|---|---|---|---|
| **M-SC1** | *Hornfelsed Longford-Down* | E95 | 56 | 196 | 215 | 0.717000 | 0.714900 |
| **M-SC2** | *Hornfelsed Longford-Down* | E98 | 56 | 131 | 251 | 0.715737 | 0.714535 |
| **M-SC3** | *Hornfelsed Longford-Down* | E96 | 56 | 183 | 229 | 0.716894 | 0.715053 |
| **M-SC4** | *Hornfelsed Longford-Down* | E97 | 56 | 118 | 242 | 0.717477 | 0.716354 |
| **M-SC5** | *Hornfelsed Longford-Down* | E100 | 56 | 405 | 17 | 0.768654 | 0.713495 |
| **M-LD-BB** | *Longford-Down* | E101 | 56 | 123 | 195 | 0.717847 | 0.716394 |
| **BWa** | *meta sed xenolith* | D837 | 56 | 178 | 1,169 | 0.709245 | 0.708870 |
| **BWb** | *meta sed xenolith* | E468 | 56 | 173 | 1,153 | 0.709383 | 0.709014 |
| **BWb re-run** | *meta sed xenolith* | D838 | 56 | 173 | 1,153 | 0.709435 | 0.709066 |
| **BWc** | *meta sed xenolith* | D839 | 56 | 237 | 1,140 | 0.709966 | 0.709453 |
| **BWd-tub** | *meta sed xenolith* | E469 | 56 | 23 | 1,118 | 0.706494 | 0.706443 |
| **BWd-tub *re-run*** | *meta sed xenolith* | D840 | 56 | 23 | 1,118 | 0.706506 | 0.706455 |

### *8.8.2. Lead*

| Sample | Rock Type | Lab Number | Age (Ma) | U (ppm) | Th (ppm) | Pb (ppm) | $^{206}Pb/^{204}Pb$ age-corrected | $^{207}Pb/^{204}Pb$ age-corrected | $^{208}Pb/^{204}Pb$ age-corrected |
|---|---|---|---|---|---|---|---|---|---|
| **M-SC1** | *Hornfelsed Longford-Down* | E114 | 56 | 2.2 | 9.5 | 7.0 | 18.864 | 15.638 | 38.707 |
| **M-SC2** | *Hornfelsed Longford-Down* | E117 | 56 | 2.2 | 9.0 | 8.0 | 18.929 | 15.644 | 38.848 |
| **M-SC3** | *Hornfelsed Longford-Down* | E115 | 56 | - | - | - | - | - | - |
| **M-SC4** | *Hornfelsed Longford-Down* | E116 | 56 | 2.3 | 10.3 | 7.8 | 18.890 | 15.635 | 38.764 |
| **M-SC5** | *Hornfelsed Longford-Down* | E115 | 56 | - | - | - | - | - | - |
| **M-LD-BB** | *Longford-Down* | E1120 | 56 | 2.4 | 9.5 | 7.2 | 19.049 | 15.632 | 38.830 |
| **BWB** | *Meta-igneous xenolith* | N482 | 56 | 1.2 | 1.4 | 18.5 | 18.465 | 15.622 | 38.008 |
| **BWC** | *Meta-igneous xenolith* | N475 | 56 | 1.7 | 0.9 | 18.6 | 18.571 | 15.600 | 37.929 |
| **BWD-TUB** | *Meta-igneous xenolith* | N483 | 56 | 0.9 | 3.6 | 18.9 | 18.869 | 15.612 | 38.589 |

# Appendix 9. Slieve Gullion

## 9.1. Sample locations

| metres | Sample reference | Orientation faces on sample | GPS reference | Notes | Trinity College Collection Number |
|---|---|---|---|---|---|
| 21m | SG-FM-1 (G) | 050/75 SE<br>135/80 NE | J08130 14905 | Porphyritic microgranite with tuffisite | TCD P.19127 |
| 30m | SG-FM-1.5 (G) | | | Porphyritic microgranite | TCD P.19128 |
| 35m | SG-FM-1.7 (G) | | | Porphyritic microgranite with enclaves | TCD P.19129 |
| 50m | SG-FM-2 (G) | 044/82 SE<br>128/70 SW | J07984 14678 | Porphyritic microgranite, altered (brown) | TCD P.19130 |
| 51m | SG-FM-3 (G) | 050/90<br>135/72 SW | | Porphyritic microgranite, fresh | TCD P.19131 |
| 63m | SG-FM-4 (G) | 010/40 SE<br>025/85 NW | | Porphyritic microgranite near to Longford-Down metasediment. Sample 60cm from the contact. | TCD P.19132 |
| 63m | SG-FM-5 (G) | 055/55 NW<br>070/55 NW | | Porphyritic microgranite sample adjacent to contact with fine groundmass | TCD P.19133 |
| 63m | SG-FM-6 (LD) | 045/65 NW<br>120/65 SW | | Longford-Down metasediment; sample adjacent to contact, altered | TCD P.19134 |
| 63m | SG-FM-7 (LD) | 055/70 SE<br>010/40 SE | | Longford-Down metasediment sample 70cm from the contact | TCD P.19135 |
| 105m | SG-FM-8 (D) | 005/17 NW<br>130/40 SW | J07973 14744 | Basaltic dyke, with plagioclase | TCD P.19136 |
| 137m | SG-FM-9 (D) | 060/85 NW<br>155/60 SW | J07970 14768 | Basaltic dyke, with pyrite and plagioclase | TCD P.19137 |
| 144m | SG-FM-10 (CT) | 140/50 SW<br>010/85 NW | J07971 14775 | Sample of the contact between porphyritic rhyolite apophysis and Longford-Down | TCD P.19138 |
| 163m | SG-FM-11 (PR) | 000/40 E<br>120/50 SW | J07969 14797 | Porphyritic rhyolite sample 50cm from the contact | TCD P.19139 |

| | | | | | |
|---|---|---|---|---|---|
| 155m | SG-FM-11.5 (PR) | | | Porphyritic rhyolite with strongly zoned crystals and basaltic enclaves plus fragment of Newry Granodiorite (x2) | TCD P.19140 |
| 163m | SG-FM-12 (PR) | 090/75 N<br>020/90 | J07969 14798 | Porphyritic rhyolite sample adjacent to contact. Generally smaller crystal size than 11.5 | TCD P.19141 |
| 163m | SG-FM-13 (LD) | 015/85 SE | | Longford-Down metasediment sample adjacent to contact, hornfelsed | TCD P.19142 |
| ~163m | SG-FM-14 (LD) | 005/40 E<br>010/75 NW | J07960 14799 | Longford Down metasediment sample 110cm from contact, hornfelsed | TCD P.19143 |
| 220m | SG-FM-14.5 (LD) | | | Longford Down, sheared with fragmental tuffisite and cataclasite | TCD P.19144 |
| 221 – 225m | SG-FM-15 (LD) | 150/60 NE | | Longford Down metasediment small pieces of sample near to the contact | TCD P.19145 |
| 223m | SG-FM-15.4 (CZ) | | | Crush zone rock with Longford-Down and igneous fragmentsin a fine-grained cataclastic matrix | TCD P.19146 |
| 221-225m | SG-FM-16 (CT) | 160/65 SW | J07953 14854 | Contact of Longford-Down and microgranite, both sheared | TCD P.19147 |
| 221-225m | SG-FM-17 (G) | 060/30 NW<br>080/80 NW | J07967 14863 | Porphyritic microgranite sample near to contact with abundant tuffisite veins | TCD P.19148 |
| 227m | SG-FM-17.2 (G) | | J07966 14844 | Porphyritic microgranite with broken up crystals and tuffisite veins from near contact | TCD P.19149 |
| ~250m | SG-FM-17.5 (G) | | | Porphyritic microgranite (regular) | TCD P.19150 |
| ~260m | SG-FM-17.7 (G) | | | Porphyritic microgranite (regular and small tuffisite veins) | TCD P.19151 |
| 274m | SG-FM-18 (G) | 100/30 NE | J07957 14899 | Porphyritic microgranite (coarse) | TCD P.19152 |
| 275m | SG-FM-19 (G) | | | Microgranite with basaltic dyke contact | TCD P.19153 |
| 276m | SG-FM-20 (D) | | J07967 14895 | Pure basalt from dyke | TCD P.19154 |

(G)= porphyritic microgranite
(LD)= Longford-Down metasediment
(CT)= contact sample
(PR)= porphyritic rhyolite
(D) = dyke, basaltic
(CZ) = Crush zone